Hybrid Multimeric Architectures for Enhanced Receptor Targeting and Intracellular Delivery of Bioactive Cargoes

TECHNISCHE
UNIVERSITÄT
DARMSTADT

Vom Fachbereich Chemie
der Technischen Universität Darmstadt

zur Erlangung des Grades
Doctor rerum naturalium
(Dr. rer. nat.)

Dissertation

von Simon Peter Englert, M. Sc.
aus Erlenbach am Main

Erstgutachter:	Prof. Dr. Harald Kolmar
Zweitgutachter:	Prof. Dr. Katja Schmitz

Darmstadt 2023

Englert, Simon Peter: Hybrid Multimeric Architectures for Enhanced Receptor Targeting and Intracellular Delivery of Bioactive Cargoes.

Darmstadt, Technische Universität Darmstadt

Jahr der Veröffentlichung der Dissertation of TUprints: 2023

URN: urn:nbn:de:tuda-tuprints-244930

URL: https://tuprints.ulb.tu-darmstadt.de/id/eprint/24493

Tag der Einreichung: 14. Februar 2023

Tag der mündlichen Prüfung: 29. März 2023

Der experimentelle Teil der vorliegenden Arbeit wurde unter der Leitung von Herr Prof. Dr. Harald Kolmar am Clemens-Schöpf-Institut für Organische Chemie und Biochemie der Technischen Universität Darmstadt von Dezember 2016 bis September 2021 angefertigt.

Publications derived from this work:

B. Becker*, **S. Englert***, H. Schneider, D. Yanakieva, S. Hofmann, C. Dombrowsky, A. Macarrón Palacios,S. Bitsch, A. Elter, T. Meckel, B. Kugler, A. Schirmacher, O. Avrutina, U. Diederichsen, H. Kolmar, Multivalent dextran hybrids for efficient cytosolic delivery of biomolecular cargoes, *Journal of Peptide Science,* **2021**, 27, e3298.

H. Schneider*, **S. Englert***, A. Macarrón Palacios, J. A. Lerma-Romero, A. Ali, O. Avrutina, H. Kolmar, Synthetic Integrin-Targeting Dextran-Fc Hybrids Efficiently Inhibit Tumor Proliferation *In Vitro*, *Frontiers in Chemistry*, **2021**, 9, 693097.

* These authors contributed equally to this work.

Further publications during doctoral thesis:

A. Ali, D. Happel, J. Habermann, K. Schoenfeld, A. Macarrón Palacios, S. Bitsch, **S. Englert**, H. Schneider O. Avrutina, S. Fabritz, H. Kolmar, Sactipeptide Engineering by probing the Substrate Tolerance of a Thioether bond forming Sactisynthase, *Angewandte Chemie International Edition*, **2022**, 61, e202210883.

H. Schneider, D. Yanakieva, A. Macarrón, L. Deweid, B. Becker, **S. Englert**, O. Avrutina, H. Kolmar, TRAIL-Inspired Multivalent Dextran Conjugates Efficiently Induce Apoptosis upon DR5 Receptor Clustering, *ChemBioChem*, **2019**, 20, 3006-3012.

H. Schneider, L. Deweid, T. Pirzer, D. Yanakieva, **S. Englert**, B. Becker, O. Avrutina, H. Kolmar, Dextramabs: A Novel Format of Antibody-Drug Conjugates Featuring a Multivalent Polysaccharide Scaffold, ChemistryOpen **2019**, 8, 354-357.

L. Deweid, L. Neureiter, **S. Englert**, H. Schneider, J. Deweid, D. Yanakieva, J. Sturm, S. Bitsch, A. Christmann, O. Avrutina, H.-L. Fuchsbauer, H. Kolmar, Directed Evolution of a Bond-Forming Enzyme: Ultrahigh-Throughput Screening of Microbial Transglutaminase Using Yeast Surface Display, *Chemistry – A European Journal*, **2018**, 24, 15195-15200.

Contributions to conferences:

S. Englert, B. Becker, H. Schneider, S. Knauer, G. Baumann, T. Pirzer, O. Avrutina, H. Kolmar, Cube-octameric silsesquioxanes for intracellular delivery of therapeutic cargoes, *GDCh-Wisschenschaftsforum Chemie 2017 – Jubiläumskongress "GDCh – 150 Jahre"*, (10. – 14.09.2017).

Table of Contents

1 Abstract

1.1 Zusammenfassung

In den letzten Jahrzehnten hat sich das Spektrum der verfügbaren Therapeutika durch das ständig wachsende Feld der Biopharmazeutika erweitert. Im Vergleich zu ihren niedermolekularen Konkurrenten zeichnen sich Biotherapeutika wie Peptide, Proteine und Nukleinsäuren aufgrund ihrer molekularen strukturellen und funktionellen Diversität durch vorteilhafte Eigenschaften wie hohe Spezifität und Potenz aus. Allerdings ist die Anwendung von Biotherapeutika meist auf die extrazelluläre Umgebung beschränkt, da sie die Zellmembran nicht durchdringen können. Um diese Hürde zu überwinden und das Spektrum möglicher Angriffspunkte für Biotherapeutika auf das Zellinnere zu erweitern, wurden zahlreiche Stragien wie zellpenetrierende Peptide (*cell-penetrating peptides*, CPPs) entwickelt. Während eine erfolgreiche intrazelluläre Verabreichung durch einfache Konjugation dieser kationischen Peptide mit Frachtmolekülen möglich ist, können aufwändigere und ausgefeiltere Architekturen entwickelt werden, um die Transduktionseffizienz weiter zu verbessern. Die Darstellung von multimeren CPPs auf Gerüstmolekülen ist einer der vielversprechenden Ansätze, um dieses Ziel zu erreichen. Analog dazu könnten auch Peptide, die auf Rezeptoren ausgerichtet sind, von der Multimerisierung auf einer geeigneten Plattform profitieren.

Die vorliegende Dissertation fasst die Ergebnisse einer umfassenden Studie zusammen, die auf die Entwicklung hybrider multimerer Architekturen für die intrazelluläre Lieferung von Biomakromolekülen und die Verbesserung der Leistung von Peptiden mit Rezeptortargetierung abzielt.

Der erste Teil der Arbeit befasste sich mit der Evaluierung verschiedener CPPs, nicht-peptidischer alternativer Strukturen sowie das CPP L17E, welches auf dem Polysaccharid Dextran multimerisiert wurde, hinsichtlich ihrer Fähigkeiten, die zelluläre Aufnahme von bioaktiver 18mer Peptid-Nukleinsäure (*peptide nucleic acid*, PNA) als Frachtmolekül zu ermöglichen. Dabei wurde der eGFP654-Fehlsplicing-Korrekturtest als funktioneller Test verwendet, der einen quantitativen Vergleich der Translokationsmodule ermöglichte. Aufgrund der bemerkenswerten Leistung von Dextran-L17E Hybriden im PNA-basierten Test sollte die Architektur in einem zusätzlichen funktionellen Test einer weiteren Validierung unterzogen werden, welche auf der zytosolischen Translokation eines 16mer Peptids basiert. Der Dextran-L17E Ansatz war in der Lage, die zelluläre Aufhnahme des bioaktiven Peptids zu ermöglichen, welche die Wiederherstellung der Fluoreszenz eines nicht-funktionellen grün-fluoreszierenden Proteins (*green fluorescent protein*, GFP) durch Komplementierung zur Folge hatte.

Desweiteren wurden Dextran-CPP Hybride hinsichtlich ihrer Fähigkeiten zur intrazellulären Lieferung von Biomakromolekülen evaluiert. In einer *proof-of-concept* Studie wurden CPP-Dextran-Chimären mit Biotin modifiziert und als Transfermodule von fluoreszenzmarkiertem Streptavidin (Sav) als Modellprotein eingesetzt. L17E-funktionalisiertes Dextran war in der Lage, die intrazellulären Lieferung des Ankerproteins Sav sowie biotin-markiertem GFP als zusätzliche Fracht zu vermitteln. Allerdings ging die eindrucksvolle Leistung der effizienten intrazellulären Proteinlieferung mit einem zumindest für therapeutische Anwendungen nicht tolerierbaren Maß an Toxizität einher.

Der erste Teil der Arbeit bestätigte die Fähigkeit von L17E-Dextran Hybriden als vielseitig einsetzbare Plattform für die intrazelluläre Lieferung relevanter Biomakromoleküle. Neben PNA und Peptiden ermöglichten diese Architekturen auch die zelluläre Aufnahme von Proteinen als Frachtmoleküle, auch wenn dies mit signifikanter Zytotoxizität einherging. Daher könnten zukünftige Untersuchungen entweder die Optimierung von L17E-Dextran Hybriden angehen beziehungsweise das Peptid durch neue, hocheffiziente CPPs ersetzen.

Der zweite Teil der vorliegenden Arbeit untersuchte den Dextran-Sav-Hybridansatz als neue Plattform für die Multimerisierung rezeptorbindender Peptide. Dextran, welches mit mehreren Kopien des *death receptor 5 targeting peptide (*DR5TP) ausgerüstet war, war in der Lage, Apoptose in krebsrelevanten Zellen im Bereich niedriger nanomolarer Konzentration auszulösen. Die Potenz des mit DR5TP-dekorierten Dextrans konnte noch einmal deutlich erhöht werden, indem es auf dem Ankerprotein Sav multimerisiert wurde.

Für weitere Evaluierung des Dextran-Sav-Hybridansatzes als Multimerisierungsplattform für rezeptorbindende Peptide wurden Integrin-bindende zyklische Peptide ausgewählt, welche das RGD Motiv enthalten. Dextran, ausgestattet mit mehreren Kopien des zyklischen RGD Peptids, war zwar in der Lage, den isolierten Rezeptor zu binden, allerdings übertrug sich dieses Ergebnis nicht auf einen zellbasierten Test mit fluoreszenzmarkiertem Sav als Ankerprotein. Mit Hilfe eines Antikörperfragments (Fc) als Dimerisierungsplattform von RGD-modifiziertem Dextran konnten Integrin-überexprimierende Krebszellen effizient addressiert werden und zudem war das Gebilde in der Lage, ein Zytotoxin in die Zielzellen zu liefern.

Der zweite Teil der Arbeit präsentierte den Dextran-Sav-Hybridansatz als vielversprechende Plattform für rezeptorbindende Peptide, wobei das Spektrum von erfolgreich-addressierbaren Rezeptoren in weiteren Studien untersucht werden sollte. Als Alternative verbleiben Fc-Dextran Hybride als hocheffizientes Gerüst für die Multimerisierung rezeptorbindender Peptide.

1.2 Abstract

In recent decades, the spectrum of available therapeutics has been expanded by the ever-growing field of biopharmaceuticals such as peptides, proteins, and nucleic acids, which are characterized by advantageous properties including high specificity and potency as a consequence of their molecular structural and functional diversity. However, the application of biotherapeutics is mostly limited to the extracellular environment due to their intrinsic disability to traverse the cellular membrane. In order to overcome this obstacle and expand the range of potential targets for biotherapeutics into the cell´s interior, numerous strategies such as cell-penetrating peptides (CPPs) have been developed. While these cationic peptides facilitate cellular uptake by simple conjugation to the cargo molecule, more sophisticated architectures can be designed to further improve the transduction efficiency. Multimeric presentation of CPPs on scaffold molecules is one of the promising approaches to reach this goal. Analogously, receptor-targeting peptides could also benefit from multimerization on a suited platform.

The presented doctoral thesis summarizes results of a comprehensive study aimed at the development of hybrid multimeric architectures for intracellular delivery of bioactive cargoes and enhancing the performance of receptor-targeting peptides.

The first part of the work addressed the evaluation of various monomeric CPPs, non-peptidic architectures and the CPP L17E, multimerized on the polysaccharide dextran, in their ability to facilitate cellular uptake of bioactive 18mer peptide nucleic acid (PNA) as payload. Thereby, the eGFP654 mis-splicing correction assay was performed as functional assay that allowed for comparison of the delivery modules in a quantitative fashion. Due to the remarkable performance of dextran-L17E hybrids in the mis-splicing assay, the architecture was subjected to further validation in a second functional assay based on the cytosolic delivery of a 16mer peptide. The dextran-L17E approach was able to facilitate cellular uptake of the bioactive peptide, which induced restoration of fluorescence upon complementation to non-functional green fluorescent protein (GFP).

Additionally, dextran-CPP chimeras were assessed in their capabilities to mediate intracellular transport of large payload. In a proof-of-concept study, dextran-CPP hybrids were equipped with biotin and employed as delivery modules for fluorescently labeled streptavidin (Sav) as model cargo. L17E-functionalized dextran was able to facilitate intracellular delivery of the core protein Sav and, furthermore, a biotinylated GFP as additional cargo. However, the impressive performance of efficient protein delivery was accompanied by intolerable cytotoxicity, at least for therapeutic applications.

The first part of this work confirmed the capability of L17E-dextran hybrids as versatile platform for intracellular delivery of relevant payload. Beside PNA and peptides, these architectures could facilitate the cellular uptake of cargo proteins, albeit with significant cytotoxicity. Thus, future investigations could optimize the architecture of dextran-L17E hybrids or replace the peptide by novel, high-performing CPPs.

The second part of this work assessed dextran-Sav hybrids as novel architectures for multimerization of receptor-binding peptides. Dextran equipped with multiple copies of death receptor 5 targeting peptide (DR5TP) was able to efficiently induce apoptosis in a cancer-relevant cell line at low nanomolar concentrations. The apoptotic potency of DR5TP-decorated dextran was distinctly increased upon further multimerization on Sav as centerpiece.

For further evaluation of dextran-Sav architectures as multimerization platform for receptor-targeting peptides, integrin binding cyclic peptides harboring the RGD motif were chosen. While dextran bearing multiple copies of cyclic RGD peptides was able to bind to the isolated target integrin, these results did not translate into a cell-based assay using fluorescently labeled Sav as core protein. Using an antibody fragment (Fc) as dimerization platform for RGD-modified dextran, integrin overexpressing cancer cells could be efficiently targeted and, furthermore, the architecture was suited to deliver a cytotoxic agent into the target cells.

The second part of this work presented dextran-Sav hybrids as promising platform for multimeric receptor-targeting peptides, whereby the scope of successfully-addressable receptors should be the subject of further research. As an alternative, Fc-dextran hybrids remain a highly efficient framework for multimerization of receptor-targeting peptides.

2 Introduction

Since the beginning of the scientific revolution and the consequent accumulation of knowledge in form of technologies, methods, and concepts in this ever faster growing field of drug research, some ideas have remained relevant and inspiring even after decades or centuries. Amongst those, targeted therapy, first outlined by Paul Ehrlich in the 1900s as the "magic bullet" concept is a desirable yet unreached goal in pharmaceutical science.[1] It is based on the idea of neutralizing pathogens while remaining non-toxic to healthy tissues. While this concept was formulated for the therapy of infections, it can be extended to other diseases like cancer as well. Classical chemotherapy is employing small molecule cytotoxins to target abnormally proliferating cancer cells. Although this approach is efficient and, therefore, remains the mainstay of anticancer therapy to date, it is also accompanied by side effects due to damaging healthy tissues.[2] While efficient and specific small molecule drugs like kinase inhibitors[3] and proteolysis targeting chimeras (PROTACs)[4] have been introduced during the last decades displaying less off-target toxicity, the focus shifted more towards the development of biotherapeutics. Compared to their "classical" counterparts, biomacromolecules in form of peptides and proteins are structurally more complex and can interact efficiently with binding partners in processes like molecular recognition.[5a, 5b] However, their application range is mostly limited to the extracellular environment due to an inherent inability to cross the cellular membrane and, therefore, a plethora of biotherapeutic architectures has been developed which target extracellular structures, e. g. receptors, to gain a therapeutic effect. Amongst receptor-targeting biologicals, monoclonal antibodies in particular gained interest as novel therapeutics.[6] In addition to these complex and large structures, receptor-binding peptides have also been employed.[7] The specificity of both architectures can be combined with the potency of small molecule toxins to generate chimeras like antibody-drug conjugates (ADCs)[8] and peptide-drug conjugates (PDCs)[7]. Without the ability to enter cells, the vast majority of targets for biopharmaceuticals is not addressable, limiting their therapeutic potential drastically. Unsurprisingly, a lot of effort has been directed into strategies to overcome this issue. Cell-penetrating peptides (CPPs), for instance, can efficiently enter cells and facilitate the cytoplasmic delivery of attached payload.[9]

Although CPP-mediated delivery is possible by linking the vehicle to the payload, more complex and sophisticated architectures can be designed to increase the transduction efficiency. This could be realized by multimeric presentation of CPPs on a suitable platform. Not only CPPs, but also receptor-binding peptides could benefit from multimerization on scaffold molecules. Hence, this work mainly addresses the combination of the polysaccharide dextran and the tetrameric protein streptavidin (Sav) for efficient display of bioactive peptides in a multimeric fashion. The following section provides an overview of the relevant modules employed in this work: The first part addresses different multimerization strategies for peptides with an emphasis on dextran and Sav, the second part presents the bioactive modules employed in this thesis.

2.1 Multimerization Strategies for Peptides

Multimerization of bioactive compounds is a frequently used strategy to enhance their intended effects. Inspired by nature, which often relies on this strategy to strengthen non-covalent interactions, e. g. multivalent interactions between ligands and receptors,[10] different strategies for multimeric presentation of bioactive compounds like peptides have been developed. Receptor targeting peptides can benefit from multimerization by increasing their efficacy by simultaneous binding of multiple receptors, which requires sufficient distance between the binding moieties in order to reach adjacent receptors.[11] However, even if this condition is not met, the high local concentration of the multimerized peptides can also increase the chance of rebinding a single receptor thus reducing the off-rate.[11] Furthermore, the multimeric display of CPPs can also result in enhanced properties compared to their solitary counterparts.[12] These multimerization strategies differ in various points, like the quantity of employed peptides, the presence of conjugation sites for payload, the origin of the scaffold and its flexibility as well as the spatial orientation of the presented peptides. Since these criteria make it difficult to provide a comprehensive overview, only some representative examples are given below.

It is important to note that the use of a scaffold is not mandatory for the multimerization of peptides; e. g. dimerization of peptides can be achieved by introduction of a disulfide bond. This strategy was successfully employed to enhance the efficacy of CPPs[13a, 13b] and a receptor-targeting peptide.[14] Alternatively, the multimerization of a CPP in a linear fashion with up to 6 CPP repeats interrupted by linker sequences yielded an efficient delivery system for a genetically fused cargo protein.[15]

Low-valence presentation of peptides can be realized using small molecule scaffolds like adamantane and tris(hydroxymethyl)aminomethane (Tris). The latter scaffold allows for trimeric display of peptides at the hydroxyl groups and an additional orthogonal conjugation site for the payload at the amine functionality (**Figure 1**, **A**).[16] The rigid adamantane scaffold can be chemically modified to bear up to 4 conjugation sites for peptides[17] or - analogous to Tris - an additional orthogonally addressable moiety (**Figure 1**, **B**).[18] Beside small molecules, peptide-based scaffolds have also been employed due to their diversity in terms of structure and applicability to amino acids. Multimerization can be achieved on linear scaffold peptides by addressing suitable side chains, while the *N*-terminus serves for further functionalization (**Figure 1**, **C**).[12] As an alternative, peptide scaffolds like regioselectively addressable functionalized templates (RAFT) are structurally confined and provide a framework for the topological arrangement of functional peptides.[19] Thereby, head-to-tail cyclization of the decapeptide K-A-K-P-G-K-A-K-P-G resulted in a cyclic β-sheet. In order to enhance the degree of functionalization, the lysine and alanine residues, respectively, can be exchanged with orthogonally addressable amino acids (**Figure 1**, **D**).

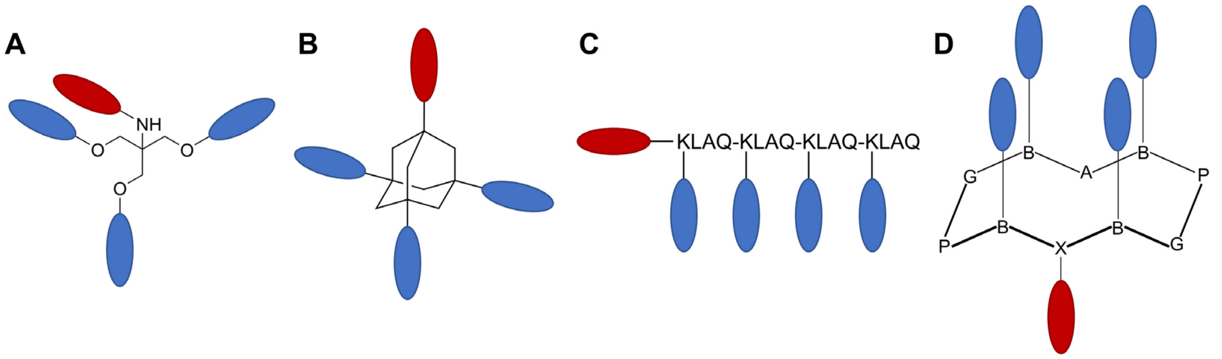

Figure 1| Small molecule and peptide based multimerization platforms for peptides (blue) and additional payload (red). **A**: Tris based scaffold with peptides on the hydroxyl groups and the payload at the amine functionality. **B**: Adamantane based scaffold containing three peptides and a payload. **C**: Linear peptide scaffold with repetitive sequence containing lysine residues for peptide conjugation and additional *N*-terminal payload. **D**: RAFT scaffold with two orthogonal amino acids B and X for peptide and payload conjugation, respectively. Please note that this is only one possible layout to achieve a peptide multimerization scaffold with an additional conjugation site for cargo; the alanine for instance can be replaced with X or a third orthogonal amino acid.

Higher valence can be achieved by using macromolecules like linear polymers or dendritic structures that exhibit opposing properties. Linear polymers (**Figure 2**, **A**), either of chemical or natural origin, possess a flexible backbone and do not display their payload in a defined fashion.[20] Synthetic polymers based on a polyacrylamide backbone like poly(*N*-(2-hydroxypropyl)methacrylamide) (HPMA)[21a, 21b] are water soluble and biocompatible. Furthermore, the properties of HPMA can be adjusted by copolymerization,[22] which also allows for the introduction of different peptidic payloads during the polymerization process using a mixture of peptide labeled monomers.[23] Alternatively, carbohydrates like deacetylated amine-bearing chitosan[24] or the neutral polysaccharide dextran, which will be presented in the following section, can be used. Contrary to their linear counterparts, dendritic structures are well-defined and present a high number of addressable sites in a compact, globular fashion.[20] These architectures are based on a core molecule, which is functionalized using a monomer containing one reactive and two inactive sites. Iterative steps of dormant site activation and subsequent conjugation of monomers result in the growth of the branched molecule.[25] Dendritic structures based on lysine[12, 26] and polyamidoamine (PAMAM)[27] have been used for multimeric presentation of bioactive peptides, whereby the end groups were functionalized with the peptides and the core molecules were equipped with an additional orthogonal attachment site for a second payload (**Figure 2**, **B**).

The valence can even be further increased by subjecting the intrinsic polymeric architectures to multimerization. This strategy was employed by multimerization of peptide-presenting dendrons on the surface of liposomes.[28] Alternatively, proteins can be used as centerpiece for further multimerization, which was realized by dimerization of dextran on a Fc scaffold and subsequent conjugation of peptidic payload to the polysaccharide (**Figure 2**, **C**).[29] Tetramerization of amine-bearing dendrons was achieved by biotinylation of these architectures and subsequent assembly on tetrameric streptavidin (Sav) (**Figure 2**, **D**);[30] this scaffold which will be detailed in section **2.1.2**.

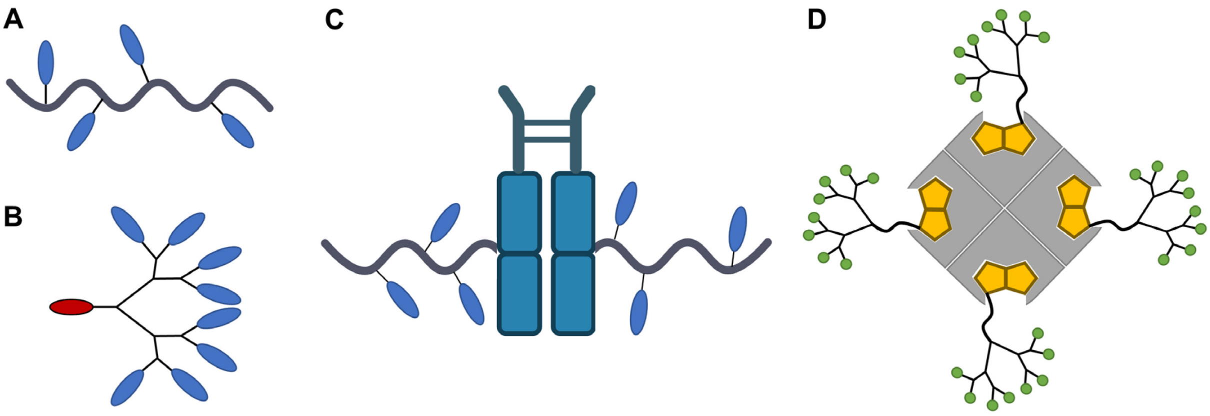

Figure 2| **A**: Linear polymer (grey) decorated with peptide payload (blue). **B**: Dendron with peptides (blue) on the end groups and additional payload (red) at the core molecule. **C**: Fc (blue centerpiece) equipped with two dextran polymers (grey) decorated with peptides (blue). **D**: Biotin (yellow) bearing dendrons with amine decorated end groups (green), tetramerized on streptavidin (grey centerpiece). Created with BioRender.com.

2.1.1 Dextran

Produced by bacteria, dextrans are neutral polysaccharides comprising an *α*-(1,6)-linked D-glucose backbone with various degree of branching in form of α-(1,2), α-(1,3) and α-(1,4) linkages. Natural synthesis of dextran is performed extracellularly by dextransucrases primarily from *Leuconostoc* and *Streptococcus* species,[31] on which the nature and degree of branching depends[32]. Dextransucrase, in this particular case from *Leuconostoc mesenteroides* (*L.m.*) NRRL B512F, catalyzes the transfer of D-glucopyranosyl residues from sucrose to dextran by forming an α-(1,6)-glycosidic bond under release of fructose, which results in a stepwise assembly of the biopolymer.[31, 33] This enzymatic process yields dextran with only 5% α-(1,3) branching[34] of which 85% comprise one or two glucose residues,[35] whereas the remaining 15% may have an average of 33 glucose units (**Figure 3**, **A**)[36]. Since a low degree of branching is accompanied with higher water solubility, dextran from *L. m.* B512F strain is of particular commercial interest.[31, 37] Produced mostly by whole cell fermentation in sucrose-rich medium, the dextran obtained has a molecular weight of up to 500 MDa and a high degree of polydispersity.[31] Commercially available dextran with lower molecular weights (M_w = 4-200 kDa) and polydispersity (~1.5) can be produced by partial hydrolysis and subsequent fractionation.[37, 38]

In addition to its good solubility, dextran combines favorable properties like stability under mild acidic and basic conditions, biocompatibility, biodegradability and low antigenicity.[31, 39] Aqueous solutions of dextran have been used for over half a century in the clinic as blood flow enhancer (M_w = 40 kDa) and plasma volume expander (M_w = 70 kDa).[36] Additionally to the aforementioned beneficial properties, dextran polymers possess high biological stability in the blood stream but are metabolized by dextranase in liver, spleen, kidney, and gastrointestinal tract.[31]

During the last decades, dextran has also come into the research focus as a carrier platform for various bioactive cargoes. In the most straightforward way, payload was attached by covalent conjugation to the polysaccharide (**Figure 3**, **B**). Using this strategy, doxorubicin-decorated dextran displayed reduced cytotoxicity and improved pharmacokinetics compared to the solitary cytotoxin in a phase I clinical trial.[40] Proteins can also benefit from conjugation to dextran. After conjugation of 4.4 dextran molecules to superoxide dismutase (SOD) the hybrid retained the majority of its initial enzyme activity and displayed significantly improved stability in blood plasma.[41] Recently, dextran was employed as multimerization site for the hydrophobic cytotoxin monomethylauristatin E (MMAE) in the generation of hydrophilic antibody-drug conjugates (ADCs).[42] Dextran is also used as building block for more complex, three dimensional architectures for delivery. Cross-linking of the dextran backbone results in the formation of hydrogels, which were utilized as framework for the site-specific release of several non-steroidal anti-inflammatory drugs (NSAIDs).[43] The drug-loaded hydrogels (**Figure 3**, **B**) were designed for the specific release of their payload, covalently attached to dextran *via* an ester linker, in the colon after oral administration. Indeed, the hydrogels did not release their cargo under conditions simulating the acidic environment of the stomach, whereas an increase in pH and the presence of dextranase and esterase liberated the conjugated drugs. Alternatively, dextran polymers are also employed as building blocks for the generation of micelles. In a study, a copolymer of dextran and poly-(DL-lactide-co-glycolide) (PLGA) was synthesized, which assembled to core-shell micelles (**Figure 3**, **C**) under aqueous conditions with the dextran component forming the outer shell.[44] Doxorubicin was incorporated in the core structure comprised of the PLGA portion of the copolymer. These cytotoxin-loaded micelles exhibited superior uptake and cytotoxicity to doxorubicin-resistant tumor cells compared to the free drug.

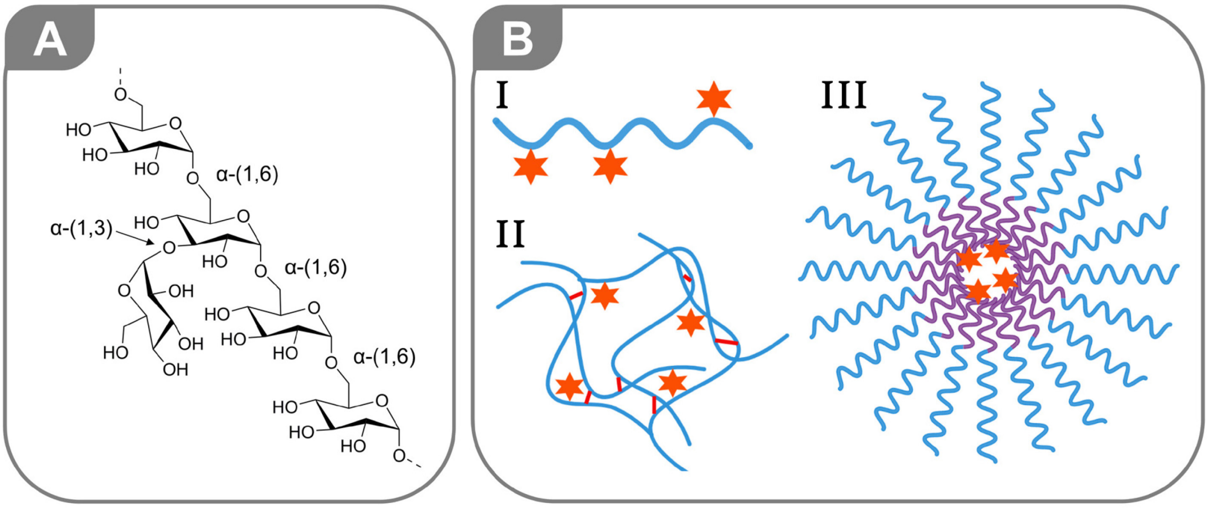

Figure 3| **A**: Structure of dextran produced from *Leuconostoc mesenteroides* NRRL B-512F strain. **B**: Schematic depictions of payload (orange star) attached to solitary dextran (**I**, blue line), dextran hydrogel (**II**) with crosslinking (red line) and micelle (**III**) comprising dextran-PLGA (violet line) micelles with incorporated payload. Created with BioRender.com.

In order to be used as a scaffold for a carrier platform, dextran must be modified chemically. The vast number of hydroxyl groups are an obvious choice for covalent conjugation. In a straightforward fashion, payload bearing carboxyl groups can be attached directly to dextran by ester bond formation.[45] For most cargo molecules an introduction of a suited chemical moiety into dextran is a prerequisite for the subsequent conjugation of a payload. This can be achieved by several strategies, like activation of the hydroxyl groups with 1,1´-carbonyldiimidazole (CDI) to form an imidazole carboxylic ester, which can further react with amines to a carbamate (**Scheme 1**, **A**). Using this approach, dextran was decorated with amine functionalities, which served as conjugation site for cytotoxic drugs.[46] Alternatively, carboxymethyl groups can be introduced by reaction of the hydroxyl groups with chloroacetic acid under basic conditions (**Scheme 1**, **B**).[47] Dextran was also decorated with azide-functionalities using 1-azido-2,3-epoxypropane, which allowed further orthogonal functionalization by copper(I)-catalyzed azide-alkyne cycloaddition (CuAAC) (**Scheme 1**, **C**).[48]

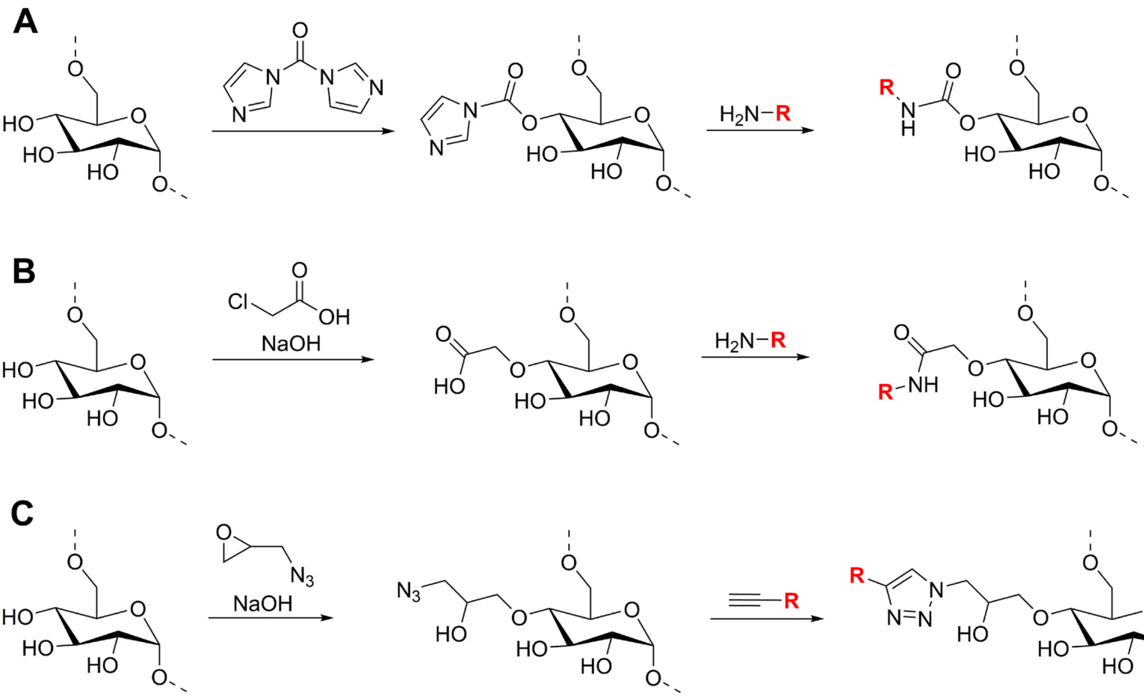

Scheme 1| Overview of strategies for chemical modification of dextran. **A:** CDI-mediated conjugation of amine bearing cargo by forming a carbamate. **B:** Carboxymethylation and subsequent amide bond formation. **C:** Introduction of azide-functionalities and CuAAC-mediated cargo conjugation. Please note that only for demonstration purposes the functionalization was displayed exclusively at position C-4.

These strategies share the drawback of unspecific conjugation to hydroxyl groups. Site-specific functionalization can be made by addressing the reducing end of the dextran polymer. Contrary to the remaining glucose units, the terminal glucose unit bears a cyclic hemiacetal at C-1 position, which is in equilibrium with its open aldehyde form (**Scheme 2**, **A**). The aldehyde can react with amines to an imine which is an equilibrium reaction. With the aim to yield a stable bond between the terminal glucose and its amine counterpart the generated imine can be reduced to an amine; a reaction called reductive amination (**Scheme 2**, **A**).[49] In addition to the reducing end modification, site-specific functionalization of dextran at the repeating units can be achieved by carboxyethylation.[50] In this method, the hydroxyl group reacts as nucleophile with acrylamide in an addition reaction under basic conditions. Subsequent increase in temperature leads to the hydrolysis of the amide and yields a carboxyl functionality, which can be further addressed upon amide bond formation (**Scheme 2**, **B**). Interestingly, structural analysis of the product revealed that functionalization took place exclusively at C-2 position.[51] Furthermore, the number of carboxyethyl groups can be adjusted in relation to the amount of acrylamide used. Both site-specific strategies can be combined to obtain a modified dextran bearing orthogonal groups at the reducing end and repeating units, respectively.[29, 42]

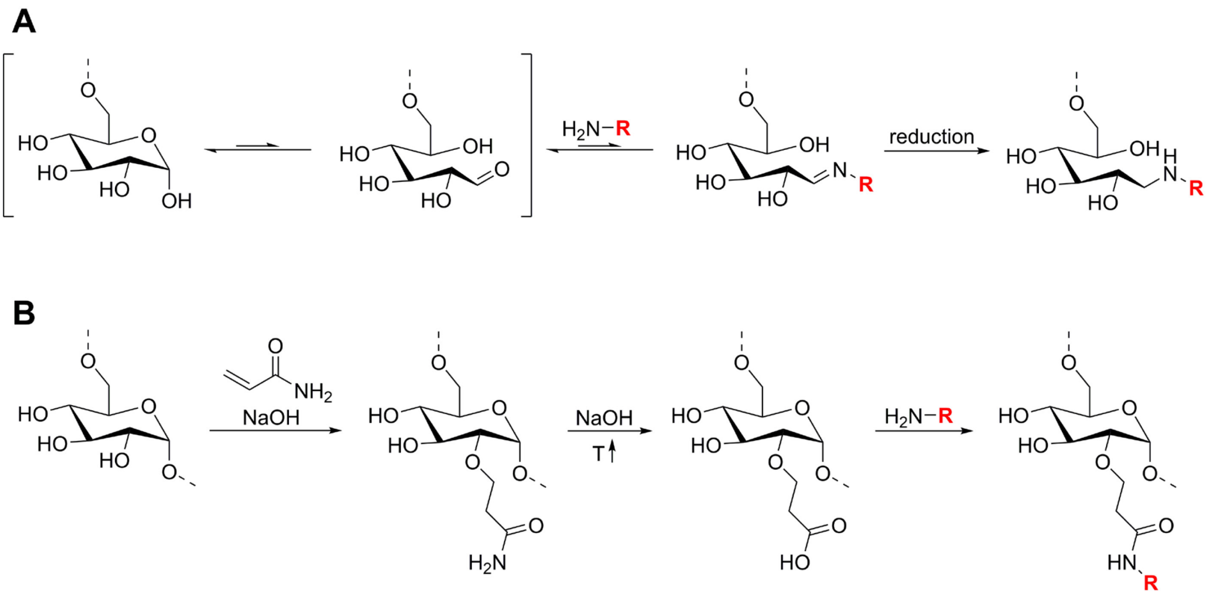

Scheme 2| A: Reductive amination of dextran at the reducing end. **B:** Carboxyethylation of dextran with subsequent amide bond formation.

2.1.2 Streptavidin

Streptavidin (Sav) is a ~60 kDa homotetrameric protein isolated from the bacterium *Streptomyces avidinii*.[52] It belongs to a group of proteins that bind up to four D-biotin molecules with very high affinity ($K_D \approx 10^{-13}$ -10^{-15} M). Other members of the group were isolated from different organisms, like avidin from chicken egg white[53] or bradavidin from the bacterium *Bradyrhizobium japonicum*[54]. Compared to the most prominent member avidin, Sav is not glycosylated and has a lower isoelectric point (pI = 5-6 versus pI = 10), which results in less non-specific interactions in biological systems.[55]

Full-length, mature Sav monomer consists of 159 amino acids and is produced in *Streptomyces avidinii* with an additional 24mer signal sequence, which blocks biotin binding.[56] Postsecretory cleavage of the terminal regions leads to a truncated variant termed natural core streptavidin (127 amino acids), whereas non- or incompletely truncated Sav tends to form non-soluble aggregates.[57] Furthermore, truncation of the terminal regions results in better accessibility of the biotin binding site.[57]

Structural crystallographic analysis revealed that each monomer comprises 8 antiparallel β-sheets with several extended hairpin loops which form a β-barrel structure. Two β-barrels form a dimer *via* hydrogen bonding at a 45° angle and, consequently, two dimers assemble to the tetrameric species, which is additionally stabilized by van der Waals interactions between the barrel surfaces (**Figure 4**, **A**).[58] Binding of biotin at the end of those β-barrels results in conformational changes, in which the initially disordered loop at the binding site becomes ordered and forms a lid over the bound biotin (**Figure 4**, **B**).[58, 59] Thereby, 8 hydrogen bonds are formed between the amino acids in the binding pocket and biotin, as well as hydrophobic and van der Waals interactions (**Figure 4**, **C**).[60a, 60b] Key amino acids for the latter interactions are four tryptophans, whereby one tryptophan is provided by a neighboring subunit.[58, 61]

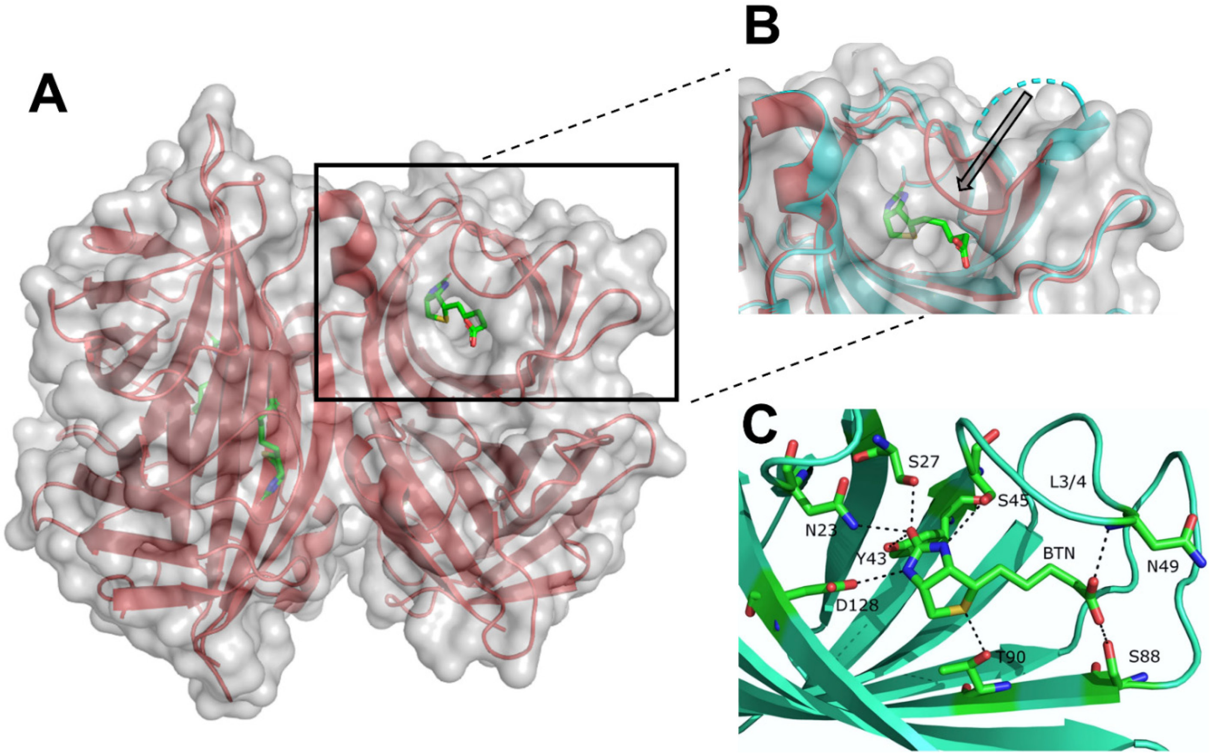

Figure 4| A: Structure of Sav tetramer (red) with bound biotin ligands (green) (PDB: 1SWE). **B:** Superimposed section of Sav binding pocket with (red, PDB: 1SWE[62]) or without (cyan, PDB: 1SWA[62]) ligand. Binding of biotin provokes a conformational change (arrow) of the initially disordered loop (dashed cyan). **C:** Hydrogen bonding between amino acids in the binding pocket and biotin ligand, modified from Liu *et al.*[60b] and distributed under the terms of the Creative Commons Attribution 4.0 International, license: CC BY 4.0.

As mentioned before, these interactions between Sav and its ligand result in a very high affinity. Nevertheless, despite the low dissociation rate constant ($k_{off} \approx 10^{-5}$ - 10^{-6} s)[63a, 63b] the interaction between Sav and biotin is not irreversible. Displacement analysis of ^{14}C-labeled biotin-Sav complexes with a large excess of unlabeled biotin (> 100 fold) revealed half-lives ranging from 3 hours[63b] to 2.9 days[55]. Thereby, factors like temperature and pH play an important role; higher temperature correlates with lower half-life, while the optimal pH for binding is around 5.[55]

Several strategies have been presented to alter the binding affinity between Sav and ligand. The exchange of two amino acids, S52G and R53D, in the loop region which forms the lid upon biotin binding results in a variant with less disorder.[63b] Structural analysis revealed that the loop region of this mutant, traptavidin, is already closed prior to biotin binding.[59] While this structural change reduces the association rate of biotin due to higher steric hindrance in the binding pocket, the dissociation rate is vastly reduced.[59, 63b] In a different approach, a disulfide bridge was incorporated by introduction of two cysteines, N49C and A86C, at opposite sides of the loop generating a reductively labile switch.[64] This variant had a decreased dissociation rate compared to wild-type Sav in its oxidized form, whereas reduction of the disulfide bond increased the dissociation rate by four orders of magnitude.[64]

For applications based on Sav, functionalization can be achieved either by covalent conjugation of biotin to the payload, direct conjugation or genetic fusion. Sav conjugates are widely used for biochemical methods, e. g. Sav-enzyme conjugates for detection of biotinylated antibodies in enzyme-linked immunosorbent assay (ELISA)[65] or western blot[66]. Furthermore, Sav conjugates are used in live-cell imaging for detection of cell surface proteins. Biotinylation of those proteins can be achieved unselectively by chemical modification of lysine side-chains[67] or selectively by employing enzymes like biotin ligase[68].

Sav was also used for intracellular delivery of various cargoes, among them biomacromolecules. In one example, Sav was decorated with a biotinylated aptamer targeting prostate-specific membrane antigen (PSMA) and biotinylated 27mer small interfering RNA (siRNA) in equimolar ratio. The conjugate displayed specificity both towards PSMA-positive cells and in inhibition of the target RNA.[69] In another publication, Sav was employed as centerpiece for the intracellular delivery of biotinylated p53 and cytochrome C, respectively.[30] Cellular uptake was achieved by using biotinylated second generation dendrons bearing terminal amine groups. The dendron-protein hybrid architectures were assembled by mixing the biotinylated compounds with Sav. Intracellular delivery of p53 and cytochrome C, respectively, was confirmed by induction of apoptosis in two different tumor cell lines.

Both examples highlight the potential of Sav as platform for multimerization of multiple compounds. Biotinylated payload of various size and origin can be employed and the assembly of the hybrids is easily performed by mixing. However, the application of Sav-based technologies in the clinical setting could be complicated by the emergence of immune response in human. In clinical trials a novel therapeutic approach called pretargeted radioimmunotherapy (PRIT) was employed for the treatment of refractory or relapsed non-Hodgkin´s lymphoma (NHL).[70] In this particular case, the method was based on a chemically conjugated Rituximab antibody-Sav chimera, which was infused in the first step to target the tumor site. Following this, a biotinylated clearing agent was administered to remove the protein chimera from circulation. Finally, biotin-DOTA as carrier for radioisotopes was infused for imaging and therapy, respectively. In comparison to conventional radioimmunotherapy, this three-step approach should reduce the circulation time of radioactivity in the body, resulting in less off-target damage. Indeed, using ^{90}Y as radioisotope, a tumor to whole body ratio of 32.5:1 was achieved and 6 out of 7 patients showed response to the therapy. Despite these promising results, in 6 out of 10 patients the treatment was accompanied by the emergence of anti-Sav antibodies 8 weeks after the beginning. The antibody titers, however, returned to baseline after 35 weeks. In a similar PRIT clinical study targeting adenocarcinoma the formation of anti-Sav antibodies was observed after just 4 weeks.[71]

2.2 Bioactive Modules to Address Cells

2.2.1 The Plasma Membrane: Composition and Endocytosis

The plasma membrane serves as barrier which fully covers the cellular surface and separates the cytoplasm from the extracellular environment. Amphiphilic glycerophospholipids and sphingolipids assemble in a lipid bilayer with the polar head groups facing towards the cytoplasm and extracellular space, respectively, whereas the variable hydrophobic acyl chains of the lipids form the hydrophobic core (**Figure 5**).[72] Sterols, in mammalian organisms cholesterol, account for up to 50 mol % of the total lipid content of the plasma membrane.[73] Cholesterol plays a pivotal role in altering properties like thickness and viscosity of the lipid bilayer.[74] In addition to lipids, the plasma membrane consists of up to 50% by weight of proteins that are either anchored to or associated with the membrane and further contribute to the complexity of the membrane (**Figure 5**).[75] They participate in various processes; e. g. serve as receptors in signal trafficking across the plasma membrane,[76] as anchoring junctions to other cells[77] and the extracellular matrix[78], respectively, as well as channels or transporters for impermeable molecules like metabolites and ions.[79] These proteins are frequently glycosylated; the carbohydrates influence the folding and stability of the proteins and participate in cellular functions such as signaling and cell-cell communication.[80] The molecular organization of the plasma membrane, with its broad spectrum of lipids, proteins, and carbohydrates, is highly complex and dynamic.

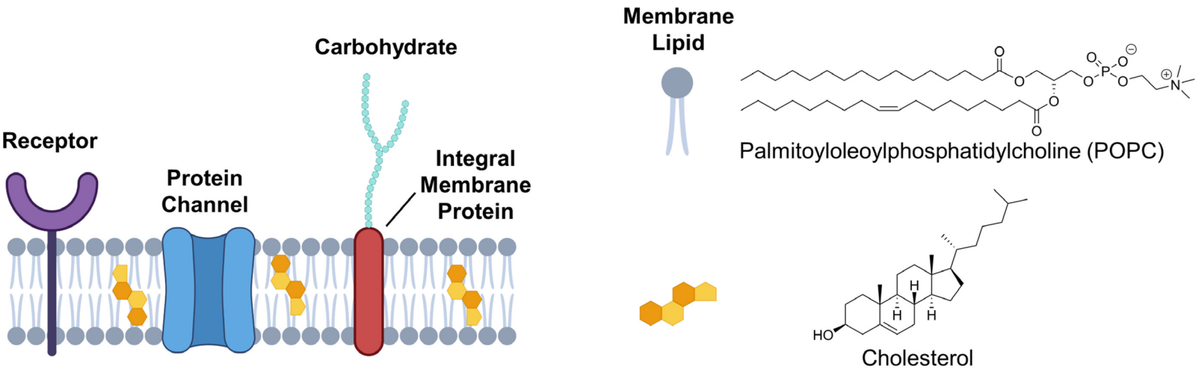

Figure 5 | Schematic depiction of the plasma membrane with different constituents and structures of cholesterol and POPC as example for glycerophospholipids. Created with BioRender.com.

Several models were proposed to describe the nature of membranes, among them the fluid mosaic model.[81] This approach describes the membrane as homogenous, two-dimensional fluid composed of the lipid bilayer and the associated proteins either floating on the surfaces or anchored within the membrane. Consequently, the compounds are subjected to permanent and free movement within the membrane in an unordered fashion, although the authors of this particular model pointed out, that the motion of those molecules could be restricted due to intrinsic or extrinsic interactions.[81, 82] A later proposal, the lipid raft model,[83] describes ordered, transient microdomains within the membrane with elevated levels of cholesterol and sphingolipids, that could be modulated and/or entered by structures like membrane-anchored proteins or the cytoskeleton.[84] These aggregations can assemble to larger domains upon certain triggers like crosslinking of those membrane-associated proteins and play an important role in cellular processes, amongst them endocytosis.[84]

Endocytosis is a cellular process involving the internalization of cargo by forming endocytic vesicles comprising extracellular molecules and membrane constituents. Several subtypes of endocytosis can take place simultaneously in mammalian cells. These can be differentiated according to the size of formed vesicles and involved proteins, respectively. Large amounts of extracellular fluid and plasma membrane can be internalized by an endocytic mechanism called micropinocytosis (**Figure 6**). This mechanism can be triggered by activation of growth factor receptors, which results in increasing rate of actin polymerization at the cell surface.[85] As a consequence, membrane ruffles, extended sheet-like structures of the membrane which are modulated by actin filaments beneath the surface,[86] can re-fuse with the membrane resulting in the enclosure of extracellular fluid in vesicles called macropinosomes.[85] In comparison to this mechanism which yields vesicles ranging from 0.2 to 10 µm in diameter,[86] micropinocytotic processes involving smaller vesicles require membrane bending. The curvature of the membrane can be mediated by coat proteins like clathrin or caveolin, after which their respective endocytic process is termed.[87]

Clathrin-mediated endocytosis is the major pathway for vesicular trafficking (**Figure 6**). The process is initiated by clustering of adaptor proteins at the inner leaflet of the plasma membrane, primarily induced by high local concentrations of cargo proteins like receptors. Following this, binding of clathrin to the nucleation site and subsequent polymerization of the coat protein to hexagons and pentagons leads to the membrane pit coated with a clathrin lattice. The actin cytoskeleton can further contribute to membrane bending and invagination. For the detachment of the clathrin coated vesicle from the membrane a scission step is required. The GTPase dynamin, amongst other proteins, forms an oligomer around the membrane neck and its constriction results in membrane fission. Vesicle uncoating releases the enveloping proteins for reuse.[88]

Caveolae, bulb shaped invaginations of the membrane (**Figure 6**), are comprised, amongst others, of the coat protein caveolin which binds directly to cholesterol.[89] These domains are similar to lipid rafts in terms of lateral motion in the plasma membrane.[89] While the complex interplay between caveolin and other proteins in this process is not fully elucidated to date,[89] caveolin-mediated endocytosis is also inducible by the presence of cargo molecules[90]. Phosphorylation of caveolin by tyrosine kinases plays an important role in caveolae internalization, whereby actin and dynamin are also key actors for membrane invagination and scission, respectively.[89]

While the exact process of cellular entry is different for the highlighted pathways, the emerging vesicles converge into early endosomes.[91] The fate of the ingested molecules is decided in these organelles. The majority of ligands is sorted into late endosomes and finally lysosomes, during which a decrease in pH and enzymatic degradation takes place.[91, 92] Receptors can also be recycled back to the plasma membrane or transported to the *trans*-Golgi network.[91] It is important to note that this "classic" endocytic trafficking is not mandatory for all endocytic vesicles; new research data indicates also direct trafficking to organelles of vesicles from clathrin-[93] and caveolin-mediated endocytosis[89], thus bypassing early endosomes.

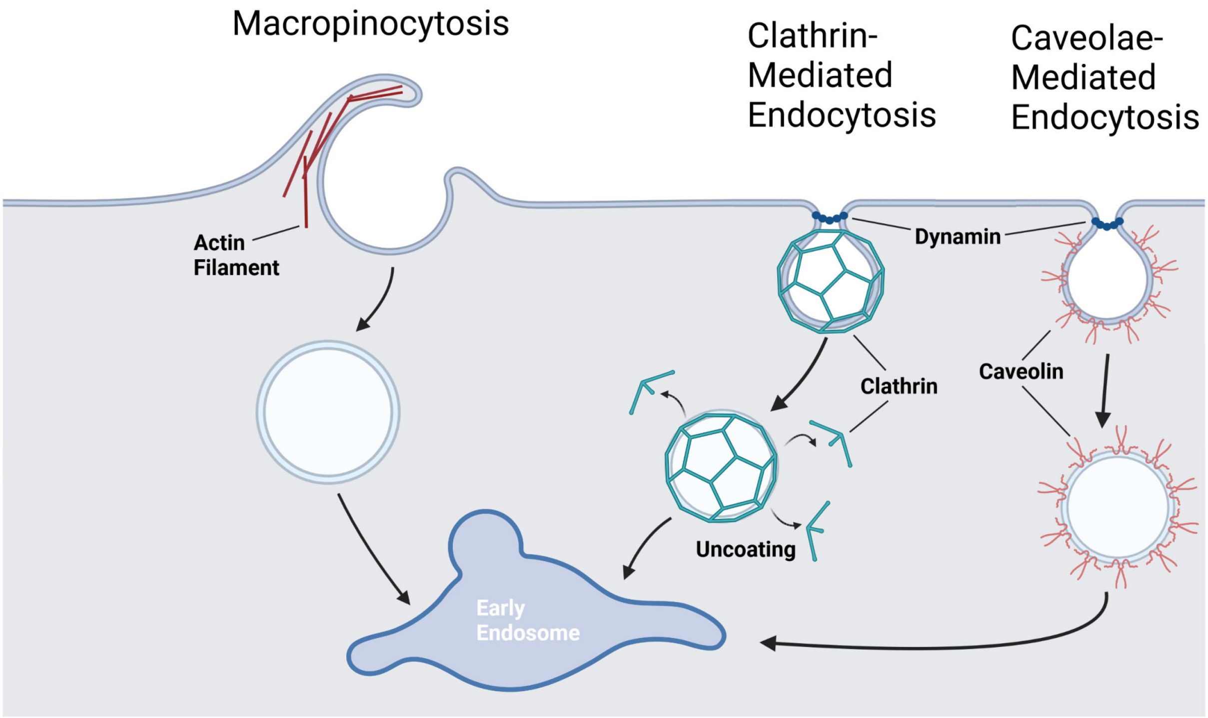

Figure 6| Subtypes of pinocytotic uptake and vesicular trafficking to early endosomes; created with BioRender.com and adapted from Mayor *et al*.[90].

2.2.2 Addressing Cells: To the Membrane and Beyond

2.2.2.1 Targeting Receptors

As mentioned before, cell membrane receptors serve as transmitters of extracellular signals into the intracellular space and, hence, are key actors in various physiological processes. While different classes, notably G protein-coupled receptors (GPCRs) and receptor tyrosine kinases (RTKs), differ in their exact function and architecture, respectively, they share basic structural features. They possess an extracellular domain (or extracellular loops in the case of GPCRs), to which specific ligands, ranging from small molecules to proteins, can bind. The receptors are anchored within the cell membrane by hydrophobic transmembrane domains; GPCRs comprise 7 transmembrane helices whereas RTKs contain a single transmembrane domain. Upon ligand binding, conformational changes in GPCRs and dimerization of RTKs, respectively, trigger an intracellular signaling cascade. This process encompasses dissociation of trimeric G-protein in GPCRs, which results in recruitment of further messenger modules. Activation of RTKs, on the other hand, leads to phosphorylation events catalyzed by their tyrosine kinase domains and subsequent signal transduction.[94a, 94b]

Dysregulation of certain receptors, e. g. overexpression, can often be observed in tumor tissue.[95] Consequently, different approaches for cancer treatment are based on the specific targeting of receptors to achieve tumor-specific therapy. Amongst those, therapeutic antibodies emerged in the last decades as promising tools.[6] Thereby, engineered immunoglobulins (Ig) can neutralize cancer cells by blocking the receptors and recruit effector cells.[96] Furthermore, antibodies can be employed in the aforementioned radioimmunotherapy for targeted delivery of radionuclides.[96] Immunoglobulins were also combined with cytotoxic agents to yield ADCs, aimed for specific release of their payload upon endocytosis.[8] While antibody-based therapeutics achieved impressive results, these complex architectures display shortcomings in their pharmacokinetic profile, i. e. low tumor penetration.[97] Thus, alternatives like receptor-binding peptides emerged in the last decades, which are much smaller in size compared to full-length antibodies.

Amongst those, receptor-binding peptides containing the motif arginine-glycine-aspartic acid (RGD) gained special interest as highly effective and versatile binders of integrins. These heterodimeric receptors are key regulators in processes like proliferation, apoptosis, migration and adhesion.[98a, 98b] Consequently, overexpression of these receptors in several subtypes of solid tumors like melanoma, glioblastoma, breast- and pancreatic cancer as well as tumor blood vessels were reported, making them attractive targets in antitumor therapy.[99] Both integrins and their specific binders will be discussed in detail in section **2.2.4.1**.

An alternative approach to antitumor therapy aims at induction of tumor cell apoptosis upon activation of specific receptors. The observation that certain proteins of the tumor necrosis factor (TNF) family exhibited efficient cell killing, gave rise to this therapeutic strategy.[100] One member of the group, TNF-related apoptosis inducing ligand (TRAIL), showed high antitumoral activity while sparing healthy cells. This protein binds several receptors on the cellular surface, of which the stimulation of two receptors, death receptor (DR) 4 and 5, results in induction of apoptosis. While clinical trials of recombinant human TRAIL, dulanermin, as monotherapy revealed insufficient activity due to a short half-life and possible resistance mechanisms, the inherent potential of this therapeutic approach provoked the development of novel TRAIL versions and TRAIL-inspired DR binders.[100] Amongst those, DR5 targeting peptide (DR5TP), identified by recombinant peptide screening, displayed high activity upon multimerization.[101] The mechanisms of apoptosis triggered by DR binding and DR5TP will be presented in greater detail in section **2.2.4.2**.

2.2.2.2 Intracellular Delivery Strategies

The challenge of intracellular transport of biomacromolecules across the plasma membrane gave rise to the development of various different strategies. These can be roughly divided into different categories, like biophysical methods (e. g. electroporation and microinjection), viral vectors and non-viral delivery strategies. For *in vivo* applications, non-viral delivery systems seem most promising since biophysical approaches are hardly applicable and viral vectors potentially bear the risk of gene insertion into the host genome.[9] Various non-viral delivery systems were developed in the last decades, with liposomes,[102] polymers,[103] CPPs and nanoparticles[104] being their prominent members. Furthermore, concepts like thiol-mediated uptake[105] gained more attention in the last years as mainstay approach and improvement of other systems, respectively. In general, these systems should meet certain prerequisites in order to be considered effective; e. g. low cytotoxicity and high delivery efficiency.

In the following section, CPPs will be discussed in greater detail as well as thiol-mediated uptake and an organic-inorganic hybrid mimicking CPPs.

2.2.3 Cell-Penetrating Peptides and Mimics

Cell-penetrating peptides are defined as short, water-soluble peptidic architectures rich in cationic and/or hydrophobic amino acids. Since the discovery of the cell-penetrating ability of the transactivator of transcription (TAT) protein in human immunodeficiency virus-1 (HIV-1) in the 1980s,[106] numerous peptides have been reported, either discovered in biological systems, of synthetic origin, or chimeras comprising motifs of different peptides.[107] The majority of CPPs can be categorized according to their physicochemical properties into amphipathic and non-amphipathic ones. Non-amphipathic CPPs comprise cationic peptides rich in basic amino acids, i.e., arginine and lysine, and the far less common hydrophobic CPPs.[108] Amphipathic CPPs comprise both cationic and hydrophobic amino acids and can be subdivided into primary and secondary amphipathic CPPs. Within the first subclass, cationic and hydrophobic amino acids are separated in the sequence and the peptides are typically rather long (more than 20 amino acids). Secondary amphipathic CPPs, on the other hand, are shorter and display a more even distribution of hydrophilic and hydrophobic residues.[107] These peptides exert their amphipathicity by contact with the phospholipid bilayer by forming α-helices and β-sheets, respectively, in which the cationic and hydrophobic residues are separated conformationally.[107, 108]

The exact internalization mechanisms of CPPs are not totally resolved to date despite extensive research in this field. Physicochemical properties of the peptides, such as length and charge distribution, influence their interactions with cell surface molecules and, consequently, the uptake pathway.[9] Beside the intrinsic properties of employed CPPs, other factors, like the size of the attached cargo, concentration and cell lines with varying membrane composition influence the mode of internalization.[108] The major uptake pathways are the energy-independent direct translocation and energy-dependent endocytosis; it is known that CPPs can use several routes concurrently.[9] In general, low concentrations and large cargoes result in predominantly endocytic pathways.[108]

Several models have been proposed for direct translocation; they all share the common feature of initial electrostatic interaction or hydrogen bonding between CPP and negatively charged moieties on the cell surface.

Direct translocation *via* transient pore formation includes the "barrel-stave" and "toroidal" models (**Figure 7**, **A**), which are in general proposed for amphipathic peptides.[9] According to the "barrel-stave" model, primary amphipathic peptides, which have a sufficient length to span the phospholipid bilayer, form as α-helices a bundle within the membrane with their hydrophobic domains facing towards the lipids and their hydrophilic residues forming the central pore.[109] Contrary to that, in the "toroidal" model the peptides form α-helices and accumulate upon contact with the membrane. This results in the bending of the membrane towards the interior and the formation of a hydrophilic gap enclosed from both the peptides and the hydrophilic headgroups.[9]

The "inverted micelle" model proposes the encapsulation of CPPs in an inverted micelle (**Figure 7**, **A**), with the polar headgroups forming a hydrophilic interior, after CPP-mediated disruption of the lipid bilayer. Destabilization of these transient structures and reopening can release the entrapped CPP into the cytoplasm.[110]

In the "carpet-like" model, the peptides associate in a carpet like manner parallel to the membrane induced by electrostatic interactions (**Figure 7**, **A**). Thereby, hydrophobic residues of the peptides are embedded within the lipid bilayer, which results in membrane reorganization and internalization. Alternatively, in the "membrane-thinning" model, the assembly of the peptides in the carpet like fashion results in membrane thinning, reduced surface tension, intercalation of the CPPs within the membrane and subsequent internalization.[9]

While these models can explain direct translocation of amphipathic and structurally defined peptides, cationic CPPs lack both a high rate of hydrophobic peptides and an ordered structure. Nevertheless, energy-independent uptake was also observed for this class of CPPs. One possible explanation is the formation of bidentate hydrogen bonds and electrostatic interactions between the guanidine functions of the peptide and their counterparts (carboxylates, phosphates etc.) on the cell surface. This results in accumulation of the CPPs on the cell surface and attenuation of the hydrophilic character of arginine side-chains, thus reducing the energy barrier for cationic CPPs to translocate. Additionally, the membrane potential could also contribute to the translocation of the positively charged peptides, since the voltage at the inner membrane leaflet is lower compared to the outside one.[111]

Endocytosis is the second large uptake pathway of CPPs and generally favored for large cargo molecules and low CPP concentration, respectively. Contrary to direct translocation, endocytic mechanisms, as described in section **2.2.1**, result in endosomal entrapment of the cargo, which is ultimately subjected to lysosomal degradation. Since the vast majority of potential biopharmaceuticals must reach the cytoplasm in order to achieve their purpose, an endosomal escape is strictly required. Several mechanisms of CPPs have been proposed to promote endosomal release. Similar to direct translocation according to the "barrel-stave" and "toroidal" model, respectively, amphipathic CPPs could facilitate transient pore formation in the endosomal membrane. Alternatively, CPPs could destabilize or disrupt the endosomal membrane, thus gaining access to the cytoplasm. Vesicle budding and collapse, a mechanism supported by experimental evidence,[112] describes the binding of CPPs to the endosomal membrane, generating CPP-rich lipid domains, which bud off as small vesicles. This process could occur multiple times in the same endosome and be enhanced by increased affinity of CPPs to the membrane induced by endosomal acidification. Disintegration and collapse of the CPP-rich budded off vesicles would release the CPPs into the cytoplasm.[113]

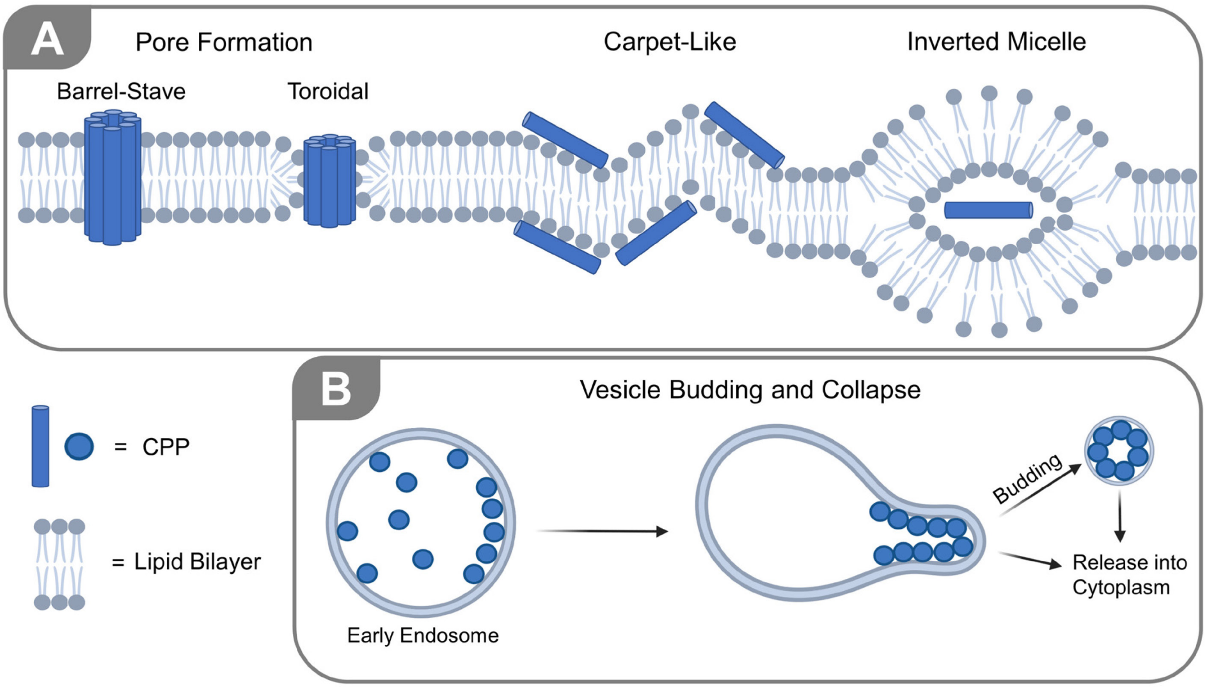

Figure 7 | A: Proposed mechanisms for direct translocation of amphipathic CPPs. Adapted from Trabulo *et al.*[114]. **B:** Schematic depiction of vesicle budding and collapse mechanism. Adapted from Pei and Buyanova[113]. Both **A** and **B** created with BioRender.com.

Despite the ability of certain CPPs to facilitate endosomal release, this process is generally inefficient and subsequently presents a bottleneck for cytoplasmic delivery of biotherapeutics, especially at lower CPP concentrations.[115] In order to overcome this crucial issue, several strategies have been developed that aim for improved delivery systems by specifically enhancing their endosomal escape capabilities and / or overall translocation efficiency.

One approach is based on the application of pH-responsive membrane-active peptides. These molecules comprise pH-sensitive residues (His, Glu, Asp), that remain deprotonated in the extracellular environment but become protonated during endosome maturation. Consequently, they undergo structural changes and an overall increase in hydrophobicity and positive charges, respectively, that enhances their membrane lytic capabilities.[115] One prominent member of this group, HA2 peptide (GLFGAIAGFIENWEGMIDGWYG) derived from the *N*-terminal region of influenza virus hemagglutinin protein, becomes more hydrophobic upon protonation of its acidic residues and able to lyse the endosomal membrane.[113] In an alternative approach, cationic haemolytic peptides were used as scaffold for the design of endosomolytic peptides. Starting with M-lycotoxin (IWLTALKFLGKHAAKHLAKQQLSKL-NH_2), an antimicrobial peptide from wolf spider *Lycosa carolinensis*,[116] Futaki and coworkers exchanged certain hydrophobic amino acids in the sequence with glutamate to attenuate its cytotoxicity at physiological pH.[117] The most promising candidate and one subject of this work which will be described in greater detail in the following section, L17E, was able to facilitate the cytoplasmic uptake of proteins like antibodies and Cre recombinase upon coincubation.[117]

A strategy to improve the general efficacy of CPPs, especially cationic peptides, is the reduction of conformational flexibility by cyclization. The stapling of TAT_{47-57} (original sequence: $YGRKKRQRRR-NH_2$) by introducing hydrocarbon-bearing amino acids at position 5 and 9, followed by cyclization yielded a variant with drastically increased helicity and cellular uptake compared to the original peptide and non-cyclized variant equipped with the non-natural amino acids, respectively.[118] Similar effects were observed upon head-to-tail cyclization of decaarginine, which proved to be an efficient intracellular delivery platform of covalently attached proteins like nanobodies[119] and mCherry[120].

Multimerization of CPPs can also be a viable option to enhance their translocation efficiency. Oxidative dimerization of a TAT derivative yielded dfTAT (CK(ε-NH-TAMRA)RKKRRQRRRG-NH_2), equipped with additional carboxytetramethylrhodamine (TAMRA) fluorophores.[13a] This construct displayed high efficacy in mediating endosomal leakage and facilitated cytosolic delivery of protein cargo.[13a] The presence of two TAMRA moieties in the construct might also contribute to its endosomolytic activity. It has been reported that TAMRA-labeled TAT acted as photosensitizer upon laser irradiation and mediated endosomal membrane rupture.[121] However, it has to be mentioned that the laser exposure time during the dfTAT experiments were kept to an absolute minimum and thus, the authors concluded that endosomal leakage facilitated by dfTAT was light-independent.[13a] Flow cytometric analysis of multimerized CPPs on a linear peptide scaffold and dendritic structures, respectively, revealed that certain CPPs like TAT and amphipathic TP10K (AGYLLGKINKLKALAALAKKIL) could benefit from dimerization on both scaffolds. The respective tetramers, however, showed only minor improvements in cellular uptake while being significantly more toxic.[12] Multimeric presentation of CPPs was also performed on dextran as scaffold. Covalent decoration of the polysaccharide with two copies of nonaarginine and 5 copies of a pro-apoptotic peptide induced apoptosis in cancer cells.[51] Further investigations in this field revealed that dextran equipped with 5 copies of nonaarginine expressed high membrane-perturbing activity and thus strongly increased cytotoxicity.[122]

2.2.3.1 L17E

With the intention to develop an endosomolytic peptide derived from M-lycotoxin (IWLTALKFLGKHAAKHLAKQQLSKL-NH_2), Futaki and coworkers exchanged different amino acids in the potential hydrophobic face with glutamic acid. The incorporation of negative charges should attenuate the membrane-lytic activity at physiological pH by disrupting hydrophobic interactions between peptide and plasma membrane. On the other hand, the peptide should retain a net positive charge for membrane adsorption and subsequent efficient endocytosis. Upon endosomal maturation accompanied by decrease in pH, protonation of the acidic residues should restore the peptides membrane-lytic activity. Different variants were screened for cytotoxicity and endosomolysis, respectively, in which one or two hydrophobic amino acids were exchanged with glutamic acid. The most promising candidate, L17E (IWLTALKFLGKHAAKHEAKQQLSKL-NH_2), displayed strongly reduced cytotoxicity compared to the parent peptide and facilitated the cytoplasmic uptake of biomacromolecules like full-length antibodies and Cre recombinase upon coincubation. Interestingly, more detailed investigations using artificial membranes revealed that the membrane-lytic activity of L17E is pH-independent and exhibited only weak helicity. The authors suggested a lipid-composition-sensitive membrane-lytic mechanism for L17E.[117]

Two years later, Futaki and coworkers presented more detailed studies on L17E and proposed a novel uptake mechanism. Contrary to the intended mechanism of action, L17E probably facilitates transient cell membrane permeabilization allowing cargo to enter cells directly and bypass endocytosis. According to the proposed mechanism, L17E interacts with the cell membrane and induces its ruffling by actin rearrangement, followed by macropinocytosis. Before the formation of the macropinosome is completed, L17E presumably ruptures the ruffled membrane transiently allowing cargo molecules to directly enter cytoplasm. [123]

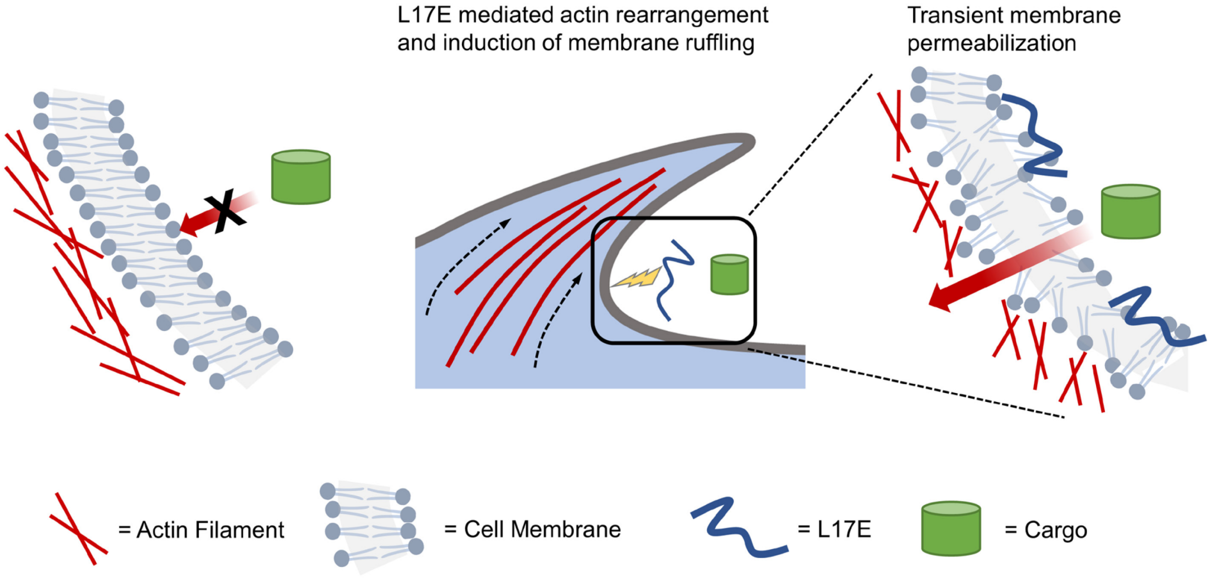

Figure 8| Proposed novel mechanism for transient membrane permeabilization mediated by L17E. Figure adapted from Akishiba and Futaki[123] and created with BioRender.com.

Beside simple coincubation, L17E was also employed in a trimerized version for intracellular antibody (IgG) delivery. Therefore, L17E was equipped with a *C*-terminal GGC extension and covalently attached *via* selective disulfide formation to a Fc region binding peptide (FcB) with additional triple cysteine linker (HWRGWV-G-C-G-C-G-C-NH_2). Mixing FcB(L17E)$_3$ with fluorophore-labeled IgG in a 2:1 ratio resulted in the formation of liquid droplets, comprising condensed IgG and FcB(L17E)$_3$. The proposed uptake pathway is based on the induction of membrane ruffling and potentially transient permeabilization (as depicted in **Figure 8**) upon contact of the droplets with the cellular membrane. More detailed investigations revealed that negative charges of cargo IgG, introduced by labeling with the anionic fluorophore Alexa488, play an important role in the formation of liquid droplets. Furthermore, the exchange of the FcB with a control peptide (KRGFYY), comprising amino acids with similar physicochemical properties and without binding affinity to Fc, did not result in reduced cellular uptake.[124]

2.2.3.2 GuCOSS

As described before, the efficacy of cyclic cationic CPPs is superior to their linear counterparts due to increased structural rigidity. It has been proposed that improved uptake efficacy by cyclization is a consequence from enhanced membrane contact facilitated by arginine residues in a maximally distant position.[125] Since further structural improvements of cyclic CPPs are limited intrinsically to their peptidic backbone, alternative frameworks gained interest to generate delivery vehicles presenting spatially oriented guanidine functions in a dense fashion. This led to the development of novel delivery modules based on non-peptidic scaffolds such as calixarenes[126], dendrimers[127] or cube-octameric silsesquioxanes (COSS)[128]. Silsesquioxanes in general refer to compounds with the general empirical formula $[RSiO_{1.5}]_n$ where R is either hydrogen or an organic residue.[129] These (organo-)silicon compounds exist in various architectures such as random structures, ladders and (partial) cage structures.[129] Being a member of the fully condensed cage structures termed polyhedral oligomeric silsesquioxanes (POSS), COSS comprises an inorganic core comprising eight silicon atoms arranged in a cubic shape (**Figure 9**, **A**).[130] The inorganic cage of COSS has a diagonal diameter of 0.53 nm,[131] which increases depending on the attached residues to an overall size of 1-3 nm. Thus, COSS could be considered as the smallest existing silica nanoparticles.[132] Beside the application as filler for composite polymers to tune their mechanical properties,[132] COSS also gained interest in the field of biochemical research due to promising characteristics. The rigid inorganic core in general possesses good thermal and chemical stability, but is prone to hydrolytic degradation under basic aqueous conditions whereby the decomposition rate is highly dependent on the corner substituents.[133] With regard to the application as delivery module, the tunable degradation of the framework can be considered advantageous. Accumulation of COSS derivatives within the biological system could be avoided and the resulting final degradation products, i.e., monomeric silsesquioxanes, possess low cytotoxicity.[128, 133] Furthermore, certain COSS derivatives displayed cell-penetrating capabilities. Octa(3-aminopropyl)-COSS, equipped with a boron-dipyrromethene (BODIPY) fluorophore at one of the pendant arms *via* amide-bond formation, was able to enter the cytoplasm of mammalian cells.[134] Additionally, amine-bearing COSS served as platform for the nuclear delivery of the fluorophore fluorescein and a 16mer peptide.[135] In an effort to enhance the cell-penetrating capabilities of COSS nanoparticles, the amine groups of the aforementioned COSS derivative were replaced by guanidine functionalities, generating octa(3-guanidinopropyl)-COSS, or short, GuCOSS (**Figure 9**, **B**).[128] Single-corner TAMRA-labeled GuCOSS displayed far superior cell-penetrating capabilities compared to its amine-bearing counterpart as well as TAMRA-heptaarginine comprising equal number of guanidine groups and other CPPs such as decaarginine and TAT.[128] The uptake was not significantly decreased at 4 °C, indicating an energy-independent uptake; the cytotoxicity of this novel delivery vehicle (LC_{50} = 84 µM) was found to be in the range of polyarginines (LC_{50} = 76 µM)[136].[128] The rather low cytotoxicity of GuCOSS could be the result of degradation of the inorganic framework under physiological conditions and, indeed, the half-life of the inorganic core was roughly 2.5 h in an intracellular environment.[128] Interestingly, fluorescently labeled GuCOSS was also able to gain access to the interior of bacteria, yeast and even archaea cells.[128]

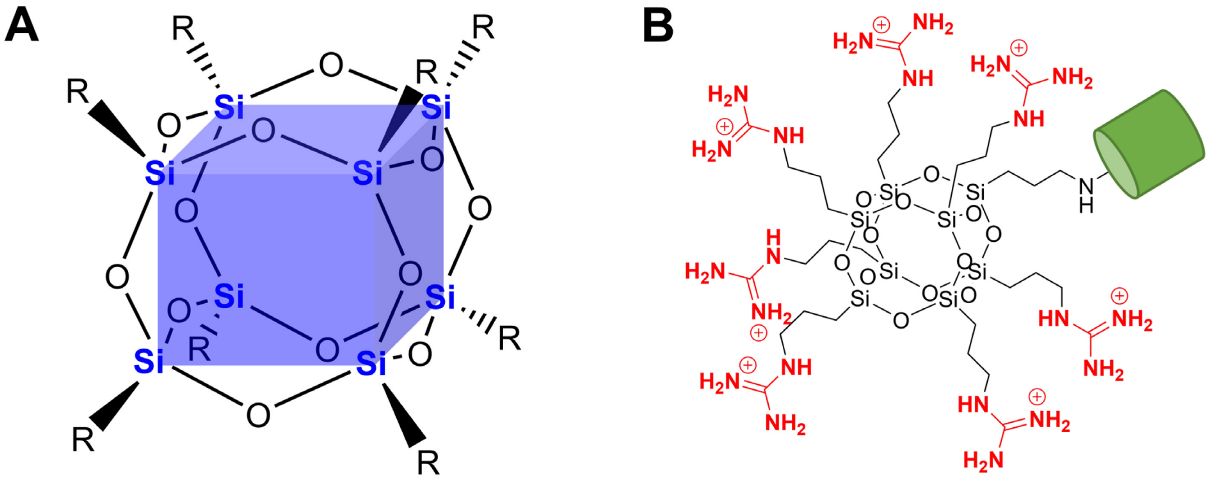

Figure 9| A: Inorganic framework of COSS with silicon atoms in a cubic arrangement (blue). **B:** General structure of GuCOSS with highlighted guanidine functions (red) and a covalently attached cargo (green).

2.2.3.3 Thiol-Mediated Uptake

Despite the impressive in vitro results reported for cationic delivery vehicles like CPPs and GuCOSS, their in vivo performance is most likely reduced by electrostatic interactions with endogenous biomacromolecules. This problem, termed as “polycationic dilemma”, refers to the attenuation of the transporters cationic character and, thus, its activity, due to interactions with polyanionic serum proteins and components of the extracellular matrix (ECM), respectively.[137] Indeed, the presence of serum in in vitro uptake experiments drastically reduces the activity of both polyarginines[138] and GuCOSS[128]. An alternative approach towards efficient intracellular delivery is based on the concept of “thiol-mediated uptake”. While a correlation between cellular entry of HIV[139] and diphtheria toxin[140] and its inhibition by thiol-reactive Ellmans reagent was reported some decades ago, only little effort was being directed at the development of novel intracellular delivery strategies based on interactions with membrane-bound thiols. Only during the last decade and thanks to pioneering work predominantly from Stefan Matile´s research group, this concept became the focus of closer attention. Their work in this field started with the development of cell-penetrating polydisulfides (CPDs). These mimics of CPPs comprise a disulfide backbone and guanidine side-chains and are obtained by ring-opening polymerization of guanidine-functionalized cyclic oligochalcogenides (COCs).[141] Being designed to minimize toxicity due to rapid depolymerization within the cytosol, CPDs also predominantly avoid endocytosis and are capable of promoting cytosolic delivery of cargoes ranging from fluorophores[141] to proteins[142] and even quantum dots[143]. Shortly after the development of CPDs, the focus shifted towards the investigation and optimization of thiol-mediated uptake of COCs. It has been proposed, that increasing ring tension in COCs as well as higher acidity of the corresponding thiols results in higher cellular uptake.[105] In acyclic disulfide bonds, the CSSC dihedral angle is 90° to optimize hyperconjugation and minimize lone pair repulsion.[105] In contrast, cyclic 1,2-dithiolanes such as lipoic acid and asparagusic acid have a smaller dihedral angle (**Figure 10**, **A**) of 35° and 27°, respectively, which is also reflected in a higher uptake activity of asparagusic acid compared to lipoic acid.[144] Maximum ring tension was achieved with epidithiodiketopiperazines (ETP; **Figure 10**, **A**), in which the dihedral angle was reduced to 0° and the acidity was increased.[145] Alternatively, the switch from sulfur to selenium yields derivatives such as diselenolipoic acid (DiSeL; **Figure 10**, **A**) with vastly improved properties.[146] Compared to its sulfur-containing predecessor, DiSeL has a dihedral angle of 0°, enabled by its longer Se-Se bond, as well as being more acidic.[105, 146] The exact uptake mechanism is not fully elucidated yet, since the reactivity of the intermediates complicate their detection.[146] Data received from thiol-exchange affinity chromatography and low-temperature trapping experiments suggest a mechanism of DiSeL as “molecular walker” along disulfides of transmembrane proteins, facilitated by rapid covalent exchange reactions (**Figure 10**, **B**).[146, 147] The uptake is initiated by formation of selenosulfides between exofacial thiols and DiSeL in a ring opening reaction, whereby the secondary position is preferred.[147] Following this, the resulting primary selenide can either attack intramolecularly to reform the diselenide, rearrange to a primary selenosulfide or attack a proximal disulfide bond.[146, 147] The intramolecular attack of the secondary selenide liberates the primary selenide again, which subsequently can attack another proximal disulfide bond. This stepwise exchange and rearrangement reactions can repeat until DiSeL is released into the cytosol. The presented hypothetical mechanism further illustrates the importance of acidity. While the rate of exchange reactions is in general dominated by the electrophile, i. e. the “migrating” thiols of the transmembrane proteins, further exchange reactions of 1,2-dithiolanes are inhibited due to protonation of their thiol groups.[147] Thus, 1,2-dithiolanes are immobilized on the surface of the proteins after the initial reaction and become entrapped after endocytosis.[147]

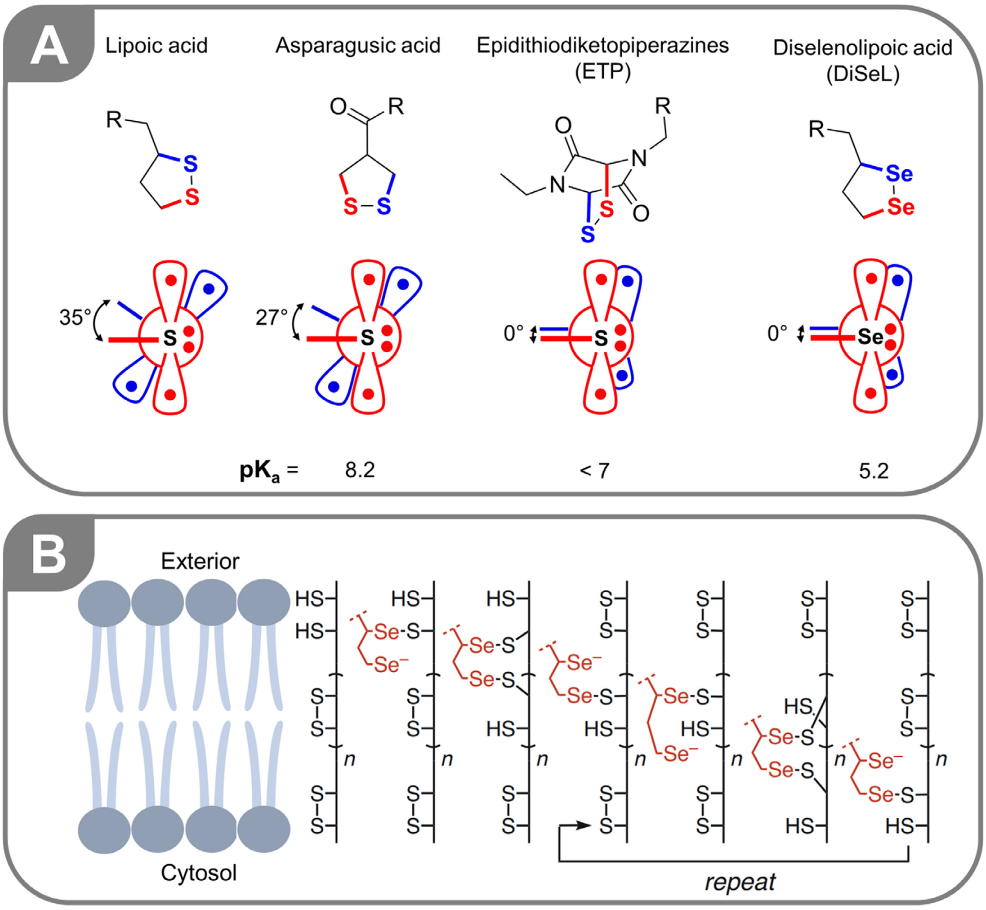

Figure 10| **A:** Structures of cyclic oligochalcogenides (COCs) with an emphasis on the CXXC angles and pKa´s of the corresponding thiols and selenols, respectively. Figure adapted from Laurent et al.[105]. **B:** Proposed uptake mechanism of DiSeL, figure adapted from Martinent *et al.*[148] and distributed under the terms of the Creative Commons Attribution-NonCommercial 4.0 international, license: CC BY-NC 4.0. **B** was created with BioRender.com.

2.2.4 Receptor Targeting

2.2.4.1 Integrins and the RGD motif

As already mentioned, the receptor class of integrins plays a pivotal role in communication between cells and their environment. Thus, integrins are key actors in processes like proliferation, apoptosis, migration and adhesion; dysregulation of their expression has been observed in several types of solid tumors.[98a, 98b, 99] Integrins are heterodimeric glycosylated transmembrane receptors; at least 24 human variants originate from a pool of 18 α- and 8 β-subunits.[149] Integrins are capable of both “inside-out” and “outside-in” signaling; the ligand-binding activity is modulated by interactions between the cytoskeleton and cytoplasmic domains of the receptors whereas extracellular stimuli trigger cytoskeletal adaptor proteins.[150] These stimuli are either ligand-binding, receptor-clustering or mechanical forces.[150] Ligation to ECM components results in the clustering of integrins on the cellular surface; these focal adhesions link the cytoskeleton to the ECM.[99]

Structure determination of integrin αvβ3 ectodomain revealed that the α-subunit contains a seven-bladed β-propeller structure as an *N*-terminal head group, followed by a "thigh" and two "calf" domains.[151] The β-subunit, on the other hand, has an βA domain looping out of an Ig-like hybrid domain as well as a PSI (plexins, semaphorins and integrins) domain[152], four epidermal growth factor (EGF) repeats and a β-tail domain (**Figure 11**, **A**).[151] The βA domain also contains metal-ion coordination sites to which bivalent cations (Mg^{2+}, Ca^{2+}, Mn^{2+}) can associate, such as the metal-ion dependent adhesion site (MIDAS), with regulatory and ligand-binding activity.[151, 153] The heterodimeric integrins exist in different conformational states with low or high affinity towards ligands.[98a] During "inside-out" signaling, the receptor initially exists in a low affinity state, in which the head groups are bent towards the cell membrane and the intracellular domains are associated by intermolecular salt bridges (**Figure 11**, **B**).[154] Binding of the proteins talin or kindlin to the intracellular domain of the β-subunit provokes the dissociation of the integrin subunits and conformational rearrangement of the ectodomains.[98a, 154] The motion from a bent to an extended form, referred to as "switchblade" mechanism, results in an erect posture of the subunits in a high affinity state.[98a] "Outside-in" signaling is triggered by ligand binding to the head pieces, followed by dissociation of the subunits (**Figure 11**, **B**). Homo-oligomerization of the subunits to complexes results in binding of talin or kindlin to the intracellular domains and subsequent activation of downstream signaling.[98a]

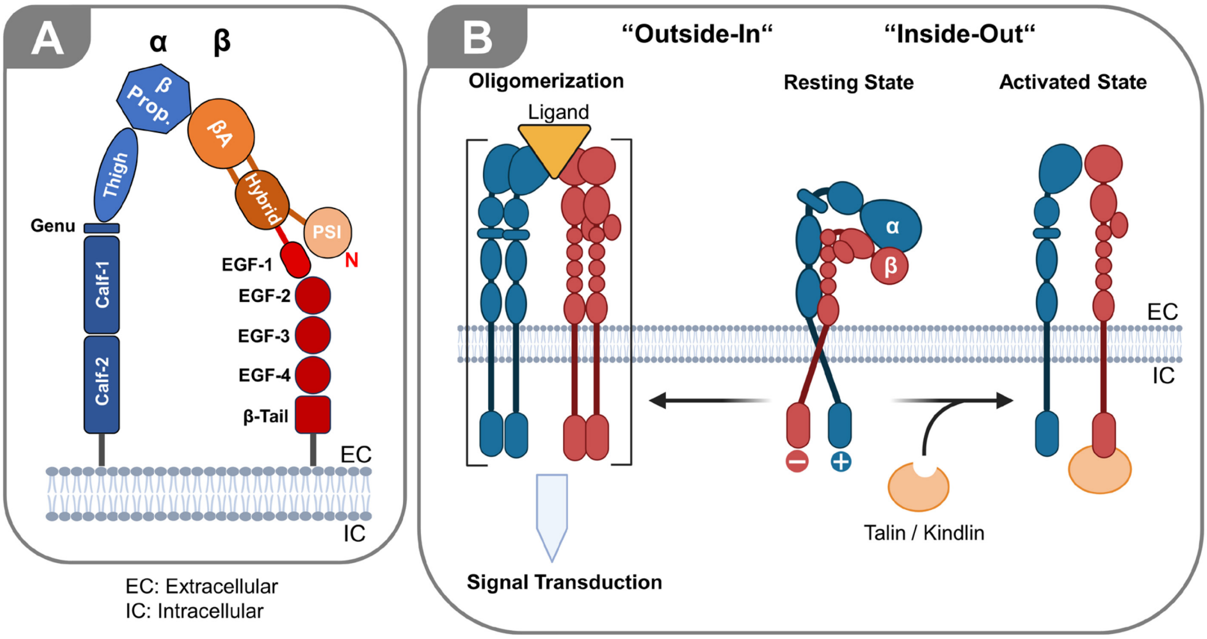

Figure 11| A: Schematic depiction of integrin αvβ3 in an extended conformation with additional highlighting of the flexible region ("Genu") in the α-subunit. Adapted from [154, 155]. **B:** Depiction of the "outside-in" and "inside-out" signaling of integrins. Adapted from Nieberler *et al*.[98a] and Feni[156] and created with BioRender.com.

The group of integrins can be categorized according to their binding motif in ECM proteins, of which the RGD-binding integrins are of special importance regarding their involvement in cancer progression.[98a] Originally discovered in the natural ligand fibronectin,[157] RGD is the recognition sequence for the integrins αvβ1, αvβ3, αvβ5, αvβ6, αvβ8, α5β1, α8β1 and αIIbβ3.[98a] It is important to note, that conformation and spatial orientation of the binding motif as well as adjacent molecular regions within ECM proteins are also essential criteria for the specificity between the ligands and their respective integrins.[98a]

Integrin αvβ3 in particular has become subject of intensive investigations due to correlating expression levels in tumors and their progression. Furthermore, the expression of this integrin has been reported in tumor blood vessels but not quiescent endothelial cells.[99] Thus, αvβ3 has become a prime target for anticancer therapy over the last decades with various platforms as antagonistic inhibitors, like antibodies, RGD-containing peptides and non RGD-based small molecules.[158a, 158b] Starting from the minimal recognition sequence RGD, various peptidic integrin binders have been designed with different properties in regard to selectivity, affinity and in vivo stability.[158a] Constraining the conformational freedom by head-to-tail macrocyclization and incorporation of D-amino acids yielded cyclic pentapeptides such as *cyclo*[RGDfV] with superior binding activity compared to their linear counterparts.[159] Further improvements could be achieved by introduction of *N*-methylated amino acids, which culminated in the design of cilengitide *cyclo*[RGDf(NMe)V].[160] This cyclic peptide displays sub nanomolar affinity towards αvβ3 while being highly selective for cancer-relevant integrins (three orders of magnitude lower affinity towards αIIbβ3).[160, 161] The latter property is of great importance for in vivo applications to avoid side effects; high affinity towards the platelet integrin αIIbβ3 could result in hemorrhagic disorders.[98a] Beside the improvements in affinity and selectivity towards αvβ3 and other cancer-relevant integrins, macrocyclization and the incorporation of *N*-methylated and D-amino acids can also enhance the stability towards enzymatic degradation in vivo.[158a, 161] More detailed investigations of the conformation of cilengitide in solution were performed by nuclear magnetic resonance (NMR) spectroscopy and molecular dynamics (MD) simulations.[160] These experiments revealed, that cyclization and *N*-methylation induce a γ-turn within the glycine residue while both arginine and aspartic acid exhibit inverse γ-turns (γ_i) (**Figure 12, A**). As a result, cilengitide comprises a distinct kink between arginine and aspartic acid within the backbone (**Figure 12, A**), which seems essential for the selective binding of αvβ3 compared with integrin αIIbβ3, favored by extended ligands.[160] The crystal structure of αvβ3 ectodomains with cilengitide elucidated, that the ligand binds within a cleft between the β-propeller of the α-subunit and the βA-domain of the β-subunit (**Figure 12, B**).[162] Thereby, the guanidinium residue of cilengitide forms both a bidentate salt bridge and another salt bridge with two Asp residues located in the β-propeller.[162] The carboxylate of cilengitide coordinates with a Mn^{2+} cation in the

MIDAS and further interacts *via* hydrogen bonding with the backbone of the βA-domain.[162] Cilengitide's glycine exhibits hydrophobic interactions in the interface between the subunits.[162] Both remaining amino acids are oriented away from the protein and can be varied to a certain degree. Replacing the D-Phe with other hydrophobic amino acids or serine results only in minor differences in affinity or selectivity; however, the *N*-terminal amide proton at this position is of great importance, which indicates its involvement in receptor binding.[163] The interchangeability of valine enables the introduction of chemically addressable moieties such as lysine for further covalent functionalization of the integrin binder.[163]

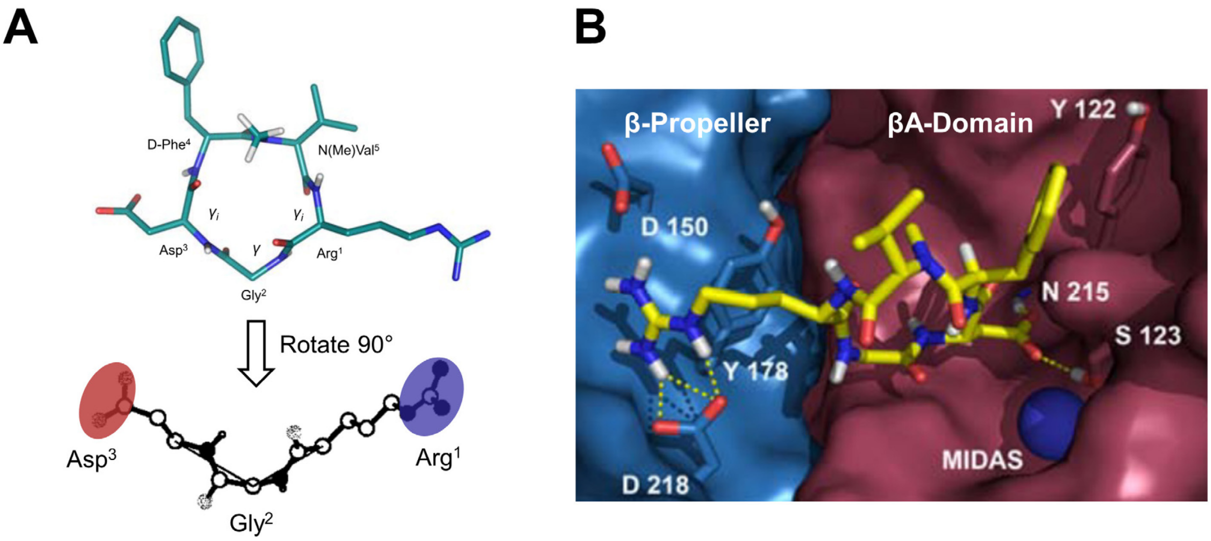

Figure 12| A: Conformation of cilengitide in solution with edge-on depiction of the cyclic peptide highlighting its kinked conformation. (Adapted with permission from Dechantsreiter *et al.*, *J. Med. Chem.*, **1999**, *42*, 3033-3040.[160] Copyright 1999 American Chemical Society) **B:** Cilengitide bound to αvβ3 at the interface between the α- and β-subunit. Figure adapted from Mas-Moruno *et al.*[161] and distributed under the terms of the Creative Commons Attribution 2.5 generic license: CC BY 2.5.

Unfortunately, the promising *in vitro* performance and the results from preclinical studies[164] did not translate into successful application of cilengitide as anticancer agent in human. Clinical trials with cilengitide for the treatment of advanced head and neck tumors, metastatic melanoma or lung cancer revealed only little impact on overall survival.[165] While the combination of cilengitide with the alkylating agent temozolomide and radiotherapy showed promising preliminary results for the treatment of glioblastoma,[166] phase III clinical trials ultimately reported no improved outcome over control therapy.[167] The failure of cilengitide in clinical applications might be attributed to the fact that in blood plasma low concentration of this cyclic peptide (which is typical for the usual administration regimen) actually stimulates tumor growth and angiogenesis.[168] At low nanomolar concentrations, cyclic RGD peptides displayed agonistic behavior in vitro by inducing structural rearrangement of αvβ3, resulting in the receptor adopting an extended structure with high affinity towards ligands.[169]

Despite the failure of cilengitide as agent in anticancer therapy, its high affinity and selectivity for cancer-relevant receptors in combination with the interchangeable position of valine make the framework attractive as receptor-targeting module. RGD-containing cyclic peptides have found clinical application as carrier platform for radioisotopes in tumor imaging *via* positron emission tomography (PET).[170] Furthermore, cilengitide analogues can be employed as peptide-drug conjugates with covalently attached cytotoxic drugs like cryptophycin[171] or paclitaxel[172]. Both affinity and rate of specific internalization, crucial factors for efficient intracellular delivery of cytotoxins, can potentially be increased by multimerization.[173] Various strategies and platforms have been used for multimeric presentation of RGD-peptides, among them dextran and streptavidin.

Dextran has been employed as carrier platform for the small molecules doxorubicin and the proteasome inhibitor bortezomib as well as *cyclo*[RGDfK] for targeted delivery.[174] The final construct was assembled by Schiff base formation between the amine-bearing *cyclo*[RGDfK] and doxorubicin and oxidized aldehyde-bearing dextran, whereas bortezomib was covalently attached *via* boronic esterification.[174] These decorated dextran polysaccharides formed micelles, which displayed higher tumor accumulation in vivo compared to a control without *cyclo*[RGDfK].[174] Moreover, both the imine and boronic ester bonds are pH-sensitive, which can result in the release of the small molecules upon receptor-mediated endocytosis and subsequent endosome maturation.[174]

Streptavidin served as centerpiece for integrin-targeted dual optical imaging and PET. Thus, Sav was labeled with a fluorescent dye and multiple copies of the metal ion complexing agent DOTA *via* amide bond formation.[175] For integrin targeting, E[*cyclo*(RGDyK)]$_2$ was equipped with biotin and subsequently tetramerized on the functionalized streptavidin.[175] The assembled construct displayed higher affinity towards αvβ3 compared to solitary E[*cyclo*(RGDyK)]$_2$.[175] Optical imaging and PET of the construct with chelated ^{64}Cu displayed higher tumor accumulation in a αvβ3 positive mouse model in comparison to ^{64}Cu-DOTA-E[*cyclo*(RGDfK)]$_2$.[175]

2.2.4.2 Death Receptor 5 Targeting

Inducing apoptosis in tumor cells while sparing healthy tissues is a very promising therapeutic approach. Certain proteins, such as TRAIL, bind to specific receptors on the cell surface and trigger signaling events, which can ultimately result in apoptosis.[100] TRAIL, expressed as trimer on the surface of natural killer cells and T cells, among others, interacts with four different membrane-bound receptors.[176] Binding to the receptors DR4 and DR5 can trigger apoptosis signaling, whereas two decoy receptors, DcR1 and DcR2, inhibit TRAIL-induced signal transduction.[176] While both decoy receptors possess similar transmembrane regions as the death receptors, DcR1 and DcR2 lack the intracellular death domain (DD) and have a dysfunctional one, respectively, which is essential for intracellular signal transduction.[177]

The apoptotic pathway is initiated by binding of TRAIL to the preorganized trimeric death receptors, inducing their oligomerization (**Figure 13**).[178] As a result, homotypic interactions of the receptor DD recruit Fas-associated with death domain (FADD), which also possesses a DD and additionally a death effector domain (DED).[179] The latter domain interacts with the DED of pro-caspase-8; the complex comprising the DD of the oligomerized receptors, FADD and caspase-8 is termed death-inducing signaling complex (DISC).[179] Following this, release of active caspase-8 results in a proteolytic cascade involving caspase-3 and caspase-7 which ultimately leads to apoptosis.[179] In certain cell types, activation of caspase-8 is insufficient for transduction of the pro-apoptotic signal.[179] Therefore, an alternative pathway *via* a mitochondrial amplification loop is required (**Figure 13**).[178] This involves caspase-8-mediated cleavage of Bid (BH3-interacting domain death agonist) to form truncated Bid (tBid), which causes oligomerization of Bak (Bcl-2 homologous antagonist/killer) and Bax (Bcl-2 associated X-protein) and subsequent pore formation in the outer mitochondrial membrane.[178] Efflux of pro-apoptotic molecules, among them cytochrome C, results in the formation of the apoptosome.[178] This large protein complex activates caspase-9, which itself participates in the apoptotic cascade by activating caspase-3 and caspase-7.[178, 179]

TRAIL-mediated apoptosis is a tightly regulated cellular process, since DR4 and DR5 are present in most human tissues.[177] Both receptors are often co-expressed on the same cells, whereby DR5 seems to be more crucial for signaling of apoptosis.[177] On a cellular surface level, TRAIL-induced apoptosis is regulated by the expression rate of the death receptors and their decoy receptors, respectively, as well as the glycosylation of DR4 and DR5.[179] Intracellular effector proteins, such as cellular FLICE-like inhibitory protein (c-FLIP), further regulate the signaling cascade. c-FLIP competes with caspase-8 for binding to FADD and consequently has an anti-apoptotic effect by preventing caspase-8 activation.[180] Further adding to the complexity of TRAIL-induced signaling is the fact, that its binding to DRs can provoke anti-apoptotic signaling in non-tumorigenic and resistant tumor cells, respectively.[181]

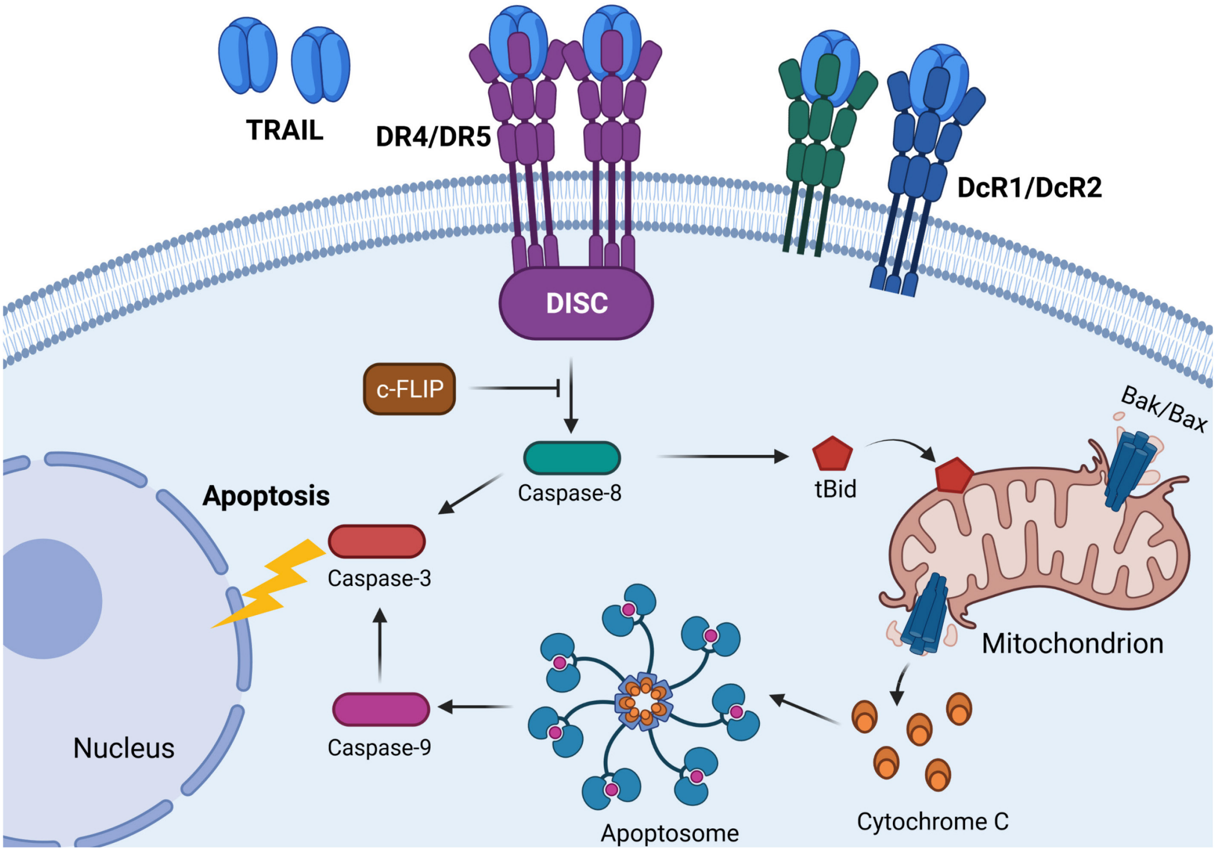

Figure 13 | TRAIL-induced intracellular signaling leading to apoptosis *via* direct pathway and mitochondrial amplification loop, respectively. Figure adapted from Schneider-Brachert *et al*.[178] and created with BioRender.com.

Being recognized as a promising target for directed antitumor therapy, various formats of DR binders have been designed within the last years. The recombinant protein dulanermin, comprising residues 114-281 of naturally occurring TRAIL, showed poor results as monotherapy in clinical trials due to a short circulation time and potential resistance mechanisms.[100] While the combination of dulanermin with chemotherapeutic agents prolonged progression-free survival in patients with advanced non-small cell lung cancer (NSCLC), it had no impact on the overall survival.[182] Alternatively, several agonistic antibodies targeting DR4 and DR5, respectively, have been developed, which showed promising results in vitro.[183] While therapeutic antibodies, such as mapatumumab and tigatuzumab targeting DR4 and DR5, respectively, were well tolerated in clinical trials, they displayed only negligible efficacy.[183] A major factor for these disappointing results is presumably the inability of the antibodies to induce sufficient receptor clustering.[184] While higher degree of effective binding of the antibodies can result from interaction with Fcγ receptors on the surface of immune cells, this effect seems insufficient to induce apoptosis.[185] Consequently, different strategies were employed to generate antibody species with increased valence. The importance of high-valence antibody formats was showcased in a recent publication, in which a pentameric IgM antibody format targeting DR5 was employed. This novel construct, termed IGM-8444, was vastly superior in cell experiments and xenograft models compared to a corresponding IgG and is currently in phase I clinical trials.[186]

The pivotal role of multimerization for efficient DR5 clustering and induction of apoptosis is not limited to antibodies or proteins in general. A 15mer peptide sequence originated from recombinant peptide screening and unrelated to TRAIL, termed DR5TP, displayed nanomolar affinity towards DR5 whilst lacking the ability to induce apoptosis.[101] Dimerization of this peptide by cross-linking of its lysine residues yielded a construct with micromolecular cytotoxicity, which could be increased 5-fold by trimerization on a Tris-based scaffold.[101] Exchange of this flexible scaffold with a rigid adamantane framework yielded a trivalent derivative with improved activity against DR5-positive cells.[187] Interestingly, a G1 dendron of adamantane with a total of 6 DR5TP ligands displayed inferior cytotoxicity towards DR5-positive cells compared to its monomeric counterpart.[187] Low nanomolar cytotoxicity in DR5-positive colorectal cancer cells could be achieved employing C4b-binding protein as scaffold molecule.[188] Thereby, the best results were achieved by genetic fusion of DR5TP to the *C*-terminus of the heptameric protein, whereas both *N*-terminal placement and enzyme-mediated conjugation of the peptide resulted in constructs with lower activity.[188] Furthermore, the highly flexible biopolymer dextran was also employed as scaffold for multimerization of a large number of DR5TPs.[29] Thus, 10 kDa dextran was dimerized using a human Fc fragment as centerpiece and decorated with DR5TP to yield constructs with a total of 22 and 27 peptides, respectively.[29] Indeed, these multivalent hybrids displayed highly efficient killing of DR5-positive cells while sparing non-malignant cells.[29]

2.2.5 Peptide Nucleic Acid

Nucleic acid-based therapeutics have got into a focus of public interest in the wake of the corona virus disease-19 (COVID-19) pandemic. Since the FDA's emergency approval of the first mRNA-based vaccine in December 2020 (BioNTech/Pfizer's BNT162b2), the global health care systems possess a specific therapeutic tool to attenuate the impact of this disease.[189] In the academic environment, the potential of nucleic acid-based therapeutics has been recognized for decades, and extensive research effort led to the development and application of several orphan drugs for the treatment of rare diseases.[190] While the usefulness of these therapeutics in a wide range of applications is unquestionable, several challenges had to be addressed. Among those, the short half-life of RNA and DNA in vivo has been concerned a major issue which initiated the development of nucleotide analogues.[191] The replacement of an oxygen atom in the phosphodiester backbone of DNA with sulfur yielded phosphorothioates (**Figure 14**) with increased stability towards enzymatic degradation.[191, 192] Beside the phosphodiester linkage, the sugar moieties within the backbone can also be modified. Introduction of a covalent linkage between the oxygen at position 2 and the carbon atom at position 4 in ribose generated locked nucleic acids (LNA, **Figure 14**).[191] As a consequence, these bicyclic nucleotide analogues display improved affinity towards their target RNA.[193] The scope of possible modifications is not limited to the (deoxy)ribose framework and phosphodiester linkage, respectively. Exchange of the natural pentose with the six-membered heterocycle morpholine and replacement of the phosphodiester with a phosphordiamidate group gave rise to phosphordiamidate morpholino oligonucleotides (PMO, **Figure 14**), also called morpholinos.[191] Contrary to their progenitor, morpholinos are uncharged under physiological conditions and highly stable towards enzymolysis.[194]

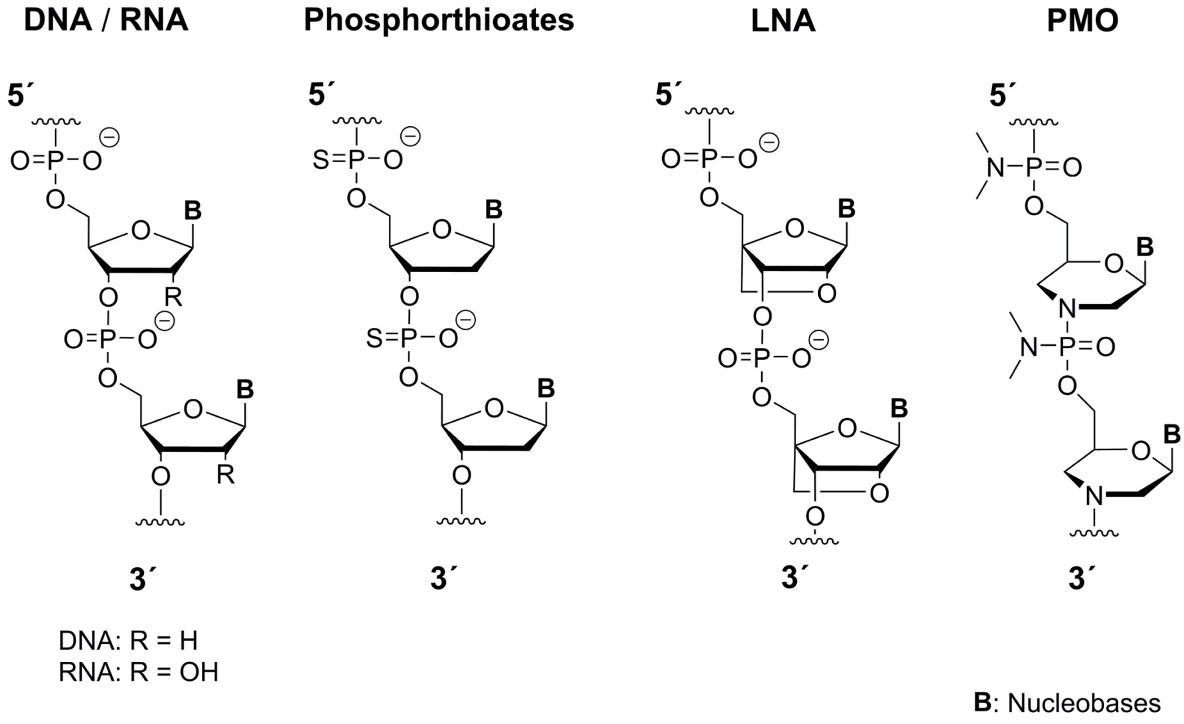

Figure 14| Structure of DNA and RNA as well as the analogues phosphorothioates, LNA and PMO.

While these examples for synthetic nucleotide analogues differ in terms of structure from their natural template to a various degree, their backbone is still comprised of the nucleobases attached to a phosphorus-containing framework *via* a cyclic adaptor module. In contrast to these structures, peptide nucleic acids (PNAs) feature a polyamide backbone based on nucleosides coupled to *N*-2-aminoethyl glycine (aeg) modules.[195] From a structural point of view, PNA could be described as hybrid with a protein backbone and an oligonucleotide. Despite the obvious differences between PNA and RNA/DNA, the synthetic oligonucleotides share the structural bond arrangement of the nucleobases with their natural counterparts.[196] Originally designed with the intent to target double helical DNA by insertion into the major groove and to form a triplex *via* Hogsteen base pairing, further investigations revealed a broad spectrum of advantageous features.[196] Indeed, PNA binds to complementary RNA/DNA in a parallel and antiparallel fashion, respectively, that exceeds naturally occurring double helices in terms of stability (ΔT_m = 1-2 °C per base in general).[196] Furthermore, suited PNA oligonucleotides are able to invade existing DNA double helices by displacing one of the DNA strands.[197] The superior affinity of PNA to complementary oligonucleotides is a consequence of the neutral pseudopeptide backbone, which, in contrast to the natural phosphodiester linkage, is not subject of salt concentration-dependent charge repulsion.[196, 198] Beside the remarkable hybridization properties of PNA, these nucleotide analogues possess further beneficial properties. PNA exhibits resistance towards both nucleases and proteases in human serum and cellular extracts.[199] Furthermore, the peptidic nature of PNA monomers with both *N*- and *C*-terminus allows for the assembly *via* well-established solid phase synthesis protocols. Thereby, commercially available building blocks usually comprise an *N*-terminal fluorenylmethoxycarbonyl (Fmoc) protection, whereas the nucleobases (with exception of thymine that requires no protecting group) bear a benzhydryloxycarbonyl (Bhoc) group.[200] Conveniently, PNA-peptide chimeras can be obtained without changing the overall synthesis strategy, whereby peptides can be introduced terminally or within the PNA oligomer.[201]

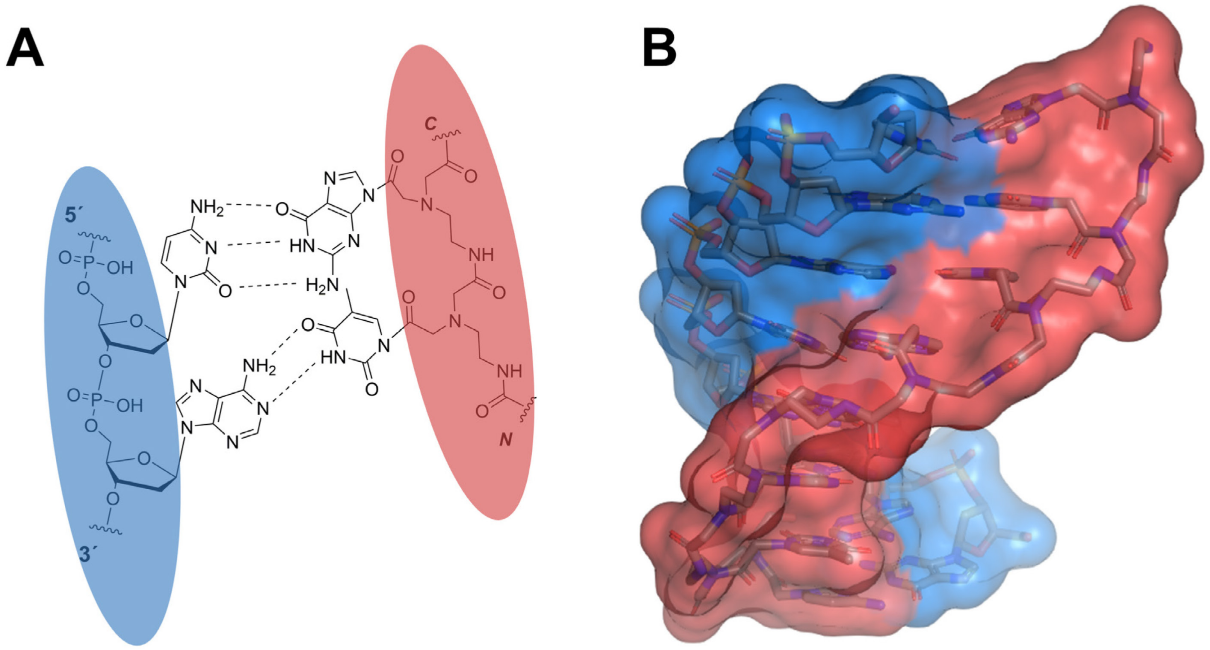

Figure 15| A: Antiparallel hybridization of DNA (blue) and PNA (red) dimers with hydrogen bonds (dashed lines). **B:** NMR-derived structure (PDB: 1PDT)[202] of DNA- (blue) and PNA-octamer (red) comprising double helix.

PNA oligomers have found application in diagnostics as fluorescence *in situ* hybridization (FISH) probes. This FDA-approved technology allows for the detection of microbial pathogens, such as *Staphylococcus aureus*[203] or *Candida albicans*[204], by targeting their ribosomal RNA (rRNA) with fluorescently labeled PNA probes. Contrary to standard methods, which can take several days, the treatment of blood samples with PNA FISH oligonucleotides and subsequent readout by fluorescence microscopy is finished within hours.[205] Combined with multicolor PNA-FISH probes to differentiate subspecies, this technology provides vital information about infections, which is of great importance for effective antibiotic treatment in hospital.[205] In addition to its effectiveness for diagnostic purposes, PNA has also great potential for therapeutic applications. Similar to the detection of microbial pathogens, these synthetic oligonucleotides could be an asset in the fight against emerging multidrug-resistant bacteria. Indeed, PNA directed at either an essential gene for fatty acid metabolism[206] or a rRNA loop in the ribosomes [207] was able to inhibit bacterial growth. PNA can also be employed as anticancer drug by blocking mRNA of oncogenic proteins. One such example is the fused *bcr*/*abl* protein, originating from the abnormal Philadelphia chromosome present in most patients with chronic myeloid leukemia (CML).[208] Targeting the mRNA of *bcr*/*abl* with complementary PNA led to significant downregulation of the mRNA and subsequent cell growth inhibition in in vitro experiments.[208] The mechanism of PNA-mediated inhibition is hereby limited to steric shielding of the corresponding mRNA target; contrary to small interfering (si)RNA, PNA is not able to activate RNA interference by entering the RNA-induced silencing complex (RISC).[209]

The potential of unmodified PNA in experiments with intact cells or even in vivo is severely hampered by its low cell penetrating capability, which is a general problem of nucleic acid-based therapeutics.[191] Consequently, various strategies have been developed to overcome this issue, among them the usage of CPPs. For application in several prokaryotic systems, such as the aforementioned PNA with antibiotic properties, *N*-terminal covalent attachment of the synthetic CPP $(KF_2)_3K$ has proven to be very effective.[206, 207] Despite the capability of this peptide to facilitate the uptake of PNA in several gram-positive and -negative organisms, respectively, it was not very effective in *Pseudomonas aeruginosa*.[206] In mammalian cells, the well-established CPPs penetratin (RQIKIWFQNRRMKWKK), TAT (GRKKRRQRRRPPQ) and nonaarginine showed only moderate effectiveness.[210] Therefore, optimized CPPs for PNA delivery in HeLa cells were identified by synthetic molecular evolution using both penetratin and TAT as template.[210] The lead candidates P14 (RKKRWFRRRRPKWKK) and P17 (GRKKRWFRRRRMKWKK) exceeded their parent peptides in intracellular delivery of PNA while keeping a moderate cytotoxic profile.[210] In order to benchmark the performance of the CPPs, a quantitative measure of successfully delivered and bioactive PNA is required. One such assay is the enhanced green fluorescent protein (eGFP)654 mis-splicing correction assay.[211] Thereby, HeLa cells are stably transfected with an eGFP gene, which is interrupted by a mutated intron from human β-globin (IVS2-654) (**Figure 16**).[211] The point mutation at position 654 of the intron activates aberrant splice sites, which are preferred over the still existing normal ones.[211] As a consequence, the spliced eGFP mRNA contains a fragment of the mutated intron and the resulting protein is non-functional.[211] Targeting position 654 with a complementary 18mer PNA oligonucleotide restores correct splicing after successful hybridization and, therefore, allows for a correlation between delivered PNA and eGFP fluorescence.[211]

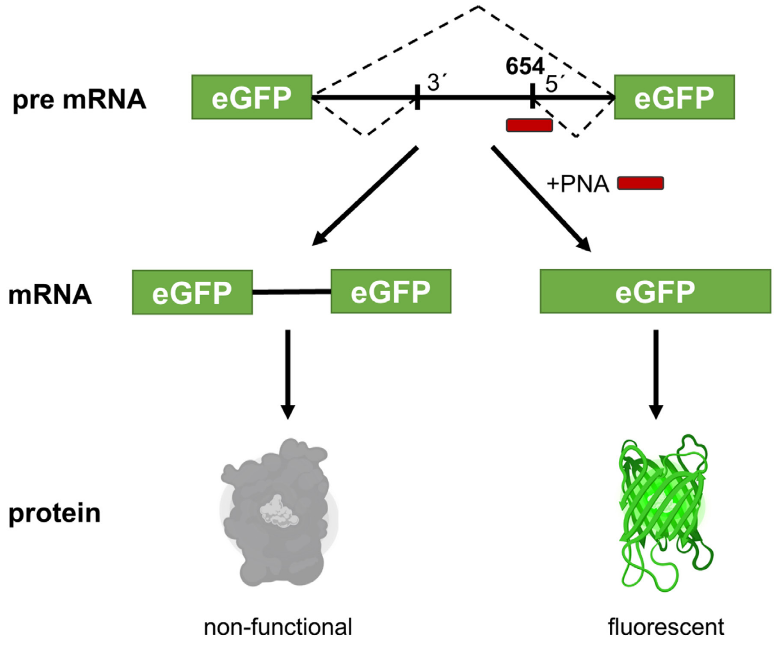

Figure 16| Schematic depiction of the eGFP654 mis-splicing assay, in which hybridization of PNA complementary to a mutated position of intron IVS2-654 results in correct splicing of eGFP mRNA and subsequent production of functional protein. Figure adapted from Sazani *et al.*[212].

3 Objective

3.1 Molecular Platforms for Intracellular Delivery of PNA: Comparative Studies

The first part of this work was aimed at the challenge of successful intracellular delivery of bioactive PNA. As shown in the introduction, PNA is a promising tool for therapeutic applications. However, to be effective in mammalian cells, these synthetic oligonucleotides must traverse the cellular membrane and enter the nucleus. Since PNA suffers from low cellular uptake, conjugation to a suited delivery platform could overcome this obstacle.

To this end, delivery platforms of various origin should be evaluated in view of their ability to facilitate cellular uptake of PNA in mammalian cells. One promising delivery module could be the silicon-based nanoparticle GuCOSS, which displayed effective cellular uptake in HeLa cells. As competitors in the field of cationic delivery modules, peptides P14 and P17, both optimized concerning their ability to facilitate cellular uptake of PNA, should serve as reference. In addition to guanidine-mediated uptake, arginine-free CPP $(KF_2)_3K$, which has shown good overall efficacy in prokaryotic systems, should also be included. Additionally, the non-cationic DiSeL, relying on an entirely different uptake mechanism, was chosen. In order to obtain results that allow the comparison of the different platforms in a quantitative fashion, the eGFP654 mis-splicing correction assay should be performed. Beside the efficacy of the employed carrier systems, their cytotoxic profile has to be evaluated.

Since simultaneous investigations of Dr. Bastian Becker revealed the potential of multimerized CPP L17E on a dextran platform, this novel scaffold was also investigated for PNA delivery. Furthermore, this hybrid system should be employed in an alternative functional assay to evaluate its general applicability. Thus, the novel polysaccharide architecture was to be adapted for the splitGFP assay, which is based on cytoplasmic recombination of an intracellularly delivered peptide fragment with its non-functional GFP counterpart. Thereby, the cytotoxicity of the L17E-dextran delivery system should also be investigated.

3.2 Modular Dextran-Streptavidin Hybrids

With regard to the effectiveness of dextran as multimerization scaffold for bioactive peptides, this platform could be combined with streptavidin to expand its spectrum of potential applications. Combining high affinity for its ligand with four binding sites, streptavidin has great potential to serve as centerpiece for a modular system. Thereby, biotinylated dextran decorated with various different effector molecules, such as CPPs and receptor-targeting peptides, could be combined with any biotin-bearing species on streptavidin as core structure. Consequently, this approach could reduce the required synthesis effort to interconnect functionalized dextran with variable cargo.

Concerning the issue of successful intracellular delivery of biomacromolecules, the novel dextran-streptavidin approach could serve multiple purposes. Since streptavidin is a protein with a molecular weight of ~60 kDa, it can be used as cargo molecule for intracellular delivery facilitated by CPP-decorated dextran. To that end, CPPs should be multimerized on biotinylated dextran and subsequently attached to fluorescently labeled streptavidin for uptake experiments. Furthermore, the intracellular delivery of the fluorescent protein eGFP, interconnected to CPP-decorated dextran *via* streptavidin, should be investigated to evaluate the potential of this modular approach. These studies should also include beside microscopic investigations of cellular uptake in mammalian cells also the impact of CPP multimerization on their cytotoxic profile.

Multimerization of DR5TP is essential for its ability to neutralize tumor cells. Former studies involving DR5TP-decorated dextran revealed a correlation between number of peptides per dextran polymer and its efficacy towards sensitive COLO205 cells. Thereby, further improvement was observed upon dimerization on human Fc as centerpiece. By employing the dextran-streptavidin approach, the potential increase of efficacy regarding the number of dextran molecules per streptavidin could be investigated. The assembly of this hybrid polysaccharide-protein architecture under stochiometric control allows for a convenient variation.

In addition to the targeting of DR5, which was already successfully addressed by DR5TP-decorated dextran and should result in direct killing of COLO205 cells, integrins were chosen as alternative target due to their pivotal role development and progression. Successful receptor-targeting *via* RGD-functionalized dextran-streptavidin hybrids could pave the way for more complex architectures comprising additional payload, such as cytotoxins, for efficient cargo delivery and subsequent killing of integrin-overexpressing cells.

4 Results and Discussion

4.1 Comparative Studies of Multiple Platforms for Intracellular Delivery of PNA

4.1.1 Design and Synthesis of the PNA-Module Hybrids

This project was focused on the evaluation of various platforms in their capabilities to facilitate intracellular delivery of covalently attached bioactive PNA. With regard to results that enable the quantitative comparison of the different delivery modules, the HeLa-eGFP654 mis-splicing correction assay was chosen. This functional assay is based on the restoration of correct splicing of eGFP upon blocking an aberrant splice site with an 18mer PNA oligonucleotide.[211] Consequently, the fluorescence of functional eGFP correlates with the level of PNA in the nuclei of the modified HeLa cells.

In order to obtain the PNA-module hybrids with a covalent linkage between the oligonucleotide and its uptake-mediating counterparts (**Figure 17**), the synthesis pathway must be designed carefully. The 18mer PNA oligonucleotide is accessible by solid-phase synthesis, whereby a *C*-terminally located lysine residue was introduced to improve the solubility of the resulting oligomer. Furthermore, *N*-terminal modification with either a chemical handle for subsequent conjugation to a delivery module or successive SPPS allows for the synthesis of CPP-PNA conjugates.

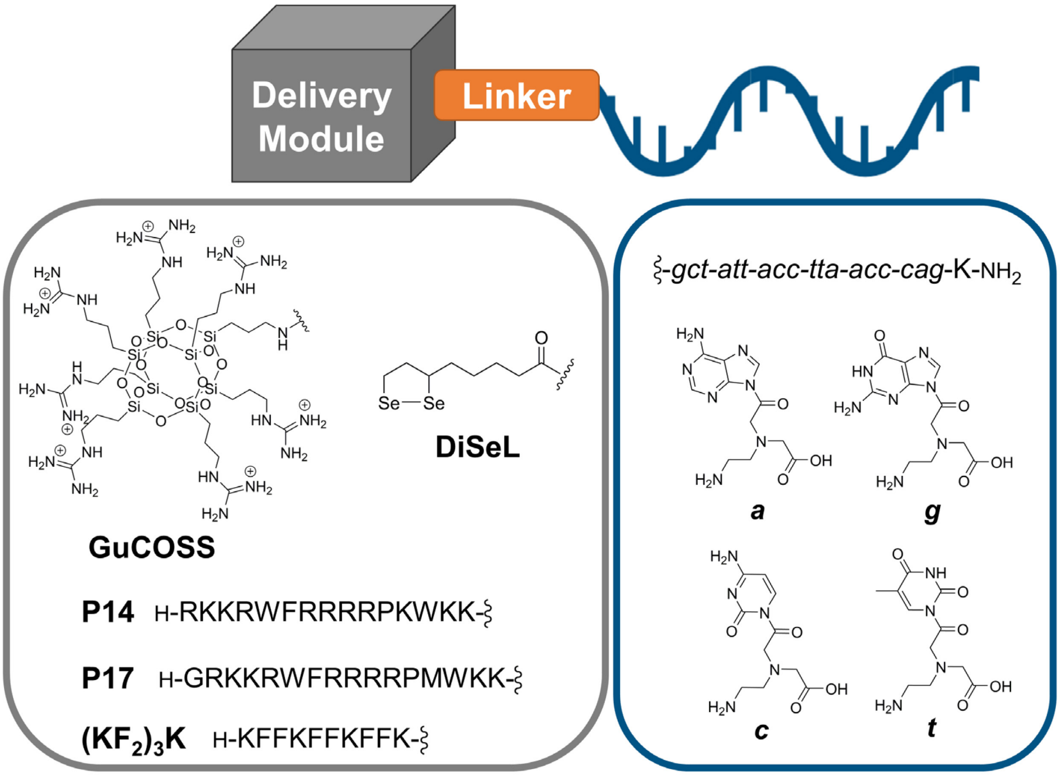

Figure 17 | General structure of the PNA-module hybrids with the respective delivery modules (gray box) and the 18mer PNA oligonucleotide with the corresponding PNA monomers (blue box).

This project initially addressed the evaluation of GuCOSS for intracellular delivery of PNA as covalently attached payload, utilizing the HeLa-eGFP654 mis-splicing correction assay. Originating from their amine-bearing precursor, which already facilitated intracellular delivery of various payloads, these guanidinylated nanoparticles have excelled as efficient delivery modules. In order to obtain the desired GuCOSS-PNA hybrids, a synthesis strategy had to be utilized that would allow efficient conjugation of GuCOSS to its PNA counterpart.

Several conjugation methods that involved the COSS framework, such as disulfide or amide bond formation or CuAAC have been employed in the past.[128, 135] Since earlier studies with GuCOSS-PNA hybrids in the working group displayed the feasibility of linking both parts *via* thiol-maleimide chemistry,[213] this strategy was also employed in the current work. To that end, both GuCOSS and PNA have to be functionalized with a thiol moiety, followed by the introduction of a bismaleimide linker **1** and subsequent interconnection (**Scheme 3**).

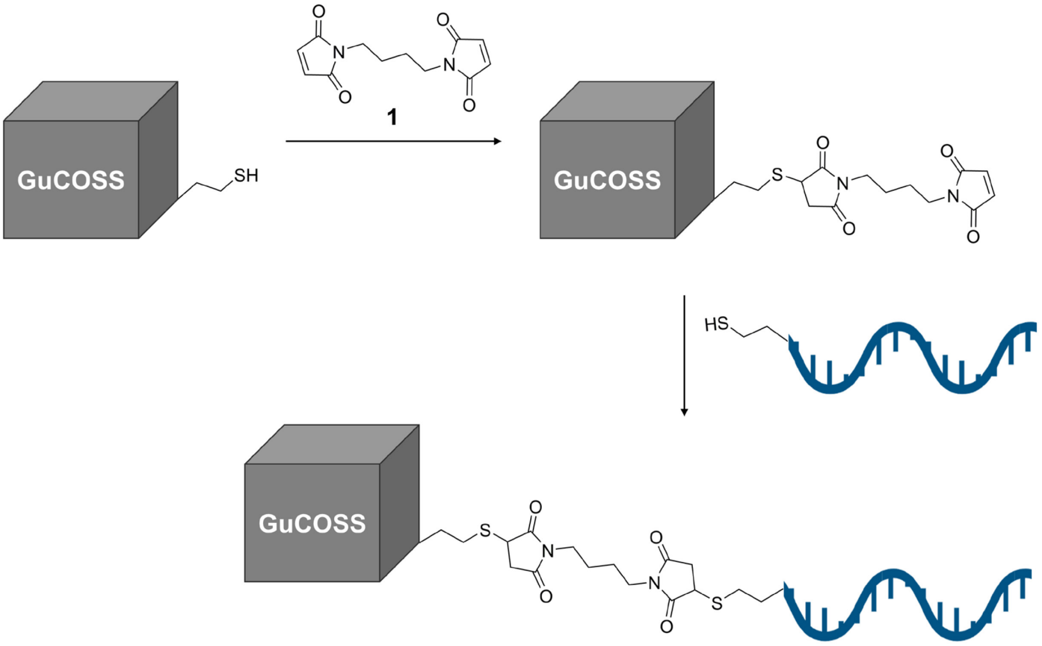

Scheme 3| General approach to GuCOSS-PNA hybrids comprising a bismaleimide linker.

Moreover, only a few adjustments are required to obtain GuCOSS-PNA hybrids comprising disulfide bonds, which are labile under reducing conditions, thus allowing for the cytosolic release of the cargo. While disulfide formation between GuCOSS and PNA could be easily realized by incubating both components in an oxidative environment, a more sophisticated strategy is preferable to avoid homodimerization. To that end, thiol-bearing GuCOSS can be modified *via* aldrithiol activation with 2,2´-dithiopyridine **2**; the resulting mixed disulfide only reacts with unmodified thiols.

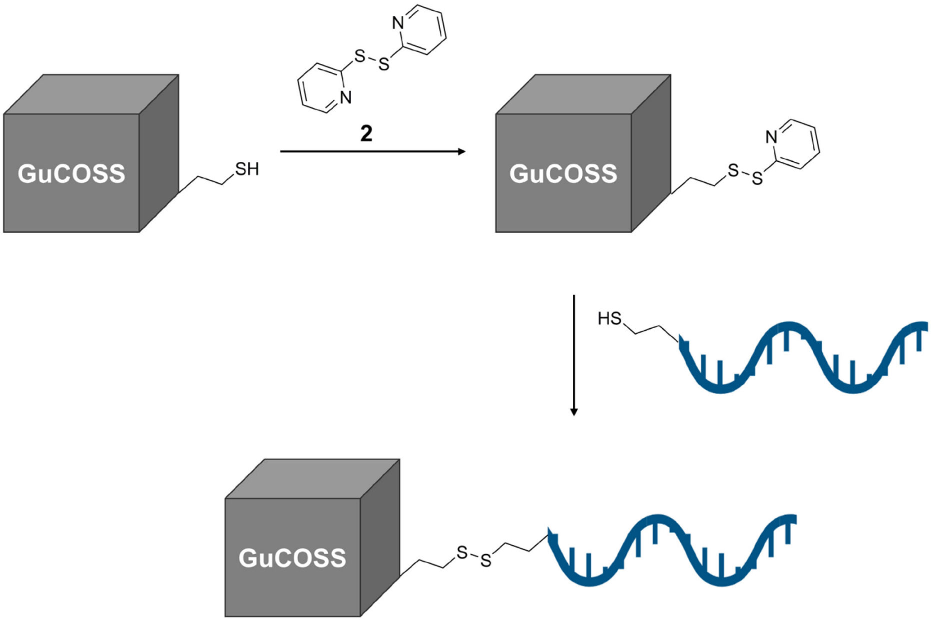

Scheme 4| Synthetic approach towards GuCOSS-PNA conjugates connected *via* disulfide bond.

The synthetic route towards thiol-modified GuCOSS started with single-corner modification of commercially available amine-bearing COSS derivative **3** according to the literature.[135] Thereby, trityl (Trt)-protected acid **5** was introduced as linker *via* amide bond formation in dimethylsulfoxide (DMSO) under anhydrous conditions to prevent hydrolysis of the COSS framework. Thereby, COSS derivative **3** was used in excess to mitigate multiple coupling of the acid. Beside the protection of the thiol moiety from unwanted side-reactions, the Trt protecting group further serves as hydrophobic anchor for subsequent purification of product **6** by reverse phase chromatography. In contrast to earlier studies involving GuCOSS-PNA conjugates in our working group, an additional β-alanine spacer was incorporated to increase the distance between GuCOSS and its polymeric cargo.

In the next step, the remaining seven amine groups were guanidinylated to afford GuCOSS nanoparticles. To that end, COSS derivative **6** was treated with 1*H*-pyrazole-1-carboxamidine hydrochloride **7** according to the literature[128]. Thereby, a large excess of guanidinylating agent **7** was used and the reaction was performed for three days to ensure complete conversion of the amine groups. Analogously to the previous reaction, the reaction was performed in DMSO under anhydrous conditions to avoid degradation of the silsesquioxane framework. After chromatographic isolation of GuCOSS derivative **8**, the Trt protecting group was removed under acidic conditions to obtain thiol bearing GuCOSS **9**.

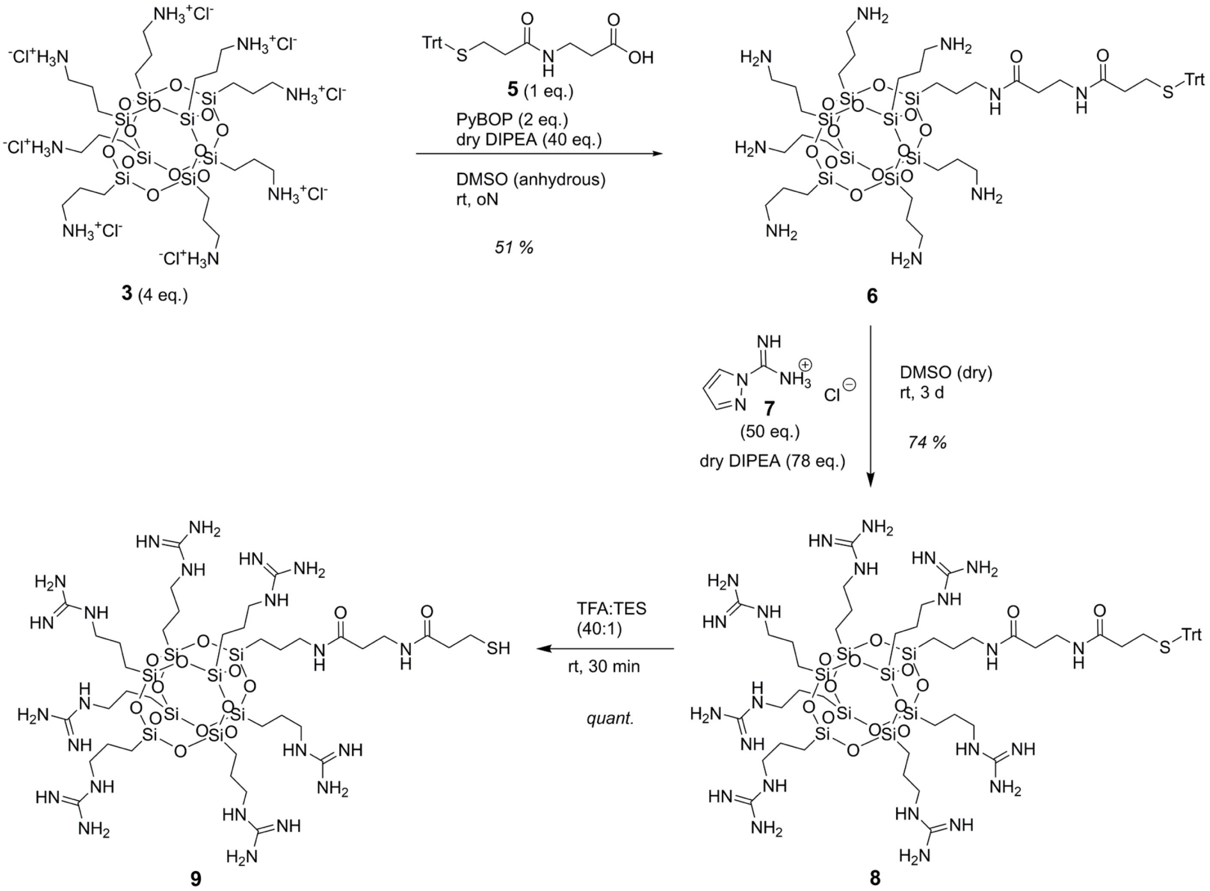

Scheme 5| Synthetic pathway leading to thiol bearing GuCOSS **9**. In the first step, linker **5** wass introduced to amine-functionalized COSS derivative **3** *via* amide bond formation. Subsequent guanidinylation of the remaining amine groups afforded GuCOSS **8**. In the final step, acidic cleavage of the Trt-protecting group yielded the target compound **9**.

In the next step, GuCOSS derivative **9** was modified for the subsequent conjugation to the PNA oligonucleotide by disulfide bond formation and thiol-maleimide reaction, respectively. To that end, bismaleimide linker **1** was coupled to GuCOSS **9**, whereby the linker was employed in excess to prevent homodimerization and, furthermore, the reaction was carried out under inert atmosphere to minimize thiol oxidation (**Scheme 6**). Aldrithiol-activation was conducted by treating GuCOSS **9** with 2,2′-dithiopyridine **2** in excess under acidic aqueous conditions in argon atmosphere (**Scheme 6**). Both maleimide-functionalized GuCOSS **10** and aldrithiol-activated GuCOSS **11** were purified by semi-preparative HPLC.

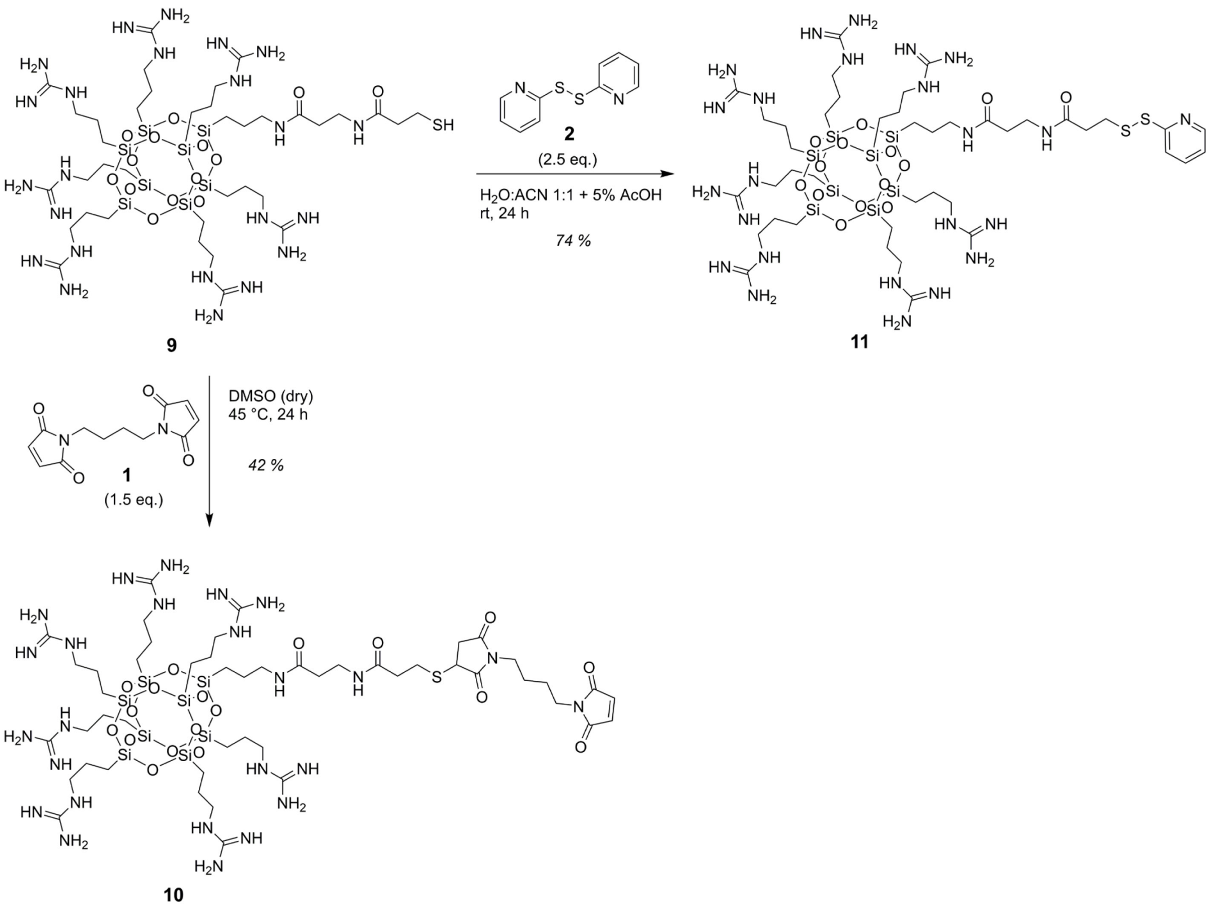

Scheme 6| Aldrithiol activation of GuCOSS **9** to afford GuCOSS derivative **11** and synthesis of maleimide-functionalized GuCOSS **10**.

The PNA oligonucleotide **12** suited for conjugation to the GuCOSS derivatives was synthesized by solid-phase synthesis using Fmoc/Bhoc strategy. As mentioned before, lysine was introduced *C*-terminally as solubility enhancer and, additionally, a thiol moiety in the shape of 3-mercaptopropionic acid was introduced at the *N*-terminus. The assembly of GuCOSS-PNA conjugate **13** interconnected by thioether bonds was performed under inert atmosphere in anhydrous DMSO. Initially, the reaction of both constituents in an equimolar ratio led to incomplete consumption of PNA **12**, wherefore the reaction was prolonged with an additional equivalent GuCOSS **10**. GuCOSS-PNA conjugate **14** comprising a disulfide bond was obtained under similar reaction conditions, whereby aldrithiol-activated GuCOSS **11** was employed in a slight excess.

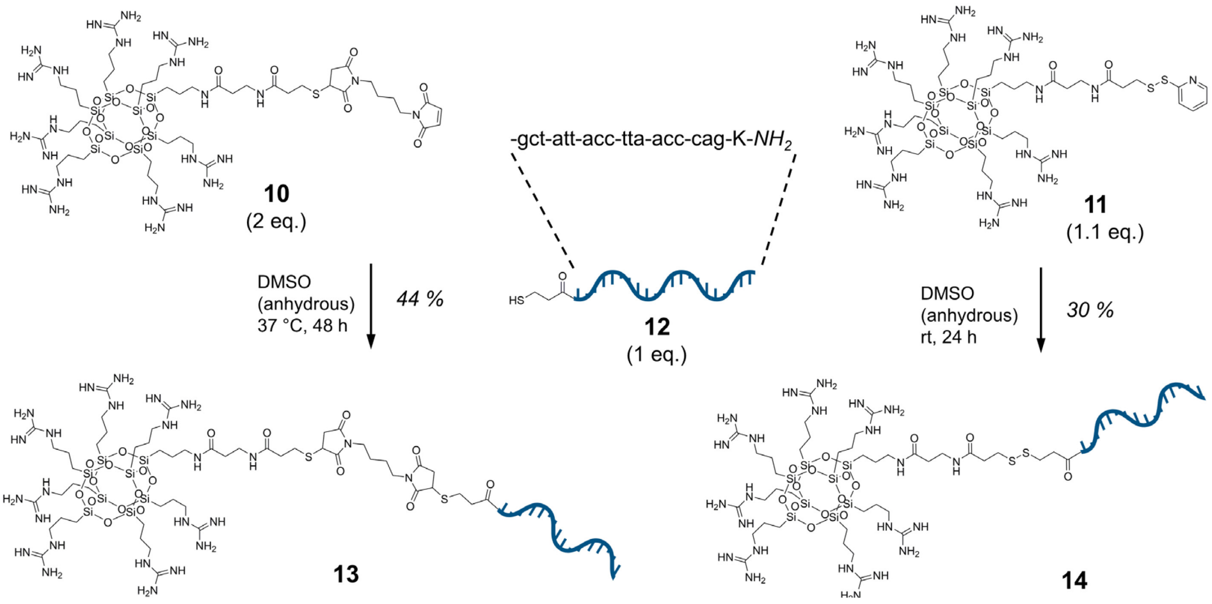

Scheme 7| Synthesis of GuCOSS-PNA conjugates **13** and **14**, interconnected by thioether and disulfide bond, respectively.

Following the successful preparation of the GuCOSS-PNA hybrids, three CPP-PNA conjugates should be synthesized that would allow for comparison of the delivery systems in the quantitative mis-splicing assay. P14 and P17, optimized for the delivery of an 18mer PNA into HeLa cells,[210] were chosen as archetypical members of arginine-rich peptides. Additionally, the arginine-free $(KF_2)_3K$ peptide was selected as an efficient PNA delivery module in prokaryotic systems.[214] In contrast to the GuCOSS-PNA hybrids, the synthesis of the CPP-PNA conjugates could be conducted entirely by solid-phase synthesis. An additional spacer, 8-amino-3,6-dioxaoctanoic acid (O2Oc, **15**), was inserted between PNA and CPP. Both $(KF_2)_3K$-PNA **16** and P17-PNA **17** were synthesized by Dr. Hendrik Schneider in the working group.

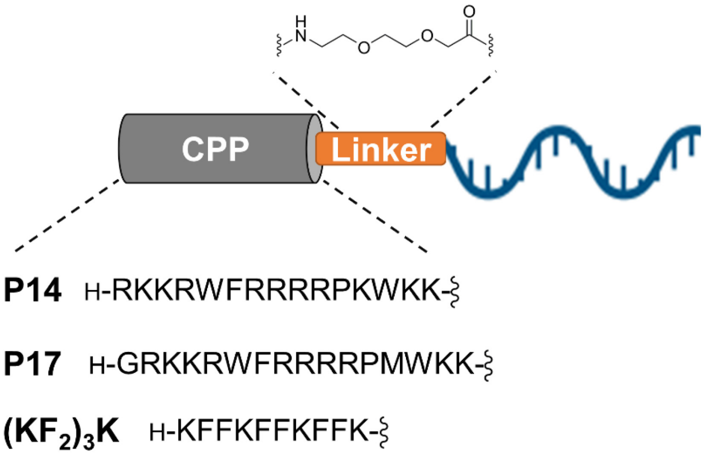

Figure 18| Structure of synthesized CPP-PNA conjugates with CPP sequence and O2Oc linker.

As mentioned previously (section **2.2.3.3**), the performance of cationic delivery vehicles in *in vivo* applications is most likely limited due to electrostatic interactions with endogenous biomacromolecules. Therefore, transporters based on alternative mechanisms for cell entry, such as “thiol-mediated uptake”, have been developed. Amongst other representatives of this particular class, cyclic diselenide DiSeL **20** displayed promising results for cytoplasmic delivery of large cargo molecules.[215] Contrary to its cationic competitors, DiSeL **20** undergoes rapid exchange reactions with exofacial thiols on the cell surface to enter the cytoplasm. Inspired by published data, displaying cytosolic delivery of Sav facilitated by a single copy of the cyclic diselenide,[215] we aimed to investigate whether the 18mer PNA would also benefit from covalently attached DiSeL **20**. To that end, DiSeL **20** should be synthesized and subsequently coupled to the *N*-terminus of the cargo PNA. DiSeL **20** is synthetically accessible by a three-step process (**Scheme 8**) according to the literature.[216] Thereby, the ester ethyl-6,8-dichlorooctanoate **19** was initially hydrolyzed under alkaline conditions in aqueous ethanol. Following this, the cyclization by selenylation was accomplished by addition of sodium diselenide. The instability of this inorganic compound towards air oxidation necessitated its *in situ* generation (**Scheme 8**). Thus, powdered selenium was reduced with sodium borohydride in water under argon atmosphere to generate sodium hydrogen selenide. After the vigorous gas formation had subsided, further selenium was added to obtain sodium diselenide. The resulting dark solution was transferred to the former reaction for selenylation and then acidified to precipitate the product as a dark brown solid. The presence of side products required additional purification steps, i.e., extraction with tetrahydrofuran and silica chromatography, further contributing to the poor yield of 8 %.

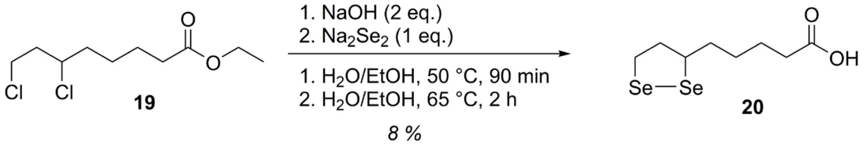

In situ generation of sodium diselenide:

$$4\,NaBH_4 + 2\,Se + 7\,H_2O \longrightarrow 2\,NaHSe + Na_2B_4O_7 + 14\,H_2$$

$$Na_2B_4O_7 + 2\,NaHSe + 2\,Se + 5\,H_2O \longrightarrow 2\,Na_2Se_2 + 4\,H_3BO_3$$

Scheme 8: Synthesis of DiSel **20** using ethyl-6,8-dichlorooctanoate **19** as starting material and *in situ* generation of sodium diselenide by reduction of selenium with sodium borohydride.

Following this, the 18mer PNA could be functionalized with DiSel **19**. The most straightforward strategy, coupling the cyclic diselenide to the *N*-terminus of the PNA on a solid support followed by TFA-mediated cleavage, seemed feasible because DiSel **19** was stable in acidic conditions during its synthesis. Analogously to the CPP-PNA conjugates, an O2Oc spacer was introduced. The *N*-terminal conjugation of DiSel **19** was performed by amide bond formation using *N*,*N*-diisopropylcarbodiimide (DIC) and Oxyma (**Scheme 9**). Cleavage from solid support was performed in aq. TFA in absence of triethylsilane (TES) to prevent reduction of the diselenide. Analysis of purified DiSel-PNA conjugate **22** revealed the presence of an M+16 species with an estimated percentage of 30 % according to the area under curve (**Figure S 32**), indicating oxidation of the product during synthesis and/or purification. Since post-hoc reduction of the oxidized impurity could lead to cleavage of the diselenide and the subsequent formation of intermolecular diselenide bonds, the product was used in the mis-splicing assay without further treatment.

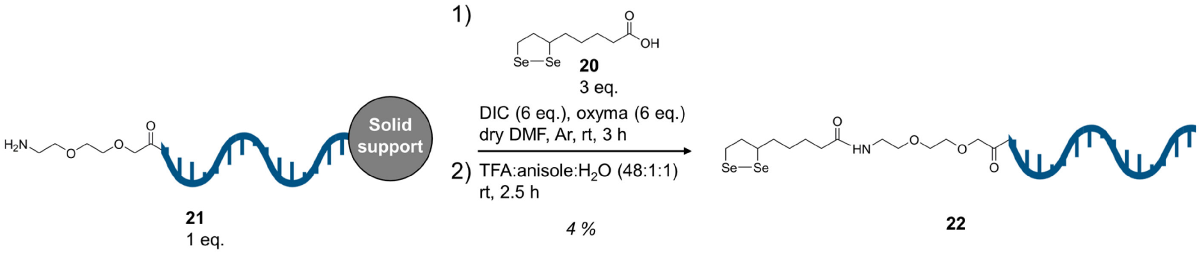

Scheme 9| *N*-terminal conjugation of DiSel **20** to O2Oc-functionalized 18mer PNA **21** on solid support, followed by TFA-mediated cleavage.

4.1.2 Evaluation of PNA-Module Hybrids in Biological Assays

Initially, both GuCOSS-PNA hybrids **13** and **14**, comprising a stable thioether linkage and reductively labile disulfide bond, respectively, were tested against each other in the HeLa-eGFP654 mis-splicing assay. To that end, HeLa-eGFP654 cells were treated with different concentrations of **13** and **14** in serum-free medium for 30 min. Thereby, the incubation was performed at either 37 °C or 4 °C to estimate the contribution of energy-dependent endocytosis on the overall uptake of the GuCOSS-PNA hybrids. After treating the cells with the compounds, the cells were incubated for further 24 h in serum-containing medium at 37 °C and subsequently trypsinized. Analysis by flow cytometry revealed that both GuCOSS-PNA hybrids induced a shift in eGFP fluorescence at a concentration of 20 µM, whereas no difference between solitary PNA **12** and cells treated only with phosphate-buffered saline (PBS) could be observed (**Figure 19**). These findings clearly highlight the necessity of a delivery module for successful cytosolic translocation of PNA. Furthermore, both GuCOSS-PNA hybrids were also able to increase eGFP fluorescence at 4 °C, suggesting, at least in part, an energy-independent uptake pathway. However, it should be noted that specific inhibitors would be required to investigate the influence of endocytosis more precisely and in greater detail. While lower temperatures reduce or inhibit the rate of endocytosis,[210] warm up of the samples during the experimental procedure could influence the cytosolic uptake and, hence, eGFP-fluorescence.

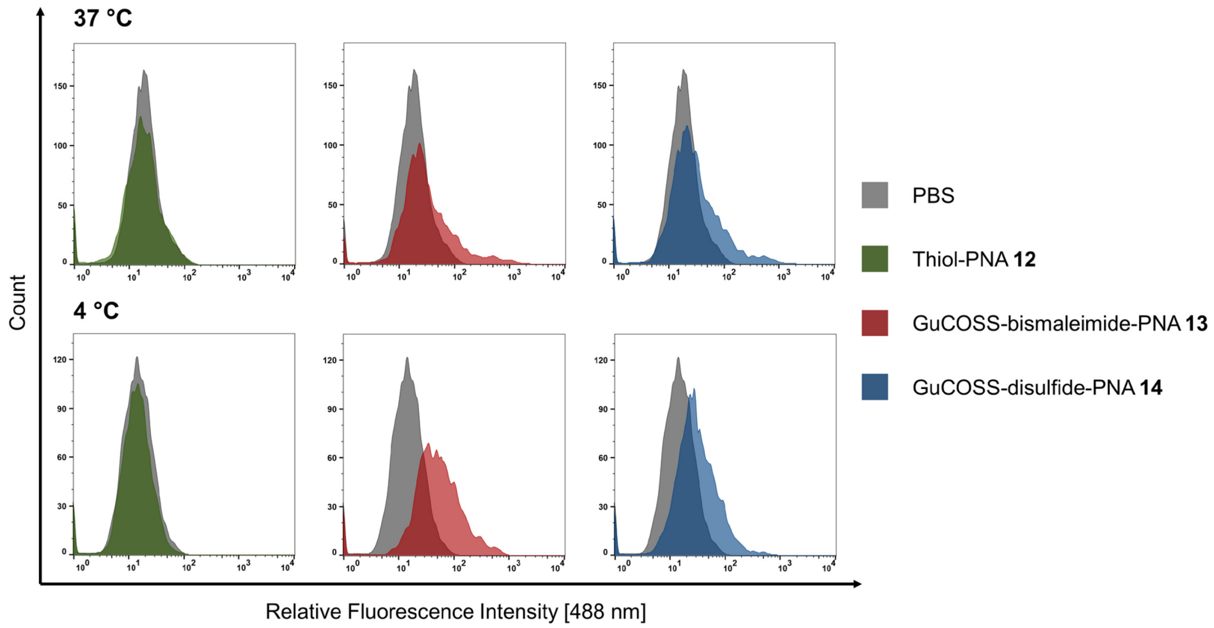

Figure 19| Flow cytometric analysis of HeLa-eGFP654 cells treated with 20 µM thiol-PNA **12** and GuCOSS-PNA conjugates **13** and **14**, respectively, at 4 °C and 37 °C. Grey histograms refer to cells incubated only with PBS at 4 °C and 37 °C.

HeLa-eGFP654 cells were also treated with both GuCOSS-PNA conjugates at lower concentrations. In order to compare the obtained results in a quantitative fashion, the mean fluorescence intensity of viable cells at 488 nm wavelength of each sample was determined. The ratio of the intensity of cells treated with PNA-compounds to the intensity of PBS-treated cells is displayed in **Figure 20**, **B**. Incubation of cells with GuCOSS-PNA conjugates **13** and **14** at lower concentrations than 20 µM did not result in a significant increase of eGFP-fluorescence. Even at 20 µM, only a relatively small population of viable cells shifted towards higher fluorescence (**Figure 19**; **Figure 20**, **B**), which could indicate, that the concentration of GuCOSS-PNA conjugates is not sufficient to effectively facilitate cytoplasmic translocation of its bioactive cargo. Alternatively, the presence of covalently attached GuCOSS in thioether-linked conjugate **13** upon cellular uptake could negatively affect the PNA to hybridize to its target site. In contrast to GuCOSS-PNA conjugate **13**, the reductively labile disulfide bond in compound **14** should be cleaved in the cytoplasm, resulting in the release of thiol-bearing PNA **12**. However, despite the differences in the linker architecture, both GuCOSS-PNA conjugates induced a similar shift in eGFP-fluorescence at 20 µM. This could suggest that translocation of the compounds into cytoplasm plays a more pivotal role than their subsequent mechanism of action.

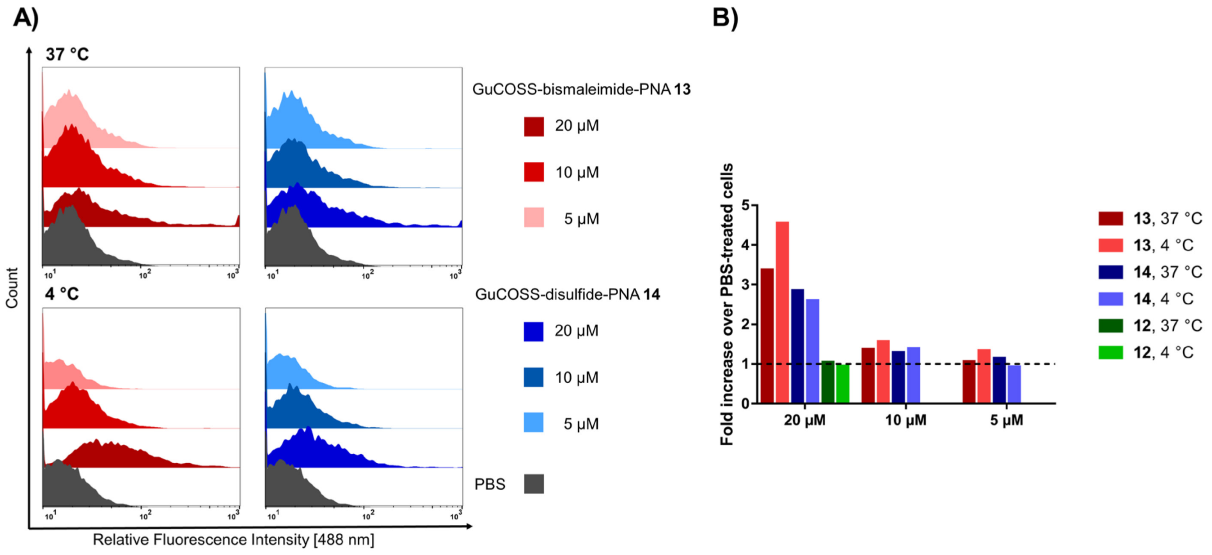

Figure 20| A: Histograms (half offset) of HeLa-eGFP654 cells treated with different concentrations of GuCOSS-PNA conjugates **13** and **14**, respectively, at 4 °C and 37 °C. **B:** Ratio of mean fluorescence intensity of cells treated with PNA-compounds to the intensity of PBS-treated cells, expressed as fold increase over PBS-treated cells.

Next on, the GuCOSS-based PNA delivery approach should be compared to its peptidic competitors. Since both GuCOSS-PNA conjugates gave similar results in the mis-splicing correction assay and the stable thioether linkage of derivative **13** is more similar to the CPP-PNA conjugates comprising the non-cleavable O2Oc linker, only this GuCOSS-PNA compound was employed in the following assays. In advance of the actual experiments, the issue of poor performance of GuCOSS-PNA conjugate **13** in the previous assay was addressed. In order to determine the amount of the conjugate more precisely, the concentration of GuCOSS-PNA conjugate **13** was measured photometrically, using the absorption of the nucleobases at λ = 260 nm (section **6.6.13**). Photometry revealed significantly lower actual concentrations of PNA compared to the initial mass, suggesting the presence of counterions such as TFA and possible weighing errors. Hence, this concentration determination procedure was also performed for the CPP-PNA conjugates.

Following that, HeLa-eGFP654 cells were incubated with GuCOSS-PNA conjugate **13**, P17-PNA **17**, P14-PNA **18** and $(KF_2)_3K$-PNA **16** under the same conditions as in the previous experiment. At 20 µM concentration and 37 °C incubation temperature, every delivery module was able to induce a distinct increase in eGFP-fluorescence (**Figure 21**). Similar results could also be observed at decreased temperature, with exception of $(KF_2)_3K$-PNA **16**, which caused only a minor shift in fluorescence (**Figure 21**). Interestingly, incubation of cells with either P14-PNA **18** or P17-PNA **17** at lower temperature resulted in a larger subpopulation with higher fluorescence compared to cells incubated at 37 °C. These results indicate a predominantly energy-independent uptake of the guanidine-based delivery modules P14, P17 and GuCOSS, whereas $(KF_2)_3K$ presumably relies more heavily on energy-dependent endocytosis to enter the cells.

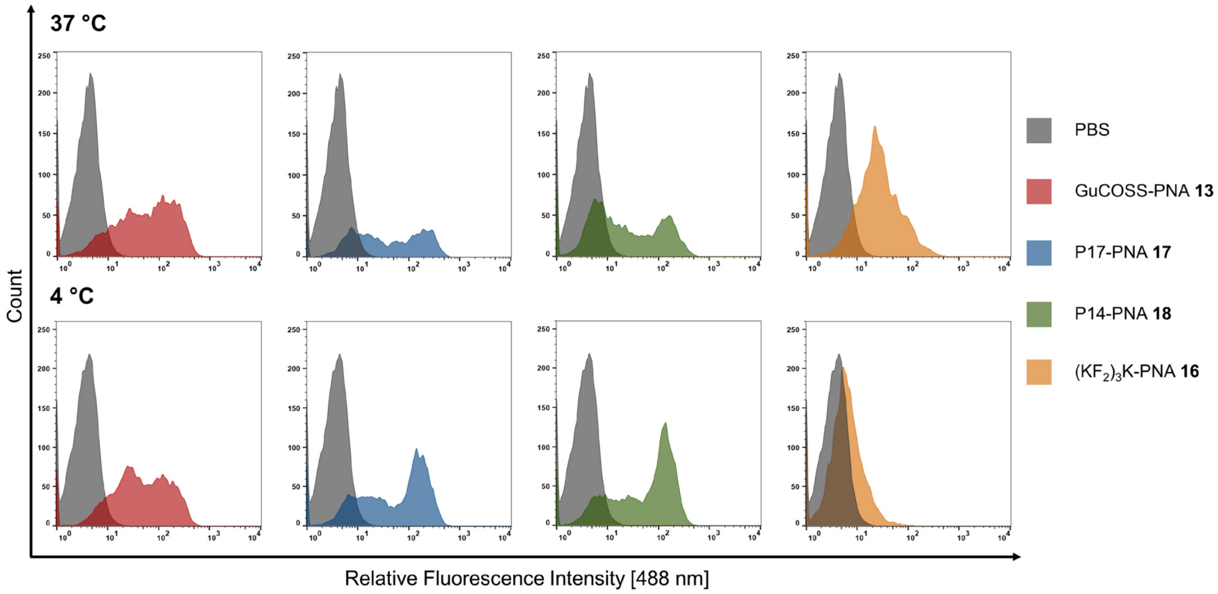

Figure 21| Flow cytometric analysis of HeLa-eGFP654 cells incubated with 20 µM GuCOSS-bismaleimide-PNA **13**, P17-PNA **17**, P14-PNA **18** and $(KF_2)_3$K-PNA **16** at 37 °C and 4 °C.

At 20 µM and 37 °C, GuCOSS is slightly better than its peptidic competitors P14 and P17 (**Figure 22**). At lower concentrations, however, the efficacy of the silicon nanoparticle rapidly declined, whereas both peptides induced increased fluorescence down to a concentration of 5 µM. Thereby, as was already reported in the literature,[210] P17 outperforms P14 by a slight margin independent from concentration and temperature. Both GuCOSS and $(KF_2)_3$K require high concentrations to deliver PNA efficiently, whereby temperature plays a pivotal role for the performance of $(KF_2)_3$K. These findings suggest for GuCOSS that a certain threshold concentration is required that enables its translocation into the target nucleus *via* energy-independent pathways.

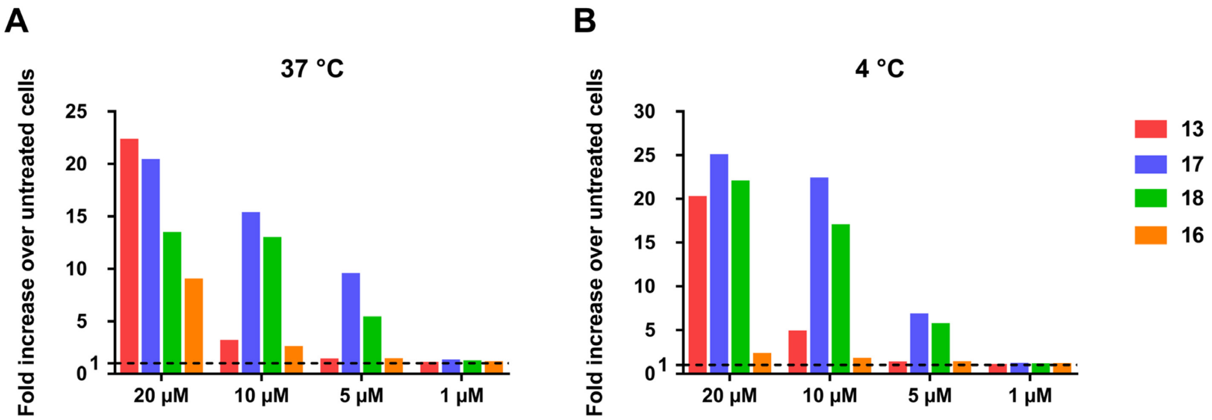

Figure 22| Ratio of mean fluorescence intensity of cells treated with PNA-compounds (GuCOSS-bismaleimide-PNA **13**, P17-PNA **17**, P14-PNA **18** and $(KF_2)_3$K-PNA **16**) to the intensity of PBS-treated cells at 37 °C (**A**) and 4 °C (**B**).

After evaluation of the delivery modules in the mis-splicing correction assay, their cytotoxic profile was investigated using the MTS assay. Unmodified HeLa cells were used because the presence of eGFP could interfere with the formazan dye employed in the proliferation assay, as both absorb light at a wavelength of 490 nm. Cells were treated with the compounds for 30 min in absence of serum, followed by further 24 h in serum-containing medium. The guanidine-rich delivery modules display cytotoxicity at concentrations higher than 10 µM, whereby no significant difference was observed (**Figure 23**). At 20 µM, all three transporters exhibit moderate cytotoxicity, suggesting for GuCOSS that significant enhancement of eGFP fluorescence is inevitably associated with cytotoxicity. Both P14 and P17, however, still facilitate intracellular PNA translocation at lower concentrations without causing side effects. In contrast to its guanidine containing competitors, $(KF_2)_3K$ had no negative effect on cell proliferation up to a concentration of 40 µM. Considering the overall low activity of this CPP in the mis-splicing correction assay, the lack of cytotoxicity may have been the result of low activity toward the cell membrane and subsequent uptake.

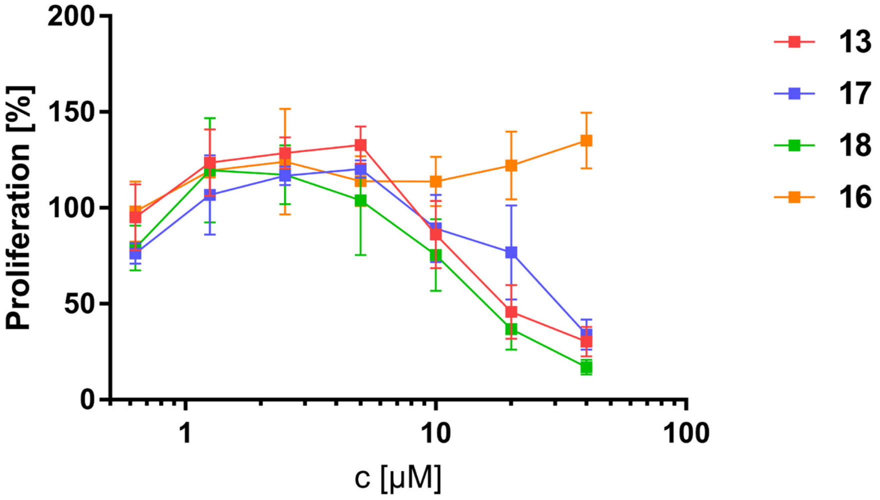

Figure 23| Cell proliferation assay: Unmodified HeLa cells were treated with GuCOSS-bismaleimide-PNA **13**, P17-PNA **17**, P14-PNA **18** and $(KF_2)_3K$-PNA **16** for 30 min in medium only, followed by further 24 h in serum-containing medium. Results are shown as the mean ± standard error of the mean and are based on triplicates.

After testing the delivery modules relying on positive charges to facilitate cellular uptake, thiol-reactive DiSel was also evaluated in the mis-splicing correction assay. In addition to DiSel-PNA **22**, P17-PNA **17** was employed as the best performing delivery module in the previous assay. Considering the long incubation time of DiSel-modified cargo reported in the literature,[215] HeLa-eGFP654 cells were incubated with DiSel-PNA **22** for 4 h, followed by further 22 h in medium only. Flow cytometry revealed that DiSel did not enhance eGFP fluorescence at concentrations of 20 µM and 10 µM, whereas P17 once again induced a strong shift in fluorescence at 20 µM. Parallel projects involving DiSel-mediated intracellular delivery displayed only low performance for fluorophores as payload, whereas no uptake could be observed for protein cargo (data not shown). Furthermore, these experiments revealed serious solubility issues in aqueous media, which was also observed during the mis-splicing correction assay. However, it should be noted that an oxidized by-product was present in DiSel-PNA **22**, which accounted for 30% according to HPLC analysis.

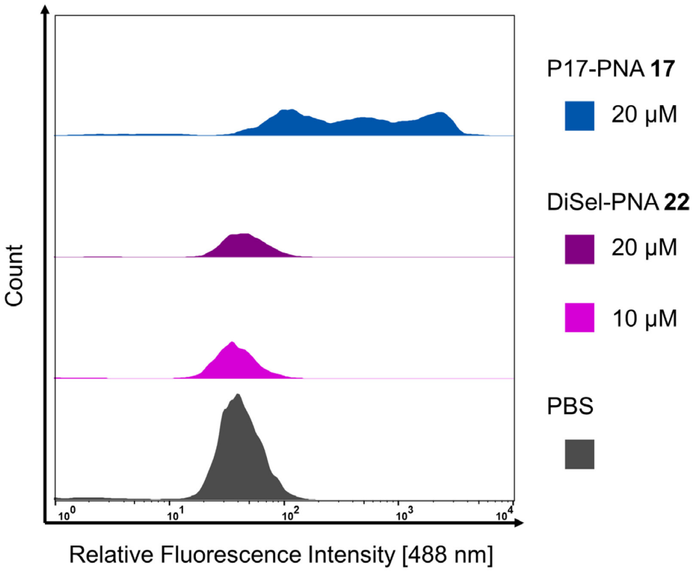

Figure 24| Histogram (half offset) of HeLa-eGFP654 cells treated with DiSel-PNA **22** or P17-PNA **17** at 37 °C.

Numerous strategies have been presented in the literature to develop novel delivery systems or to improve existing ones, such as the synthetic molecular evolution approach that resulted in P14 and P17 optimized for translocation of PNA into mammalian cells.[210] In parallel with the synthesis and evaluation of delivery modules directly conjugated to the mis-splicing correcting PNA, my colleague Dr. Bastian Becker investigated the effect of CPP-multimerization on the polysaccharide dextran as scaffold. He established dextran decorated with multiple copies of the M-lycotoxin variant L17E as an efficient architecture for intracellular delivery of covalently attached cargoes.[217] In search of payload that would confirm cytosolic and even nuclear uptake in frame of a functional assay, we decided to investigate intracellular delivery of PNA employing the L17E-dextran carrier. To that end, thiol-modified PNA **12** was conjugated by Dr. Bastian Becker to maleimide-functionalized dextran in presence of an equimolar amount of L17E-Cys, resulting in the dextran-(L17E)$_{5.3}$-(PNA)$_{5.3}$ conjugate **23** (**Figure 25, A**). HeLa-eGFP654 cells were treated under identical conditions as described before, however, after incubation with the dextran conjugate **23** for 30 min, an additional washing step with low-pH glycine buffer was performed to remove membrane-bound substance. Flow cytometric analysis displayed substantial enhancement of eGFP-fluorescence at concentrations ranging from 20 μM down to even 2.5 μM (**Figure 25, B**). Despite its complexity and size, with a molecular weight of about 50 kDa, this construct not only entered the nucleus, but was furthermore able to interact with its target RNA and correct mis-splicing.

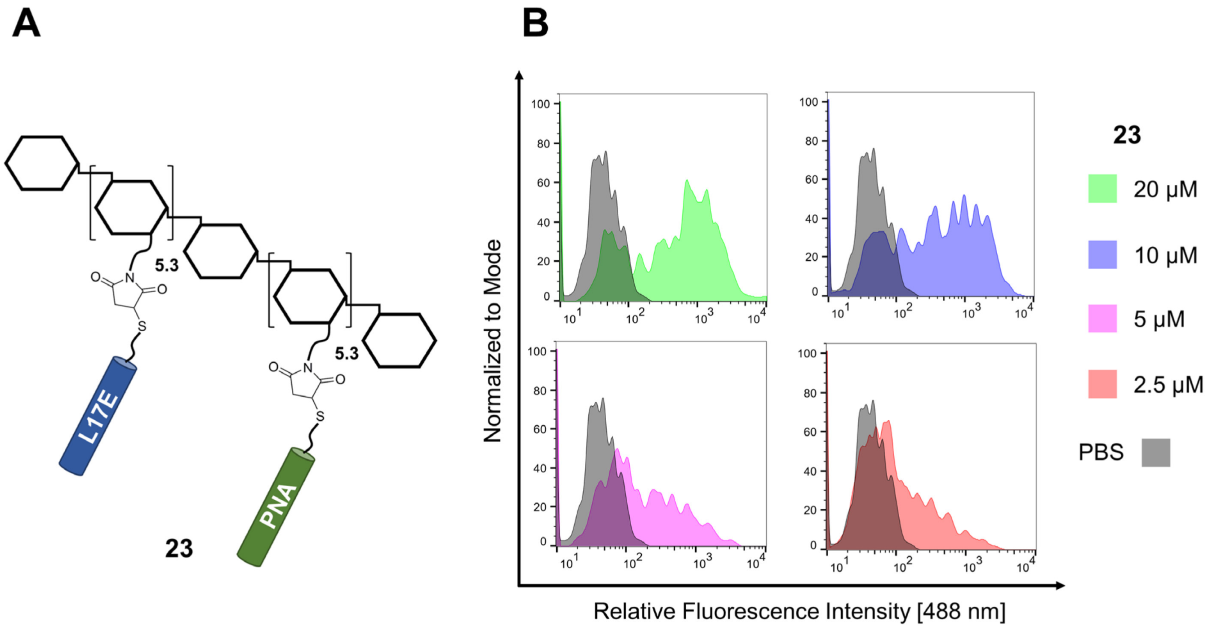

Figure 25| A: Schematic depiction of dextran-(L17E)$_{5.3}$-(PNA)$_{5.3}$ conjugate **23**. **B:** Histograms of HeLa-eGFP654 cells incubated with different concentrations of dextran-(L17E)$_{5.3}$-(PNA)$_{5.3}$ conjugate **23** at 37 °C. Adapted from Becker *et al.*[218].

4.2 Evaluation of L17E-Decorated Dextran in the Split-GFP Complementation Assay

4.2.1 Design and Synthesis

Due to the remarkable performance of dextran-L17E in the mis-splicing correction assay, the architecture should be subjected to further testing. Considering that the biological function of the delivered cargo is of greater importance for potential therapeutic applications of delivery modules than simple translocation through the cellular membrane, an additional functional assay, the GFP-complementation assay, was chosen. This assay is based on non-covalent hybridization of the 16mer peptide GFP 11, the *C*-terminal β-strand of GFP, to the nonfluorescent fragment protein GFP 1-10 resulting in the recovery of fluorescence.[219] Thus, cytoplasmic delivery of exogenous GFP 11 with a delivery module should increase GFP-fluorescence of genetically modified cells producing GFP 1-10 (**Figure 26**, **A**). Indeed, this approach has been employed frequently to validate and quantify CPP-mediated translocation of GFP 11.[210] In order to investigate dextran-L17E as transporter for GFP11 in the GFP-complementation assay, dextran polysaccharide had to be modified accordingly. In a similar geometry as described for the assembly of dextran-(L17E)$_{5.3}$-(PNA)$_{5.3}$ conjugate **23**, both L17E and GFP11 should be covalently attached to the repeating units of dextran (**Figure 26**, **B**). In addition to the peptides, the introduction of the fluorophore TAMRA at the reducing end of the polysaccharide should further confirm cellular uptake by microscopy and flow cytometry.

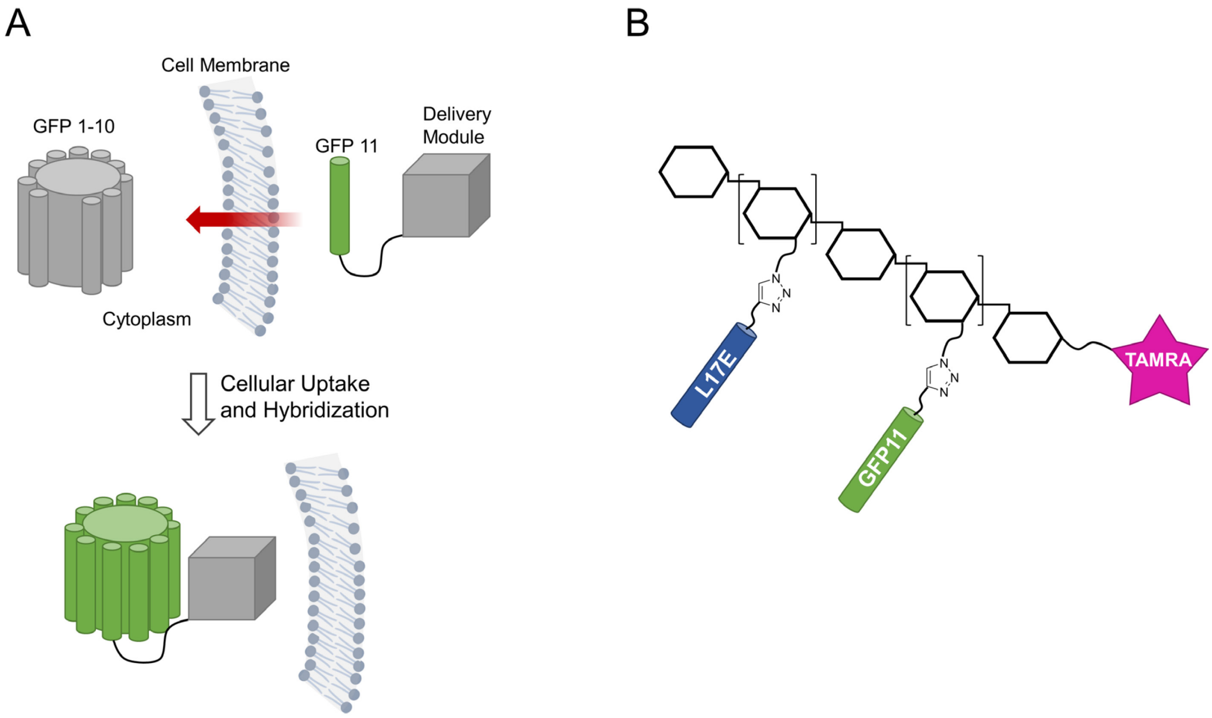

Figure 26| A: Illustration of the GFP-complementation assay. Non-fluorescent intracellular GFP 1-10 hybridizes with exogenous GFP11 to form functional GFP. Figure adapted from Cabantous *et al.*[220] **B:** Schematic depiction of dextran modified with both L17E and GFP11 at the repeating units and an additional fluorophore label at the reducing end.

The preparation of dextran as scaffold for the fluorophore TAMRA at its reducing end and L17E and GFP 11 at the repeating units followed protocols well established in our working group.[29, 42] In the first step, the reducing end of 10 kDa dextran **24** from *Leuconostoc mesenteroides* was functionalized *via* reductive amination. Thereby, an amine forms a Schiff base with the open aldehyde form of the terminal glucose unit, which is subsequently reduced to obtain an irreversible bond between dextran and its amine-bearing counterpart. To enable later conjugation of TAMRA to the reducing end *via* amide bond formation, *N*-Boc-cadaverine with a protected second amine functionality was employed. The reductive amination was performed with a large excess of *N*-Boc-cadaverine in borate buffer at pH 8.2 with sodium cyanoborohydride as reducing agent (**Scheme 10**).[42, 221] After conducting the reaction for three days to maximize functionalization of the reducing end, the product **25** was isolated by precipitation in methanol and subsequent purification by size-exclusion chromatography (SEC).

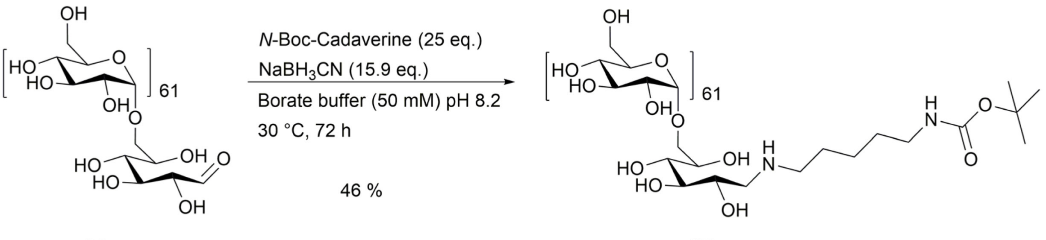

24 **25**

Scheme 10| Introduction of *N*-Boc-cadaverine at the reducing end of dextran *via* reductive amination.

The product was analyzed by NMR analysis as described in the literature.[42] Briefly, the integral of the anomeric protons **1** was set to 62 corresponding to the average number of glucose monomers in 10 kDa dextran (**Figure 27**). The integral of the signals assigned to the aliphatic chain of *N*-Boc-cadaverine, protons **2**-**6**, as well as the singlet originating from the Boc-protecting group, protons **7**, indicated quantitative functionalization of the reducing end.

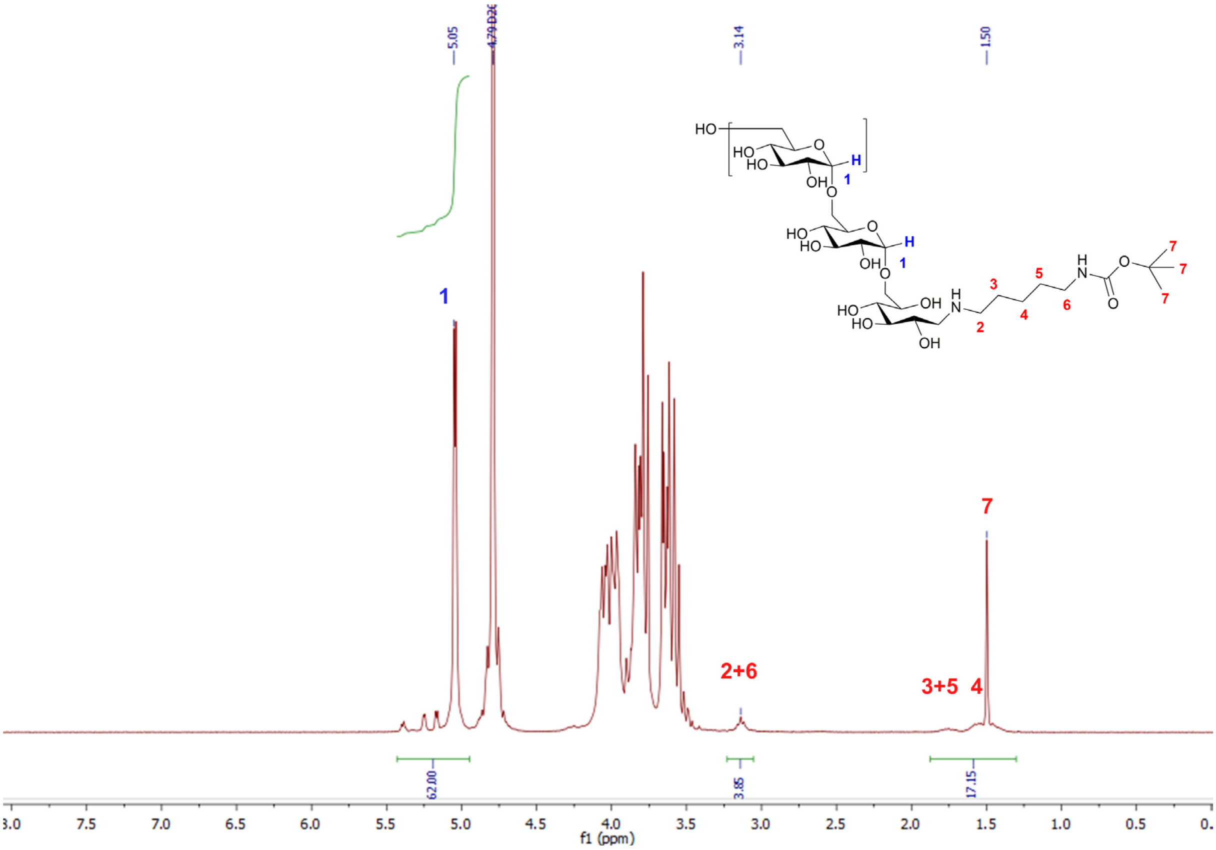

Figure 27| ^{1}H NMR spectrum of *N*-Boc-cadaverine-dextran **25:** The ratio of anomeric protons **1** to the protons of *N*-Boc-cadaverine (**2**-**7**) displayed successful functionalization of the reducing end.

In the next step, carboxyl groups were introduced into the dextran scaffold by carboxyethylation, a reaction that takes place exclusively at the C-2 position of the glucose subunits.[51] Thereby, the hydroxyl groups at C-2 position are alkylated by acrylamide, followed by hydrolysis of the amide moieties to afford the carboxylates. In addition to site-specific functionalization, this synthetic approach also allows regulation of the introduced carboxyethyl groups by the amount of acrylamide used, whereby 2.5 equivalents acrylamide yielded approximately one carboxylate residue. [42, 51] The reaction was performed under basic aqueous conditions at 30 °C for 24 h, followed by further 24 h at elevated temperature (**Scheme 11**). Product **26** was obtained after precipitation in methanol, neutralization of the carboxyl groups and purification by SEC. Low amounts of employed acrylamide afforded the product **26** with only 5.4 carboxyethyl groups per dextran on average. This was intended to minimize possible cytotoxic effects of the final product as a consequence of the number of L17E peptides attached to the polysaccharide as well as solubility issues experienced with the GFP 11 peptide.

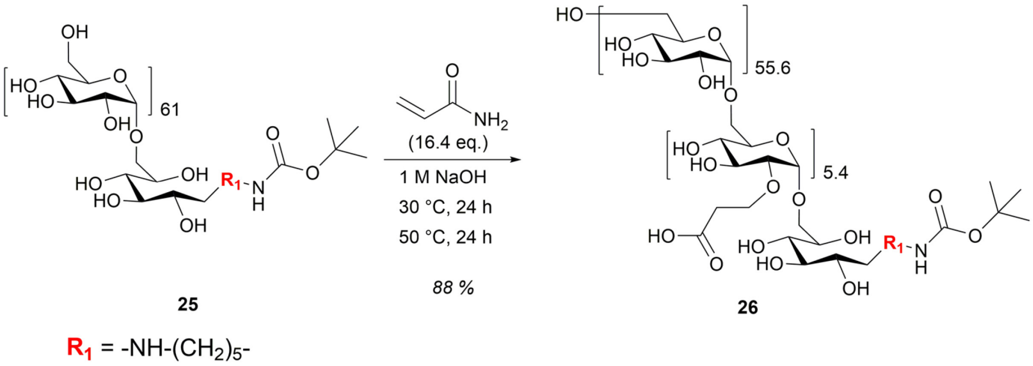

Scheme 11| Carboxyethylation of *N*-Boc-cadaverine-dextran **25**.

Quantification of introduced carboxyethyl groups was performed by NMR spectroscopy as described in the literature. [42, 51] The signal of both protons **8** in the spectrum was used to determine the number of carboxyethyl groups, which is half of the integral, i.e., approximately 6 groups per dextran (**Figure 28**). The aforementioned 5.4 carboxyethyl groups per dextran refer to analysis of the azide-functionalized dextran **29** with removed Boc-protecting group at the reducing end (**Figure 29, B**; **Equation 1**). The changing number of carboxyethyl groups as observed by NMR spectroscopy might be the result of impurities present in the product *N*-Boc-cadaverine-dextran-$CE_{5.4}$ **26**. Furthermore, the integral of *N*-Boc-cadaverine at the reducing end was also lower after carboxyethylation compared to the analysis of *N*-Boc-cadaverine-dextran **25** (**Figure 27**). This indicates the presence of either unreacted *N*-Boc-cadaverine in the product or incomplete reduction of the labile imine formed between the linker and the reducing end. As a consequence, one can assume that only approximately 80% of dextran was equipped with *N*-Boc-cadaverine at the reducing end.

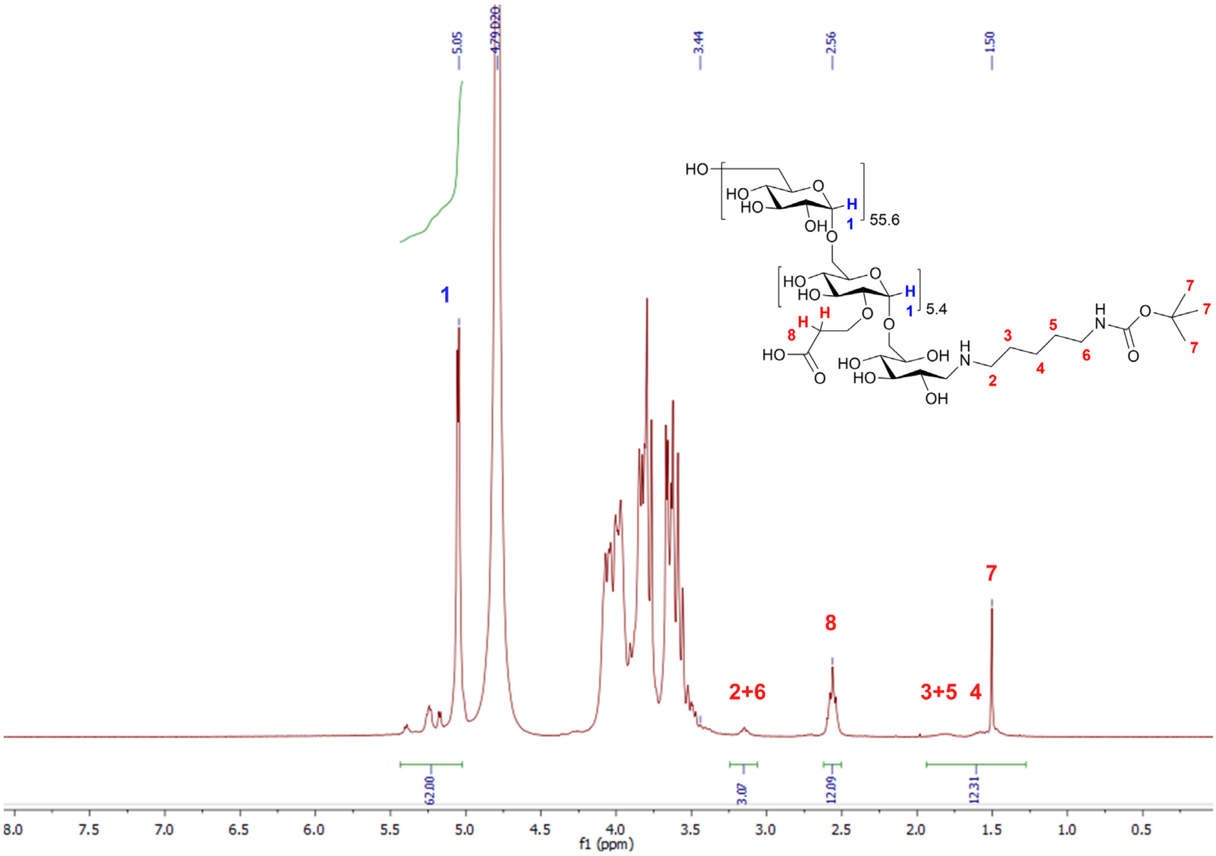

Figure 28| ^{1}H NMR of *N*-Boc-cadaverine-dextran-CE$_{5.4}$ **26**. Please note that for sake of simplification, the product is referred to as dextran with 5.4 carboxyethyl groups as determined after azide-functionalization and unmasking of the reducing end (vide infra).

For the subsequent conjugation of the peptides to the dextran scaffold by copper-catalyzed "click" reaction, azide-functionalities had to be introduced at the carboxyethyl groups. This was done by amide bond formation using bifunctional *N*-(5-aminopentyl)-2-azidoacetamide **27** as linker, comprising cadaverine as spacer to increase the distance between the peptides and dextran backbone. Conjugation of the linker to *N*-Boc-cadaverine-dextran-CE$_{5.4}$ **26** was performed using EEDQ as coupling reagent in a mixture of water and acetonitrile (**Scheme 12**).[29, 42] After isolation of the product *N*-Boc-cadaverine-dextran-(N$_3$)$_{5.4}$ **28** by precipitation and SEC-purification, the acid-labile Boc protecting group at the reducing end was removed by treatment with TFA (**Scheme 12**).

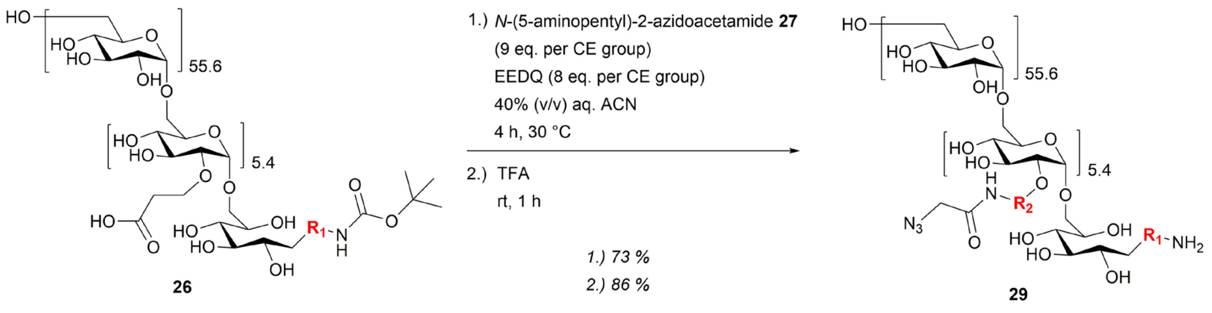

R_1 = -NH-(CH$_2$)$_5$-
R_2 = -(CH$_2$)$_2$-CO-NH-(CH$_2$)$_5$-

Scheme 12| EEDQ-mediated conjugation of azide-linker **27** to *N*-Boc-cadaverine-dextran-CE$_{5.4}$ **26**, followed by TFA-mediated removal of the Boc-protecting group at the reducing end.

The success of azide-functionalization of dextran **28** and following Boc-removal was quantified by NMR spectroscopy. Analysis of *N*-Boc-cadaverine-dextran-(N$_3$)$_{5.4}$ **28** (**Figure 29**, **A**) revealed an increase of the integrals of protons **2**+**6**, **3**+**5** and **4** in relation to the anomeric proton **1** due to an overlap of signals originating from *N*-Boc-cadaverine and the azide linker **27**, respectively. Subsequent TFA-mediated cleavage of the Boc-protecting group at the reducing end resulted in the disappearance of the singlet of protons **7** (**Figure 29**, **B**).

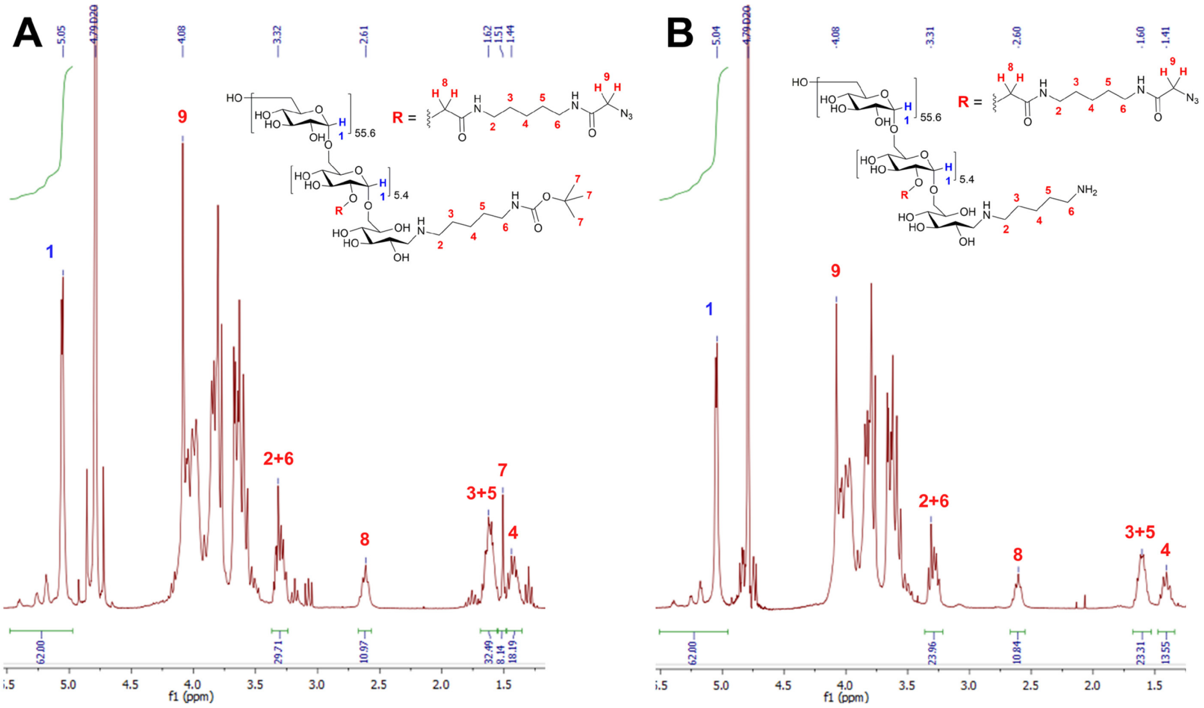

Figure 29| A: ^{1}H NMR of *N*-Boc-cadaverine-dextran-(N$_3$)$_{5.4}$ **28**. **B**: ^{1}H NMR of *N*-cadaverine-dextran-(N$_3$)$_{5.4}$ **29** upon acidic removal of the terminal protecting group.

The exact number of a covalently attached linker **27** was calculated as mean of the individual signals originating from the azide linker **27** and *N*-cadaverine at the reducing end, respectively, as described in the literature:[217]

$$\frac{N_3\ groups}{Dextran}=\frac{\frac{(\mathbf{2}+\mathbf{6})_{(total-red.end)}}{4}+\frac{(\mathbf{8})_{total}}{2}+\frac{(\mathbf{3}+\mathbf{5})_{(total-red.end)}}{4}+\frac{(\mathbf{4})_{(total-red.end)}}{2}}{4} \qquad (\mathbf{1})$$

Thereby, the integrals derived from *N*-cadaverine-dextran-$(N_3)_{5.4}$ **29** (**Figure 29**, **B**) were used and the degree of reducing end-functionalization, i.e., approximately 80%, was considered:

$$\frac{N_3-groups}{Dextran}=\frac{\frac{23.96-3.2}{4}+\frac{10.84}{2}+\frac{23.31-3.2}{4}+\frac{13.55-1.6}{2}}{4}\approx 5.4$$

Following the TFA-mediated removal of the Boc-protecting group at the reducing end, TAMRA was conjugated to *N*-cadaverine-dextran-$(N_3)_{5.4}$ **29** as fluorescent label for later microscopy or flow cytometry. This was accomplished by using NHS-activated TAMRA **30** and DIPEA in DMSO under anhydrous conditions to minimize premature hydrolysis of the NHS ester (**Scheme 13**). After isolation of TAMRA-cadaverine-dextran-$(N_3)_{5.4}$ **31**, the product was analyzed by SEC-HPLC and photometry to determine its purity and quantify the amount of fluorophore coupled to the reducing end (see section **6.7.7**). Analysis revealed that approximately 0.78 copies of TAMRA were attached per dextran molecule, which coincides with the number of *N*-Boc-cadaverine present at the reducing end as determined by NMR spectroscopy (**Figure 28**).

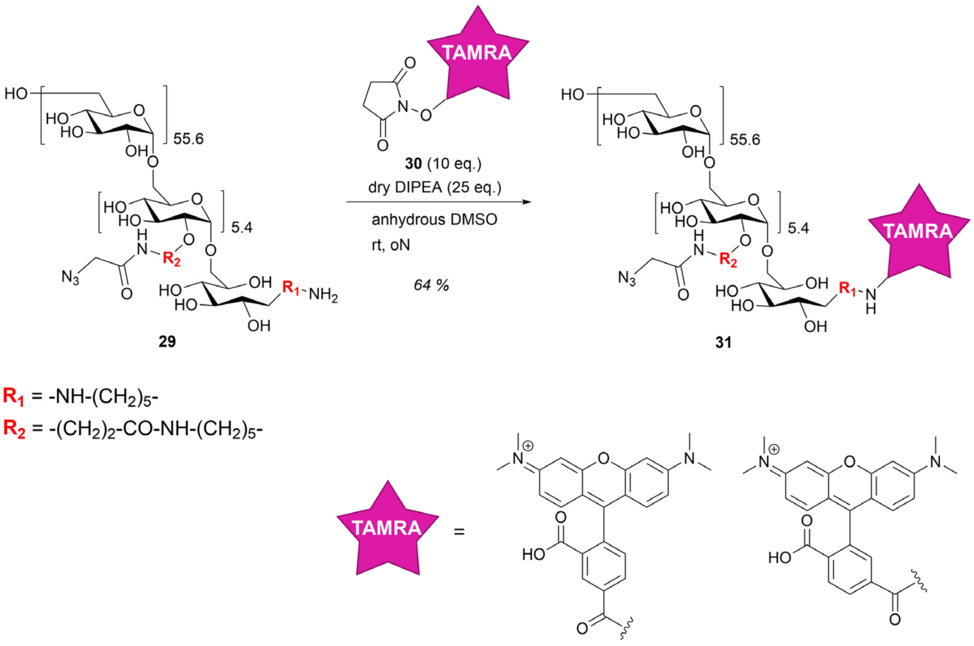

Scheme 13| Introduction of the fluorophore TAMRA at the reducing end of *N*-cadaverine-dextran-$(N_3)_{5.4}$ **29**.

The synthesis of the final dextran hybrid bearing a fluorescent label at the reducing end and the peptides L17E and GFP11 at the repeating units was accomplished by copper-catalyzed “click” reaction. In contrast to the maleimide-thiol reaction used to assemble the dextran-(L17E)$_{5.3}$-(PNA)$_{5.3}$ conjugate **23**, the chemical handles required for CuAAC, i.e., azides and alkynes, are less prone to side reactions. Furthermore, IR-spectroscopy allows for qualitative evaluation of reaction progress by monitoring of the characteristic azide band, which disappears upon reacting to the corresponding triazole.

The peptides bearing alkyne moieties were synthesized by SPPS, whereby L17E was modified *C*-terminally with propargylglycine (Pra) and GFP 11 had an *N*-terminally located 4-pentynoic acid with an additional GSSG tetrapeptide spacer. Conjugation of both peptides to the dextran scaffold was performed using an equimolar ratio of L17E-Pra **32** and alkyne-GFP11 **33** (**Scheme 14**). Since preliminary synthesis attempts revealed low solubility of alkyne-GFP 11 **33** under aqueous conditions, DMSO was used as co-solvent. Furthermore, the reaction was performed with 2-(4-((bis((1-(tert-butyl)-1H-1,2,3-triazol-4-yl)methyl)amino)methyl)-1*H*-1,2,3-triazol-1-yl)acetic acid (BTTAA, **Scheme 14**) as Cu(I) chelator, which stabilizes the catalytic ion and accelerates the reaction rate.[222] The reaction was conducted in phosphate buffer at pH 7.5 to counter the drop in pH caused by ascorbic acid and BTTAA. Isolation of TAMRA-cadaverine-dextran-(L17E, GFP 11)$_{5.4}$ **34** was achieved by consecutive SEC-HPLC runs on an analytical scale.

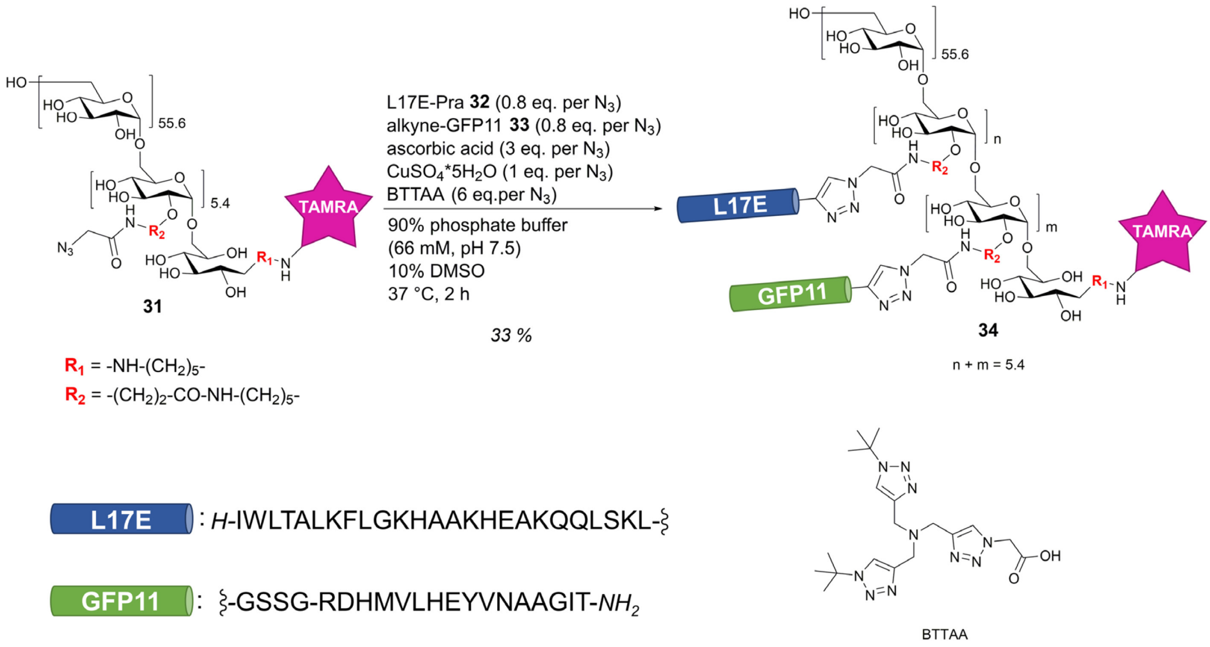

Scheme 14| CuAAC-mediated conjugation of L17E-Pra **32** and alkyne-GFP 11 **33** to TAMRA-cadaverine-dextran-(N$_3$)$_{5.4}$ **31**.

The purified product was analyzed by SEC-HPLC, which displayed a shift towards lower retention time upon functionalization with the peptides compared to the educt, and IR analysis, which revealed the disappearance of the characteristic azide band at wavenumber 2112 cm^{-1}

(**Figure 30**). It is important to note, however, that neither IR-spectroscopy nor SEC-HPLC are suited to determine the ratio of both peptides in the final dextran conjugate. Considering the 0.8 eq. of peptides per azide group, the final construct could be equipped with a particular peptide ranging from 0.2 x 5.4 = 1.08 and 0.8 x 5.4 = 4.32 copies per dextran on average.

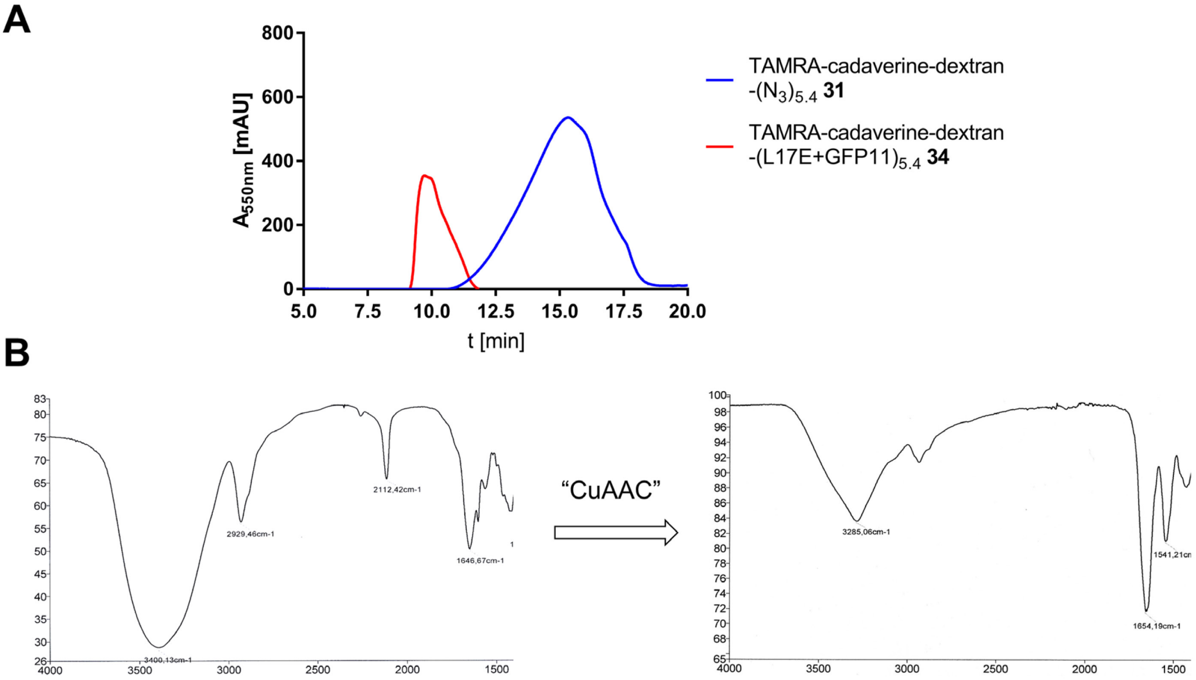

Figure 30| A: Overlay (excerpt) of the chromatographic traces, obtained by SEC-HPLC, of dextran prior and after CuAAC-mediated functionalization. **B**: Excerpt of the IR-spectra of azide-bearing dextran **31** (left) and peptide-decorated dextran **34** (right), displaying the disappearance of the azide band at 2112 cm^{-1}. Please note that for the right spectrum attenuated total reflection (ATR)-IR was employed, contrary to the left spectrum obtained by KBr-pellet based IR spectroscopy.

In addition to dextran peptide hybrid **34** bearing both peptides, a control dextran conjugate lacking uptake-mediating L17E was synthesized. Due to the aforementioned problems with the solubility of GFP 11 in aqueous media and for reasons of comparability, alkyne-GFP 11 **33** was employed in shortage in regard to the number of azide groups present in TAMRA-cadaverine-dextran-$(N_3)_{5.4}$ **31** (**Scheme 15**). SEC-analysis of the isolated product **35** displayed a shift towards lower retention time compared to the educt dextran (**Figure S 52**) and, additionally, IR-spectroscopy showed a diminished azide band (**Figure S 54**).

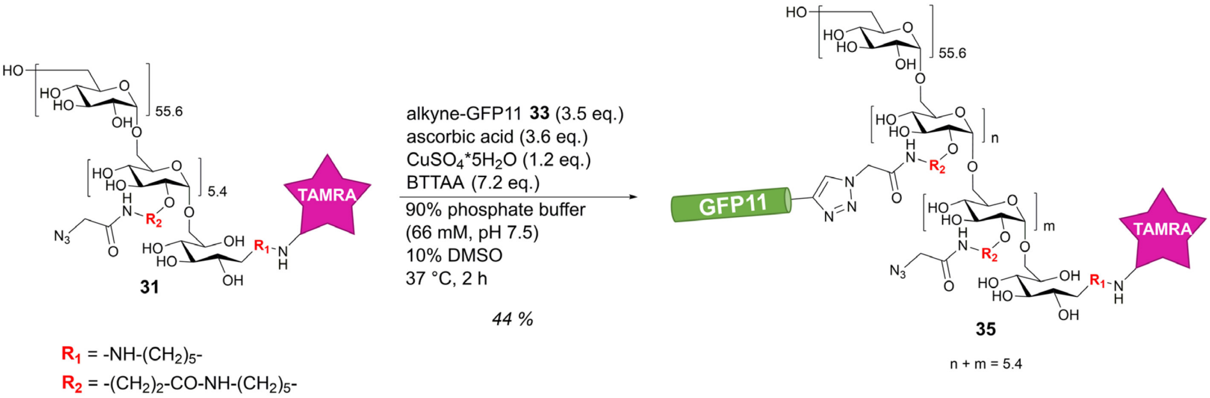

Scheme 15| Synthesis of TAMRA-cadaverine-dextran-GFP 11 **35**. Please note that contrary to the previous reaction, the equivalents refer to the amount of dextran and not its azide moieties. The yield was calculated under the assumption that all 3.5 eq. of alkyne-GFP 11 **33** were coupled to dextran.

4.2.2 GFP-Complementation and Cytotoxicity

HeLa cells stably transfected with GFP 1-10 plasmid were manufactured and maintained by Carolin Dombrowsky in our working group. The general applicability of the dextran-L17E approach for intracellular delivery of GFP 11 peptide and subsequent GFP complementation was initially investigated. To that end, HeLa GFP 1-10 cells were incubated with different concentrations of TAMRA-cadaverine-dextran-(L17E, GFP 11)$_{5.4}$ **34** for 1 h in medium without serum. Afterwards, the cells were incubated for further 24 h in serum-containing medium, followed by trypsinization and FACS analysis. Flow cytometry displayed a concentration-dependent shift in GFP-fluorescence at $\lambda = 488$ nm of cells treated with dextran peptide hybrid **34**, indicating its successful translocation to the cytoplasm and its ability to hybridize to GFP 1-10 (**Figure 31**). However, even at the highest concentration of 10 µM only a modest increase in GFP-fluorescence could be observed in a fraction of cells. This finding suggests that only a subpopulation of the genetically modified HeLa GFP 1-10 cells was susceptible towards GFP 11-induced recovery of fluorescence, possibly indicating partial absence of the plasmid despite continuous incubation of the cells in medium containing the selection marker puromycin. In contrast to the fluorescence at 488 nm excitation wavelength, the cells displayed two orders of magnitude higher TAMRA fluorescence in presence of dextran conjugate **34** compared to untreated cells, even at the lowest concentration of 2.5 µM (**Figure 31**). However, flow cytometry cannot distinguish between fluorescently labeled compounds adhering to the outside of cells and fluorophores located in the interior. In order to investigate the membrane stickiness of TAMRA-labeled dextran, HeLa GFP 1-10 cells were also incubated with TAMRA-cadaverine-dextran-$(N_3)_{5.4}$ **31**, which displayed tenfold lower TAMRA-fluorescence compared to dextran conjugate **34** equipped with L17E (**Figure S 1**).

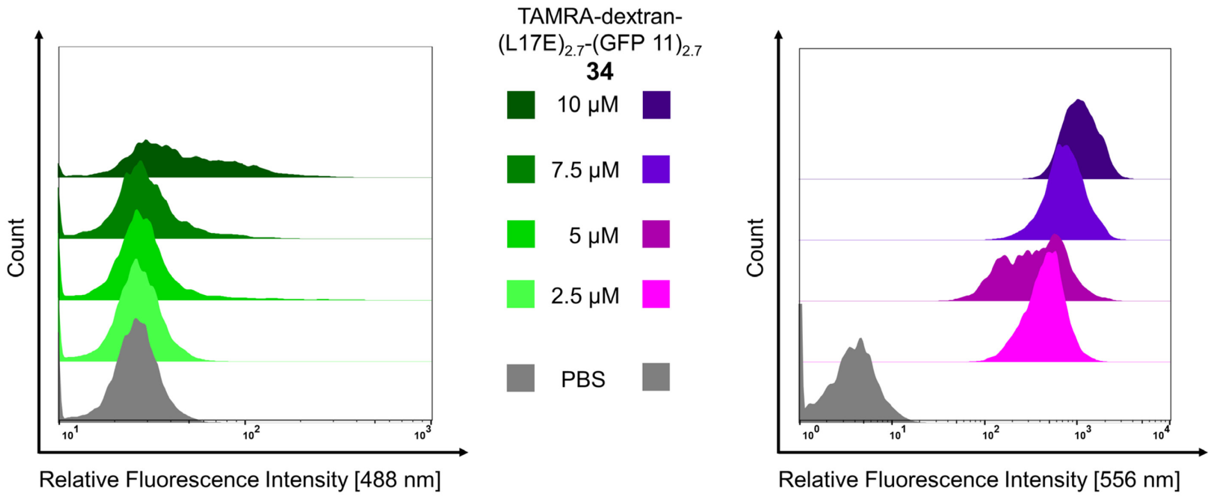

Figure 31| Histograms (half offset) showing GFP-fluorescence (λ = 488 nm) and TAMRA fluorescence (λ = 556 nm) of HeLa GFP 1-10 cells treated with TAMRA-cadaverine-dextran-(L17E, GFP 11)$_{5.4}$ **34** at 37 °C.

For more detailed investigation of the fluorescently labeled dextran peptide hybrid in the GFP complementation assay, confocal laser scanning microscopy (CLSM) was performed. To that end, HeLa GFP 1-10 cells were incubated for 1 h with different samples in absence of serum, followed by further 24 h in serum-containing medium and subsequent analysis by microscopy without fixation.

HeLa GFP 1-10 cells incubated with TAMRA-cadaverine-dextran-(L17E, GFP 11)$_{5.4}$ **34** at 15 µM displayed distinctly increased GFP fluorescence compared to cells treated with PBS only, which exhibited only minor background fluorescence (**Figure 32**). Whereas GFP was relatively evenly distributed in the cytosol (except in the nuclei) when treated with peptide-decorated dextran **34**, TAMRA fluorescence was concentrated in spots and was also absent in the nuclei. While these findings could indicate partial vesicular entrapment of the fluorescently labeled dextran conjugate, increased GFP fluorescence compared to cells treated with PBS clearly highlighted the capability of the peptide dextran architecture to enter the cytoplasm and hybridize to GFP 1-10.

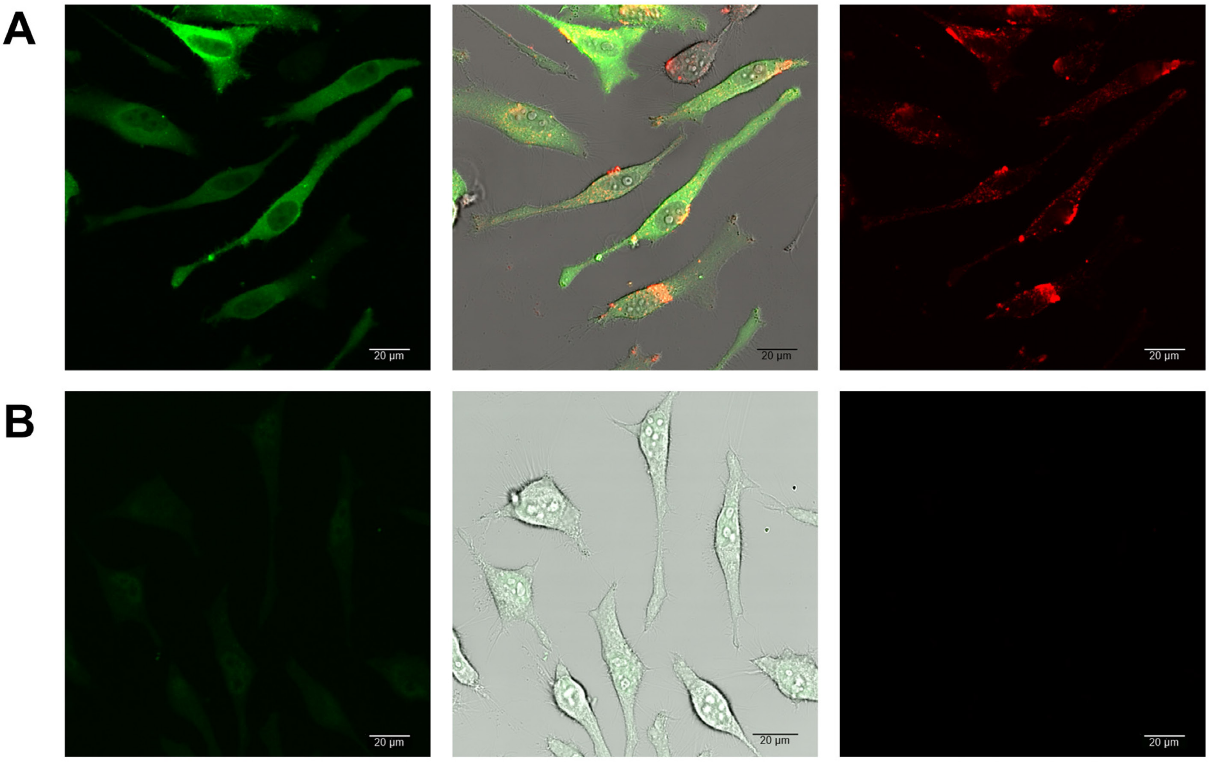

Figure 32| Live-cell CLSM images (20x) of HeLa GFP 1-10 cells treated with TAMRA-cadaverine-dextran-(L17E, GFP 11)$_{2.7}$ **34** at 15 µM (**A**) and PBS (**B**) with the GFP channel (left), TAMRA channel (right) and both fluorescence channels merged with brightfield (center). Adapted from Becker *et al*.[218].

Since FACS analysis (**Figure 31**) gave rise to the assumption that only a fraction of HeLa GFP 1-10 cells was sensitive towards GFP 11-induced GFP complementation, microscopy images comprising a larger number of cells were recorded to investigate this issue. Indeed, while some cells exhibited high levels of GFP, others were only slightly visible in the GFP fluorescence channel (**Figure 33**, **A**). At concentrations of 10 µM, the fluorescently labeled dextran conjugate **34** induced overall distinctly less GFP fluorescence compared to 15 µM, whereby a few cells still contained larger amounts of functional GFP (**Figure 33**, **B**). Nevertheless, widespread intracellular TAMRA fluorescence could be observed even at lower concentration.

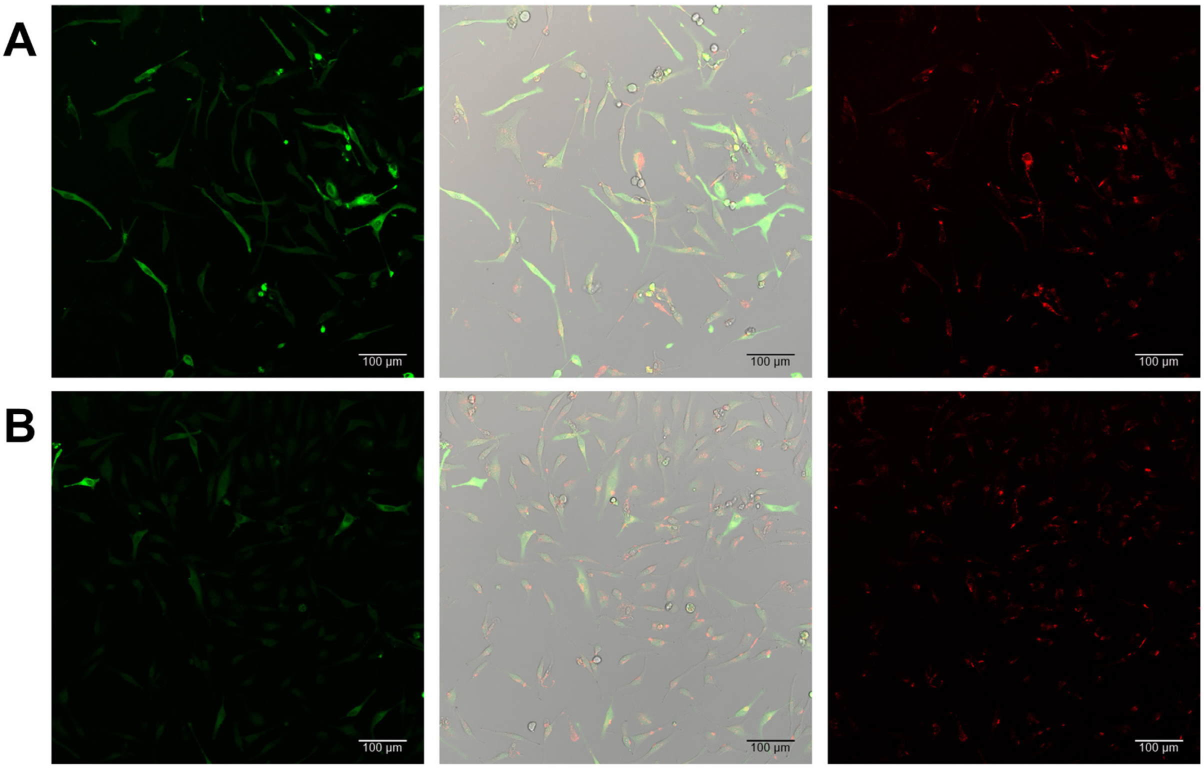

Figure 33| Live-cell wide field CLSM images (20x) of HeLa GFP 1-10 cells treated with TAMRA-cadaverine-dextran-(L17E, GFP 11)$_{5.4}$ **34** at 15 µM (**A**) and 10 µM (**B**) with the GFP channel (left), TAMRA channel (right) and both fluorescence channels merged with brightfield (center). Adapted from Becker *et al.*[218].

To confirm that covalently attached L17E was essential for the cellular uptake of fluorescently labeled dextran decorated with GFP 11 peptide, HeLa GFP 1-10 cells were incubated with the control conjugate **35** at 10 µM. As expected, cells treated with TAMRA-cadaverine-dextran-GFP 11 **35** (**Figure 34**, **A**) did not exhibit increased GFP fluorescence compared to cells treated only with PBS (**Figure 32**, **B**), highlighting the necessity of L17E to enter cytoplasm. Furthermore, no TAMRA could be detected within the cells or bound to the cellular membrane, contrary to elevated TAMRA fluorescence of cells treated with TAMRA-cadaverine-dextran-(N_3)$_{5.4}$ **31** observed during FACS analysis (**Figure S 1**).

L17E was reported to facilitate cellular uptake of various cargo by simple coincubation.[117] To investigate, whether covalent attachment of both L17E and GFP 11 to dextran was required to achieve GFP complementation, HeLa GFP 1-10 cells were treated with a mixture of L17E (synthesized by Dr. Bastian Becker) and GFP 11 **36**. Thereby, both peptides were applied at a concentration of 40.5 µM to yield equal peptide concentrations as present at 15 µM with TAMRA-cadaverine-dextran-(L17E, GFP 11)$_{2.7}$ **34**. HeLa GFP 1-10 cells incubated with the peptide mixture (**Figure 34**, **B**) did not exhibit elevated GFP fluorescence compared to PBS-treated cells (**Figure 32**, **B**). The prerequisite of covalent attachment between L17E and cargo-decorated dextran for successful intracellular translocation was already reported by Dr. Bastian Becker in the case of TAMRA and eGFP as cargo molecules.[217, 218]

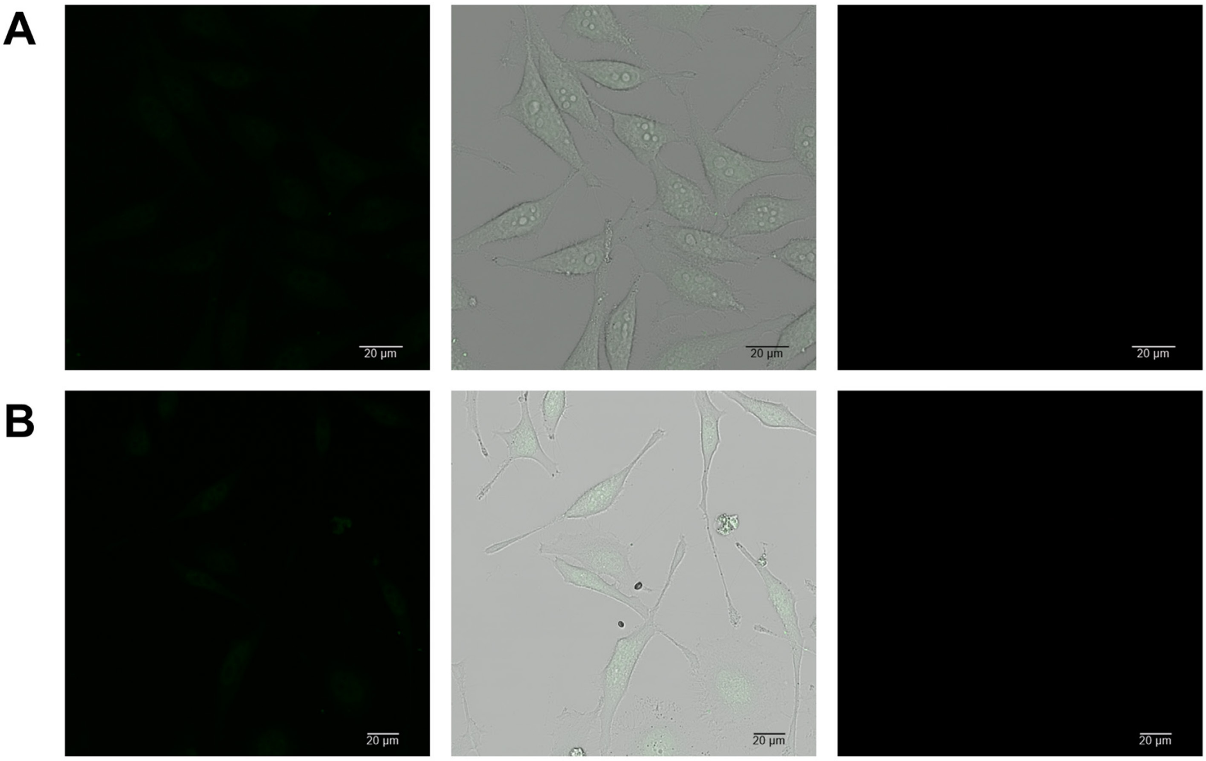

Figure 34| Live-cell CLSM images (20x) of HeLa GFP 1-10 cells treated with TAMRA-cadaverine-dextran-(GFP 11) **34** at 10 µM (**A**) and a mixture of solitary GFP11 **36** and L17E (1:1 ratio, 40.5 µM) (**B**) with the GFP-channel (left), TAMRA channel (right) and both fluorescence channels merged with brightfield (center). Adapted from Becker *et al.*[218].

As has been reported in the literature, multimerization of the CPP nonaarginine on dextran drastically increased its membrane-perturbing activity.[122] 10 kDa dextran bearing 5 copies of nonaarginine induced cytotoxicity in HeLa cells even at sub-micromolar concentrations, although solitary nonaarginine had also a negative impact on cell viability at moderate concentration of 11 µM. In contrast to the arginine-based nonaarginine, L17E revealed no significant cytotoxicity even at concentrations higher 50 µM.[117, 217, 218] The impact of L17E-multimerization on its cytotoxic profile was investigated using dextran equipped with 4.8 L17E on average. [217, 218] This construct exhibited an IC_{50} in HeLa cells of 10 µM, which was considerably lower than monomeric L17E. Considering the number of covalently attached peptides, the IC_{50} of 48 µM was roughly 1.5-fold lower compared to solitary L17E with 70 µM.

In order to assess the cytotoxic profile of TAMRA-cadaverine-dextran-(L17E, GFP 11)$_{5.4}$ **34**, unmodified HeLa cells were used once more to prevent potential interference of functional GFP with the formazan dye employed in the proliferation assay as described earlier (section **4.1.2**, **Figure 23**). TAMRA-labeled dextran **34** featuring a total of 5.4 copies of both L17E and GFP11 on average displayed only moderate cytotoxicity up to 20 µM (**Figure 35**). Considering the possible number of covalently attached L17E ranging from 1.1 – 4.3, it is difficult to compare the obtained results to L17E-equipped dextran reported in the literature. [217, 218] However, taking into account the successful GFP-complementation achieved by TAMRA-cadaverine-dextran-(L17E, GFP 11)$_{5.4}$

34 at 10 µM (**Figure 31**; **Figure 33**, **B**), the cell proliferation assay revealed that the construct was able to facilitate GFP-complementation without compromising the cells to a large extent.

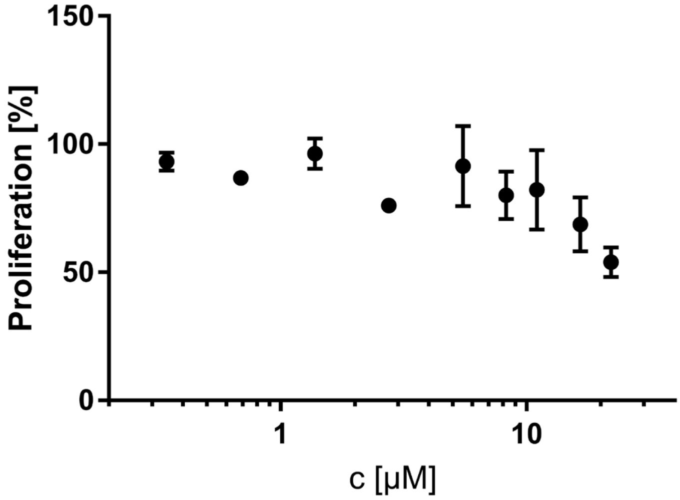

Figure 35| Cell proliferation assay of TAMRA-cadaverine-dextran-(L17E, GFP 11)$_{5.4}$ **34** on HeLa cells. Cells were incubated for 1 h with a serial dilution of the construct in medium lacking serum, followed by further 24 h in serum-containing medium. Results are shown as the mean ± standard error of the mean and are based on triplicates.

4.3 Modular Dextran-Streptavidin Hybrids: Cellular Uptake

4.3.1 Design and Synthesis

The preceding experiments highlighted the potential of L17E-dextran hybrids as promising delivery platform for both PNA and peptides as bioactive payloads. With regard to biomacromolecules, such as proteins, as emerging class of novel therapeutics, their inherent inability to cross the cellular membrane has been recognized as serious bottleneck calling for the development and optimization of efficient delivery modules. By introduction of a covalent linkage between eGFP as payload and L17E-decorated dextran, Dr. Bastian Becker in our working group was able to efficiently deliver the cargo protein into the cytoplasm of HeLa cells.[217] Encouraged by these results, we opted for an alternative protein to further investigate the potential of L17E-dextran hybrids. We chose Sav as cargo protein due to several beneficial properties. In contrast to eGFP, no covalent attachment of the protein to L17E-dextran is required due to the remarkably high affinity of Sav towards its ligand biotin. Thus, dextran-Sav hybrids could be conveniently assembled by mixing biotinylated dextran with the protein. The presence of 4 biotin binding pockets per Sav molecule further allows for adjustable ratio between dextran and protein under stochiometric control. Additionally, more sophisticated constructs, comprising additional functionalities bearing biotin, could be assembled using Sav as core structure. Sav has already been employed as centerpiece for intracellular delivery of a plethora of biotinylated payloads ranging from fluorophores over proteins to quantum dots, in which the ability to penetrate cells was provided by thiol reactive compounds.[215, 223] For experiments concerning the general feasibility of the dextran-Sav strategy, cellular uptake of fluorescently labeled Sav should be investigated. The most straightforward way to introduce a fluorophore into Sav is *via* direct covalent attachment. Since TAMRA was reported to act potentially as photosensitizer which induced endosomolysis upon laser irradiation,[121] two alternative fluorophores, ATTO 647 and AF647, were employed (**Figure 36**). Additionally, the intracellular delivery of an additional biotinylated cargo protein should be investigated. To that end, eGFP as fluorescent protein was chosen and modified to bear a biotin moiety (**Figure 36**). The uptake-mediating delivery module, i.e., L17E-decorated dextran, should bear a biotin functionality at its reducing end. Furthermore, the arginine-rich CPP P14 should also be multimerized on dextran polysaccharide and examined as potential alternative to L17E. While P14 performed worse in the intracellular delivery of bioactive PNA compared with the related P17 (section **4.1.2**), P14 proved superior in the GFP-complementation assay as reported by the literature.[210] To investigate, whether L17E and P14 could also benefit from an alternative way of multimerization apart from dextran, the monomeric peptides should be biotinylated and tetramerized on fluorescently labeled Sav as core structure.

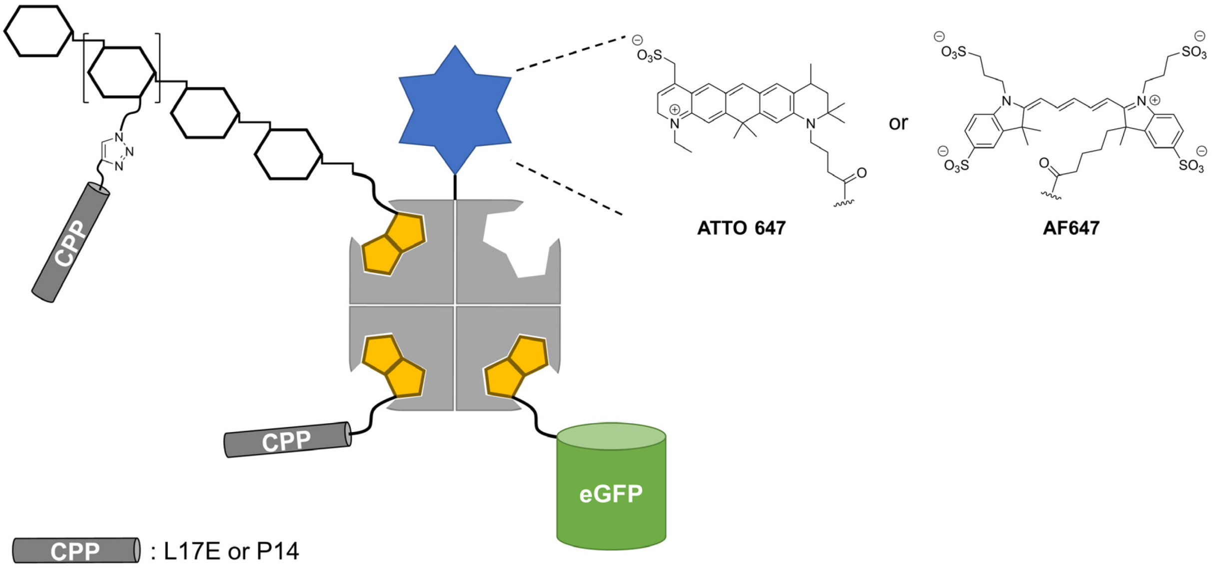

Figure 36| Depiction of Sav as centerpiece that allowed for the assembly of biotinylated (yellow) dextran, peptides or eGFP. Additionally, a fluorescent label (blue star), either ATTO 647 or AF647, could be introduced *via* direct coupling to Sav.

For the synthesis of biotinylated dextran equipped with either L17E or P14, respectively, biotin was introduced as NHS-ester at the reducing end of *N*-cadaverine-dextran-$(N_3)_{5.4}$ **29** *via* amide bond formation (**Scheme 16**). Analogous to the introduction of TAMRA at the reducing end of dextran (**Scheme 13**), the reaction was performed with an excess of NHS ester in DMSO with DIPEA as base under anhydrous conditions.

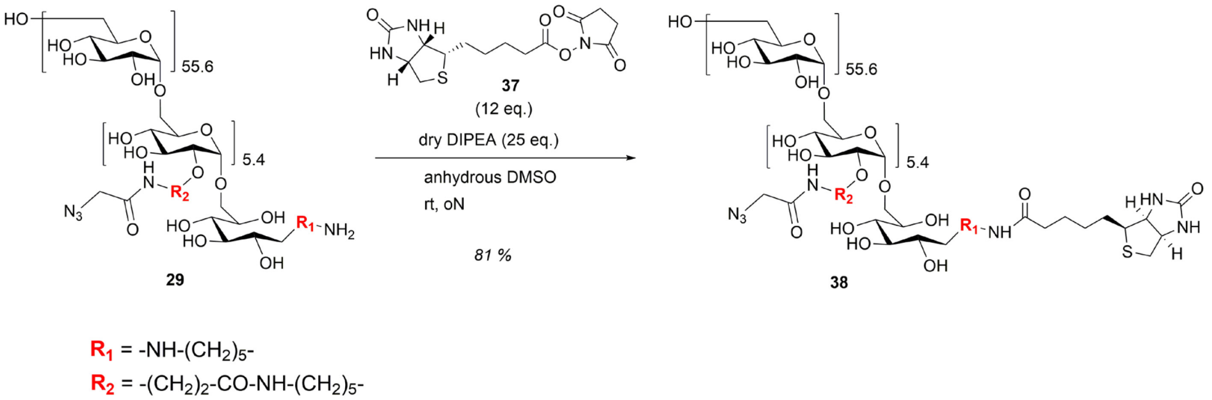

Scheme 16| Introduction of biotin at the reducing end of *N*-cadaverine-dextran-$(N_3)_{5.4}$ **29** *via* amide bond formation.

Following the biotin-functionalization of dextran **29**, the polysaccharide was decorated with either L17E or P14 at the repeating units *via* CuAAC. Contrary to the “click”-reactions involving GFP 11 peptide (**Scheme 14**, **Scheme 15**), which required DMSO in phosphate buffer as solvent system and the usage of BTTAA as chelating agent stabilizing the Cu(I)-species, the reactions were performed in plain water (**Scheme 17**). Both L17E-decorated biotin-dextran **40** and P14-decorated biotin-dextran **41** were isolated by consecutive SEC-HPLC on an analytical scale. While SEC-analysis of both peptide-dextran hybrids displayed a distinct shift towards shorter retention time, IR-spectroscopy of biotin-cadaverine-dextran-$(L17E)_{5.4}$ **40** still displayed a minor azide band (**Figure S 63**), indicating incomplete functionalization of the repeating units.

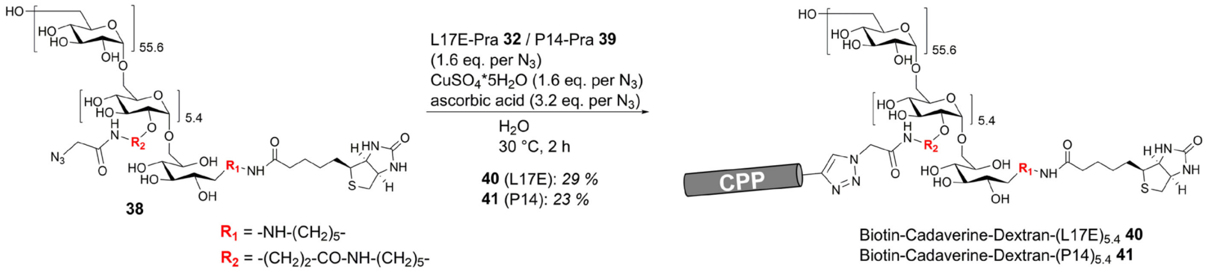

Scheme 17| Synthesis of L17E-decorated dextran **40** and P14-decorated dextran **41** *via* CuAAC.

The synthesis of biotin-functionalized monomeric L17E and P14 was performed by SPPS. With the aim to introduce biotin site-specifically, both peptides comprised a *C*-terminally located lysine with an orthogonal *N*-[1-(4,4-dimethyl-2,6-dioxocyclohex-1-ylidene)ethyl] (Dde)-protecting group. Upon completion of the peptides *via* SPPS, the *N*-terminal Fmoc-protecting group was removed and replaced by Boc. Dde was removed with hydrazine while conserving the remaining side-chain protecting groups. In order to increase the distance between biotin and the peptide, 6-aminohexanoic acid (Ahx) as additional spacer was introduced, following by NHS-mediated coupling of biotin (**Figure 37**).

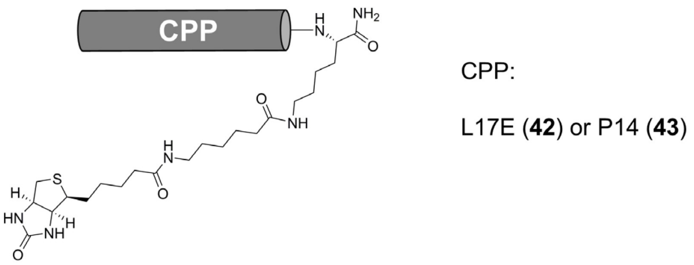

Figure 37| Depiction of L17E-Biotin **42** and P14-Biotin **43** displaying the *C*-terminally located biotin with additional Ahx spacer.

In addition to the delivery modules, eGFP as fluorescent cargo protein also had to be biotinylated. While the synthesis of eGFP-biotin could easily be accomplished by incubation of the protein with biotin-NHS, this strategy would result in a heterogenous product with a varying degree of functionalization. As a consequence, eGFP harboring two or more copies of biotin could act as linker to interconnect two Sav molecules or occupy multiple biotin binding pockets simultaneously. Thus, a more elaborated synthesis strategy was designed, based on enzyme-mediated introduction of biotin site-specifically. To that end, lipoic acid protein ligase (LplA) from *Escherichia coli* (*E. coli*) was chosen, which specifically addresses a 13 amino acid recognition sequence (GFEIDKVWYDLDA) called lipoic acid acceptor peptide (LAP).[224] This enzyme catalyzes the amide bond formation between the lysine residue of the recognition sequence and a suited carboxylate.[224] While the substrate promiscuity was increased *via* mutation of a gatekeeper amino acid (W37V) to accept carboxylate donors apart from the natural substrate lipoic acid,[225] the ligation efficiency is highly dependent on the linker length.[226] Since sufficient distance between eGFP and biotin deemed crucial for the assembly of Sav-eGFP hybrids, the functionalization of eGFP with biotin was planned as a two-step process. In the first step, eGFP harboring the LAP-tag in a loop between E172 and D173,[226] should be modified with a bicyclo[6.1.0]nonyne (BCN) substrate *via* LplA-catalysis (**Scheme 18**). Following that, a biotin derivative comprising an additional aliphatic spacer and an azide-functionality, could be introduced by strain-promoted azide-alkyne cycloaddition (SPAAC) (**Scheme 18**).

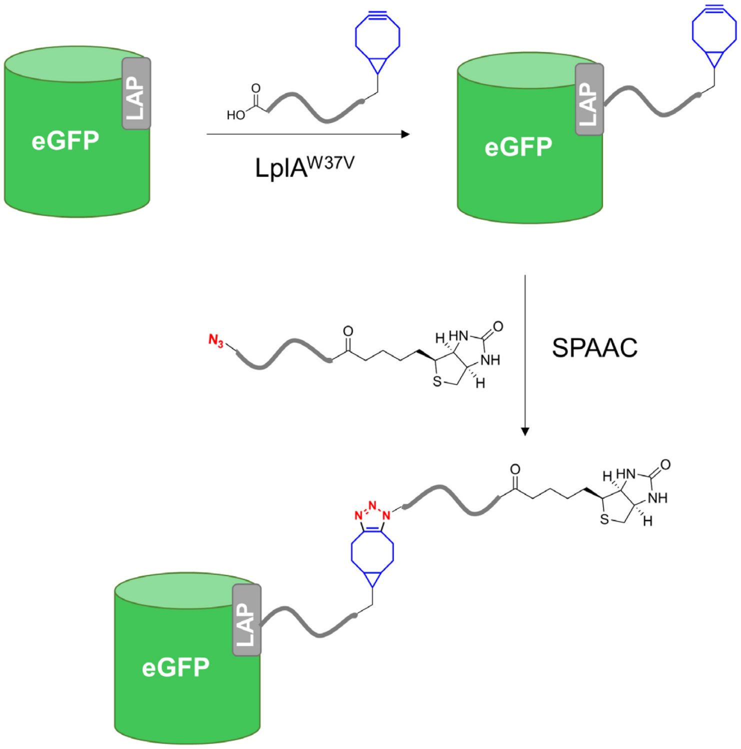

Scheme 18| Synthetic approach to biotin-functionalized eGFP. In the first step, a BCN-functionalized substrate is introduced *via* LplA-mediated amide bond formation. Afterwards, conjugation of azide-bearing biotin derivative by SPAAC affords the final product a site-specifically labeled eGFP.

The synthetic pathway leading to BCN substrate **51** was performed as initiated by the synthesis of BCN-OH **48** according to the literature.[227] Thereby, the bicyclo[6.1.0]nonyne framework was established by cyclopropanation of an excess of 1,5-cyclooctadiene with ethyl diazoacetate and Rh(II) acetate dimer as catalyst (**Scheme 19**). The resulting mixture of *endo* **44** and *exo* **45** diastereomers were separated by silica chromatography. *Exo* isomer **45**, despite slightly lower reaction rate of the final BCN-OH **48**,[228] was employed in the subsequent reactions due to a higher obtained yield. In the next step, the ester functionality was reduced to alcohol **46** using lithium aluminium hydride, followed by bromination of the olefine to afford dibromide **47** (**Scheme 19**). Both products, which required no additional chromatographic purification, were obtained in good yields. In the last step, dehydrobromination with potassium tert-butoxide resulted in BCN alcohol **48** (**Scheme 19**), which was isolated by silica chromatography.

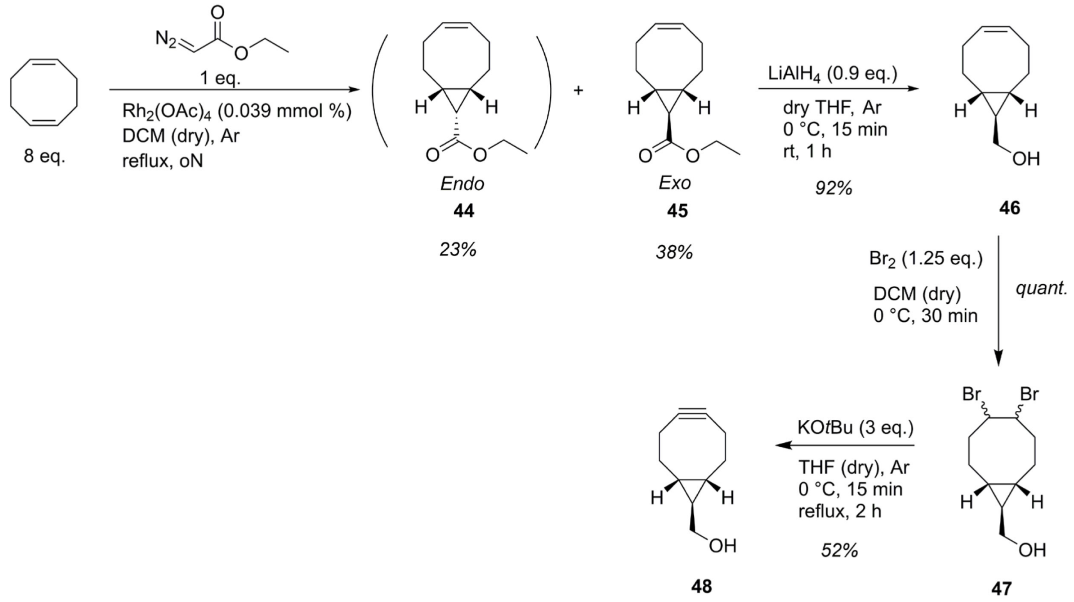

Scheme 19| Synthetic pathway leading to BCN alcohol **48**. Cyclopropanation of 1,5-cyclooctadiene yielded diastereomer **44** (*endo*) and **45** (*exo*). Following that, reduction of the ester group with lithium aluminium hydride afforded olefin **46**, which was subsequently brominated. Dehydrobromination of dibromide **47** resulted in the final compound BCN alcohol **48**.

For the subsequent coupling of BCN-OH **48** to 5-aminopentanoic acid as linker that displayed the highest conversion rate for BCN substrate in the literature,[226] the alcohol was activated as mixed carbonate ester. To that end, BCN-OH **48** was reacted with a slight excess of bis(4-nitrophenyl) carbonate **49** under basic conditions (**Scheme 20**). Following the isolation of carbonate ester **50** by automated silica flash chromatography, conjugation to 5-aminopentanoic acid was achieved by carbamate formation (**Scheme 20**).

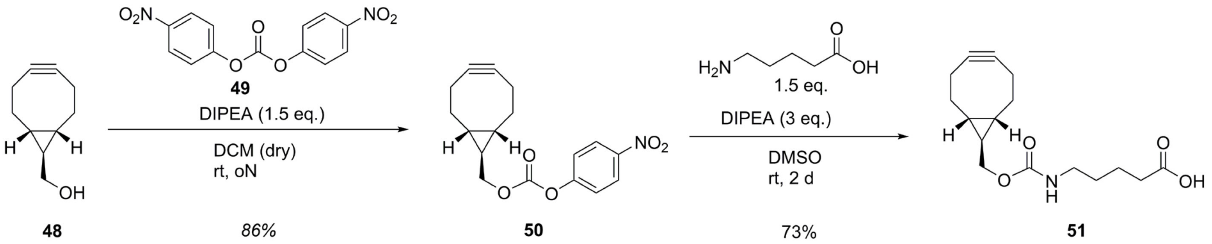

Scheme 20| Activation of BCN-OH **48** as mixed carbonate ester **50**, followed by conjugation to 5-aminopentanoic acid by carbamate formation.

The synthesis of azide-bearing biotin derivative **54** started with NHS activation of biotin (**Scheme 21**). Following that, biotin-NHS **37** was reacted with *N*-Boc-cadaverine *via* amide bond formation (**Scheme 21**). Subsequent cleavage of the Boc-protecting group with TFA afforded biotin-cadaverine **52** (**Scheme 21**). 2-azidoacetic acid was activated as NHS-ester **53** and coupled to the second amine functionality of biotin-cadaverine, resulting in biotin-cadaverine-azide **54** (**Scheme 21**).

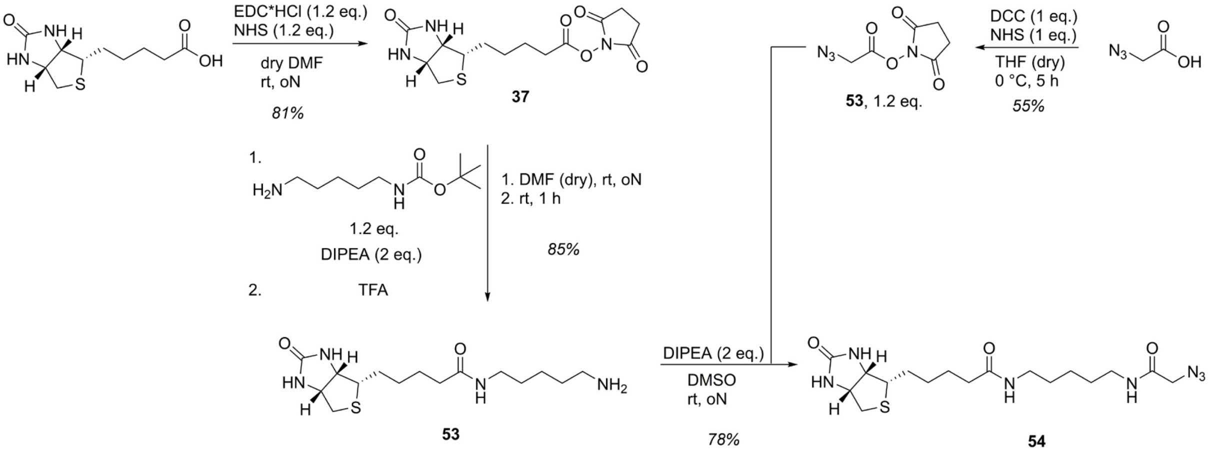

Scheme 21| Synthetic route leading to azide-functionalized biotin derivative **54**. Biotin was activated as NHS-ester and coupled to *N*-Boc-cadaverine, followed by acidic cleavage of the protecting group. NHS-activated 2-azidoacetic acid **53** was conjugated to the unprotected amine functionality of biotin-cadaverine **52**, affording the final product **54**.

Having assembled both alkyne- and azide-functionalized chemical handles required for site-specific biotinylation of eGFP, the fluorescent protein was modified enzymatically. To that end, eGFP-LAP **55** was incubated with LplA^{W37V} and an excess BCN substrate **51** in the presence of cosubstrate adenosin triphosphate (ATP) for 2 h at 37 °C (**Scheme 22**). Afterwards, product **56** was purified by dialysis to remove excessive BCN-substrate **51** and the biotin handle was introduced by SPAAC-mediated conjugation of azide-functionalized biotin derivative **54** (**Scheme 22**).

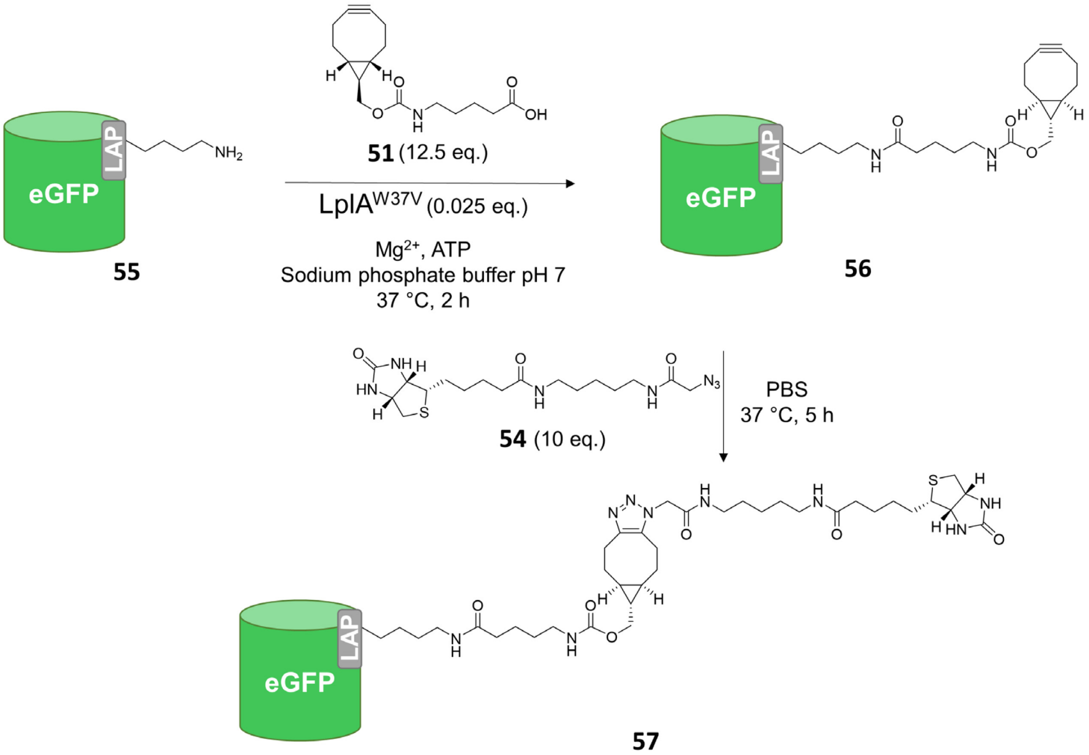

Scheme 22| Synthesis of eGFP-biotin **57**. After LplA-mediated conjugation of BCN substrate **51**, the resulting eGFP-BCN **56** was equipped with a biotin handle *via* SPAAC.

Both reactions were monitored by hydrophobic interaction chromatography (HIC), which displayed nearly quantitative turnover of eGFP-LAP, expressed as shift towards higher retention time (**Figure 38**, **A**). Conversion of eGFP-BCN **55** to the corresponding eGFP-biotin **57** *via* SPAAC led to slightly lower retention time of the product (**Figure 38**, **A**). All eGFP-derivatives displayed distinct shoulders in the chromatogram, which suggests impurities already present in educt eGFP-LAP. Since sodium dodecyl sulfate polyacrylamide gel electrophoretic (SDS-PAGE) analysis of eGFP-LAP displayed only minimal impurities with varying molecular weight (**Figure 38**, **B**), these data suggest that the heterogenous peak in the HIC chromatogram could have been the result from post-translational modifications such as misfolding and oxidation. However, the SDS-PAGE of eGFP-BCN **56** displayed some minor bands at higher molecular weights (**Figure 38**, **B**), possibly as a result from side-reactions facilitated by LplA or BCN substrate **51**.

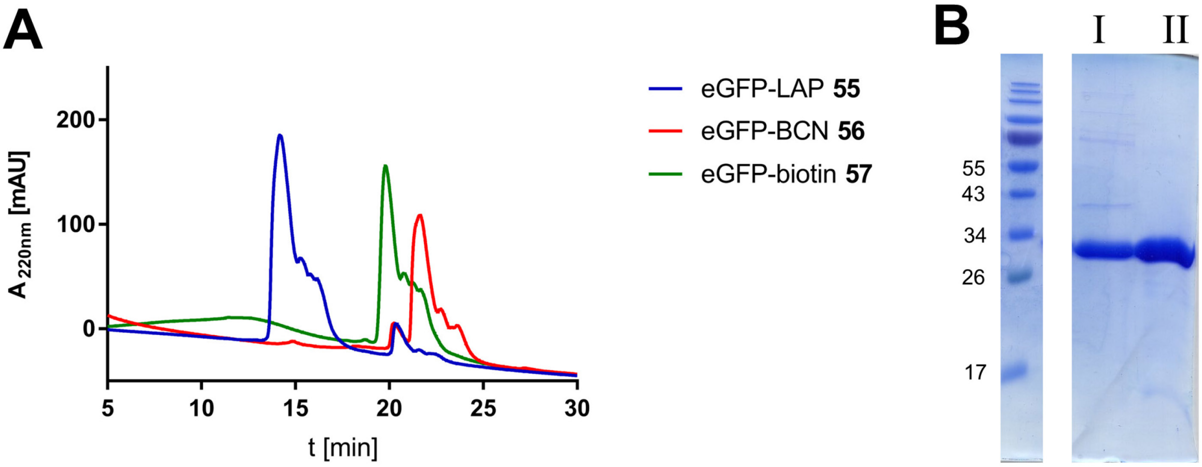

Figure 38| **A**: Overlay of HIC chromatographic traces of eGFP-LAP **55**, eGFP-BCN **56** and eGFP-biotin **57**. **B**: SDS-PAGE analysis of eGFP-LAP **55** (lane II, M_w = 29565.11 Da) and eGFP-BCN **56** (lane I, M_w = 29840.47 Da)

After successful synthesis of eGFP comprising a site-specifically located biotin moiety, it should be investigated whether the compound was indeed able to bind to Sav. To that end, eGFP-biotin **57** (1 eq.) was preincubated with an excess of solitary biotin (3 eq.), followed by addition to Sav (1 eq.). Mixing of biotin and eGFP-biotin was performed to minimize binding of the biotinylated protein in a stochastic fashion. The resulting mixture was incubated for 1 h at 4 °C and subsequently analyzed by SEC. Sav incubated with both biotin and eGFP-biotin **57** resulted in a peak at lower retention time compared to Sav alone, indicating successful binding of eGFP. The relative homogeneity of the presumed Sav-eGFP peak with only a small shoulder at lower retention time suggested the assembly mostly in a 1:1 ratio. However, since unmodified Sav was still present in the protein mixture, eGFP-biotin was applied in a 1.5-fold excess in regard to Sav in the upcoming cellular uptake experiments to increase the ratio of fluorescently labeled Sav.

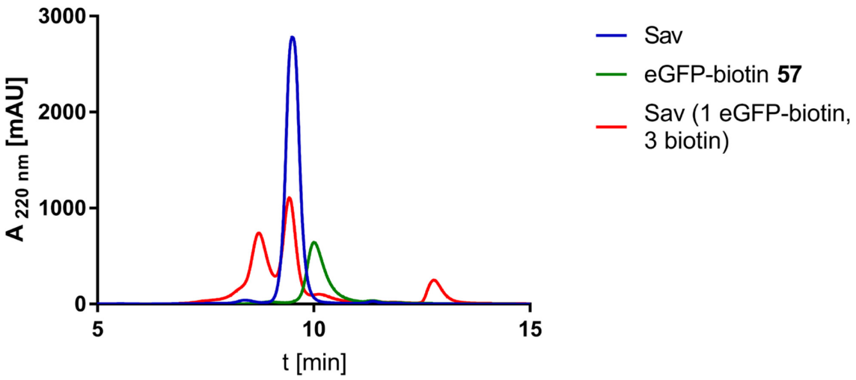

Figure 39| SEC analysis of Sav (M_w = 53326 Da), eGFP-biotin **57** (M_w = 30252 Da) and Sav incubated with biotin and eGFP-biotin **57** (M_w = 84311 Da, calculated for binding of 3 molecules biotin and 1 molecule eGFP-biotin **57** to Sav).

After biotinylation of the cargo and delivery modules, respectively, Sav was fluorescently labeled with either ATTO 647 or AF647. To that end, Sav was incubated with commercially available NHS-esters of the fluorophores (**Scheme 23**), followed by removal of unconjugated dye using size exclusion spin columns and determination of dye-to-protein ratios (DPR) by photometry.

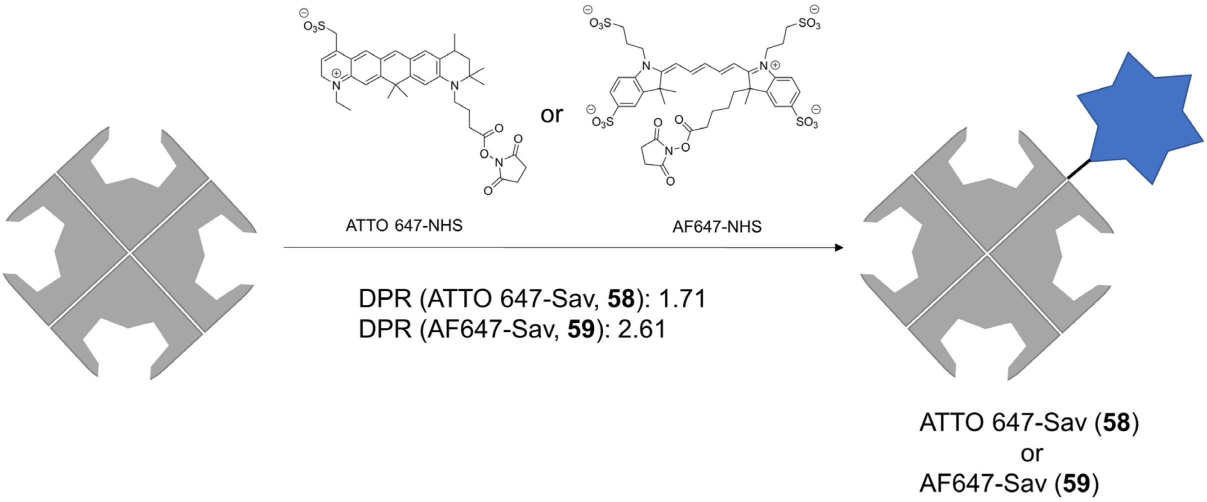

Scheme 23| Fluorescent labeling of Sav with ATTO 647-NHS and AF647-NHS, respectively.

4.3.2 Cellular Uptake and Cytotoxicity

Cellular uptake of fluorescently labeled Sav facilitated by biotinylated monomeric CPPs and their multimerized counterparts on dextran, respectively, was studied in HeLa cells using confocal microscopy. For preliminary experiments concerning the general applicability of this approach, CPP-decorated dextran conjugates **40** (L17E) and **41** (P14) should be employed in a ratio of 2:1 with regard to Sav-ATTO 647 **58**. Monomeric L17E **42** and P14 **43** equipped with biotin at their *C*-terminus were assembled on Sav-ATTO 647 core structure in a 4:1 ratio in order to maximize the amount of attached peptide per Sav core structure.

The Sav-dextran conjugates were assembled by premixing 2 eq. solitary biotin with 2 eq. biotinylated CPP-dextran hybrids and subsequent addition to Sav-ATTO 647 **58**. The resulting mixture was incubated for 2 h at 4 °C under vigorous shaking and were subsequently used without further purification. Sav-ATTO 647 **58** equipped with monomeric CPPs was obtained in a similar fashion without additional solitary biotin, and as a control, Sav-ATTO 647 **58** was functionalized with 4 eq. biotin. HeLa cells were incubated for 30 min with the constructs in medium without serum at 37 °C, followed by fixation and analysis by CLSM. Please note that in the following cell experiments involving Sav, the stated concentrations refer to the concentration of the protein as core structure.

HeLa cells treated with Sav-ATTO 647 decorated with 4 biotin molecules did not display fluorescence located in the cell interior or adherent to the membrane at 3 µM concentration (**Figure S 2**). In contrast, Sav-ATTO 647 **58** equipped with two copies of biotin-cadaverine-dextran-(L17E)$_{5.4}$ **40** displayed distinct intracellular fluorescence at 3 µM (**Figure 40**). While the fluorescence was evenly distributed within the cytoplasm, the construct seemed to have accumulated in the nuclei of the treated cells, possibly the nucleoli. However, the brightfield image comprises a large amount of small dense spots, which also display strong fluorescence. In combination with cell-shaped negatives in the fluorescence image completely absent of fluorophore, probably caused by detachment of cells prior to the fixation, these findings indicate membrane-lytic activity of Sav-ATTO 647 **58** equipped with two copies of biotin-cadaverine-dextran-(L17E)$_{5.4}$ **40**. As a consequence, the construct could bind to fragments of the membrane by electrostatic interactions, resulting in the highly fluorescent spots observable in the fluorescence image. At lower concentration of 0.75 µM no extracellular fluorescent spots could be observed (**Figure 40**). While fluorescence was distinctly lower compared to 3 µM, the fluorophore is still located in the cells. Considering the overall molecular weight of the construct around 109 kDa, the cellular uptake observable at sub-micromolecular concentrations deemed rather promising for the design. However, the presumable membrane fragmentation observed at 3 µM suggest a concentration-dependent cytotoxicity of biotin-cadaverine-dextran-(L17E)$_{5.4}$ **40** dimerized on fluorescently labeled Sav.

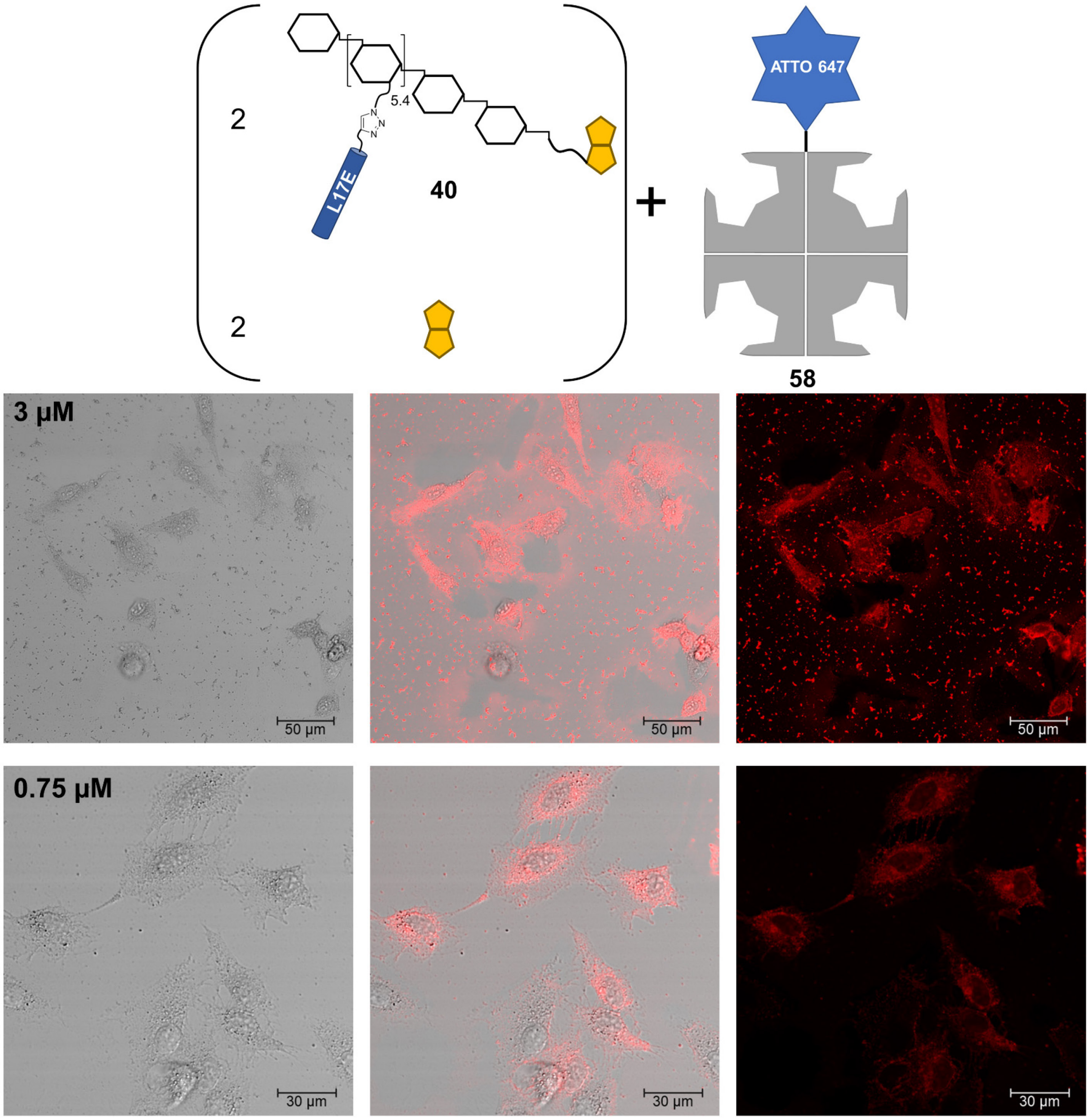

Figure 40| CLSM images (20x) of HeLa cells incubated with Sav-ATTO 647 **58** equipped with 2 copies of biotin-cadaverine-dextran-(L17E)$_{5.4}$ **40** at 3 µM (top) and 0.75 µM (bottom) with brightfield (left), overlay (middle) and fluorescence channel (right).

Next, cellular uptake of fluorescently labeled Sav equipped with two copies of biotin-cadaverine-dextran-(P14)$_{5.4}$ **41** was investigated. HeLa cells treated with 3 µM of the construct comprised strong, heterogeneously-distributed fluorescence in the interior, which coincides with dark nuclei visible in the brightfield channel (**Figure 41**). This suggests accumulation of the construct, harboring a total of 2 (dextran polymer) x 5.4 (functionalized repeating units) x 6 (number of arginine residues per P14) = 64.8 arginine residues on average in the nuclei, probably due to electrostatic interactions with negatively charged DNA. Compared to L17E-decorated counterpart **40**, fewer but more condensed fluorescent spots are visible outside the cells. At lower concentrations, only a portion of cells exhibit fluorescence as large spots in their interior, whereas other cells display fluorescence located at their membrane (**Figure 41**). Unlike its L17E-comprising competitor **40**, which has less intracellular fluorescence at decreasing concentrations, a certain threshold concentration seems required for biotin-cadaverine-dextran-(P14)$_{5.4}$ **41** to facilitate successful intracellular delivery of the protein cargo.

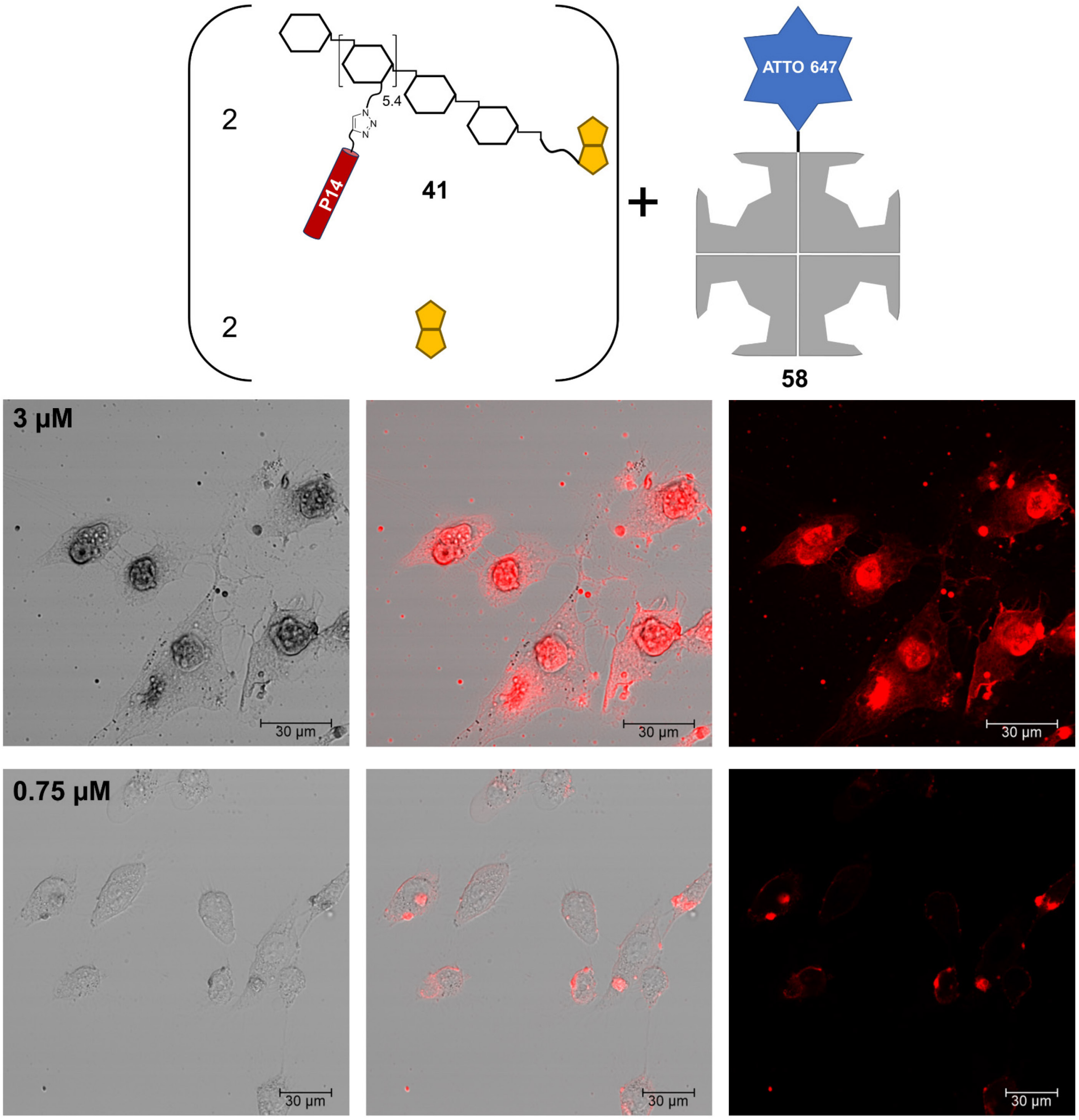

Figure 41| CLSM images (20x) of HeLa cells incubated with Sav-ATTO 647 **58** equipped with 2 copies of biotin-cadaverine-dextran-(P14)$_{5.4}$ **41** at 3 µM (top) and 0.75 µM (bottom) with brightfield (left), overlay (middle) and fluorescence channel (right).

Sav comprising 4 biotin binding sites allows for an alternative way of CPP-multimerization without the use of dextran as framework. In order to investigate, whether biotinylated L17E **42** and P14 **43** could facilitate cellular uptake of Sav as their tetramerization platform, HeLa cells were treated with Sav-ATTO 647 harboring 4 copies of either L17E and P14. Thereby, L17E-decorated Sav-ATTO 647 at 3 µM displayed some intracellular spots in the fluorescence channel (**Figure 42**), which could indicate vesicular localization upon cellular entry, presumably by endocytosis. In contrast, Sav-ATTO 647 equipped with 4 copies of P14-biotin did not show distinct intracellular signals in the fluorescence channel (**Figure 42**), only some minor labeling of the cellular membrane. Both peptide-decorated conjugates, however, are concentrated in condensed spots in the brightfield channel, which is probably the result of binding to cellular debris.

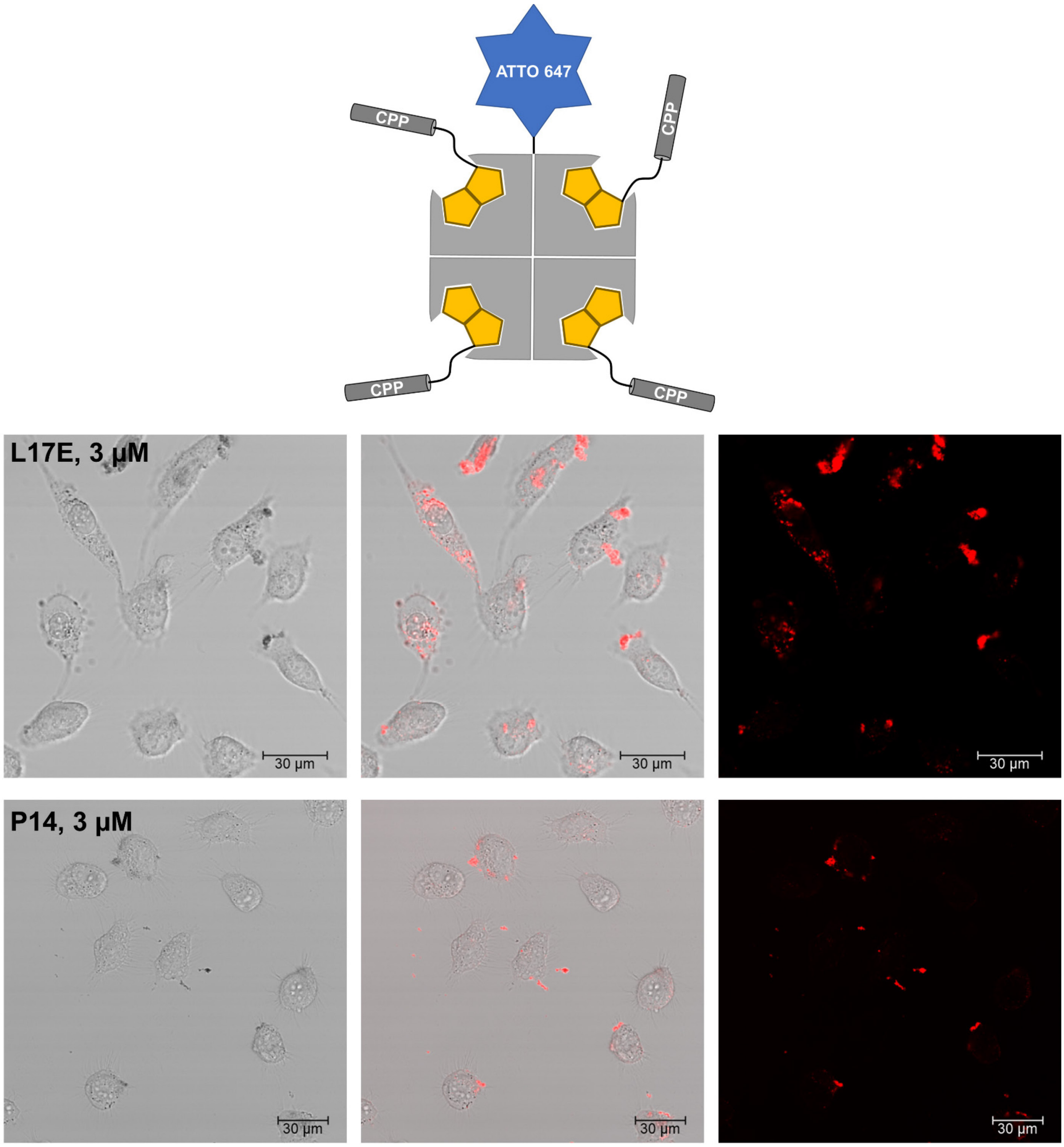

Figure 42| CLSM images (20x) of HeLa cells incubated with Sav-ATTO 647 **58** equipped with 4 copies of biotinylated L17E **42** (top) and P14 **43** (bottom), respectively, at 3 µM with brightfield (left), overlay (middle) and fluorescence channel (right).

These experiments illustrated the general feasibility of peptide-decorated dextran in combination with Sav as cargo protein for intracellular delivery, with L17E proving superior to P14, especially at lower concentrations. Furthermore, tetramerization of the solitary CPPs was not sufficient to induce cellular uptake of Sav in an efficient manner. However, cellular uptake of Sav facilitated by both CPP-decorated dextran was also accompanied by changes in cell morphology and, presumably, cytotoxicity. Thus, for the upcoming experiments, only L17E-bearing dextran **40**, being the most promising delivery module, was investigated in greater detail. Therefore, Sav labeled with AF647 as fluorophore was chosen as cargo protein and dextran was employed in both 1:1 and 2:1 ratio with regard to the protein.

Treating HeLa cells with solitary Sav-AF647 **59** at 3 µM did not result in intracellular fluorescence (**Figure S 3**). Addition of 2 eq. biotin-cadaverine-dextran-(L17E)$_{5.4}$ **40** to Sav-647 at 3 µM led to strong intracellular fluorescence in the majority of cells (**Figure 43**). In a similar fashion as already observed for Sav-ATTO 647 equipped with 2 copies of the functionalized dextran, cellular uptake was accompanied again by highly fluorescent cellular debris, even though to a lesser degree. Although cell viability is always subject to external factors, such as experimental handling, the two different fluorophores could also play an important role. Both fluorophores have similar optical properties, however, ATTO 647 (**Figure 36**) is an electrically neutral zwitterion. AF647 (**Figure 36**), on the other hand, has a net charge of -3 as a consequence of the excess of negatively charged sulfonates. The presence of 2.6 copies of AF647 per Sav on average could have had an attenuating effect on L17E as positively charged CPP. Mixing L17E-decorated dextran **40** and Sav-AF647 **59** in an equimolar ratio resulted in distinctly lower cellular uptake compared to the 2:1 construct (**Figure 43**). Interestingly, while some cells displayed only little fluorescence outlining their circumference, other cells harbor relatively high levels of fluorophore in their interior.

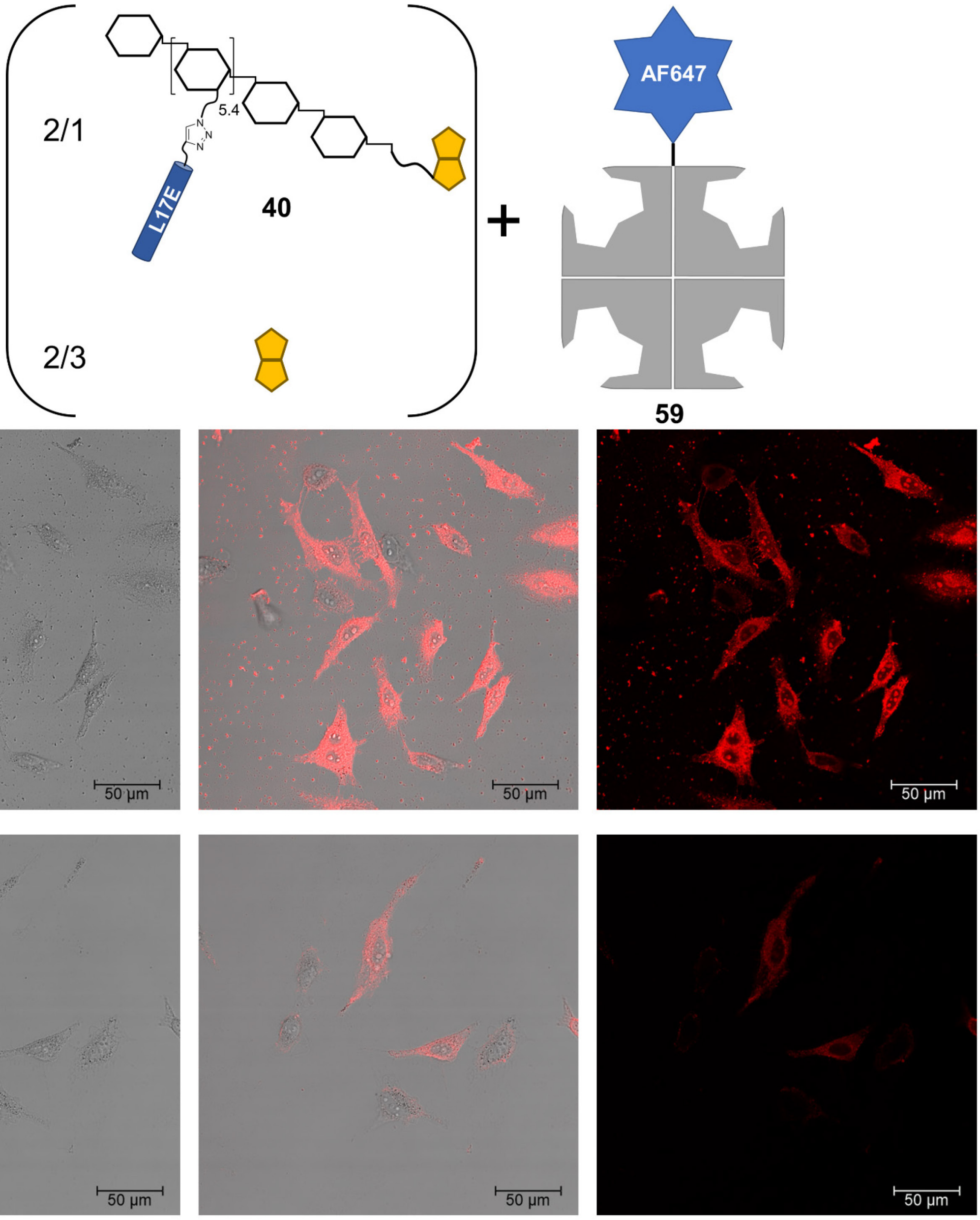

Figure 43| CLSM images (20x) of HeLa cells incubated with Sav-AF647 **59** equipped with 2 (top) and 1 (bottom) copies, respectively, of biotin-cadaverine-dextran-(L17E)$_{5.4}$ **40** at 3 µM (top) with brightfield (left), overlay (middle) and fluorescence channel (right).

At half the concentration, i.e. 1.5 µM, HeLa cells treated with Sav-647 and 2 eq. biotin-cadaverine-dextran-(L17E)$_{5.4}$ **40** displayed strong intracellular fluorescence in the majority of cells, whereby some nuclear localization of the fluorescently labeled cargo protein can be observed (**Figure 44**). In addition, the substantially reduced amount of extracellular staining indicates a lower membrane-lytic activity compared to cells treated with 3 µM of the 2:1 construct. While the 1:1 construct was incapable of translocate into most of the cells at 3 µM, some few cells still harbored considerable amounts of the construct at 1.5 µM (**Figure 44**). Further reduction of the concentration to 0.75 µM resulted for the 2:1 construct in low intracellular fluorescence predominantly located in close proximity of the cellular membranes, whereas the 1:1 construct was absent from the cell interior (**Figure S 4**).

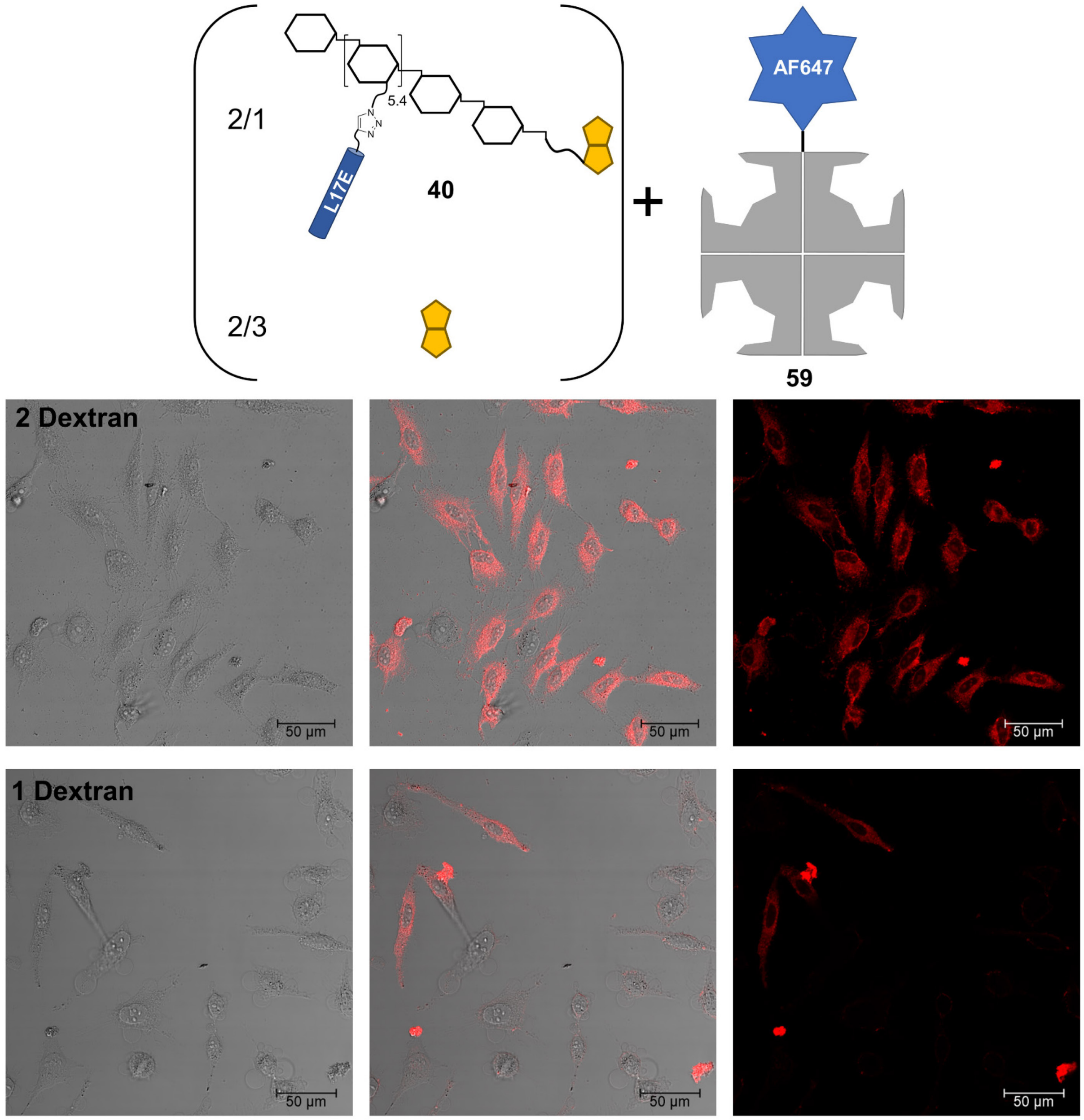

Figure 44| CLSM images (20x) of HeLa cells incubated with Sav-AF647 **59** equipped with 2 (top) and 1 (bottom) copies, respectively, of biotin-cadaverine-dextran-(L17E)$_{5.4}$ **40** at 1.5 µM (top) with brightfield (left), overlay (middle) and fluorescence channel (right).

Confocal microscopy with fluorescently labeled Sav and biotin-cadaverine-dextran-(L17E)$_{5.4}$ **40** as delivery module displayed strong cellular uptake of the cargo protein equipped with 2 copies of dextran, although presumably accompanied by cytotoxicity. In contrast, the application of L17E-decorated dextran in a 1:1 ratio with regard to Sav led to poor translocation at concentrations ranging from 0.75 to 3 µM, highlighting the need for 2 copies of dextran per Sav for efficient uptake. Interestingly, the choice of fluorophore had a great impact on cellular uptake, whereby non-charged ATTO 647 led to higher intracellular levels of fluorophore, but also presumably higher toxicity, compared to anionic AF647. In order to determine the cytotoxicity caused by solitary dextran **40**-decorated Sav, several constructs were employed in a cell proliferation assay. Thereby, biotin-cadaverine-dextran-(L17E)$_{5.4}$ **40** attached to unlabeled Sav in a 2:1 and 1:1 ratio was assessed, as well as solitary dextran. Additionally, Sav-AF647 in combination with 2 eq. of biotin-cadaverine-dextran-(L17E)$_{5.4}$ **40** was also included to investigate the potential attenuating effect of AF647 on the membrane-lytic activity of the delivery module. To that end, HeLa cells were treated with a serial dilution of the constructs for 30 min in medium without serum, followed by further 3 h in medium and analysis using the MTS assay. This assay displayed strong cytotoxicity of biotin-cadaverine-dextran-(L17E)$_{5.4}$ **40** in both unbound form and coupled to Sav (**Figure 45**). Since no significant difference can be observed in presence or absence of Sav, the results indicate that dimerization of dextran on the protein did not enhance its cytotoxic effect. Interestingly, incorporation of AF647 reduced toxicity of the dextran-Sav 2:1 hybrid to a greater extent than omitting one dextran polysaccharide in the construct (**Figure 45**). Considering the translocation efficiency of the fluorescently labeled protein mediated by dextran **40**, successful cellular uptake was always accompanied by cytotoxicity. Only at 1.5 µM Sav-AF647 **59** equipped with 2 copies of dextran was capable of efficient cellular uptake while being only moderately cytotoxic (**Figure 44**).

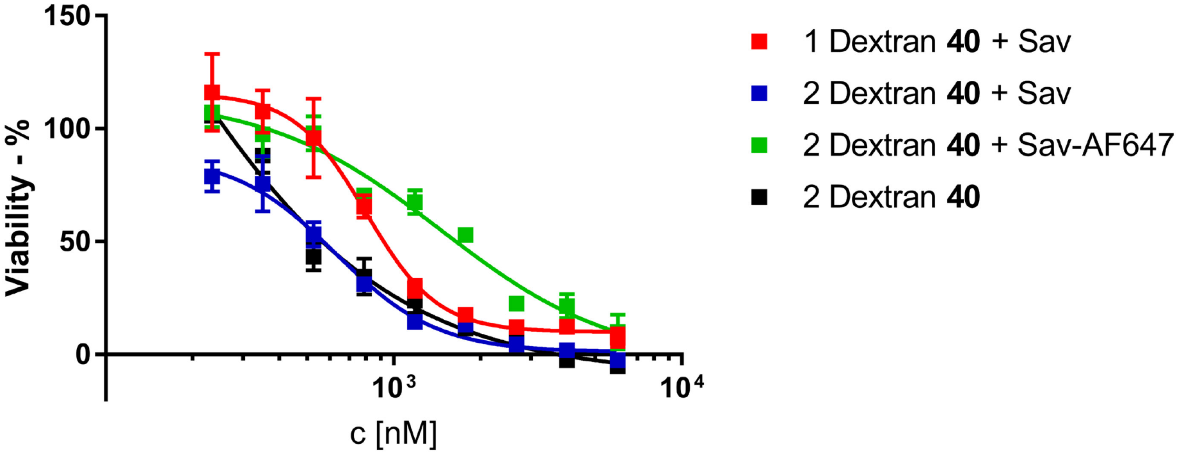

Figure 45| Cell proliferation assay: HeLa cells were treated with solitary dextran **40**, dextran-Sav hybrids (2:1, 1:1) and dextran-Sav 647 for 30 min in medium only, followed by further 3 h in serum-containing medium. Results are shown as the mean ± standard error of the mean and are based on triplicates.

The cytotoxic profiles were quantified by determining the lethal concentration 50 (LC$_{50}$) value of the different constructs (**Figure S 5**). As could already be observed, cytotoxicity of biotin-cadaverine-dextran-(L17E)$_{5.4}$ **40** is essentially unaffected from additional Sav present (**Table 1**). The dextran-Sav 1:1 hybrid displayed distinctly higher cytotoxicity with regard to the dextran concentration, compared to the 2:1 constructs. The introduction of the anionic fluorophore AF647 reduced the cytotoxicity of Sav-dextran hybrids by a factor more than 2.

Table 1| LC_{50} values of dextran-Sav hybrids (2:1, 1:1) and dextran-Sav 647 (2:1) referring to the cytotoxicity of the constructs and dextran, respectively.

Construct	LC_{50} [nM] Construct	LC_{50} [nM] Dextran
Dextran **40** + Sav (1:1)	801	801
Dextran **40** + Sav (2:1)	629	1257
Dextran **40** + Sav-AF647 (2:1)	1461	2923
Dextran **40** (2x)	609	1217

Despite the strong cytotoxicity expressed by the dextran-Sav hybrids, the approach was further validated in delivering eGFP as an additional protein cargo into HeLa cells. To that end, both biotinylated dextran **40** and eGFP **57** were assembled on Sav as core structure. As mentioned before, eGFP-biotin **57** was employed in 1.5 eq. to compensate for the incomplete binding to Sav as determined by SEC (**Figure 39**). Since the dextran-Sav 1:1 hybrid was not able to efficiently translocate into the cells, only the 2:1 conjugate was used. Furthermore, cellular uptake experiments were also performed at 4 °C to determine the influence of energy-dependent endocytosis on the overall translocation.

HeLa cells treated with 3 µM of Sav bearing 2 copies of dextran **40** and 1.5 copies of eGFP **57** on average displayed strong intracellular fluorescence, which also extended into the nuclei (**Figure 46**). Compared to HeLa cells treated with 3 µM of 2:1 hybrids of dextran with either Sav-ATTO 647 **58** (**Figure 40**) or Sav-AF647 **59** (**Figure 43**), significantly less extracellular fluorescent spots were visible, which suggests reduced membrane-lytic activity of the construct or lower adherence to the resulting membrane debris. Distinct intracellular fluorescence could also be observed in HeLa cells treated at 4 °C (**Figure 46**), suggesting that energy-independent pathways were at least partially responsible for cellular uptake. While decreased temperatures reduce or inhibit endocytosis,[210] the application of more specific inhibitors of endocytosis would be required to confidently rule out endocytosis as a major uptake pathway. Interestingly, while the amount of fluorophore within the cytosol appears quite similar at both temperatures, the big spots of fluorophore within the nuclei were not present at 4 °C. This finding indicates, that energy-dependent mechanisms were necessary for the construct to enter the nucleus.

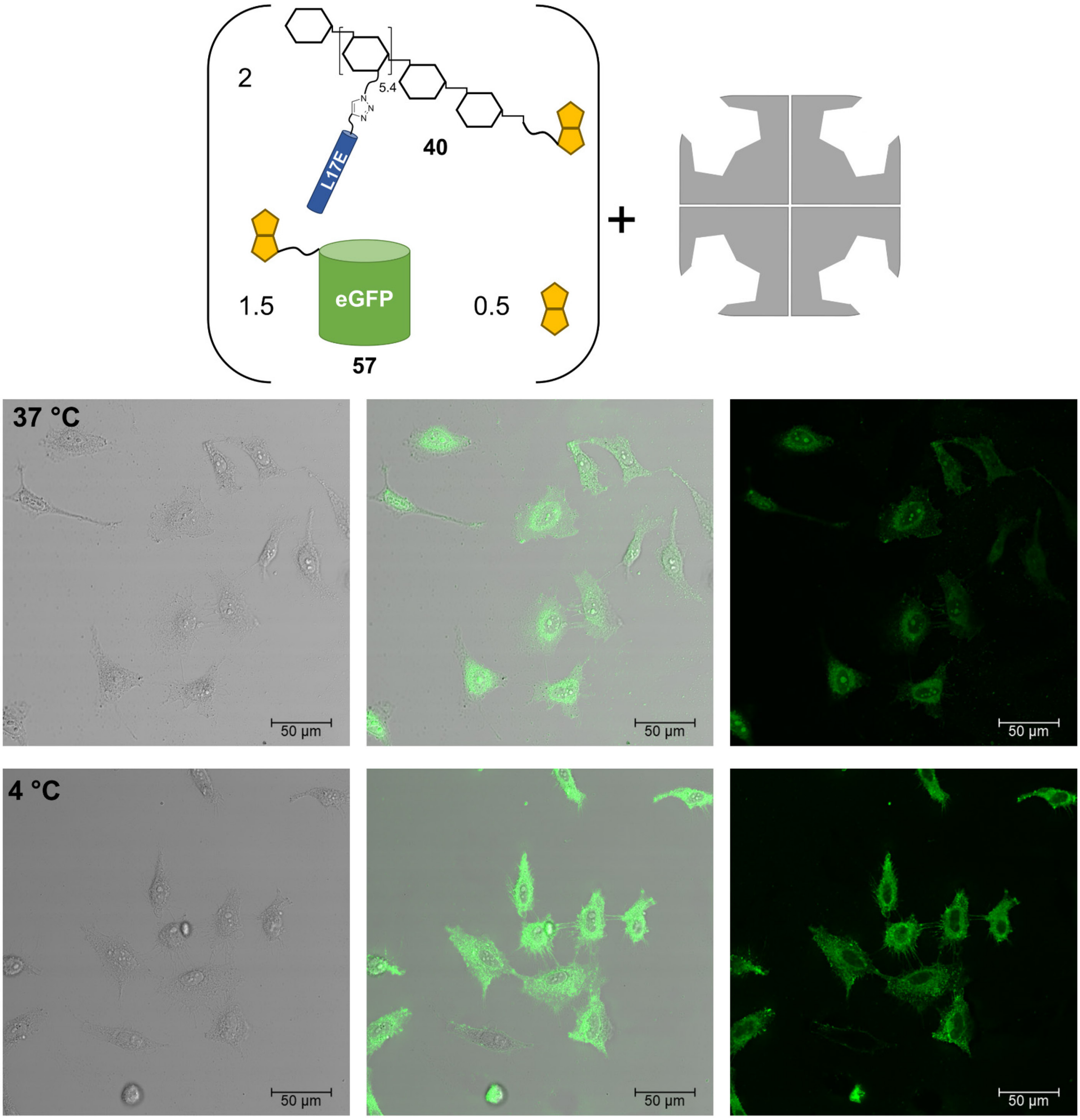

Figure 46| CLSM images (20x) of HeLa cells incubated with 3 µM Sav equipped with 2 copies of biotin-cadaverine-dextran-(L17E)$_{5.4}$ **40** and 1.5 copies of biotinylated eGFP **56** at 37 °C (top) and 4 °C (bottom) with brightfield (left), overlay (middle) and fluorescence channel (right).

Incubation of HeLa cells with 1.5 µM of Sav bearing 2 copies of dextran **40** and 1.5 copies of eGFP **56** on average resulted in much lower intracellular fluorescence compared to 3 µM. The cells predominantly did not show evenly distributed fluorophores within the cells, regardless of incubation temperature. While the cells incubated at 37 °C harbored the fluorophore more towards the center of the cells, at 4 °C the construct is mainly localized at the cell membrane. This could indicate that endocytosis is the main uptake pathway at this concentration, which transferred the construct into the interior of the cells upon binding to the membrane. Initial association of the dextran-protein hybrid to the plasma membrane would also take place at 4 °C, however, due to the compromised endocytotic pathways required for subsequent transport, the construct would remain mostly located at the outside of the cells.

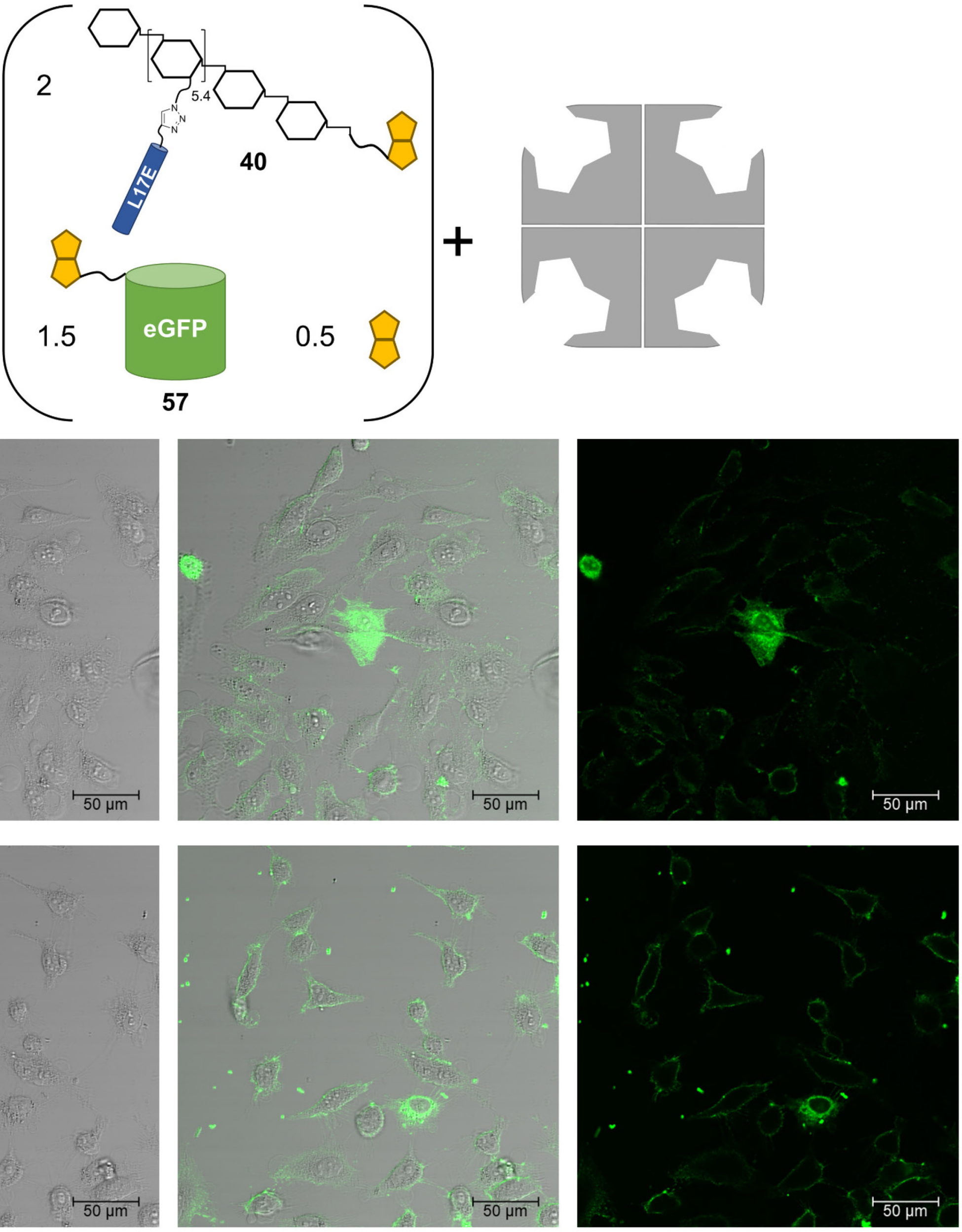

Figure 47| CLSM images (20x) of HeLa cells incubated with 1.5 µM Sav equipped with 2 copies of biotin-cadaverine-dextran-(L17E)$_{5.4}$ **40** and 1.5 copies of biotinylated eGFP **56** at 37 °C (top) and 4 °C (bottom) with brightfield (left), overlay (middle) and fluorescence channel (right).

The experiments regarding cellular uptake of Sav promoted by biotinylated dextran confirmed the general feasibility of the approach. 2 copies of L17E-decorated dextran could facilitate the cellular uptake of non-covalently attached Sav at low micromolar concentration. Furthermore, the site-specific biotinylation of eGFP enabled by enzyme-mediated protein functionalization and “click”-reaction allowed for convenient assembly of dextran-eGFP hybrids using Sav as centerpiece. The resulting construct efficiently translocated into HeLa cells at 3 µM even at low incubation temperature. Considering the overall molecular weights ranging from 109 kDa (fluorescently labeled Sav) to approximately 139 kDa (eGFP as additional cargo), L17E-decorated dextran displayed remarkable efficiency in delivering these large cargo molecules. However, the prospect of further application is curtailed by high intrinsic cytotoxicity of L17E-decorated dextran. In comparison to dextran **34** equipped with 5.4 copies GFP 11 peptide and L17E in total, comprising the same *N*-cadaverine-dextran-$(N_3)_{5.4}$ **29** as framework, biotinylated dextran **40** was far more toxic. Additionally, the degree of functionalization of approximately 80% at the reducing end meant that some of dextran **40** was actually not equipped with biotin and was therefore unable to bind to Sav. Thus, in the upcoming series of experiments, it will be required to simultaneously detect intracellular delivery of eGFP and cell viability, e.g., by co-application of live cell imaging fluorophors such as 7-amino actinomycin (7-AAD), which can only traverse damaged cell membrane.[229]

Hence, further optimization of both dextran framework functionalization and careful decoration with L17E would be required to yield a delivery module capable of facilitating intracellular delivery of protein cargo whilst causing less side-effects. With such an optimized delivery module, the scope of Sav-dextran hybrid mediated intracellular delivery could be expanded to bear additional biotinylated functionalities. Cargoes of great interest would be antibody(-fragments), which could be either directed at extracellular targets, like receptors, to enable cell specific delivery, or directed at intracellular targets. Alternatively, receptor-targeting peptides could be employed to impart cell specificity to the construct, a strategy presented in the upcoming sections.

4.4 Modular Dextran-Streptavidin Hybrids: Targeting Death Receptor 5

4.4.1 Design and Synthesis

The preceding experiments concerning intracellular delivery of Sav, mediated by biotin-functionalized dextran, confirmed the general compatibility of the polysaccharide and protein in the designed architecture. Encouraged by these results, the effect of dextran tetramerization on Sav as core structure should be evaluated in an alternative approach, based on receptor-targeting peptides. One particular member of these peptidic entities, death-receptor 5 targeting peptide (DR5TP), is of great interest due to its innate capability to induce apoptosis of cancer cells by clustering its target receptor on the cellular surface. While DR5TP in its monomeric form is not capable to trigger programmed cell death, multimerization of the peptide is paramount to induce receptor clustering and subsequent apoptosis in DR5-sensitive cells. Several scaffolds were reported for the display of DR5TP in a multimeric fashion, of which the heptameric protein C4-binding protein[188] as well as dextran[29] displayed efficacy in low nanomolar range. The potency of the dextran-based design could be further increased by additional dimerization on Fc as centerpiece.

These experiments with DR5TP-functionalized dextran suggest the application of Sav in conjunction with DR5TP-decorated dextran (**Figure 48**), to further investigate the impact of multimerization at a higher order than solitary polysaccharide as platform. The Sav-based design bears the advantage of easy assembly of protein and fully-functionalized dextran, in which the ratio of protein and biopolymer can be tuned by stochiometric control. Analogous to the previous section, monomeric DR5TP equipped with biotin should also be assembled on Sav to investigate the potential activity tetramerized peptide in absence of dextran.

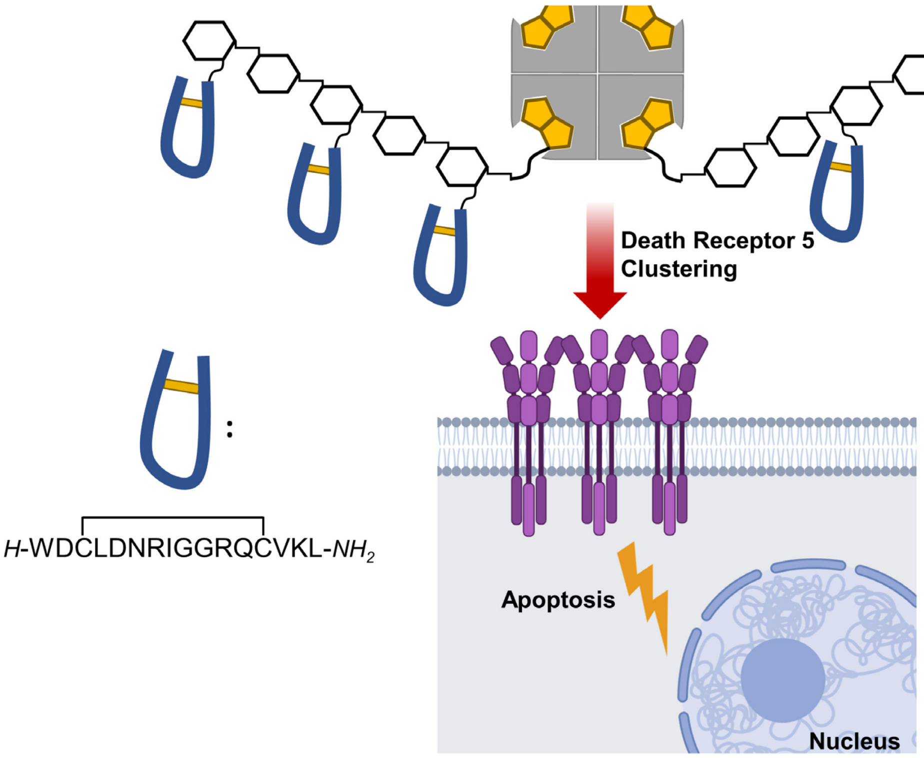

Figure 48| Depiction of apoptosis induced by DR5TP-decorated dextran attached to Sav as core structure. Created with BioRender.com.

The synthesis of DR5TP-functionalized dextran was performed with biotin-cadaverine-dextran-$(N_3)_{5.4}$ **38** as scaffold, whereby the peptide was introduced as alkyne-modified derivative **60** (provided by Dr. Hendrik Schneider) *via* CuAAC. The amount of both $CuSO_4$ and ascorbic acid were reduced to minimize cleavage of the intracellular disulfide bond by ascorbic acid as reducing agent and the reaction was performed in presence of BTTAA in phosphate buffer (**Scheme 24**).

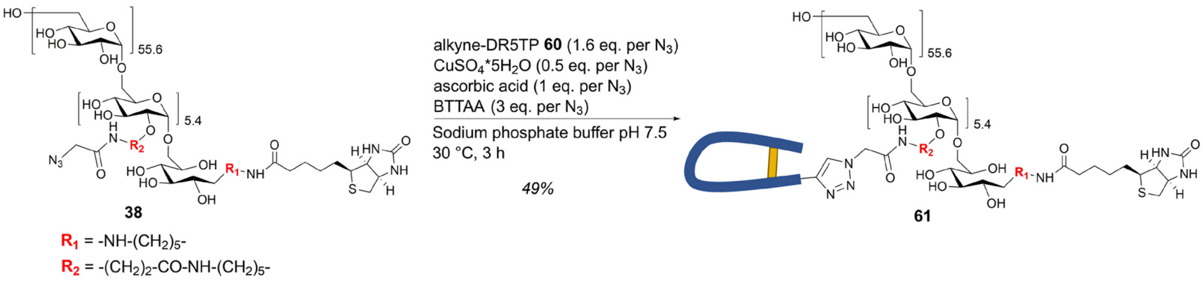

Scheme 24| CuAAC-mediated coupling of alkyne-DR5TP **60** to biotin-cadaverine-dextran-$(N_3)_{5.4}$ **38**.

Biotin-functionalized monomeric DR5TP (**Figure 49**) was obtained by solid-phase peptide synthesis. Upon completion of the peptide sequence, Ahx was introduced *N*-terminally as spacer, followed by conjugation of biotin. Oxidative cyclization was achieved by bubbling with pressurized air through a highly diluted solution of the crude peptide in a mixture of DMSO and ammonium carbonate buffer (pH = 8.35).

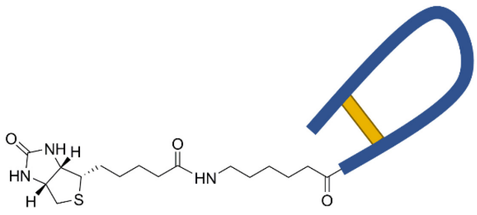

62

Figure 49| Schematic depiction of DR5TP *N*-terminally equipped with Ahx as spacer, and biotin.

4.4.2 Cell Killing Studies

Initial experiments were performed to confirm the general activity of DR5TP-decorated dextran against DR5-overexpressing COLO205 cells, as previously reported by Schneider et al.[29] Additionally, the potential increase in efficiency upon dextran-tetramerization using Sav as framework should be investigated. Beside DR5TP displayed on dextran in multiple copies, the biotinylated DR5TP derivative **62** should also be subjected to tetramerization on Sav and its cytotoxic profile should be assessed. To that end, COLO205 cells were treated with serial dilutions of both DR5TP-functionalized dextran **61** and biotin-bearing DR5TP **62**, respectively, in presence or absence of Sav for 72 h, followed by evaluation *via* cell proliferation assay. As expected, dextran **61** induced cell killing in the low nanomolar range (**Figure 50**, **A**), which is in accordance with the literature.[29] Additional Sav in a 1:4 ratio with regard to dextran **61** enhanced cytotoxicity of the peptide-decorated polysaccharide significantly, strongly suggesting an additive effect originating from tetramerization. On the other hand, monomeric biotin-DR5TP **62** was not able to affect viability of COLO205 cells regardless of concentration (**Figure 50**, **B**), which was expected since multimerization of the peptide is required to trigger programmed cell death.[29, 188] However, tetramerization of the solitary peptide on Sav had no effect on the ability of the peptide to induce apoptosis, indicating that multiple DR5TP moieties could not bind to their target receptors simultaneously as a consequence of either spatial orientation or steric hindrance of the core protein. Valldorf and colleagues tetramerized DR5TP on Fc as scaffold protein *via* sortase A-mediated conjugation, which increased its affinity towards isolated DR5 whilst no improved induction of apoptosis compared to monomeric DR5TP could be observed.[188] These findings highlight the importance of a suited multimerization platform to efficiently target DR5-sensitive cells.

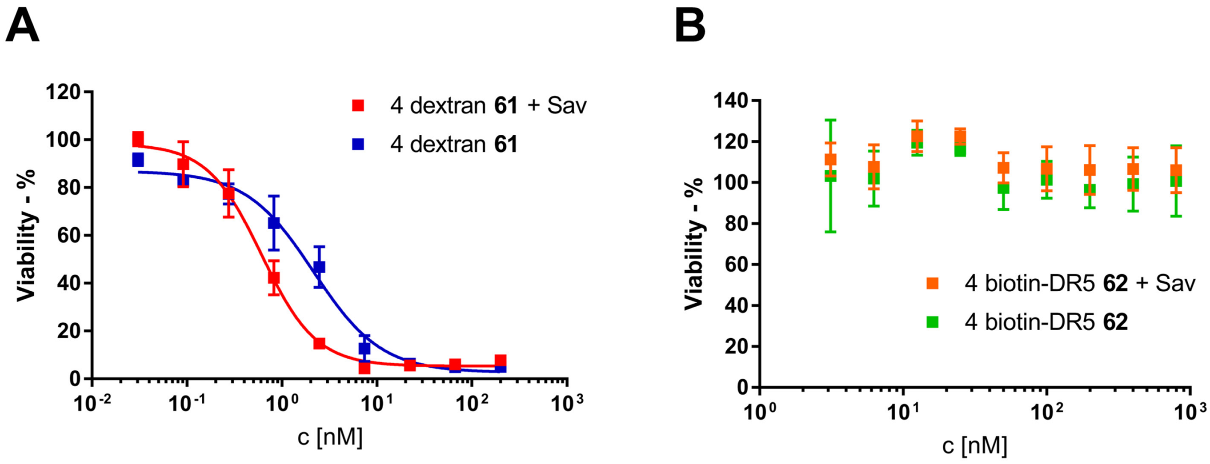

Figure 50| A: Cell viability assay of DR5TP-decorated dextran **61** in presence or absence of Sav as tetramerization platform. **B**: Cell viability assay of biotinylated DR5TP **62** +/- Sav. In both experiments, DR5-overexpressing COLO205 cells were incubated with serial dilutions of the constructs for 72 h in serum-containing medium, followed by a colorimetric MTS assay to determine cell viability. Results are shown as the mean ± standard error of the mean and are based on triplicates.

The apoptotic potency of biotin-cadaverine-dextran-(DR5TP)$_{5.4}$ **61**, individually or tetramerized on Sav, was quantified as effective concentration 50 (EC$_{50}$) values (**Table 2**), which were in the picomolar range for dextran **58** hybridized to Sav. Compared to solitary dextran **61**, the addition of Sav increased cytotoxicity by a factor of 3.5. Interestingly, the potency of dextran **61**, equipped with 5.4 copies of DR5TP on average, is considerably higher compared to the effective concentrations of 10 kDa dextran polymer harboring 11 and 13.4 DR5TP moieties reported in the literature, which displayed EC$_{50}$ values of 16.9 and 15.5 nM, respectively.[29] This could indicate that sufficient spacing between DR5TP units on dextran as scaffold is required to achieve enhanced apoptosis, triggered by receptor clustering.

Table 2| EC$_{50}$ values of dextran-Sav hybrids (4:1) and solitary dextran **61**, referring to the cytotoxicity of the constructs and dextran, respectively.

Construct	EC$_{50}$ [nM] Construct	EC$_{50}$ [nM] Dextran
Dextran **61** + Sav (4:1)	0.61	2.45
Dextran **61** (4x)	2.15	8.61

One of the outstanding features of DR5-targeted strategies is specific triggering of apoptosis in DR5-positive cells while sparing normal tissue. To investigate nonspecific cytotoxicity induced by the employed dextran-Sav constructs, human embryonic kidney (HEK) cells lacking DR5 on their cellular surface were treated with dextran **61** in presence or absence of Sav analogously to the COLO205 cells. Indeed, neither solitary dextran **61** nor its Sav conjugate induced significant cytotoxicity – up to 900 nM Sav – in DR5-negative HEK cells (**Figure 51**, **B**). In addition to the assessment of cell specificity, it should be determined whether enhanced potency of Sav-dextran hybrids compared to solitary polysaccharide **61** is actually attributable to tetramerization rather than Sav itself. To that end, Sav was incubated with a large excess (20 eq.) biotin for 1 h, followed by addition of 4 eq. biotin-cadaverine-dextran-(DR5TP)$_{5.4}$ **61**. As control, dextran **61** was incubated with biotin lacking Sav and subsequently COLO205 cells were treated with serial dilutions of both mixtures. Incubation of Sav with excessive biotin prior to addition of biotinylated dextran should prevent hybridization of the polysaccharide to a large extent. Indeed, both mixtures displayed no significant differences in the cell viability assay (**Figure 51**, **A**), strongly suggesting that the formation of Sav-dextran hybrids is the pivotal factor for increased potency.

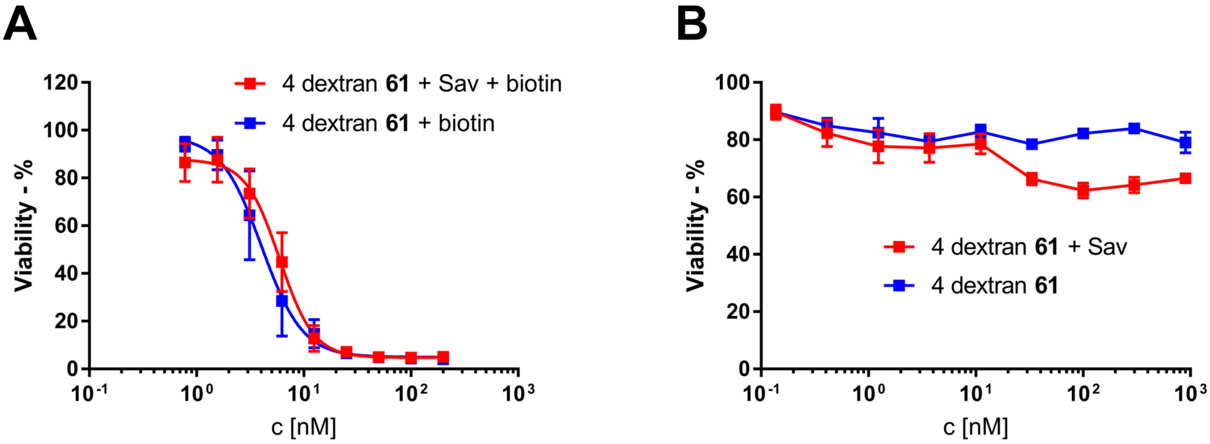

Figure 51| A: Cell viability assay of DR5TP-decorated dextran **61** and a large excess of biotin in presence or absence of Sav in COLO205 cells. **B**: Cell viability assay of DR5TP-decorated dextran **61** +/- Sav in DR5-negative HEK cells. Results are shown as the mean ± standard error of the mean and are based on triplicates.

Having evaluated the capabilities of the Sav-dextran approach to trigger apoptosis in COLO205 cells, its binding to these DR5-overexpressing cells was investigated. Therefore, AF647-labeled Sav **59** was decorated with 4 copies of biotin-cadaverine-dextran-(DR5TP)$_{5.4}$ **61** and COLO205 cells were treated with serial dilutions of this construct for 45 min at 4 °C. In addition, binding to U87MG glioblastoma cells, which express DR5 on their cell surface but are more or less insensitive to TRAIL-induced apoptosis due to resistance mechanisms, was investigated.[230] A distinct concentration-dependent increase in fluorescence was observed in both cell lines (**Figure 52**), with the entire population of U87MG cells shifting upon addition of the DR5TP-containing dextran-Sav hybrid. COLO205 cells, on the other hand, comprised a subpopulation with lower fluorescence that disappeared only at the highest concentration. The negative control, biotin-decorated Sav-AF647, induced only little increase in fluorescence in both cell lines at high concentrations (**Figure 52**).

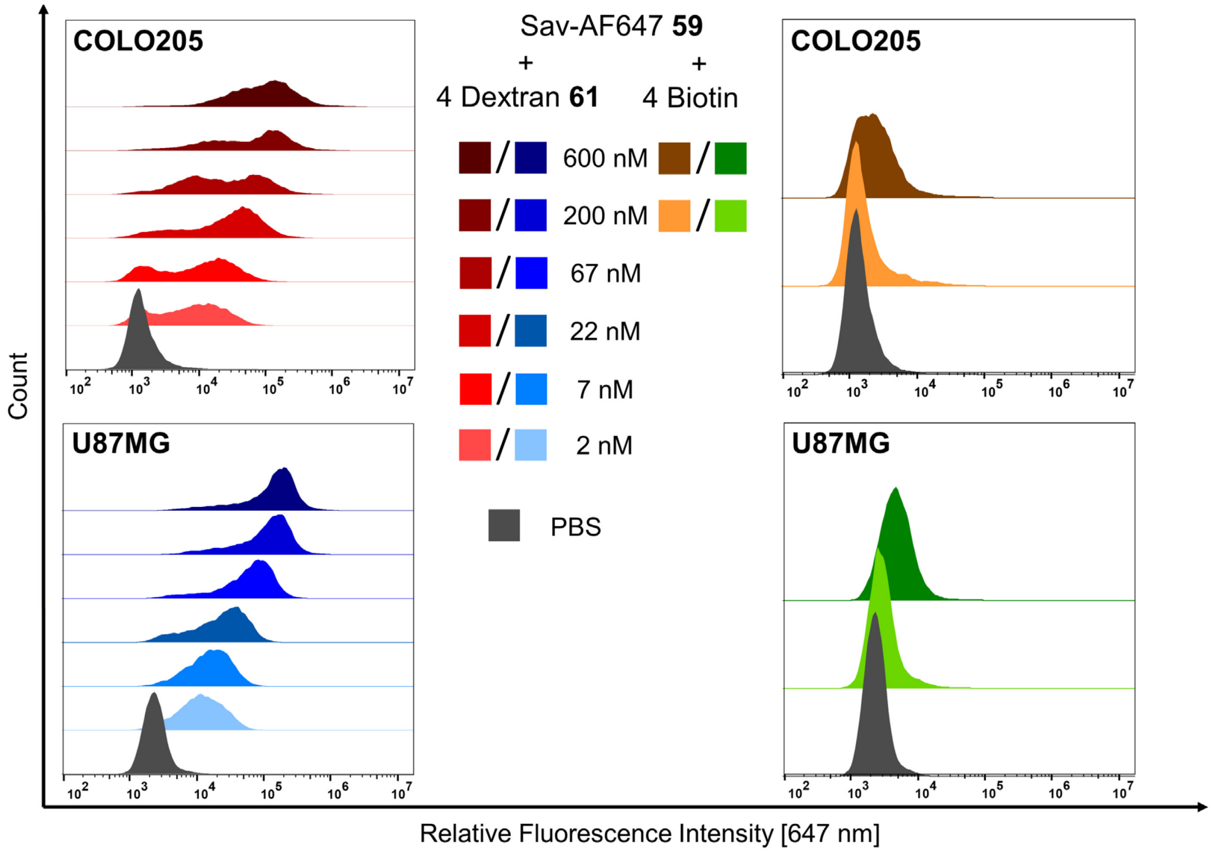

Figure 52| Histograms (half offset) showing AF647-fluorescence (λ = 647 nm) of COLO205 cells (top) and U87MG cells (bottom) treated with Sav-AF647 **59**, decorated with 4 eq. biotin-cadaverine-dextran-(DR5TP)$_{5.4}$ **61** (left) and 4 eq. biotin (right).

The initial experiments regarding cell killing of DR5-overexpressing COLO205 cells mediated by DR5TP-decorated dextran revealed a 3.5-fold increase in potency upon tetramerization on Sav. To further evaluate the influence of multimerization on Sav, the protein was equipped with 4, 3, 2 and 1 eq. biotin-cadaverine-dextran-(DR5TP)$_{5.4}$ **61**, on average, and subjected to assessment *via* cell viability assay in COLO205 cells. Sav equipped with 3 and 4 copies of DR5-decorated dextran **61**, respectively, displayed the highest apoptosis-inducing potency (**Figure 53**). Further reduction of biotin-cadaverine-dextran-(DR5TP)$_{5.4}$ **61** in relation to Sav led to distinctly lower effectiveness (**Figure 53**).

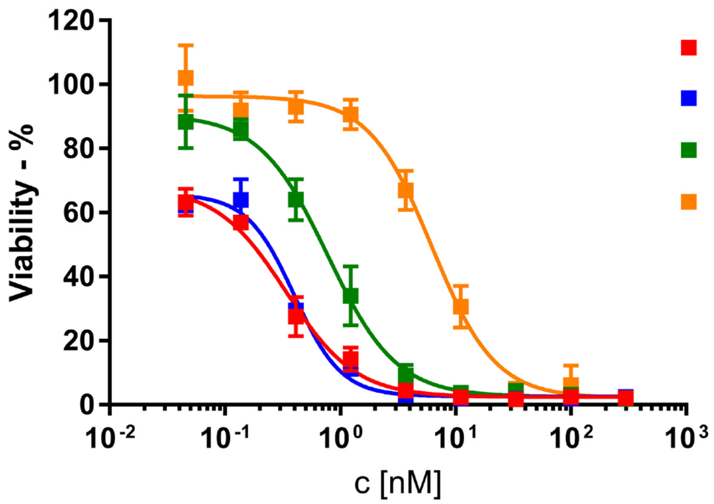

Figure 53| Cell viability assay of Sav equipped with 4, 3, 2 and 1 eq. biotin-cadaverine-dextran-(DR5TP)$_{5.4}$ **61**, on average, in COLO205 cells. Results are shown as the mean ± standard error of the mean and are based on triplicates.

In order to quantify the impact of multimerization on the potency of Sav-dextran hybrids, the EC$_{50}$ values of the different constructs were determined (**Table 3**). Sav equipped with more than one copy of DR5-decorated dextran displayed EC$_{50}$ values in the subnanomolar range, strongly suggesting an additive effect as a consequence of multimerization. Considering the concentrations of dextran in the hybrid architecture (**Table 3**), a fourfold increase in efficiency could be observed upon dimerization compared to its counterpart harboring equal amounts of Sav and dextran. Constructs with an even higher ratio of dextran to Sav showed only slight improvements, which could indicate that only two copies of DR5TP-decorated dextran bound to Sav are capable to interact with their target receptors simultaneously, possibly due to unfavorable spatial orientation of the additional dextran ligands.

Table 3| EC$_{50}$ values of dextran-Sav hybrids harboring 4, 3, 2 and 1 eq. DR5TP-decorated dextran **61** with regard to Sav, referring to the cytotoxicity of the constructs and dextran, respectively.

Construct	EC$_{50}$ [nM] Construct	EC$_{50}$ [nM] Dextran
4 Dextran **61** + Sav	0.34	1.36
(3 Dextran **61** + 1 biotin) + Sav	0.40	1.19
(2 Dextran **61** + 2 biotin) + Sav	0.77	1.55
(1 Dextran **61** + 3 biotin) + Sav	6.24	6.24

The experiments regarding the specific targeting of DR5 overexpressing COLO205 cells with DR5TP-decorated dextran **61** assembled on Sav as centerpiece, that allowed for additional tetramerization of the peptide-polysaccharide hybrid, demonstrated the general feasibility of the strategy. Compared to unbound dextran **61**, its efficiency could be enhanced distinctly by dimerization on the protein scaffold, whereas a higher ratio of dextran to Sav did not result in increased induction of apoptosis. Encouraged by these results, the scope of application of receptor-targeting peptides, multimerized on dextran as primary backbone and Sav as additional centerpiece, should be extended to an alternative target.

4.5 Modular Dextran-Streptavidin Hybrids: Targeting Integrin Receptor αvβ3

4.5.1 Design and Synthesis

The preceding experiments confirmed the general applicability of peptide-decorated dextran, equipped with a biotin handle at its reducing end, in conjunction with its counterpart Sav as efficient inducers of apoptosis in receptor-overexpressing cells. Thereby, the inherent potency of DR5TP-decorated dextran towards malignant cells could be further amplified upon multimerization on Sav as scaffold. Encouraged by these results, an alternative class of addressable receptors were chosen, to further evaluate the potential of dextran-Sav hybrid architecture. Out of the plethora of potential target proteins, integrins have gained special interest in the last decades due to their pivotal involvement in cancer progression. Thus, much effort is being directed towards designing and improving binders targeting integrins, with a focus on the integrin receptor αvβ3. Initiated by the discovery of the minimal recognition sequence RGD in natural protein ligands, optimization strategies culminated in the development of the cyclic peptide cilengitide (*cyclo*[RGDf(NMe)V]).[160] While clinical trials revealed the ineffectiveness of cilengitide in treatment of various cancers due to induction of adverse side effects at low plasma concentrations, the framework of this cyclic peptide remains an attractive motif for the development of novel integrin targeting strategies. Thanks to the interchangeability of valine, which allows for the incorporation of addressable amino acids like lysine or glutamate, the cyclic peptide was employed in covalent constructs either in monomeric fashion or multimerized on scaffolds, among them dextran[231] and Sav[175], to potentially increase affinity or rate of internalization.

In contrast to the preceding experiments regarding specific targeting of DR5-overexpressing cancer cells thereby inducing apoptosis at low nanomolar concentrations, successful addressing of αvβ3-expressing cells using the dextran-Sav hybrid architecture is not expected to result in programmed cell death of the target. Nevertheless, Sav could serve as centerpiece for a multifunctional construct harboring peptide-functionalized dextran as targeting module (**Figure 54**), combined with additional functionalities such as fluorophores for imaging or cytotoxins for targeted therapy. To investigate the general feasibility of this approach, dextran should be functionalized in an analogous fashion to the previous sections with biotin at its reducing end and RGD-containing cyclic peptides (*cyclo*[RGDfK], **71**, **Figure 54**) at the repeating units, followed by tetrameric assembly on fluorescently labeled Sav as core structure and employment in cell binding studies. A cyclic peptide containing alanine (*cyclo*[RADfK], **72**,

Figure 54) instead of glycine should be used as a negative control, and in addition, the effect of tetramerization of the cyclic peptides in the absence of dextran as backbone should be investigated.

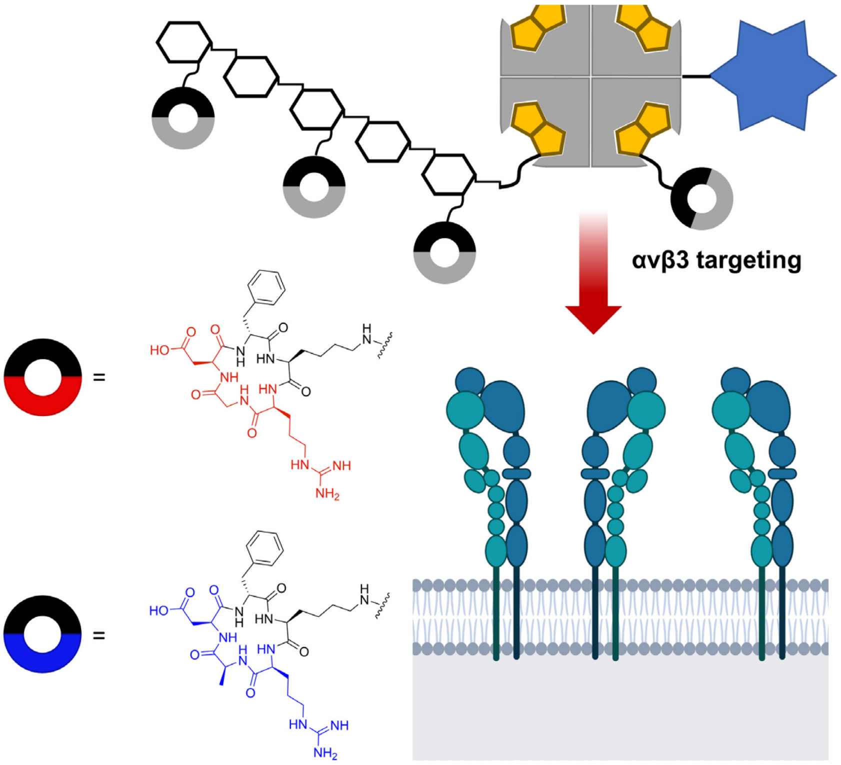

Figure 54| Depiction of fluorescently labeled Sav equipped with either solitary biotinylated cyclic peptides (circular shape, with general depiction (gray), *cyclo*[RGDfK] (red) and *cyclo*[RADfK] (blue)) or biotinylated dextran decorated with multiple copies of the cyclic peptides. Figure adapted from Schneider et al.[232]

For the assembly of biotinylated dextran equipped with either *cyclo*[RGDfK] or the negative control *cyclo*[RADfK], the framework of dextran with biotin at its reducing end and azide functionalities at the repeating units was synthesized as described before (**Scheme 25**). However, in the previous synthesis of TAMRA-cadaverine-dextran-$(N_3)_{5.4}$ **31**, both NMR and photometric analysis revealed that only approximately 80% of dextran polymer was functionalized at its reducing end, probably as a consequence of incomplete covalent attachment of *N*-Boc-cadaverine in the first step. Thus, the reductive amination was analyzed in greater detail, which revealed an increased pH of around 11 upon addition of *N*-Boc-cadaverine. Readjustment of the pH to 8.2 with hydrochloric acid resulted in a product, which displayed a degree of reducing-end functionalization of approximately 90% according to NMR analysis (**Figure S 96**) upon carboxyethylation. Interestingly, carboxyethylation with the same equivalents of acrylamide as described for the synthesis of dextran **26** afforded *N*-Boc-cadaverine-dextran-$(N_3)_{6.3}$ **63** equipped with an additional carboxyethyl group on average. Azide functionalities were introduced by conjugation of *N*-(5-aminopentyl)-2-azidoacetamide **27**, followed by acidic cleavage of the Boc-protecting group at the reducing end and the deprotected amine was subsequently biotinylated with biotin-NHS **37** (**Scheme 25**).

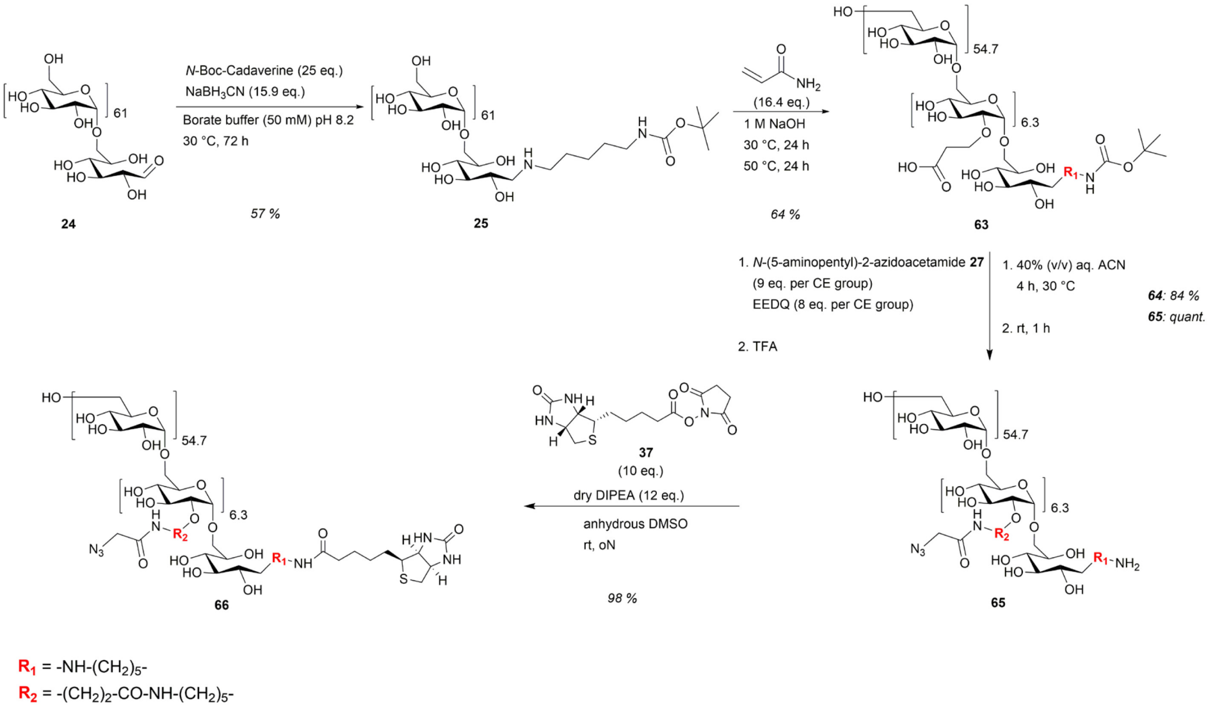

Scheme 25| Functionalization of dextran to afford final product biotin-cadaverine-dextran-$(N_3)_{6.3}$ **66**.

After completion of the dextran modification, both peptides *cyclo*[RGDfK] **74** and *cyclo*[RADfK] **75** were prepared. To that end, the linear precursors **67** and **68** were prepared by SPPS on 2-chlorotrityl chloride resin to afford the free *C*-terminus upon cleavage from solid support, which was performed under mild acidic conditions to conserve the side chain protecting groups (**Scheme 26**).[233] Following that, head-to-tail cyclization of the linear peptides afforded the cyclic peptides **69** and **70**, which was conducted at low concentrations to minimize side reactions such as dimerization (**Scheme 26**).[234] Subsequent cleavage of the side chain protecting groups in a mixture of TFA and DCM yielded *cyclo*[RGDfK] **71** and *cyclo*[RADfK] **72** (**Scheme 26**), whereby the latter product was compromised of two species with different retention time in the HPLC (**Figure S 109**, **Figure S 111**) but identical m/z signals. These findings indicate the formation of stereoisomers, probably during head-to-tail cyclization of the linear precursor peptide, as has been reported in the literature.[235] This assumption is supported by the fact that this was the case only for *H*-D(OtBu)-f-K(Boc)-R(Pbf)-A-*OH* **67** comprising a *C*-terminal alanine, but not for the analogue *H*-D(OtBu)-f-K(Boc)-R(Pbf)-G-*OH* **68** harboring the non-chiral glycine. The obtained cyclic peptides had to be modified at the lysine residue for the subsequent coupling to biotin-cadaverine-dextran-$(N_3)_{6.3}$ **66** *via* CuAAC by introduction of an alkyne functionality. Since *in situ* activation of 4-pentynoic acid was not possible due to the presence of aspartate in the cyclic peptides, the alkyne bearing acid was preactivated as NHS-ester **73** (synthesis performed by Dr.

Hendrik Schneider) and then reacted with the lysine residue under anhydrous conditions using DIPEA as base (**Scheme 26**).

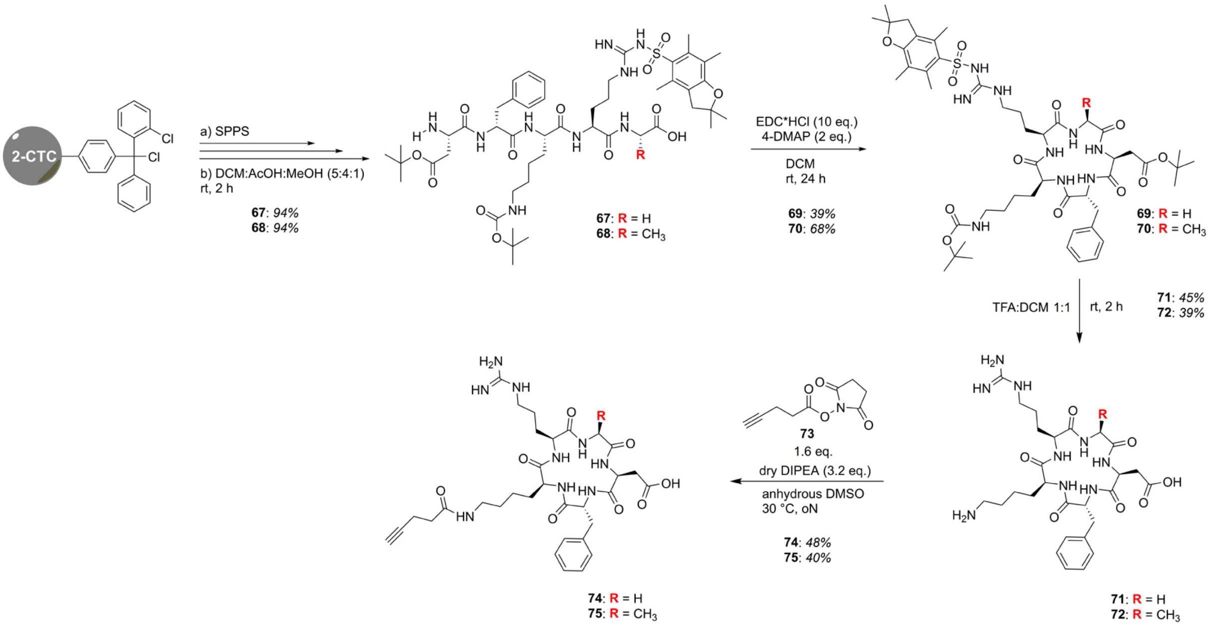

Scheme 26| Synthetic approach towards alkyne-modified *cyclo*[RGDfK] **74** and *cyclo*[RADfK] **75**.

Decoration of biotin-cadaverine-dextran-$(N_3)_{6.3}$ **63** with either *cyclo*[RGDfK] **71** or *cyclo*[RADfK] **72** at the repeating units was performed by CuAAC. The reaction was performed in sodium phosphate buffer using BTTAA as chelating agent and *in situ* generation of Cu(I) catalyst overnight (**Scheme 27**), followed by isolation of the products **76** and **77** by consecutive SEC-HPLC runs on an analytical scale. Success of the reactions was confirmed by IR spectroscopy, which displayed the absence of azide bands in both products (**Figure S 118**, **Figure S 120**).

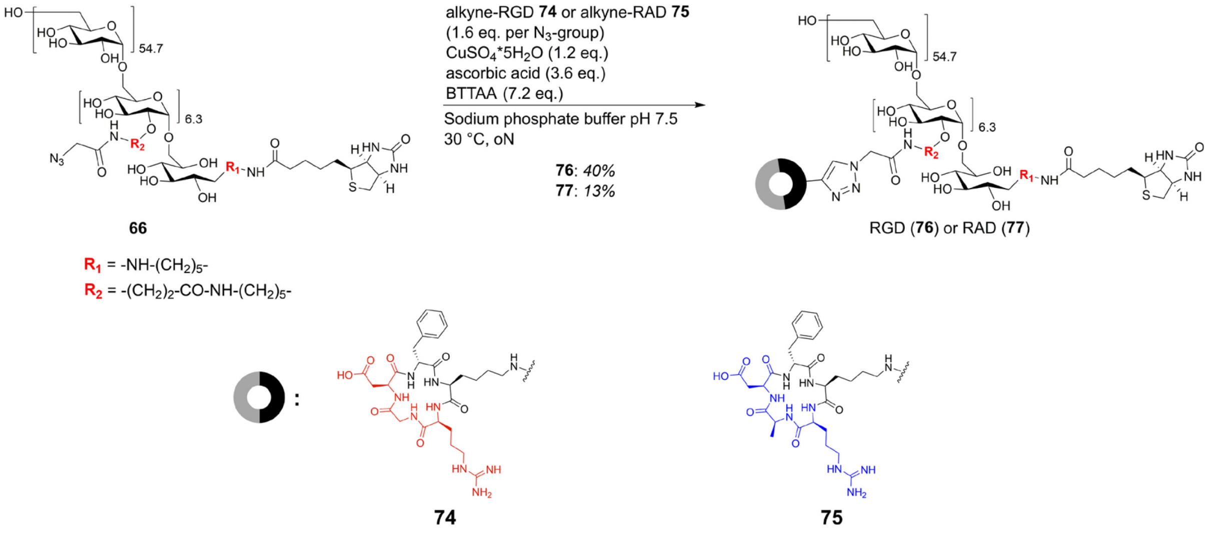

Scheme 27| CuAAC-mediated synthesis of biotin-dextran equipped with either *cyclo*[RGDfK] **74** or *cyclo*[RADfK] **75** at the repeating units.

Analogous to the previous sections regarding Sav-dextran hybrids for cellular uptake and DR5-directed cell killing, respectively, the studies should also include peptides tetramerized on Sav in absence of dextran as scaffold. Thus, derivatives of both cyclic peptides were required comprising a biotin handle, separated from the receptor binding RGD motif by a spacer molecule. To that end, Ahx was modified with biotin at its *N*-terminus using solid phase synthesis (**Scheme 28**). After cleavage from solid support, linker **78** was activated as NHS ester and subsequently conjugated to either *cyclo*[RGDfK] **71** or *cyclo*[RADfK] **72**.

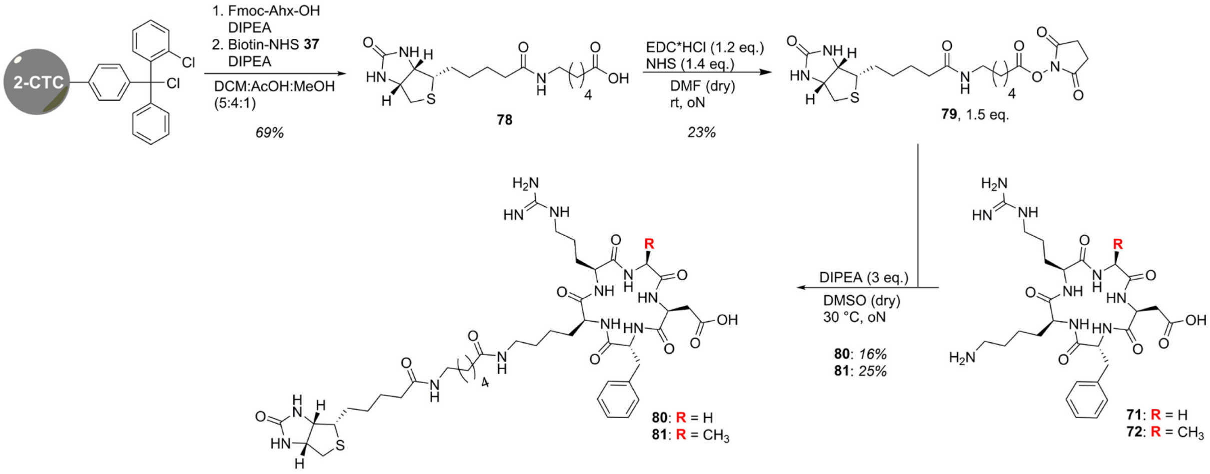

Scheme 28| Synthetic pathway leading to biotinylated *cyclo*[RGDfK] **80** and *cyclo*[RADfK] **81**.

4.5.2 Receptor Binding Studies

Initially, the binding capabilities of both solitary biotin functionalized *cyclo*[RGDfK] **80** and biotin-cadaverine-dextran-[RGDfK]$_{6.3}$ **76** towards their target receptor integrin αvβ3 should be assessed. To that end, these structures were employed in an ELISA assay using the natural integrin ligand vitronectin as competitor. Thus, the compounds were mixed at different concentrations with vitronectin at constant concentration and added to immobilized recombinant αvβ3, followed by quantification of the binding of the biotinylated species using streptavidin-horse radish peroxidase (Sav-HRP) and photometric measurement of the emerging chromophore at 405 nm wavelength (**Figure 55**, **A**). This assay displayed strong binding of all compounds, including RAD-containing species, to the receptor at high concentrations (**Figure 55**, **B**). At lower concentrations down to the picomolar range, both biotinylated solitary RGD **80** and RGD-decorated dextran **76** could compete successfully with their counterpart vitronectin, whereby monomeric RGD **80** displayed better performance than multimeric dextran **76**. The overall higher degree of binding, expressed as absorption of the chromophore, of monomeric RGD **80** could be explained by the fact, that the ratio of RGD to biotin moiety is 1:1, whereas RGD-decorated dextran **76** comprises at least six RGD molecules per biotin in its backbone. In contrast, dextran **77** equipped with 6.3 copies of RAD on average displayed higher binding capabilities in comparison to its monomeric counterpart **81** at higher concentrations, suggesting unspecific binding caused by either multimerization or the polysaccharide backbone itself.

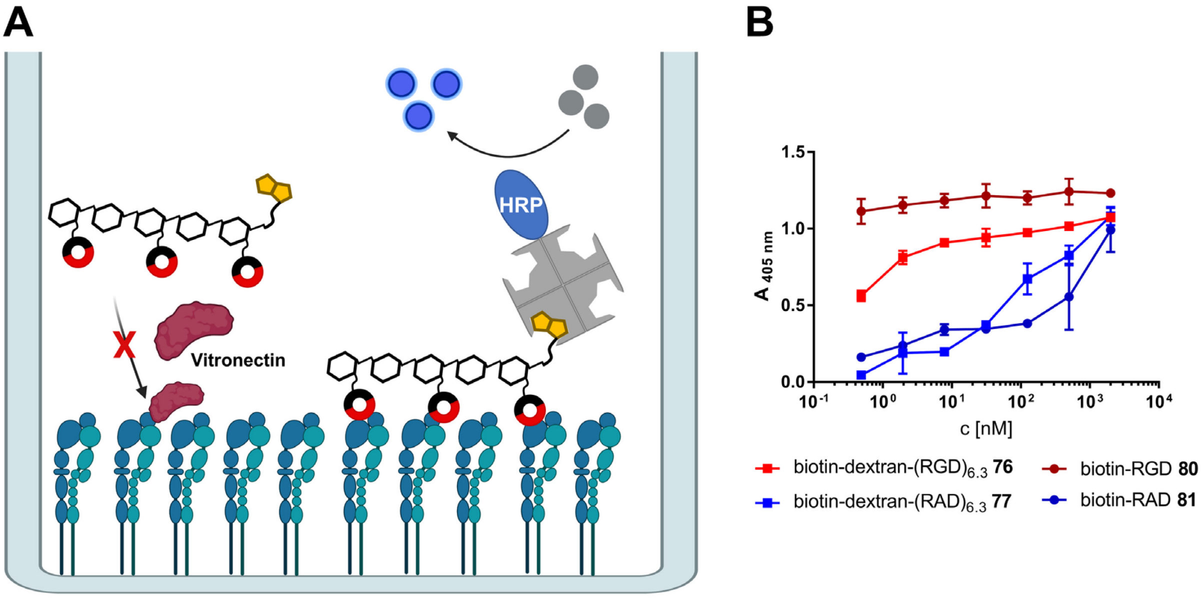

Figure 55| A: Schematic depiction of the employed vitronectin competition assay. Biotinylated RGD- and RAD-species were mixed at different concentrations with a fixed concentration of vitronectin and added to recombinant immobilized αvβ3. After incubation and removal of the supernatant, Sav-HRP was added, which binds to the biotinylated compounds, followed by quantification *via* enzymatic turnover of colorless substrate to the chromophore. **B**: Concentration-dependent binding of the various RGD and RAD containing species to immobilized αvβ3 in competition with the natural ligand vitronectin.

Next on, the binding characteristics of both solitary biotin-functionalized *cyclo*[RGDfK] **80** and biotin-cadaverine-dextran-[RGDfK]$_{6.3}$ **76** were examined on αvβ3-positive U87MG cells[236]. To that end, AF647-labeled Sav **59** was decorated with 4 copies of biotin-*cyclo*[RGDfK] **80** and biotin-cadaverine-dextran-[RGDfK]$_{6.3}$ **76**, or their respective alanine-containing counterparts **78** and **74** as negative control, and added to the cells. Flow cytometry displayed generally only a minor shift in fluorescence upon addition of the probes assembled on Sav-AF647 **59** (**Figure 56**) at the highest concentration of 500 nM. Furthermore, no significant difference between the RGD-containing compounds and their negative controls could be observed (**Figure 56**).

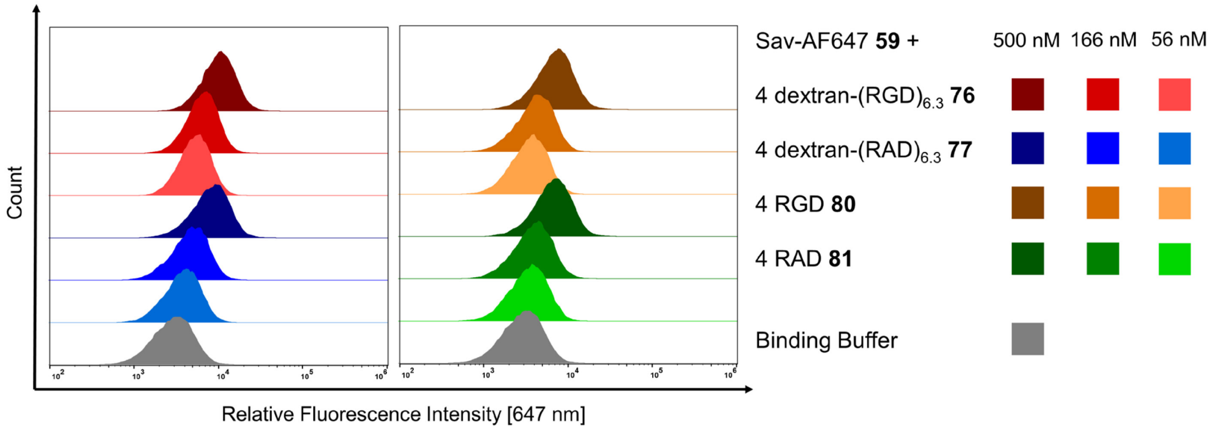

Figure 56| Histograms (half offset) showing AF647-fluorescence (λ = 647 nm) of U87MG cells treated with Sav-AF647, decorated with 4 eq. biotinylated RGD-dextran **76**, RAD-dextran **77** (left) or solitary biotin-RGD **80** and biotin RAD **81** (right).

The inaptitude of the RGD-containing probes to target αvβ3-positive U87MG cells, despite the successful receptor-targeting in the ELISA assay (**Figure 55**, **B**), could indicate a negative influence of the core protein Sav on the binding capability, possibly as a result of steric hindrance due to formation of a molecular assembly with an expected very large hydrodynamic radius of four hydrated dextran molecules assembled on the Sav centerpiece. Nevertheless, this finding requires further elucidation, e.g., by performing binding studies of dextran-RGD in absence of Sav followed after removal of unbound dextran by addition of Sav-647 as detection agent. Thus, the initial strategy based on Sav as centerpiece for the assembly of integrin-targeting dextran was terminated. In an alternative design based on the preceding work by Dr. Hendrik Schneider and in collaboration with him, RGD-functionalized dextran was dimerized on human Fc as centerpiece, which will be presented in detail in the following section.

4.5.3 Alternative Approach: Integrin-Targeting Dextran-Fc Hybrids

Specific targeting of αvβ3-positive U87MG cells *via* RGD-functionalized dextran tetramerized on Sav as centerpiece failed due to a lack of receptor-binding capabilities in a cell-based assay. In preceding experiments conducted by Dr. Hendrik Schneider, DR5TP-decorated dextran dimerized on human Fc as centerpiece proved efficient in DR5-targeting and induction of apoptosis in COLO205 cells.[29] Hence, in collaboration with Dr. Hendrik Schneider, this approach was utilized for specific targeting of integrin overexpressing cells (**Figure 57**). Additionally, the introduction of a cytotoxin, i.e., monomethyl auristatin E (MMAE), should enable targeted cell killing upon receptor-mediated endocytosis. For the subsequent intracellular release of the toxin, an additional valine-citrulline-PAB (*p*-aminobenzyl alcohol) linker was introduced, which is cleavable by the enzyme cathepsin B present in lysosomes.[237]

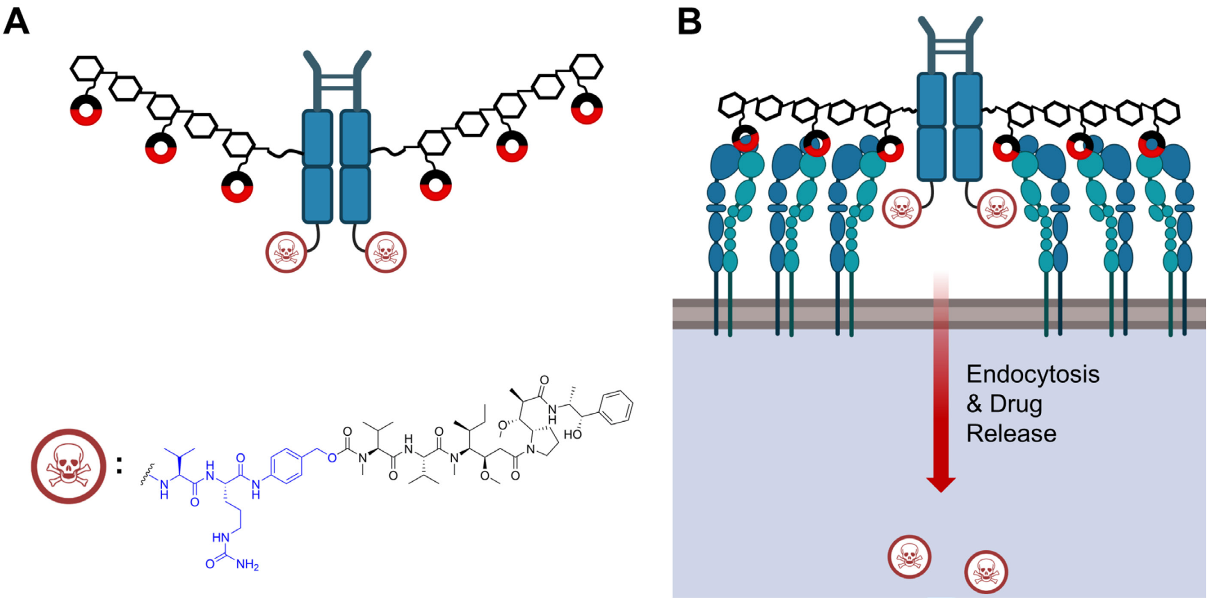

Figure 57| A: Schematic depiction of the integrin-targeting dextran-Fc hybrid, equipped with multiple copies of RGD and further functionalized with the cytotoxic agent MMAE (blue: Val-Cit-PAB linker). **B**: Intended mechanism of action: Binding of αvβ3 on the cell surface by the construct results in receptor-mediated endocytosis and subsequent release of free cytotoxin. Figure adapted from Schneider et al.[232]

Assembly of the multifunctional construct was based on orthogonal enzyme reactions and subsequent "click" modification. Two orthogonal enzyme modification sites were introduced in human Fc, i.e. a *C*-terminal LPETGG tag as recognition sequence for sortase A,[238] as well as a N297A mutation, which results in an aglycosylated Fc **82** and allows for enzymatic addressing of Q295 *via* microbial transglutaminase (mTG).[42] In the first step, the cytotoxin was introduced as GGG-PEG$_3$-Val-Cit-Pab-MMAE by sortase A-catalyzed condensation (**Scheme 29**), which resulted in a drug-to-protein ratio of 1.6 according to HIC analysis.[232] Following that, *N*-cadaverine-dextran-(N$_3$)$_{15.6}$ **83** harboring 15.6 azide groups on average was covalently introduced at position Q295 by mTG-mediated transamidation (**Scheme 29**).[232] In the ultimate step, dextran polysaccharide was decorated with either alkyne-functionalized *cyclo*[RGDfK] **74** or *cyclo*[RADfK] **75** *via* CuAAC, resulting in the ultimate dextran-Fc hybrids **86** and **87** (**Scheme 29**).[232] Additionally, two dextran-Fc hybrids **88** and **89** lacking cytotoxic cargo MMAE were also synthesized (**Figure 60**, **A**).[232]

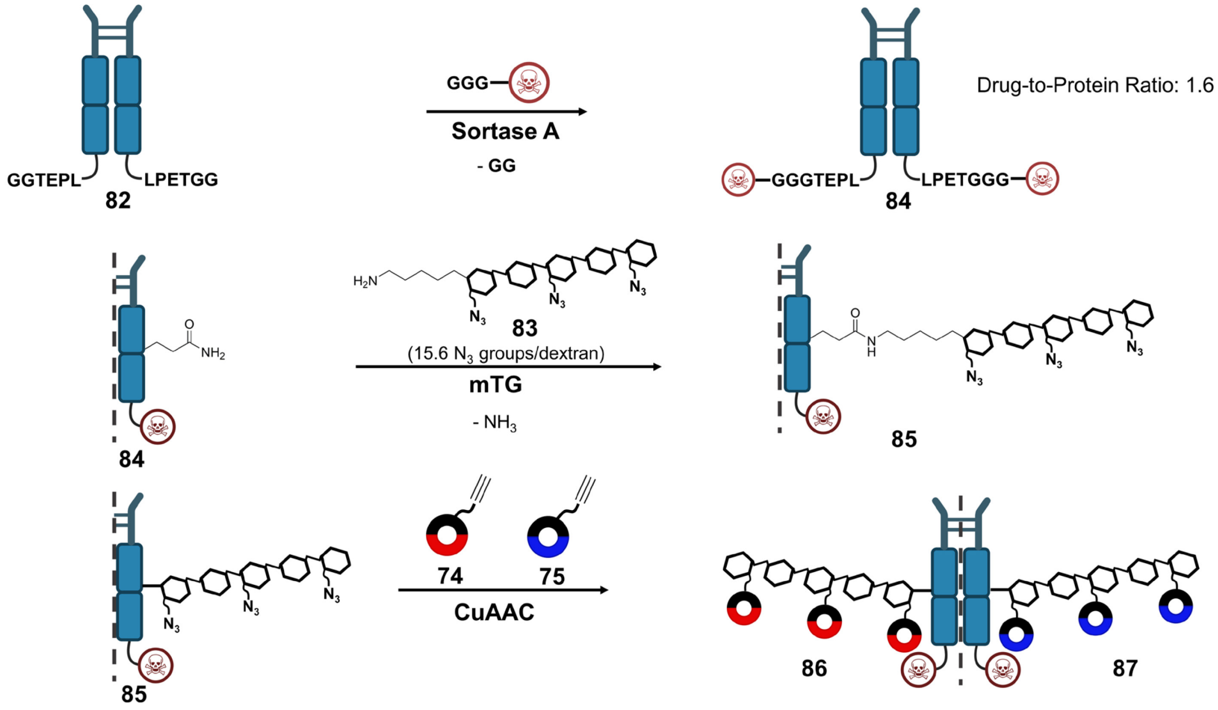

Scheme 29| Synthetic pathway towards integrin-targeting dextran-Fc hybrids. In the first step, cytotoxin MMAE (skull and crossbones) is introduced *via* Sortase A-catalyzed condensation. Following this, mTG-mediated transamidation at position Q295 allowed for the introduction of azide-functionalized dextran **83**. Finally, dextran polymers were decorated with either *cyclo*[RGDfK] **74** or *cyclo*[RADfK] **75** *via* CuAAC to afford the final products **86** and **87**. Please note that for the sake of simplification some symmetrical compounds are displayed as half structure, with the mirror axis as dashed line. Scheme adapted from Schneider *et al.*[232]

The receptor-binding capabilities of the novel Fc-dextran hybrids **86** and **87** were assessed on U87MG cells *via* flow cytometry.[232] In contrast to the preceding dextran-Sav approach (**Figure 56**), RGD-functionalized Fc-dextran **86** displayed distinct binding of αvβ3-positive U87MG cells even at low nanomolar concentration (**Figure 58**). The negative control, RAD-decorated Fc-dextran **87**, only showed little binding at relatively high concentrations (**Figure 58**).

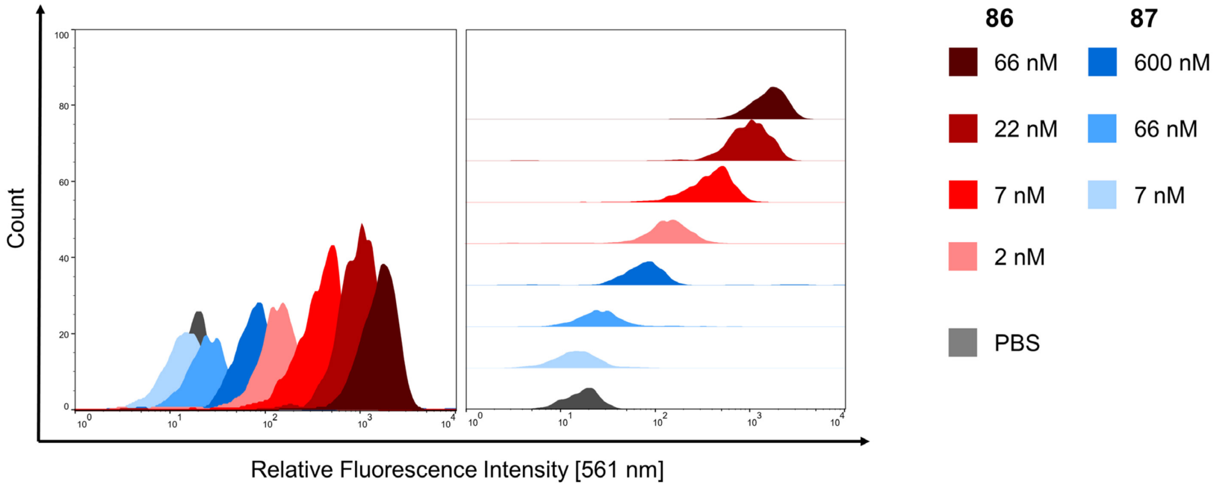

Figure 58| Binding of Fc-dextran hybrids **86** and **87** functionalized with RGD and RAD, respectively, to U87MG cells. Depicted as histogram (left) and half offset (right). Figure adapted from Schneider *et al.*[232]

Next on, the cytotoxic profile of Fc-dextran chimeras was assessed.[232] In addition to the peptide-functionalized constructs **86** and **87**, MMAE-functionalized Fc **84** was also included in order to investigate potential off-target toxicity as a consequence of non-specific endocytic. RGD-decorated Fc-dextran hybrid **86** induced significantly higher cytotoxicity in U87MG cells compared to its RAD-bearing counterpart **87** or MMAE-functionalized Fc **84** (**Figure 59**). This finding strongly suggests higher intracellular uptake of construct **86** as a consequence of specific integrin-targeting, followed by receptor-mediated endocytosis and enzymatic release of the toxin. Treatment of U87MG cells with RAD-functionalized construct **87** resulted in moderate toxicity at high concentrations, which could also be observed for Fc **84** lacking dextran. This could indicate integrin-independent uptake by macropinocytosis or the presence of Fc receptors on the cellular surface. Alternatively, hydrolysis of the linkage between Fc and MMAE could have resulted in the premature release of the cytotoxin, which is membrane-permeable in free form.

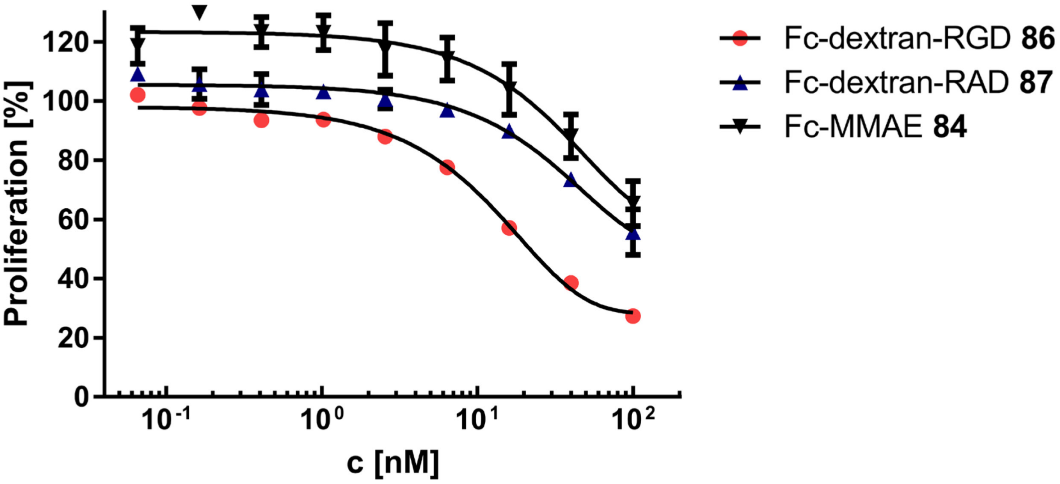

Figure 59| Cell proliferation assay of Fc-dextran decorated with RGD (**86**, red), RAD (**87**, blue) and Fc-MMAE **84** on U87MG cells. Figure adapted from Schneider *et al*.[232]

In order to elucidate whether integrin clustering induced by RGD-decorated Fc-dextran would also result in an antiproliferative effect in absence of MMAE as payload, U87MG cells were treated with constructs **88** and **89** (**Figure 60**, **A**).[232] However, the cell proliferation assay revealed no cytotoxic effect up to a concentration of 100 nM (**Figure 60**, **B**).

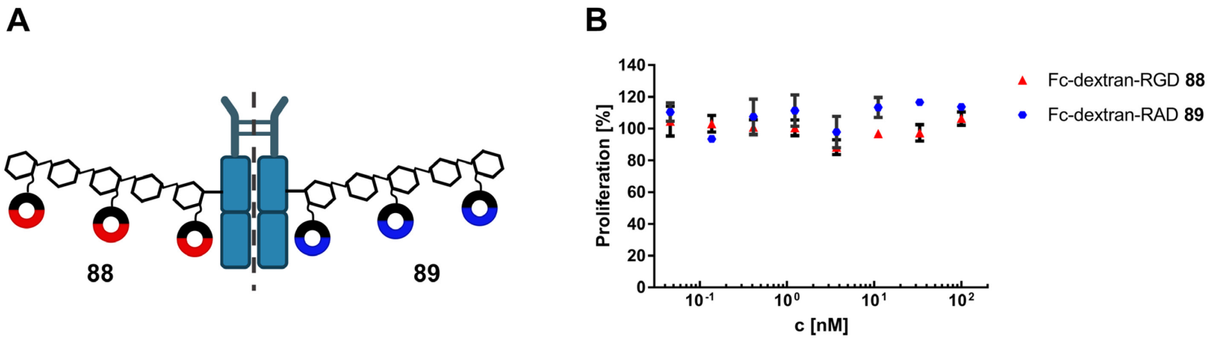

Figure 60| **A**: Schematic depiction of Fc-dextran construct **88** and **89** lacking cytotoxin MMAE. **B**: Cell proliferation assay of Fc-dextran decorated with RGD (**88**, red), RAD (**89**, blue). Figure adapted from Schneider et *al.*[232]

5 Summary and Outlook

In recent decades, the spectrum of available therapeutics has been expanded by the ever-growing field of biopharmaceuticals. Compared to their small molecule competitors, biotherapeutics such as peptides, proteins, and nucleic acids are characterized by advantageous properties such as high specificity and potency as a consequence of their molecular complexity and tunability.[239] However, the application of biotherapeutics is mostly limited to the extracellular environment due to their intrinsic disability to traverse the cellular membrane. Motivated by the challenge of overcoming this obstacle and expanding the range of potential targets for biotherapeutics into the cell´s interior, numerous strategies have been developed over the past years. Among those, cell-penetrating peptides have proven effective in facilitating the cytoplasmic delivery of attached payload.[9] While successful intracellular delivery can be achieved by simple conjugation of these cationic peptides to its cargo, more elaborate and sophisticated architectures can be designed to further improve the transduction efficiency. Multimeric presentation of CPPs on scaffold molecules is one of the promising approaches to reach this goal. Analogously, receptor-targeting peptides could also benefit from multimerization on a suited platform.

The presented doctoral thesis summarizes results of a comprehensive study aimed at development of hybrid multimeric architectures for intracellular delivery of bioactive cargoes and enhancing the performance of receptor-targeting peptides.

The first study addressed the evaluation of different architectures in their ability to facilitate cellular uptake of bioactive 18mer PNA as payload. Thereby, the eGFP654 mis-splicing correction assay was performed as functional assay that allowed for comparison of the delivery modules in a quantitative fashion.[211] Three different CPPs, i.e., the arginine-rich peptides P14 and P17 as well as $(KF_2)_3K$, were employed. Additionally, the silicon-based nanoparticle GuCOSS and non-cationic DiSeL were chosen as non-peptidic alternatives. Initially, GuCOSS-PNA conjugates comprising either a stable thioether linkage (conjugate **13**) or a reductively-labile disulfide bond (conjugate **14**) were evaluated in the mis-splicing correction assay, which is based on the formation of functional eGFP upon successful translocation into modified HeLa cells. While flow-cytometric analysis displayed increased eGFP fluorescence in cells treated with either conjugate, no distinct differences in efficacy could be observed. GuCOSS-PNA hybrid **13** was subsequently benchmarked against its peptidic competitors, of which both P14 and P17 were optimized in their ability to facilitate translocation of PNA into mammalian cells,[210] whereas $(KF_2)_3K$ has proven efficacious in prokaryotes.[214] At the highest concentration of 20 µM and 37 °C, GuCOSS-PNA conjugate **13** outperformed the arginine-rich CPP-PNA conjugates by a slight margin. However, at lower concentration a rapid decline in performance of the silicon-based nanoparticle could be observed, whereas both P14 and P17 were effective down to a concentration of 5 µM. Arginine-free

$(KF_2)_3K$-PNA conjugate **16**, on the other hand, displayed only moderate activity at 37 °C, strongly suggesting energy-dependent endocytosis as the major uptake pathway. The remaining candidate, DiSeL-PNA conjugate **22**, which in contrast to its competitors relies on thiol-exchange reactions to facilitate cellular uptake,[215] failed to restore eGFP fluorescence even at 20 µM concentration. Beside the uptake-enhancing capabilities for bioactive payload, a beneficial cytotoxic profile of the delivery modules is paramount to be considered for potential future application in therapy. With exception of $(KF_2)_3K$, which displayed no cytotoxicity up to 40 µM, whereas the guanidine-bearing P14 and P17 as well as GuCOSS were increasingly toxic beyond 10 µM. The data indicates for GuCOSS that significant enhancement of eGFP fluorescence is inevitably associated with cytotoxicity. Both P14 and P17, however, still facilitate intracellular PNA translocation at lower concentrations without causing side effects.

In parallel with the synthesis and evaluation of delivery modules directly conjugated to the mis-splicing correcting PNA, my colleague Dr. Bastian Becker investigated the effect of L17E-multimerization on the polysaccharide dextran as scaffold.[217] The 25mer CPP, with attenuated cytotoxicity compared to its parent peptide M-lycotoxin, was capable of cytosolic delivery of full-length antibodies into mammalian cells upon simple coincubation.[117] Starting from this, Dr. Bastian Becker established dextran decorated with multiple copies of L17E as an efficient architecture for intracellular delivery of covalently attached cargo, using eGFP as model protein.[217] In search of payload that would validate cytosolic and even nuclear uptake in frame of a functional assay, the L17E-dextran carrier was functionalized to carry multiple copies of mis-splicing correcting PNA. Dextran-$(L17E)_{5.3}$-$(PNA)_{5.3}$ conjugate **23** was able to induce substantial enhancement of eGFP-fluorescence at concentrations ranging from 20 µM down to even 2.5 µM, despite its molecular weight of approximately 50 kDa.

Due to the remarkable performance of dextran-L17E in the mis-splicing correction assay, the architecture should be subjected to further validation in an additional functional assay. The GFP-complementation assay was chosen, which is based on non-covalent hybridization of the 16mer peptide GFP 11, the *C*-terminal β-strand of GFP, to the nonfluorescent fragment protein GFP 1-10 resulting in the recovery of fluorescence.[219] In order to investigate dextran-L17E as delivery module for GFP11 in the GFP-complementation assay, both L17E and GFP11 were covalently attached to the repeating units of dextran in a similar approach as described by Dr. Bastian Becker for the dextran-$(L17E)_{5.3}$-$(PNA)_{5.3}$ conjugate **23**. In addition to the peptides, the introduction of the fluorophore TAMRA at the reducing end of the polysaccharide should further confirm cellular uptake by microscopy and flow cytometry. The final construct, TAMRA-cadaverine-dextran-$(L17E, GFP\ 11)_{5.4}$ **34**, was able to induce GFP-complementation in GFP 1-10 producing HeLa cells, whereby successful translocation of the construct was further confirmed by intracellular TAMRA fluorescence. Furthermore, the assessment of cytotoxicity revealed that the construct was able to facilitate GFP-complementation without compromising the cells to a large extent.

The preceding experiments highlighted the potential of L17E-dextran hybrids as promising delivery platform of both PNA and peptides as bioactive payloads. In order to further validate the capabilities of CPP-dextran chimeras in the context of large payload, streptavidin was chosen as model protein due to its advantageous intrinsic properties. The extraordinarily high affinity of Sav towards its ligand biotin would allow for the convenient assembly of Sav-dextran hybrids without covalent linkage between protein and polysaccharide. Furthermore, the presence of 4 biotin binding pockets per Sav molecule further enabled an adjustable ratio between dextran and protein under stochiometric control. In the frame of a proof-of-concept study, dextran was decorated with 5.4 copies of either L17E or P14 at the repeating units and a single biotin label, site-specifically introduced at the reducing end. The cargo protein Sav was equipped with a fluorescent label that allowed for the intracellular localization *via* confocal microscopy. Preliminary experiments involving ATTO 647-labeled Sav **58** revealed successful uptake into HeLa cells upon decoration with two copies of L17E-dextran **40** even at submicromolar concentration, which was, however, accompanied by cytotoxic effects. Sav equipped with P14-functionalized dextran **41** in a 1:2 ratio induced morphologically abnormal changes of the treated HeLa cells, probably as a consequence of interactions between the highly positively-charged construct with DNA in the nuclei. Experiments with solitary biotinylated L17E and P14, respectively, in absence of dextran resulted in only negligible cellular uptake, highlighting the uptake-enhancing effects of CPPs multimerized on the polysaccharide backbone. Subsequent experiments displayed evenly distributed AF647 labeled Sav **59** in the cytosol of HeLa cells upon functionalization with L17E-dextran **40** in a 1:2 ratio at low micromolar concentration. Assembly of Sav-dextran hybrids in an equimolar ratio, however, significantly reduced intracellular localization of the fluorescently labeled protein. In order to quantify the cytotoxic effects observable in the microscopic images, the cytotoxic profile of L17E-dextran **40** was assessed. Solitary L17E-dextran **40** induced strong toxicity in HeLa cells, which was not significantly influenced by the presence of unlabeled Sav. Interestingly, the introduction of approximately 2.5 copies of AF647 per Sav reduced the cytotoxicity of the dextran-Sav hybrid by a factor more than 2, which suggests attenuation of the membrane-lytic activity of L17E-dextran **40** by the overall negatively-charged fluorophore. Considering the translocation efficiency of the fluorescently labeled protein mediated by dextran **40**, successful cellular uptake was always accompanied by cytotoxicity. Only at 1.5 µM Sav-AF647 equipped with 2 copies of dextran was capable of efficient cellular uptake while being only moderately cytotoxic.

Despite the considerable cytotoxic effect expressed by L17E-decorated dextran **40**, the approach was further validated as delivery platform of site-specifically biotinylated eGFP as additional cargo protein. HeLa cells treated with 3 µM of Sav bearing 2 copies of dextran **40** and 1.5 copies of biotinylated eGFP on average displayed strong intracellular fluorescence even at 4 °C, suggesting that energy-independent pathways were at least partially responsible for cellular uptake.

In conclusion of the first part of this doctoral thesis, multimeric presentation of L17E on dextran polysaccharide is a promising technique to enhance cellular uptake of various bioactive cargoes. Conceived by my colleague Dr. Bastian Becker, this approach was effective in mediating translocation of peptides, PNA and even proteins. Successful cytoplasmic localization of the peptide GFP10 was confirmed by the functional GFP-complementation assay. Efficient nuclear delivery of 18mer PNA, mediated by L17E-decorated dextran, was demonstrated in collaboration with Dr. Bastian Becker in a mis-splicing assay, whereby the multimeric construct **23** even exceeded the CPPs P14 and P17, both optimized for PNA delivery into mammalian cells. In a modular design based on the tetrameric protein Sav as centerpiece, biotin-functionalized L17E-dextran **40** was not only capable of facilitating cellular uptake of the core protein, but also eGFP as additional cargo. However, the impressive performance of efficient protein delivery was accompanied by intolerable levels of toxicity.

Thus, the design remains to be optimized in regard to its cytotoxic profile in order to be a reliable asset for intracellular protein delivery. This could be accomplished by carefully tuning the number of L17E per dextran polymer to achieve optimal performance at intracellular delivery whilst keeping the toxicity at moderate levels. Alternatively, L17E could be replaced by novel, high-performing CPPs.

The second part of this thesis, multimerization of receptor-targeting peptides, was inspired by the modular dextran-Sav hybrid approach. Combining the high affinity of Sav towards its natural ligand biotin, which allows for the convenient assembly of Sav-dextran chimeras by simple co-incubation, with four addressable biotin binding sites, the design deemed optimal to study the effect of receptor-targeting peptide multimerization.

In a preceding project of my colleague Dr. Hendrik Schneider, the potency of DR5TP-decorated dextran was considerably increased upon dimerization on human Fc as centerpiece.[29] Thus, Sav presented itself as optimal core structure to investigate the potential performance enhancement of DR5TP functionalized dextran, induced by multimerization on the protein. To that end, a biotinylated dextran derivative **61** was synthesized, equipped with 5.4 copies of DR5TP on average. The apoptotic potency of dextran **61**, individually or tetramerized on Sav, was assessed on DR5TP-sensitive COLO205 cells. While solitary dextran **61** had an EC_{50} value in the low nanomolar range, its potency was further enhanced by a factor of approximately 3.5 upon tetramerization on Sav. To further elucidate the effect of multimerization on the apoptotic potency, Sav was equipped with 4, 3, 2 and 1 copy of DR5TP-decorated dextran **61**, respectively, and employed in a cell proliferation assay. Thereby, a fourfold increase in efficiency could be observed upon dimerization compared to its counterpart harboring equal amounts of Sav and dextran **61**. Further multimerization of the functionalized dextran did not result in significantly increased cytotoxicity, suggesting that only two copies of DR5TP-decorated dextran bound to Sav are capable to interact with their target receptors simultaneously, possibly due to unfavorable spatial orientation of the additional dextran ligands.

To further evaluate the potential of dextran-Sav hybrid architectures as efficient platform for multimeric presentation of receptor-targeting peptides, integrins were chosen as alternative target. In order to investigate the general feasibility of integrin-targeting dextran-Sav architectures, dextran was functionalized analogously to the previous projects with biotin at its reducing end and, additionally, RGD-containing cyclic peptides as the receptor-binding entities. To that end, biotin functionalized dextran **66** comprising 6.3 azide groups on average was assembled and subsequently decorated *via* CuAAC with either alkyne-RGD **74** or alkyne-RAD **75** as negative control. Additionally, biotinylated monomeric RGD **80** and RAD **81** were synthesized to elucidate the potential effect of tetramerization of the cyclic peptides in absence of dextran as backbone. These constructs were initially employed in an ELISA with recombinant integrin αvβ3 as target and the natural ligand vitronectin as competitor. This assay, conducted in absence of Sav as core structure, revealed the binding capabilities of both RGD-decorated dextran **76** as well as biotinylated RGD derivative **80**, whereby the monomeric peptide **80** showed superior performance. However, in a cell-based assay using αvβ3-overexpressing U87MG glioblastoma cells and Sav-AF647 **59** as core structure, none of the RGD-containing compounds were able to bind efficiently to their target receptors.

In collaboration with Dr. Hendrik Schneider, Fc-dextran hybrids with multiple copies of RGD were synthesized as an alternative to dextran-Sav hybrids. Additionally equipped with the cytotoxic agent MMAE, Fc-dextran **86** was able to efficiently target and deliver its toxic payload into U87MG cells.

In conclusion, the second part of this doctoral thesis evaluated dextran-Sav hybrids as novel architectures for multimerization of receptor-binding peptides. Death receptor 5 has already been targeted successfully by a variety of constructs with multimeric DR5TP, of which peptide-decorated dextran dimerized on human Fc showed promising results.[29] Based on these findings of my colleague Dr. Hendrik Schneider,[29] Sav was employed as core structure to investigate the impact of multimerization on the apoptotic potency of DR5TP functionalized dextran. A fourfold increase in efficiency could be observed upon dimerization of dextran **61** on Sav compared to monomeric dextran, whereby higher levels of multimerization did not result in significantly increased potency. To further validate dextran-Sav hybrids in an alternative setup, integrin αvβ3 was chosen and addressed with RGD-decorated dextran **76**. While both dextran **76** as well as monomeric RGD derivative **80** could efficiently bind to isolated αvβ3 in an ELISA competition assay in absence of Sav, none of the constructs proved successful in targeting αvβ3-presenting U87MG cells with Sav-AF647 **59** as centerpiece. These projects presented dextran-Sav hybrids as promising platform for multimeric receptor-targeting peptides, whereby the scope of successfully-addressable receptors should be the subject of further research. As an alternative, Fc-dextran hybrids remain a highly efficient architecture to target both DR5 as well as αvβ3.

6 Experimental Part

6.1 General

6.1.1 Reagents

Reagents were purchased from *Sigma Aldrich* (part of *Merck KGaA*, Darmstadt, Germany), *Carl Roth GmbH + Co. KG* (Karlsruhe, Germany), *Acros Organics* (part of Thermo Fisher Scientific, Dreieich, Germany), *Fisher Scientific* (part of *Thermo Fisher Scientific*), *TCI* (Eschborn, Germany), *Carbolution Chemicals GmbH* (St. Ingbert, Germany) and *Alfa Aesar* (Karlsruhe, Germany). Building blocks for peptide synthesis were ordered from *Iris Biotech GmbH* (Marktredwitz, Germany) or *Carbolution Chemicals GmbH.* PNA building blocks were obtained from *PNA BIO Inc* (Newbury Park, CA, USA).

6.1.2 Solvents

Solvents were obtained from *Carl Roth GmbH + Co. KG*, *Acros Organics*, *Fisher Scientific* and *Sigma Aldrich* and used without further purification unless stated otherwise. Solvents for solid phase synthesis, i.e., *N,N*-dimethylformamide (DMF), trifluoroacetic acid (TFA) and *N,N*-diisopropylethylamine (DIPEA) were of peptide synthesis grade. Anhydrous dimethyl sulfoxide (DMSO), DMF, DCM and tetrahydrofuran (THF) were purchased from *Acros Organics.*

Acetonitrile (ACN) was dried by storage over 3 Å molecular sieve. Anhydrous DIPEA was obtained by addition of 25 g/L calcium hydride and stirring at 90 °C for 3 h, followed by distillation under reduced pressure. The received solvent was stored layered with argon and in the dark.

6.1.3 Buffers and Solutions

Table 4| Composition of buffers and solutions used.

Buffer / Solution	Content
Phosphate-buffered saline (PBS)	137 mM NaCl 2.7 mM KCl 10 mM NaH_2PO_4 1.8 mM KH_2PO_4
Eluent A (HPLC)	0.1% (v/v) aqueous (aq.) TFA
Eluent B (HPLC)	0.1% (v/v) TFA in 90% (v/v) aq. ACN
Eluent A (LC-MS)	0.1% (v/v) aq. formic acid

Eluent B (LC-MS)	0.1% (v/v) formic acid in ACN
HIC buffer A (pH 7.5)	25 mM Tris*HCl 1.5 M $(NH_4)_2SO_4$
HIC buffer B (pH 7.5)	25 mM Tris*HCl
Coomassie destaining solution	10% (v/v) aq. acetic acid
Coomassie staining solution	0.2% (w/v) Coomassie Brilliant Blue R-250 0.2% (w/v) Coomassie Brilliant Blue G-250 30% (v/v) aq. isopropanol 7.5% (v/v) aq. acetic acid
SDS-PAGE 4× running gel buffer (pH 8.8)	3 M Tris*HCl 4 g/L sodium dodecyl sulfate (SDS)
SDS-PAGE 4× stacking gel buffer (pH 6.8)	0.5 M Tris*HCl 4 g/L SDS
SDS-PAGE 5× sample buffer (pH 8)	0.25 M Tris*HCl 7.5% (w/v) SDS 25% (v/v) glycerol 12.5% (v/v) β-mercaptoethanol 0.25 g/L bromophenol blue
SDS-PAGE running buffer (pH 8.8)	50 mM Tris*HCl 190 mM glycine 1 g/L SDS
ELISA coating buffer (pH 7.4)	20 mM Tris*HCl 150 mM NaCl 1 mM $MnCl_2$ 2 mM $CaCl_2$ 1 mM $MgCl_2$
ELISA blocking buffer (pH 7.4)	20 mM Tris*HCl 150 mM NaCl 1 mM $MnCl_2$ 2 mM $CaCl_2$ 1 mM $MgCl_2$ 5% (w/v) bovine serum albumin (BSA)

6.1.4 Solvent Removal

Solvents were evaporated under reduced pressure using a *Büchi Labortechnik AG* (Essen, Germany) *Rotavapor R-300* rotary evaporator.

6.1.5 Lyophilization

Freeze-drying was performed using an *Alpha 2-4 LSC* device from *Martin Christ Gefriertrocknungsanlagen GmbH* (Osterode am Harz, Germany) equipped with an *Ilmvac Typ 109012* high vacuum pump from *Ilmvac GmbH* (now *Welch by Gardner Denver*, Ilmenau, Germany).

6.1.6 Centrifugation

Centrifugation of substances in micro tubes was performed with either an *Eppendorf AG* (Hamburg, Germany) *type 5415 R* or *Fisher Scientific accuSpin Micro 17* centrifuge. A *Multifuge 3 L-R* centrifuge from *Heraeus* (Hanau, Germany) was used for larger volumes. For centrifugation of 96 well plates an *Eppendorf AG 5804 R* device was used.

6.1.7 Sonication

A *DIGITAL ULTRASONIC CLEANER* (*Digital Pro+*) ultrasonic bath was used for dissolving poorly soluble substances.

6.2 Analysis

6.2.1 Reversed-Phase (RP) High Performance Liquid Chromatography (HPLC)

RP-HPLC analysis was performed either on an *Agilent 1100 device* (*Agilent Technologies Germany GmbH & Co. KG*, Waldbronn, Germany) equipped with an *Agilent ZORBAX Eclipse Plus* (C18, 100×4.6 mm, 3.5 µm, 95Å) column or an *Agilent 1260* device equipped with an *Interchim* (Montluçon, France) *Uptisphere Strategy RP* column (C18-HQ, 3 µm, 100×4.6 mm, 100 Å). The eluent system consisted of eluent A (0.1 % (v/v) TFA in H_2O) and eluent B (0.1 % (v/v) TFA in 90% (v/v) aqueous (aq.) ACN) at 0.6 ml/min. 3 min of isocratic flow (starting concentration of eluent B) was followed by a linear gradient over 20 min and a subsequent washing phase at 100 % eluent B for 4 min. The column was finally washed for further 5 min at the starting concentration of eluent B.

6.2.2 Size Exclusion Chromatography (SEC)

SEC analysis was performed using a *Phenomenex* (Aschaffenburg, Germany) *BioSep SEC-s2000* column (300×7.8 mm, 5 µm, 145 Å) in combination with either an *Agilent 1100* device or *Agilent 1260* device at a flow rate of 0.6 ml/min. Same eluents as for RP-HPLC were used and samples were eluted at an isocratic flow of 30% eluent B.

For SEC analysis of proteins, a *TOSOH Bioscience* (Grießheim, Germany) *TSKgel® Super-SW3000* (300×4.6 mm, 4 µm, 250 Å) column on an *Agilent 1260* device was used. A flow rate of 0.35 ml/min and phosphate buffered saline (PBS, 137 mM NaCl, 2.7 mM KCl, 10 mM Na_2HPO_4, 1.8 mM KH_2PO_4, pH 7.4) as eluent were employed.

6.2.3 Hydrophobic Interaction Chromatography (HIC)

HIC analysis was conducted on an *Agilent 1260* device equipped with a *TSKgel® Butyl-NPR* (35×4.6 mm, 2.5 µm) column from *TOSOH Bioscience* at a flow rate of 0.9 ml/min. The eluent system consisted of HIC buffer A (25 mM Tris*HCl, 1.5 M $(NH_4)_2SO_4$, pH 7.5) and HIC buffer B (25 mM Tris*HCl, pH 7.5).

6.2.4 Electrospray Ionization (ESI) Mass Spectrometry (MS)

ESI-MS spectra were obtained from a *Shimadzu* (Grießheim, Germany) *LCMS-2020* device equipped with a *Phenomenex Synergy 4 u Fusion-RP 80* (C-18, 250×4.6 mm, 2 µm, 80 Å) column at a flow rate of 0.7 ml/min and 37 °C using a linear gradient over 13.5 min. Eluent system consisted of eluent A (0.1 % (v/v) formic acid (FA) in H_2O, LCMS grade, *Fisher Scientific*) and eluent B (0.1 % (v/v) formic acid in acetonitrile, LCMS grade, *Fisher Scientific*).

High-resolution (HR) ESI-MS spectra were obtained using an *Impact II* (*Bruker Daltonik GmbH*, Bremen, Germany) equipped with a quadrupole time-of-flight (QTOF) detector.

6.2.5 Nuclear Magnetic Resonance (NMR)

NMR spectroscopy was performed on a *Bruker BioSpin GmbH* (Rheinstetten, Germany) *Avance III* and *Avance II* (^1H: 300 MHz, ^{13}C: 75 MHz) or alternatively on a *Bruker BioSpin GmbH DRX 500* (^1H: 500 MHz, ^{13}C: 150 MHz). The chemical shifts are stated as δ-values in parts per million (ppm) downfield shifted corresponding to remaining proton signals of the deuterated solvents and tetramethylsilane (TMS), respectively. Substances were dissolved in deuterium oxide, $CDCl_3$, DMSO-d_6 and CD_3OD purchased from *Sigma-Aldrich*.

6.2.6 Infrared (IR) Spectroscopy

IR spectra were obtained from a *FTIR-Spectrometer Spectrum Two* (*PerkinElmer*, Rodgau, Germany) using homogenous potassium bromide pellets or by attenuated total reflection (ATR)-IR. Wave number area: 8.300-350 cm^{-1}, spectral solution 0.5 cm^{-1}; wave number accuracy better than 0,01 cm^{-1} at 3.000 cm^{-1}; wave number correctness: 0,1 cm^{-1} at 3.000 cm^{-1}; signal-to-noise-ratio: 9.300: 1 Peak to Peak, 5 s and 32.000: 1 Peak to Peak, 1 min.

6.2.7 UV/Vis Spectroscopy

UV/Vis-spectroscopy was performed on a *Shimadzu UVmini 1240* device using *Quarzglas Suprasil* quartz cuvettes (10 mm path length) obtained from *Hellma Analytics* (Müllheim, Germany).

Protein concentrations were determined using a *BioSpec-nano* device from *Shimadzu*. To that end, the absorption at λ = 280 nm was measured photometrically and the concentration was calculated using the ExPAsy ProtParam online tool (https://web.expasy.org/protparam/).

An *Infinite F200 pro* from *TECAN* (Crailsheim, Germany) was used for the readout of multiwell plates.

6.2.8 Thin Layer Chromatography (TLC)

TLC analysis was performed with *ALUGRAM® Xtra SIL G/UV254* 0.2 mm silica gel 60 plates with fluorescent indicator from *Macherey-Nagel* (Düren, Germany). The visualization of spots was either performed using UV light at λ = 254 nm or $KMnO_4$-stain (1.5 g $KMnO_4$, 10 g K_2CO_3 and 1.25 ml 10% (w/v) NaOH dissolved in 200 ml water).

6.2.9 Flow Cytometry

Flow Cytometry was conducted on either an *Influx* (*BD Bioscience*, Heidelberg, Germany) Fluorescence-Activated Cell Sorting device (FACS), or a *CytoFLEX S* cytometer (*Beckman Coulter*, Krefeld, Germany).

6.2.10 SDS-Polyacrylamide Gel Electrophoresis (SDS-PAGE)

Reducing SDS-PAGE was performed by heating the protein samples (3-5 µg in 12 µL) with 3 µL 5× sample buffer at 98 °C for 5 min to facilitate reduction of disulfide bridges and denaturation of the sample. Afterwards, the samples were loaded onto the polyacrylamide gel (stacking gel: 4%, separation gel: 15%) and the analysis was performed at 300 V and 40 mA. As ladder, blue prestained protein standard, broad range (11 – 250 kDa) from *New England Biolabs* (Ipswich, MA, USA) was used. Upon completion of the electrophoretic separation, the polyacrylamide gel was stained with Coomassie staining solution, followed by destaining with 10% (v/v) aq. acetic acid.

6.2.11 Confocal Microscopy

Confocal laser scanning microscopy was performed on a *Leica TSC SP8* confocal microscope (*Leica Microsystems* CMS GmbH, Wetzlar, Germany).

6.3 Chromatographic Purification

6.3.1 Semi-Preparative HPLC

Peptides were purified on a semi-preparative RP-HPLC *Interchim Puriflash 4250* equipped with a semi-preparative *Interchim Uptisphere Strategy* (C18-HQ, 5 µm, 250×21.2 mm) column. At a flow rate of 18 ml/min, 5 min of isocratic flow (starting concentration of eluent B) was followed by 20 min of gradient flow using the same eluent system as for analytical RP-HPLC.

6.3.2 Silica Chromatography

Silica chromatography was performed with silica gel 60 (0.04 – 0.063 mm, 230 – 400 mesh) purchased from *Carl Roth GmbH + Co. KG* either by gravity column chromatography or (automated) flash chromatography. Thereby, the retention factor of the substance was adjusted to 0.2 – 0.4, determined by TLC.

For manual chromatography the crude product was dissolved in a suited solvent and added to the silica column, followed by elution with a solvent mixture. Compressed air (1 - 3.5 bar) was applied for manual flash chromatography. The eluate was fractionated and analyzed by TLC, whereafter the product fractions were combined and evaporated.

Automated flash chromatography was performed using the *Interchim Puriflash 4250* device. The crude product was dissolved in a suited solvent and adsorbed on silica gel by evaporation under reduced pressure. The charged silica gel was transferred into 12 g flash cartridges and layered with sand, followed by chromatographic separation using a linear gradient at a flow rate of 26 ml/min utilizing 40 g flash cartridges filled with silica gel. Detection of the compounds was conducted by either UV absorption or using an evaporative light scattering detector (ELSD).

6.4 Cell Lines

Mammalian cell lines were incubated under standard conditions at 37 °C in a humidified incubator with 5% CO_2. HeLa-eGFP654 cells[211] were ordered from the *UNC Tissue Culture* facility (Chapel Hill, NC, USA).

HeLa-GFP1-10 cells were generated by Carolin Dombrowsky using the following procedure: HeLa cells were seeded in a 12-well plate in a density of 5.5×10^4 cells/well and incubated for 24 h under standard conditions in Dulbecco´s Modified Eagle´s Medium (DMEM, *Sigma Aldrich*) without penicillin/streptomycin (pen/strep). The cells were transfected with *pQCXIP-GFP1-10* plasmid[240] (*Addgene* plasmid #68715, gifted from Yutaka Hata) using lipofectamine 2000 (*Invitrogen*, supplier *Thermo Fisher Scientific*) following the instructions of the supplier. For the selection of stably transfected cells, the cells were treated 72 h after transfection with 0.5 µg/ml puromycin. The concentration of puromycin was increased stepwise over two weeks to a final concentration of 1.2 µg/ml.

The following culture media were used for cultivation of the cell lines used in this work:

Table 5| Cell lines and their cultivation conditions.

Cell Line	Description	Culture Medium
HeLa	Human Cervix Adenocarcinoma cells (Henrietta Lacks)	DMEM with 10% fetal bovine serum (FBS) (*Merck KGaA*) and 1× pen/strep (*Life Technologies*, Carlsbad, CA, USA)
HeLa-eGFP654	HeLa cells stably transfected with eGFP plasmid interrupted with IVS-654 intron (mutation at nucleotide 654 of the human β-globin intron-2)	Same conditions as for HeLa cells
HeLa-GFP1-10	HeLa cells stably transfected with GFP1-10 plasmid	Same conditions as for HeLa cells
HEK	Human Embryonic Kidney cells	Same conditions as for HeLa cells
U87MG	Glioblastoma Cells (Uppsala 87 Malignant Glioma)	Minimum Essential Medium (MEM, *Sigma Aldrich*) supplemented with 10% FBS
COLO205	Human Colon Adenocarcinoma cells	Roswell Park Memorial Institute (RPMI) 1640 medium (*Gibco*, supplier *Thermo Fisher Scientific*) with 10% FBS

6.5 Solid Phase Synthesis using Fmoc/tBu Strategy

6.5.1 Resins

Solid phase peptide synthesis (SPPS) was performed using either 2-chlorotrityl chloride (2-CTC) resin (1.60 mmol/g) from *Iris Biotech* or *AmphiSpheres 40* Rink Amide (RAM) resin (0.34 – 0.35 mmol/g) from *Agilent Technologies*.

PNA and PNA-peptide hybrids were synthesized exclusively on *AmphiSpheres 40* RAM resin.

6.5.2 Loading of the First Amino Acid

In a reaction vessel equipped with a frit, *AmphiSpheres 40* Rink Amide (RAM) resin was swollen for 30 min in DCM and washed afterwards twice with DMF. The Fmoc protecting group was removed and the first amino acid was preactivated by mixing 4 eq. amino acid, 3.95 eq. 3-[bis(dimethylamino)methyliumyl]-3*H*-benzotriazol-1-oxide hexafluorophosphate (HBTU) and 8-eq. of DIPEA in DMF for 3 min. The preactivated amino acid mixture was added to the resin, which was shaken for 1 h at room temperature. After removal of the supernatant the resin was washed thoroughly with DMF and was ready for further use. The coupling of non-natural amino acids was accomplished by pre-activation of 3 eq. amino acid, 2.95 eq. 1-[bis(dimethylamino)methylene]-1H-1,2,3-triazolo[4,5-b]pyridinium 3-oxide hexafluoro-phosphate (HATU) and 6 eq. DIPEA for 3 min. The coupling time and workup was analogous to the coupling of natural amino acids.

The loading of the first amino acid onto 2-CTC resin was performed by swelling the resin in anhydrous DCM for 30 min in a reaction vessel equipped with a frit. The amino acid (1.2 - 2 eq.) and DIPEA (2.4 - 4 eq.) were dissolved in dry DCM. In case of poorly soluble amino acids, dry DMF was added to facilitate the dissolution. The mixture was added to the resin and the reaction vessel was shaken at room temperature for 90 min, followed by thorough washing of the resin with DMF.

6.5.3 Fmoc Deprotection (Peptide Synthesis)

Fmoc protecting groups were removed by treating the swollen and washed resin with 20% (v/v) piperidine in DMF for 3 min under shaking. Afterwards the supernatant was removed, the resin was washed thrice with DMF and fresh piperidine solution was added. The resin was shaken for further 10 min, whereafter the solution was removed, the resin was washed DMF (10×) and was ready for further treatment.

6.5.4 Coupling (Peptide Synthesis)

Prolongation of the peptide chain on solid support was achieved by pre-activation of 4 eq. amino acid using 3.95 eq. HBTU and 8 eq DIPEA in DMF for 5 min, followed by addition of the mixture to resin containing an *N*-terminally deprotected amino acid. The resulting slurry was shaken for 1 h at ambient temperature, whereafter the supernatant was removed and the resin was washed with DMF (5×).

The procedure was adapted according to the employed amino acid: Non-natural amino acids (3 eq.) were activated with HATU (2.95 eq.) and DIPEA (6 eq.); for the coupling of racemizationsensitive L-cysteine and L-histidine collidine instead of DIPEA was used. For challenging coupling steps, i.e., L-arginine and amino acids subsequent to L-proline, the conjugation was performed as double coupling, whereby after 45 min the reaction mixture was replaced by fresh one and the resin was treated for further 45 min.

6.5.5 Automated Peptide Synthesis

Automated peptide synthesis was performed using the *Liberty Blue™* system from *CEM* (Kamp-Lintfort, Germany). *AmphiSpheres 40* RAM resin was used either pre-loaded (in case of non-natural amino acids as first amino acid) or un-loaded. Amino acid conjugation was performed as double coupling using the ethyl cyanohydroxyiminoacetate (Oxyma)/*N,N*-diisopropylcarbodiimide (DIC) activation system utilizing microwave irradiation (90 °C, 10min; L-cysteine and L-histidine: 50 °C). Deprotection was achieved using 0.1 M Oxyma in 20% (v/v) piperidine in DMF, also microwave-assisted (90 °C, 1 min).

6.5.6 Fmoc Deprotection (PNA and PNA-Peptide Hybrids Synthesis)

Fmoc protecting groups of PNA building blocks were removed using 20% (v/v) in DMF. After addition of the deprotection solution the resin was shaken for 2 min at room temperature, whereafter the supernatant was removed, the resin was washed thrice with DMF and the deprotection step was repeated twice for 3 min. After the final deprotection step the resin was washed with DMF (10×).

Fmoc protecting group removal of amino acids during PNA-peptide hybrid synthesis was performed analogous to Fmoc deprotection procedure during peptide synthesis.

6.5.7 Coupling (PNA and PNA-Peptide Hybrids Synthesis)

Coupling of PNA building blocks was accomplished by pre-activation of 1.5 eq. PNA building block using 1.45 eq. HATU and 3 eq. DIPEA in DMF for 3 min. The activated mixture was added to the resin which was shaken for 45 min at ambient temperature. After removal of the supernatant and washing with DMF (3×) the procedure was repeated with fresh reagents. The resin was washed after the double coupling thoroughly with DMF (10×) and was ready for further treatment.

After coupling of three PNA building blocks a test cleavage was performed to confirm the success of the synthesis.

6.5.8 Storage of the Resins

Unless stated otherwise, the resins were stored over night and for a longer period of time in a desiccator. Hence, after completion of coupling and deprotection, respectively, the swollen resin was washed thoroughly with DMF (10×), DCM (5×) and diethyl ether (DEE, 5×). The washed resin was dried in the airstream of the suction pump for a short period of time and then stored in a desiccator.

6.5.9 Cleavage and Workup

PNA test cleavages were performed by treating a spatula tip of dried resin with 500 µL cleavage cocktail consisting of TFA: triethylsilane (TES): anisole: H_2O (47:1:1:1, v:v:v:v) for 1 h at ambient temperature. Afterwards the PNA was precipitated in 1.5 mL cold DEE and centrifuged. After discarding the supernatant, the residue was washed with cold DEE and centrifuged again (2× 1 mL). The residue was dried, dissolved in 5% (v/v) aqueous acetic acid and analyzed by RP-HPLC and ESI-MS.

Final cleavage from solid support as well as side chain deprotection was achieved by treating the resin with cleavage cocktail (5 mL for 500 mg loaded resin) for 2-3 h at ambient temperature. Crude product was precipitated in cold DEE (45 mL for 5 mL cleavage cocktail) and centrifuged. The residue was washed with cold DEE and centrifuged again (2× 20 mL). After the resin was dry it was dissolved in aqueous acetic acid (5% v/v) or aqueous formic acid (0.1% v/v) and freeze-dried. For poorly soluble substances ACN (up to 40% v/v) was added. After freeze-drying the residue was analyzed by RP-HPLC and ESI-MS and purified by semi-preparative HPLC, if necessary.

For final cleavage from resin under preservation of the side chain protecting groups (only for 2-CTC resin) a mixture of DCM:acetic acid:methanol (MeOH) (5:4:1, v:v:v) as cleavage cocktail (5 mL for 500 mg loaded resin) was used. After treatment of the resin for 3 h at room temperature the cleavage cocktail was evaporated under reduced pressure to receive the crude product.

6.6 Comparative Studies of Multiple Platforms for Intracellular Delivery of PNA

6.6.1 Synthesis of *S*-3-Tritylmercaptopropionic Acid 4

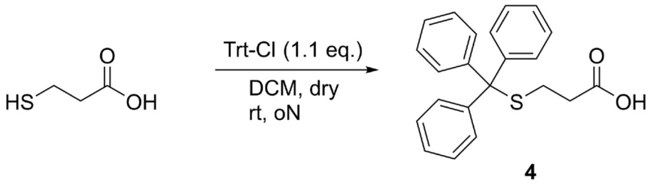

4

Scheme 30| Synthesis of *S*-3-tritylmercaptopropionic acid **4**.

The synthesis was performed as described in literature.[241] 2 mL 3-mercaptopropionic acid (2.45 g, 23 mmol, 1 eq.) were dissolved in 35 mL anhydrous DCM. 7.05 g trityl chloride (25.3 mmol, 1.1 eq.) were dissolved in dry 15 mL DCM and added dropwise and the reaction was stirred over night at room temperature, whereby a colorless solid precipitated. The suspension was filtered and the residue was washed thoroughly with DEE and dried in airstream. 7.32 g (21.0 mmol, 91%) of *S*-3-tritylmercaptopropionic acid **4** were yielded as colorless solid.

^{1}H NMR (300 MHz, DMSO-d6): δ = 7.37 – 7.28 (m, 12H), 7.27 – 7.20 (m, 3H), 2.36 – 2.26 (m, 2H), 2.22 – 2.14 (m, 2H).

6.6.2 Synthesis of (*S*-3-(Tritylmercapto)propionyl)-β-Ala-OH 5

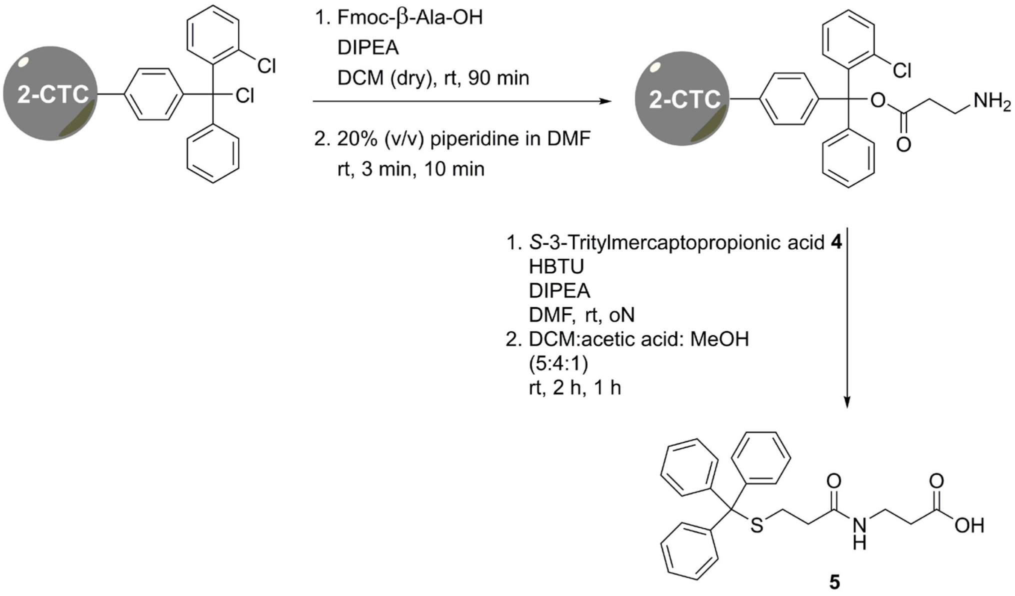

Scheme 31| Solid phase synthesis of (*S*-3-(tritylmercapto)propionyl)-β-Ala-OH **5**.

1 g 2-CTC resin (1.6 mmol/g, scale: 1.6 mmol) were transferred to a syringe equipped with a frit and swollen in anhydrous DCM for 90 min. 0.75 g Fmoc-β-Ala-OH (2.41 mmol, 1.5 eq.) and 0.84 mL DIPEA (0.62 g, 4.79 mmol, 3 eq.) were dissolved in dry DCM and added to the resin, which was shaken for 90 min at ambient temperature. After thorough washing with DMF the Fmoc-protecting group was removed using 20% (v/v) piperidine in DMF (3 min, 10 min). 1.39 g (4 mmol, 2.5 eq.) *S*-3-tritylmercaptopropionic acid **4** were activated with HBTU (1.49 g, 3.92 mmol, 2.45 eq.) and 1.39 mL DIPEA (1.03 g, 8 mmol, 5 eq.) in DMF for 5 min and added to the resin. After shaking over night, the supernatant was removed, the resin was washed with DMF, DCM and DEE and dried in the desiccator. Cleavage from solid support was performed under mild conditions by shaking the resin in 10 mL DCM: acetic acid: MeOH (5:4:1, v:v:v) for 2 h. The procedure was repeated for 1 h and the cleavage cocktails were pooled. After evaporation under reduced pressure an oily residue was received which was dissolved in ACN, precipitated by addition of H_2O and freeze-dried. 615 mg (1.46 mmol, 91%) of (*S*-3-(tritylmercapto)propionyl)-β-Ala-OH **5** were yielded as bright, fluffy solid.

^{1}H NMR (500 MHz, DMSO-d6) δ = 7.86 (t, J = 5.6 Hz, 1H), 7.37 – 7.28 (m, 12H), 7.26 – 7.22 (m, 3H), 3.20 (td, J = 6.9, 5.5 Hz, 2H), 2.34 (t, J = 6.9 Hz, 2H), 2.25 (t, J = 7.6 Hz, 2H), 2.13 (t, J = 7.4 Hz, 2H).

6.6.3 Synthesis of (*S*-3-(Tritylmercapto)propionyl)-β-Ala-Heptaammonium-COSS 6

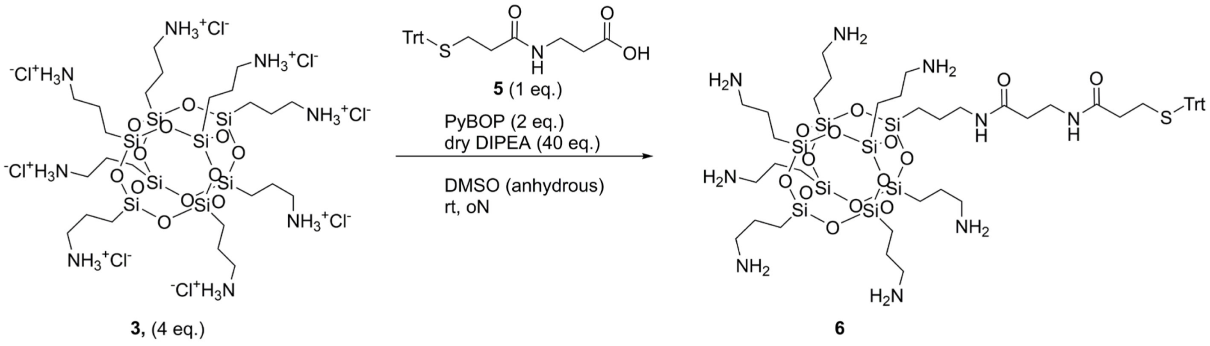

Scheme 32| Synthesis of (*S*-3-(tritylmercapto)propionyl)-β-Ala-heptaammonium-COSS **6**.

The synthesis was performed as a modified variant from literature.[128] 4.73 g (4.03 mmol, 4 eq.) octaammonium COSS hydrochloride **3** (purchased from *Hybrid Plastics* (Hattiesburg, MS, USA)) and 6.33 mL (4.7 g, 36.4 mmol, 33.6 eq.) dry DIPEA were dissolved in 120 mL anhydrous DMSO. 0.42 g (1.01 mmol, 1 eq.) (*S*-3-(tritylmercapto)propionyl)-β-Ala-OH **5**, 1.05 g (2.02 mmol, 2 eq.) (Benzotriazol-1-yloxy)tripyrrolidinophosphonium hexafluorophosphate (PyBOP) and 0.7 mL (0.52 g, 4.02 mmol, 4 eq.) anhydrous DIPEA in 20 mL dry DMSO were preactivated for 20 minutes. This solution was added to the COSS-containing solution *via* dropping funnel over 2 hours. The reaction mixture was stirred over night, whereafter the volume was reduced by freeze-drying. The remaining viscous oil was precipitated and washed with anhydrous ACN, followed by dissolution in 5% (v/v) aqueous acetic acid and lyophilization. Purification of the crude product was conducted by semi-preparative HPLC, yielding 664 mg (0.52 mmol, 51%) as colorless solid.

RP-HPLC (10 to 80% eluent B, 220 nm): Retention time (t_R) = 14.856 min.

ESI-MS: Calc. for $C_{49}H_{87}N_9O_{14}SSi_8$: m/z: $[M+2H]^{2+}$ = 642.51 (obs. 642.56), $[M+3H]^{3+}$ = 428.67 (obs. 428.85).

6.6.4 Synthesis of (3-Mercapto)propionyl)-β-Ala-Heptaguanidinium-COSS 9

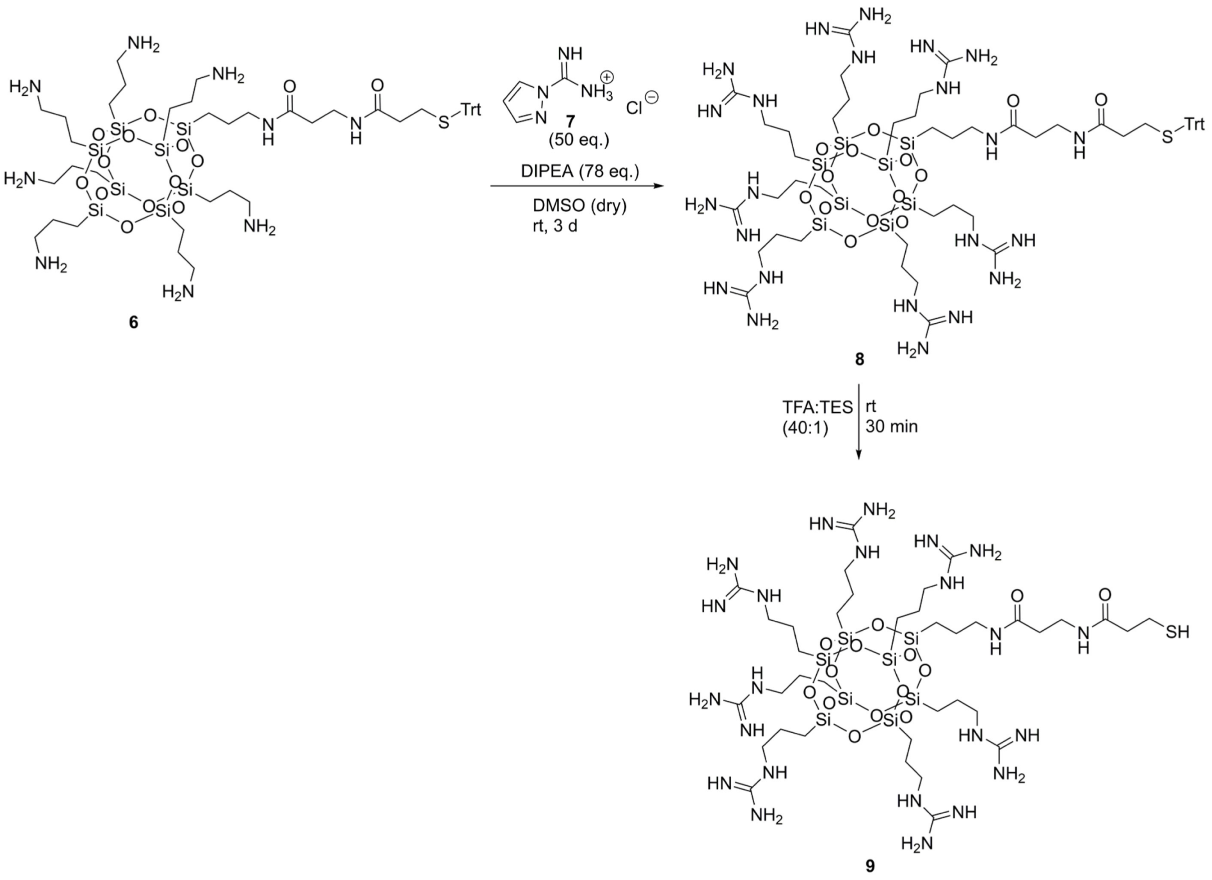

Scheme 33| Guanidinylation of COSS **6**, followed by TFA-mediated deprotection leading to Thiol-bearing GuCOSS **9**.

The synthesis was performed according to a protocol modified from literature.[128] 0.42 g (0.33 mmol, 1 eq.) (*S*-3-(tritylmercapto)propionyl)-β-Ala-heptaammonium-COSS **6** and 2.42 g (16.5 mmol, 50 eq.) 1*H*-pyrazole-1-carboxamidine hydrochloride **7** were dissolved in 40 mL anhydrous DMSO. 4.49 mL (3.33 g, 25.8 mmol, 78 eq.) dry DIPEA were added and the reaction was stirred for 3 d at ambient temperature. 4.43 mL (4.64 g, 77.4 mmol, 234 eq.) glacial acetic acid were added and the solution was diluted with 1% (v/v) aqueous acetic acid. After lyophilization the oily residue was dissolved in 1% (v/v) aqueous acetic acid and purified by semi-preparative HPLC, yielding 386 mg (0.25 mmol, 74%) of product **8**.

Trt protected GuCOSS **8** was dissolved in a mixture of TFA:TES (40:1) and stirred for 30 min at ambient temperature. Subsequently, the solvent was evaporated under reduced pressure and the residue was suspended in 1% (v/v) aqueous acetic acid. The suspension was filtered and the solution was freeze-dried, yielding 326 mg (0.25 mmol, quantitative) final product **9** as colorless solid.

GuCOSS **8**:

RP-HPLC (10 to 80% eluent B, 220 nm): t_R = 15.447 min.

ESI-MS: Calc. for $C_{56}H_{101}N_{23}O_{14}SSi_8$: m/z: $[M+2H]^{2+}$ = 789.66 (obs. 789.76), $[M+3H]^{3+}$ = 526.77 (obs. 526.85).

GuCOSS **9**:

ESI-MS:Calc. for $C_{37}H_{87}N_{23}O_{14}SSi_8$ (GuCOSS **9**): m/z: $[M+2H]^{2+}$ = 668.50 (obs. 668.56), $[M+3H]^{3+}$ = 446.00 (meas. 446.15).

6.6.5 Synthesis of Maleimide-Functionalized GuCOSS 10

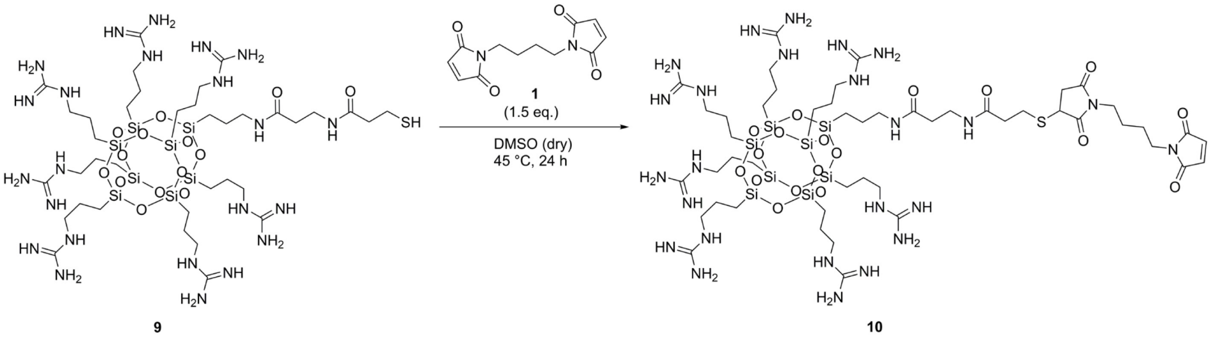

Scheme 34| Functionalization of GuCOSS **9** with bismaleimide linker **1**.

In a microtube, 8.4 mg (33.8 µmol, 1.5 eq.) 1,4-bismaleimido butane **1** were suspended in 600 µL anhydrous DMSO. A solution of 30 mg (22.5 µmol, 1 eq.) GuCOSS **9** in 200 µL dry DMSO was added, the mixture was layered with argon and the microtube was sealed. The reaction was shaken for 24 h at 45 °C, whereafter it was diluted with 5% (v/v) aqueous acetic acid and purified by semi-preparative HPLC. 15 mg (9.5 µmol, 42%) were yielded as product **10**.

RP-HPLC (0 to 40% eluent B, 220 nm): t_R = 18.893 min.

ESI-MS: Calc. for $C_{49}H_{99}N_{25}O_{18}SSi_8$: m/z: $[M+2H]^{2+}$ = 792.61 (obs. 792.66), $[M+3H]^{3+}$ = 528.74 (obs. 528.85).

6.6.6 Synthesis of Aldrithiol-Activated GuCOSS 11

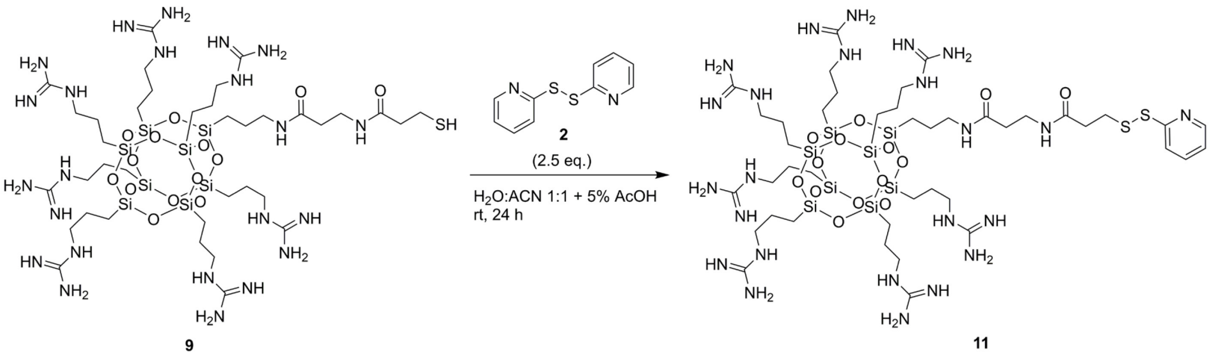

Scheme 35| Aldrithiol-activation of GuCOSS **9**.

8.3 mg (37.5 µmol, 2.5 eq.) 2,2´-dithiopyridine **2** were dissolved in 500 µL of a mixture of H_2O:ACN 1:1 + 5% AcOH. 20 mg (15 µmol, 1 eq.) GuCOSS **9** were dissolved in the same solvent mixture (300 µL) and added to the previous solution. The reaction, which turned yellow, was shaken at room temperature for 24 h and subsequently diluted and subjected to purification by semi-preparative HPLC, yielding 16 mg (11.1 µmol, 74%) product **11**.

RP-HPLC (10 to 50% eluent B, 220 nm): t_R = 13.714 min.

ESI-MS: Calc. for $C_{42}H_{90}N_{24}O_{14}S_2Si_8$: m/z: $[M+2H]^{2+}$ = 723.07 (obs. 723.06), $[M+3H]^{3+}$ = 482.38 (obs. 482.45).

6.6.7 Synthesis of Thiol-PNA 12

3-mercaptopropionic acid-gct-att-acc-tta-acc-cag-K-*NH₂*

$C_{201}H_{258}N_{102}O_{56}S$

$M_w = 5030.91$ g/mol

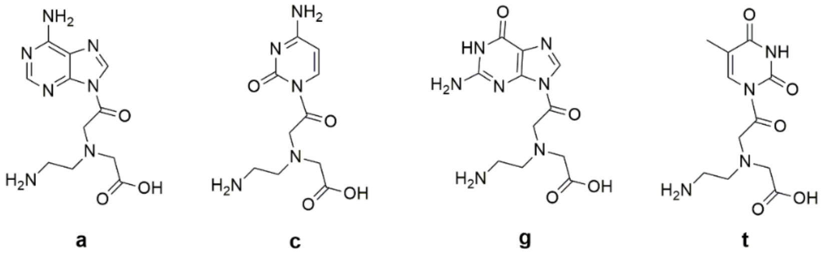

Figure 61 | Structure of the PNA monomers present in thiol-PNA **12**.

In a syringe equipped with a frit 143 mg *AmphiSpheres 40* RAM resin (capacity: 0.35 mmol/g, scale: 0.05 mmol) were swollen in DCM. After removal of the Fmoc protecting group, Fmoc-Lys(Boc)-OH (4 eq.) was coupled using HATU (3.95 eq.) and DIPEA (8 eq.) (double coupling: 2 h, 3 h). Subsequent assembly of the PNA oligomer was performed as described in section **6.5**. Upon completion, the resin was split and half of the batch (25 µmol) was further modified. *S*-3-tritylmercaptopropionic acid **4** (4 eq.) was activated with HATU (3.95 eq.) and DIPEA (8 eq.) in DMF and added to the resin, which was shaken for 2 h at ambient temperature. After drying over night in a desiccator, the resin was treated with cleavage cocktail (TFA:TES:anisole:H_2O 47:1:1:1) for 2 h, followed by precipitation in cold DEE (40 mL). The resulting suspension was centrifuged and the residue was washed twice with cold DEE (40 mL). After drying in a desiccator, the residue was dissolved in 5% (v/v) aq. AcOH and freeze-dried. 32 mg (6.4 µmol, 25%) of thiol-PNA **12** were yielded as slightly yellow solid and used without further purification.

RP-HPLC (10 to 60% eluent B, 220 nm): $t_R = 9.436$ min.

ESI-MS: Calc. for $C_{201}H_{258}N_{102}O_{56}S$: m/z: $[M+4H]^{4+} = 1258.73$ (obs. 1258.98), $[M+5H]^{5+} = 1007.18$ (obs. 1007.37), $[M+6H]^{6+} = 839.49$ (obs. 839.66), $[M+7H]^{7+} = 719.70$ (obs. 719.96), $[M+8H]^{8+} = 629.86$ (obs. 630.06).

6.6.8 Synthesis of GuCOSS-PNA Conjugate 13 with Thioether Linkage

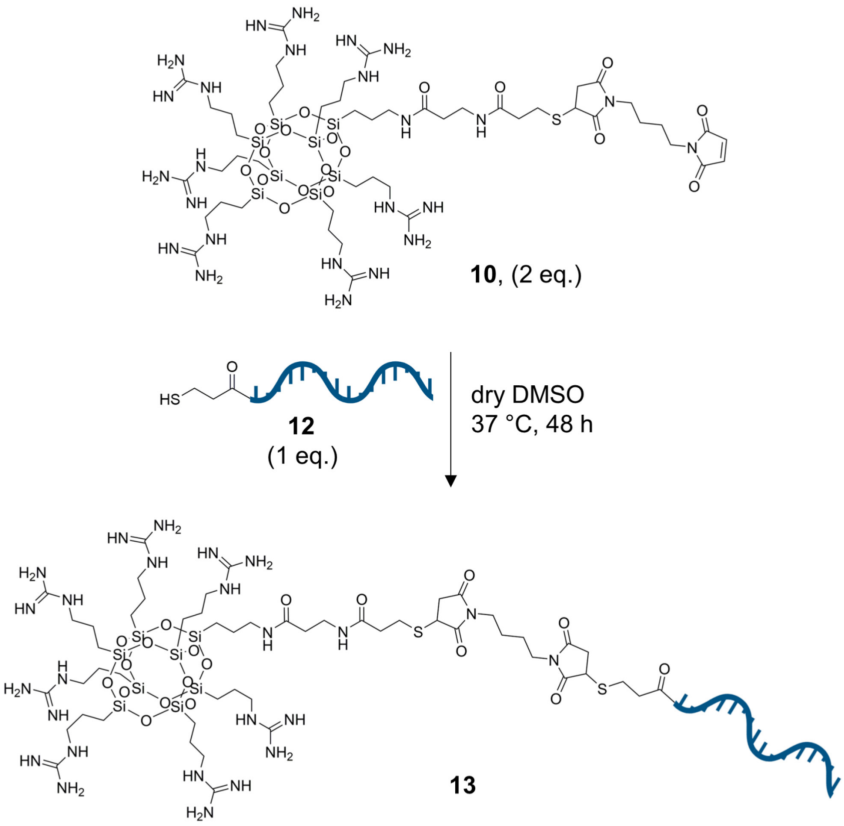

Scheme 36| Conjugation of thiol-PNA **12** to maleimide-functionalized GuCOSS **10**.

3.8 mg (2.4 µmol, 1 eq.) maleimide-bearing GuCOSS **10** were dissolved in 200 µL anhydrous DMSO and added to a solution of 12.1 mg (2.4 µmol, 1 eq.) thiol-PNA **12** in 400 µL DMSO. The resulting mixture was layered with argon and shaken for 24 h at 37 °C, whereafter HPLC analysis indicated incomplete turnover of thiol-PNA **12**. Hence, an additional equivalent GuCOSS **10** was added and the reaction was shaken for further 24 h at 37 °C. After 48 h the reaction was terminated and the product was isolated by semi-preparative HPLC, yielding 7.0 mg (1.1 µmol, 44%) GuCOSS-PNA conjugate **13**.

RP-HPLC (10 to 60% eluent B, 220 nm): t_R = 11.652 min.

ESI-MS: Calc. for $C_{250}H_{357}N_{127}O_{74}S_2Si_8$: m/z: $[M+6H]^{6+}$ = 1103.36 (obs. 1103.57), $[M+7H]^{7+}$ = 945.88 (obs. 946.17), $[M+8H]^{8+}$ = 827.77 (obs. 827.96), $[M+9H]^{9+}$ = 735.90 (obs. 736.06), $[M+10H]^{10+}$ = 662.41 (obs. 662.56).

6.6.9 Synthesis of GuCOSS-PNA Conjugate 14 with Disulfide Linkage

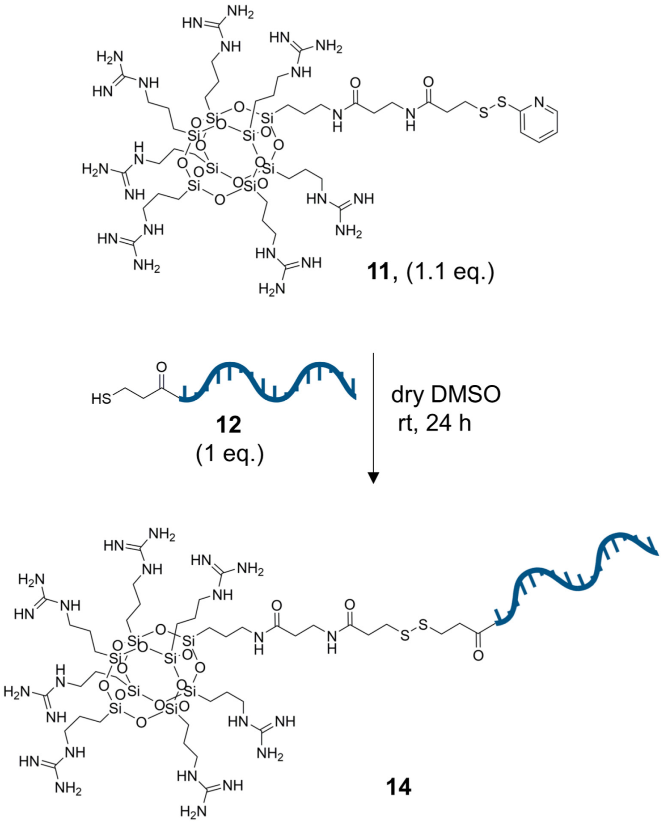

Scheme 37| Conjugation of thiol-PNA **12** to aldrithiol-activated GuCOSS **11**.

5.1 mg (3.5 µmol, 1.1 eq.) aldrithiol-activated GuCOSS **11** and 16 mg (3.2 µmol, 1 eq.) thiol-PNA **12** were dissolved in 600 µL DMSO and layered with argon. The mixture was shaken for 24 h at room temperature, whereafter the product was isolated by semi-preparative HPLC. 6 mg (0.9 µmol, 30%) PNA-conjugate **14** were yielded as product.

RP-HPLC (0 to 40% eluent B, 220 nm): t_R = 16.942 min.

ESI-MS: Calc. for $C_{238}H_{343}N_{125}O_{70}S_2Si_8$: m/z: $[M+7H]^{7+}$ = 910.13 (obs. 910.27), $[M+8H]^{8+}$ = 796.49 (obs. 796.66), $[M+9H]^{9+}$ = 708.10 (obs. 708.26), $[M+10H]^{10+}$ = 637.39 (obs. 637.56), $[M+11H]^{11+}$ = 579.54 (obs. 579.66).

6.6.10 Synthesis of $(KF_2)_3K$-PNA Conjugate 16

H-KFFKFFKFFK-O2Oc- gct-att-acc-tta-acc-cag-K-*NH₂*
$C_{282}H_{367}N_{117}O_{68}$
M_w = 6483.79 g/mol

The synthesis of $(KF_2)_3K$-PNA conjugate **16** was performed by Dr. Hendrik Schneider on a 0.025 mmol scale.

RP-HPLC (0 to 80% eluent B, 220 nm): t_R = 13.747 min.

ESI-MS: Calc. for $C_{282}H_{367}N_{117}O_{68}$: m/z: $[M+6H]^{6+}$ = 1081.63 (obs. 1081.77), $[M+7H]^{7+}$ = 927.26 (obs. 927.37), $[M+8H]^{8+}$ = 811.47 (obs. 811.66), $[M+9H]^{9+}$ = 721.42 (obs. 721.56), $[M+10H]^{10+}$ = 649.38 (obs. 649.56), $[M+11H]^{11+}$ = 590.44 (obs. 590.56).

6.6.11 Synthesis of P17-PNA Conjugate 17

H-GRKKRWFRRRRMKWKK-O2Oc- gct-att-acc-tta-acc-cag-K-*NH₂*
$C_{308}H_{438}N_{144}O_{74}S$
M_w = 7373.89 g/mol

The synthesis of P17-PNA conjugate **17** was performed by Dr. Hendrik Schneider on a 0.025 mmol scale.

RP-HPLC (0 to 80% eluent B, 220 nm): t_R = 11.457 min.

ESI-MS: Calc. for $C_{308}H_{438}N_{144}O_{74}S$: m/z: $[M+7H]^{7+}$ = 1054.41 (obs. 1054.57), $[M+8H]^{8+}$ = 922.74 (obs. 922.87), $[M+9H]^{9+}$ = 820.32 (obs. 820.46), $[M+10H]^{10+}$ = 738.39 (obs. 738.56), $[M+12H]^{12+}$ = 615.49 (obs. 615.49).

6.6.12 Synthesis of P14-PNA Conjugate 18

H-RKKRWFRRRRPWKKK-O2Oc- gct-att-acc-tta-acc-cag-K-*NH₂*
$C_{306}H_{433}N_{143}O_{73}$
M_w = 7282.76 g/mol

The assembly of the PNA was performed as described in section **6.6.7**. After completion of the PNA sequence the resin was split and one half (25 µmol) was further modified by double coupling of the Fmoc-protected spacer O_2Oc **15** (3 eq.) using HATU (2.95 eq.) and DIPEA (8 eq). Amino acids were introduced as single coupling (5 eq. amino acid), activated with HATU (4.95 eq.) and DIPEA (10 eq.). Following that, the product was cleaved from solid support using the TFA:TES:anisole:H_2O (47:1:1:1) cleavage cocktail. After precipitation in cold DEE and subsequent washing with cold DEE the crude product was split in half. One half was purified by semi-preparative HPLC, yielding 7 mg (0.96 µmol, 8% based on half of the batch). Further 21 mg (2.88 µmol, 23% based on half of the batch) of P14-PNA conjugate **18** were yielded as crude product.

RP-HPLC (0 to 80% eluent B, 280 nm): t_R = 11.037 min.

ESI-MS: Calc. for $C_{306}H_{433}N_{143}O_{73}$: m/z: $[M+6H]^{6+}$ = 1214.79 (obs. 1214.78), $[M+7H]^{7+}$ = 1041.39 (obs. 1041.37), $[M+8H]^{8+}$ = 911.35 (obs. 911.37), $[M+9H]^{9+}$ = 810.20 (obs. 810.16), $[M+10H]^{10+}$ = 663.07 (obs. 663.06).

6.6.13 UV/Vis Determination of PNA Concentration

In order to determine the amount of active compound in the PNA-conjugates **13**, **16**, **17** and **18** more precisely, the concentration was determined by photometry. To that end, the molecular extinction coefficients of the conjugates were calculated as sum of the extinction coefficients of the UV absorbing components at λ = 260 nm according to the following formula:

$$\varepsilon_{PNA-Conjugate} = \sum_i \varepsilon_i * n_i \qquad (2)$$

The extinction coefficients of the nucleotides were obtained from the manufacturer (PNA Bio Inc: "Guidelines for PNA Oligomers", https://www.pnabio.com/pdf/PNA_oligomer_handling_PNABio.pdf). Photometrical data of the aromatic amino acids phenylalanine as well as tryptophane were available from the internet (https://omlc.org/spectra/PhotochemCAD, updated September 2018). The obtained extinction coefficients are summarized in the following table:

Table 6| Molecular extinction coefficients at λ = 260 nm of the relevant building blocks in the PNA conjugates.

Building Block	Molecular Extinction Coefficient [$L*mol^{-1}*cm^{-1}$] at λ = 260 nm
a	$1.37 * 10^4$
g	$1.17 * 10^4$
c	$6.6 * 10^3$
t	$8.8 * 10^3$
F	143
W	3721

Photometric determination of PNA-conjugate concentration was performed by dissolving 20 µg (according to weighted sample; three samples per conjugate) of the conjugates in 300 µL H_2O, followed by diluting the samples 1:4 and subsequent measurement of absorption at $\lambda = 260$ nm. Using the molecular extinction coefficients of the PNA-conjugates derived from formula **2**, the concentration of the conjugates was determined and a correction factor F defined (formula **3**):

$$F = \frac{c_{weighted}}{c_{UV/Vis}} \qquad (\mathbf{3})$$

Both molecular extinction coefficients of the PNA-conjugates as well as the calculated correction factors are summarized in the following table:

Table 7| Molecular extinction coefficients of PNA-conjugates **14**, **16**, **17** and **18** and their respective correction factor F.

Conjugate	$\varepsilon_{PNA\text{-}conjugate}$ [L*mol^{-1}*cm^{-1}] at $\lambda = 260$ nm	F
14	$1.755 * 10^5$	0.287
16	$1.764 * 10^5$	0.468
17	$1.831 * 10^5$	0.549
18	$1.831 * 10^5$	0.805

6.6.14 Synthesis of DiSeL 20

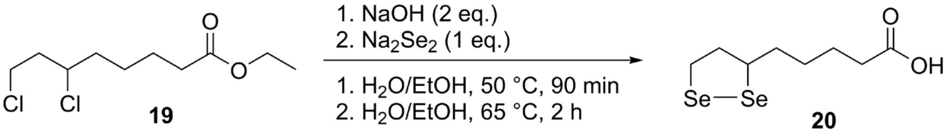

Scheme 38| Synthesis of DiSeL **20**.

The synthesis was performed as modified variant described in literature.[216] In a two-necked round bottom flask with reflux condenser and bubble counter 2.71 mL ethyl-6,8-dichlorooctanoate **19** (3 g, 12.4 mmol, 1 eq.) were dissolved in 5 mL degassed EtOH under argon atmosphere. 5% (w/v) aq. NaOH (20 mL, 24.8 mmol, 2 eq) was added and the solution was stirred at 50 °C for 90 min. Aqueous Na_2Se_2 solution* was added and the reaction was stirred for 2 h at 65 °C. Afterwards, the reaction was allowed to cool down to 40 °C and 4 g activated charcoal were added. The reaction was stirred for further 30 min, whereafter it was filtered. The filtrate was diluted with 200 mL H_2O and was cooled in an ice bath. The pH of the dark solution was adjusted to 1 with 10% hydrochloric acid (HCl) whereby a brownish-red solid precipitated. The solid was filtered off and washed with water. 1.5 g crude product were yielded after drying under reduced pressure. Since the crude product was not fully soluble in organic solvents, 40 mL dry THF were added and the suspension was stirred for 30 min. After filtration and evaporation of the solvent 600 mg product were received as dark, sticky solid. TLC analysis (n-hexane (Hex):ethyl acetate (EA) 1:1 +1% (v/v) AcOH, $KMnO_4$-staining) revealed the supposed product (R_f = 0.4) as well as a side product (R_f = 0). Hence, the crude product was purified by silica column chromatography (Hex:EA 3:2 + 1% (v/v) AcOH). Pooling of the product fractions and evaporation under reduced pressure yielded 300 mg (1 mmol, 8%) as brown solid.

**In situ* generation of aqueous Na_2Se_2 solution was performed as described in literature.[242] In a two-necked round bottom flask with dropping funnel, reflux condenser and bubble counter 1.18 g (15 mmol, 1 eq.) selenium powder were suspended in 8 mL degassed H_2O under argon atmosphere. 1.25 g (33 mmol, 2.2 eq.) $NaBH_4$ were dissolved in 8 mL degassed H_2O and added dropwise to the selenium suspension, resulting in a vigorous reaction with gas formation. After complete addition of aq. $NaBH_4$ a colorless solution was yielded, to which an additional equivalent selenium powder (1.18 g, 15 mmol, 1 eq.) was added. The resulting red-dark mixture was heated briefly to 50 °C to complete the reaction. Subsequently, the solution was transferred to the first reaction.

TLC Analysis (Hex:EA 1:1 +1% (v/v) AcOH): R_f = 0.4.

RP-HPLC (30 to 100% eluent B, 220 nm): t_R = 4.802 min.

ESI-MS: Calc. for $C_8H_{14}O_2Se_2$: $[M-H]^-$ = 300.93 (biggest isotope peak) (obs. 301.15), 298.93 (second biggest isotope peak) (obs. 299.15).

^{1}H NMR (300 MHz, DMSO-d_6): δ = 12.01 (s, 1H), 4.22 – 3.76 (m, 1H), 3.34 – 3.26 (m, 2H)*, 2.95 – 2.80 (m, 1H), 2.48 – 2.33 (m, 1H), 2.20 (t, J = 7.2 Hz, 2H), 1.85 – 1.70 (m, 1H), 1.70 – 1.57 (m, 1H), 1.56 – 1.43 (m, 2H), 1.42 – 1.29 (m, 2H).

*: Overlap with residual water peak.

6.6.15 Synthesis of DiSeL-PNA Conjugate 22

DiSeL-O2Oc- gct-att-acc-tta-acc-cag-K-*NH₂*
$C_{212}H_{277}N_{103}O_{59}Se_2$
M_w = 5370.04 g/mol

AmphiSpheres 40 RAM resin (batch: 25 µmol) preloaded with O2Oc functionalized 18mer PNA **21** was assembled as described in section **6.6.12** with some modifications. Incorporation of the O2Oc linker **15** was performed as double coupling (2× 1 h), using 2 eq. building block, HATU (1.95 eq.) and DIPEA (4 eq.). After Fmoc removal the resin was dried over night in a desiccator. 28.9 mg (75 µmol, 3 eq.) selenolipoic acid **20** and 21.3 mg Oxyma (0.15 mmol, 6 eq.) were dissolved in 5 mL anhydrous DMF. 23.2 µL (18.9 mg, 0.15 mmol, 6 eq.) DIC were added and the brown solution was shaken for 5 min under argon atmosphere. The mixture was added to the dry resin which was shaken for 3 h at ambient temperature. After removal of the supernatant, the resin was washed and dried in a desiccator over night. Cleavage from solid support and simultaneous deprotection of the side-chains was achieved using a mixture of TFA:anisole:H_2O (48:1:1) for 2.5 h. After precipitation and centrifugation of the crude product in cold DEE the residue was washed twice with cold DEE. The residue was dried in a desiccator and purified by semi-preparative HPLC. 4.7 mg (0.88 µmol, 4%) were yielded as brownish solid. The chromatographic trace revealed the presence of an impurity (t_R = 11.602 min, ~ 30% according to the area under curve at λ = 220 nm). MS analysis displayed the presence of a M+16 species, indicating the formation of an oxidized side product.

RP-HPLC (0 to 80% eluent B, 220 nm): t_R = 12.316 min.

ESI-MS: Calc. for $C_{306}H_{433}N_{143}O_{73}$ (main product): m/z: $[M+4H]^{4+}$ = 1343.53 (obs. 1343.48), $[M+5H]^{5+}$ = 1075.03 (obs. 1074.87), $[M+6H]^{6+}$ = 896.02 (obs. 895.97), $[M+7H]^{7+}$ = 768.16 (obs. 768.16), $[M+8H]^{8+}$ = 672.27 (obs. 672.26), $[M+9H]^{9+}$ = 597.68 (obs. 597.66).
Calc. for $C_{306}H_{433}N_{143}O_{74}$ (side product): m/z: $[M+4H]^{4+}$ = 1347.53 (obs. 1347.78), $[M+5H]^{5+}$ = 1078.23 (obs. 1078.07), $[M+6H]^{6+}$ = 898.69 (obs. 898.67), $[M+7H]^{7+}$ = 770.45 (obs. 770.36), $[M+8H]^{8+}$ = 674.27 (obs. 674.36).

6.6.16 PNA Mis-Splicing Correction Assay

Assay at 37 °C:

HeLa-eGFP654 cells were seeded into 48-well plates in a density of 3.0×10^4 cells/well and incubated under standard conditions for 24 h. The supernatant was removed and the cells were washed PBS. Afterwards 270 µL DMEM without L-cystine, L-glutamine, L-methionine and FBS was added, followed by 30 µL of the constructs (10× concentrated in PBS pH 5.9). After 30 min incubation at 37 °C the supernatant was aspirated and the cells were washed with PBS and 400 µL DMEM (+ 10% FBS) was added. The cells were incubated for further 24 h in the humidified incubator, washed afterwards with PBS and trypsinized with 100 µL 0.05% trypsin-EDTA (*Sigma Aldrich*) solution. After 10 min incubation at 37 °C DMEM (+ 10% FBS) was added and the suspended cells were transferred into a 96-well plate. The trypsinized cells were spun down at 500 g for 5 min, resuspended in PBS and transferred into FACS tubes. Restored eGFP-fluorescence was quantified by measuring the fluorescence at λ = 488 nm.

Assay at 4 °C:

HeLa-eGFP654 cells were seeded into 48-well plates in a density of 3.0×10^4 cells/well and incubated under standard conditions for 24 h. The supernatant was removed and the cells were washed with ice-cold PBS. Ice-cold DMEM (270 µL) without L-cystine, L-glutamine, L-methionine and FBS was added, followed by 30 µL of the constructs (10× concentrated in PBS pH 5.9). The cells were incubated in the refrigerator at 4 °C for 30 min, whereafter the cells were treated analogously to the assay at 37 °C.

Assay with DiSeL-PNA 22 and P17-PNA 17 at 37 °C:

HeLa-eGFP654 cells were seeded into 24-well plates in a density of 1.0×10^5 cells/well and incubated under standard conditions for 24 h. The supernatant was removed and the cells were washed PBS. Afterwards 360 µL DMEM without L-cystine, L-glutamine, L-methionine and FBS was added, followed by 40 µL of the constructs (10× concentrated in PBS pH 5.9). After 30 min incubation at 37 °C the supernatant of cells treated with P17-PNA conjugate **17** were removed, whereas cells were incubated for 4 h at 37 °C with DiSeL-PNA conjugate **22**. After further 22 h incubation with medium containing 10% FBS, cells were trypsinized and analyzed analogously to the previous procedures.

6.6.17 Cell Proliferation Assay

HeLa cells (1.2×10^4 cells/well) were seeded in 96-well plates and incubated under standard conditions for 24 h. The supernatant was aspirated and the cells were washed with PBS. 60 µL DMEM without L-cystine, L-glutamine, L-methionine and FBS was added, followed by 40 µL of the constructs (2.5× concentrated in PBS pH 5.9;) in triplicates. Cells were incubated for 30 min at 37 °C and 5% CO_2 whereafter the supernatant was removed and the cells were washed with PBS. 100 µL DMEM (10% FBS, 1× pen/strep) was added and the cells were incubated under standard conditions for 24 h. 10 µL *CellTiter96® AQueous One Solution Cell Proliferation Assay* MTS solution (*Promega GmbH*, Walldorf, Germany) were added and after appropriate incubation time under standard conditions absorption at λ = 490 nm was measured using the *Infinite F200 pro* plate reader. The absorption of medium without cells was subtracted as background; absorption of cells treated with medium only was set as reference to 100% proliferation.

6.7 Evaluation of L17E-Decorated Dextran in the Split-GFP Complementation Assay

6.7.1 Synthesis of *N*-Boc-Cadaverine-Dextran 25

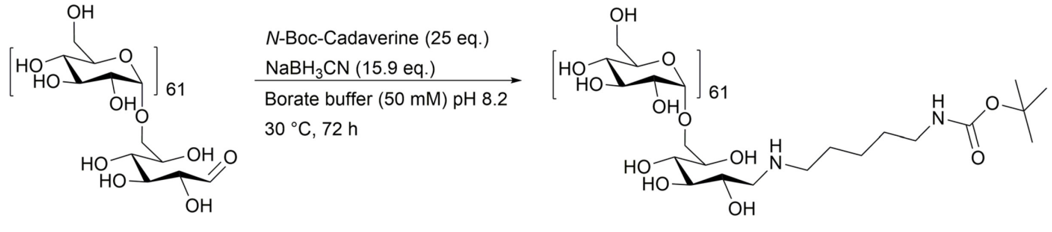

24

25

Scheme 39| Introduction of *N*-Boc-cadaverine at the reducing end of 10 kDa dextran **24** *via* reductive amination.

Variant A:

The synthesis was conducted as described in literature.[42] 1 g (0.1 mmol, 1 eq.) dextran **24** (10 kDa, average molecular weight: 9000 – 11000, from *Leuconostoc mesenteroides*, supplier: *Sigma Aldrich*) were dissolved in 5 mL borate buffer (50 mM, pH 8.2). 0.52 mL (0.51 g, 2.5 mmol, 25 eq.) *N*-Boc-cadaverine and 0.1 g (1.59 mmol, 15.9 eq.) $NaBH_3CN$ were added and the reaction was stirred in the dark for 72 h at 30 °C. The crude product was precipitated in cold methanol, centrifuged and washed twice with cold methanol. After the residue had dried, it was dissolved in H_2O and freeze-dried. The crude product was dissolved in H_2O again and purified using PD10 desalting columns following the instructions of the manufacturer. Freeze-drying of the eluate yielded 0.47 g (46.15 µmol, 46%) of *N*-Boc-cadaverine-dextran **25** as colorless solid.

Variant B:

The synthesis was performed analogously to the procedure described in **Variant A** with one difference: After dissolution of all reactants in borate buffer the pH (now at ~ 11) was readjusted with 1 M HCl to pH 8.2. After 72 h reaction time the pH was checked again (no significant change) and the workup of the product was performed as described in **Variant A**. 0.59 g (57.3 µmol, 57%) of *N*-Boc-cadaverine-dextran **25** were yielded.

^{1}H NMR (300 MHz, D_2O, **Variant A**): δ = 5.48 – 4.96 (m, 62H, anomeric **H**), 4.16 – 3.46 (m, (C2-C6)**H**), 3.21 – 3.07 (m, 4H, -NH-C**H**$_2$-(CH$_2$)$_3$-C**H**$_2$-NHBoc), 1.89 – 1.33 (m, 17H, -NH-CH$_2$-(C**H**$_2$)$_3$-CH$_2$-NH-CO-O-C(C**H**$_3$)$_3$).

^{1}H NMR (300 MHz, D_2O, **Variant B**): δ = 5.35 – 4.90 (m, 62H, anomeric H), 4.07 – 3.37 (m, (C2-C6)**H**), 3.15 – 2.98 (m, 4H, -NH-C**H**$_2$-(CH$_2$)$_3$-C**H**$_2$-NHBoc), 1.77 – 1.29 (m, 15H, -NH-CH$_2$-(C**H**$_2$)$_3$-CH$_2$-NH-CO-O-C(C**H**$_3$)$_3$).

6.7.2 Synthesis of *N*-Boc-Cadaverine-Dextran-CE$_{5.4}$ 26

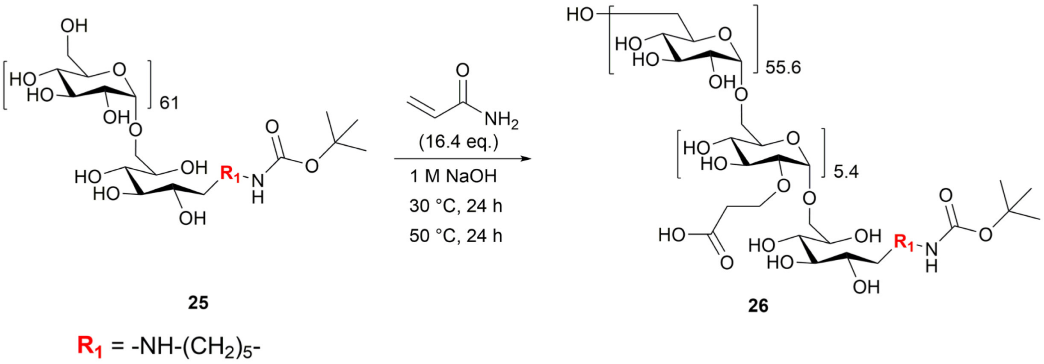

Scheme 40| Synthesis of N-Boc-cadaverine-dextran-CE$_{5.4}$ **26**.

The synthesis was performed as described in literature.[42] 470 mg (46.2 µmol, 1 eq.) *N*-Boc-cadaverine-dextran **25** were dissolved in 5 mL 1 M NaOH. Acrylamide (54 mg, 0.754 mmol, 16.4 eq.) was added and the reaction was stirred for 24 h at 30 °C, whereafter the reaction was increased to 50 °C and the reaction was stirred for further 24 h. The crude product was precipitated and washed with cold MeOH and subsequently dried in airstream. It was dissolved in H_2O and neutralized with 0.1 M HCl followed by freeze-drying. The residue was dissolved in H_2O and purified using PD10 desalting columns. 429 mg (40.6 µmol, 88 %) were yielded as colorless solid.

^{1}H NMR (300 MHz, D_2O): δ = 5.46 – 4.98 (m, 62H, anomeric **H**), 4.18 – 3.42 (m, (C2-C6)**H**), 3.21 – 3.10 (m, 3H, -NH-C**H**$_2$-(CH_2)$_3$-C**H**$_2$-NHBoc), 2.63 – 2.50 (m, 12H, -C**H**$_2$-CH_2-COOH), 1.92 – 1.29 (m, 10H, -NH-CH_2-(C**H**$_2$)$_3$-CH_2-NH-CO-O-C(C**H**$_3$)$_3$).

6.7.3 Synthesis of *N*-(5-Aminopentyl)-2-Azidoacetamide 27

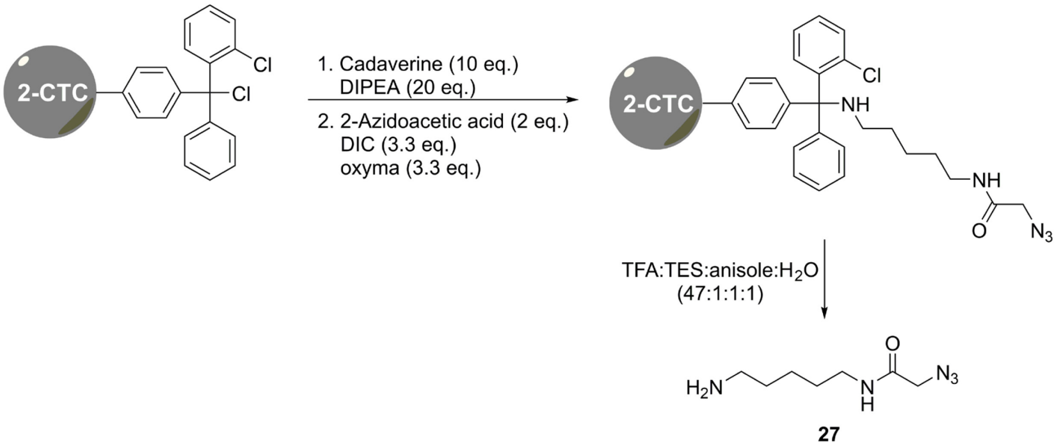

Scheme 41| Solid phase synthesis of azide-bearing linker **27**.

The synthesis was performed as described in literature.[29] 1.25 g 2-CTC resin (capacity: 1.60 mmol/g, scale: 2 mmol) was evenly split and transferred into two syringes equipped with a frit and swollen in dry DCM. A solution of 2.91 mL (2.04 g, 20 mmol, 10 eq.) cadaverine and 6.97 mL (5.13 g, 40 mmol, 20 eq.) DIPEA in DMF were added to the resin and shaken for 3 h at ambient temperature. After washing the resin thoroughly with DMF, a solution of 0.3 mL (0.4 g, 4 mmol, 2 eq.) 2-azidoacetic acid, 1.02 mL (0.83 g, 6.6 mmol, 3.3 eq.) DIC and 0.94 g (6.6 mmol, 3.3 eq.) Oxyma in DMF were added and the resin was shaken over night. The supernatant was removed, the resin was dried *in vacuo* and subsequently mixed with cleavage cocktail (TFA:TES:anisole:H_2O, 47:1:1:1). After shaking for 3 h the crude product was mixed with cold DEE which resulted in the formation of an emulsion. Centrifugation sedimented the crude product as highly viscous yellowish oil. After discarding the supernatant, the oil was dissolved in H_2O and subjected to purification by semi-preparative HPLC. 251 mg (1.36 mmol, 68%) of *N*-(5-aminopentyl)-2-azidoacetamide **27** were obtained.

RP-HPLC (0 to 40% eluent B, 220 nm): t_R = 7.322 min.

ESI-MS: Calc. for $C_7H_{15}N_5O$: m/z: $[M+H]^+$ = 186.24 (obs. 186.48).

6.7.4 Synthesis of *N*-Boc-Cadaverine-Dextran-$(N_3)_{5.4}$ 28

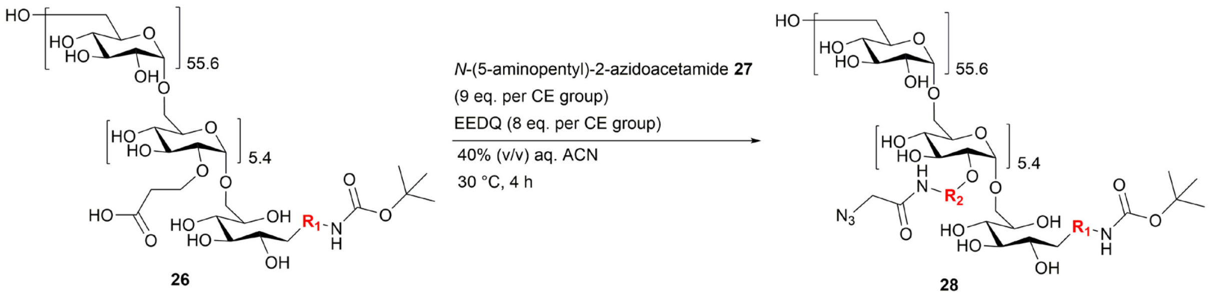

R_1 = -NH-$(CH_2)_5$-
R_2 = -$(CH_2)_2$-CO-NH-$(CH_2)_5$-

Scheme 42 | EEDQ-mediated coupling of linker **27** to dextran **26**.

The synthesis (batch 1) was performed as described in literature.[29] 50 mg (4.7 µmol, 1 eq.) *N*-Boc-cadaverine-dextran-$CE_{5.4}$ **26** were dissolved in 1.6 mL 40% (v/v) aq. ACN and heated to 30 °C. 49.5 mg (0.2 mmol, 8 eq. per CE group) *N*-ethoxycarbonyl-2-ethoxy-1,2-dihydroquinoline (EEDQ) in 500 µL 40% aq. ACN were added and the reaction was stirred for 1 h. 43 mg (0.23 mmol, 9 eq. per CE group) linker **27** in 400 µL 40% ACN was added to the reaction which was stirred for further 3 h at 30 °C. Following this, the product was purified using a PD10 desalting column. Lyophilization of the eluate yielded 40 mg (3.45 µmol, 73%) product as colorless solid.

The synthesis was repeated (batch 2) with equal amounts of dextran **26** (50 mg, 4.7 µmol, 1 eq.), EEDQ (49.5 mg, 0.2 mmol, 8 eq. per CE group) and linker **27** (43 mg, 0.23 mmol, 9 eq. per CE group). Yield after PD10 purification and freeze-drying: 51 mg (4.39 µmol, 93%).

Batch 1:

^{1}H NMR (300 MHz, D_2O): δ = 5.47 – 4.99 (m, 62H, anomeric **H**), 4.23 – 3.47 (m, (C2-C6)**H** and NH-CO-C**H**$_2$-N_3), 3.40 – 3.23 (m, 30H, -NH-C**H**$_2$-$(CH_2)_3$-C**H**$_2$-NH-), 2.71 – 2.54 (m, 11H, -C**H**$_2$-CH_2-COOH), 1.70 – 1.54 (m, 33H, -NH-CH_2-C**H**$_2$-CH_2-C**H**$_2$-CH_2-NH-), 1.51 (s, 8H, CO-O-C(C**H**$_3$)$_3$), 1.49 – 1.35 (m, 18H, -NH-CH_2-CH_2-C**H**$_2$-CH_2-CH_2-NH-).

Batch 2:

^{1}H NMR (300 MHz, D_2O): δ = 5.50 – 4.94 (m, 62H, anomeric **H**), 4.25 – 3.38 (m, (C2-C6)**H** and NH-CO-C**H**$_2$-N_3), 3.37 – 3.22 (m, 30H, -NH-C**H**$_2$-$(CH_2)_3$-C**H**$_2$-NH-), 2.69 – 2.54 (m, 11H, -C**H**$_2$-CH_2-COOH), 1.68 – 1.53 (m, 32H, -NH-CH_2-C**H**$_2$-CH_2-C**H**$_2$-CH_2-NH-), 1.51 (s, 8H, CO-O-C(C**H**$_3$)$_3$), 1.48 – 1.34 (m, 18H, -NH-CH_2-CH_2-C**H**$_2$-CH_2-CH_2-NH-).

6.7.5 Synthesis of Cadaverine-Dextran-$(N_3)_{5.4}$ 29

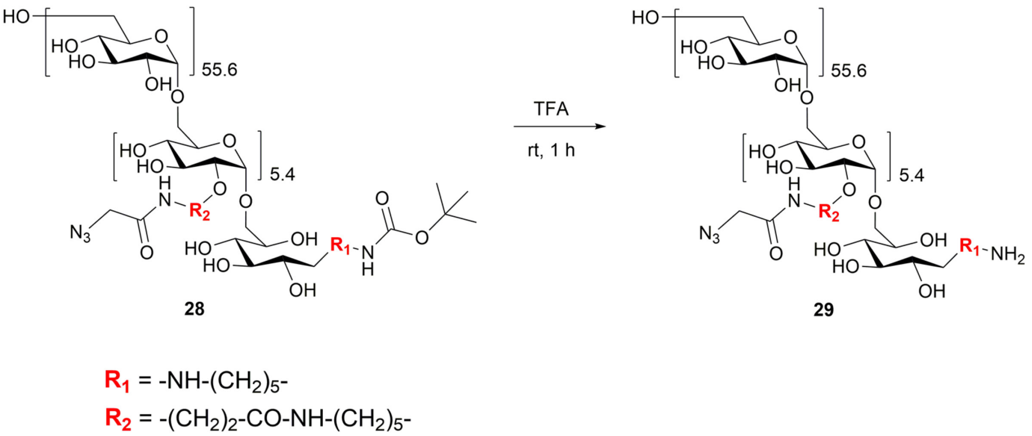

Scheme 43| TFA-mediated deprotection of the Boc protecting group of *N*-Boc-cadaverine-dextran-$(N_3)_{5.4}$ **28**.

The synthesis was accomplished as described in literature.[29] 40 mg (3.45 µmol) *N*-Boc-cadaverine-dextran-$(N_3)_{5.4}$ **28** (batch 1) were suspended in 2 mL TFA. The reaction was stirred at ambient temperature for 1 h whereby the solid dissolved completely. The product was precipitated and washed with cold MeOH. After the residue had dried it was dissolved in H_2O and purified using a disposable PD10 column. Freeze-drying yielded 34 mg (2.96µmol, 86%) of the title compound as colorless solid.

Deprotection of dextran **28** (batch 2) was performed analogously, yielding 47 mg (4.08 µmol, 93%) of the title compound.

Batch 1:

^{1}H NMR (300 MHz, D_2O): δ = 5.51 – 4.95 (m, 62H, anomeric **H**), 4.21 – 3.51 (m, (C2-C6)**H** and NH-CO-C**H**$_2$-N_3), 3.37 – 3.22 (m, 24H, -NH-C**H**$_2$-$(CH_2)_3$-C**H**$_2$-NH-), 2.73 – 2.52 (m, 11H, -C**H**$_2$-CH_2-COOH), 1.68 – 1.53 (m, 23H, -NH-CH_2-C**H**$_2$-CH_2-C**H**$_2$-CH_2-NH-), 1.49 – 1.30 (m, 14H, -NH-CH_2-CH_2-C**H**$_2$-CH_2-CH_2-NH-).

Batch 2:

^{1}H NMR (300 MHz, D_2O): δ = 5.41 – 4.91 (m, 62H, anomeric **H**), 4.16 – 3.43 (m, (C2-C6)**H** and NH-CO-C**H**$_2$-N_3), 3.36 – 3.22 (m, 25H, -NH-C**H**$_2$-$(CH_2)_3$-C**H**$_2$-NH-), 2.69 – 2.52 (m, 11H, -C**H**$_2$-CH_2-COOH), 1.67 – 1.53 (m, 23H, -NH-CH_2-C**H**$_2$-CH_2-C**H**$_2$-CH_2-NH-), 1.47 – 1.34 (m, 14H, -NH-CH_2-CH_2-C**H**$_2$-CH_2-CH_2-NH-).

6.7.6 Synthesis of TAMRA-Cadaverine-Dextran-$(N_3)_{5.4}$ 31

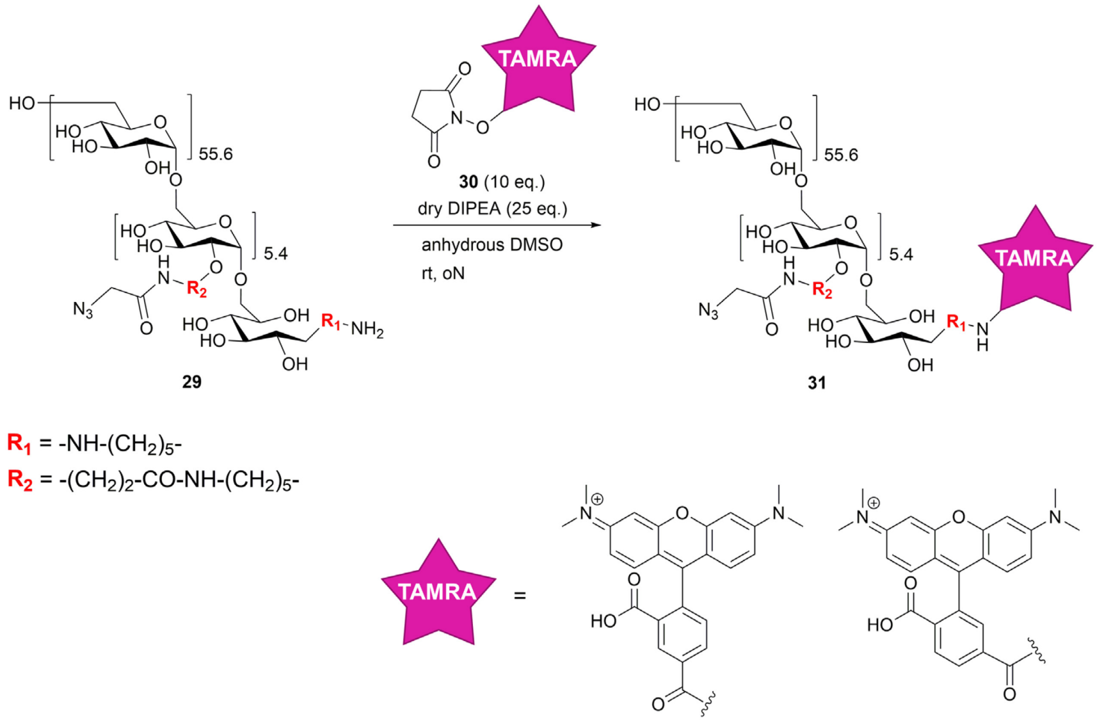

Scheme 44| Synthesis of TAMRA-cadaverine-dextran-$(N_3)_{5.4}$ **31** and structure of TAMRA isomers.

24 mg (2.11 µmol, 1 eq.) *N*-cadaverine-dextran-$(N_3)_{5.4}$ **29** (batch 1) were dissolved in 400 µL anhydrous DMSO. A solution of 11.1 mg (21.1µmol, 10 eq.) 5(6)-TAMRA-NHS **30** and 9.2 µL dry DIPEA (6.8 mg, 52.8 µmol, 25 eq.) in 200 µL anhydrous DMSO was added and the resulting dark solution was shaken over night at ambient temperature. The crude product was precipitated in MeOH, washed with MeOH and subsequently with ACN. Following that, the residue was dissolved in H_2O and purified using a PD10 desalting column. After lyophilization of the eluate 16 mg (1.36µmol, 64%) were obtained as violet solid. The product was analyzed by SEC-HPLC and IR spectroscopy.

SEC-HPLC (30% B isocratic flow, 220 nm): t_R = 15.259 min.

6.7.7 Quantification of TAMRA-functionalization of TAMRA-Cadaverine-Dextran-$(N_3)_{5.4}$ 31

Reducing end-functionalization of TAMRA-cadaverine-dextran-$(N_3)_{5.4}$ **31** was quantified by chromatography and UV/Vis photometry. Purity of the obtained product was analyzed by SEC-HPLC:

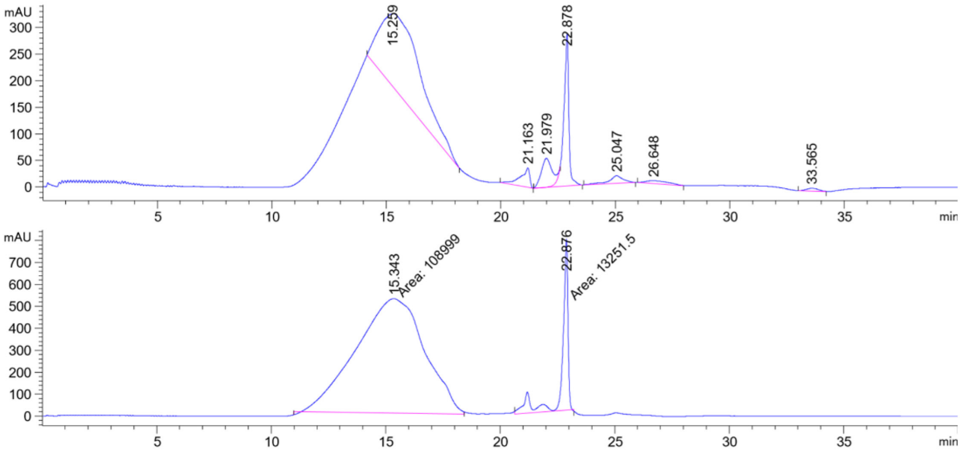

Figure 62| SEC-chromatogram of TAMRA-cadaverine-dextran-$(N_3)_{5.4}$ **31**, 30 % B isocratic flow over 40 min, λ = 220 nm (top), λ = 550 nm (bottom).

The ratio of TAMRA-cadaverine-dextran-$(N_3)_{5.4}$ ($t_R \sim 11 - 18$ min) to impurities ($t_R \sim 21$ -23 min) was estimated upon peak surface area calculated by the software and was 89%. For quantification of reducing end-functionalization, the molecular extinction coefficient of TAMRA was determined using a TAMRA calibration curve:

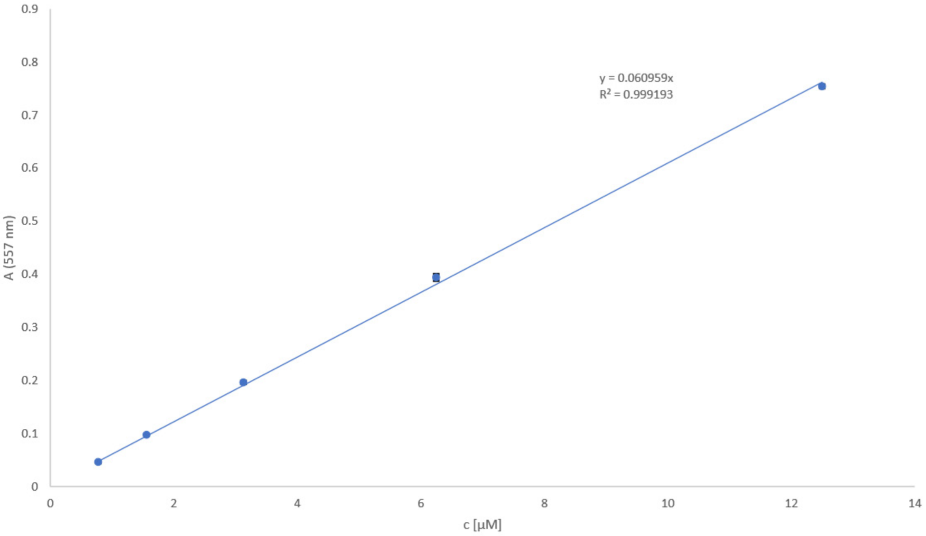

Figure 63| Calibration curve of 5(6)-TAMRA-NHS **30** in water at λ = 557 nm. The molecular extinction coefficient is the slope of the linear regression and was determined as ε = 60959 $L{*}mol^{-1}{*}cm^{-1}$.

TAMRA-cadaverine-dextran-$(N_3)_{5.4}$ **31** was dissolved in water and diluted 1:500, followed by measurement of the absorption at λ = 557 nm. Using the Lambert-Beer law (formula **4**), the TAMRA concentration of the diluted product **31** was calculated:

$$A = \varepsilon * c * d \qquad (\mathbf{4})$$

A_{557}(sample) = 0.072 (1:500 dilution)
d = 1 cm
ε_{557}(TAMRA-NHS) = 60959 L/(mol*cm)
c (sample, according to weight) = 672 µM

$$c = \frac{0.072}{60959 \frac{L}{mol * cm} * 1\ cm} = 1.18\ \mu M; \quad c\ (undiluted) = 590\ \mu M$$

According to the SEC-chromatogram, 89 % of TAMRA in the product was coupled to dextran, hence the concentration of TAMRA-cadaverine-dextran-$(N_3)_{5.4}$ **31** is c = 525 µM.

$$TAMRA\ per\ dextran: \frac{c_{photometric}}{c_{weight}} = \frac{525\ \mu M}{672\ \mu M} = 0.78$$

6.7.8 Synthesis of L17E-Pra 32

H-IWLTALKFLGKHAAKHEAKQQLSKL-Pra-*NH₂*

$C_{139}H_{225}N_{39}O_{32}$

M_w = 2954.57 g/mol

The synthesis was performed on 735 mg *AmphiSpheres 40 RAM* resin (capacity: 0.34 mmol/g, scale: 0.25 mmol). According to the general procedure the first amino acid, Fmoc-Pra-OH (3 eq.), was loaded by single coupling upon HATU (2.95 eq.) and DIPEA (6 eq.) activation. The remaining sequence was assembled by automated SPPS on the *Liberty Blue™* system. The peptide was cleaved from solid support by treating the resin with TFA:TES:anisole:H_2O (47:1:1:1) cleavage cocktail for 3 h. The crude product was precipitated and washed with cold DEE. Peptide purification was conducted by semi-preparative HPLC yielding 339 mg (0.115 mmol, 46%) of L17E-Pra **32**.

RP-HPLC (10 to 80% eluent B, 220 nm): t_R = 12.951 min.

ESI-MS: Calc. for $C_{139}H_{225}N_{39}O_{32}$: m/z: $[M+3H]^{3+}$ = 985.86 (obs. 985.87), $[M+4H]^{4+}$ = 739.64 (obs. 739.66), $[M+5H]^{5+}$ = 591.91 (obs. 591.96), $[M+6H]^{6+}$ = 493.43 (obs. 493.55).

6.7.9 Synthesis of Alkyne-GFP11 33

4-pentynoic acid-GSSG-RDHMVLHEYVNAAGIT-*NH_2*

$C_{94}H_{145}N_{29}O_{30}S$

M_w = 2193.40 g/mol

SPPS was performed using 735 mg *AmphiSpheres 40 RAM* resin (capacity: 0.34 mmol/g, scale: 0.25 mmol). The peptide sequence GSSGRDHMVLHEYVNAAGIT was assembled by automated peptide synthesis using the *Liberty Blue™* system. Following that, the alkyne functionality was introduced *N*-terminally by conjugation of 4-pentynoic acid. Hence, 98 mg (1 mmol, 4 eq.) 4-pentynoic acid and 213 mg (1.5 mmol, 6 eq.) Oxyma were dissolved in DMF. 232 µL (189 mg, 1.5 mmol, 6 eq.) DIC were added and the solution was activated for 5 min. The resin was shaken with the activated mixture over night at room temperature. After washing and storing the resin over night in a desiccator the peptide was cleaved from solid support using TFA:TES:anisole:H_2O (47:1:1:1) cleavage cocktail for 3 h. The crude product was precipitated and washed with DEE and subsequently purified by semi-preparative HPLC. 66 mg (30.1 µmol, 12%) of the title compound were obtained as colorless solid.

RP-HPLC (20 to 80% eluent B, 220 nm): t_R = 9.838 min.

ESI-MS: Calc. for $C_{94}H_{145}N_{29}O_{30}S$: m/z: $[M+2H]^{2+}$ = 1097.70 (obs. 1097.67), $[M+3H]^{3+}$ = 732.13 (obs. 732.16), $[M+4H]^{4+}$ = 549.35 (obs. 549.35).

6.7.10 Synthesis of TAMRA-Cadaverine-Dextran-(L17E,GFP11)$_{5.4}$ 34

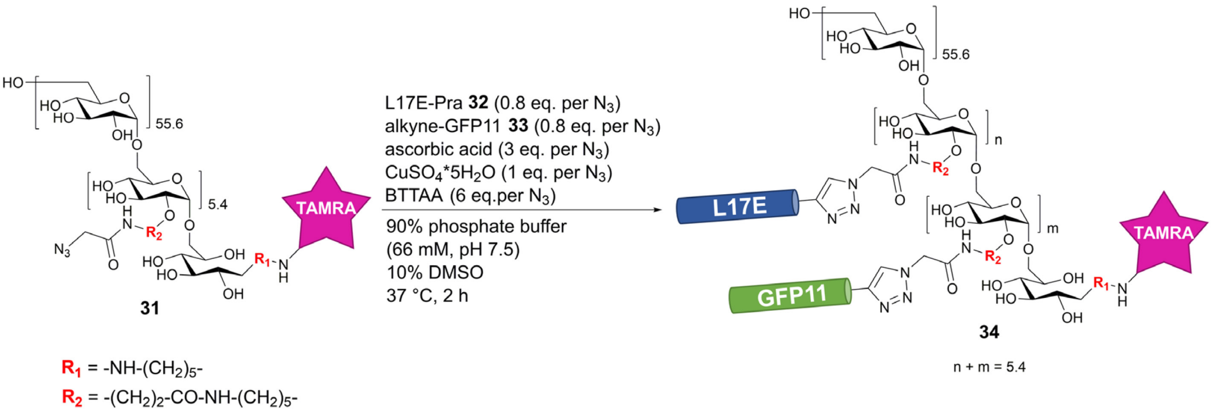

Scheme 45 | Synthesis of TAMRA-cadaverine-dextran-L17E-GFP11 **34**.

10 mg (0.87 µmol ≙ 4.71 µmol N_3-group, 1 eq.) TAMRA-cadaverine-dextran-$(N_3)_{5.4}$ **31** were dissolved in phosphate buffer (600 µL, 100 mM, pH 7.5). 12.2 mg (28.28 µmol, 6 eq per N_3-group) BTTAA were suspended in H_2O and freshly prepared stocks of $CuSO_4 \cdot 5H_2O$ (1.2 mg, 4.71 µmol, 1 eq. per N_3-group) and ascorbic acid (2.5 mg, 14.14 µmol, 3 eq. per N_3-group) were added (V_{total} = 300 µL). The blue solution which formed upon addition of $CuSO_4 \cdot 5H_2O$ faded after addition of ascorbic acid. The Cu(I)-solution was shaken for 5 min at room temperature. 11.1 mg (3.77µmol, 0.8 eq. per N_3-group) L17E-Pra **32** and 8.3 mg (3.77µmol, 0.8 eq. per N_3-group) alkyne-GFP11 **33** were dissolved in 100 µL anhydrous DMSO and added to the dextran solution. The Cu(I)-solution was added and the violet reaction mixture was shaken for 2 h at 37 °C. The product was isolated by consecutive SEC-HPLC runs, which yielded 7.4 mg (0.29 µmol, 33%) of the title compound after lyophilization.

SEC-HPLC (30% B isocratic flow, 220 nm): t_R = 9.742 min.

6.7.11 Synthesis of TAMRA-Cadaverine-Dextran-GFP11 35

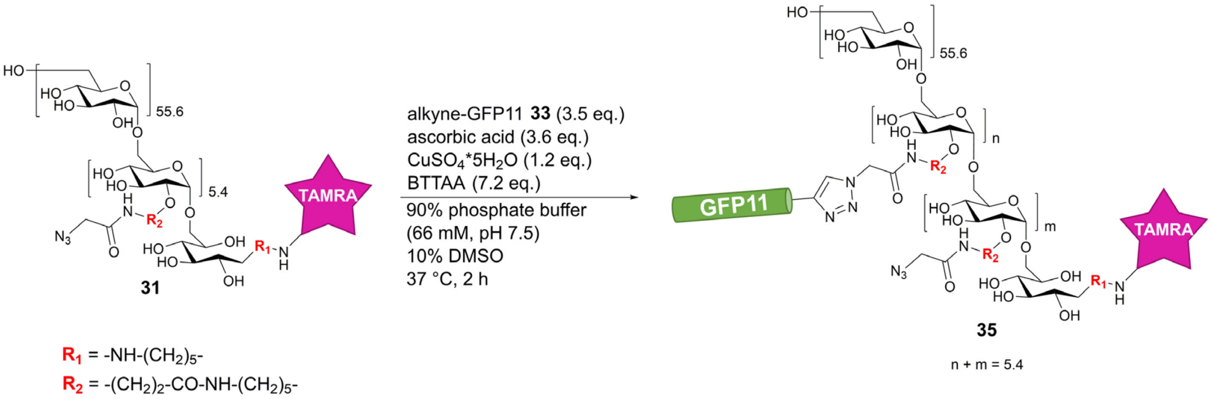

Scheme 46| CuAAC-mediated conjugation of alkyne-GFP11 **33** to TAMRA-cadaverine-dextran-$(N_3)_{5.4}$ **31**.

5 mg (0.42 µmol, 1 eq.) TAMRA-cadaverine-dextran-$(N_3)_{5.4}$ were dissolved in phosphate buffer (300 µL, 100 mM, pH 7.5). Freshly prepared aqueous solutions of $CuSO_4 \cdot 5H_2O$ (0.12 mg, 0.5 µmol, 1.2 eq.) and ascorbic acid (0.26 mg, 1.51 µmol, 3.6 eq.) were added to a suspension of 1.3 mg BTTAA (3.02 µmol, 7.2 eq.) in H_2O (V_{total} = 150 µL). 3.2 mg (1.47 µmol, 3.5 eq.) alkyne-GFP11 **33** were dissolved in 50 µL DMSO and added to the dextran solution. The Cu(I)-solution was added and the reaction was shaken for 2 h at 37 °C. The product was purified by consecutive SEC-HPLC runs, yielding 3.6 mg (0.19 µmol, 44%)* of TAMRA-cadaverine-dextran-GFP11 **35** as violet solid.

*: Since the exact number of conjugated GFP11 could not be determined, the molecular weight of product was calculated under the assumption that all 3.5 eq. of the peptide were coupled.

SEC-HPLC (30% B isocratic flow, 220 nm): t_R = 10.775 min.

6.7.12 Synthesis of GFP11 36

H-RDHMVLHEYVNAAGIT-*NH₂*
$C_{79}H_{125}N_{25}O_{23}S$
M_w: 1825.06 g/mol

The peptide was synthesized by automated SPPS in a 0.1 mmol scale on *AmphiSpheres 40 RAM* resin (capacity: 0.34 mmol/g, 294 mg) using the *Liberty Blue™* synthesizer. After completion of the synthesis the peptide was cleaved from solid support using TFA:TES:anisole:H_2O (47:1:1:1) cleavage cocktail for 3 h. The crude product was obtained after precipitation and washing with cold DEE. Purification of the product was performed by semi-preparative HPLC yielding 9 mg (4.9 µmol, 5%) as colorless solid.

RP-HPLC (10 to 60% eluent B, 220 nm): t_R = 13.257 min.

ESI-MS: Calc. for $C_{79}H_{125}N_{25}O_{23}S$: m/z: $[M+2H]^{2+}$ = 913.53 (obs. 913.57), $[M+3H]^{3+}$ = 609.35 (obs. 609.36), $[M+4H]^{4+}$ = 457.25 (obs. 457.37).

6.7.13 Flow Cytometric Analysis of GFP-Complementation

HeLa-GFP1-10 cells were seeded into 48-well plates in a density of 4.0×10^4 cells/well and incubated under standard conditions overnight. Afterwards, the medium was removed and the cells washed twice with PBS. 270 µL serum-free DMEM was added, followed by 30 µL of the compounds (10× concentrated in PBS). After incubation for 1 h the supernatant was removed, the cells were washed twice with PBS and further incubated for 24 h in 300 µL DMEM (+10% FBS). Following that, the cells were washed twice with PBS and subsequently detached from the plate using 0.05% trypsin-EDTA. After 10 min incubation at 37 °C DMEM (+ 10% FBS) was added and the suspended cells were transferred into a 96-well plate. The trypsinized cells were spun down at 500 g for 5 min, washed twice with PBS, resuspended in PBS and transferred into FACS tubes. eGFP-fluorescence was quantified by measuring the fluorescence at λ = 488 nm, TAMRA-fluorescence was measured at λ = 556 nm.

6.7.14 Live Cell CLSM of GFP-Complementation

HeLa-GFP1-10 cells were seeded in 8-well microscopy slides (*µ-Slide 8 Well*, *ibidi GmbH*, Gräfelfing, Germany) in a density of 1.5×10^4 cells/well. After incubation under standard conditions overnight, the medium was removed and the cells washed twice with PBS. 180 µL serum-free DMEM was added, followed by 20 µL of the compounds (10× concentrated in PBS). After incubation for 1 h the supernatant was removed, the cells were washed twice with PBS and further incubated for 24 h in 250 µL DMEM (+10% FBS). Prior to microscopy, the medium was aspirated and the cells were washed twice with PBS and finally covered with Hank´s solution (0.35 g/L $NaHCO_3$, with Ca^{2+} and Mg^{2+}).

6.7.15 Cell Proliferation Assay

HeLa cells were seeded in a 96-well plate in a density of 1.0×10^4 cells/well in a volume of 100 µL DMEM (+ 10% FBS). After incubation for 24 h under standard conditions the medium was aspirated and the cells were washed twice with PBS. 90 µL serum-free DMEM were added and a serial dilution of construct **34** in 10 µL PBS were added in triplicates. After incubation for 1 h at 37 °C and 5% CO_2 the supernatant was removed and the cells were washed twice with PBS. DMEM (+ 10% FBS) was added and the cells were incubated for further 24 hours. Afterwards, 10 µL *CellTiter96® AQueous One Solution Cell Proliferation Assay* MTS solution was added and after appropriate incubation time under standard conditions absorption at λ = 490 nm was measured using the *Infinite F200 pro* plate reader. The absorption of medium without cells was subtracted as background; absorption of cells treated with medium only was set as reference to 100% proliferation.

6.8 Modular Dextran-Streptavidin Hybrids: Cellular Uptake

6.8.1 Synthesis of Biotin-NHS 37

Scheme 47| Synthesis of biotin-NHS **37**.

The synthesis was performed according to the literature.[243] 1 g (4.1 mmol, 1 eq.) D-biotin were suspended in 35 mL anhydrous DMF. 0.57 g (4.92 mmol, 1.2 eq.) NHS and 0.94 g (4.92 mmol, 1.2 eq.) EDC·HCl were added and the mixture was stirred over night at ambient temperature during which the reactants dissolved completely. The solvent was removed under reduced pressure yielding a sticky solid. The product was recrystallized from EtOH:AcOH:H_2O (95:1:4). For completion of the crystallization the suspension was stored over night in a refrigerator. Following that, the suspension was filtered and the residue was washed with cold recrystallization mixture and dried *in vacuo*. 1.13 g (3.31 mmol, 81%) of biotin-NHS **37** were obtained.

^{1}H NMR (300 MHz, DMSO-d_6): δ = 6.40 (s, 1H), 6.34 (s, 1H), 4.35 – 4.27 (m, 1H), 4.19 – 4.12 (m, 1H), 3.15 – 3.07 (m, 1H), 2.87 – 2.82 (m, 1H), 2.81 (s, 4H), 2.67 (t, *J* = 7.3 Hz, 2H), 2.62 – 2.55 (m, 1H), 1.75 – 1.36 (m, 6H).

6.8.2 Synthesis of Biotin-Cadaverine-Dextran-(N_3)$_{5.4}$ 38

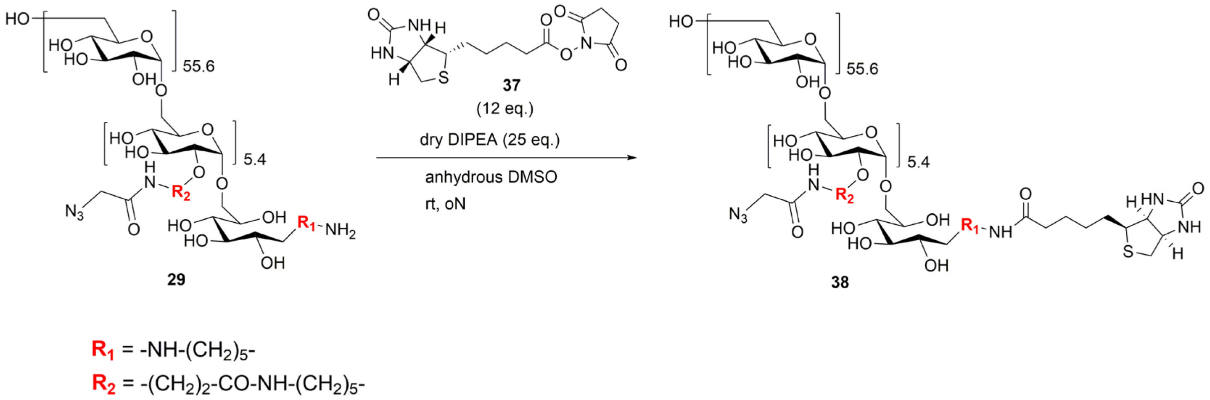

Scheme 48| Synthesis of biotin-cadaverine-dextran-(N_3)$_{5.4}$ **38**.

30 mg (2.64 µmol, 1 eq.) *N*-cadaverine-dextran-(N_3)$_{5.4}$ **29** (batch 2) were dissolved in anhydrous DMSO (400 µL). A solution of 10.8 mg (31.4 µmol, 12 eq.) Biotin-NHS **37** in 200 µL dry DMSO were added, followed by 11.5 µL (8.5 mg, 66 µmol, 25 eq.) anhydrous DIPEA. The reaction was shaken over night at room temperature and subsequently precipitated in MeOH. The residue was washed with MeOH and ACN and subsequently dissolved in H_2O. The product was purified using a PD10 desalting column yielding 25 mg (2.15 µmol, 81%) after freeze-drying of the eluate.

^{1}H NMR (300 MHz, D_2O): δ = 5.47 – 4.97 (m, 62H, anomeric **H**), 4.58 – 4.46 (m, 1H, -NH-C$_{\text{bridge}}$**H**-CH$_x$-S- (biotin)), 4.19 – 3.53 (m, (C2-C6)**H** and NH-CO-C**H**$_2$-N$_3$), 3.38 – 3.19 (m, 24H, -NH-C**H**$_2$-(CH$_2$)$_3$-C**H**$_2$-NH-), 2.68 – 2.56 (m, 11H, -C**H**$_2$-CH$_2$-COOH), 2.33 (t, *J* = 7.3 Hz, 2H, -CH$_2$-C**H**$_2$-CO-NH-(biotin)), 1.72 – 1.56 (m, 25H, -NH-CH$_2$-C**H**$_2$-CH$_2$-C**H**$_2$-CH$_2$-NH-), 1.51 – 1.36 (m, 14H, -NH-CH$_2$-CH$_2$-C**H**$_2$-CH$_2$-CH$_2$-NH-).

6.8.3 Synthesis of P14-Pra 39

H-RKKRWFRRRRPKWKK-Pra-*NH₂*

$C_{107}H_{176}N_{42}O_{16}$

M_w = 2306.81 g/mol

The peptide was assembled by manual SPPS in a 0.2 mmol scale on *AmphiSpheres 40 RAM* resin (capacity: 0.34 mmol/g, 588 mg). Fmoc-Pra-OH was loaded onto the resin by single coupling (3 eq.) using HATU (2.95 eq.) and DIPEA (6 eq.). The remaining sequence was assembled by single coupling using 5 eq. amino acid, 4.95 eq HATU and 10 eq. DIPEA. After final Fmoc-deprotection the resin was dried in a desiccator and subsequently cleavage from solid support and simultaneous side chain deprotection was achieved using cleavage cocktail (TFA:TES:anisole:H_2O, 47:1:1:1) for 3 h. The crude peptide was precipitated and washed with cold DEE. Purification of the title compound was accomplished by semi-preparative HPLC yielding 62 mg (27 µmol, 14%) as colorless solid.

RP-HPLC (0 to 40% eluent B, 220 nm): t_R = 14.783 min.

ESI-MS: Calc. for $C_{107}H_{176}N_{42}O_{16}$: m/z: $[M+3H]^{3+}$ = 769.94 (obs. 769.96), $[M+4H]^{4+}$ = 577.70 (obs. 577.76), $[M+5H]^{5+}$ = 462.36 (obs. 462.45).

6.8.4 Synthesis of Biotin-Cadaverine-Dextran-(L17E)$_{5.4}$ 40

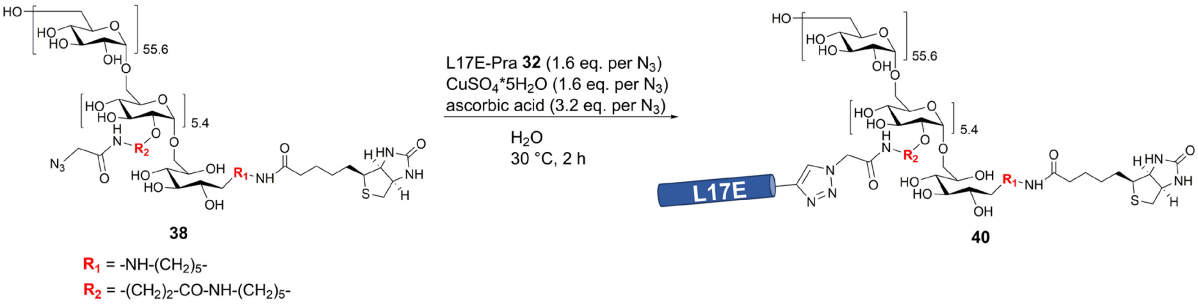

Scheme 49| CuAAC-mediated conjugation of L17E-Pra **32** to biotin-cadaverine-dextran-$(N_3)_{5.4}$ **38**.

6 mg (0.52 µmol ≙ 2.79 µmol N_3-group, 1 eq.) biotin-cadaverine-dextran-$(N_3)_{5.4}$ **38** and 13.2 mg (4.46 µmol, 1.6 eq. per N_3-group) L17E-Pra **32** were dissolved in H_2O. Freshly prepared stocks of $CuSO_4 \cdot 5H_2O$ (1.1 mg, 4.46 µmol, 1.6 eq. per N_3-group) and ascorbic acid (1.6 mg, 8.93 µmol, 3.2 eq. per N_3-group) were mixed and shaken at 30 °C for 5 min, whereafter the Cu(I)-solution was added to the dextran solution (V_{total} = 600 µL). The reaction mixture was shaken for 2 h at 30 °C and the

product was subsequently isolated by consecutive SEC-HPLC runs. Lyophilization of the product fractions yielded 4.2 mg (0.15 µmol, 29%) of the title compound.

SEC-HPLC (30% B isocratic flow, 220 nm): t_R = 9.797 min.

6.8.5 Synthesis of Biotin-Cadaverine-Dextran-(P14)$_{5.4}$ 41

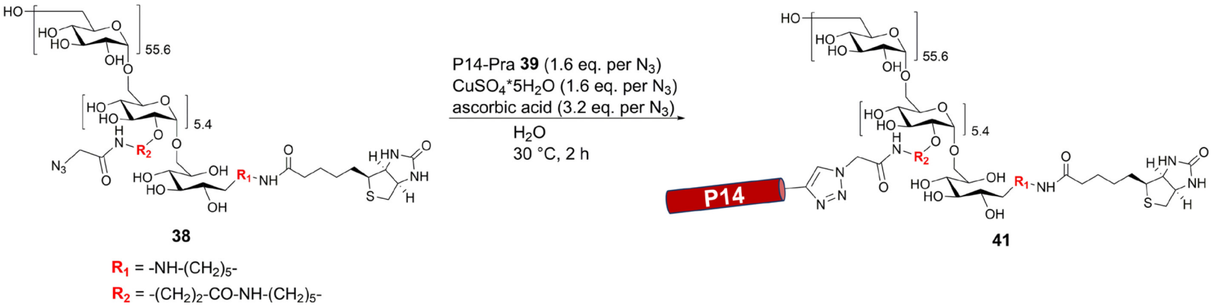

Scheme 50| CuAAC-mediated conjugation of P14-Pra **39** to biotin-cadaverine-dextran-(N$_3$)$_{5.4}$ **38**.

6 mg (0.52 µmol ≙ 2.79 µmol N$_3$-group, 1 eq.) biotin-cadaverine-dextran-(N$_3$)$_{5.4}$ **38** and 10.3 mg (4.46 µmol, 1.6 eq. per N$_3$-group) P14-Pra **39** were dissolved in H_2O. Freshly prepared stocks of $CuSO_4 \cdot 5H_2O$ (1.1 mg, 4.46 µmol, 1.6 eq. per N$_3$-group) and ascorbic acid (1.6 mg, 8.93 µmol, 3.2 eq. per N$_3$-group) were mixed and shaken at 30 °C for 5 min, whereafter the Cu(I)-solution was added to the dextran solution (V_{total} = 600 µL). The reaction mixture was shaken for 2 h at 30 °C and the product was subsequently isolated by consecutive SEC-HPLC runs. Lyophilization of the product fractions yielded 2.9 mg (0.12 µmol, 23%) of the title compound.

SEC-HPLC (30% B isocratic flow, 220 nm): t_R = 9.640 min.

6.8.6 Synthesis of L17E-K(Ahx-Biotin) 42

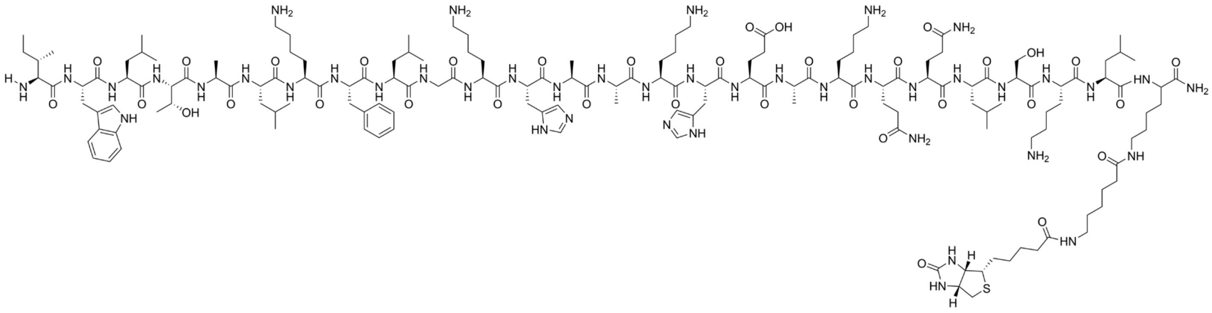

Figure 64| Structure of L17E-K(Ahx-biotin) **42**.

H-IWLTALKFLGKHAAKHEAKQQLSKL-K(Ahx-biotin)-*NH*$_2$
$C_{156}H_{257}N_{43}O_{35}S$
M_w = 3327.10 g/mol

The synthesis was performed on a 0.1 mmol scale on *AmphiSpheres 40 RAM* resin (capacity: 0.34 mmol/g, 294 mg). Fmoc-Lys(Dde)-OH (3 eq.) was loaded onto the resin mediated by HATU/DIPEA (2,95 eq/6 eq.) activation. The remaining sequence was assembled using the *Liberty Blue*^{TM} synthesizer. After completion a Boc protecting group was introduced *N*-terminally using 230 µL (218 mg, 1.00 mmol, 10 eq.) di-*tert*-butyl dicarbonate and 348 µL (258 mg, 2.00 mmol, 20 eq.) DIPEA in DMF for 2 h. The resin was washed and dried in a desiccator over night. The *C*-terminal Dde protecting group was removed following the literature.[244] A solution of 2% (v/v) hydrazine monohydrate in anhydrous DMF was prepared (15 mL). The dried resin was shaken with 5 mL of the hydrazine solution for 3 min (3×). Following that, the resin was dried and the success of the protecting group removal was confirmed by RP-HPLC and ESI-MS. The 6-aminohexanoic acid (Ahx) spacer was introduced as Fmoc-(Ahx)-OH (3.00 eq.) using HATU/DIPEA (2,95 eq/6 eq.). After Fmoc-removal 68 mg (0.20 mmol, 2 eq.) biotin-NHS **37** with 70 µL (52 mg, 0.40 mmol, 4 eq.) DIPEA in DMF were conjugated over night. The crude product was cleaved from solid support following to the general procedure. After precipitation and washing with cold DEE the peptide was purified by semi-preparative HPLC. 12.2 mg (3.7 µmol, 4%) were yielded as colorless solid.

RP-HPLC (0 to 80% eluent B, 220 nm): t_R = 15.860 min.

ESI-MS: Calc. for $C_{107}H_{176}N_{42}O_{16}$: m/z: $[M+3H]^{3+}$ = 1110.03 (obs. 1110.17), $[M+4H]^{4+}$ = 832.78 (obs. 832.86), $[M+5H]^{5+}$ = 666.42 (obs. 666.46), $[M+6H]^{6+}$ = 555.52 (obs. 555.55).

6.8.7 Synthesis of P14-K(Ahx-Biotin) 43

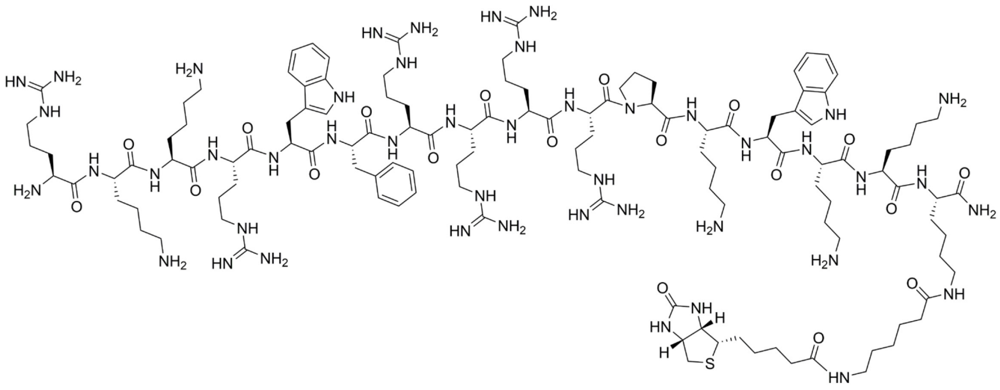

Figure 65| Structure of P14-K(Ahx-biotin) **43**.

H-RKKRWFRRRRPKWKK-K(Ahx-Biotin)-*NH₂*
$C_{124}H_{208}N_{46}O_{19}S$
M_w = 2679.34 g/mol

The synthesis was performed analogous to the synthesis of L17E-K(Ahx-biotin) **42** described in section **6.8.6**. After loading Fmoc-Lys(Dde)-OH onto the resin the remaining sequence was assembled by automated SPPS. Conjugation of Fmoc-Ahx-OH was conducted after Boc protection of the *N*-terminus and subsequent Dde removal. Following this, the *N*-terminus of Ahx was biotinylated and the peptide was cleaved from solid support. Isolation of the peptide yielded 7 mg (2.6 µmol, 3%), which was analyzed by RP-HPLC and HR-ESI-MS.

RP-HPLC (0 to 80% eluent B, 220 nm): t_R = 12.982 min.

HR-ESI-MS: Calc. for $C_{124}H_{208}N_{46}O_{19}S$: m/z: $[M+3H]^{3+}$ = 893.88988 (obs. 893.88880), $[M+4H]^{4+}$ = 670.66923 (obs. 670.66877), $[M+5H]^{5+}$ = 536.73684 (obs. 536.73671).

6.8.8 Synthesis of (1R,8S,9S,Z)-Ethyl Bicyclo[6.1.0]non-4-ene-9-carboxylate 44 and (1R,8S,9R,Z)-Ethyl Bicyclo[6.1.0]non-4-ene-9-carboxylate 45

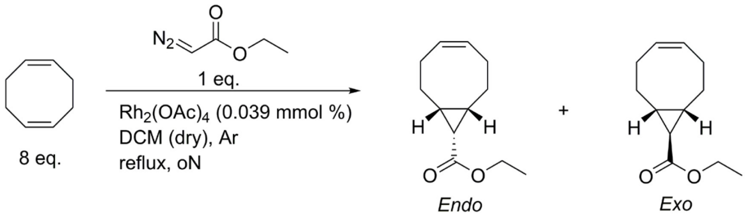

44 45

Scheme 51| Synthesis of *endo* and *exo* ethyl-bicyclo[6.1.0]non-4-ene-9-carboxylate **44** and **45**, respectively.

The synthesis was performed as a modified variant described in literature.[227] In a flame-dried three-necked round bottom flask with reflux condenser and dropping funnel under Ar atmosphere, 84.4 mL (74.4 g, 688 mmol, 8 eq.) 1,5-cyclooctadiene were mixed with 100 mL anhydrous DCM. 15 mg (33.9 µmol, 0.039 mol %) Rh(II)-acetate dimer were added, followed by dropwise addition of ethyl diazoacetate (85% in DCM, 11.6 g, 86 mmol, 1 eq.). The reaction mixture was stirred over night at reflux and subsequently the solvent was removed under reduced pressure. Excessive 1,5-cyclooctadiene was removed under high vacuum and further by a short silica column (cyclohexane (Cy):EA 25:1). 11.7 g of product were yielded as mixture of the isomers. The isomers were separated by silica flash chromatography (Hex:EA 25:1) whereby the *endo* isomer **44** eluted first. 3.89 g (20.0 mmol, 23%) *endo* isomer **44** and 6.37 g (32.8 mmol, 38%) *exo* isomer **45** were yielded as colorless oils.

For the following reactions only *exo* isomer **45** was used.

(1R,8S,9S,Z)-ethyl bicyclo[6.1.0]non-4-ene-9-carboxylate (*Endo*) 44:

^{1}H NMR (500 MHz, $CDCl_3$): δ = 5.68 – 5.53 (m, 2H), 4.10 (q, J = 7.1 Hz, 2H), 2.55 – 2.43 (m, 2H), 2.26 – 2.14 (m, 2H), 2.09 – 1.98 (m, 2H), 1.86 – 1.77 (m, 2H), 1.69 (t, J = 8.8 Hz, 1H), 1.44 – 1.33 (m, 2H), 1.25 (t, J = 7.2, 3H).

^{13}C NMR (126 MHz, $CDCl_3$): δ = 172.37, 129.57, 59.81, 27.21, 24.30, 22.81, 21.38, 14.53.

(1R,8S,9R,Z)-ethyl bicyclo[6.1.0]non-4-ene-9-carboxylate (*Exo*) 45:

^{1}H NMR (500 MHz, $CDCl_3$): δ = 5.69 – 5.57 (m, 2H), 4.09 (q, J = 7.1 Hz, 2H), 2.35 – 2.25 (m, 2H), 2.24 – 2.14 (m, 2H), 2.12 – 2.03 (m, 2H), 1.59 – 1.52 (m, 2H), 1.51 – 1.43 (m, 2H), 1.24 (t, J = 7.1 Hz, 3H), 1.17 (t, J = 4.6 Hz, 1H).

^{13}C NMR (126 MHz, $CDCl_3$): δ = 174.49, 130.04, 60.34, 28.41, 28.02, 27.83, 26.79, 14.42.

6.8.9 Synthesis of (1R,8S,9R,Z)-Bicyclo[6.1.0]non-4-ene-9-ylmethanol 46

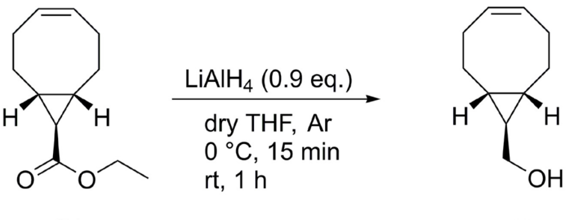

45 **46**

Scheme 52| Synthesis of *exo* ((1R,8S,9R,Z)-bicyclo[6.1.0]non-4-ene-9-yl)methanol **46**.

The reaction was performed as a modified variant described in literature.[227] 3.19 g (16.4 mmol, 1 eq.) (1R,8S,9R,Z)-ethyl bicyclo[6.1.0]non-4-ene-9-carboxylate **45** were dissolved in 25 mL anhydrous THF under Ar atmosphere in a flame-dried two-necked round bottom flask. The solution was cooled to 0 °C and $LiAlH_4$ (1 M in THF, 14.76 mmol, 0.9 eq.) was added dropwise. After stirring the reaction at ambient temperature for 1 h TLC analysis (Cy:EA 2:1, $KMnO_4$ stain) indicated complete turnover of the educt. The reaction was cooled to 0 °C and 5 mL AcOH:MeOH:H_2O (1:3:1, v:v:v) were added slowly whereby a precipitate was formed. The precipitate was dissolved with 3 mL AcOH and 20 mL H_2O was added. The aqueous phase was extracted thrice with DCM and the combined organic phase was washed with brine and dried over Na_2SO_4. Removal of the solvent under reduced pressure yielded the crude product which was further purified by flash chromatography (Cy:EA 3:2). 2.30 g (15.11 mmol, 92%) of the title compound were obtained as colorless oil after evaporation of the solvent.

^{1}H NMR (500 MHz, $CDCl_3$): δ = 5.69 – 5.54 (m, 2H), 3.45 (d, J = 7.0 Hz, 2H), 2.32 – 2.23 (m, 2H), 2.20 – 2.11 (m, 2H), 2.09 – 2.00 (m, 2H), 1.87 (s, 1H), 1.45 – 1.34 (m, 2H), 0.81 – 0.71 (m, 2H), 0.67 – 0.59 (m, 1H).

^{13}C NMR (126 MHz, $CDCl_3$): δ = 130.25, 67.28, 29.13, 28.94, 27.19, 22.23.

6.8.10 Synthesis of (1R,8S,9R)-4,5-Dibromobicyclo[6.1.0]nonan-9-ylmethanol 47

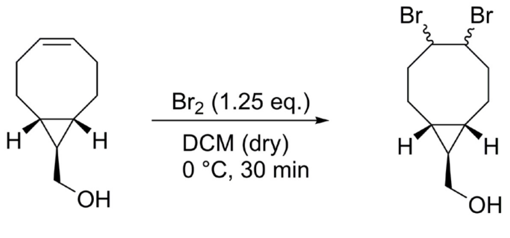

46

47

Scheme 53| Synthesis of ((1R,8S,9R)-4,5-dibromobicyclo[6.1.0]nonan-9-yl)methanol **47**.

The synthesis was as described in literature with some modifications.[227] 2.30 g (15.11 mmol, 1 eq.) ((1R,8S,9R,Z)-bicyclo[6.1.0]non-4-ene-9-yl)methanol **46** were dissolved in 80 mL anhydrous DCM. The reaction was cooled to 0 °C and a solution of bromine (967 µL, 3.02 g, 18.89 mmol, 1.25 eq.) in 15 mL dry DCM was added dropwise until the brown color persisted. The reaction was stirred for further 10 min and 20 mL 0.2% (w/v) aq. $Na_2S_2O_3$ solution was added causing a discoloration of the mixture. The phases were separated and the aqueous phase was extracted thrice with DCM. The combined organic phases were washed with brine and dried over Na_2SO_4. Evaporation of the solvent yielded 4.73 g (15.15 mmol, quantitative) of the title compound as viscous, yellow oil.

^{1}H NMR (500 MHz, $CDCl_3$): δ = 4.87 – 4.75 (m, 2H), 3.51 (d, *J* = 7.1, Hz, 2H), 2.73 – 2.56 (m, 2H), 2.31 – 2.20 (m, 1H), 2.15 – 2.02 (m, 3H), 1.64 – 1.29 (m, 3H), 0.98 – 0.81 (m, 2H), 0.71 – 0.63 (m, 1H).

^{13}C NMR (126 MHz, $CDCl_3$) δ = 66.73, 56.35, 53.40, 35.10, 34.98, 28.34, 24.56, 23.82, 22.66, 19.94.

6.8.11 Synthesis of (1R,8S,9R)-Bicyclo[6.1.0]non-4-yn-9-ylmethanol 48

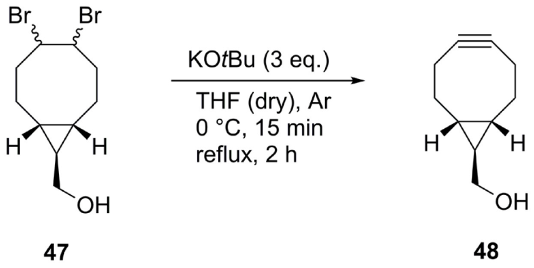

Scheme 54| Synthesis of (1R,8S,9R)-bicyclo[6.1.0]non-4-yn-9-ylmethanol (BCN-OH) **48**.

The synthesis was performed as a modified variant described in literature.[227] 4.73 g (15.15 mmol, 1 eq.) (1R,8S,9R)-4,5-dibromobicyclo[6.1.0]nonan-9-ylmethanol **47** was transferred to a flame-dried three-necked round bottom flask equipped with reflux condenser and dropping funnel under Ar atmosphere. The educt was dissolved in 40 mL anhydrous THF and cooled to 0 °C. KO*t*Bu (1.6 M in THF, 45.45 mmol, 3 eq.) was added dropwise, whereby the solution turned orange and a precipitate was formed. Following that, the reaction mixture was stirred for 2 h at reflux. After cooling to room temperature 10 mL saturated aq. NH_4Cl was added, followed by 30 mL H_2O. The reaction mixture was extracted thrice with DCM and the combined organic layers were washed with brine and dried over $MgSO_4$. Evaporation of the solvent yielded the crude product which was subjected to flash chromatography (Hex:EA 1:1). 1.19 g (7.9 mmol, 52%) of BCN-OH **48** were yielded as yellowish, waxy solid.

^{1}H NMR (300 MHz, $CDCl_3$): δ = 3.56 – 3.48 (m, 2H), 2.45 – 2.34 (m, 2H), 2.34 – 2.19 (m, 2H), 2.17 – 2.07 (m, 2H), 1.65 (s, 1H), 1.47 – 1.28 (m, 2H), 0.75 – 0.57 (m, 3H).

^{13}C NMR (75 MHz, $CDCl_3$): δ = 98.92, 67.17, 33.53, 27.40, 22.69, 21.57.

6.8.12 Synthesis of BCN-*p*NP 50

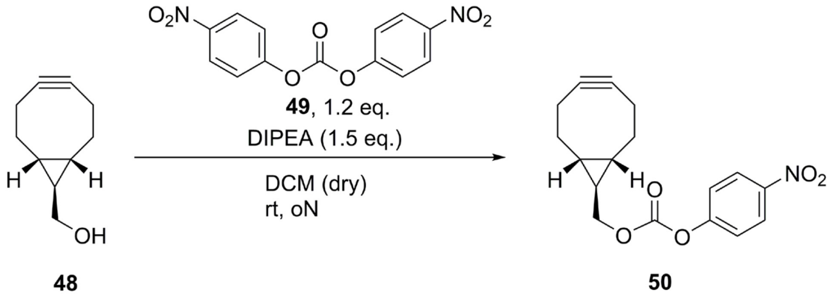

Scheme 55| Synthesis of BCN-*p*NP **50**.

200 mg (1.33 mmol, 1 eq.) BCN-OH **48** and 486 mg (1.6 mmol, 1.2 eq.) carbonate **49** were transferred to a flame-dried Schlenck flask under Ar atmosphere and dissolved in 9 mL anhydrous DCM. 348 µL (258 mg, 2 mmol, 1.5 eq.) dry DIPEA were added through a septum, whereby the solution turned yellow. The reaction was stirred over night at ambient temperature and in the dark. TLC analysis (Cy:EA 2:1) indicated complete consumption of BCN-OH **48** and the product was purified by automated flash chromatography (40 g silica cartridge, 5 to 25% EA in Cy over 25 min). Evaporation of the product fractions yielded 359 mg (1.14 mmol, 86%) of the title compound as opaque oil.

^{1}H NMR (500 MHz, $CDCl_3$): δ = 8.35 – 8.18 (m, 2H), 7.47 – 7.34 (m, 2H), 4.21 (d, J = 6.9 Hz, 2H), 2.48 – 2.41 (m, 2H), 2.36 – 2.25 (m, 2H), 2.22 – 2.14 (m, 2H), 1.47 – 1.35 (m, 2H), 0.92 – 0.78 (m, 3H).

^{13}C NMR (126 MHz, $CDCl_3$): δ = 155.75, 152.72, 145.51, 125.41, 121.89, 98.78, 74.07, 33.27, 23.41, 23.14, 21.41.

6.8.13 Synthesis of BCN-Aminopentanoic Acid 51

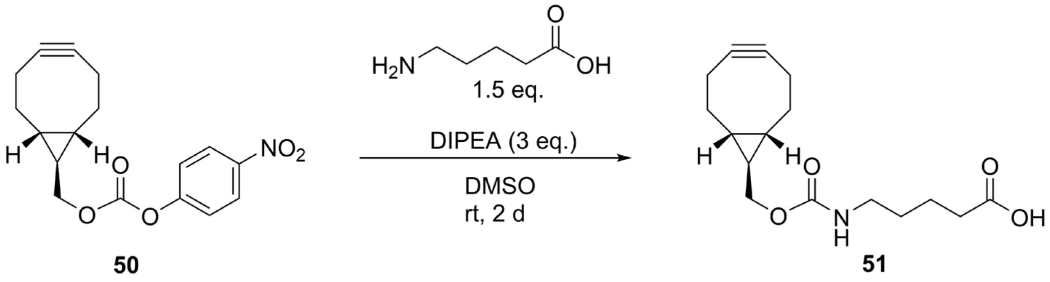

Scheme 56| Synthesis of BCN-aminopentanoic acid **51**.

The synthetic procedure was modified from literature.[226] 50 mg (0.158 mmol, 1 eq.) BCN-*p*NP **50** and 28 mg (0.237 mmol, 1.5 eq.) 5-aminopentanoic acid were transferred to a flame-dried Schlenck flask under Ar atmosphere and dissolved in anhydrous DMSO (2 mL). 83 µL (62 mg, 0.474 mmol, 3 eq.) dry DIPEA was added through a septum whereby the reaction mixture turned yellow. The reaction was stirred for 2 d at ambient temperature in the dark. Subsequently the solvent was removed by freeze-drying and the product was isolated by manual flash chromatography (DCM:EA 9:1 + 0.5% (v/v) AcOH). Evaporation of the product fractions yielded 34 mg (0.116 mmol, 73%) of the title compound.

^{1}H NMR (500 MHz, $CDCl_3$): δ = 4.76 (s, 1H), 4.10 – 3.91 (m, 2H), 3.26 – 3.10 (m, 2H), 2.42 – 2.34 (m, 4H), 2.32 – 2.23 (m, 2H), 2.18 – 2.11 (m, 2H), 1.73 – 1.62 (m, 2H), 1.61 – 1.52 (m, 2H), 1.44 – 1.30 (m, 2H), 0.79 – 0.63 (m, 3H).

^{13}C NMR (126 MHz, $CDCl_3$): δ = 178.69, 157.00, 98.93, 69.23, 40.63, 33.59, 33.44, 29.53, 23.90, 23.03, 21.92, 21.52.

6.8.14 Synthesis of Biotin-Cadaverine 52

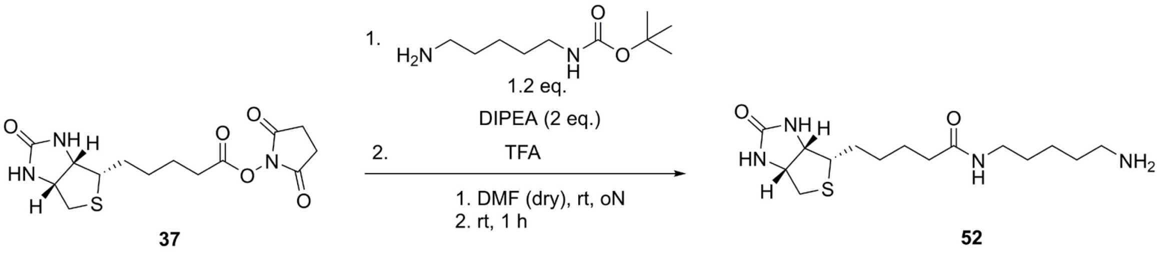

Scheme 57| Synthesis of biotin-cadaverine **52**.

400 mg (1.17 mmol, 1 eq.) biotin-NHS **37** and 293 µL (284 mg, 1.41 mmol, 1.2 eq.) *N*-Boc-cadaverine were dissolved in anhydrous DMF. 408 µL (302 mg, 2.34 mmol, 2 eq.) dry DIPEA were added and the reaction was stirred over night at room temperature. The solvent was evaporated under reduced pressure yielding a colorless oil. TFA was added and the solution was stirred for 1 h followed by removal of the solvent *in vacuo*. The crude product was purified by semi-preparative HPLC, yielding 327 mg (0.99 mmol, 85%) biotin-cadaverine **52** as colorless solid.

^{1}H NMR (300 MHz, DMSO-d_6): δ = 7.93 – 7.58 (m, 4H), 6.41 (s, 1H), 6.36 (s, 1H), 4.36 – 4.26 (m, 1H), 4.19 – 4.07 (m, 1H), 3.15 – 2.94 (m, 3H), 2.89 – 2.67 (m, 3H), 2.62 – 2.53 (m, 1H), 2.05 (t, *J* = 7.3 Hz, 2H), 1.68 – 1.35 (m, 8H), 1.34 – 1.19 (m, 4H).

6.8.15 Synthesis of 2-Azidoacetic Acid-NHS 53

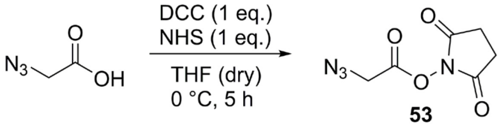

Scheme 58| Synthesis of 2-azidoacetic acid-NHS **53**.

The synthesis was performed according to literature.[245] 190 µL (256 mg, 2.53 mmol, 1 eq.) 2-azidoacetic acid were dissolved in 2 mL anhydrous THF and cooled to 0 °C. 292 mg (2.53 mmol, 1 eq.) NHS were added and the solution was stirred for further 30 min. A solution of 523 mg (2.53 mmol, 1 eq.) *N,N´*-dicyclohexylcarbodiimide (DCC) in 1.5 mL THF was added dropwise whereby a precipitate was formed. After stirring for further 4 h at 0 °C the suspension was filtered and the filtrate was mixed with DEE. The mixture was stored at 4 °C over night in a refrigerator whereby the product precipitated as colorless solid. Filtration and drying in a desiccator yielded 276 mg (1.39 mmol, 55%) of 2-azidoacetic acid-NHS **53**.

^{1}**H NMR** (500 MHz, DMSO-d_6): δ = 4.70 (s, 2H), 2.84 (s, 4H).

6.8.16 Synthesis of Biotin-Cadaverine-Azide 54

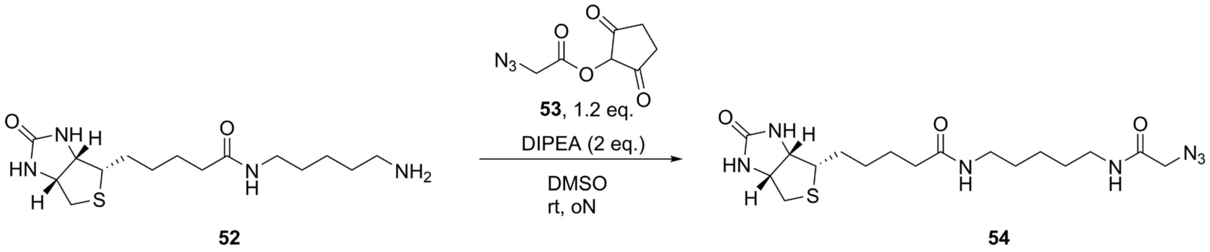

Scheme 59| Synthesis of biotin-cadaverine-azide **54**.

50 mg (0.15 mmol, 1 eq.) biotin-cadaverine **52** were dissolved in 4 mL anhydrous DMSO. 36 mg (0.18 mmol, 1.2 eq.) 2-azidoacetic acid-NHS **53** and 52 µL (39 mg, 0.3 mmol, 2 eq.) dry DIPEA were added and the reaction was stirred at room temperature over night. The solvent was removed by freeze-drying and the residue was dissolved in H_2O:ACN and purified by semi-preparative HPLC. Lyophilization of the product fractions yielded 48 mg (0.12 mmol, 78%) of the title compound.

RP-HPLC (20 to 80% eluent B, 220 nm): t_R = 7.282 min.

ESI-MS: Calc. for $C_{17}H_{29}N_7O_3S$: m/z: $[M+H]^+$ = 412.53 (obs. 412.36).

^{1}**H NMR** (300 MHz, DMSO-d6): δ = 8.05 (t, J = 5.5 Hz, 1H), 7.72 (t, J = 5.6 Hz, 1H), 6.49 – 6.27 (m, 2H), 4.39 – 4.25 (m, 1H), 4.19 – 4.08 (m, 1H), 3.78 (s, 2H), 3.18 – 2.94 (m, 5H), 2.88 – 2.76 (m, 1H), 2.63 – 2.53 (m, 1H), 2.04 (t, J = 7.3 Hz, 2H), 1.69 – 1.15 (m, 12H).

6.8.17 Synthesis of eGFP-BCN 56

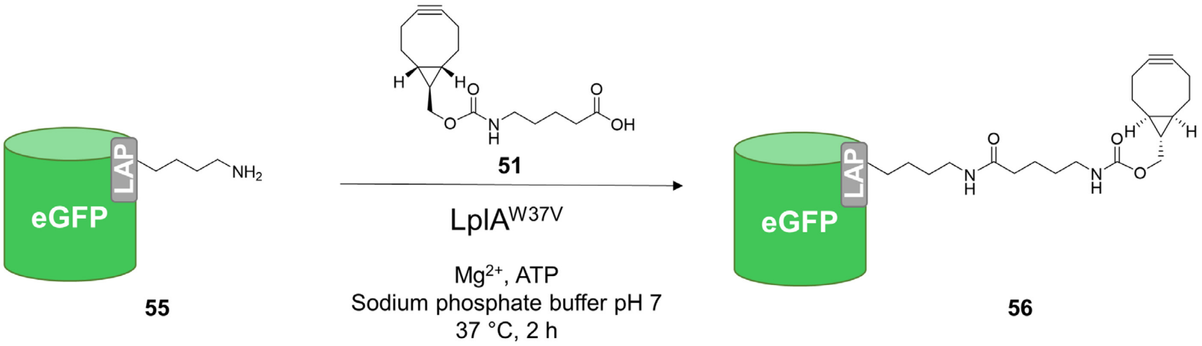

Scheme 60| LplA-mediated BCN-functionalization of eGFP-LAP **55**.

Functionalization of eGFP-LAP was performed using the following reaction mixture:

Table 8| Composition of the reaction mixture for LplA-mediated BCN-functionalization of eGFP-LAP.

Compound	c_{Final}	Eq.
eGFP-LAP **55**	20 µM	1
LplA^{W37V}	0.5 µM	0.025
BCN-aminopentanoic acid **51**	250 µM	12.5
Sodium phosphate pH 7.0	25 mM	-
ATP	5 mM	-
Mg(OAc)$_2$	5 mM	
ddH$_2$O	Filled up to 1.25 mL	

The reactants were incubated for 2 h at 37 °C whereafter HIC-analysis indicated nearly complete conversion of the educt eGFP-LAP **55**. Hence, the reaction mixture was dialyzed against PBS over night and ultimately concentrated using *Amicon Ultra* (*Merck Millipore*, part of *Merck KGaA*) centrifugation filters (3 kDa cutoff). 23.5 nmol (recovery: 94%) eGFP-BCN **56** were obtained.

HIC-HPLC (0 to 100% HIC buffer B, 220 nm) t_R = 21.632 min.

6.8.18 Synthesis of eGFP-Biotin 57

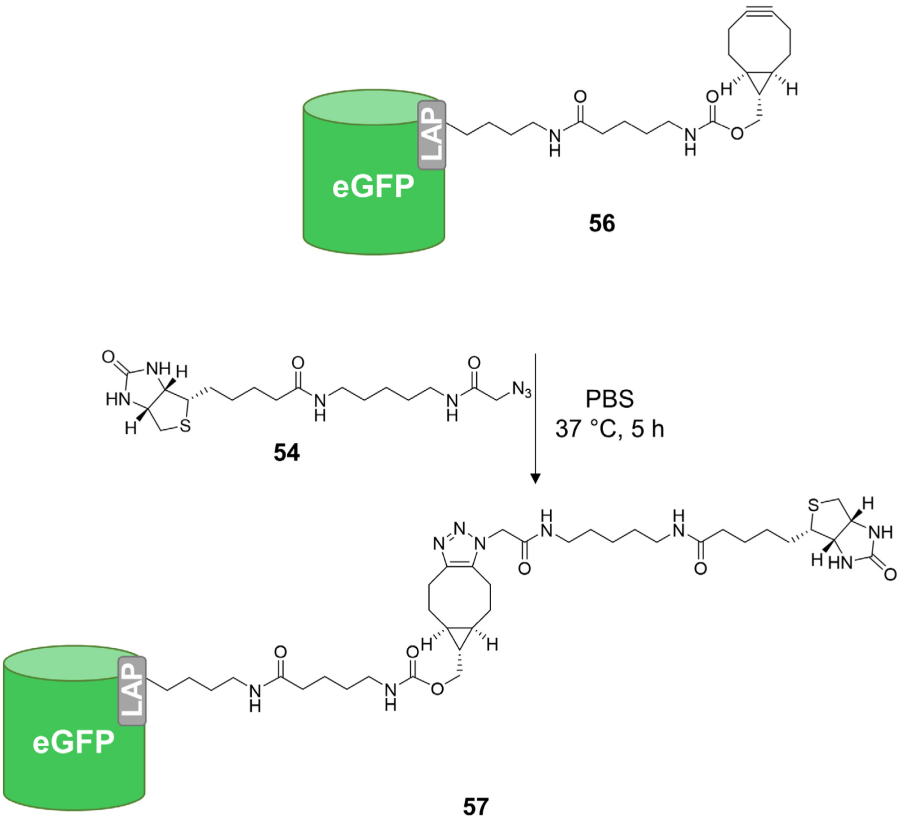

Scheme 61| SPAAC-mediated synthesis of eGFP-Biotin **57**.

eGFP-BCN **56** (16.8 nmol, c_{final} =40 µM, 1 eq.) and biotin-cadaverine-azide **54** (168 nmol, stock: 50 mM in DMSO, c_{final} = 400 µM, 10 eq.) in PBS were incubated for 5 h at 37°C. After HIC analysis indicated the consumption of eGFP-BCN **56** the reaction mixture was dialyzed against PBS over night. The product eGFP-Biotin **57** was concentrated using *Amicon Ultra* centrifugation filters (3 kDa cutoff) yielding 7.5 nmol (recovery: 45%) product.

HIC-HPLC (0 to 100% HIC buffer B, 220 nm) t_R = 19.803 min.

6.8.19 Synthesis of ATTO 647-Sav 58 and AF647-Sav 59

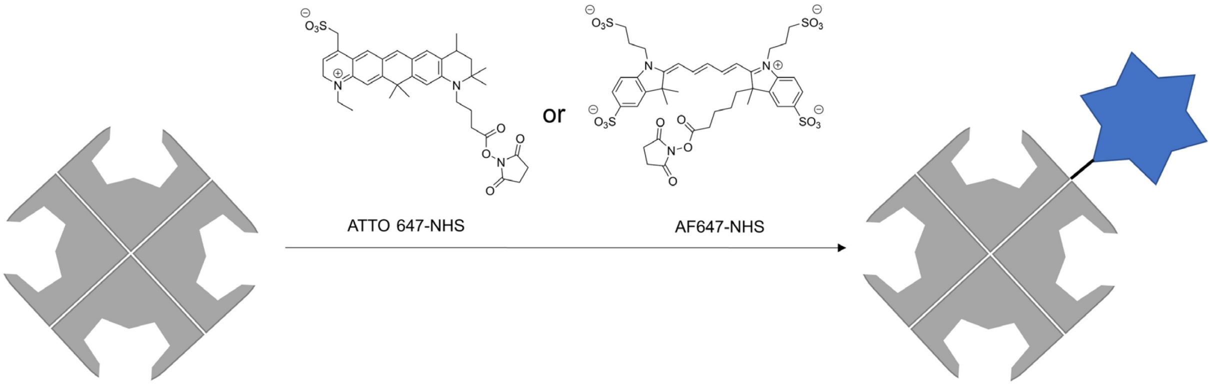

ATTO 647-Sav (**58**)
or
AF647-Sav (**59**)

Scheme 62| Fluorescent labeling of Sav with either ATTO 647 or AF647.

Synthesis of ATTO 647-Sav 58:

Sav was purchased from *IBA-lifesciences GmbH* (Göttingen, Germany) as lyophilized powder and reconstituted according to the supplier´s protocol. The protein (stock in potassium phosphate buffer pH 6.5) was diluted with PBS (c_{final} = 25 µM, 1 eq.) and mixed with ATTO 647-NHS (stock in anhydrous DMSO, c_{final} = 75 µM, 3 eq.), purchased from *ATTO-TEC GmbH* (Siegen, Germany). The resulting blue solution was shaken at 900 rpm for 1 h at room temperature in the dark, followed by purification (3 × PBS) and concentration using *Amicon Ultra* centrifugation filters (10 kDa cutoff). The dye-to-protein ratio of the fluorescently labeled protein **58** was determined as described below.

Synthesis of AF647-Sav 59:

Sav (stock in potassium phosphate buffer pH 6.5) was diluted with PBS (c_{final} = 37 µM, 1 eq.) and mixed with AF647-NHS (stock in anhydrous DMSO, c_{final} = 111 µM, 3 eq.), purchased from *Lumiprobe GmbH* (Hannover, Germany). The resulting blue solution was shaken at 900 rpm for 1 h at 30 °C in the dark, followed by purification (4 × PBS) and concentration using *Amicon Ultra* centrifugation filters (10 kDa cutoff). The dye-to-protein ratio of the fluorescently labeled protein **59** was determined as described below.

Determination of dye-to-protein ratio:

The DPR was determined according to the product information sheet provided by the supplier (*ATTO-TEC*: “Product Information: ATTO NHS-Esters”, revised: March 23, 2021; https://www.atto-tec.com/images/ATTO/Procedures/NHS.pdf); the document also included the photometric properties of ATTO 647 dye. Since no sufficient data regarding the data of AF647 was available, the photometric properties of Alexa Fluor 647® dye were used (Thermo Fisher Scientific: “Alexa Fluor® Succinimidyl Esters (NHS esters)”, revised: October 12, 2012, https://tools.thermofisher.com/content/sfs/manuals/mp10168.pdf). The molecular extinction coefficient of Sav was calculated using the ExPAsy ProtParam online tool. The DPR was calculated using the following formula:

$$DPR = \frac{A_{647} * \varepsilon_{280,Protein}}{\left(A_{280} - (A_{647} * CF_{280})\right) * \varepsilon_{647}} \qquad \textbf{(5)}$$

The photometric data employed and obtained DPR are summarized in the following table:

Table 9 | Photometric data employed for the calculation of the DPR of Sav conjugates **58** and **59**, respectively, with correction factor $CF_{280} = \varepsilon_{280} / \varepsilon_{647}$.

Compound	$\varepsilon_{280,Protein}$ [$L*mol^{-1}*cm^{-1}$]	ε_{647} [$L*mol^{-1}*cm^{-1}$]	CF_{280}	DPR
ATTO 647-Sav **58**	$1.68*10^5$	$1.20*10^5$	0.04	1.71
AF647-Sav **59**	$1.68*10^5$	$2.39*10^5$	0.03	2.61

6.8.20 General Procedure for the Assembly of Sav-Compound Architectures

The Sav-compound architectures were assembled by preincubation of either the pure protein or fluorescently labeled Sav **58** and **59** with the respective amounts of biotinylated species in PBS. To that end, the biotinylated compounds were premixed according to their stoichiometry in PBS, followed by addition of Sav. The resulting mixtures were shaken at 1000 rpm for 2 h at 4 °C and were used afterwards without purification.

6.8.21 Cellular Uptake of Sav-Compound Hybrids

HeLa cells were seeded in 8-well microscopy slides (*µ-Slide 8 Well*) in a density of 1.5×10^4 cells/well and grown to ~ 70% confluency overnight, afterwards the medium was removed and the cells washed twice with PBS. 180 µL serum-free DMEM was added, followed by 20 µL of the Sav-compound hybrids (10 × concentrated in PBS, assembled as described in section **6.8.20**). After incubation for 30 min the supernatant was removed and the cells were washed three times with PBS. Following that, cells were fixated with 250 µL 4% paraformaldehyde (PFA) in PBS for

15 min at rt. After removal of the supernatant, the cells were washed three times with PBS, covered with 300 µL PBS and stored in the refrigerator until analysis by microscopy.

Cellular uptake assays at 4 °C were performed analogously, however, after growing the cells over night to ~ 70% confluency, the slides were stored for 30 min in the refrigerator whereafter the medium was aspirated and the cells were washed twice with ice-cold PBS. 180 µL cold serum-free DMEM was added, followed by 20 µL of the Sav-compound hybrids. After incubation for 30 min at 4 °C, the supernatant was removed and the cells were washed three times with ice-cold PBS, followed by fixation.

6.8.22 Cell Proliferation Assay

HeLa cells were seeded in a 96-well plate in a density of 1.0×10^4 cells/well in a volume of 100 µL DMEM (+ 10% FBS). After incubation for 24 h under standard conditions the medium was aspirated and the cells were washed twice with PBS. 90 µL serum-free DMEM were added and a serial dilution of the Sav-dextran hybrids (assembled as described in section **6.8.20**) in 10 µL PBS were added in triplicates. After incubation for 30 min at 37 °C and 5% CO_2 the supernatant was removed and the cells were washed twice with PBS. 100 µL DMEM (+ 10% FBS) was added and the cells were incubated for further 3 hours. Afterwards, 10 µL *CellTiter96® AQueous One Solution Cell Proliferation Assay* MTS solution was added and after appropriate incubation time under standard conditions absorption at λ = 490 nm was measured using the *Infinite F200 pro* plate reader. The absorption of medium without cells was subtracted as background; absorption of cells treated with medium only was set as reference to 100% proliferation.

6.9 Modular Dextran-Streptavidin Hybrids: Targeting Death Receptor 5

6.9.1 Synthesis of Biotin-Cadaverine-Dextran-(DR5TP)$_{5.4}$ 61

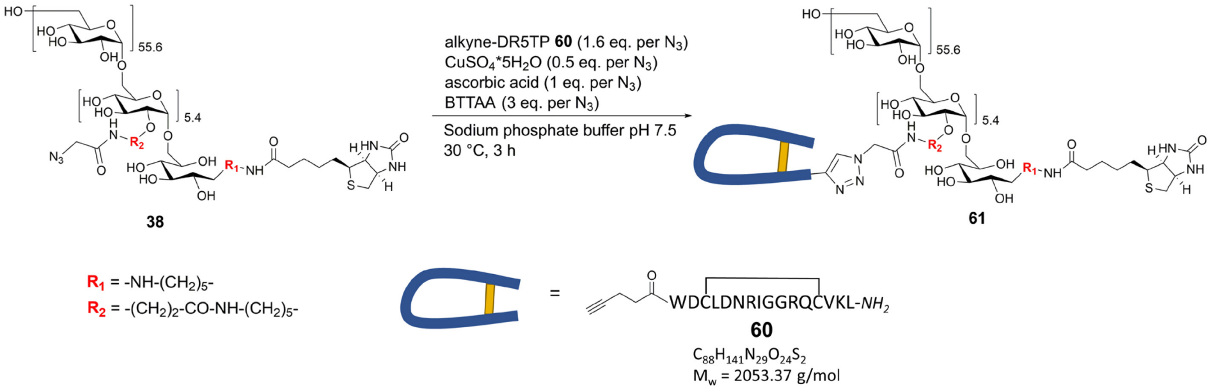

Scheme 63| Synthesis of biotin-cadaverine-dextran-DR5TP$_{5.4}$ **61**.

6 mg (0.52 µmol ≙ 2.79 µmol N_3-group, 1 eq.) biotin-cadaverine-dextran-(N_3)$_{5.4}$ **38** and 9.2 mg alkyne-DR5TP **60** (4.46 µmol, 1.6 eq. per N_3-group, synthesized by Dr. Hendrik Schneider) were dissolved in 400 µL sodium phosphate buffer (100 mM, pH 7.5). 3.6 mg (8.37 µmol, 3 eq. per N_3-group) BTTAA were suspended in H_2O and freshly prepared aq. $CuSO_4 \cdot 5H_2O$ (0.35 mg, 1.40 µmol, 0.5 eq. per N_3-group) was added which resulted in a blue solution. The addition of fresh aq. ascorbic acid (0.49 mg, 2.8 µmol, 1 eq. per N_3-group) discolorized the solution (V_{total} =200 µL) which was shaken for 5 min at 37 °C. Subsequently, the Cu(I)-solution was added to the dextran solution and the reaction mixture was shaken at 37 °C for 3 h. The reaction mixture was dialyzed against PBS over night and concentrated *via Amicon Ultra* centrifugation filters (3 kDa cutoff). The product was purified by consecutive SEC-HPLC runs yielding 5.8 mg (0.26 µmol, 49%) of the title compound.

SEC-HPLC (30% B isocratic flow, 220 nm): t_R = 9.872 min.

6.9.2 Synthesis of Biotin-Ahx-DR5TP 62

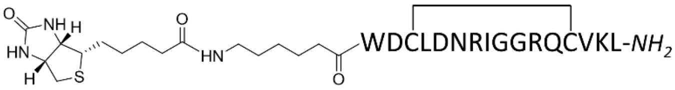

$C_{99}H_{163}N_{33}O_{25}S_3$

M_w = 2311.78 g/mol

The peptide sequence WDCLDNRIGGRQCKKL was assembled in a 0.1 mmol scale on *AmphiSpheres 40 RAM* resin (capacity: 0.34 mmol/g, 294 mg) by automated SPPS. Upon completion, Fmoc-Ahx-OH (3 eq.) was coupled using HATU/DIPEA (2.95 eq./6 eq.) activation. The dried and *N*-terminally deprotected peptidyl resin was subsequently biotinylated by adding a solution of 69 mg (0.20 mmol, 2 eq.) biotin-NHS **37** and 70 µL (52 mg, 0.40 mmol, 4.00 eq.) dry DIPEA in anhydrous DMF. The reaction was shaken over night at ambient temperature and the peptide was subsequently cleaved from solid support following the general procedure. Precipitation of the peptide and subsequent washing with cold DEE afforded 87 mg crude product. The peptide was cyclized following an adapted procedure from literature.[188] 40 mg of the crude product were dissolved (c = 1 mg/mL) in a mixture of 10% (v/v) DMSO in ammonium carbonate buffer (50 mM, pH 8.35). The resulting solution was stirred vigorously over night at ambient temperature and, additionally, pressurized air was bubbled through the solution. The solvent was removed by lyophilization and the product was isolated by semi-preparative HPLC yielding 6 mg (2.6 µmol, 15% based on 40 mg crude product; overall yield: 3%) of the title compound.

RP-HPLC (0 to 80% eluent B, 220 nm): t_R = 13.538 min.

ESI-MS: Calc. for $C_{99}H_{163}N_{33}O_{25}S_3$: m/z: $[M+2H]^{2+}$ = 1156.89 (obs. 1156.87), $[M+3H]^{3+}$ = 771.59 (obs. 771.56), $[M+3H]^{3+}$ = 578.95 (obs. 578.96).

6.9.3 Cell Proliferation Assay

COLO205 cells were seeded in a 96-well plate in a density of 1.0×10^4 cells/well in a volume of 90 µL RPMI medium (+ 10% FBS). After incubation for 24 h under standard conditions a serial dilution of the Sav-compound hybrids (assembled as described in section **6.8.20**) in 10 µL PBS were added in triplicates. The cells were incubated for further 72 h under standard conditions. Afterwards, 10 µL *CellTiter96® AQueous One Solution Cell Proliferation Assay* MTS solution was added and after appropriate incubation time under standard conditions absorption at λ = 490 nm was measured using the *Infinite F200 pro* plate reader. The absorption of medium without cells was subtracted as background; absorption of cells treated with medium only was set as reference to 100% proliferation.

HEK cells were treated analogously (96-well plate, 1.0×10^4 cells/well) in DMEM.

6.9.4 Cell Binding Assay

Trypsinized COLO205 or U87MG cells were washed twice with ice-cold PBS + 0.1% (w/v) bovine serum albumin (BSA) by centrifugation at 500 × g for 5 min at 4 °C and transferred afterwards to U-bottom 96-well plates (2.0×10^5 cells/well). Cells were incubated with a serial dilution of the Sav-compound hybrids (50 µL, assembled as described in section **6.8.20**) in PBS + 0.1% (w/v) BSA for 45 min on ice. Afterwards, the cells were washed twice with ice-cold PBS + 0.1% (w/v) BSA and transferred to FACS tubes, followed by flow cytometric analysis.

6.10 Modular Dextran-Streptavidin Hybrids: Targeting Integrin Receptor αvβ3

6.10.1 Synthesis of *N*-Boc-Cadaverine-Dextran-CE$_{6.3}$ 63

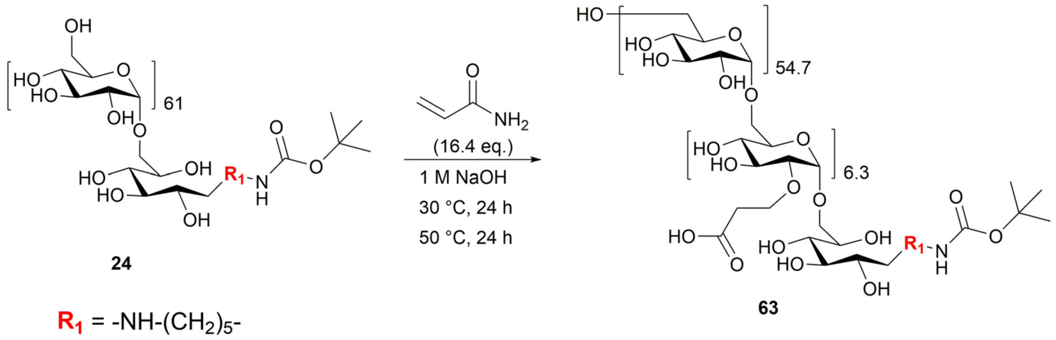

Scheme 64| Synthesis of *N*-Boc-Cadaverine-Dextran-CE$_{6.3}$ **63**.

The synthesis was performed as described in literature.[42] 300 mg (29.5 µmol, 1 eq.) *N*-Boc-cadaverine-dextran **25** (obtained from **Variant B**) were dissolved in 3 mL 1 M NaOH. Acrylamide (34 mg, 485 µmol, 16.4 eq.) was added and the reaction was stirred for 24 h at 30 °C, whereafter the reaction was increased to 50 °C and the reaction was stirred for further 24 h. The crude product was precipitated and washed with cold MeOH and subsequently dried in airstream. It was dissolved in H_2O and neutralized with 0.1 M HCl followed by freeze-drying. The residue was dissolved in H_2O and purified using PD10 desalting columns. 200 mg (18.8 µmmol, 64%) were yielded as colorless solid.

^{1}H NMR (300 MHz, D_2O): δ = 5.37 – 4.90 (m, 62H, anomeric **H**), 4.12 – 3.37 (m, (C2-C6)**H**), 3.13 – 3.04 (m, 2H, -NH-C**H**$_2$-$(CH_2)_3$-C**H**$_2$-NHBoc), 2.58 – 2.43 (m, 14H, -C**H**$_2$-CH_2-COOH), 1.84 – 1.30 (m, 13H, -NH-CH_2-(C**H**$_2$)$_3$-CH_2-NH-CO-O-C(C**H**$_3$)$_3$).

6.10.2 Synthesis of *N*-Boc-Cadaverine-Dextran-$(N_3)_{6.3}$ 64

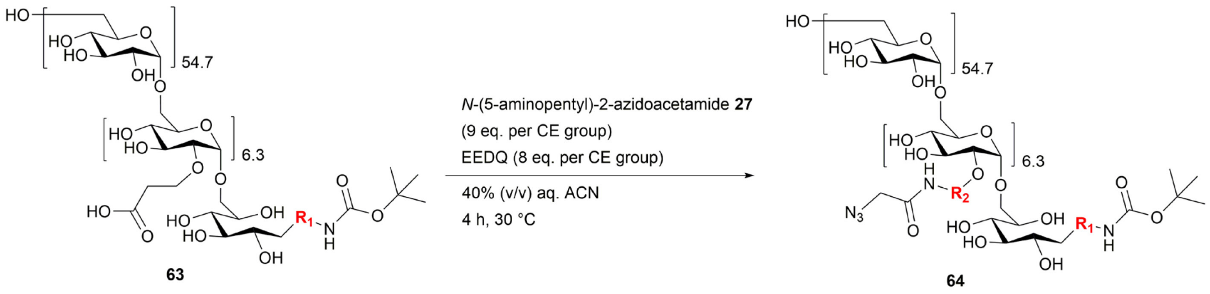

R1 = -NH-$(CH_2)_5$-
R2 = -$(CH_2)_2$-CO-NH-$(CH_2)_5$-

Scheme 65 | Synthesis of *N*-Boc-cadaverine-dextran-$(N_3)_{6.3}$ **64**.

The synthesis was performed as described in literature.[29] 200 mg (18.8 µmol≙ 0.132 mmol N_3-group, 1 eq) *N*-Boc-cadaverine-dextran-$CE_{6.3}$ **63** were dissolved in 3 mL H_2O and heated to 30 °C. 262 mg (1.06 mmol, 8 eq. per CE group) EEDQ in 2 mL ACN was added and the reaction was stirred for 1 h. 220 mg (1.19 mmol, 9 eq. per CE group) linker **27** in 1 mL 40% (v/v) ACN was added to the reaction which was stirred for further 3 h at 30 °C. Following this, the product was precipitated and washed with cold MeOH. After the residue was dry it was dissolved in H_2O and purified using PD10 desalting columns. Lyophilization of the eluate yielded 185 mg (15.8 µmol, 84%) product as colorless solid.

^{1}H NMR (300 MHz, D_2O): δ = 5.39 – 4.93 (m, 62H, anomeric **H**), 4.09 – 3.42 (m, (C2-C6)**H** and NH-CO-C**H**$_2$-N_3), 3.33 – 3.20 (m, 30H, -NH-C**H**$_2$-$(CH_2)_3$-C**H**$_2$-NH-), 2.68 – 2.50 (m, 12H, -C**H**$_2$-CH_2-COOH), 1.66 – 1.51 (m, 32H, -NH-CH_2-C**H**$_2$-CH_2-C**H**$_2$-CH_2-NH-), 1.39 (s, 9H, CO-O-C(C**H**$_3$)$_3$), 1.45 – 1.31 (m, 18H, -NH-CH_2-CH_2-C**H**$_2$-CH_2-CH_2-NH-).

6.10.3 Synthesis of *N*-Cadaverine-Dextran-(N_3)$_{6.3}$ 65

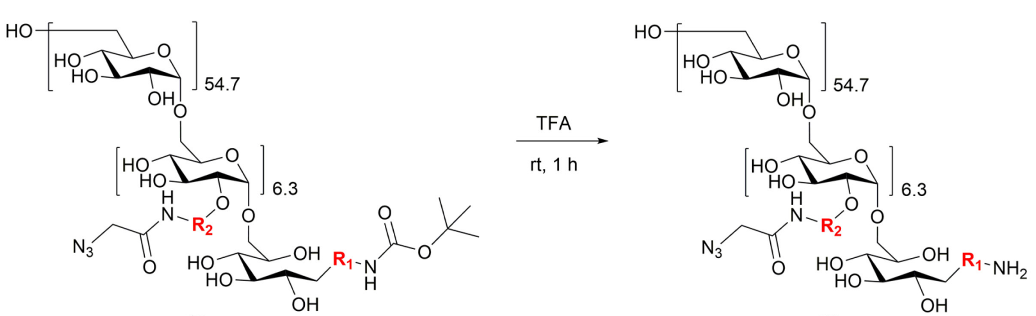

64 **65**

R_1 = -NH-(CH_2)$_5$-

R_2 = -(CH_2)$_2$-CO-NH-(CH_2)$_5$-

Scheme 66| Synthesis of cadaverine-dextran-(N_3)$_{6.3}$ **65**.

The synthesis was performed as described in literature.[29] 185 mg (15.8 µmol) *N*-Boc-cadaverine-dextran-(N_3)$_{6.3}$ **64** were suspended in 5 mL TFA. The reaction was stirred for 1 h at ambient temperature whereby the solid dissolved completely. The solvent was removed under reduced pressure and the residue was dissolved in H_2O. Freeze-drying of the solution yielded 185 mg (15.8 µmol, quantitative) of the title compound as colorless solid.

^{1}H NMR (300 MHz, D_2O): δ = 5.39 – 4.94 (m, 62H, anomeric **H**), 4.17 – 3.42 (m, (C2-C6)**H** and NH-CO-C**H**$_2$-N_3), 3.32 – 3.16 (m, 29H, -NH-C**H**$_2$-(CH_2)$_3$-C**H**$_2$-NH-), 2.65 – 2.48 (m, 12H, -C**H**$_2$-CH_2-COOH), 1.63 – 1.47 (m, 29H, -NH-CH_2-C**H**$_2$-CH_2-C**H**$_2$-CH_2-NH-), 1.42 – 1.29 (m, 16H, -NH-CH_2-CH_2-C**H**$_2$-CH_2-CH_2-NH-).

6.10.4 Synthesis of Biotin-Cadaverine-Dextran-$(N_3)_{6.3}$ 66

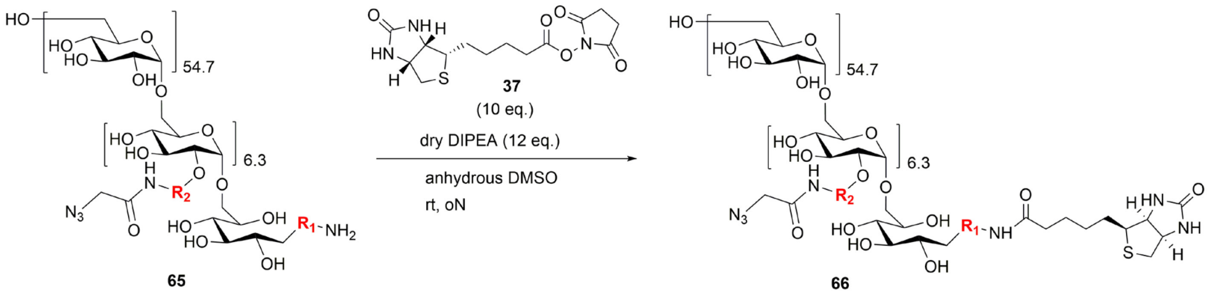

R$_1$ = -NH-$(CH_2)_5$-
R$_2$ = -$(CH_2)_2$-CO-NH-$(CH_2)_5$-

Scheme 67| Synthesis of biotin-cadaverine-dextran-$(N_3)_{6.3}$ **66**.

40 mg (3.74 µmol, 1 eq.) *N*-cadaverine-dextran-$(N_3)_{6.3}$ **65** were dissolved in 400 µL anhydrous DMSO. A solution of 13 mg (37.4 µmol, 10 eq.) Biotin-NHS **37** in 200 µL dry DMSO was added, followed by 7.8 µL (5.8 mg, 44.9 µmol, 12 eq.) anhydrous DIPEA. The reaction was shaken over night at room temperature and subsequently precipitated in MeOH. The residue was washed with MeOH and ACN and subsequently dissolved in H_2O. The product was purified using a PD10 desalting column yielding 40 mg (3,66 µmol, 98%) after freeze-drying of the eluate.

^{1}H NMR (300 MHz, D_2O): δ = 5.43 – 4.95 (m, 62H, anomeric **H**), 4.51 – 4.43 (m, 1H, -NH-C$_{\mathrm{bridge}}$**H**-CH$_x$-S- (biotin)), 4.18 – 3.51 (m, (C2-C6)**H** and NH-CO-C**H**$_2$-N$_3$), 3.34 – 3.18 (m, 26H, -NH-C**H**$_2$-(CH$_2$)$_3$-C**H**$_2$-NH-), 2.68 – 2.52 (m, 13H, -C**H**$_2$-CH$_2$-COOH), 2.30 (t, *J* = 7.3 Hz, 2H, -CH$_2$-C**H**$_2$-CO-NH-(biotin)), 1.67 – 1.49 (m, 27H, -NH-CH$_2$-C**H**$_2$-CH$_2$-C**H**$_2$-CH$_2$-NH-), 1.46 – 1.31 (m, 16H, -NH-CH$_2$-CH$_2$-C**H**$_2$-CH$_2$-CH$_2$-NH-).

6.10.5 Synthesis of *H*-D(OtBu)-f-K(Boc)-R(Pbf)-G-*OH* 67 and *H*-D(OtBu)-f-K(Boc)-R(Pbf)-A-*OH* 68

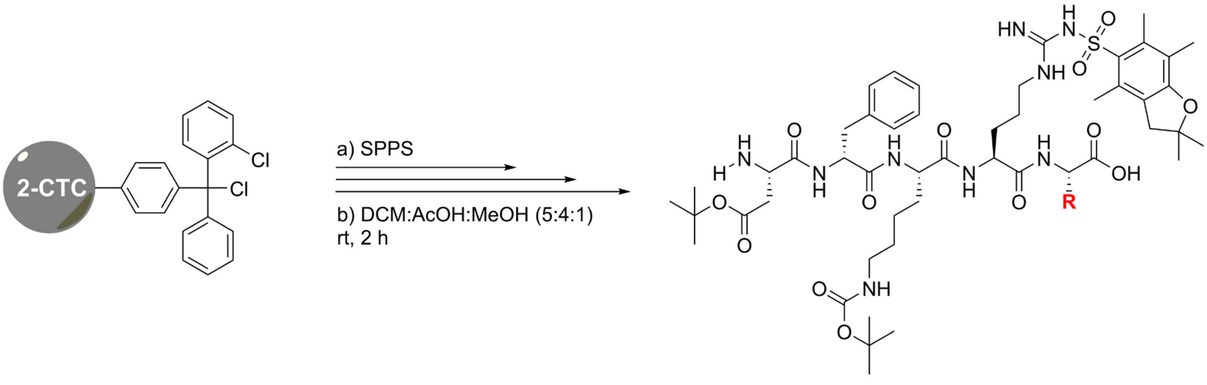

67: R = H
68: R = CH_3

Scheme 68| SPPS of side-chain protected peptides **67** and **68**, respectively.

The synthesis was performed adapting a procedure from literature.[233] 2-CTC resin (capacity: 1.59 mmol/g, scale: 0.75 mmol, 472 mg) was swollen in anhydrous DCM and subsequently, Fmoc-Gly-OH (for peptide **67**) or Fmoc-Ala-OH (for peptide **68**) were loaded onto the resin using a solution of 2 eq. Fmoc-amino acid and 4 eq DIPEA in anhydrous DCM. Following that, the remaining building blocks were coupled using 3 eq. Fmoc protected amino acid and HATU/DIPEA (2.95 eq./6 eq.) activation. The peptides were cleaved from solid support under mild conditions treating the dried resins with 10 mL DCM:AcOH:MeOH 5:4:1 for 2 h. This procedure was repeated for 1 h and subsequently, the pooled cleavage cocktails were evaporated under reduced pressure. The oily residues were dissolved in ACN and precipitated by addition of H_2O. The suspensions were freeze-dried yielding 726 mg (0.70 mmol, 94%) *H*-D(OtBu)-f-K(Boc)-R(Pbf)-G-*OH* **67** and 733 mg (0.70 mmol, 94%) *H*-D(OtBu)-f-K(Boc)-R(Pbf)-A-*OH* **68** which were used without further purification.

***H*-D(OtBu)-f-K(Boc)-R(Pbf)-G-*OH* 67:**

RP-HPLC (30 to 100% eluent B, 220 nm): t_R = 15.098 min.

ESI-MS: Calc. for $C_{49}H_{75}N_9O_{13}S$: m/z: $[M+H]^+$ = 1030.53 (obs. 1030.67), $[M+2H]^{2+}$ = 516.27 (obs. 516.15).

***H*-D(OtBu)-f-K(Boc)-R(Pbf)-A-*OH* 68:**

RP-HPLC (30 to 100% eluent B, 220 nm): t_R = 15.082 min.

ESI-MS: Calc. for $C_{50}H_{77}N_9O_{13}S$: m/z: $[M+H]^+$ = 1044.54 (obs. 1044.77), $[M+2H]^{2+}$ = 522.77 (obs. 523.15).

6.10.6 Synthesis of *Cyclo*[D(OtBu)-f-K(Boc)-R(Pbf)-G] 69 and *Cyclo*[D(OtBu)-f-K(Boc)-R(Pbf)-A] 70

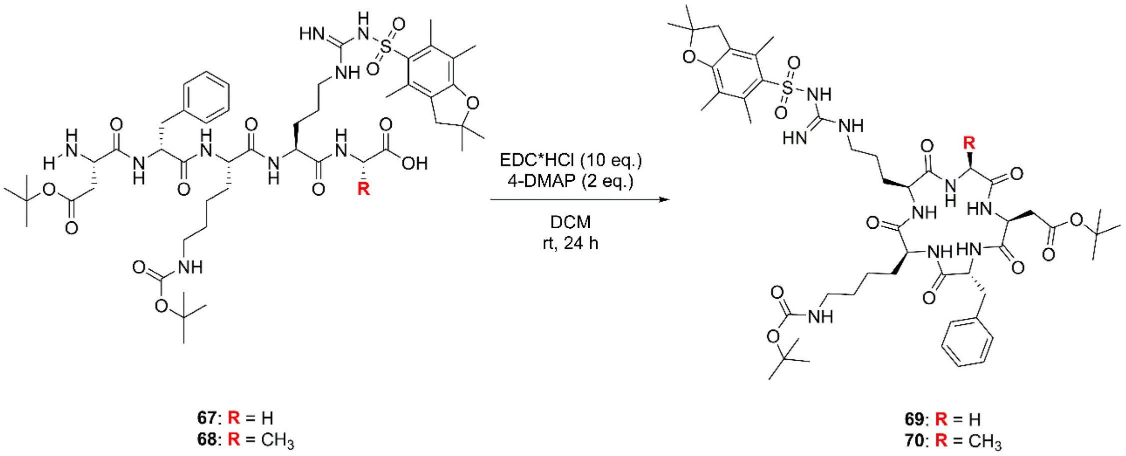

Scheme 69| Head-to-tail cyclization leading to *cyclo*[D(OtBu)-f-K(Boc)-R(Pbf)-G] **69** and *cyclo*[D(OtBu)-f-K(Boc)-R(Pbf)-A] **70**.

The synthesis was performed following a procedure adapted from literature:[234]

Synthesis of *Cyclo*[D(OtBu)-f-K(Boc)-R(Pbf)-G] 69:

361 mg (0.35 mmol, 1 eq.) *H*-D(OtBu)-f-K(Boc)-R(Pbf)-G-*OH* **67** were dissolved in DCM (1mM) followed by the addition of 86 mg (0.70 mmol, 2 eq.) 4-dimethylaminopyridine (4-DMAP) and 671 mg (3.5 mmol, 10 eq.) EDC·HCl. The resulting solution was stirred over night at ambient temperature whereafter HPLC analysis displayed complete turnover of the educt and, hence, the reaction mixture was concentrated *in vacuo*. The organic phase was extracted thrice with 2% (v/v) formic acid, twice with saturated aq. $NaHCO_3$, three times with brine and evaporated under reduced pressure. The residue was dissolved in ACN, precipitated with H_2O and freeze-dried. 137 mg (0.135 mmol, 39%) of the title compound were obtained and used without further purification.

***Cyclo*[D(OtBu)-f-K(Boc)-R(Pbf)-G] 69:**

RP-HPLC (30 to 100% eluent B, 220 nm): t_R = 17.099 min.

Synthesis of *Cyclo*[D(OtBu)-f-K(Boc)-R(Pbf)-A] 70:

The synthesis was performed analogously to the previous reaction. 365 mg (0.35 mmol, 1 eq.) *H*-D(OtBu)-f-K(Boc)-R(Pbf)-A-*OH* **68** were cyclized with 86 mg (0.70 mmol, 2 eq.)

4-dimethylaminopyridine (4-DMAP) and 671 mg (3.5 mmol, 10 eq.) EDC·HCl. After workup 245 mg (0.239 mmol, 68%) of the title compound were received and used without further purification.

Cyclo[D(OtBu)-f-K(Boc)-R(Pbf)-A] 68:

RP-HPLC (30 to 100% eluent B, 220 nm): t_R = 17.262 min.

6.10.7 Synthesis of *Cyclo*[RGDfK] 71 and *Cyclo*[RADfK] 72

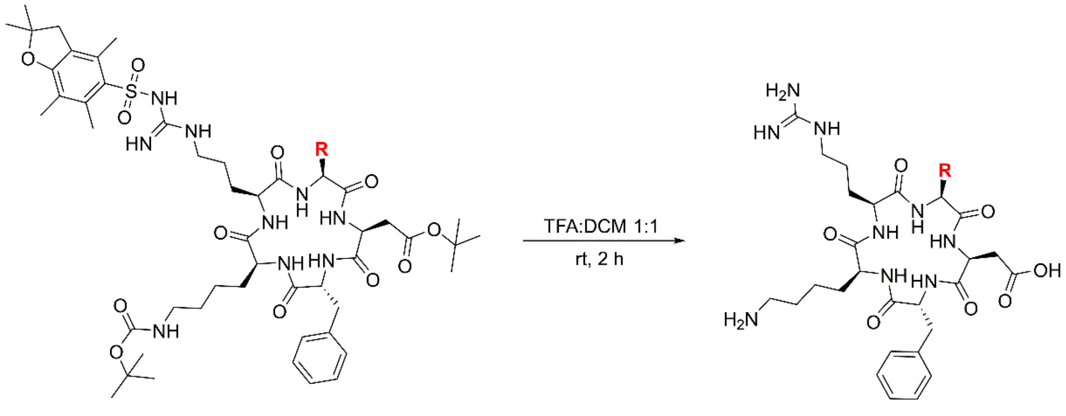

69: R = H
70: R = CH_3

71: R = H
72: R = CH_3

Scheme 70| Synthesis of *cyclo*[RGDfK] **71** and *cyclo*[RADfK] **72**.

Synthesis of _Cyclo_[RGDfK] 71:

137 mg (0.135 mmol) *cyclo*[D(OtBu)-f-K(Boc)-R(Pbf)-G] **69** were dissolved in a mixture of TFA:DCM 1:1 and stirred for 2 h at room temperature. The crude product was precipitated and washed with cold DEE. Purification of the product was performed by semi-preparative HPLC yielding 37 mg (0.061 mmol, 45%) of *cyclo*[RGDfK] **71**.

RP-HPLC (0 to 40% eluent B, 220 nm): t_R = 13.744 min.

ESI-MS: Calc. for $C_{27}H_{41}N_9O_7$: m/z: $[M+H]^+$ = 604.32 (obs. 604.37), $[M+2H]^{2+}$ = 302.66 (obs. 302.96), $[M-H]^-$ = 602.31 (obs. 602.37).

Synthesis of _Cyclo_[RADfK] 72:

245 mg (0.239 mmol) *cyclo*[D(OtBu)-f-K(Boc)-R(Pbf)-A] **70** were dissolved in a mixture of TFA:DCM 1:1 and stirred for 2 h at room temperature. The crude product was precipitated and washed with cold DEE. Purification of the product was performed by semi-preparative HPLC. Two product fractions with 22 mg (0.036 mmol, 15%, lower retention time: #1) and 35 mg

(0.057 mmol, 24%, higher retention time: #2) were obtained. MS analysis displayed identical m/z patterns for both fractions indicating presence of isomers.

#1:

RP-HPLC (0 to 40% eluent B, 220 nm): t_R = 13.637 min.

ESI-MS: Calc. for $C_{28}H_{43}N_9O_7$: m/z: $[M+H]^+$ = 618.34 (obs. 618.48), $[M+2H]^{2+}$ = 309.67 (obs. 309.96), $[M-H]^-$ = 616.32 (obs. 616.38).

#2:

RP-HPLC (0 to 40% eluent B, 220 nm): t_R = 14.363 min.

ESI-MS: Calc. for $C_{28}H_{43}N_9O_7$: m/z: $[M+H]^+$ = 618.34 (obs. 618.48), $[M+2H]^{2+}$ = 309.67 (obs. 310.06), $[M-H]^-$ = 616.32 (obs. 616.38).

6.10.8 Synthesis of *Cyclo*[RGDfK(4-Pentynoic Acid)] 74 and *Cyclo*[RADfK(4-Pentynoic Acid)] 75

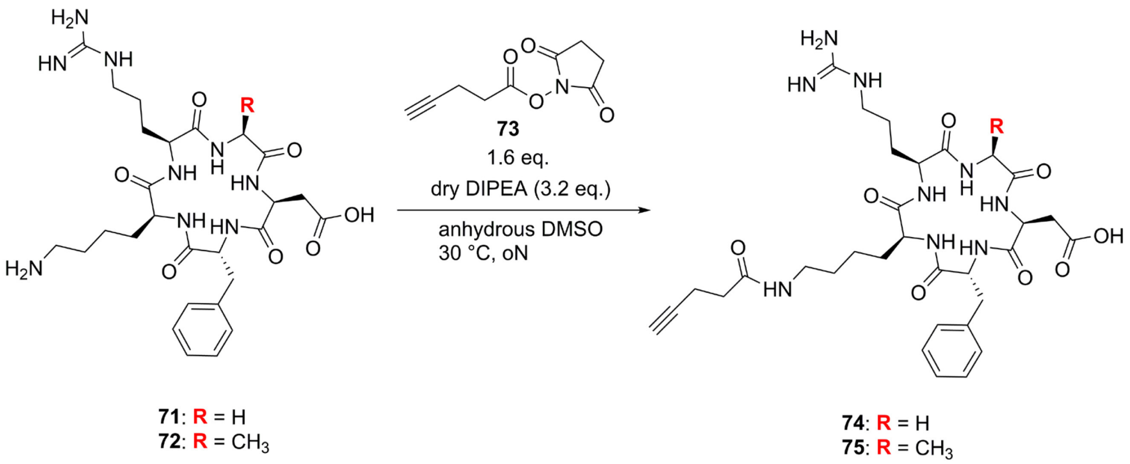

Scheme 71 | Synthesis of *cyclo*[RGDfK(4-pentynoic acid)] **74** and *cyclo*[RADfK(4-pentynoic acid)] **75**.

Synthesis of *Cyclo*[RGDfK(4-Pentynoic acid)] 74:

37 mg (0.061 mmol, 1 eq.) *cyclo*[RGDfK] **71** and 19 mg (0.098 mmol, 1.6 eq.) 4-pentynoic acid-NHS **73** (synthesized by Dr. Hendrik Schneider) were dissolved in 2 mL anhydrous DMSO. 34 µL (25 mg, 0.196 mmol, 3.2 eq.) dry DIPEA were added and the reaction was shaken over night at 30 °C. The solvent was removed by freeze-drying and the residue was subjected to semi-preparative HPLC. 20 mg (0.029 mmol, 48%) of the title compound were obtained.

RP-HPLC (0 to 40% eluent B, 220 nm): t_R = 19.008 min.

ESI-MS: Calc. for $C_{32}H_{45}N_9O_8$: m/z: $[M+H]^+$ = 684.38 (obs. 684.48), $[M-H]^-$ = 682.38 (obs. 682.38).

Synthesis of *Cyclo*[RADfK(4-Pentynoic acid)] 75:

The synthesis was conducted analogously to the previous reaction. 35 mg (0.057 mmol, 1 eq., #2) *cyclo*[RADfK] **72** and 18 mg (0.91 mmol, 1.6 eq.) 4-pentynoic acid-NHS **73** were dissolved in 2 mL anhydrous DMSO. 32 µL (23 mg, 0.181 mmol, 3.2 eq.) dry DIPEA were added and the reaction was stirred at 30 °C over night. After workup and purification 16 mg (0.023 mmol, 40%) of the title compound were obtained.

RP-HPLC (0 to 40% eluent B, 220 nm): t_R = 19.163 min.

ESI-MS: Calc. for $C_{33}H_{47}N_9O_8$: m/z: $[M+H]^+$ = 698.36 (obs. 698.38), $[M-H]^-$ = 696.28 (obs. 682.35).

6.10.9 Synthesis of Biotin-Cadaverine-Dextran-(RGD)$_{6.3}$ 76

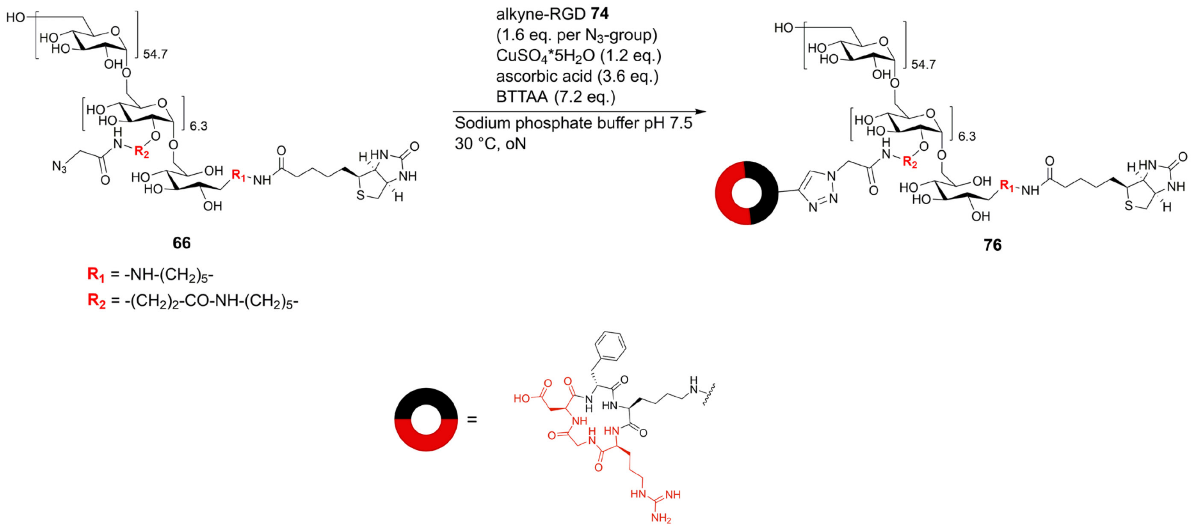

Scheme 72| Synthesis of biotin-cadaverine-dextran-(RGD)$_{6.3}$ **76**.

6 mg (0.51 µmol ≙ 3.21 µmol N_3-group, 1 eq.) biotin-cadaverine-dextran-$(N_3)_{6.3}$ **66** and 3.5 mg alkyne-RGD **74** (5.14 µmol, 1.6 eq. per N_3-group) were dissolved in 400 µL sodium phosphate buffer (100 mM, pH 7.5). 1.6 mg (3.67 µmol, 7.2 eq) BTTAA were suspended in H_2O and freshly prepared aq. $CuSO_4 \cdot 5H_2O$ (0.15 mg, 0.61 µmol, 1.2 eq.) was added which resulted in a blue solution. The addition of fresh aq. ascorbic acid (0.32 mg, 1.84 µmol, 3.6 eq.) discolorized the solution (V_{total} = 200 µL) which was shaken for 5 min at 30 °C. Subsequently, the Cu(I)-solution was added to the dextran solution and the reaction mixture was shaken over night at 30 °C. The

product was isolated by consecutive SEC-HPLC runs yielding 3.3 mg (0.21 µmol, 40%) of the title compound.

SEC-HPLC (30% B isocratic flow, 220 nm): t_R = 11.623 min.

6.10.10 Synthesis of Biotin-Cadaverine-Dextran-(RAD)$_{6.3}$ 77

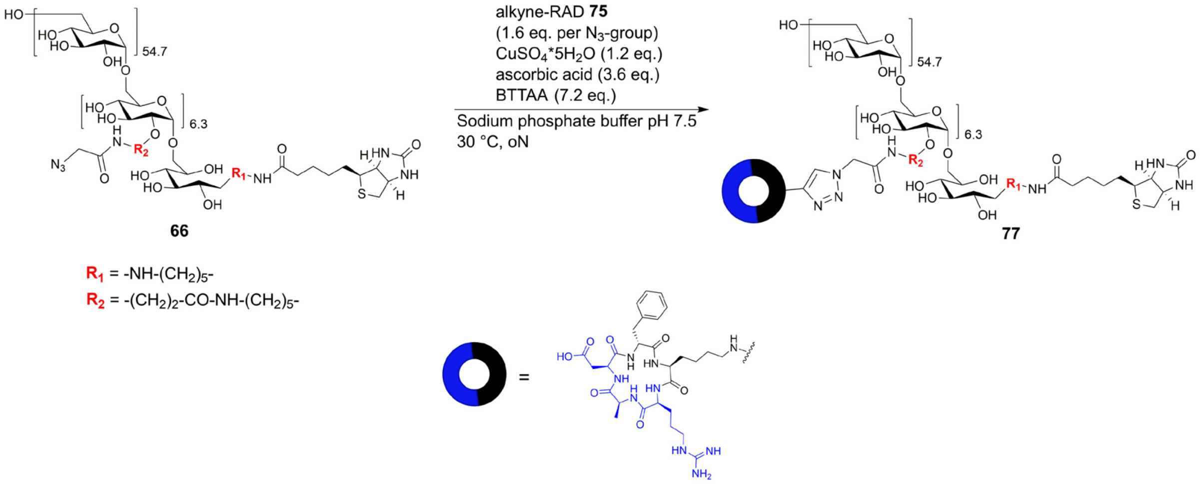

Scheme 73| Synthesis of biotin-cadaverine-dextran-(RAD)$_{6.3}$ **77**.

6 mg (0.51 µmol ≙ 3.21 µmol N_3-group, 1 eq.) biotin-cadaverine-dextran-(N_3)$_{6.3}$ **66** and 3.6 mg alkyne-RAD **75** (5.14 µmol, 1.6 eq. per N_3-group) were dissolved in 400 µL sodium phosphate buffer (100 mM, pH 7.5). 1.6 mg (3.67 µmol, 7.2 eq) BTTAA were suspended in H_2O and freshly prepared aq. $CuSO_4 \cdot 5H_2O$ (0.15 mg, 0.61 µmol, 1.2 eq.) was added which resulted in a blue solution. The addition of fresh aq. ascorbic acid (0.32 mg, 1.84 µmol, 3.6 eq.) discolorized the solution (V_{total} 200 µL) which was shaken for 5 min at 30 °C. Subsequently, the Cu(I)-solution was added to the dextran solution and the reaction mixture was shaken over night at 30 °C. The product was isolated by consecutive SEC-HPLC runs yielding 1.1 mg (0.07 µmol, 13%) of the title compound.

SEC-HPLC (30% B isocratic flow, 220 nm): t_R = 11.615 min.

6.10.11 Synthesis of Biotin-Ahx 78

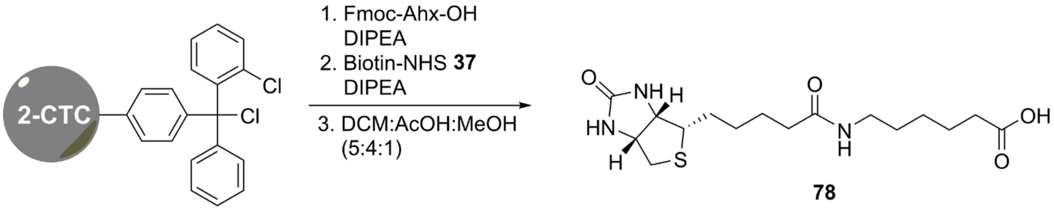

Figure 66| Solid phase synthesis of biotin-Ahx **78**.

2-CTC resin (capacity: 1.59 mmol/g, scale: 0.7 mmol, 440 mg) was swollen in anhydrous DCM. Fmoc-Ahx-OH (1.7 eq.) and dry DIPEA (3.4 eq.) were dissolved in dry DCM and added to the resin. After shaking for 2 h the Fmoc protecting group was removed and the resin was dried over night in a desiccator. Biotin-NHS **37** (2.2 eq.) and dry DIPEA (4.4 eq.) were dissolved in dry DMF and added to the resin, which was shaken over night. The product was cleaved from solid support using DCM:AcOH:MeOH (5:4:1) for 2 h. The cleavage cocktail was evaporated under reduced pressure and the residue was dissolved in H_2O:ACN. Freeze-drying yielded 170 mg (0.48 mmol, 69%) product which was used without further purification.

^{1}H NMR (500 MHz, DMSO-d_6): δ = 11.94 (s, 1H), 7.71 (t, J = 5.7 Hz, 1H), 6.48 – 6.31 (m, 2H), 4.33 – 4.28 (m, 1H), 4.15 – 4.10 (m, 1H), 3.13 – 3.06 (m, 1H), 3.04 – 2.98 (m, 2H), 2.86 – 2.78 (m, 1H), 2.61 – 2.54 (m, 1H), 2.18 (t, J = 7.4 Hz, 2H), 2.04 (t, J = 7.4 Hz, 2H), 1.67 – 1.20 (m, 10H)*.

*: Overlap with impurities.

6.10.12 Synthesis of Biotin-Ahx-NHS 79

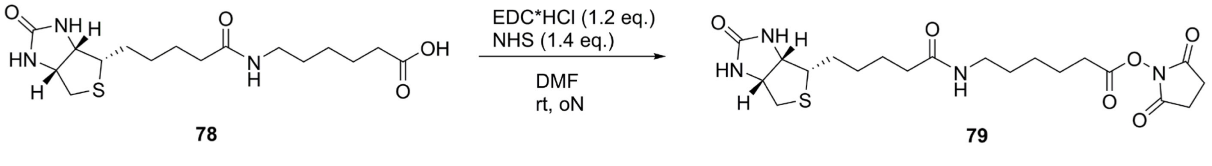

Figure 67| Synthesis of biotin-Ahx-NHS **79**.

170 mg (0.476 mmol, 1 eq.) biotin-Ahx **78** were dissolved in anhydrous DMF. 110 mg (0.571 mmol, 1.2 eq.) EDC·HCl and 77 mg (0.666 mmol, 1.4 eq.) NHS were added and the reaction was stirred over night at room temperature. The solvent was removed *in vacuo* and the residue was suspended in EA. After filtration the organic phase was extracted with 2% (v/v) formic acid

and once with brine. The organic layer was dried over $MgSO_4$ and evaporated. The residue was dissolved in H_2O:ACN and freeze-dried yielding 51 mg (0.112 mmol, 23%) of the title compound.

LC-MS (30 to 100% eluent B, gradient: 13.5 min, 220 nm): t_R = 9.625 min.

ESI-MS: Calc. for $C_{20}H_{30}N_4O_6S$: m/z: $[M+H]^+$ = 455.19 (obs. 455.36), $[2M+H]^+$ = 909.36 (obs. 909.49).

6.10.13 Synthesis of *Cyclo*[RGDfK(Ahx-Biotin)] 80 and *Cyclo*[RADfK(Ahx-Biotin)] 81

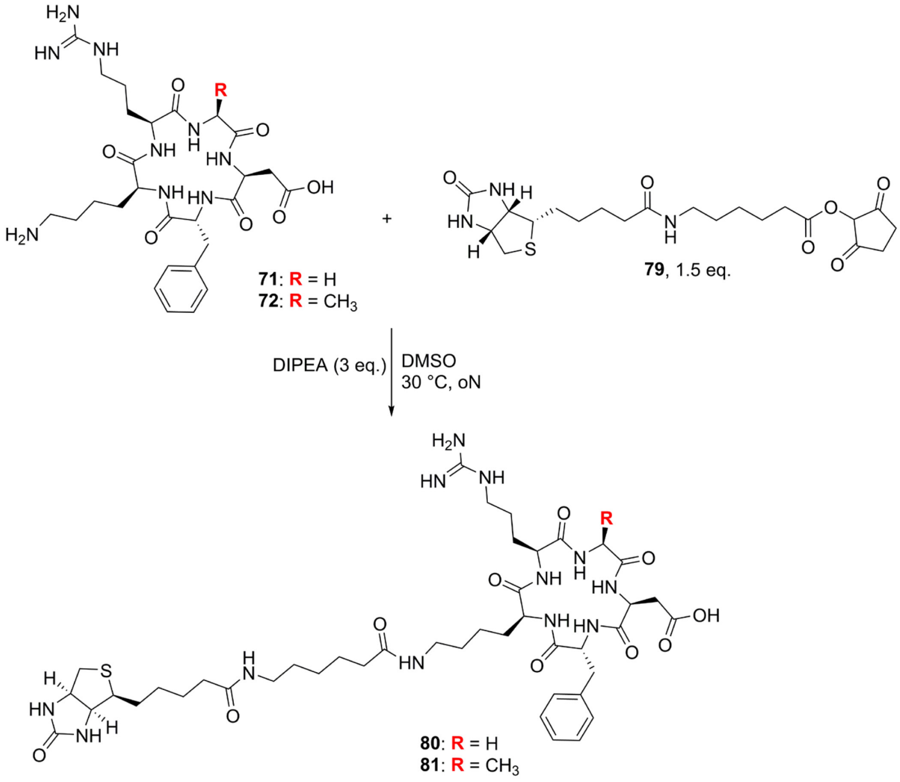

Figure 68| Synthesis of *cyclo*[RGDfK(Ahx-biotin)] **80** and *cyclo*[RADfK(Ahx-biotin)] **81**.

Synthesis of *Cyclo*[RGDfK(Ahx-Biotin)] 80:

15 mg (24.8 µmol, 1 eq.) *cyclo*[RGDfK] **71** and 17 mg (37.2 µmol, 1.5 eq.) biotin-Ahx-NHS **79** were dissolved in 2 mL anhydrous DMSO. 13 µL (9.6 mg, 74.4 µmol, 3 eq.) dry DIPEA was added and the reaction was shaken over night at 30 °C. The solvent was removed by lyophilization and the crude product was purified by semi-preparative HPLC. 3.8 mg (4.0 µmol, 16%) of the title compound were obtained as colorless solid.

RP-HPLC (10 to 60% eluent B, 220 nm): t_R = 14.445 min.

ESI-MS: Calc. for $C_{43}H_{66}N_{12}O_{10}S$: m/z: $[M+H]^+$ = 943.48 (obs. 943.67), $[M+2H]^{2+}$ = 472.24 (obs. 472.65).

Synthesis of *Cyclo*[RADfK(Ahx-Biotin)] 81:

15 mg (24.3 µmol, 1 eq., #1) *cyclo*[RADfK] **72** and 16.5 mg (36.4 µmol, 1.5 eq.) biotin-Ahx-NHS **37** were dissolved in 2 mL anhydrous DMSO. 12.7 µL (9.4 mg, 72.9 µmol, 3 eq.) dry DIPEA was added and the reaction was shaken over night at 30 °C. The solvent was removed by lyophilization and the crude product was purified by semi-preparative HPLC. 5.7 mg (6.0 µmol, 25%) of cyclo[RADfK(Ahx-biotin)] **81** were obtained as colorless solid.

RP-HPLC (10 to 60% eluent B, 220 nm): t_R = 14.391 min.

ESI-MS: Calc. for $C_{43}H_{66}N_{12}O_{10}S$: m/z: $[M+H]^+$ = 957.50 (obs. 957.67), $[M+2H]^{2+}$ = 479.25 (obs. 479.65).

6.10.14 ELISA

Integrin αvβ3 (*ACROBiosystems*, Newark, DE, USA) was reconstituted according to the supplier´s protocol and subsequently diluted in ELISA coating buffer (final concentration of the protein: 1 µg/mL). 100 µL of the solution were transferred into *Nunc MaxiSorp* ELISA plates and incubated over night at 4 °C. Following this, the supernatant was removed and the wells were washed thrice with ELISA coating buffer. Subsequently, the wells were blocked with 200 µL ELISA blocking buffer for 1 h at room temperature, followed by three washing steps with coating buffer. The constructs were diluted in coating buffer (2× concentrated, in 50 µL) and mixed with 50 µL of vitronectin (*ACROBiosystems*) in coating buffer (2 µg/mL). The mixture was transferred to the integrin-coated wells and incubated for 1 h at rt, followed by three washing steps with coating buffer. Thereafter, StrepTactin-HRP conjugate (*BioRad*, Herkules, CA, USA) was added, following the supplier´s protocol, and the plate was incubated for 1 h at rt. After removal of the supernatant and three washing steps with coating buffer, 100 µL *TMB One substrate solution* (*Promega GmbH*) was added and the plates were incubated at rt, until a sufficient color change to blue could be observed. The reaction was stopped with 100 µL 1M HCl, which resulted in a color change from blue to yellow and the assay was analyzed in the *Infinite F200 pro* plate reader at 405 nm wavelength.

6.10.15 Cell Binding Assay

Trypsinized U87MG cells were washed twice with ice-cold ELISA coating buffer + 0.1% (w/v) BSA by centrifugation at 500 × g for 5 min at 4 °C and transferred afterwards to U-bottom 96-well plates (2.0×10^5 cells/well). Cells were incubated with a serial dilution of the Sav-compound hybrids (50 µL, assembled as described in section **6.8.20**) in ELISA coating buffer + 0.1% (w/v) BSA for 45 min on ice. Afterwards, the cells were washed twice with ice-cold ELISA coating buffer + 0.1% (w/v) BSA and transferred to FACS tubes, followed by flow cytometric analysis.

7 References

[1] K. Strebhardt, A. Ullrich, *Nat. Rev. Cancer,* **2008**, *8*, 473-480.

[2] N. Batis, J. M. Brooks, K. Payne, N. Sharma, P. Nankivell, H. Mehanna, *Adv. Drug Del. Rev.,* **2021**, 113854.

[3] K. S. Bhullar, N. O. Lagarón, E. M. McGowan, I. Parmar, A. Jha, B. P. Hubbard, et al., *Mol. Cancer,* **2018**, *17*, 48-48.

[4] X. Sun, H. Gao, Y. Yang, M. He, Y. Wu, Y. Song, et al., *Signal Transduct Target Ther,* **2019**, *4*, 64.

[5] a) N. Tsomaia, *Eur. J. Med. Chem.,* **2015**, *94*, 459-470; b) Alex M. Chapman, Brian R. McNaughton, *Cell Chem. Biol.,* **2016**, *23*, 543-553.

[6] R.-M. Lu, Y.-C. Hwang, I. J. Liu, C.-C. Lee, H.-Z. Tsai, H.-J. Li, et al., *J. Biomed. Sci.,* **2020**, *27*, 1.

[7] D. J. Worm, S. Els-Heindl, A. G. Beck-Sickinger, *Peptide Sci,* **2020**, *112*, e24171.

[8] P. Khongorzul, C. J. Ling, F. U. Khan, A. U. Ihsan, J. Zhang, *Mol. Cancer Res.,* **2020**, *18*, 3-19.

[9] I. Ruseska, A. Zimmer, *Beilstein J. Nanotechnol.,* **2020**, *11*, 101-123.

[10] M. Mammen, S.-K. Choi, G. M. Whitesides, *Angew. Chem. Int. Ed.,* **1998**, *37*, 2754-2794.

[11] C. Chittasupho, *Ther. Deliv.,* **2012**, *3*, 1171-1187.

[12] G. A. Eggimann, S. Buschor, T. Darbre, J.-L. Reymond, *Org. Biomol. Chem.,* **2013**, *11*, 6717-6733.

[13] a) A. Erazo-Oliveras, K. Najjar, L. Dayani, T.-Y. Wang, G. A. Johnson, J.-P. Pellois, *Nat. Methods,* **2014**, *11*, 861-867; b) Y. Nomura, K. Sakamoto, M. Akishiba, T. Iwata, H. Hirose, S. Futaki, *Bioorg Med Chem Lett,* **2020**, *30*, 127362.

[14] S. Duggineni, S. Mitra, I. Lamberto, X. Han, Y. Xu, J. An, et al., *ACS Med. Chem. Lett.,* **2013**, *4*, 344-348.

[15] J. H. Oh, S.-E. Chong, S. Nam, S. Hyun, S. Choi, H. Gye, et al., *Adv. Sci.,* **2018**, *5*, 1800240.

[16] J. Zhao, S. Li, Y. Jin, J. Y. Wang, W. Li, W. Wu, et al., *Molecules,* **2019**, *24*, 817.

[17] H. Kubas, M. Schäfer, U. Bauder-Wüst, M. Eder, D. Oltmanns, U. Haberkorn, et al., *Nucl. Med. Biol.,* **2010**, *37*, 885-891.

[18] K. C. Collins, K. D. Janda, *Bioconjug. Chem.,* **2014**, *25*, 593-600.

[19] O. Avrutina, M. Empting, S. Fabritz, M. Daneschdar, H. Frauendorf, U. Diederichsen, et al., *Org. Biomol. Chem.,* **2009**, *7*, 4177-4185.

[20] C. Fasting, C. A. Schalley, M. Weber, O. Seitz, S. Hecht, B. Koksch, et al., *Angew. Chem. Int. Ed.,* **2012**, *51*, 10472-10498.

[21] a) K. Koschek, V. Durmaz, O. Krylova, M. Wieczorek, S. Gupta, M. Richter, et al., *Beilstein J. Org. Chem.,* **2015**, *11*, 837-847; b) B. Říhová, *Compos. B. Eng.,* **2007**, *38*, 386-397.

[22] J. Kopecek, P. Kopecková, *Adv. Drug Del. Rev.,* **2010**, *62*, 122-149.

[23] D. S. H. Chu, M. J. Bocek, J. Shi, A. Ta, C. Ngambenjawong, R. C. Rostomily, et al., *J. Control. Release,* **2015**, *205*, 155-161.

[24] T. H. C. Petrin, V. Fadel, D. B. Martins, S. A. Dias, A. Cruz, L. M. Sergio, et al., *Biomacromolecules,* **2019**, *20*, 2743-2753.

[25] E. Abbasi, S. F. Aval, A. Akbarzadeh, M. Milani, H. T. Nasrabadi, S. W. Joo, et al., *Nanoscale Res Lett,* **2014**, *9*, 247-247.

[26] G. Thumshirn, U. Hersel, S. L. Goodman, H. Kessler, *Chem. Eur. J.,* **2003**, *9*, 2717-2725.

[27] C. Wängler , S. Maschauer, O. Prante, M. Schäfer, R. Schirrmacher, P. Bartenstein, et al., *ChemBioChem,* **2010**, *11*, 2168-2181.

[28] B. P. Gray, S. Li, K. C. Brown, *Bioconjug. Chem.,* **2013**, *24*, 85-96.

[29] H. Schneider, D. Yanakieva, A. Macarrón, L. Deweid, B. Becker, S. Englert, et al., *ChemBioChem,* **2019**, *20*, 3006-3012.

[30] D. Y. W. Ng, J. Fahrer, Y. Wu, K. Eisele, S. L. Kuan, H. Barth, et al., *Adv. Healthc. Mater.,* **2013**, *2*, 1620-1629.

[31] T. Heinze, T. Liebert, B. Heublein, S. Hornig, in *Polysaccharides II, Vol. 205*, 1 ed. (Ed.: D. Klemm), Advances in Polymer Science, **2006**, pp. 199-291.

[32] A. Jeanes, W. C. Haynes, C. A. Wilham, J. C. Rankin, E. H. Melvin, M. J. Austin, et al., *J. Am. Chem. Soc.,* **1954**, *76*, 5041-5052.

[33] J. F. Robyt, B. K. Kimble, T. F. Walseth, *Arch. Biochem. Biophys.,* **1974**, *165*, 634-640.

[34] J. W. Van Cleve, W. C. Schaefer, C. E. Rist, *J. Am. Chem. Soc.,* **1956**, *78*, 4435-4438.

[35] O. Larm, B. Lindberg, S. Svensson, *Carbohydr. Res.,* **1971**, *20*, 39-48.

[36] C. Larsen, *Adv. Drug Del. Rev.,* **1989**, *3*, 103-154.

[37] R. Mehvar, *J Control Release,* **2000**, *69*, 1-25.

[38] I. Wolff, C. L. Mehltretter, R. L. Mellies, P. R. Watson, B. T. Hofreiter, P. L. Patrick, et al., *Ind. Eng. Chem. Res.,* **1954**, *46*, 2605-2610.

[39] M. Naessens, A. Cerdobbel, W. Soetaert, E. J. Vandamme, *J. Chem. Technol. Biotechnol.,* **2005**, *80*, 845-860.

[40] S. Danhauser-Riedl, E. Hausmann, H.-D. Schick, R. Bender, H. Dietzfelbinger, J. Rastetter, et al., *Invest. New Drugs,* **1993**, *11*, 187-195.

[41] Y. Perez, A. Valdivia, L. Gomez, B. K. Simpson, R. Villalonga, *Macromol. Biosci.,* **2005**, *5*, 1220-1225.

[42] H. Schneider, L. Deweid, T. Pirzer, D. Yanakieva, S. Englert, B. Becker, et al., *ChemistryOpen,* **2019**, *8*, 354-357.

[43] M. Feeney, M. Giannuzzo, P. Paolicelli, M. A. Casadei, *Drug Deliv.,* **2007**, *14*, 87-93.

[44] Y.-I. Jeong, D. H. Kim, C.-W. Chung, J.-J. Yoo, K. H. Choi, C. H. Kim, et al., *Int. J. Nanomed.,* **2011**, *6*, 1415-1427.

[45] C. Larsen, *Int. J. Pharm.,* **1989**, *52*, 55-61.

[46] J. Nakamura, N. Nakajima, K. Matsumura, S.-H. Hyon, *Anticancer Res.,* **2010**, *30*, 903-909.

[47] S. Okuno, M. Harada, T. Yano, S. Yano, S. Kiuchi, N. Tsuda, et al., *Cancer Res.,* **2000**, *60*, 2988-2995.

[48] H.-K. Yang, M. Qi, L. Mo, R.-M. Yang, X.-D. Xu, J.-F. Bao, et al., *RSC Adv.,* **2016**, *6*, 114519-114531.

[49] M. Yalpani, D. E. Brooks, *J. Polym. Sci., Polym. Chem. Ed.,* **1985**, *23*, 1395-1405.

[50] S. Weinert, S. Jabs, C. Supanchart, M. Schweizer, N. Gimber, M. Richter, et al., *Science,* **2010**, *328*, 1401-1403.

[51] M. Richter, A. Chakrabarti, I. R. Ruttekolk, B. Wiesner, M. Beyermann, R. Brock, et al., *Chem. Eur. J.,* **2012**, *18*, 16708-16715.

[52] L. Chaiet, F. J. Wolf, *Arch. Biochem. Biophys.,* **1964**, *106*, 1-5.

[53] P. György, C. S. Rose, R. E. Eakin, E. E. Snell, R. J. Williams, *Science,* **1941**, *93*, 477-478.

[54] H. R. Nordlund, V. P. Hytönen, O. H. Laitinen, M. S. Kulomaa, *J. Biol. Chem.,* **2005**, *280*, 13250-13255.

[55] N. Michael Green, in *Methods Enzymol., Vol. 184* (Eds.: M. Wilchek, E. A. Bayer), Academic Press, **1990**, pp. 51-67.

[56] R. Modanloo Jouybari, A. Sadeghi, B. Khansarinejad, S. Sadoogh Abbasian, H. Abtahi, *Rep. Biochem. Mol. Biol.,* **2018**, *6*, 178-185.

[57] T. Sano, M. W. Pandori, X. Chen, C. L. Smith, C. R. Cantor, *J. Biol. Chem.,* **1995**, *270*, 28204-28209.

[58] P. Weber, D. Ohlendorf, J. Wendoloski, F. Salemme, *Science,* **1989**, *243*, 85-88.

[59] C. E. Chivers, A. L. Koner, E. D. Lowe, M. Howarth, *Biochem. J.,* **2011**, *435*, 55-63.

[60] a) D. E. Hyre, I. Le Trong, E. A. Merritt, J. F. Eccleston, N. M. Green, R. E. Stenkamp, et al., *Protein Sci.,* **2006**, *15*, 459-467; b) F. Liu, J. Z. H. Zhang, Y. Mei, *Sci. Rep.,* **2016**, *6*, 27190.

[61] A. Chilkoti, P. H. Tan, P. S. Stayton, *Proc. Natl. Acad. Sci. U. S. A.,* **1995**, *92*, 1754-1758.

[62] R. E. Stenkamp, I. L. Trong, L. Klumb, P. S. Stayton, S. Freitag, *Protein Sci.,* **1997**, *6*, 1157-1166.

[63] a) U. Piran, W. J. Riordan, *J. Immunol. Methods,* **1990**, *133*, 141-143; b) C. E. Chivers, E. Crozat, C. Chu, V. T. Moy, D. J. Sherratt, M. Howarth, *Nat. Methods,* **2010**, *7*, 391-393.

[64] J. M. Marangoni, S.-C. Wu, D. Fogen, S.-L. Wong, K. K. S. Ng, *Sci. Rep.,* **2020**, *10*, 12483.

[65] T. Lakshmipriya, S. C. B. Gopinath, T.-H. Tang, *PLoS One,* **2016**, *11*, e0151153-e0151153.

[66] M. Mishra, S. Tiwari, A. Gunaseelan, D. Li, B. D. Hammock, A. V. Gomes, *Electrophoresis,* **2019**, *40*, 1731-1739.

[67] K. Tanaka, S. Yokoi, K. Morimoto, T. Iwata, Y. Nakamoto, K. Nakayama, et al., *Biorg. Med. Chem.,* **2012**, *20*, 1865-1868.

[68] I. Chen, M. Howarth, W. Lin, A. Y. Ting, *Nat. Methods,* **2005**, *2*, 99-104.

[69] T. C. Chu, K. Y. Twu, A. D. Ellington, M. Levy, *Nucleic Acids Res.,* **2006**, *34*, e73-e73.

[70] P. L. Weiden, H. B. Breitz, O. Press, J. W. Appelbaum, J. K. Bryan, S. Gaffigan, et al., *Cancer Biother Radiopharm,* **2000**, *15*, 15-29.

[71] H. B. Breitz, P. L. Weiden, P. L. Beaumier, D. B. Axworthy, C. Seiler, F.-M. Su, et al., *J. Nucl. Med.,* **2000**, *41*, 131-140.

[72] A. Luchini, G. Vitiello, *Biomimetics,* **2020**, *6*.

[73] F. R. Maxfield, G. van Meer, *Curr. Opin. Cell Biol.,* **2010**, *22*, 422-429.

[74] F. de Meyer, B. Smit, *Proc. Natl. Acad. Sci. U. S. A.,* **2009**, *106*, 3654-3658.

[75] J. Bernardino de la Serna, G. J. Schütz, C. Eggeling, M. Cebecauer, *Front. Cell Dev. Biol.,* **2016**, *4*.

[76] I. J. Uings, S. N. Farrow, *MP, Mol. Pathol.,* **2000**, *53*, 295-299.

[77] M. A. Garcia, W. J. Nelson, N. Chavez, *Cold Spring Harb. Perspect. Biol.,* **2018**, *10*.

[78] A. Zuidema, W. Wang, A. Sonnenberg, *Bioessays,* **2020**, *42*, 2000119.

[79] A. Schwab, A. Fabian, P. J. Hanley, C. Stock, *Physiol. Rev.,* **2012**, *92*, 1865-1913.

[80] Y.-Y. Zhao, M. Takahashi, J.-G. Gu, E. Miyoshi, A. Matsumoto, S. Kitazume, et al., *Cancer Sci.,* **2008**, *99*, 1304-1310.

[81] S. J. Singer, G. L. Nicolson, *Science,* **1972**, *175*, 720-731.

[82] M. Leabu, *Discoveries,* **2013**, *1*, e7-e7.

[83] K. Simons, E. Ikonen, *Nature,* **1997**, *387*, 569-572.

[84] D. Lingwood, K. Simons, *Science* **2010**, *327*, 46-50.

[85] M. C. Kerr, R. D. Teasdale, *Traffic,* **2009**, *10*, 364-371.

[86] J. A. Swanson, *Nat. Rev. Mol. Cell Bio.,* **2008**, *9*, 639-649.

[87] S. Kumari, S. Mg, S. Mayor, *Cell Res.,* **2010**, *20*, 256-275.

[88] M. Kaksonen, A. Roux, *Nat. Rev. Mol. Cell Bio.,* **2018**, *19*, 313-326.

[89] C. Matthaeus, J. W. Taraska, *Front. Cell Dev. Biol.,* **2021**, *8*.

[90] S. Mayor, R. E. Pagano, *Nat. Rev. Mol. Cell Bio.,* **2007**, *8*, 603-612.

[91] M. J. O'Sullivan, A. J. Lindsay, *Int. J. Mol. Sci.,* **2020**, *21*, 6074.

[92] H. Schulze, T. Kolter, K. Sandhoff, *Biochim. Biophys. Acta,* **2009**, *1793*, 674-683.

[93] Z. Wei, W. Su, H. Lou, S. Duan, G. Chen, *J. Mol. Cell. Biol.,* **2018**, *10*, 539-548.

[94] a) M. A. Lemmon, J. Schlessinger, *Cell,* **2010**, *141*, 1117-1134; b) D. M. Rosenbaum, S. G. F. Rasmussen, B. K. Kobilka, *Nature,* **2009**, *459*, 356-363.

[95] Z. Du, C. M. Lovly, *Mol. Cancer,* **2018**, *17*, 58.

[96] D. Zahavi, L. Weiner, *Antibodies,* **2020**, *9*, 34.

[97] N. Krall, J. Scheuermann, D. Neri, *Angew. Chem. Int. Ed.,* **2013**, *52*, 1384-1402.

[98] a) M. Nieberler, U. Reuning, F. Reichart, J. Notni, H. J. Wester, M. Schwaiger, et al., *Cancers,* **2017**, *9*; b) J. D. Humphries, A. Byron, M. J. Humphries, *J. Cell Sci.,* **2006**, *119*, 3901-3903.

[99] J. S. Desgrosellier, D. A. Cheresh, *Nat. Rev. Cancer,* **2010**, *10*, 9-22.

[100] O. Micheau, S. Shirley, F. Dufour, *Br. J. Pharmacol.,* **2013**, *169*, 1723-1744.

[101] Y. M. Angell, A. Bhandari, M. N. De Francisco, B. T. Frederick, J. M. Green, K. Leu, et al., *Adv. Exp. Med. Biol.,* **2009**, *611*, 101-103.

[102] B. Chatin, M. Mével, J. Devallière, L. Dallet, T. Haudebourg, P. Peuziat, et al., *Mol. Ther. Nucleic Acids,* **2015**, *4*, e244.

[103] Y. Cheng, *Chin. J. Chem .* **2021**, *39*, 1443-1449.

[104] M. Yu, J. Wu, J. Shi, O. C. Farokhzad, *J Control Release,* **2016**, *240*, 24-37.

[105] Q. Laurent, R. Martinent, B. Lim, A.-T. Pham, T. Kato, J. López-Andarias, et al., *JACS Au,* **2021**, *1*, 710-728.

[106] A. D. Frankel, C. O. Pabo, *Cell,* **1988**, *55*, 1189-1193.

[107] S. Reissmann, *J. Pept. Sci.,* **2014**, *20*, 760-784.

[108] F. Wang, Y. Wang, X. Zhang, W. Zhang, S. Guo, F. Jin, *J Control Release,* **2014**, *174*, 126-136.

[109] D. M. Copolovici, K. Langel, E. Eriste, Ü. Langel, *ACS Nano,* **2014**, *8*, 1972-1994.

[110] H. Derakhshankhah, S. Jafari, *Biomed. Pharmacother.,* **2018**, *108*, 1090-1096.

[111] S. Futaki, I. Nakase, *Acc. Chem. Res.,* **2017**, *50*, 2449-2456.

[112] A. Sahni, Z. Qian, D. Pei, *ACS Chem. Biol.,* **2020**, *15*, 2485-2492.

[113] D. Pei, M. Buyanova, *Bioconjug. Chem.,* **2019**, *30*, 273-283.
[114] S. Trabulo, A. L. Cardoso, M. Mano, M. C. P. De Lima, *Pharmaceuticals,* **2010**, *3*, 961-993.
[115] F. Nadal-Bufí, S. T. Henriques, *Peptide Sci,* **2020**, *112*, e24168.
[116] L. Yan, M. E. Adams, *J. Biol. Chem.,* **1998**, *273*, 2059-2066.
[117] M. Akishiba, T. Takeuchi, Y. Kawaguchi, K. Sakamoto, H. H. Yu, I. Nakase, et al., *Nat. Chem.,* **2017**, *9*, 751-761.
[118] S. Li, X. Zhang, C. Guo, Y. Peng, X. Liu, B. Wang, et al., *Chem. Commun.,* **2020**, *56*, 15655-15658.
[119] H. D. Herce, D. Schumacher, A. F. L. Schneider, A. K. Ludwig, F. A. Mann, M. Fillies, et al., *Nat. Chem.,* **2017**, *9*, 762-771.
[120] A. F. L. Schneider, A. L. D. Wallabregue, L. Franz, C. P. R. Hackenberger, *Bioconjug. Chem.,* **2019**, *30*, 400-404.
[121] D. Srinivasan, N. Muthukrishnan, G. A. Johnson, A. Erazo-Oliveras, J. Lim, E. E. Simanek, et al., *PLoS One,* **2011**, *6*, e17732.
[122] A. Chakrabarti, J. J. Witsenburg, M. D. Sinzinger, M. Richter, R. Wallbrecher, J. C. Cluitmans, et al., *Biochim. Biophys. Acta,* **2014**, *1838*, 3097-3106.
[123] M. Akishiba, S. Futaki, *Mol. Pharm.,* **2019**, *16*, 2540-2548.
[124] T. Iwata, H. Hirose, K. Sakamoto, Y. Hirai, J. V. V. Arafiles, M. Akishiba, et al., *Angew. Chem. Int. Ed.,* **2021**, *60*, 19804-19812.
[125] G. Lättig-Tünnemann, M. Prinz, D. Hoffmann, J. Behlke, C. Palm-Apergi, I. Morano, et al., *Nat. Commun.,* **2011**, *2*, 453.
[126] I. Morbioli, A. Casnati, J. D. Esko, Y. Tor, F. Sansone, *Org. Biomol. Chem.,* **2021**, *19*, 6598-6602.
[127] C. Kojima, R. Kameyama, M. Yamada, M. Ichikawa, T. Waku, A. Handa, et al., *Bioconjug. Chem.,* **2015**, *26*, 1804-1810.
[128] S. Hörner, S. Knauer, C. Uth, M. Jöst, V. Schmidts, H. Frauendorf, et al., *Angew. Chem. Int. Ed.,* **2016**, *55*, 14842-14846.
[129] R. H. Baney, M. Itoh, A. Sakakibara, T. Suzuki, *Chem. Rev.,* **1995**, *95*, 1409-1430.
[130] D. B. Cordes, P. D. Lickiss, F. Rataboul, *Chem. Rev.,* **2010**, *110*, 2081-2173.
[131] X. You, H. Wu, Y. Su, J. Yuan, R. Zhang, Q. Yu, et al., *J. Mater. Chem. A,* **2018**, *6*, 13191-13202.
[132] E. Ayandele, B. Sarkar, P. Alexandridis, *Nanomaterials,* **2012**, *2*, 445-475.
[133] S. Fabritz, S. Hörner, O. Avrutina, H. Kolmar, *Org. Biomol. Chem.,* **2013**, *11*, 2224-2236.
[134] C. McCusker, J. B. Carroll, V. M. Rotello, *Chem. Commun.,* **2005**, 996-998.
[135] S. Hörner, S. Fabritz, H. D. Herce, O. Avrutina, C. Dietz, R. W. Stark, et al., *Org. Biomol. Chem.,* **2013**, *11*, 2258-2265.
[136] S. W. Jones, R. Christison, K. Bundell, C. J. Voyce, S. M. V. Brockbank, P. Newham, et al., *Br. J. Pharmacol.,* **2005**, *145*, 1093-1102.
[137] A. Bernkop-Schnürch, *Adv. Drug Del. Rev.,* **2018**, *136-137*, 62-72.
[138] M. Kosuge, T. Takeuchi, I. Nakase, A. T. Jones, S. Futaki, *Bioconjug. Chem.,* **2008**, *19*, 656-664.
[139] H. J. P. Ryser, R. Flückiger, *Drug Discovery Today,* **2005**, *10*, 1085-1094.
[140] H. J. Ryser, R. Mandel, F. Ghani, *J. Biol. Chem.,* **1991**, *266*, 18439-18442.
[141] G. Gasparini, E.-K. Bang, G. Molinard, D. V. Tulumello, S. Ward, S. O. Kelley, et al., *J. Am. Chem. Soc.,* **2014**, *136*, 6069-6074.
[142] L. Qian, J. Fu, P. Yuan, S. Du, W. Huang, L. Li, et al., *Angew. Chem. Int. Ed.,* **2018**, *57*, 1532-1536.
[143] E. Derivery, E. Bartolami, S. Matile, M. Gonzalez-Gaitan, *J. Am. Chem. Soc.,* **2017**, *139*, 10172-10175.
[144] G. Gasparini, G. Sargsyan, E. K. Bang, N. Sakai, S. Matile, *Angew. Chem. Int. Ed.,* **2015**, *54*, 7328-7331.
[145] L. Zong, E. Bartolami, D. Abegg, A. Adibekian, N. Sakai, S. Matile, *ACS Cent. Sci.,* **2017**, *3*, 449-453.

[146] N. Chuard, A. I. Poblador-Bahamonde, L. Zong, E. Bartolami, J. Hildebrandt, W. Weigand, et al., *Chem. Sci.,* **2018**, *9*, 1860-1866.
[147] Q. Laurent, N. Sakai, S. Matile, *Helv. Chim. Acta,* **2019**, *102*, e1800209.
[148] R. Martinent, Q. Laurent, N. Sakai, S. Matile, *Chimia,* **2019**, *73*, 304-307.
[149] H. Yousefi, M. Vatanmakanian, M. Mahdiannasser, L. Mashouri, N. V. Alahari, M. R. Monjezi, et al., *Oncogene,* **2021**, *40*, 1043-1063.
[150] S. Huveneers, E. H. Danen, *J. Cell Sci.,* **2009**, *122*, 1059-1069.
[151] J.-P. Xiong, T. Stehle, B. Diefenbach, R. Zhang, R. Dunker, D. L. Scott, et al., *Science,* **2001**, *294*, 339-345.
[152] P. Bork, T. Doerks, T. A. Springer, B. Snel, *Trends Biochem. Sci.,* **1999**, *24*, 261-263.
[153] D. Craig, M. Gao, K. Schulten, V. Vogel, *Structure,* **2004**, *12*, 2049-2058.
[154] I. D. Campbell, M. J. Humphries, *Cold Spring Harb. Perspect. Biol.,* **2011**, *3*, a004994.
[155] E. J. Park, P. K. Myint, A. Ito, M. G. Appiah, S. Darkwah, E. Kawamoto, et al., *Front. Cell Dev. Biol.,* **2020**, *8*.
[156] L. Feni, *Doctoral Dissertation, Improving cargo delivery in cancer therapy with the help of cell-penetrating peptides,* Universität Köln **2019**.
[157] M. D. Pierschbacher, E. Ruoslahti, *Nature,* **1984**, *309*, 30-33.
[158] a) T. G. Kapp, F. Rechenmacher, S. Neubauer, O. V. Maltsev, E. A. Cavalcanti-Adam, R. Zarka, et al., *Sci. Rep.,* **2017**, *7*, 39805; b) C. J. Avraamides, B. Garmy-Susini, J. A. Varner, *Nat. Rev. Cancer,* **2008**, *8*, 604-617.
[159] M. Aumailley, M. Gurrath, G. Müller, J. Calvete, R. Timpl, H. Kessler, *FEBS Lett.,* **1991**, *291*, 50-54.
[160] M. A. Dechantsreiter, E. Planker, B. Mathä, E. Lohof, G. Hölzemann, A. Jonczyk, et al., *J. Med. Chem.,* **1999**, *42*, 3033-3040.
[161] C. Mas-Moruno, F. Rechenmacher, H. Kessler, *Anticancer Agents Med. Chem.,* **2010**, *10*, 753-768.
[162] J. P. Xiong, T. Stehle, R. Zhang, A. Joachimiak, M. Frech, S. L. Goodman, et al., *Science,* **2002**, *296*, 151-155.
[163] R. Haubner, R. Gratias, B. Diefenbach, S. L. Goodman, A. Jonczyk, H. Kessler, *J. Am. Chem. Soc.,* **1996**, *118*, 7461-7472.
[164] D. A. Reardon, L. B. Nabors, R. Stupp, T. Mikkelsen, *Expert Opin Investig Drugs,* **2008**, *17*, 1225-1235.
[165] M. Tucci, S. Stucci, F. Silvestris, *Lancet Oncol.,* **2014**, *15*, e584-e585.
[166] D. A. Reardon, B. Neyns, M. Weller, J. C. Tonn, L. B. Nabors, R. Stupp, *Future Oncol.,* **2011**, *7*, 339-354.
[167] R. Stupp, M. E. Hegi, T. Gorlia, S. C. Erridge, J. Perry, Y.-K. Hong, et al., *Lancet Oncol.,* **2014**, *15*, 1100-1108.
[168] A. R. Reynolds, I. R. Hart, A. R. Watson, J. C. Welti, R. G. Silva, S. D. Robinson, et al., *Nat. Med.,* **2009**, *15*, 392-400.
[169] J. Takagi, B. M. Petre, T. Walz, T. A. Springer, *Cell,* **2002**, *110*, 599-611.
[170] H. Chen, G. Niu, H. Wu, X. Chen, *Theranostics,* **2016**, *6*, 78-92.
[171] M. Nahrwold, C. Weiß, T. Bogner, F. Mertink, J. Conradi, B. Sammet, et al., *J. Med. Chem.,* **2013**, *56*, 1853-1864.
[172] X. Chen, C. Plasencia, Y. Hou, N. Neamati, *J. Med. Chem.,* **2005**, *48*, 1098-1106.
[173] S. Lucie, G. Elisabeth, F. Stéphanie, S. Guy, H. Amandine, A.-R. Corinne, et al., *Mol. Ther.,* **2009**, *17*, 837-843.
[174] D. Li, T. Su, L. Ma, F. Yin, W. Xu, J. Ding, et al., *Eur. J. Med. Chem.,* **2020**, *199*, 112367.
[175] C. M. Kang, H.-J. Koo, G. I. An, Y. S. Choe, J. Y. Choi, K.-H. Lee, et al., *EJNMMI Research,* **2015**, *5*, 60.
[176] A. Thorburn, *J. Thorac. Oncol.,* **2007**, *2*, 461-465.
[177] M. E. Guicciardi, G. J. Gores, *FASEB J.,* **2009**, *23*, 1625-1637.
[178] W. Schneider-Brachert, U. Heigl, M. Ehrenschwender, *Int. J. Mol. Sci.,* **2013**, *14*, 14475-14503.
[179] S. Shirley, A. Morizot, O. Micheau, *Recent Pat. Anticancer Drug Discov.,* **2011**, *6*, 311-323.

[180] D. Sarhan, P. D'Arcy, A. Lundqvist, *Int. J. Mol. Sci.,* **2014**, *15*, 18557-18573.

[181] Y. Shlyakhtina, V. Pavet, H. Gronemeyer, *Cell Death Dis.,* **2017**, *8*, e3025-e3025.

[182] X. Ouyang, M. Shi, F. Jie, Y. Bai, P. Shen, Z. Yu, et al., *Invest. New Drugs,* **2018**, *36*, 315-322.

[183] M. Snajdauf, K. Havlova, J. Vachtenheim, A. Ozaniak, R. Lischke, J. Bartunkova, et al., *Front. Mol. Biosci.,* **2021**, *8*.

[184] A. Dubuisson, O. Micheau, *Antibodies,* **2017**, *6*, 16.

[185] P. M. Holland, *Cytokine Growth Factor Rev.,* **2014**, *25*, 185-193.

[186] B. T. Wang, T. Kothambawala, L. Wang, T. J. Matthew, S. E. Calhoun, A. K. Saini, et al., *Mol. Cancer Ther.,* **2021**.

[187] G. Lamanna, C. R. Smulski, N. Chekkat, K. Estieu-Gionnet, G. Guichard, S. Fournel, et al., *Chem. Eur. J.,* **2013**, *19*, 1762-1768.

[188] B. Valldorf, H. Fittler, L. Deweid, A. Ebenig, S. Dickgiesser, C. Sellmann, et al., *Angew. Chem. Int. Ed.,* **2016**, *55*, 5085-5089.

[189] F. P. Polack, S. J. Thomas, N. Kitchin, J. Absalon, A. Gurtman, S. Lockhart, et al., *N. Engl. J. Med.,* **2020**, *383*, 2603-2615.

[190] J. A. Kulkarni, D. Witzigmann, S. B. Thomson, S. Chen, B. R. Leavitt, P. R. Cullis, et al., *Nat. Nanotechnol,* **2021**, *16*, 630-643.

[191] S. Agrawal, M. J. Gait, in *Advances in Nucleic Acid Therapeutics*, The Royal Society of Chemistry, **2019**, pp. 1-21.

[192] F. Eckstein, *Angew. Chem. Int. Ed.,* **1983**, *22*, 423-439.

[193] J. Wengel, M. Petersen, K. E. Nielsen, G. A. Jensen, A. E. Håkansson, R. Kumar, et al., *Nucleosides Nucleotides Nucl. Acids,* **2001**, *20*, 389-396.

[194] Y. Nan, Y.-J. Zhang, *Front. Microbiol.,* **2018**, *9*.

[195] P. E. Nielsen, M. Egholm, R. H. Berg, O. Buchardt, *Science,* **1991**, *254*, 1497-1500.

[196] P. E. Nielsen, G. Haaima, *Chem. Soc. Rev.,* **1997**, *26*, 73-78.

[197] D. Y. Cherny, B. P. Belotserkovskii, M. D. Frank-Kamenetskii, M. Egholm, O. Buchardt, R. H. Berg, et al., *Proc. Natl. Acad. Sci. U.S.A.,* **1993**, *90*, 1667.

[198] J. Li, S. S. Wijeratne, X. Qiu, C.-H. Kiang, *Nanomaterials,* **2015**, *5*, 246-267.

[199] V. V. Demidov, V. N. Potaman, M. D. Frank-Kamenetskii, M. Egholm, O. Buchard, S. H. Sönnichsen, et al., *Biochem. Pharmacol.,* **1994**, *48*, 1310-1313.

[200] A. Y. Shaikh, F. Björkling, P. E. Nielsen, H. Franzyk, *Eur. J. Org. Chem.,* **2021**, *2021*, 2792-2801.

[201] E. Uhlmann, A. Peyman, G. Breipohl, D. W. Will, *Angew. Chem. Int. Ed.,* **1998**, *37*, 2796-2823.

[202] M. Eriksson, P. E. Nielsen, *Nat. Struct. Biol.,* **1996**, *3*, 410-413.

[203] G. N. Forrest, S. Mehta, E. Weekes, D. P. Lincalis, J. K. Johnson, R. A. Venezia, *J. Antimicrob. Chemother.,* **2006**, *58*, 154-158.

[204] K. Oliveira, G. Haase, C. Kurtzman, J. r. Hyldig-Nielsen Jens, H. Stender, *J. Clin. Microbiol.,* **2001**, *39*, 4138-4141.

[205] G. N. Forrest, M.-C. Roghmann, L. S. Toombs, J. K. Johnson, E. Weekes, D. P. Lincalis, et al., *Antimicrob. Agents Chemother.,* **2008**, *52*, 3558-3563.

[206] A. Ghosal, P. E. Nielsen, *Nucleic Acid Ther.,* **2012**, *22*, 323-334.

[207] M. Kulik, A. Markowska-Zagrajek, M. Wojciechowska, R. Grzela, T. Wituła, J. Trylska, *Biochimie,* **2017**, *138*, 32-42.

[208] V. Rapozzi, B. E. A. Burm, S. Cogoi, G. A. van der Marel, J. H. van Boom, F. Quadrifoglio, et al., *Nucleic Acids Res.,* **2002**, *30*, 3712-3721.

[209] S. Montazersaheb, M. S. Hejazi, H. Nozad Charoudeh, *Adv Pharm Bull,* **2018**, *8*, 551-563.

[210] W. B. Kauffman, S. Guha, W. C. Wimley, *Nat. Commun.,* **2018**, *9*, 2568.

[211] P. Sazani, S. H. Kang, M. A. Maier, C. Wei, J. Dillman, J. Summerton, et al., *Nucleic Acids Res.,* **2001**, *29*, 3965-3974.

[212] P. Sazani, F. Gemignani, S.-H. Kang, M. A. Maier, M. Manoharan, M. Persmark, et al., *Nat. Biotechnol.,* **2002**, *20*, 1228-1233.

[213] S. Englert, *Master Thesis, COSS-Based Synthetic Conjugates for Intracellular Delivery of Peptide Nucleic Acids and Cytotoxins,* Technical University Darmstadt **2016**.

[214] N. Brodyagin, M. Katkevics, V. Kotikam, C. A. Ryan, E. Rozners, *Beilstein J. Org. Chem.,* **2021**, *17*, 1641-1688.

[215] E. Bartolami, D. Basagiannis, L. Zong, R. Martinent, Y. Okamoto, Q. Laurent, et al., *Chem. Eur. J.,* **2019**, *25*, 4047-4051.

[216] F. Xu, Z.-Z. Yang, S.-J. Zhang, *Phosphorus Sulfur Silicon Relat Elem,* **2013**, *188*, 1312-1319.

[217] B. Becker, *Doctoral Dissertation, Peptide-conjugated dextran hybrids: Generation of a versatile module for cytosolic delivery of biomolecular cargoes,* Technical University Darmstadt **2021**.

[218] B. Becker, S. Englert, H. Schneider, D. Yanakieva, S. Hofmann, C. Dombrowsky, et al., *J. Pept. Sci.,* **2021**, *27*, e3298.

[219] S. Cabantous, T. C. Terwilliger, G. S. Waldo, *Nat. Biotechnol.,* **2005**, *23*, 102-107.

[220] S. Cabantous, H. B. Nguyen, J.-D. Pedelacq, F. Koraïchi, A. Chaudhary, K. Ganguly, et al., *Sci. Rep.,* **2013**, *3*, 2854.

[221] M. S. Verma, F. X. Gu, *Carbohydr. Polym.,* **2012**, *87*, 2740-2744.

[222] C. Besanceney-Webler, H. Jiang, T. Zheng, L. Feng, D. Soriano del Amo, W. Wang, et al., *Angew. Chem. Int. Ed.,* **2011**, *50*, 8051-8056.

[223] J. López-Andarias, J. Saarbach, D. Moreau, Y. Cheng, E. Derivery, Q. Laurent, et al., *J. Am. Chem. Soc.,* **2020**, *142*, 4784-4792.

[224] S. Hauke, M. Best, T. T. Schmidt, M. Baalmann, A. Krause, R. Wombacher, *Bioconjug. Chem.,* **2014**, *25*, 1632-1637.

[225] M. Fernández-Suárez, H. Baruah, L. Martínez-Hernández, K. T. Xie, J. M. Baskin, C. R. Bertozzi, et al., *Nat. Biotechnol.,* **2007**, *25*, 1483-1487.

[226] M. Baalmann, L. Neises, S. Bitsch, H. Schneider, L. Deweid, P. Werther, et al., *Angew. Chem. Int. Ed.,* **2020**, *59*, 12885-12893.

[227] N. Stuhr-Hansen, C.-D. Vagianou, O. Blixt, *Chem. Eur. J.,* **2017**, *23*, 9472-9476.

[228] J. Dommerholt, S. Schmidt, R. Temming, L. J. A. Hendriks, F. P. J. T. Rutjes, J. C. M. van Hest, et al., *Angew. Chem. Int. Ed.,* **2010**, *49*, 9422-9425.

[229] M. Tsuneki, J. A. Madri, *Mol Cell Biol,* **2014**, *34*, 4485-4499.

[230] M. Khan, Y. Bi, J. I. Qazi, L. Fan, H. Gao, *Mol Med Rep,* **2015**, *11*, 257-262.

[231] X. Xue, Y. Wu, X. Xu, B. Xu, Z. Chen, T. Li, in *Polymers, Vol. 13*, **2021**.

[232] H. Schneider, S. Englert, A. Macarrón Palacios, J. A. Lerma Romero, A. Ali, O. Avrutina, et al., *Front. Chem.,* **2021**, *9*.

[233] X. Dai, Z. Su, J. O. Liu, *Tetrahedron Lett.,* **2000**, *41*, 6295-6298.

[234] A. I. Fernández-Llamazares, J. García, V. Soto-Cerrato, R. Pérez-Tomás, J. Spengler, F. Albericio, *Chem. Commun.,* **2013**, *49*, 6430-6432.

[235] J. S. Davies, *J. Pept. Sci.,* **2003**, *9*, 471-501.

[236] S. Benedetto, R. Pulito, S. G. Crich, G. Tarone, S. Aime, L. Silengo, et al., *Magn. Reson. Med.,* **2006**, *56*, 711-716.

[237] G. M. Dubowchik, R. A. Firestone, L. Padilla, D. Willner, S. J. Hofstead, K. Mosure, et al., *Bioconjug Chem,* **2002**, *13*, 855-869.

[238] A. Macarrón Palacios, J. Grzeschik, L. Deweid, S. Krah, S. Zielonka, T. Rösner, et al., *Front. Immunol.,* **2020**, *11*, 560244.

[239] M. Kesik-Brodacka, *Biotechnol Appl Biochem,* **2018**, *65*, 306-322.

[240] M. Kodaka, Z. Yang, K. Nakagawa, J. Maruyama, X. Xu, A. Sarkar, et al., *Exp. Cell Res.,* **2015**, *336*, 171-181.

[241] C. J. Benjamin, K. J. Wright, S.-H. Hyun, K. Krynski, G. Yu, R. Bajaj, et al., *Langmuir,* **2016**, *32*, 551-559.

[242] D. L. Klayman, T. S. Griffin, *J. Am. Chem. Soc.,* **1973**, *95*, 197-199.

[243] J. Wang, M. Uttamchandani, L. P. Sun, S. Q. Yao, *Chem. Commun.,* **2006**, 717-719.

[244] W. C. Chan, B. W. Bycroft, D. J. Evans, P. D. White, *J. Chem. Soc., Chem. Commun.,* **1995**, 2209-2210.

[245] N. Thamban Chandrika, K. D. Green, J. L. Houghton, S. Garneau-Tsodikova, *ACS Med. Chem. Lett.,* **2015**, *6*, 1134-1139.

8 Appendix

8.1 Supplementary Figures

8.1.1 FACS-Analysis of TAMRA-Dextran-Cadaverine-$(N_3)_{5.4}$ on HeLa GFP 1-10 Cells

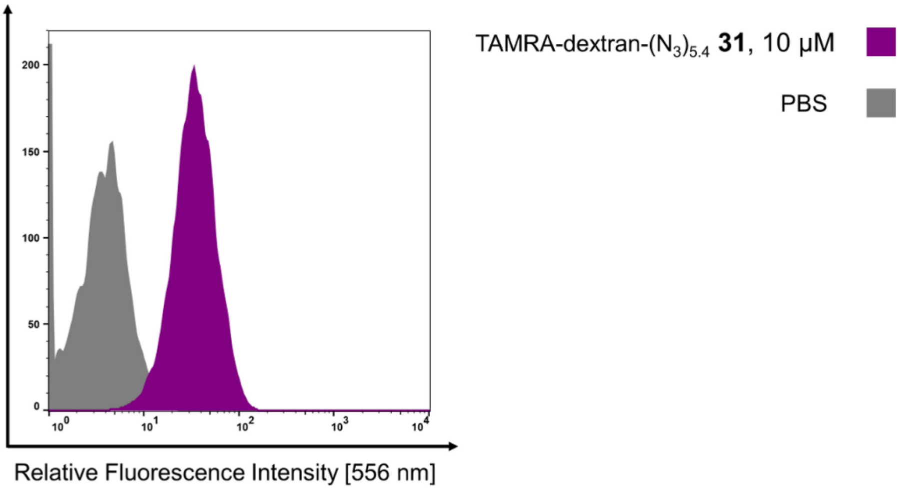

Figure S 1| Histogram showing TAMRA fluorescence (λ = 556 nm) of HeLa GFP 1-10 cells treated with 10 µM TAMRA-cadaverine-dextran-$(N_3)_{5.4}$ **31** at 37 °C.

8.1.2 CLSM of Sav- ATTO 647 58 (4x Biotin) on HeLa Cells

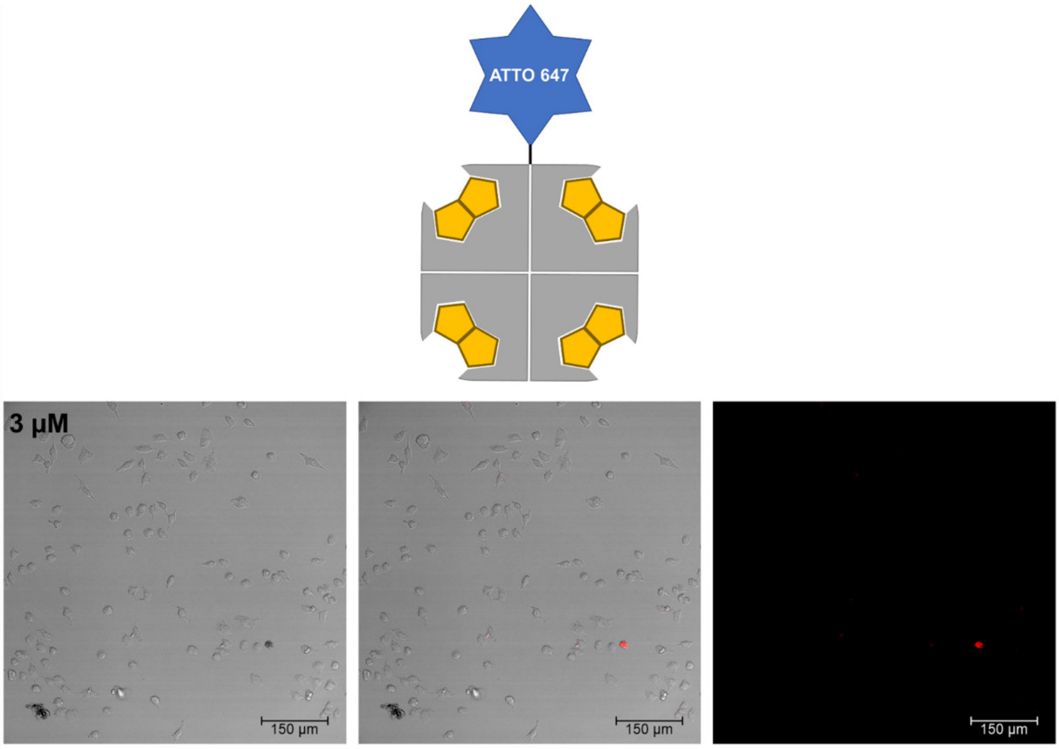

Figure S 2| CLSM images (20x) of HeLa cells incubated with Sav-ATTO 647 **58** equipped with 4 copies of biotin at 3 µM with brightfield (left), overlay (middle) and fluorescence channel (right).

8.1.3 CLSM of Sav- AF647 59 (4x Biotin) on HeLa Cells

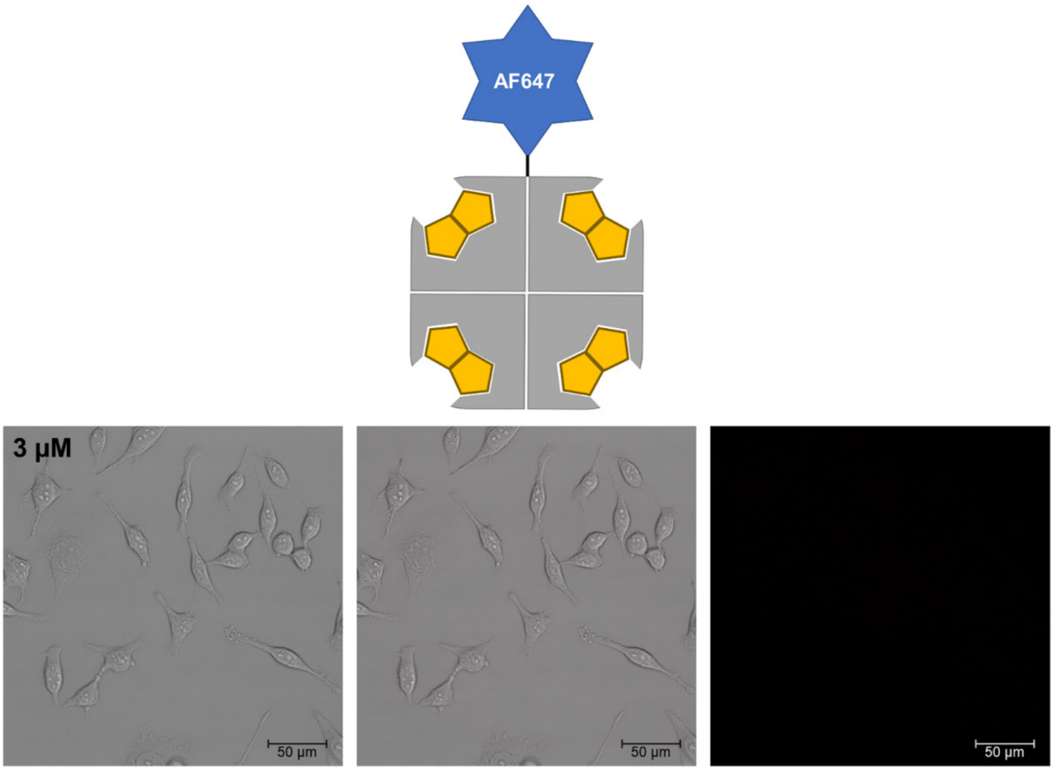

Figure S 3| CLSM images (20x) of HeLa cells incubated with Sav-AF647 **59** equipped with 4 copies of biotin at 3 µM with brightfield (left), overlay (middle) and fluorescence channel (right).

8.1.4 CLSM of Sav- AF647 59 (2x / 1x Dextran 40) on HeLa Cells

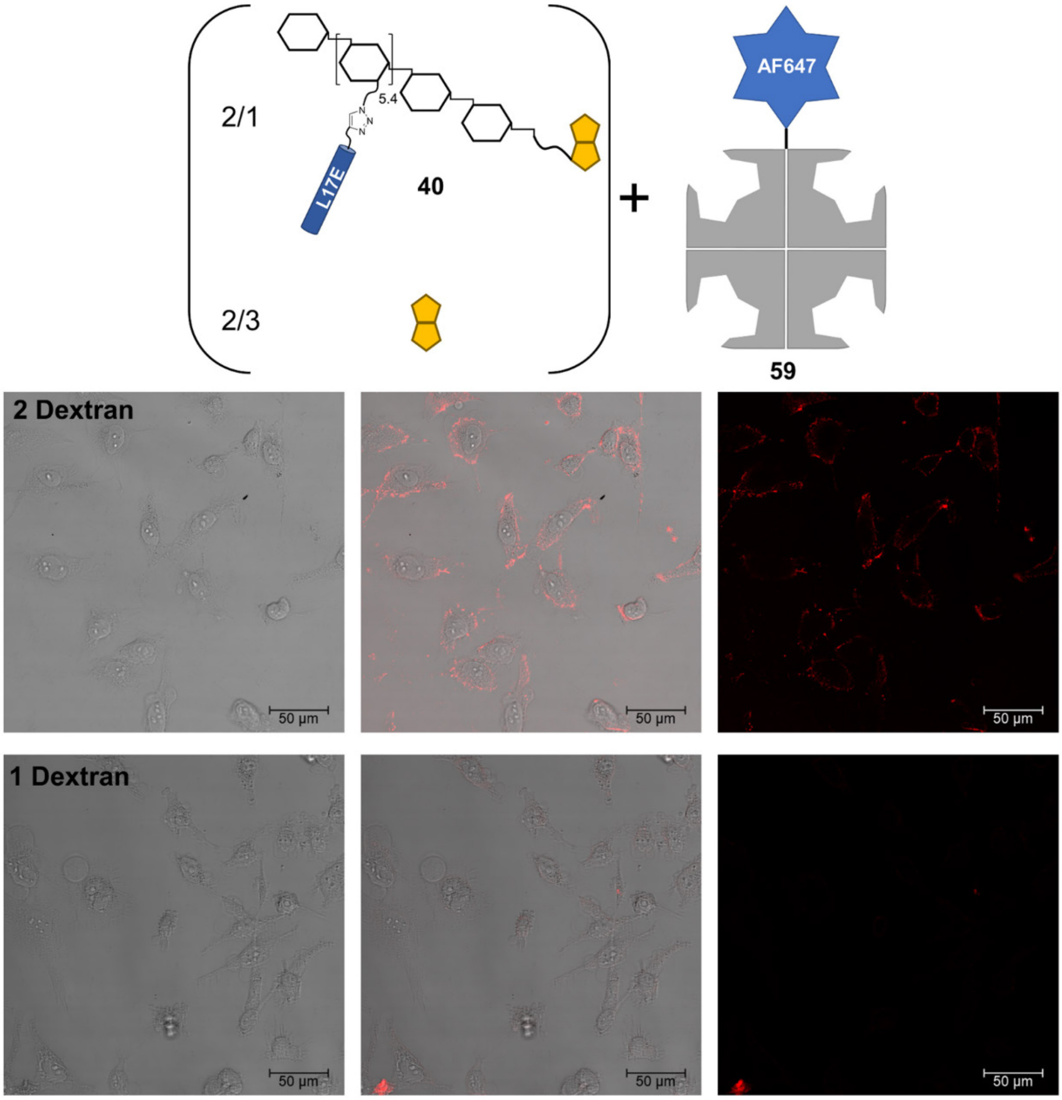

Figure S 4| CLSM images (20x) of HeLa cells incubated with Sav-AF647 **59** equipped with 2 (top) and 1 (bottom) copies, respectively, of biotin-cadaverine-dextran-(L17E)$_{5.4}$ **40** at 0.75 µM (top) with brightfield (left), overlay (middle) and fluorescence channel (right).

8.1.5 LC_{50} Determination of L17E-decorated Dextran – Sav Hybrids

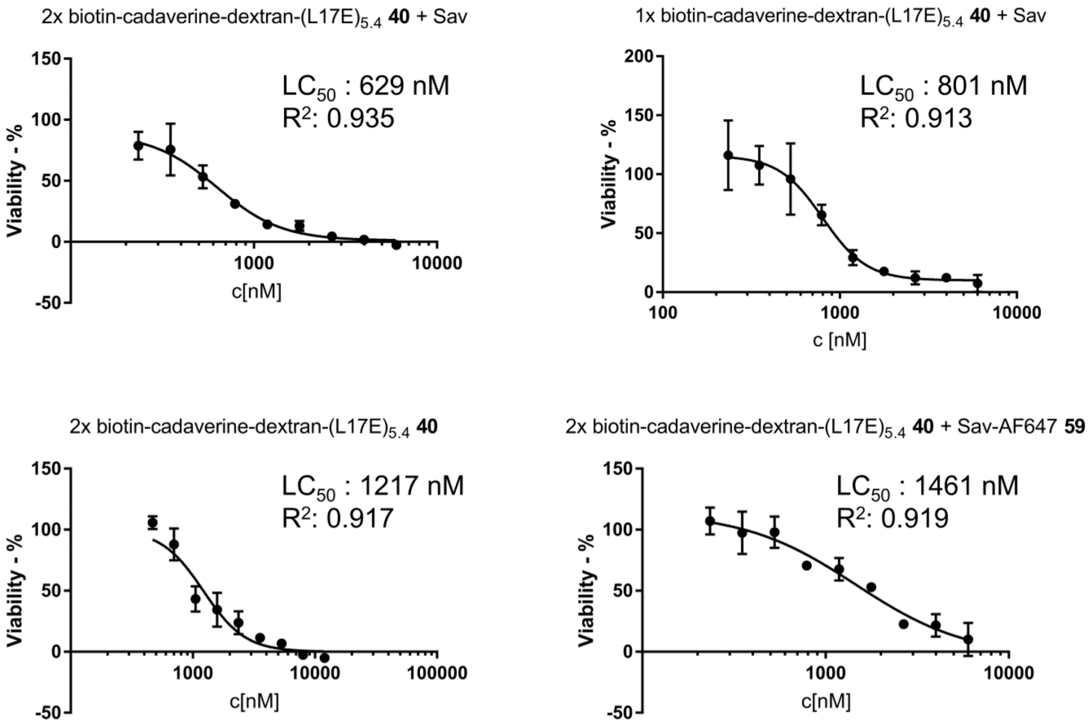

Figure S 5| LC_{50} calculation of dextran **40** – Sav hybrids. The LC_{50} values refer to the concentration of Sav in the architectures, with exception of bottom left, which refers to the concentration of dextran

8.2 Analytical Data of Synthesized Compounds

8.2.1 Analytical Data of *S*-3-Tritylmercaptopropionic Acid 4

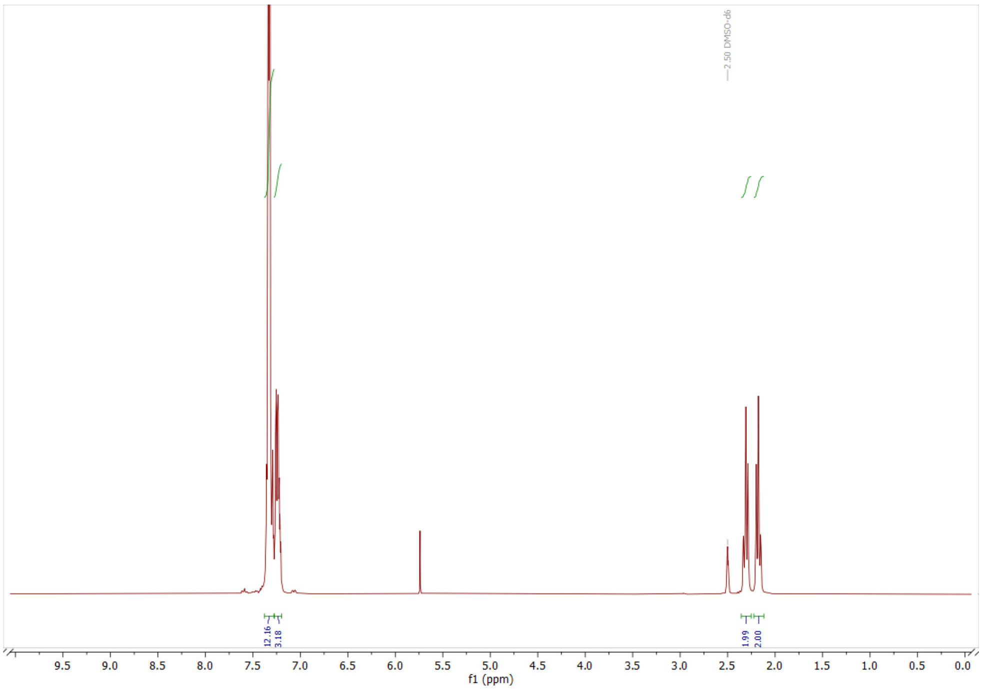

Figure S 6| ^{1}H NMR (300 MHz, DMSO-d6) of *S*-3-tritylmercaptopropionic acid **4**.

8.2.2 Analytical Data of (*S*-3-(Tritylmercapto)propionyl)-β-Ala-OH 5

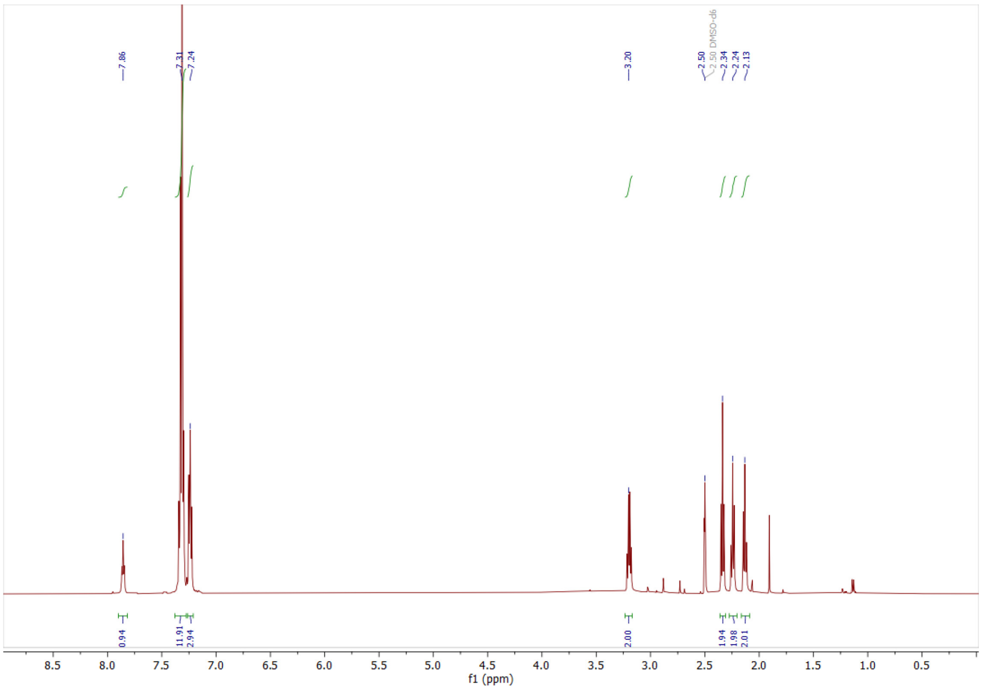

Figure S 7| ^{1}H NMR (500 MHz, DMSO-d_6) of (*S*-3-(tritylmercapto)propionyl)-β-Ala-OH **5**.

8.2.3 Analytical Data of (*S*-3-(Tritylmercapto)propionyl)-β-Ala-heptaammonium-COSS 6

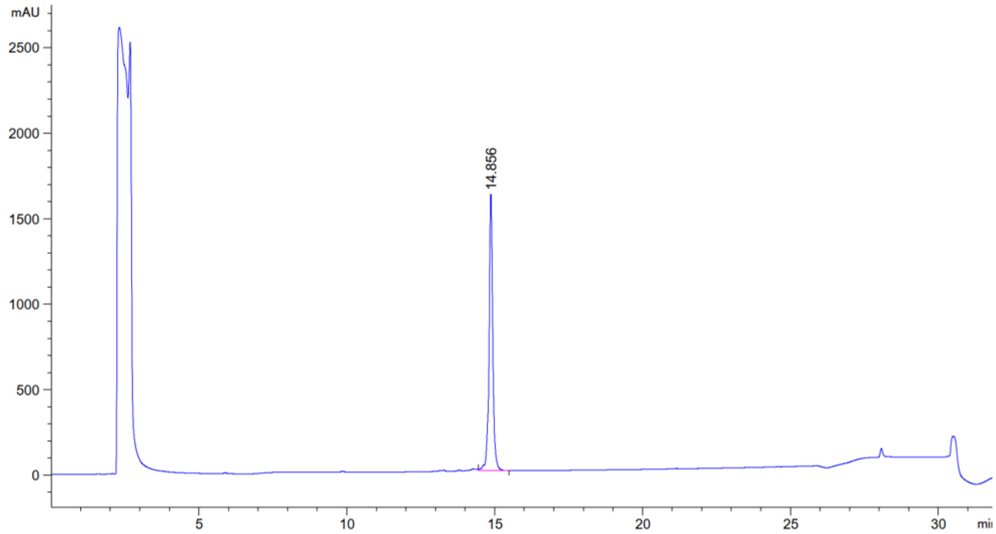

Figure S 8| Analytical RP-HPLC chromatogram of (*S*-3-(tritylmercapto)propionyl)-β-Ala-heptaammonium-COSS **6**, 10 to 80 % eluent B (20 min gradient), 220 nm, t_R = 14.856 min.

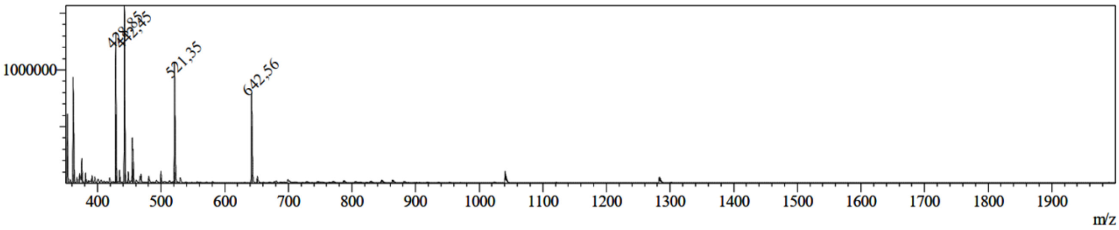

Figure S 9| ESI-MS of (*S*-3-(tritylmercapto)propionyl)-β-Ala-heptaammonium-COSS **6**. Calc. for $C_{49}H_{87}N_9O_{14}SSi_8$: m/z: $[M+2H]^{2+}$ = 642.51 (obs. 642.56), $[M+3H]^{3+}$ = 428.67 (obs. 428.85).

8.2.4 Analytical Data of (3-Mercapto)propionyl)-β-Ala-heptaguanidinium-COSS 9

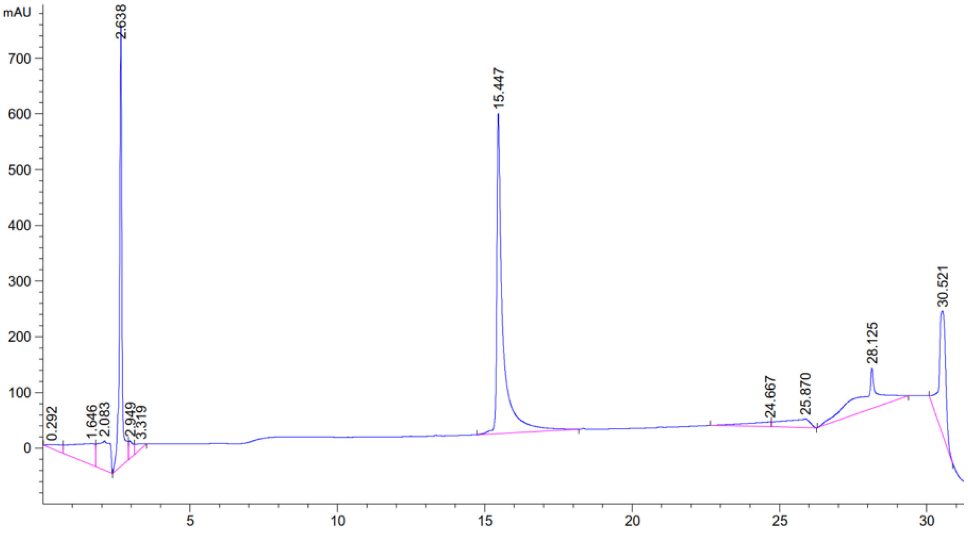

Figure S 10| Analytical RP-HPLC chromatogram of (*S*-3-(tritylmercapto)propionyl)-β-Ala-heptaguanidinium-COSS **8**, 10 to 80 % eluent B (20 min gradient), 220 nm, t_R = 15.447 min.

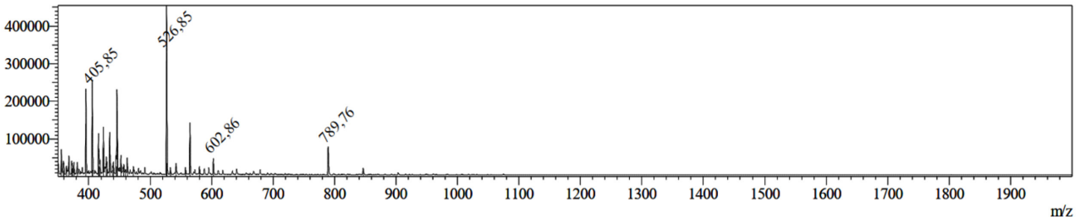

Figure S 11| ESI-MS of (*S*-3-(tritylmercapto)propionyl)-β-Ala-heptaguanidinium-COSS **8**. Calc. for $C_{56}H_{101}N_{23}O_{14}SSi_8$: m/z: $[M+2H]^{2+}$ = 789.66 (obs. 789.76), $[M+3H]^{3+}$ = 526.77 (obs. 526.85).

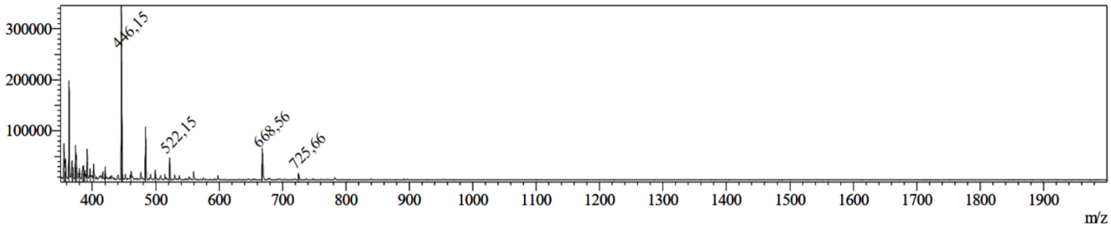

Figure S 12| ESI-MS of (3-mercapto)propionyl)-β-Ala-heptaguanidinium-COSS **9**. Calc. for $C_{37}H_{87}N_{23}O_{14}SSi_8$: m/z: $[M+2H]^{2+}$ = 668.50 (obs. 668.56), $[M+3H]^{3+}$ = 446.00 (meas. 446.15).

8.2.5 Analytical Data of Maleimide-Functionalized GuCOSS 10

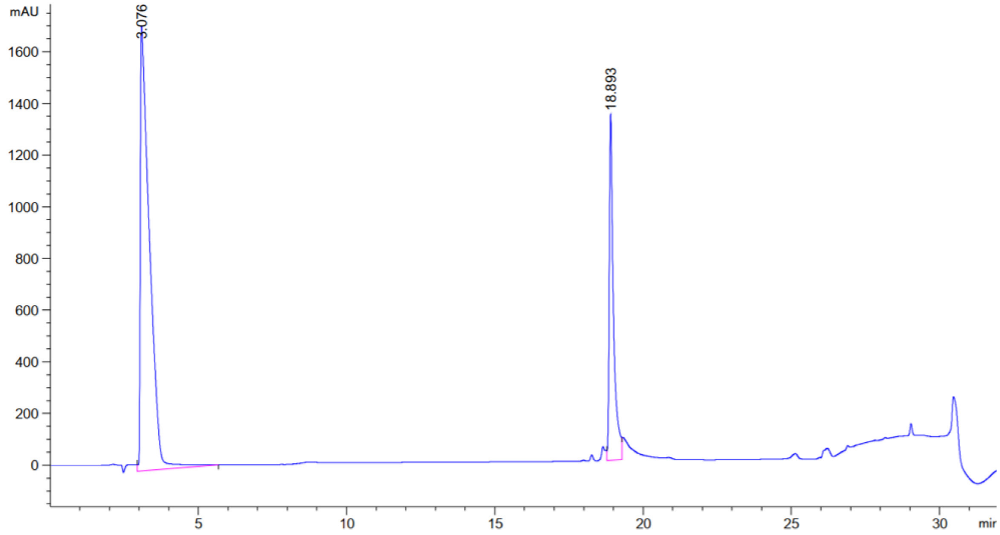

Figure S 13| Analytical RP-HPLC chromatogram of maleimide functionalized GuCOSS **10**, 0 to 40 % eluent B (20 min gradient), 220 nm, t_R = 18.893 min.

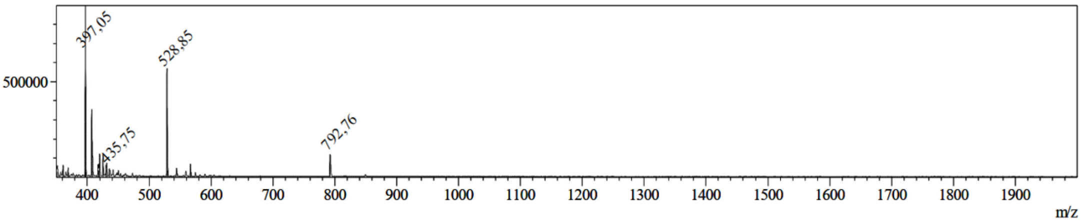

Figure S 14| ESI-MS of maleimide functionalized GuCOSS **10**. Calc. for $C_{49}H_{99}N_{25}O_{18}SSi_8$: m/z: $[M+2H]^{2+}$ = 792.61 (obs. 792.66), $[M+3H]^{3+}$ = 528.74 (obs. 528.85).

8.2.6 Analytical Data of Aldrithiol-Activated GuCOSS 11

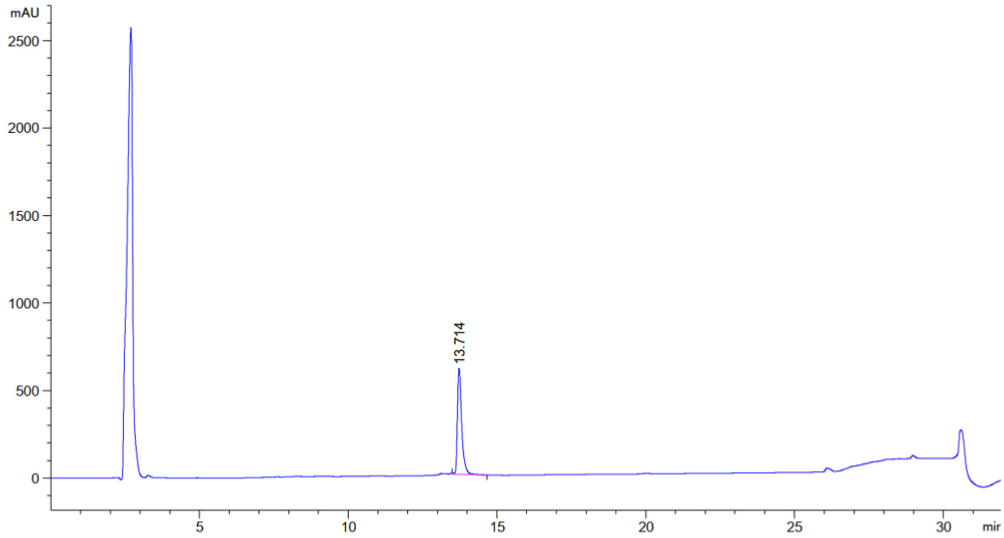

Figure S 15| Analytical RP-HPLC chromatogram of aldrithiol-activated GuCOSS **11**, 10 to 50 % eluent B (20 min gradient), 220 nm, t_R = 13.714 min.

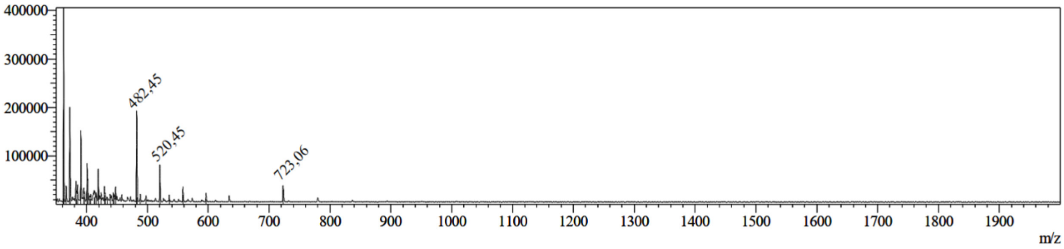

Figure S 16| ESI-MS of aldrithiol-activated GuCOSS **11**. Calc. for $C_{42}H_{90}N_{24}O_{14}S_2Si_8$: m/z: $[M+2H]^{2+}$ = 723.07 (obs. 723.06), $[M+3H]^{3+}$ = 482.38 (obs. 482.45).

8.2.7 Analytical Data of Thiol-PNA 12

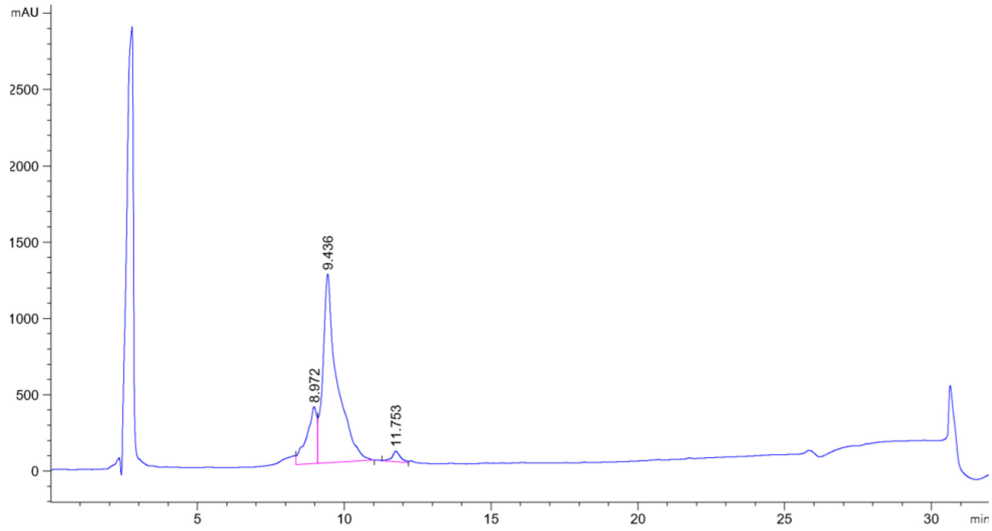

Figure S 17| Analytical RP-HPLC chromatogram of thiol-PNA **12**, 10 to 60 % eluent B (20 min gradient), 220 nm, t_R = 9.436 min.

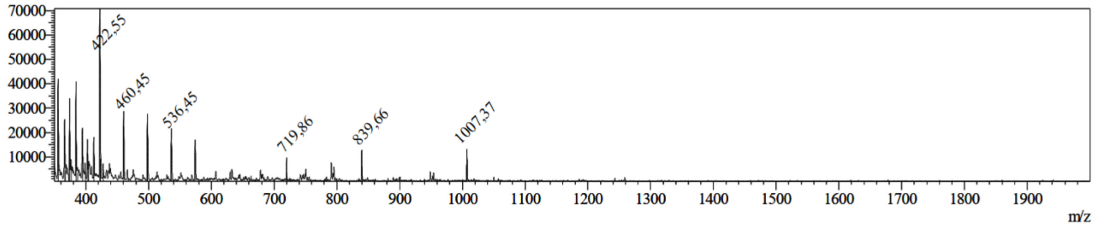

Figure S 18| ESI-MS of thiol-PNA **12**. Calc. for $C_{201}H_{258}N_{102}O_{56}S$: m/z: $[M+4H]^{4+}$ = 1258.73 (obs. 1258.98), $[M+5H]^{5+}$ = 1007.18 (obs. 1007.37), $[M+6H]^{6+}$ = 839.49 (obs. 839.66), $[M+7H]^{7+}$ = 719.70 (obs. 719.96), $[M+8H]^{8+}$ = 629.86 (obs. 630.06).

8.2.8 Analytical Data of GuCOSS-PNA Conjugate 13 with Thioether Linkage

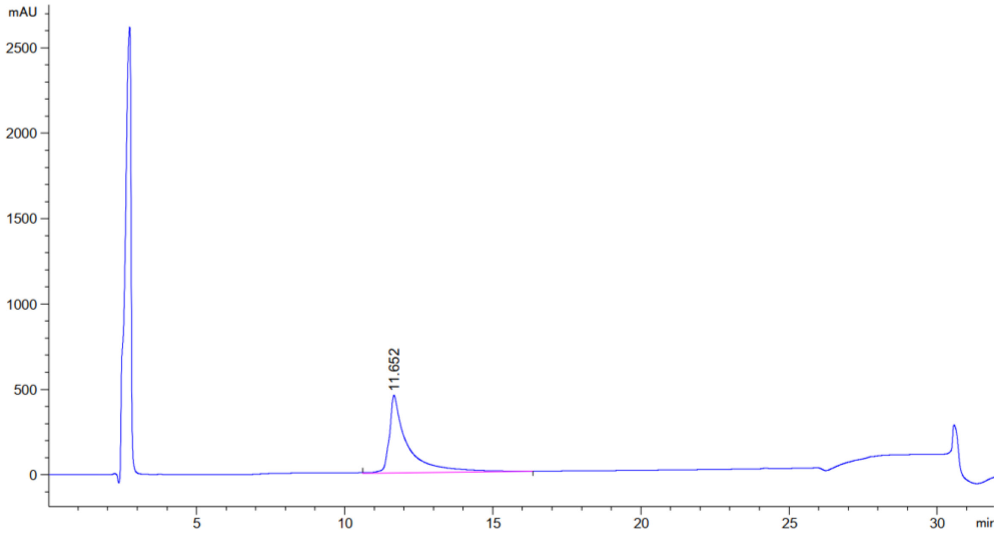

Figure S 19| Analytical RP-HPLC chromatogram of GuCOSS-PNA Conjugate **13**, 10 to 60 % eluent B (20 min gradient), 220 nm, t_R = 11.652 min.

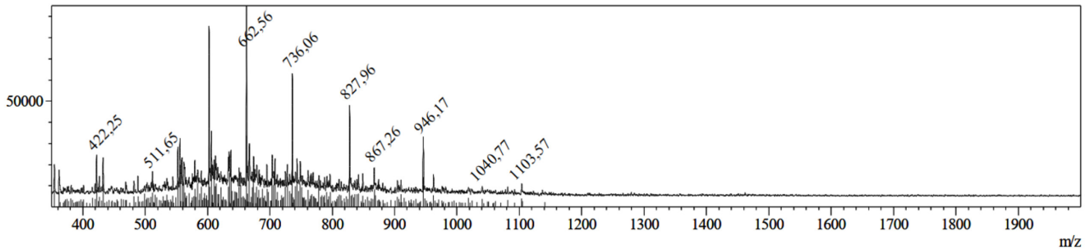

Figure S 20| ESI-MS of GuCOSS-PNA Conjugate **13**. Calc. for $C_{250}H_{357}N_{127}O_{74}S_2Si_8$: m/z: $[M+6H]^{6+}$ = 1103.36 (obs. 1103.57), $[M+7H]^{7+}$ = 945.88 (obs. 946.17), $[M+8H]^{8+}$ = 827.77 (obs. 827.96), $[M+9H]^{9+}$ = 735.90 (obs. 736.06), $[M+10H]^{10+}$ = 662.41 (obs. 662.56).

8.2.9 Analytical Data of GuCOSS-PNA Conjugate 14 with Disulfide Linkage

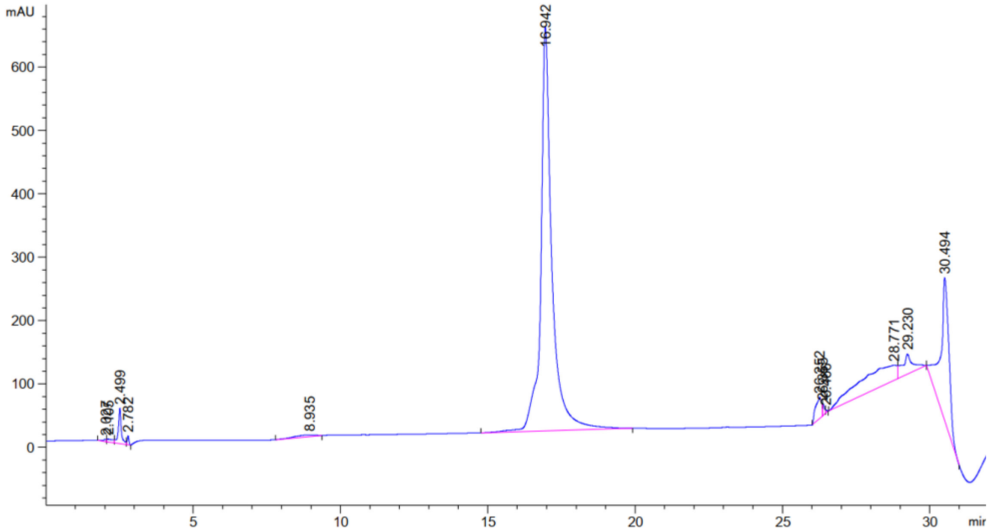

Figure S 21| Analytical RP-HPLC chromatogram of GuCOSS-PNA Conjugate **14**, 0 to 40 % eluent B (20 min gradient), 220 nm, t_R = 16.942 min.

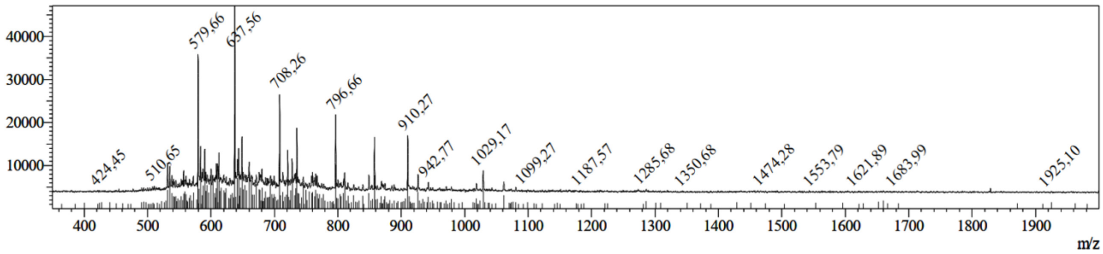

Figure S 22| ESI-MS of GuCOSS-PNA Conjugate **14**. Calc. for $C_{238}H_{343}N_{125}O_{70}S_2Si_8$: m/z: $[M+7H]^{7+}$ = 910.13 (obs. 910.27), $[M+8H]^{8+}$ = 796.49 (obs. 796.66), $[M+9H]^{9+}$ = 708.10 (obs. 708.26), $[M+10H]^{10+}$ = 637.39 (obs. 637.56), $[M+11H]^{11+}$ = 579.54 (obs. 579.66).

8.2.10 Analytical Data of $(KF_2)_3K$-PNA Conjugate 16

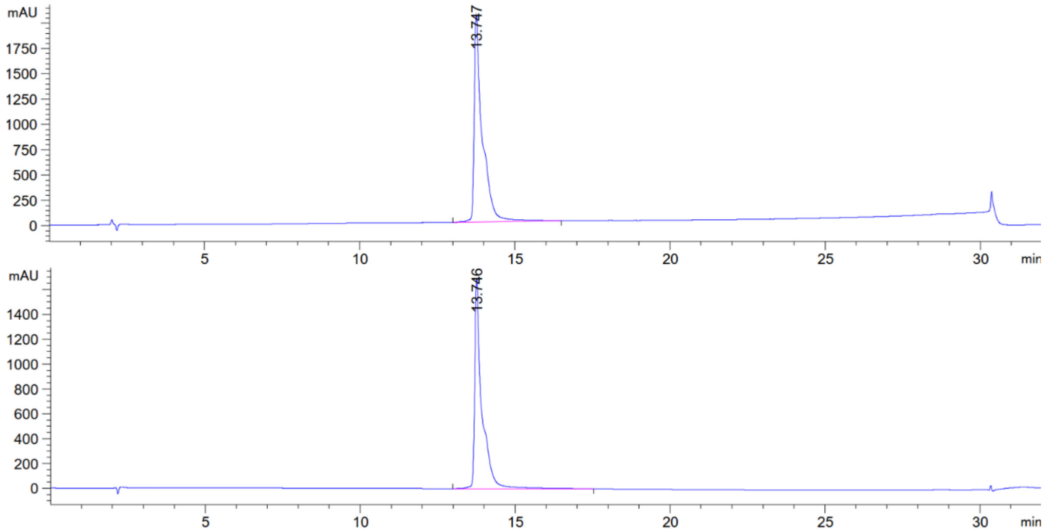

Figure S 23| Analytical RP-HPLC chromatogram of $(KF_2)_3K$-PNA Conjugate **16**, 0 to 80 % eluent B (20 min gradient), 220 nm (top), 280 nm (bottom), t_R = 13.747 min.

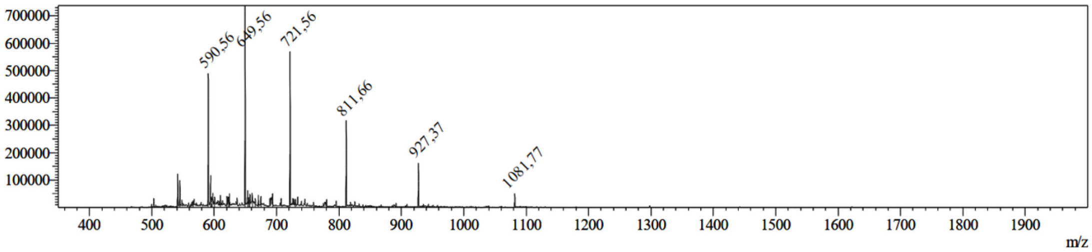

Figure S 24| ESI-MS of $(KF_2)_3K$-PNA Conjugate **16**. Calc. for $C_{282}H_{367}N_{117}O_{68}$: m/z: $[M+6H]^{6+}$ = 1081.63 (obs. 1081.77), $[M+7H]^{7+}$ = 927.26 (obs. 927.37), $[M+8H]^{8+}$ = 811.47 (obs. 811.66), $[M+9H]^{9+}$ = 721.42 (obs. 721.56), $[M+10H]^{10+}$ = 649.38 (obs. 649.56), $[M+11H]^{11+}$ = 590.44 (obs. 590.56).

8.2.11 Analytical Data of P17-PNA Conjugate 17

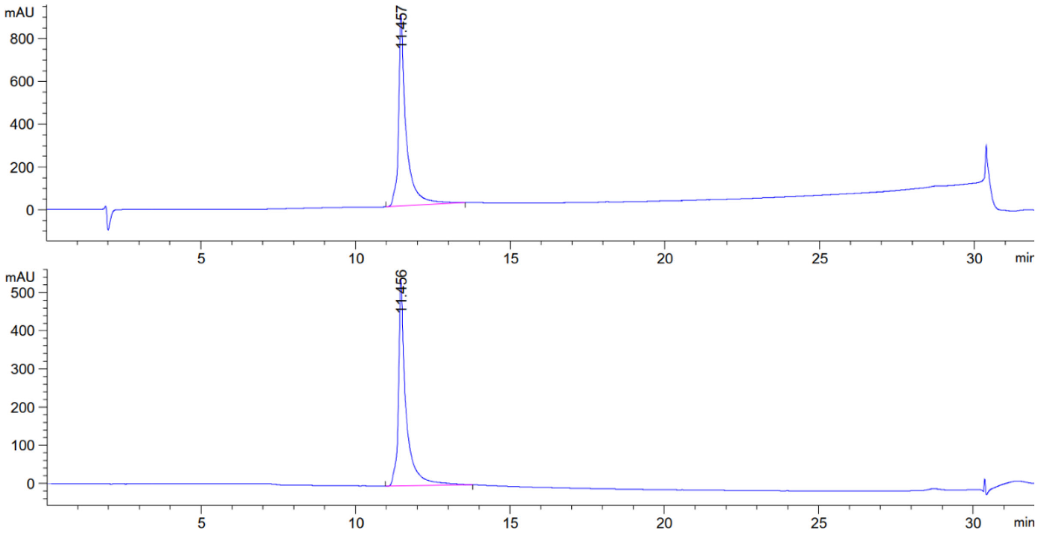

Figure S 25| Analytical RP-HPLC chromatogram of P17-PNA conjugate **17**, 0 to 80 % eluent B (20 min gradient), 220 nm (top), 280 nm (bottom), t_R = 11.457 min.

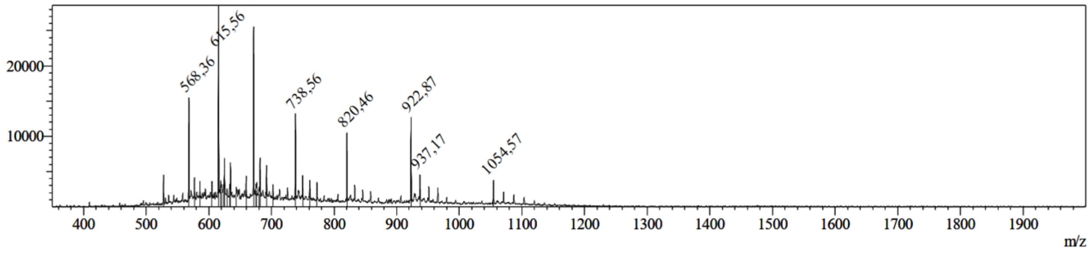

Figure S 26| ESI-MS of P17-PNA conjugate **17**. Calc. for $C_{308}H_{438}N_{144}O_{74}S$: m/z: $[M+7H]^{7+}$ = 1054.41 (obs. 1054.57), $[M+8H]^{8+}$ = 922.74 (obs. 922.87), $[M+9H]^{9+}$ = 820.32 (obs. 820.46), $[M+10H]^{10+}$ = 738.39 (obs. 738.56), $[M+12H]^{12+}$ = 615.49 (obs. 615.49).

8.2.12 Analytical Data of P14-PNA Conjugate 18

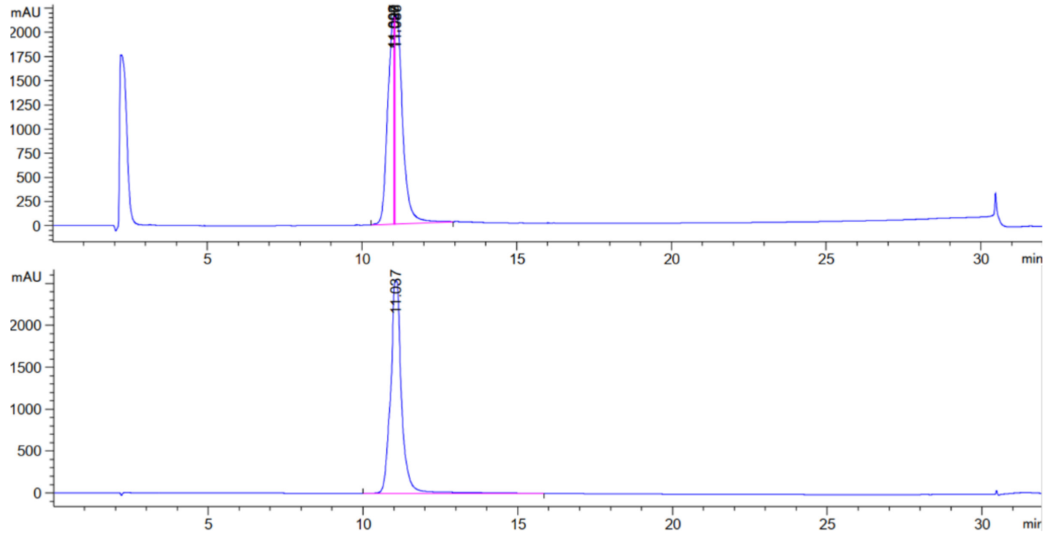

Figure S 27| Analytical RP-HPLC chromatogram of P14-PNA conjugate **18**, 0 to 80 % eluent B (20 min gradient), 220 nm (top), 280 nm (bottom), t_R = 11.037 min.

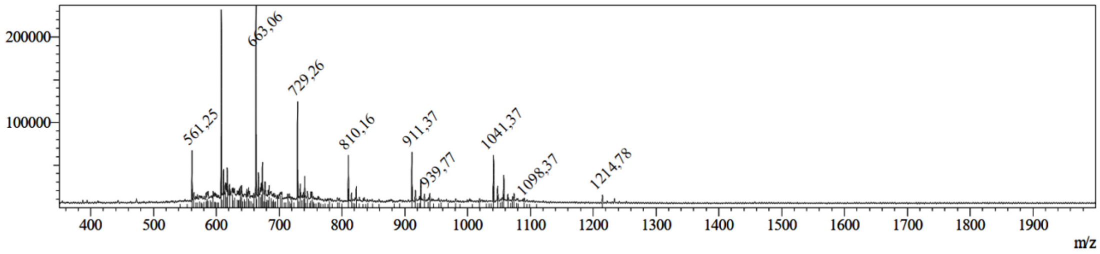

Figure S 28| ESI-MS of P14-PNA conjugate **18**. Calc. for $C_{306}H_{433}N_{143}O_{73}$: m/z: $[M+6H]^{6+}$ = 1214.79 (obs. 1214.78), $[M+7H]^{7+}$ = 1041.39 (obs. 1041.37), $[M+8H]^{8+}$ = 911.35 (obs. 911.37), $[M+9H]^{9+}$ = 810.20 (obs. 810.16), $[M+10H]^{10+}$ = 663.07 (obs. 663.06).

8.2.13 Analytical Data of DiSeL 20

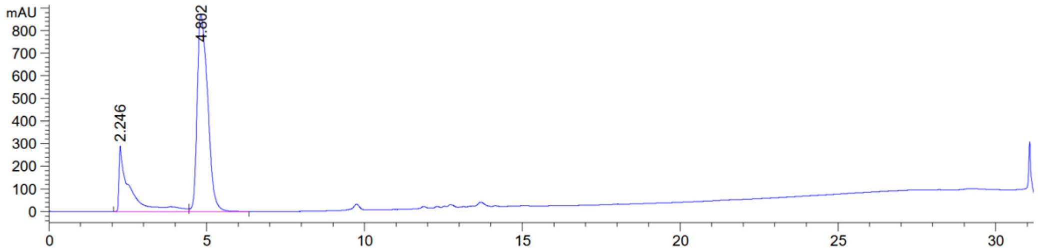

Figure S 29| Analytical RP-HPLC chromatogram of DiSeL **20**, 30 to 100 % eluent B (20 min gradient), 220 nm (top), t_R = 4.802 min.

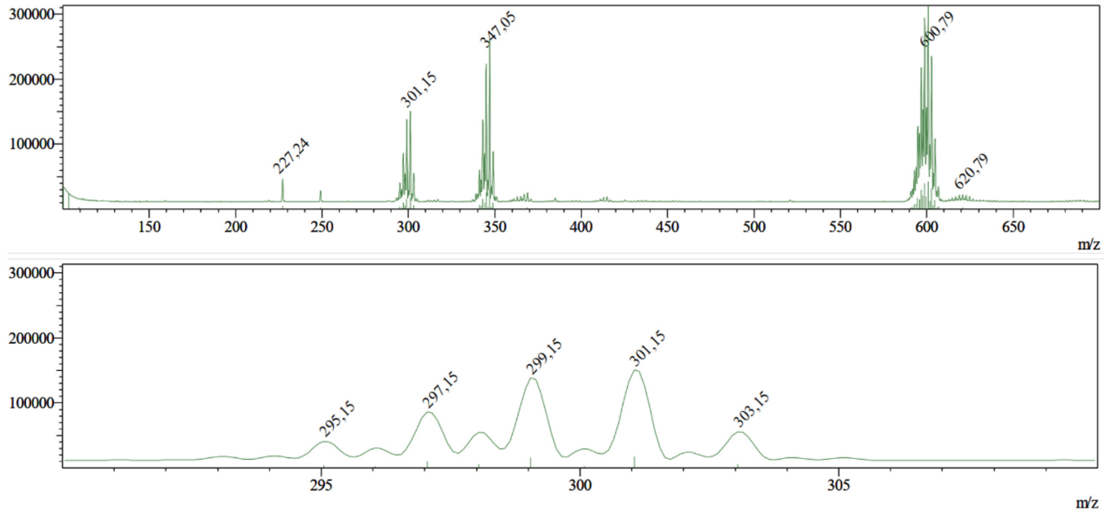

Figure S 30| ESI-MS of DiSeL **20** with complete spectrum (top) and excerpt (bottom, m/z = 290 – 310). Calc. for $C_8H_{14}O_2Se_2$: $[M-H]^-$ = 300.93 (biggest isotope peak) (obs. 301.15), 298.93 (second biggest isotope peak) (obs. 299.15).

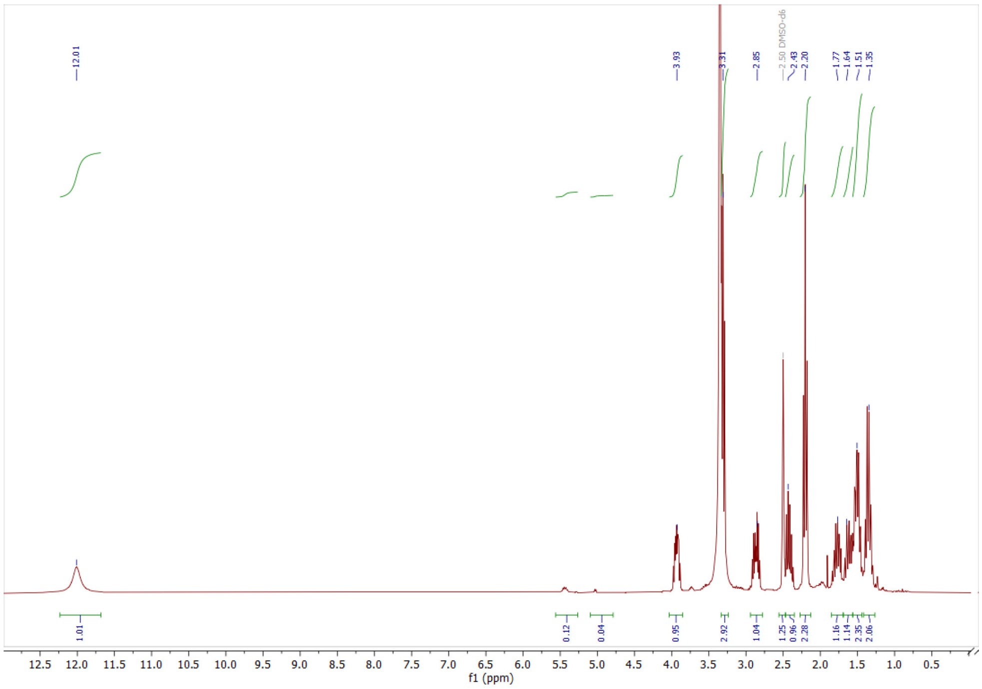

Figure S 31| ^{1}H NMR (300 MHz, DMSO-d_6) of DiSeL **20**.

8.2.14 Analytical Data of DiSeL-PNA Conjugate 22

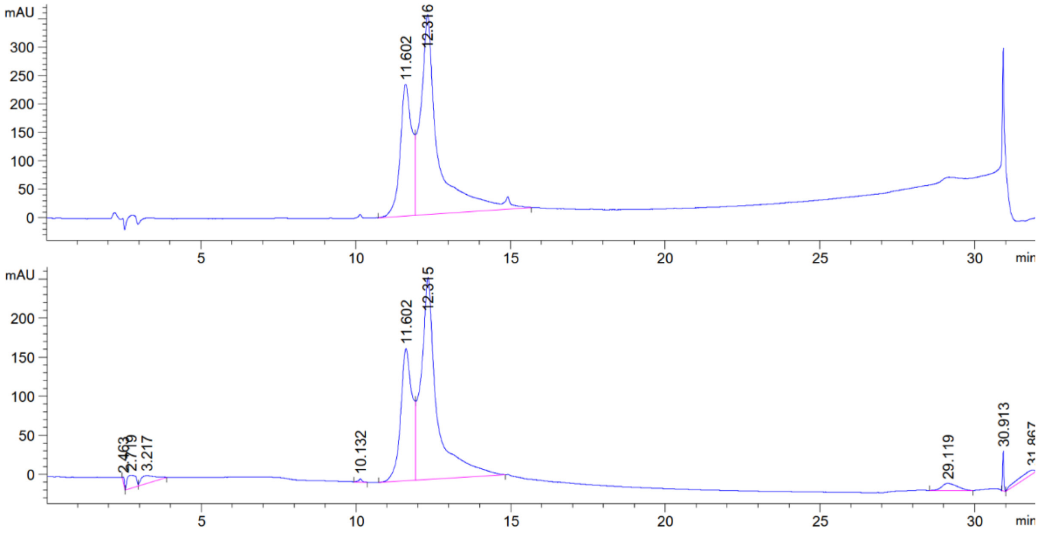

Figure S 32| Analytical RP-HPLC chromatogram of DiSeL-PNA conjugate **22**, 0 to 80 % eluent B (20 min gradient), 220 nm (top), 280 nm (bottom), t_R = 12.316 min (product), t_R = 11.602 min (side-product).

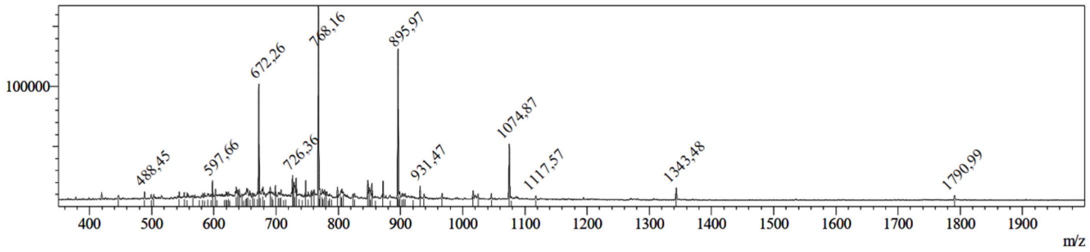

Figure S 33| ESI-MS of DiSeL-PNA conjugate **22** (product). Calc. for $C_{306}H_{433}N_{143}O_{73}$ (main product): m/z: $[M+4H]^{4+}$ = 1343.53 (obs. 1343.48), $[M+5H]^{5+}$ = 1075.03 (obs. 1074.87), $[M+6H]^{6+}$ = 896.02 (obs. 895.97), $[M+7H]^{7+}$ = 768.16 (obs. 768.16), $[M+8H]^{8+}$ = 672.27 (obs. 672.26), $[M+9H]^{9+}$ = 597.68 (obs. 597.66).

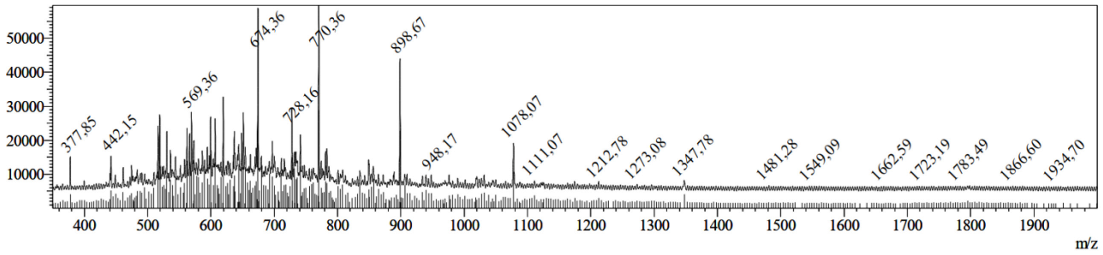

Figure S 34| ESI-MS of DiSeL-PNA conjugate **22** (side-product). Calc. for $C_{306}H_{433}N_{143}O_{74}$ (side product): m/z: $[M+4H]^{4+}$ = 1347.53 (obs. 1347.78), $[M+5H]^{5+}$ = 1078.23 (obs. 1078.07), $[M+6H]^{6+}$ = 898.69 (obs. 898.67), $[M+7H]^{7+}$ = 770.45 (obs. 770.36), $[M+8H]^{8+}$ = 674.27 (obs. 674.36).

8.2.15 Analytical Data of *N*-Boc-Cadaverine-Dextran 25 (Variant A)

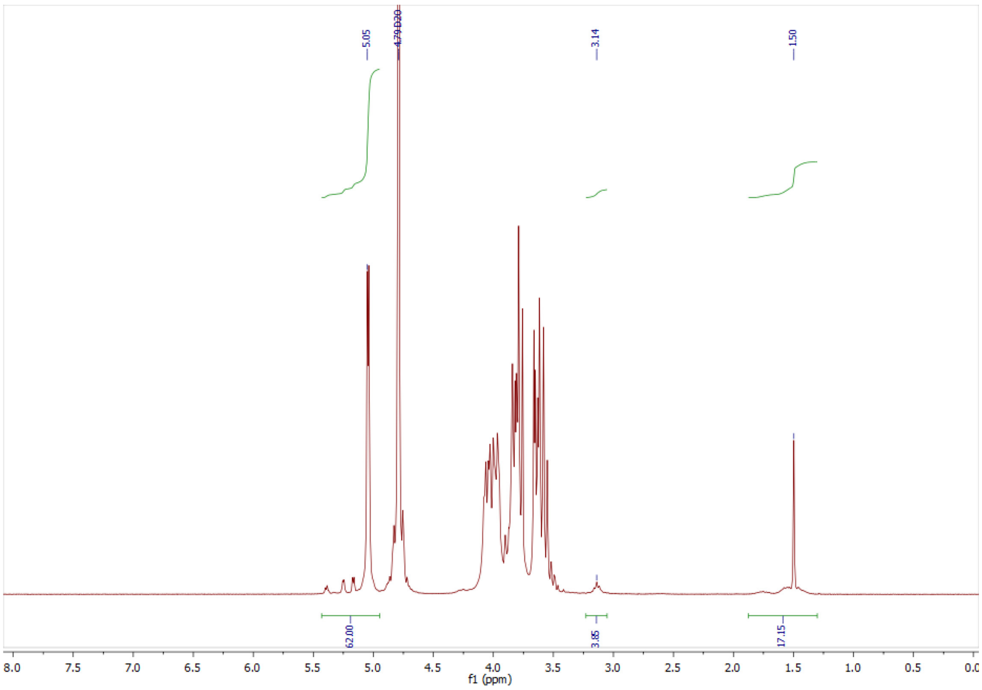

Figure S 35| ^{1}H NMR (300 MHz, D_2O) of *N*-Boc-cadaverine-dextran **25** (obtained by variant A).

8.2.16 Analytical Data of *N*-Boc-Cadaverine-Dextran 25 (Variant B)

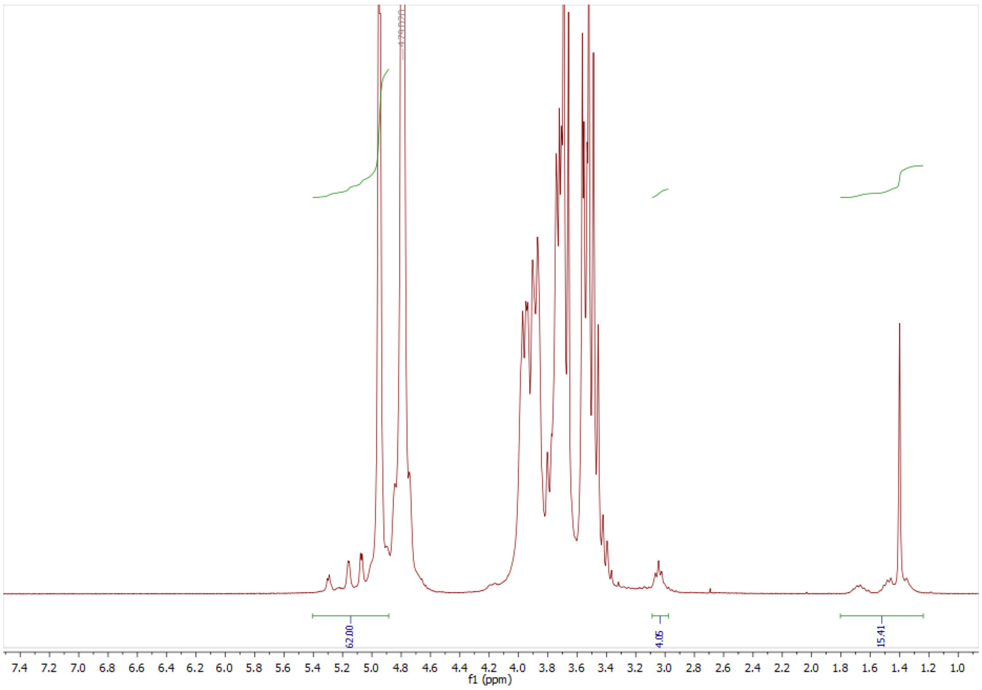

Figure S 36| ^{1}H NMR (300 MHz, D_2O) of *N*-Boc-cadaverine-dextran **25** (obtained by variant B).

8.2.17 Analytical Data of *N*-Boc-Cadaverine-Dextran-(CE)$_{5.4}$ 26

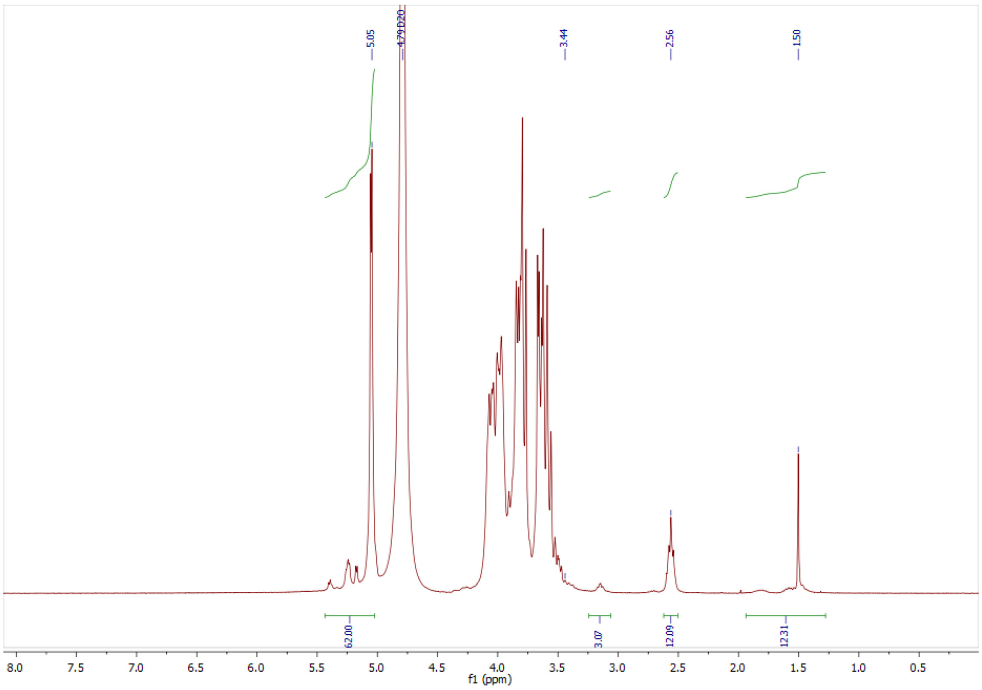

Figure S 37| ^{1}H NMR (300 MHz, D_2O) of *N*-Boc-cadaverine-dextran-(CE)$_{5.4}$ **26**.

8.2.18 Analytical Data of *N*-(5-Aminopentyl)-2-Azidoacetamide 27

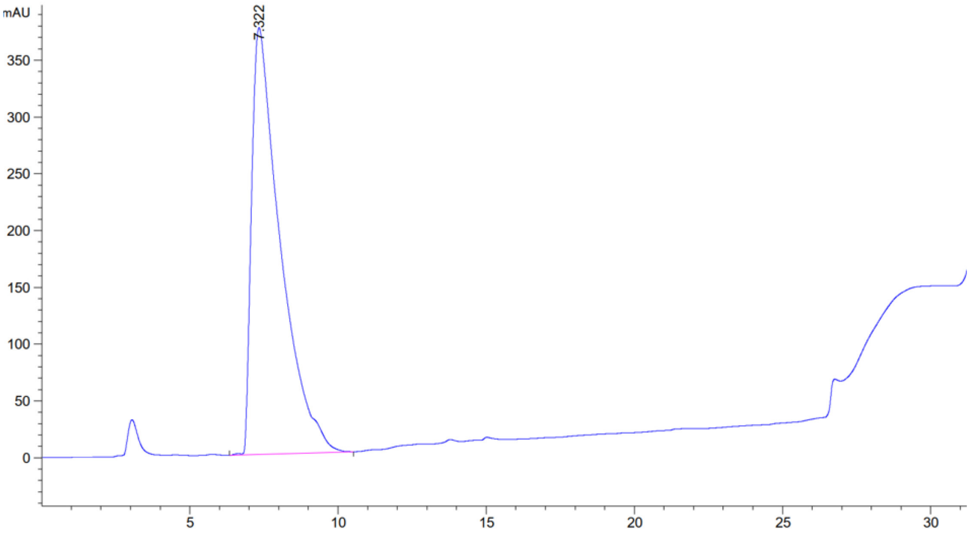

Figure S 38| Analytical RP-HPLC chromatogram of *N*-(5-aminopentyl)-2-azidoacetamide **27**, 0 to 40 % eluent B (20 min gradient), 220 nm, t_R = 7.322 min.

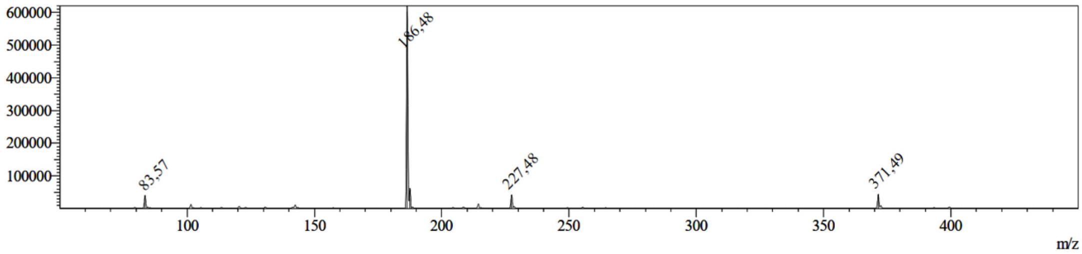

Figure S 39| ESI-MS of *N*-(5-aminopentyl)-2-azidoacetamide **27**. Calc. for $C_7H_{15}N_5O$: m/z: $[M+H]^+$ = 186.24 (obs. 186.48).

8.2.19 Analytical Data of *N*-Boc-Cadaverine-Dextran-$(N_3)_{5.4}$ 28, Batch 1

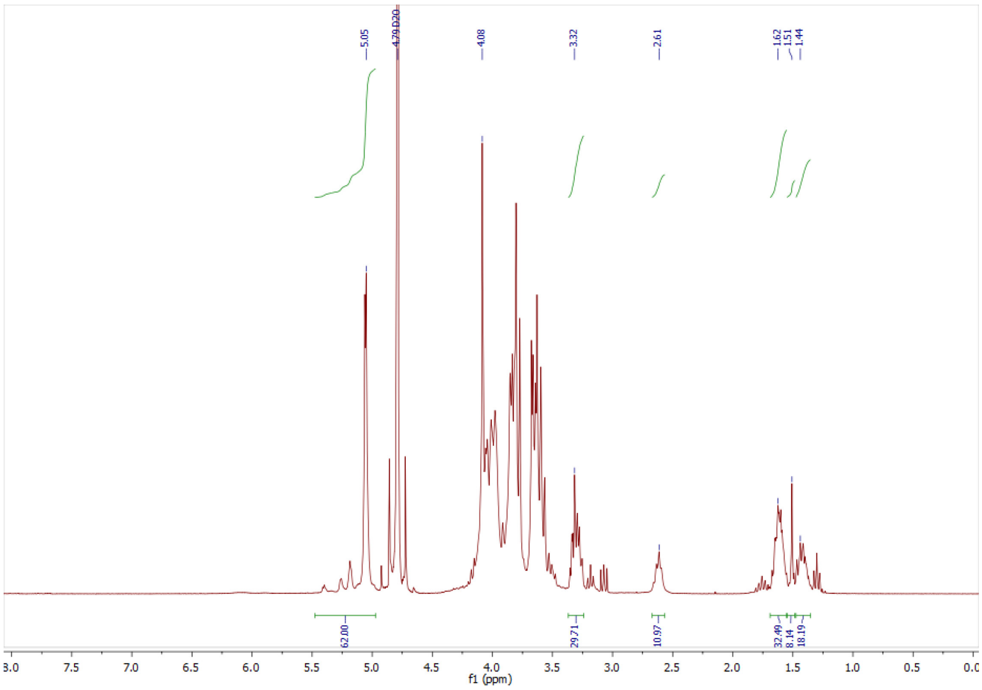

Figure S 40| ^1H NMR (300 MHz, D_2O) of *N*-Boc-cadaverine-dextran-$(N_3)_{5.4}$ **28**, batch 1.

8.2.20 Analytical Data of *N*-Boc-Cadaverine-Dextran-$(N_3)_{5.4}$ 28, Batch 2

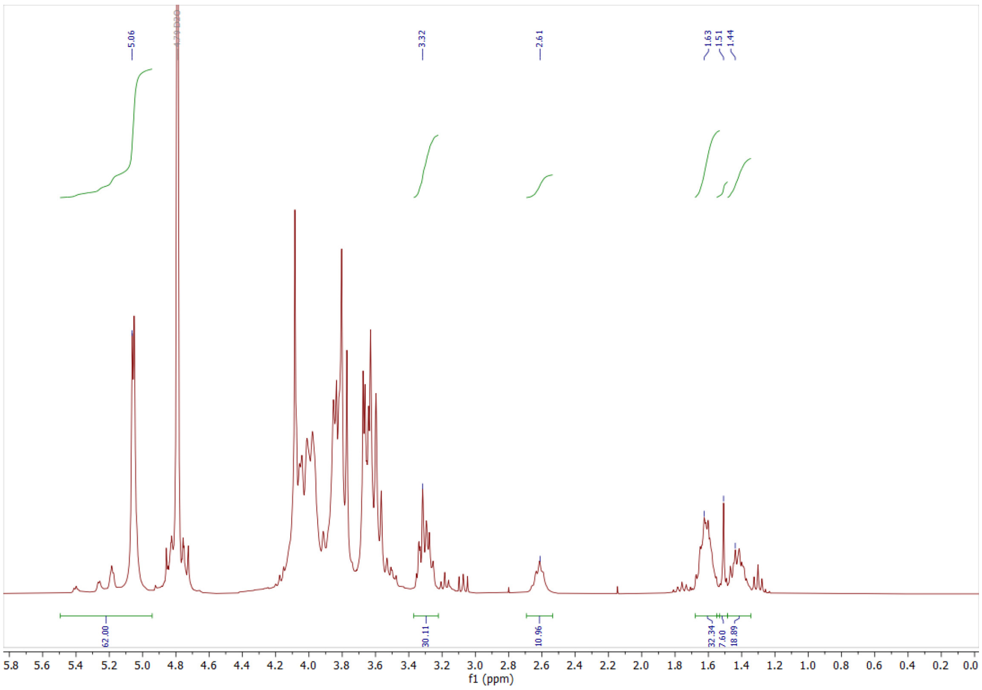

Figure S 41| ^1H NMR (300 MHz, D_2O) of *N*-Boc-cadaverine-dextran-$(N_3)_{5.4}$ **28**, batch 2.

8.2.21 Analytical Data of Cadaverine-Dextran-$(N_3)_{5.4}$ 29, Batch 1

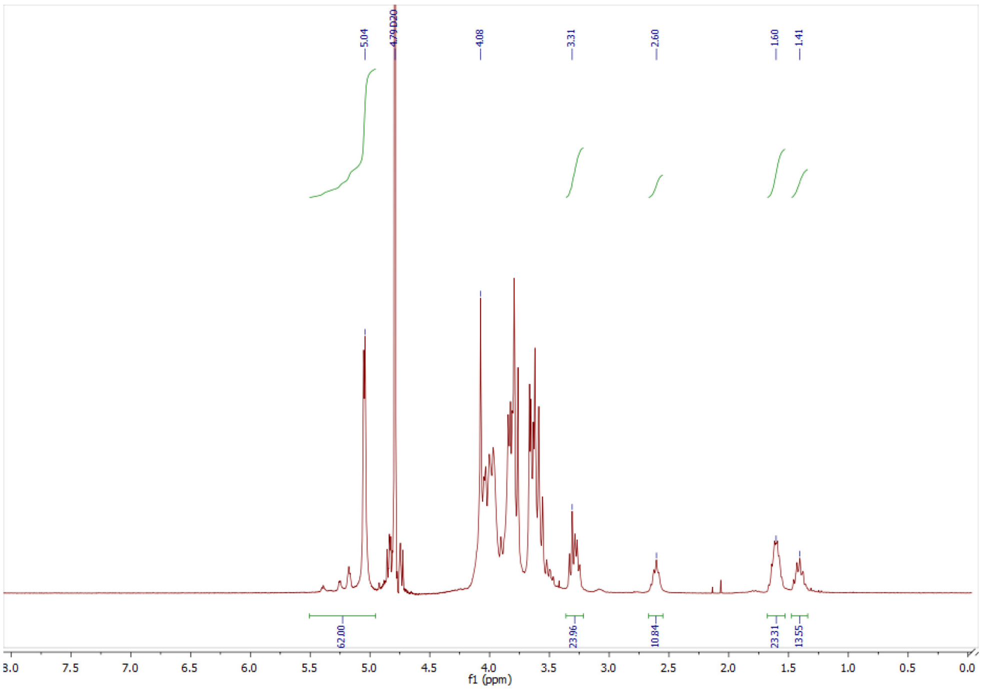

Figure S 42| ^1H NMR (300 MHz, D_2O) of cadaverine-dextran-$(N_3)_{5.4}$ **29**, batch 1.

8.2.22 Analytical Data of Cadaverine-Dextran-$(N_3)_{5.4}$ 29, Batch 2

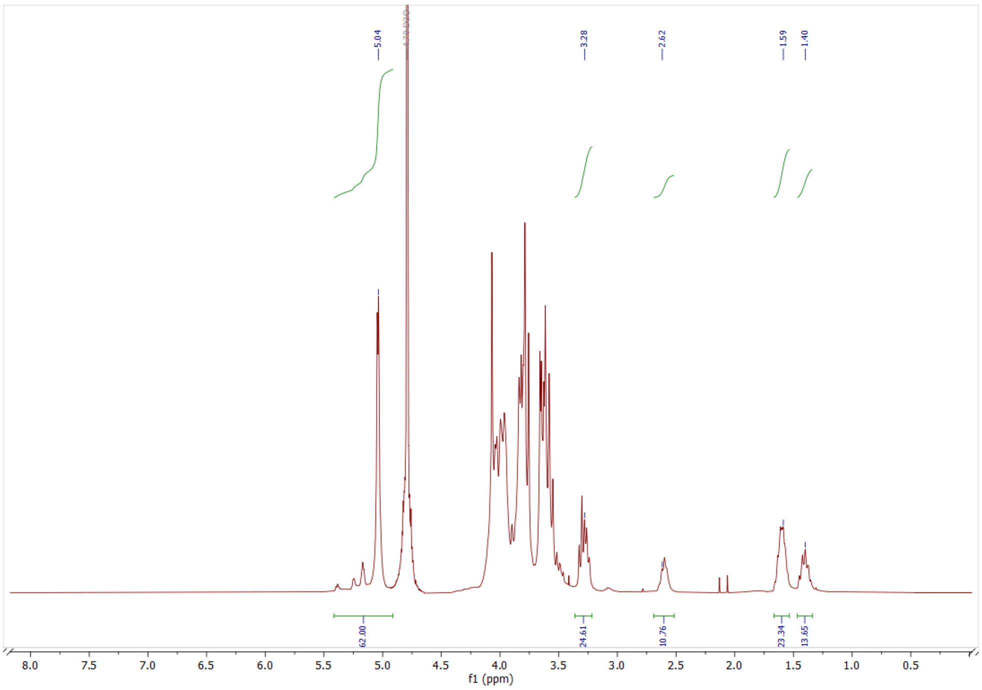

Figure S 43| ^{1}H NMR (300 MHz, D_2O) of cadaverine-dextran-$(N_3)_{5.4}$ **29**, batch 2.

8.2.23 Analytical Data of TAMRA-Cadaverine-Dextran-$(N_3)_{5.4}$ 31

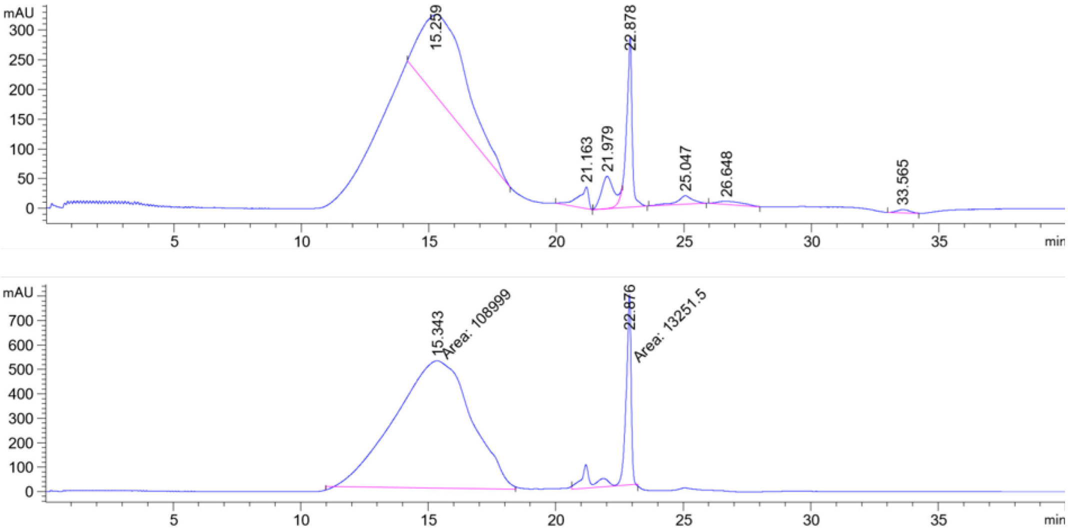

Figure S 44| Analytical SEC-HPLC chromatogram of TAMRA-cadaverine-dextran-$(N_3)_{5.4}$ **31**, isocratic 30% B (40 min), 220 nm (top), 550 nm (bottom), t_R = 15.259 min.

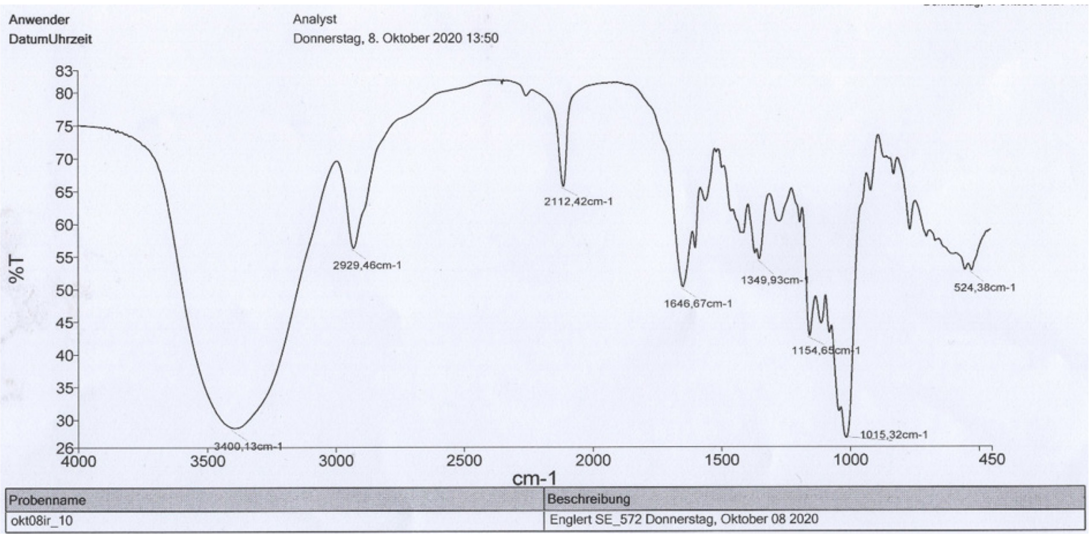

Figure S 45| IR spectrum (KBr pellet) of TAMRA-cadaverine-dextran-$(N_3)_{5.4}$ **31** with azide band at a wavenumber of 2112.42 cm^{-1}.

8.2.24Analytical Data of L17E-Pra 32

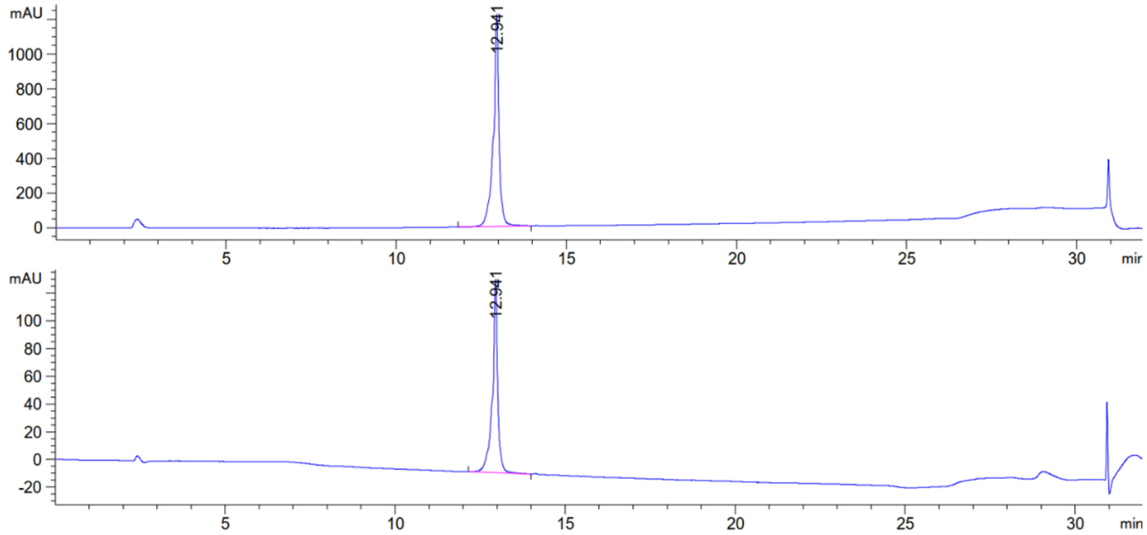

Figure S 46| Analytical RP-HPLC chromatogram of L17E-Pra **32**, 10 to 80 % eluent B (20 min gradient), 220 nm, t_R = 12.941 min.

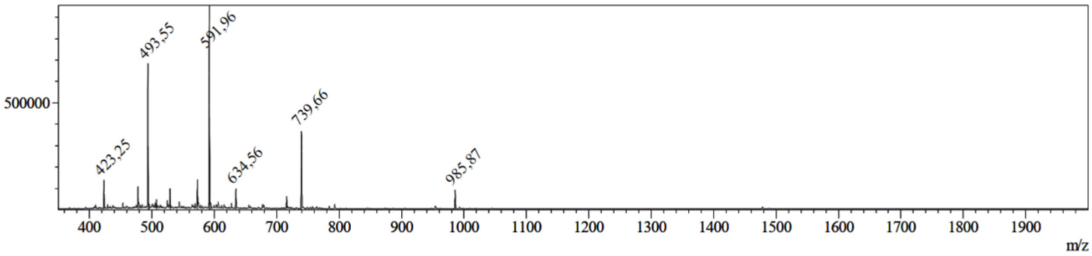

Figure S 47| ESI-MS of L17E-Pra **32**. Calc. for $C_{139}H_{225}N_{39}O_{32}$: m/z: $[M+3H]^{3+}$ = 985.86 (obs. 985.87), $[M+4H]^{4+}$ = 739.64 (obs. 739.66), $[M+5H]^{5+}$ = 591.91 (obs. 591.96), $[M+6H]^{6+}$ = 493.43 (obs. 493.55).

8.2.25Analytical Data of Alkyne-GFP11 33

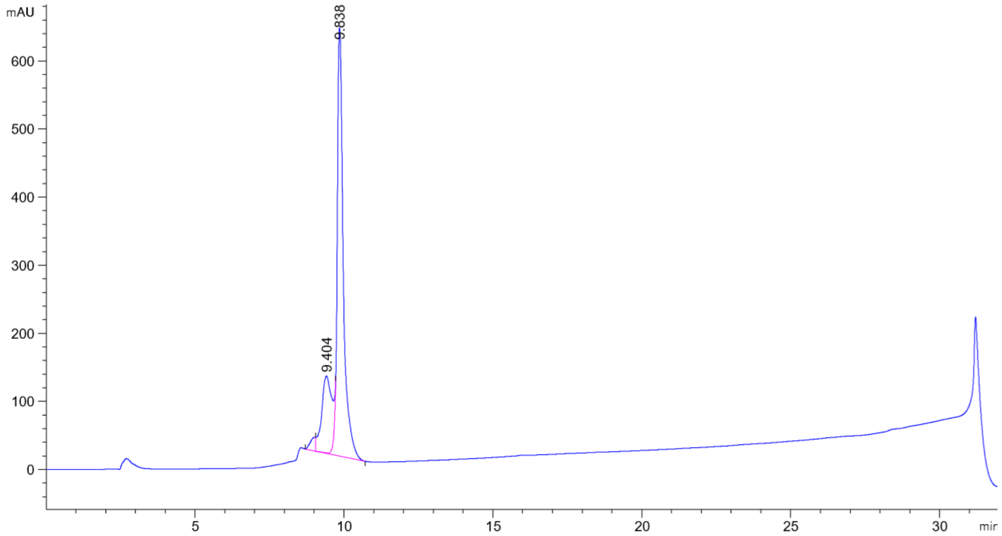

Figure S 48| Analytical RP-HPLC chromatogram of alkyne-GFP11 **33**, 20 to 80 % eluent B (20 min gradient), 220 nm, t_R = 9.838 min.

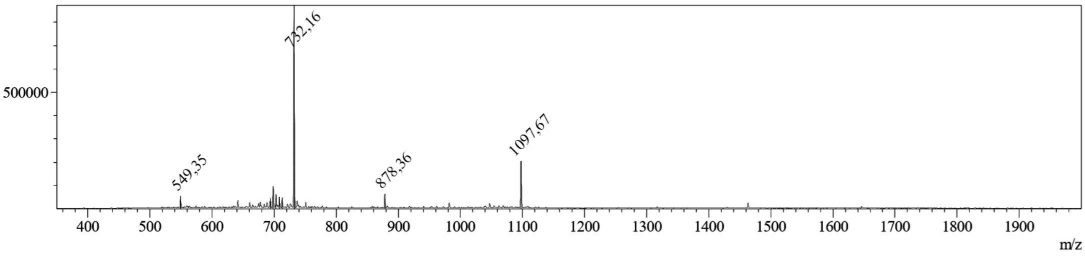

Figure S 49| ESI-MS of alkyne-GFP11 **33**. Calc. for $C_{94}H_{145}N_{29}O_{30}S$: m/z: $[M+2H]^{2+}$ = 1097.70 (obs. 1097.67), $[M+3H]^{3+}$ = 732.13 (obs. 732.16), $[M+4H]^{4+}$ = 549.35 (obs. 549.35).

8.2.26 Analytical Data of TAMRA-Cadaverine-Dextran-L17E-GFP11 34

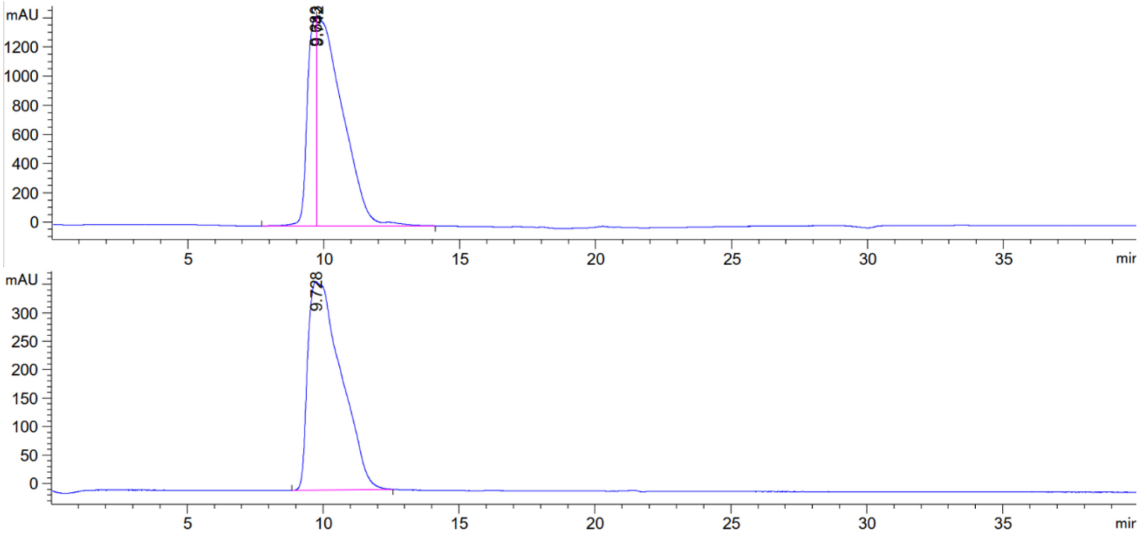

Figure S 50| Analytical SEC-HPLC chromatogram of TAMRA-cadaverine-dextran-L17E-GFP11 **34**, isocratic 30% B (40 min), 220 nm (top), 550 nm (bottom), t_R = 9.742 min.

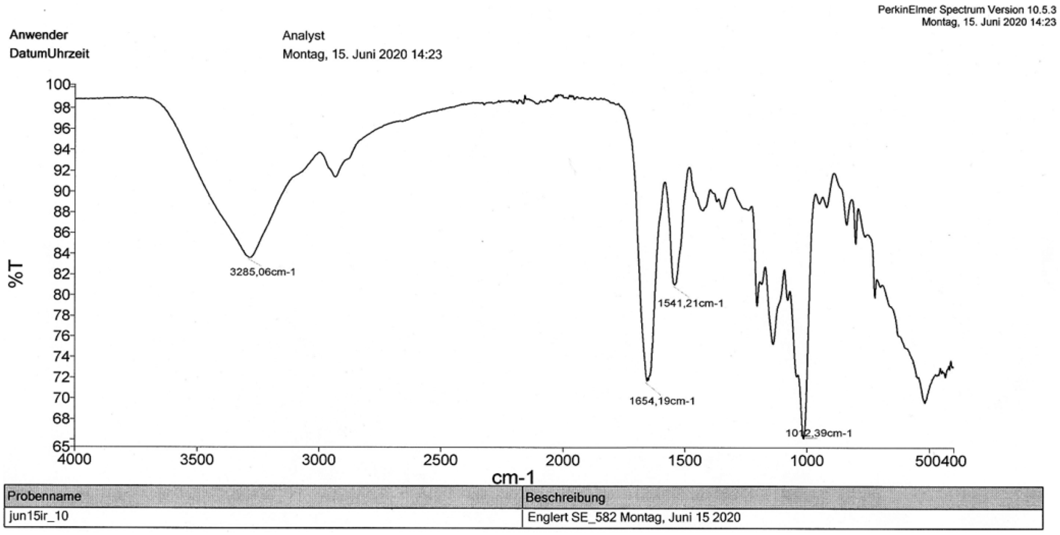

Figure S 51| IR spectrum (ATR) of TAMRA-cadaverine-dextran-L17E-GFP11 **34**. The azide band at wavenumber 2112 cm^{-1} from the parent dextran **31** completely disappeared.

8.2.27 Analytical Data of TAMRA-Cadaverine-Dextran-GFP11 35

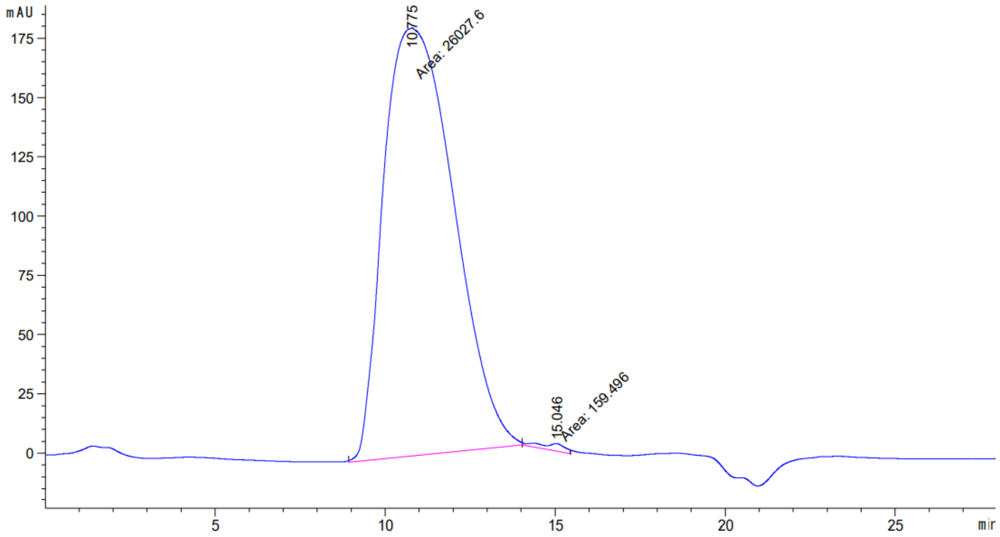

Figure S 52| Analytical SEC-HPLC chromatogram of TAMRA-cadaverine-dextran-GFP11 **35**, isocratic 30% B (28 min), 220 nm, t_R = 10.775 min.

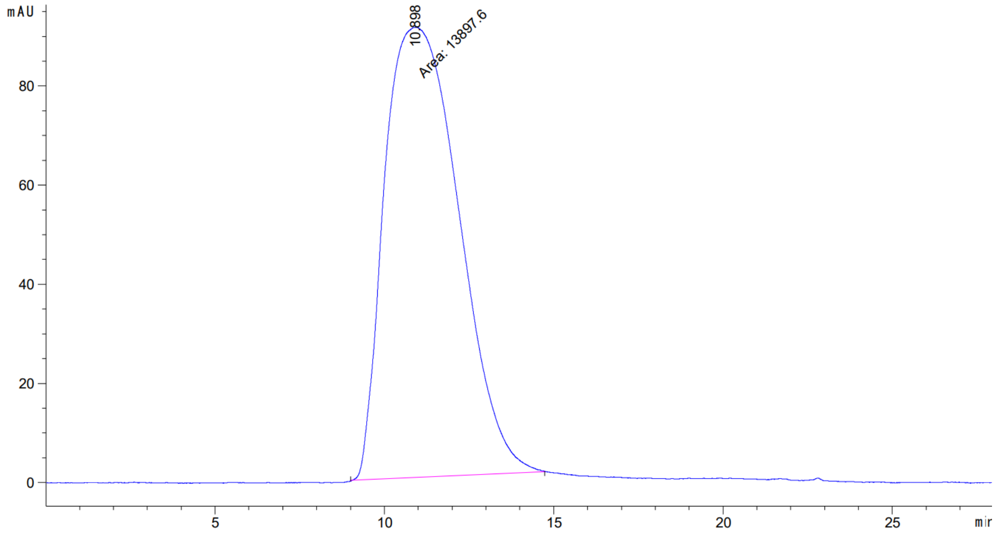

Figure S 53| Analytical SEC-HPLC chromatogram of TAMRA-cadaverine-dextran-GFP11 **35**, isocratic 30% B (28 min), 550 nm.

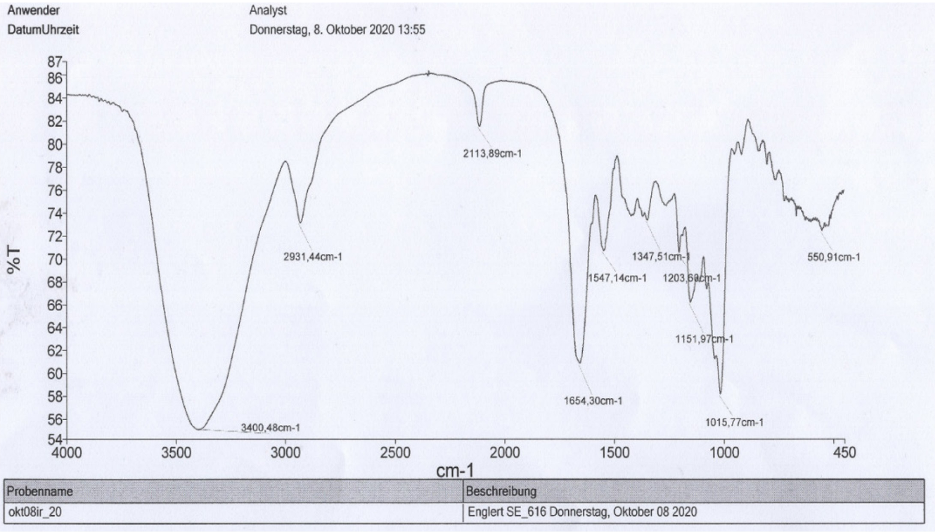

Figure S 54| IR spectrum (KBr pellet) of TAMRA-cadaverine-dextran-GFP11 **35** with azide band at a wavenumber of 2113.89 cm^{-1}. Compared to the parent dextran **31**, the intensity of the azide band is distinctly reduced.

8.2.28 Analytical Data of GFP11 36

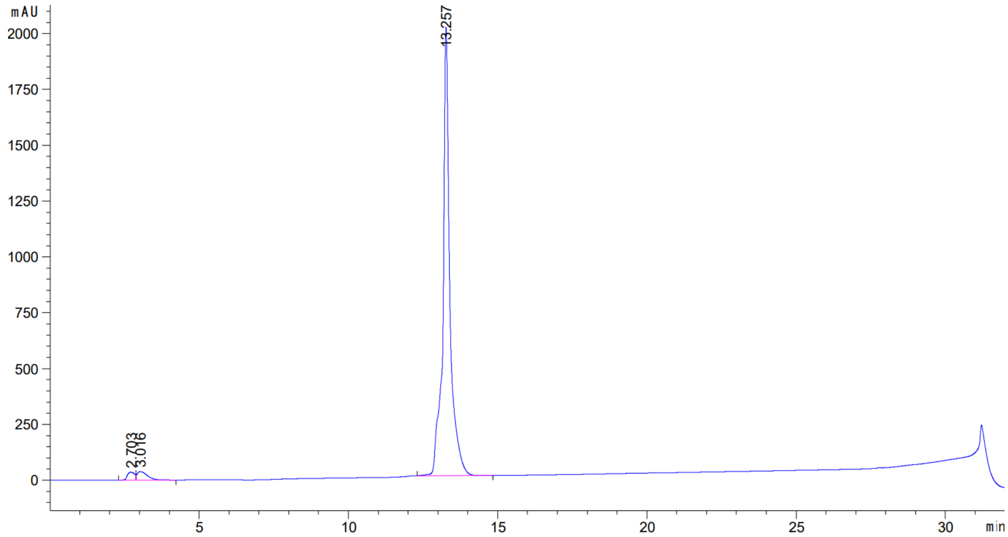

Figure S 55| Analytical RP-HPLC chromatogram of GFP11 **36**, 10 to 60 % eluent B (20 min gradient), 220 nm, t_R = 13.257 min.

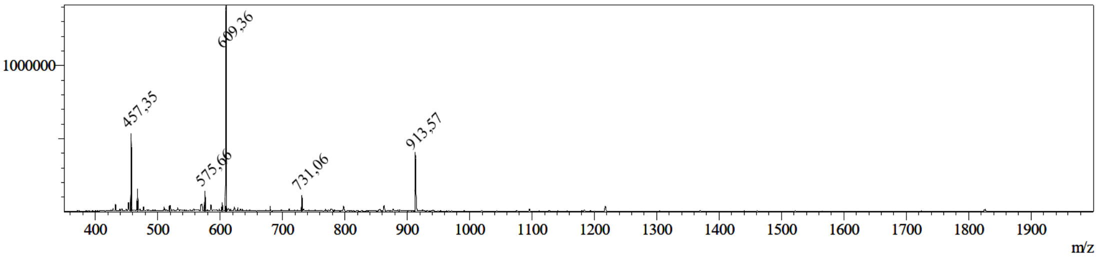

Figure S 56| ESI-MS of GFP11 **36**. Calc. for $C_{79}H_{125}N_{25}O_{23}S$: m/z: $[M+2H]^{2+}$ = 913.53 (obs. 913.57), $[M+3H]^{3+}$ = 609.35 (obs. 609.36), $[M+4H]^{4+}$ = 457.25 (obs. 457.37).

8.2.29 Analytical Data of Biotin-NHS 37

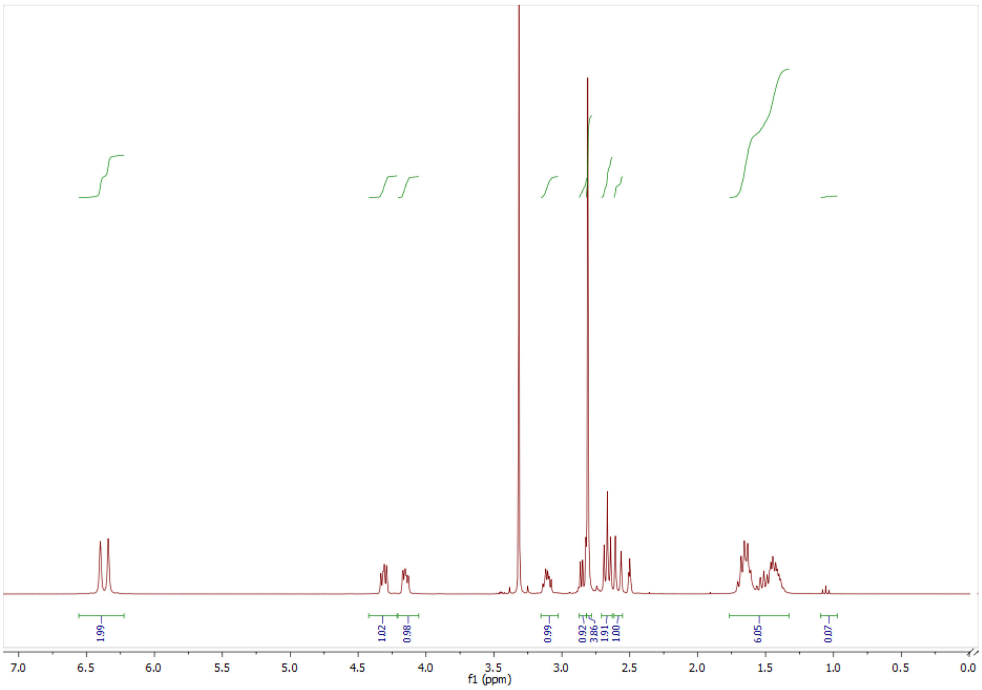

Figure S 57| ^{1}H NMR (300 MHz, DMSO-d_6) of biotin-NHS **37**.

8.2.30 Analytical Data of Biotin-Cadaverine-Dextran-$(N_3)_{5.4}$ 38

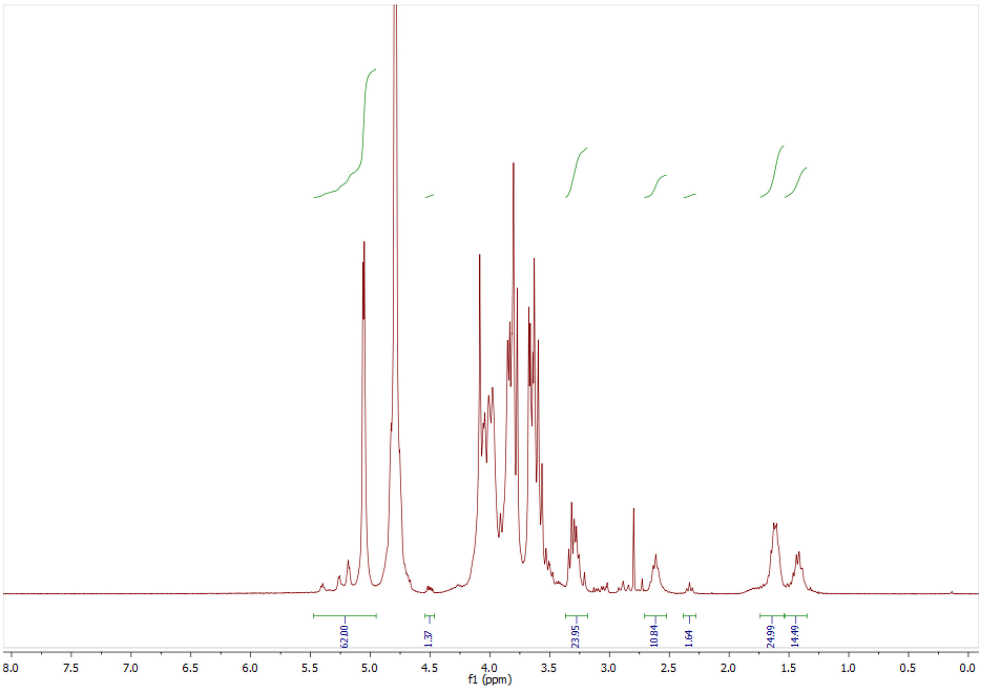

Figure S 58| ^{1}H-NMR (300 MHz, D_2O) of biotin-cadaverine-dextran-$(N_3)_{5.4}$ **38**.

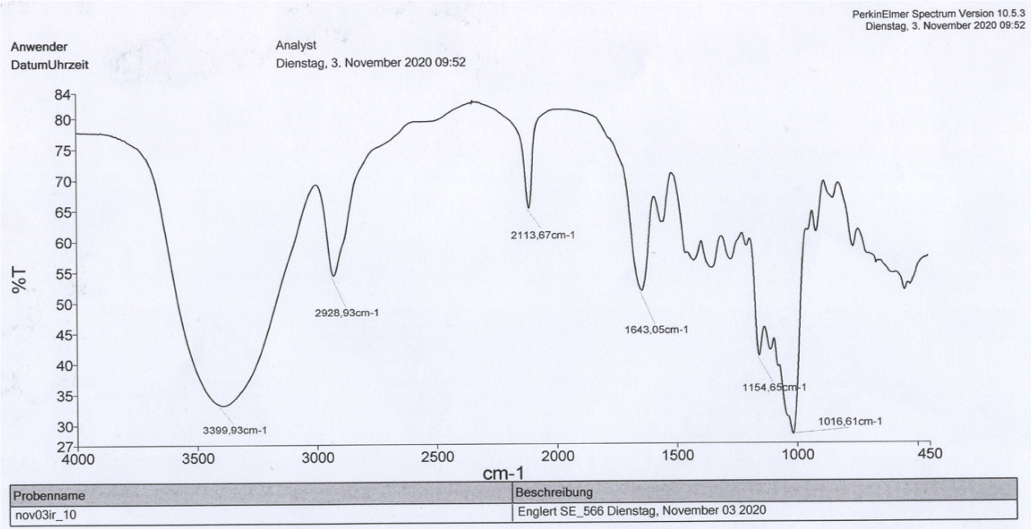

Figure S 59| IR spectrum (KBr pellet) of biotin-cadaverine-dextran-$(N_3)_{5.4}$ **38** with azide band at wavenumber of 2113.67 cm^{-1}.

8.2.31 Analytical Data of P14-Pra 39

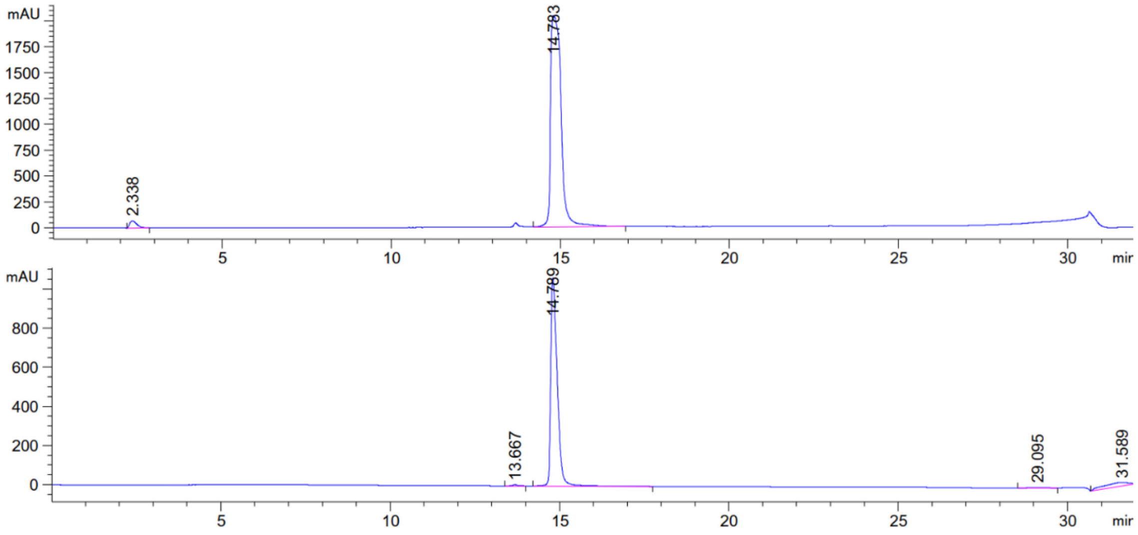

Figure S 60| Analytical RP-HPLC chromatogram of P14-Pra **39**, 0 to 40 % eluent B (20 min gradient), 220 nm (top), 280 nm (bottom) t_R = 14.783 min.

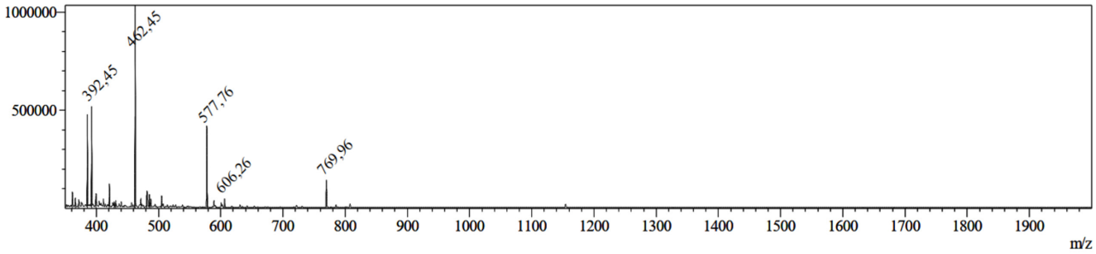

Figure S 61| ESI-MS of P14-Pra **39**. Calc. for $C_{107}H_{176}N_{42}O_{16}$: m/z: $[M+3H]^{3+}$ = 769.94 (obs. 769.96), $[M+4H]^{4+}$ = 577.70 (obs. 577.76), $[M+5H]^{5+}$ = 462.36 (obs. 462.45).

8.2.32 Analytical Data of Biotin-Cadaverine-Dextran-L17E$_{5.4}$ 40

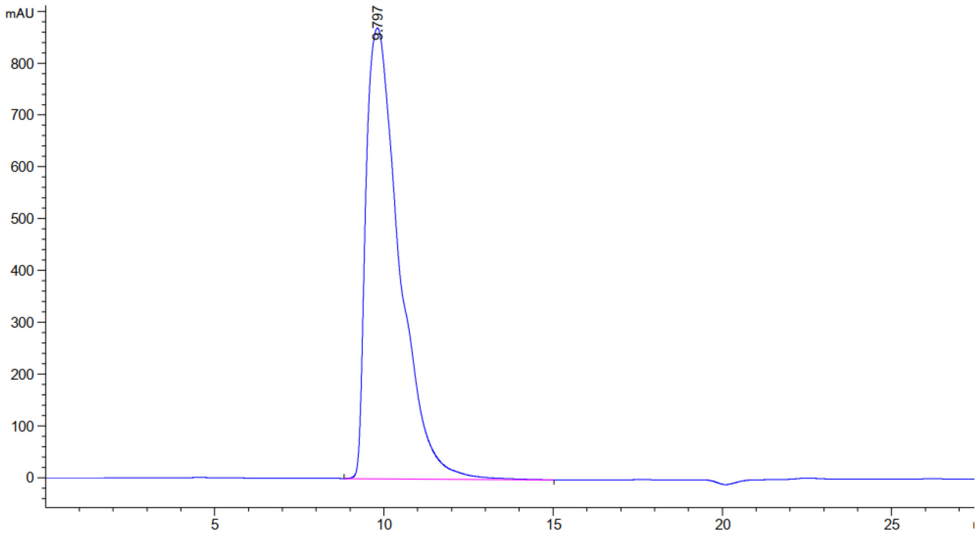

Figure S 62| Analytical SEC-HPLC chromatogram of biotin-cadaverine-dextran-L17E$_{5.4}$ **40**, isocratic 30% B (28 min), 220 nm, t_R = 9.797 min.

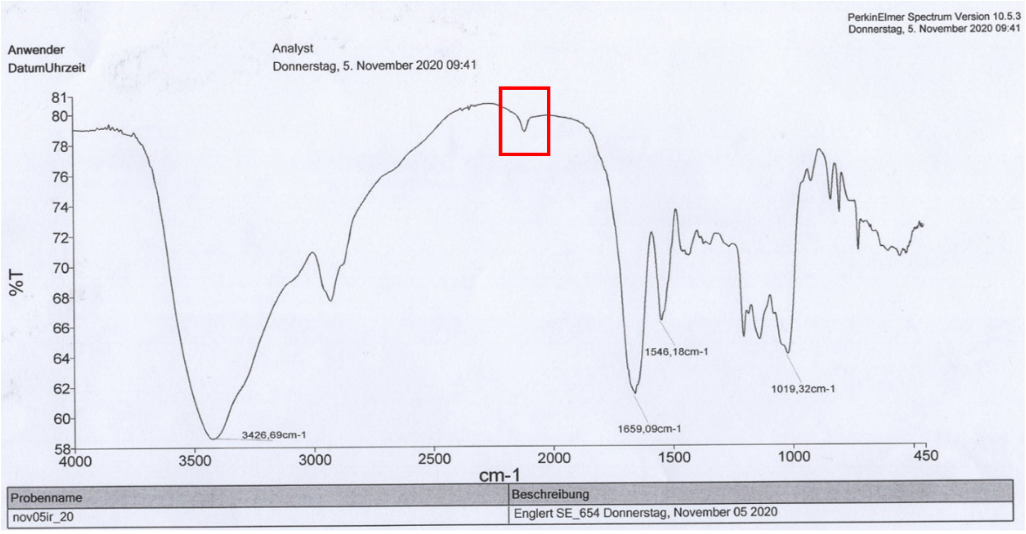

Figure S 63| IR spectrum (KBr pellet) of biotin-cadaverine-dextran-L17E$_{5.4}$ **40**. Compared to the parent dextran **38**, the intensity of the azide band (red box) is distinctly reduced.

8.2.33 Analytical Data of Biotin-Cadaverine-Dextran-P14$_{5.4}$ 41

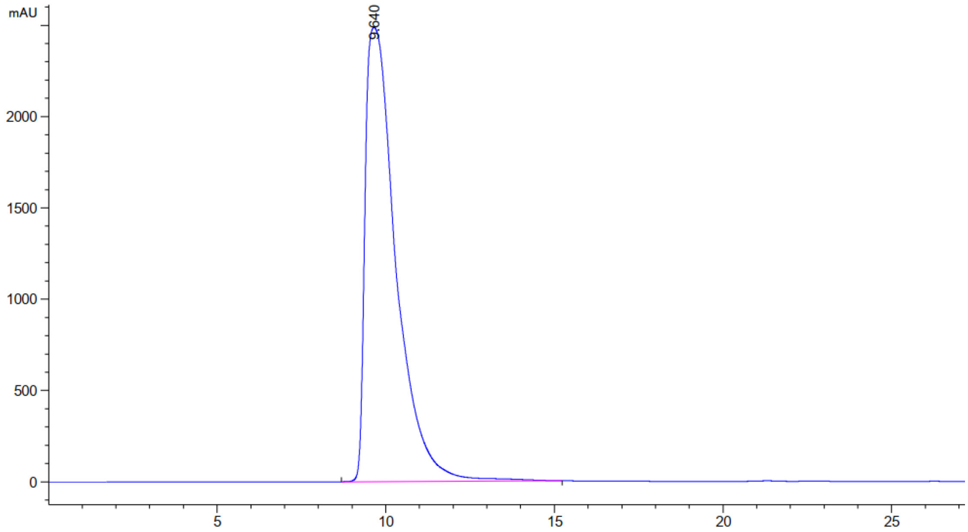

Figure S 64| Analytical SEC-HPLC chromatogram of biotin-cadaverine-dextran-P14$_{5.4}$ **41**, isocratic 30% B (28 min), 220 nm, t_R = 9.640 min.

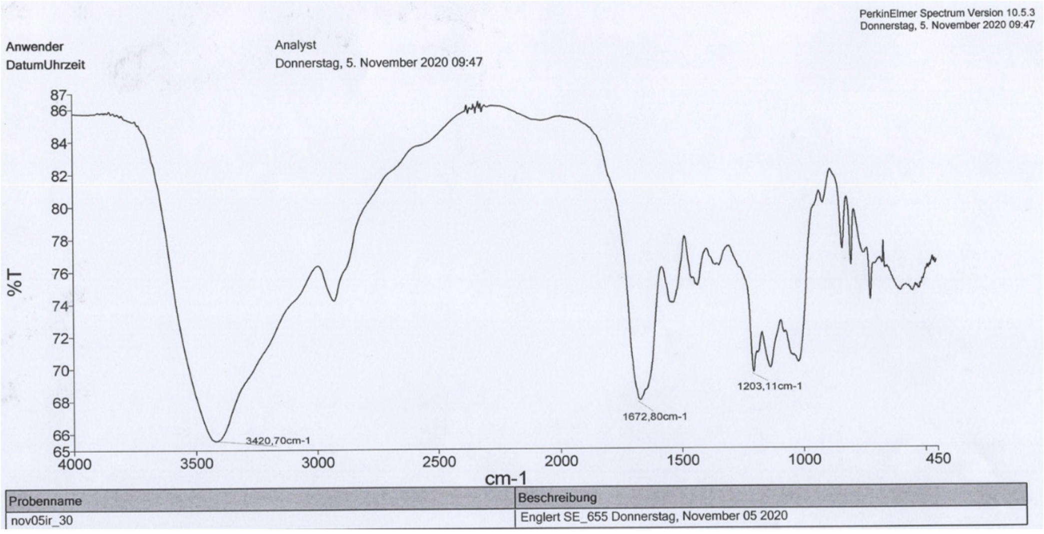

Figure S 65| IR spectrum (KBr pellet) of biotin-cadaverine-dextran-P14$_{5.4}$ **41**. Compared to the parent dextran **38**, the azide band at 2113.67 cm^{-1} disappeared.

8.2.34 Analytical Data of L17E-K(Ahx-Biotin) 42

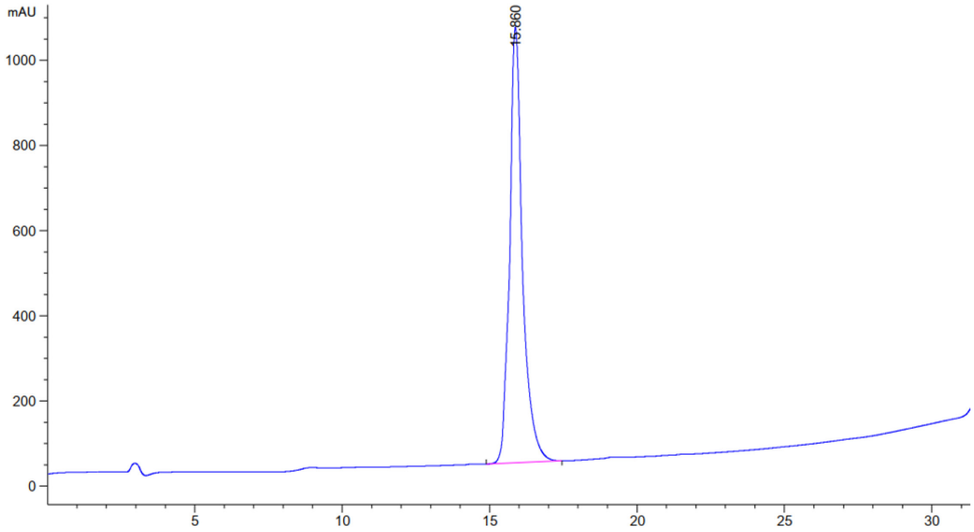

Figure S 66| Analytical RP-HPLC chromatogram of L17E-K(Ahx-Biotin) **42**, 0 to 80 % eluent B (20 min gradient), 220 nm, t_R = 15.860 min.

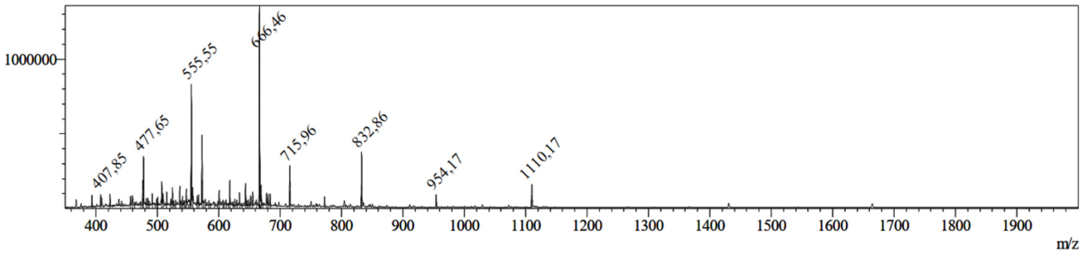

Figure S 67| ESI-MS of L17E-K(Ahx-Biotin) **42**. Calc. for $C_{107}H_{176}N_{42}O_{16}$: m/z: $[M+3H]^{3+}$ = 1110.03 (obs. 1110.17), $[M+4H]^{4+}$ = 832.78 (obs. 832.86), $[M+5H]^{5+}$ = 666.42 (obs. 666.46), $[M+6H]^{6+}$ = 555.52 (obs. 555.55).

8.2.35 Analytical Data of P14-K(Ahx-Biotin) 43

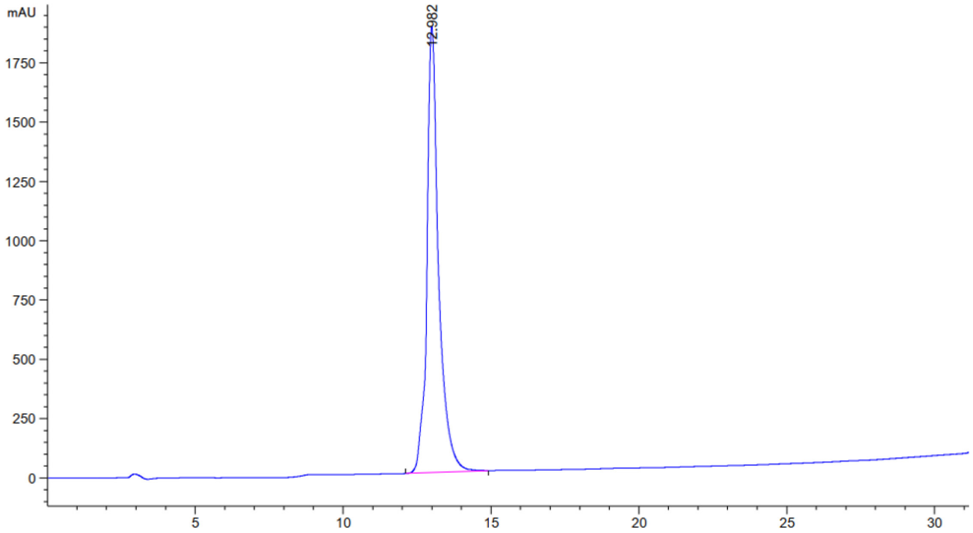

Figure S 68| Analytical RP-HPLC chromatogram of P14-K(Ahx-biotin) **43**, 0 to 80 % eluent B (20 min gradient), 220 nm, t_R = 12.982 min.

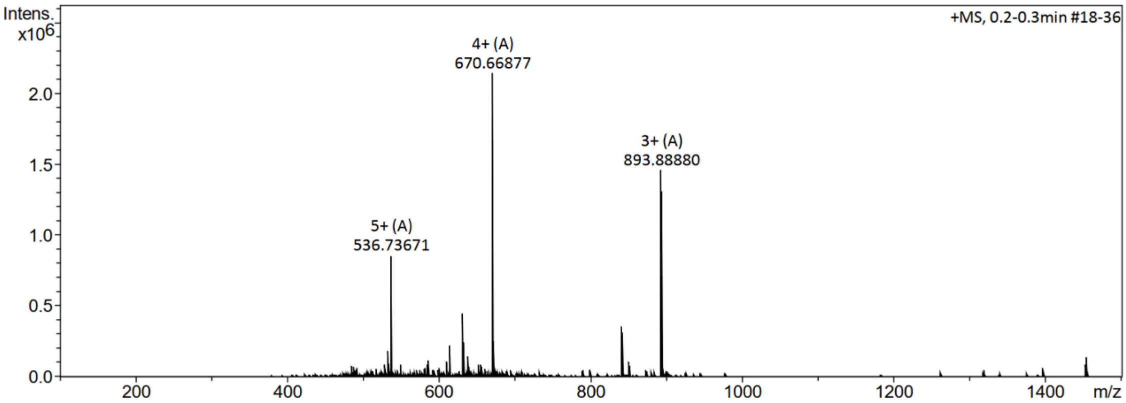

Figure S 69| HR-ESI-MS of P14-K(Ahx-biotin) **43**. Calc. for $C_{124}H_{208}N_{46}O_{19}S$: m/z: $[M+3H]^{3+}$ = 893.88988 (obs. 893.88880), $[M+4H]^{4+}$ = 670.66923 (obs. 670.66877), $[M+5H]^{5+}$ = 536.73684 (obs. 536.73671).

8.2.36 Analytical Data of (1R,8S,9S,Z)-Ethyl bicyclo[6.1.0]non-4-ene-9-carboxylate 44

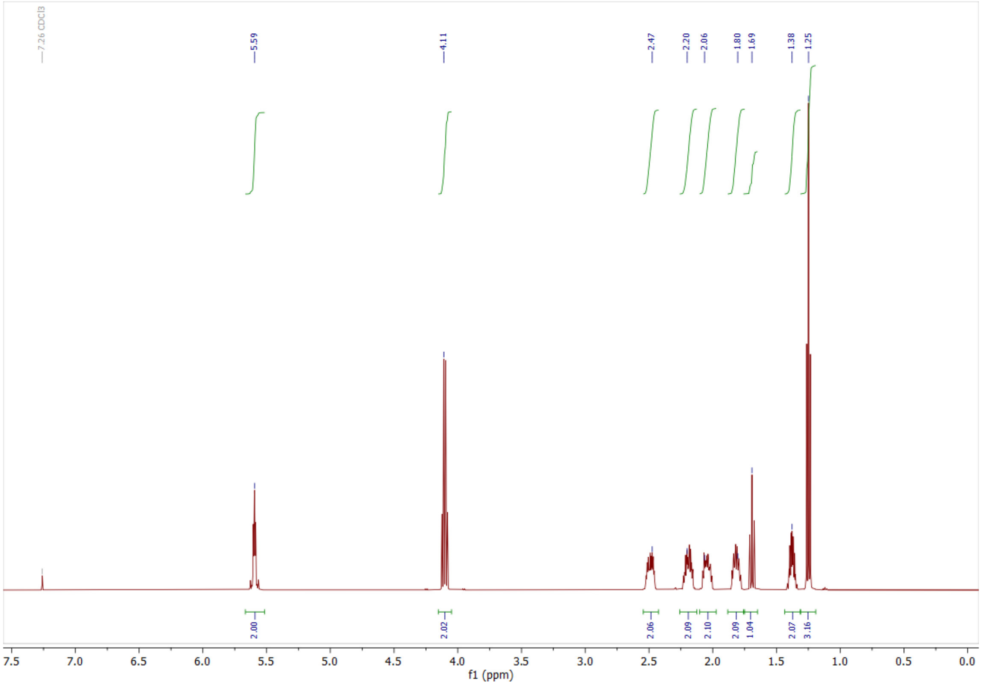

Figure S 70| ^{1}H NMR (500 MHz, $CDCl_3$) of (1R,8S,9S,Z)-ethyl bicyclo[6.1.0]non-4-ene-9-carboxylate (Endo) **44**.

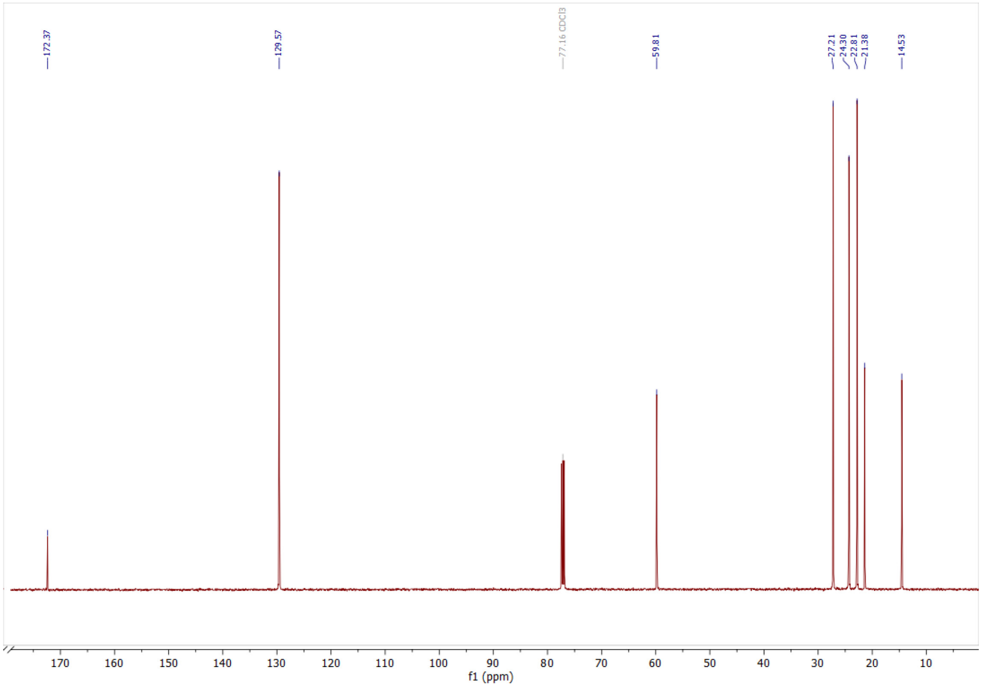

Figure S 71| ^{13}C NMR (126 MHz, $CDCl_3$) of (1R,8S,9S,Z)-ethyl bicyclo[6.1.0]non-4-ene-9-carboxylate (Endo) **44**.

8.2.37 Analytical Data of (1R,8S,9R,Z)-Ethyl bicyclo[6.1.0]non-4-ene-9-carboxylate 45

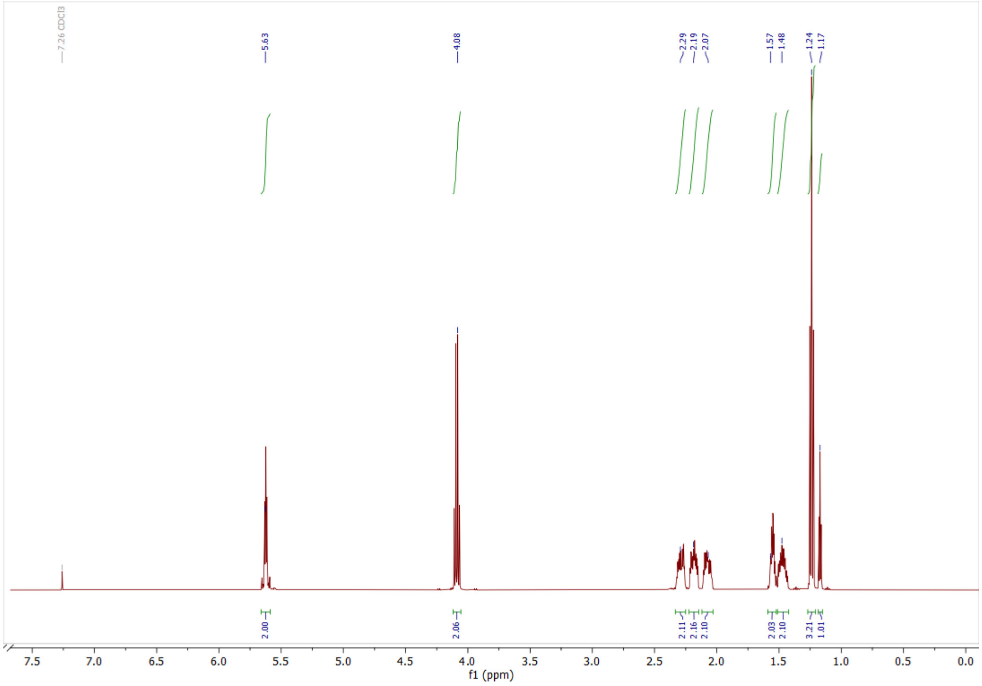

Figure S 72| ^{1}H NMR (500 MHz, $CDCl_3$) of (1R,8S,9R,Z)-ethyl bicyclo[6.1.0]non-4-ene-9-carboxylate (*Exo*) **45**.

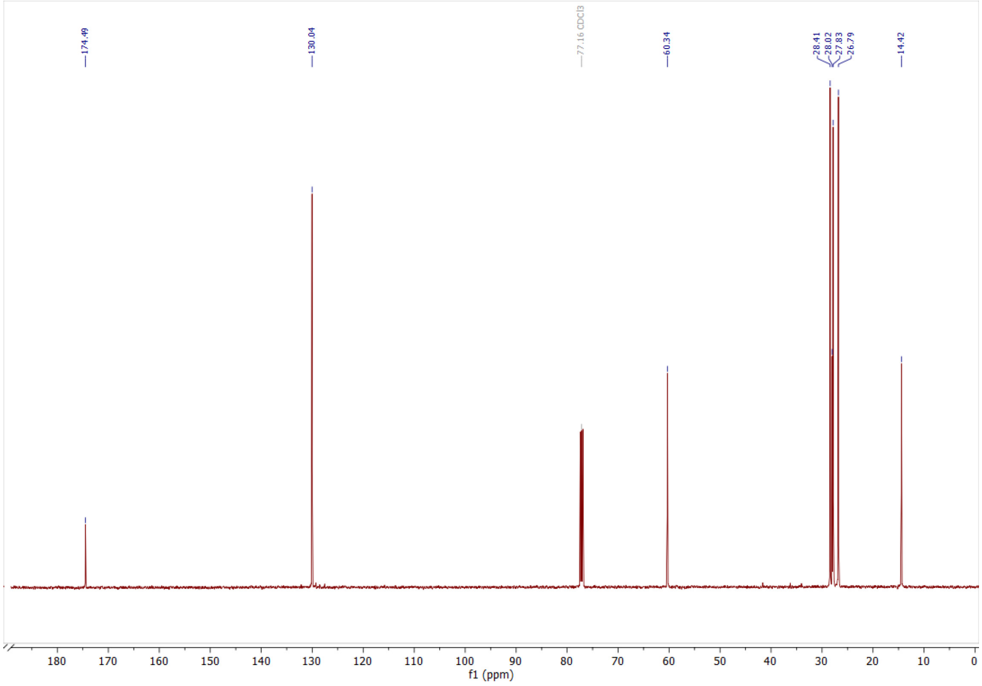

Figure S 73| ^{13}C NMR (126 MHz, $CDCl_3$) of (1R,8S,9R,Z)-ethyl bicyclo[6.1.0]non-4-ene-9-carboxylate (*Exo*) **45**.

8.2.38 Analytical Data of (1R,8S,9R,Z)-bicyclo[6.1.0]non-4-ene-9-ylmethanol 46

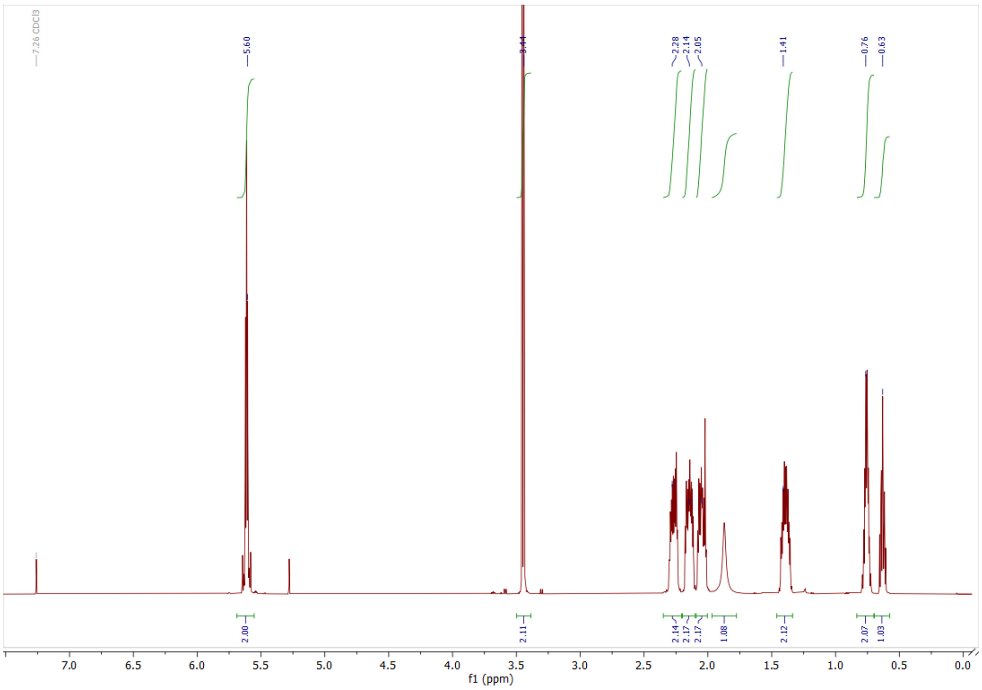

Figure S 74| ^{1}H NMR (500 MHz, $CDCl_3$) of (1R,8S,9R,Z)-bicyclo[6.1.0]non-4-ene-9-ylmethanol **46**.

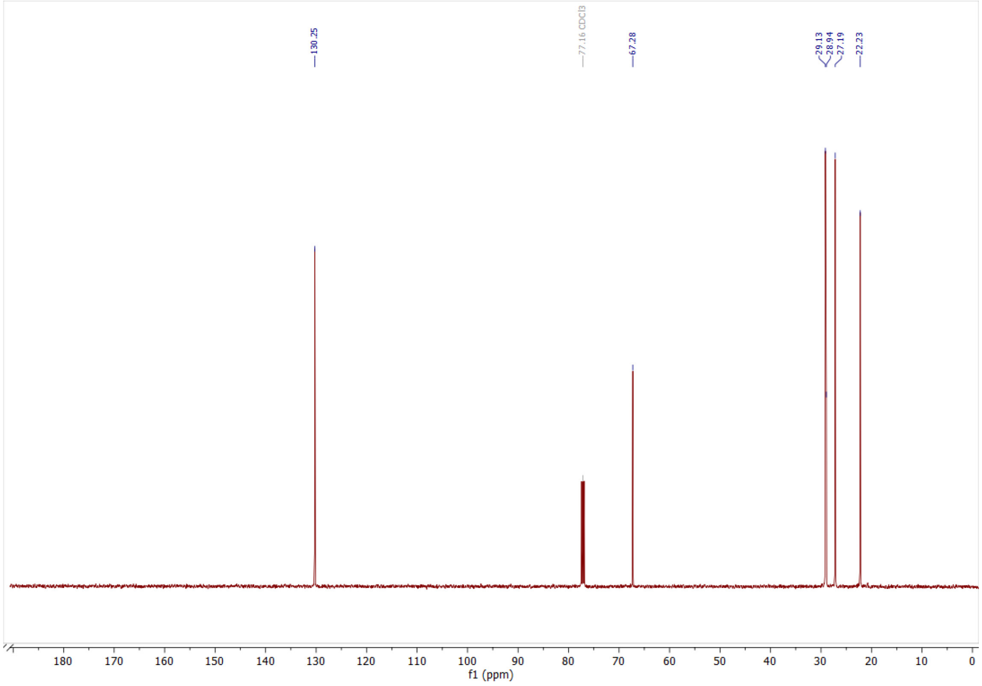

Figure S 75| ^{13}C NMR (126 MHz, $CDCl_3$) of (1R,8S,9R,Z)-bicyclo[6.1.0]non-4-ene-9-ylmethanol **46**.

8.2.39 Analytical Data of (1R,8S,9R)-4,5-Dibromobicyclo[6.1.0]nonan-9-ylmethanol 47

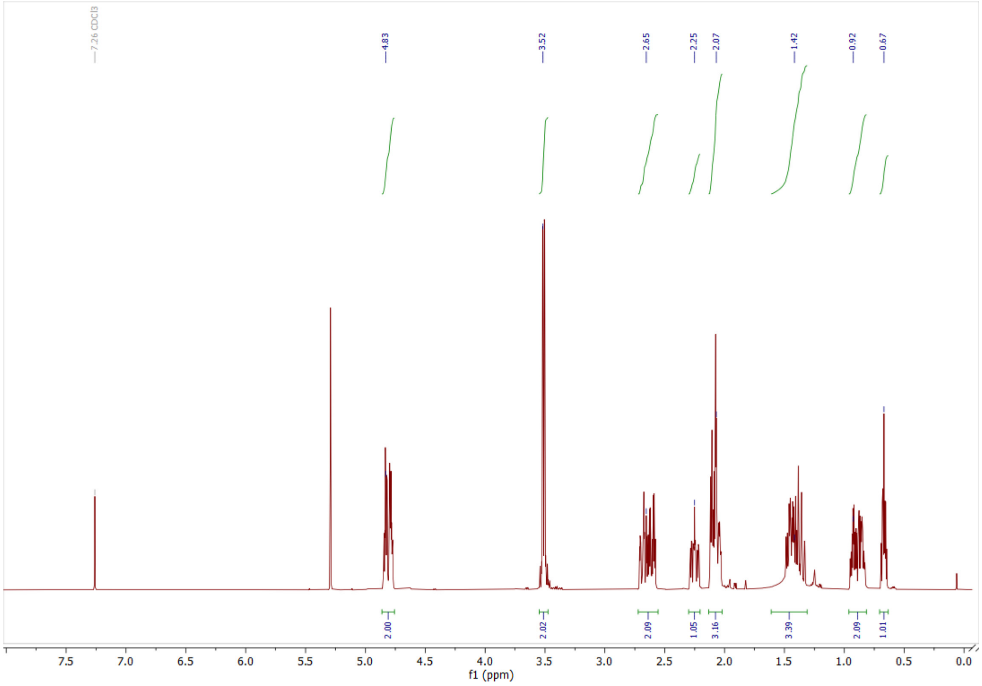

Figure S 76| ^{1}H NMR (500 MHz, $CDCl_3$) of (1R,8S,9R)-4,5-dibromobicyclo[6.1.0]nonan-9-ylmethanol **47**.

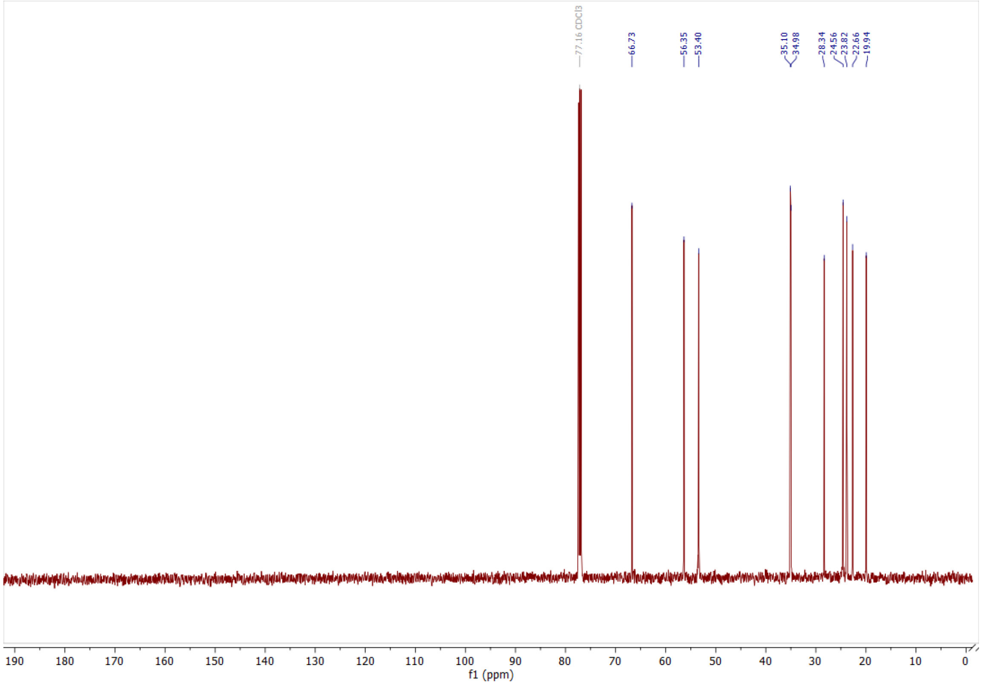

Figure S 77| ^{13}C NMR (126 MHz, $CDCl_3$) of (1R,8S,9R)-4,5-dibromobicyclo[6.1.0]nonan-9-ylmethanol **47**.

8.2.40 Analytical Data of (1R,8S,9R)-Bicyclo[6.1.0]non-4-yn-9-ylmethanol 48

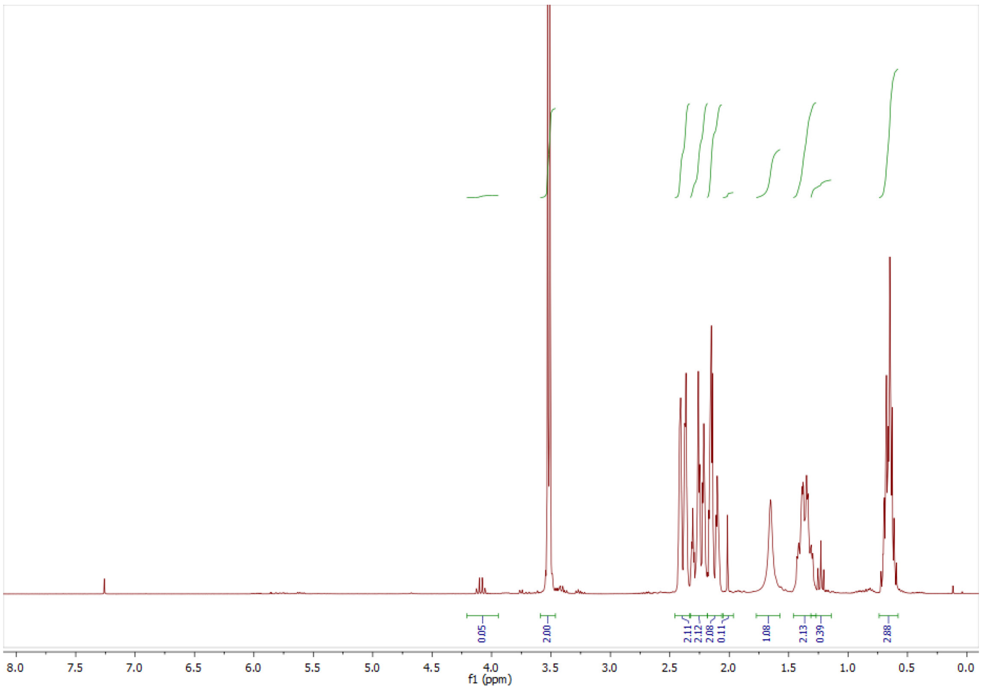

Figure S 78| ^{1}H NMR (500 MHz, $CDCl_3$) of (1R,8S,9R)-bicyclo[6.1.0]non-4-yn-9-ylmethanol **48**.

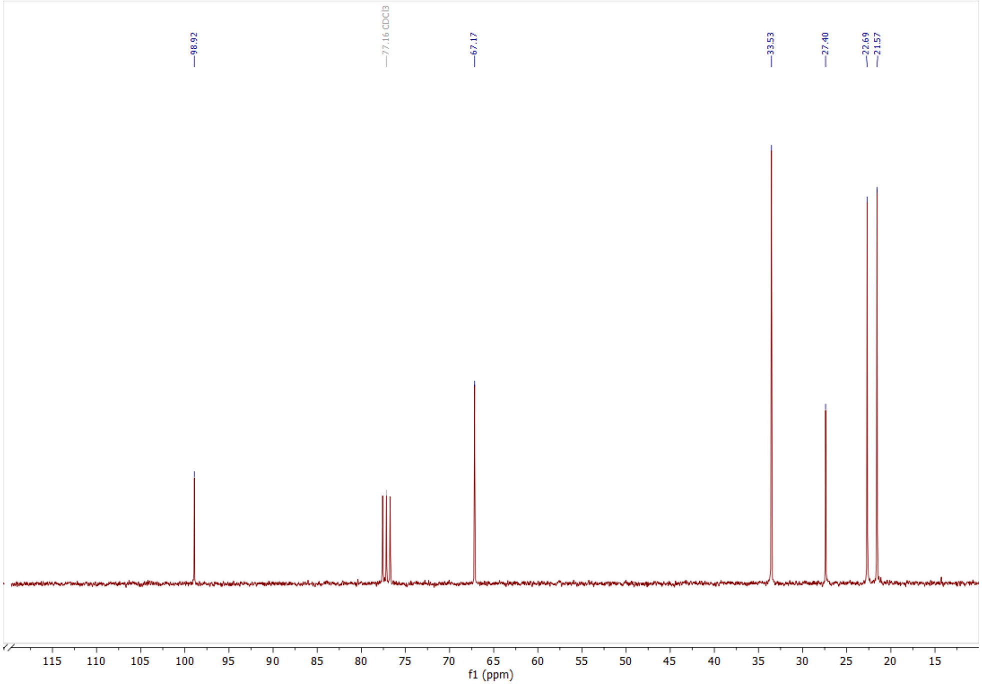

Figure S 79| ^{13}C NMR (126 MHz, $CDCl_3$) of (1R,8S,9R)-bicyclo[6.1.0]non-4-yn-9-ylmethanol **48**.

8.2.41 Analytical Data of BCN-*p*NP 50

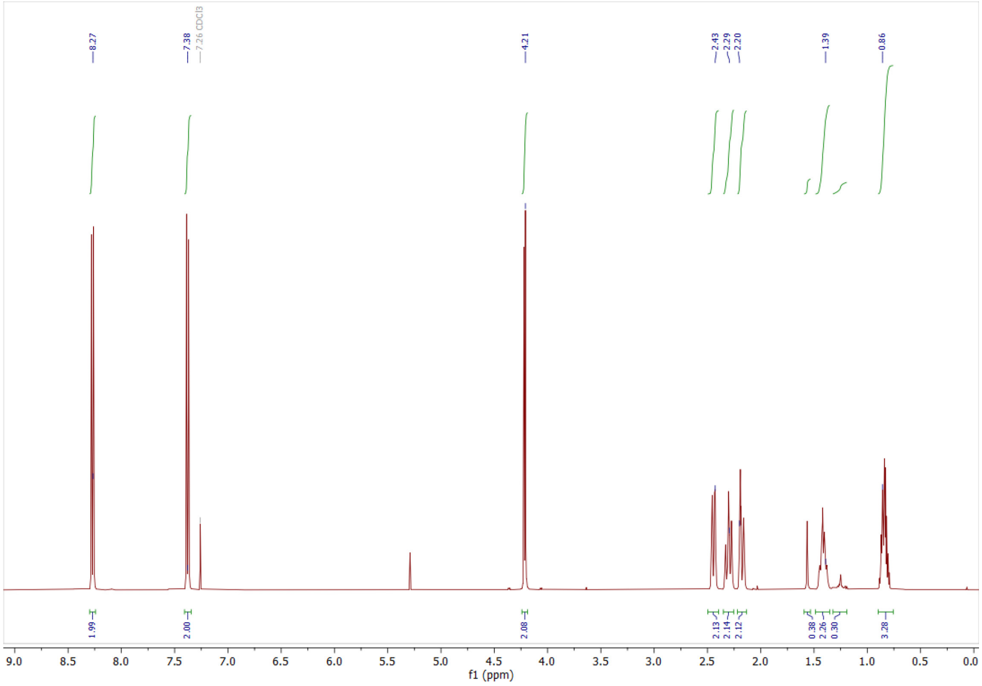

Figure S 80| ^{1}H NMR (500 MHz, CDCl$_3$) of BCN-*p*NP **50**.

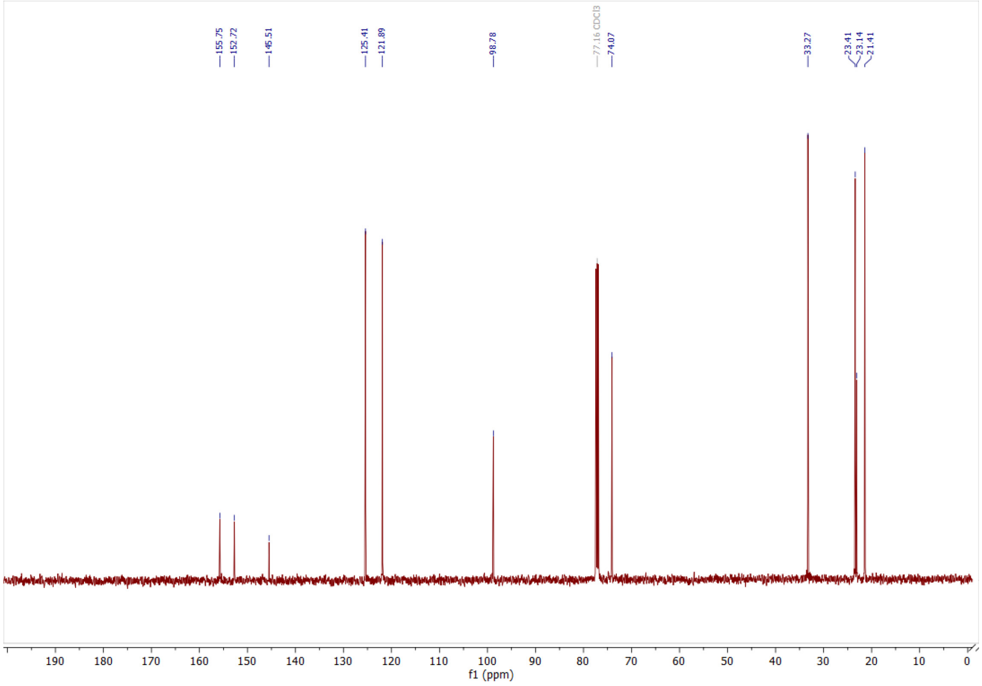

Figure S 81| ^{13}C NMR (126 MHz, CDCl$_3$) of BCN-*p*NP **50**.

8.2.42 Analytical Data of BCN-Aminopentanoic Acid 51

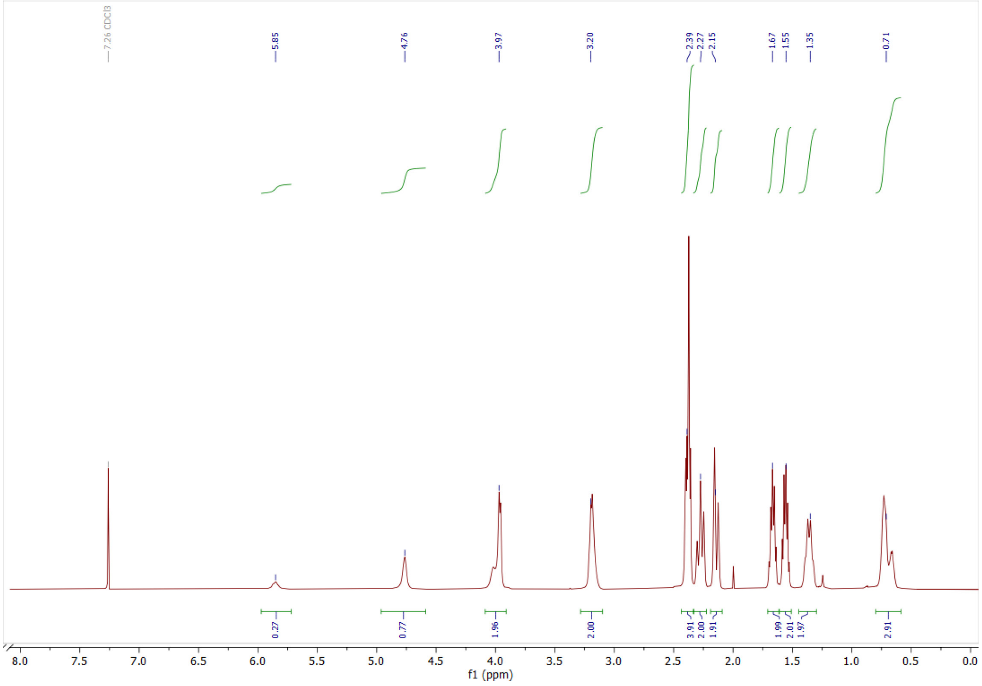

Figure S 82| ^{1}H NMR (500 MHz, $CDCl_3$) of BCN-aminopentanoic acid **51**.

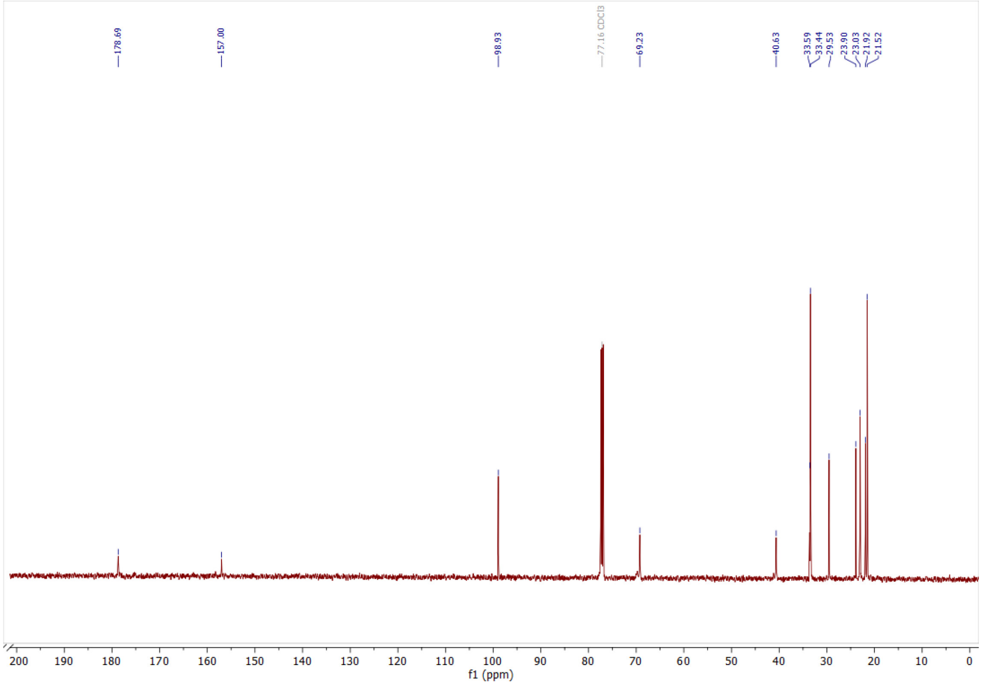

Figure S 83| ^{13}C NMR (126 MHz, $CDCl_3$) of BCN-aminopentanoic acid **51**.

8.2.43 Analytical Data of Biotin-Cadaverine 52

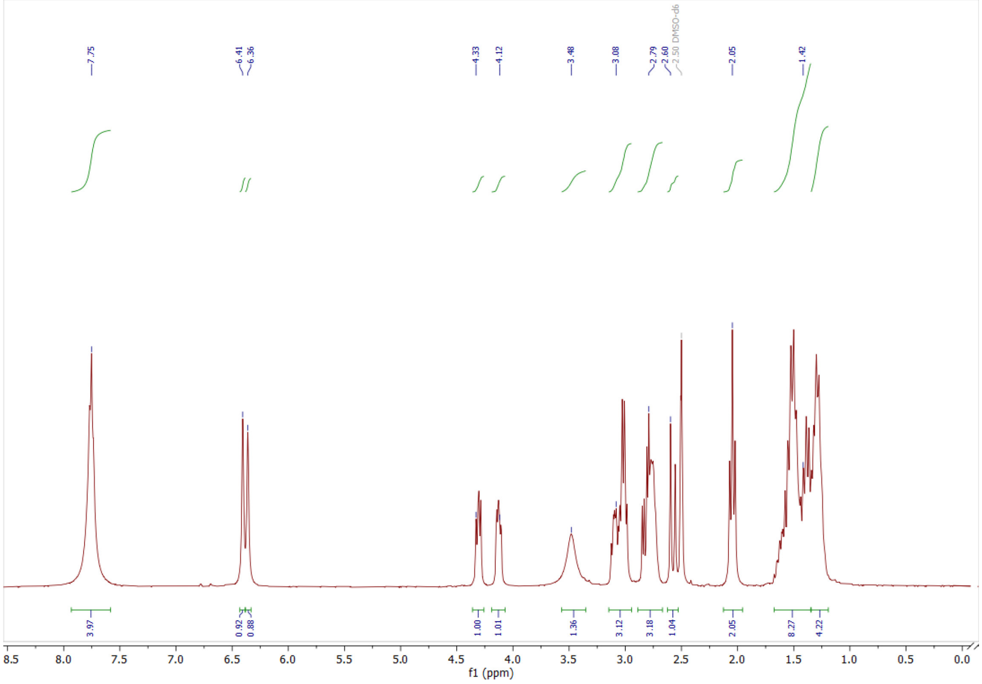

Figure S 84| ^{1}H NMR (300 MHz, DMSO-d_6) of biotin-cadaverine **52**.

8.2.44 Analytical Data of 2-Azidoacetic Acid-NHS 53

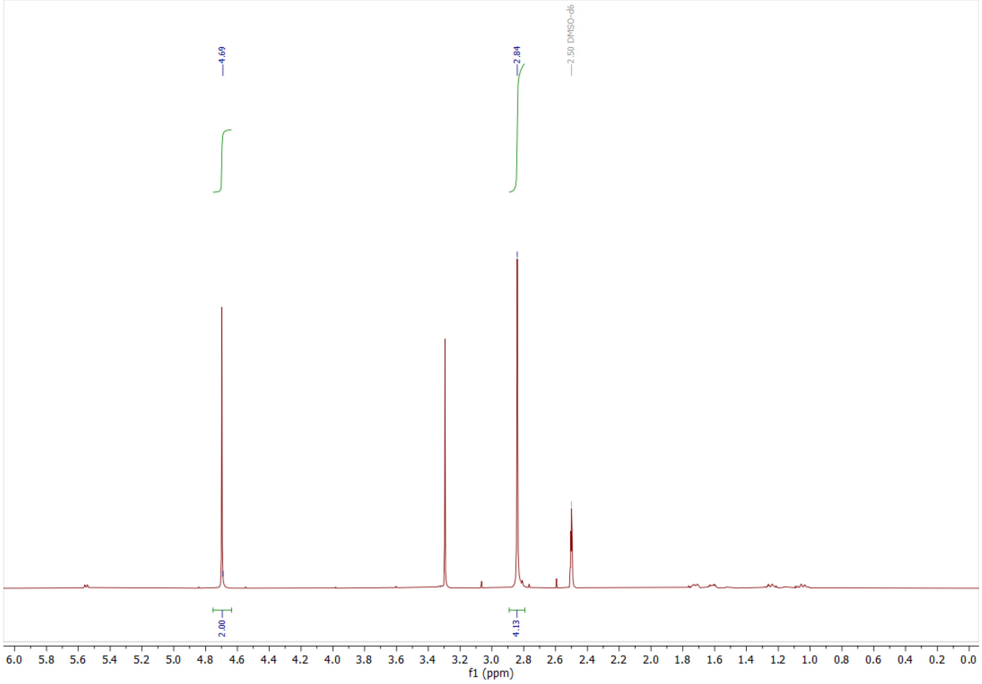

Figure S 85| ^{1}H NMR (500 MHz, DMSO-d_6) of 2-azidoacetic acid-NHS **53**.

8.2.45 Analytical Data of Biotin-Cadaverine-Azide 54

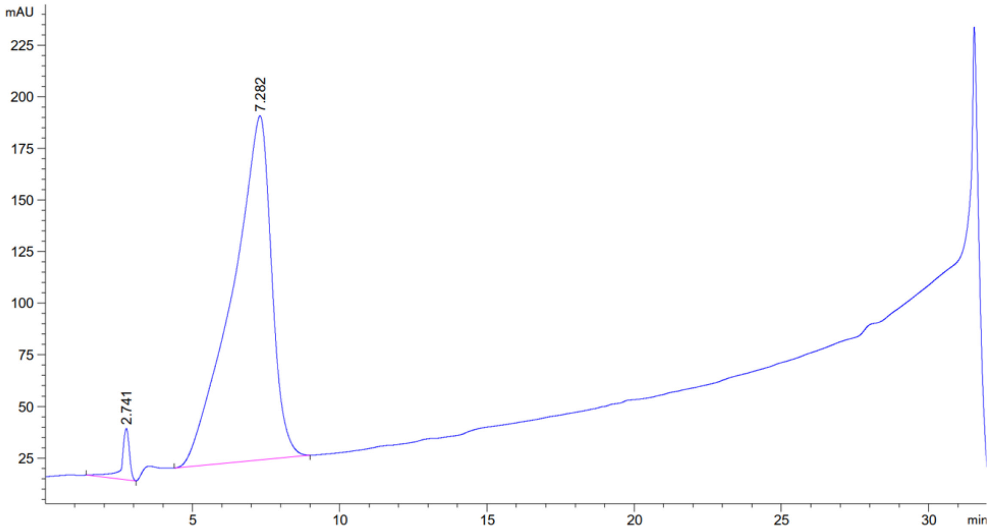

Figure S 86| Analytical RP-HPLC chromatogram of biotin-cadaverine-azide **54**, 20 to 80 % eluent B (20 min gradient), 220 nm, t_R = 7.282 min.

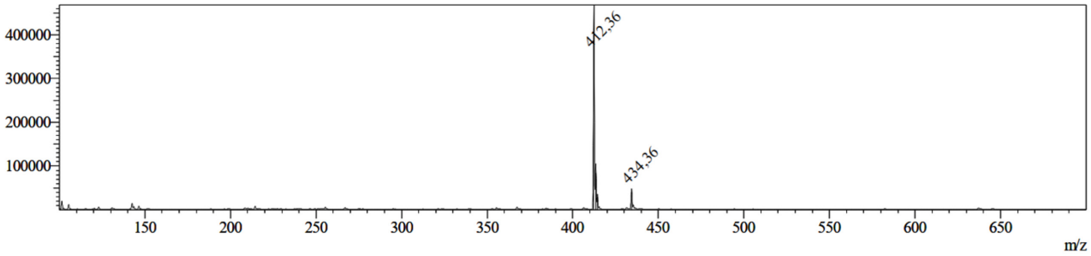

Figure S 87| ESI-MS of biotin-cadaverine-azide **54**. Calc. for $C_{17}H_{29}N_7O_3S$: m/z: $[M+H]^+$ = 412.53 (obs. 412.36).

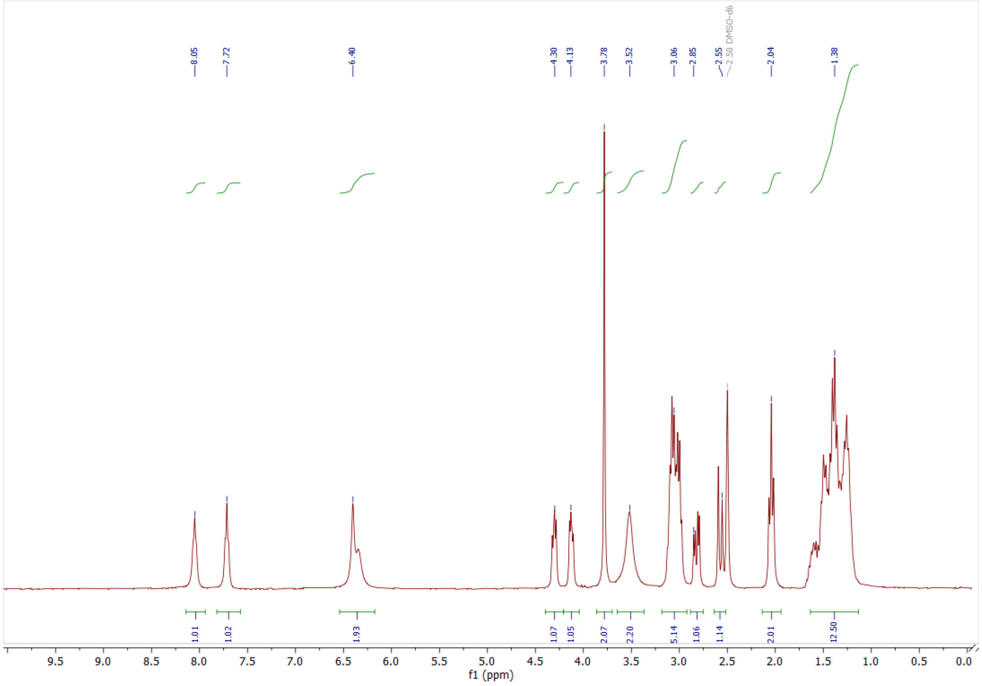

Figure S 88| ^{1}H NMR (300 MHz, DMSO-d_6) of biotin-cadaverine-azide **54**.

8.2.46 Analytical Data of eGFP-LAP 55

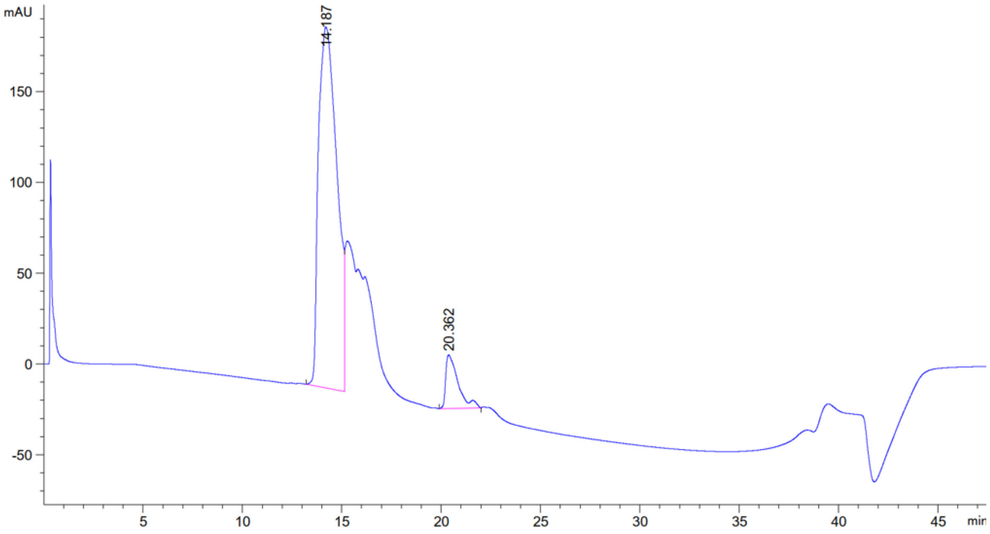

Figure S 89| Analytical HIC-HPLC chromatogram of eGFP-LAP **55**, 0 to 100 % HIC buffer B (35 min gradient), 220 nm, t_R = 14.187 min.

8.2.47 Analytical Data of eGFP-BCN 56

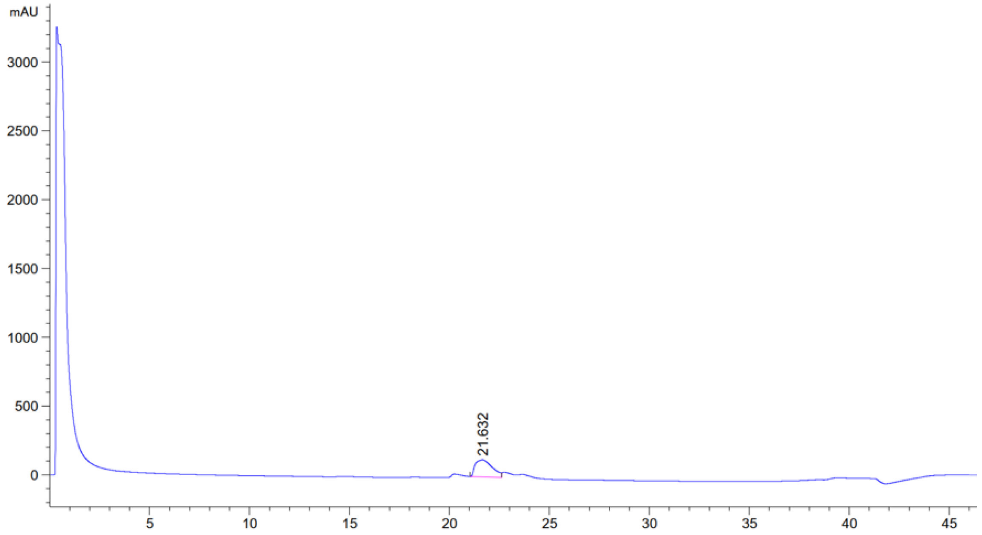

Figure S 90| Analytical HIC-HPLC chromatogram of eGFP-BCN **56**, 0 to 100 % HIC buffer B (35 min gradient), 220 nm, t_R = 21.632 min.

8.2.48 Analytical Data of eGFP-Biotin 57

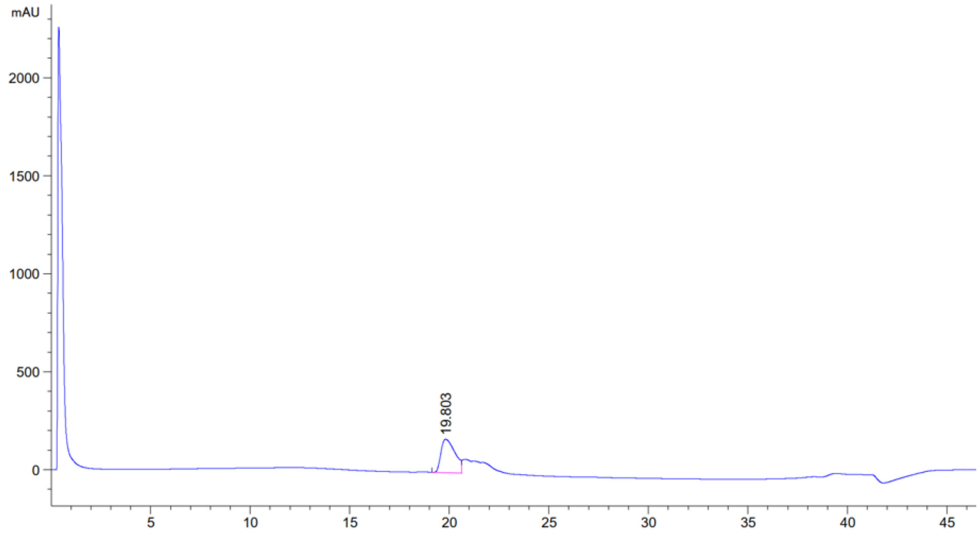

Figure S 91| Analytical HIC-HPLC chromatogram of eGFP-biotin **57**, 0 to 100 % HIC buffer B (35 min gradient), 220 nm, t_R = 19.803 min.

8.2.49 Analytical Data of Biotin-Cadaverine-Dextran-DR5TP$_{5.4}$ 61

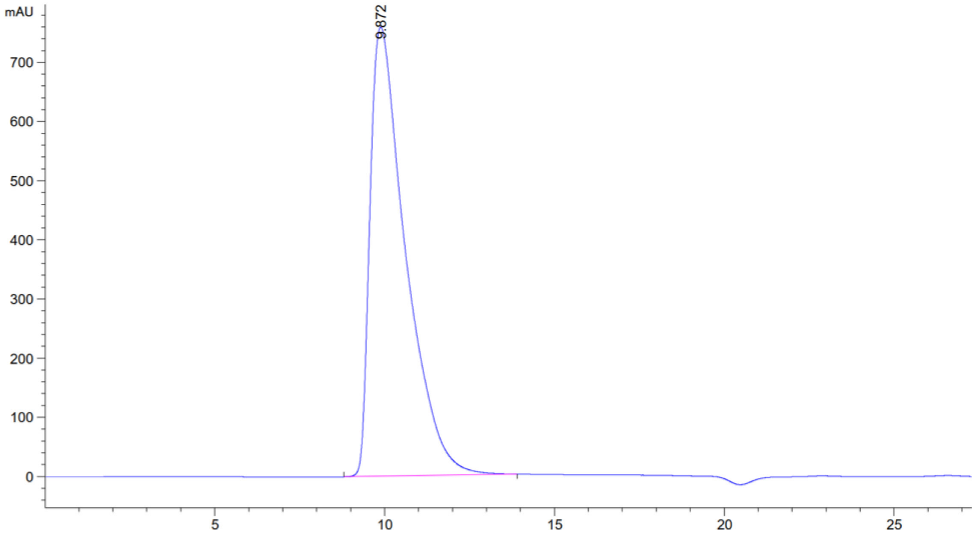

Figure S 92| Analytical SEC-HPLC chromatogram of biotin-cadaverine-dextran-DR5TP$_{5.4}$ **61**, isocratic 30% B (28 min), 220 nm, t_R = 9.872 min.

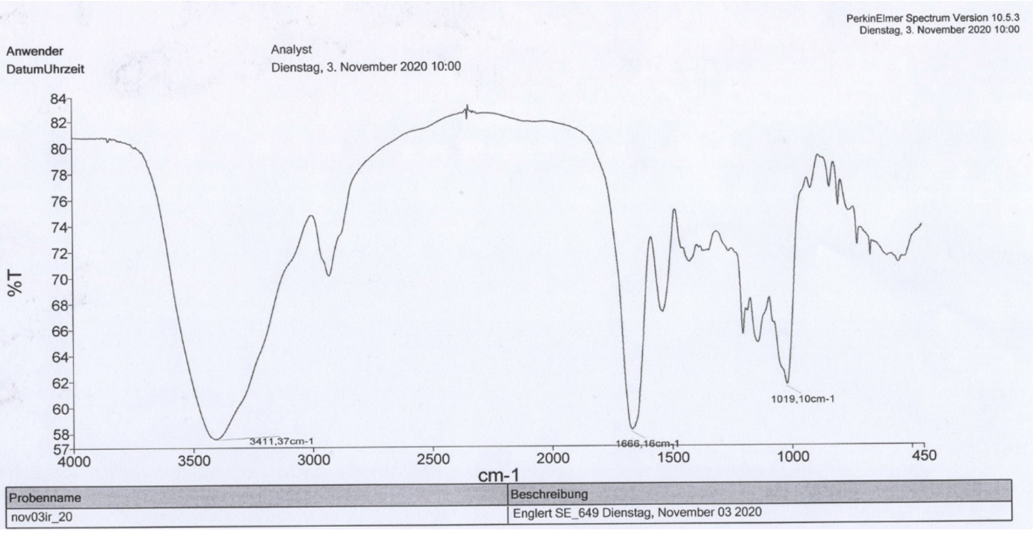

Figure S 93| IR spectrum (KBr pellet) of biotin-cadaverine-dextran-DR5TP$_{5.4}$ **61**. Compared to the parent dextran **38**, the azide band at 2113.67 cm^{-1} disappeared.

8.2.50 Analytical Data of Biotin-Ahx-DR5TP 62

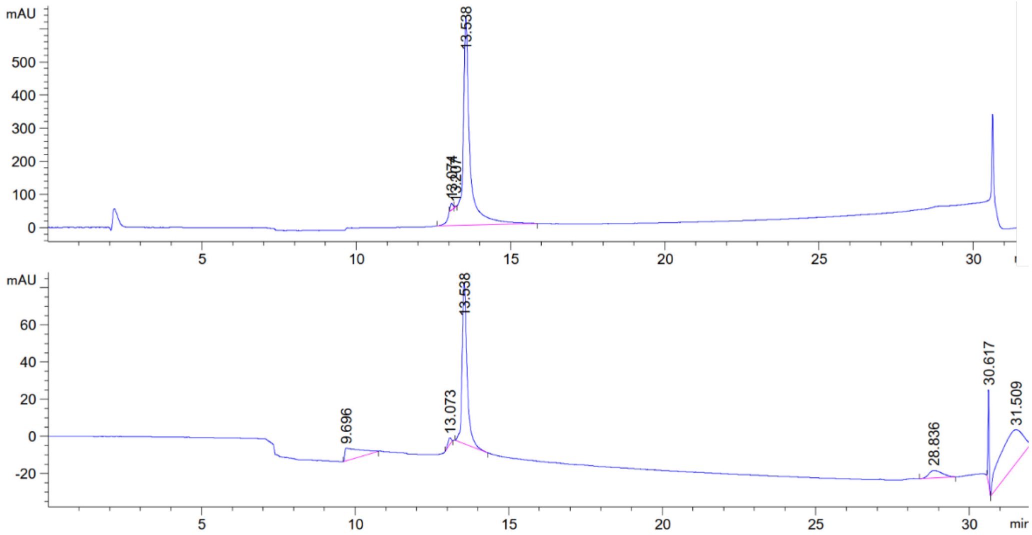

Figure S 94| Analytical RP-HPLC chromatogram of biotin-Ahx-DR5TP **62**, 0 to 80 % eluent B (20 min gradient), 220 nm (top), 280 nm (bottom), t_R = 13.538 min.

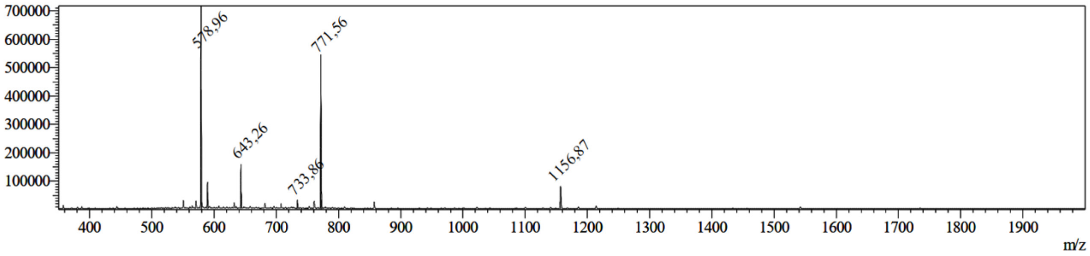

Figure S 95| ESI-MS of biotin-Ahx-DR5TP **62**. Calc. for $C_{99}H_{163}N_{33}O_{25}S_3$: m/z: $[M+2H]^{2+}$ = 1156.89 (obs. 1156.87), $[M+3H]^{3+}$ = 771.59 (obs. 771.56), $[M+3H]^{3+}$ = 578.95 (obs. 578.96).

8.2.51 Analytical Data of *N*-Boc-Cadaverine-Dextran-CE$_{6.3}$ 63

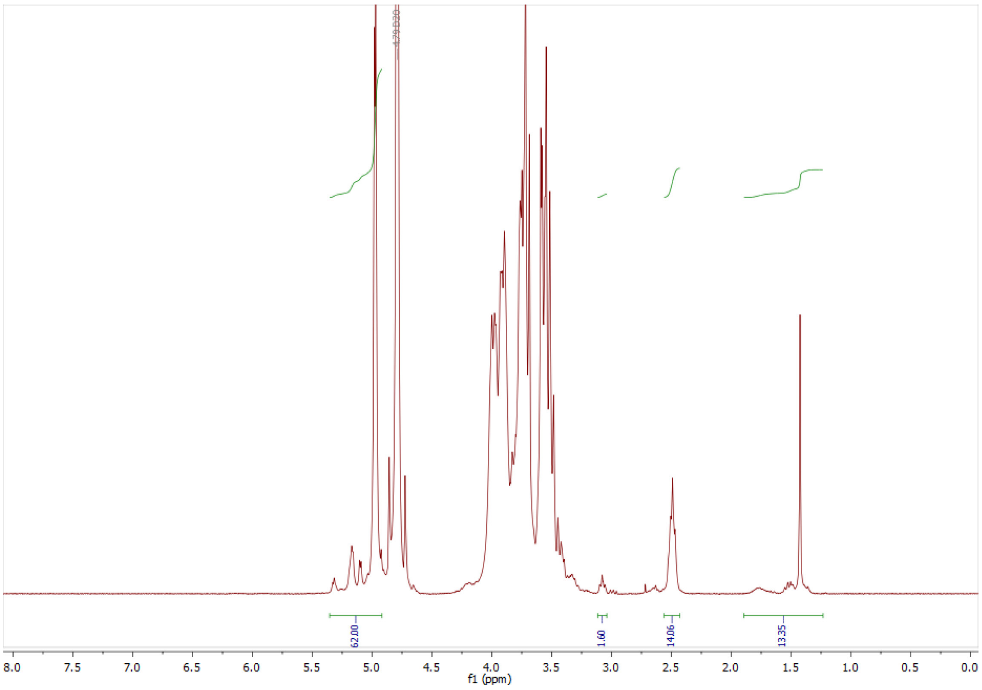

Figure S 96| ^{1}H NMR (300 MHz, D_2O) of *N*-Boc-cadaverine-dextran-CE$_{6.3}$ **63**.

8.2.52 Analytical Data of *N*-Boc-Cadaverine-Dextran-(N$_3$)$_{6.3}$ 64

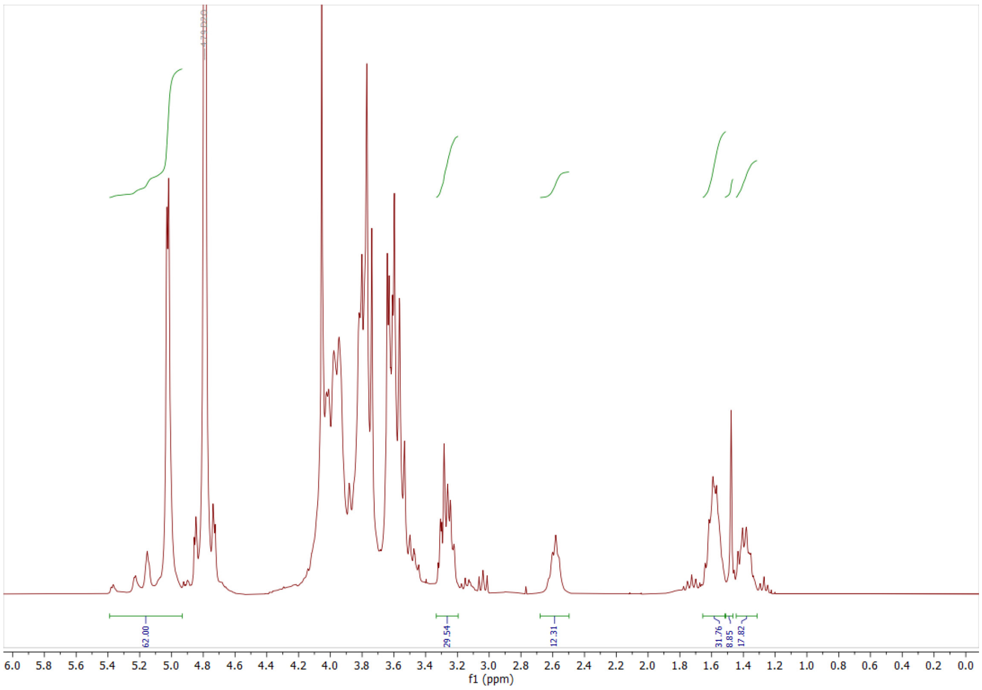

Figure S 97| ^{1}H NMR (300 MHz, D_2O) of *N*-Boc-cadaverine-dextran-(N$_3$)$_{6.3}$ **64**.

8.2.53 Analytical Data of Cadaverine-Dextran-$(N_3)_{6.3}$ 65

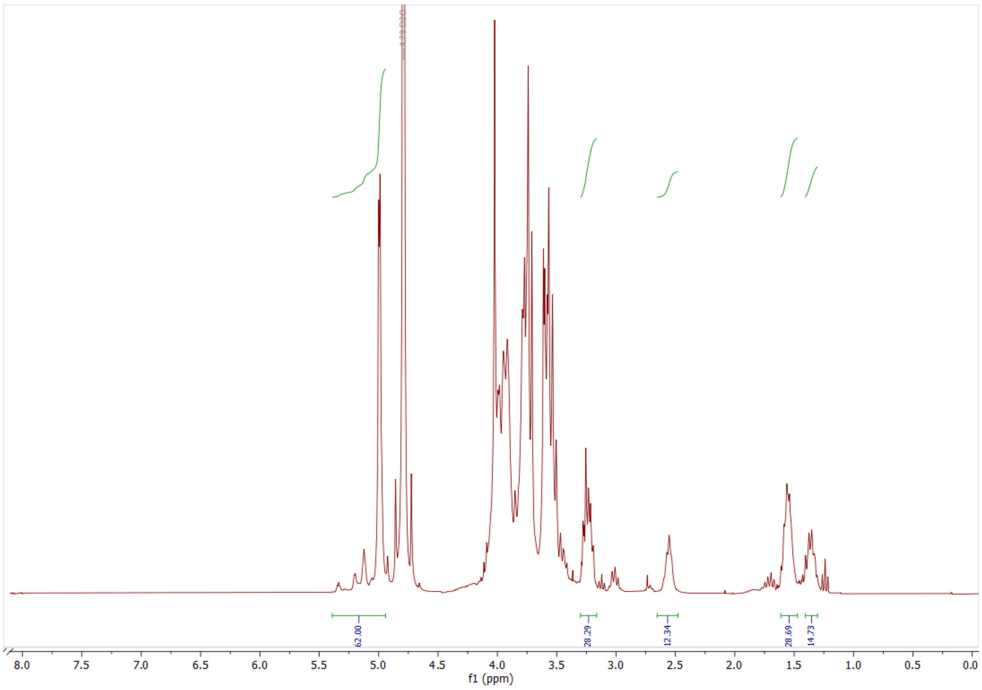

Figure S 98| ^1H NMR (300 MHz, D_2O) of cadaverine-dextran-$(N_3)_{6.3}$ **65**.

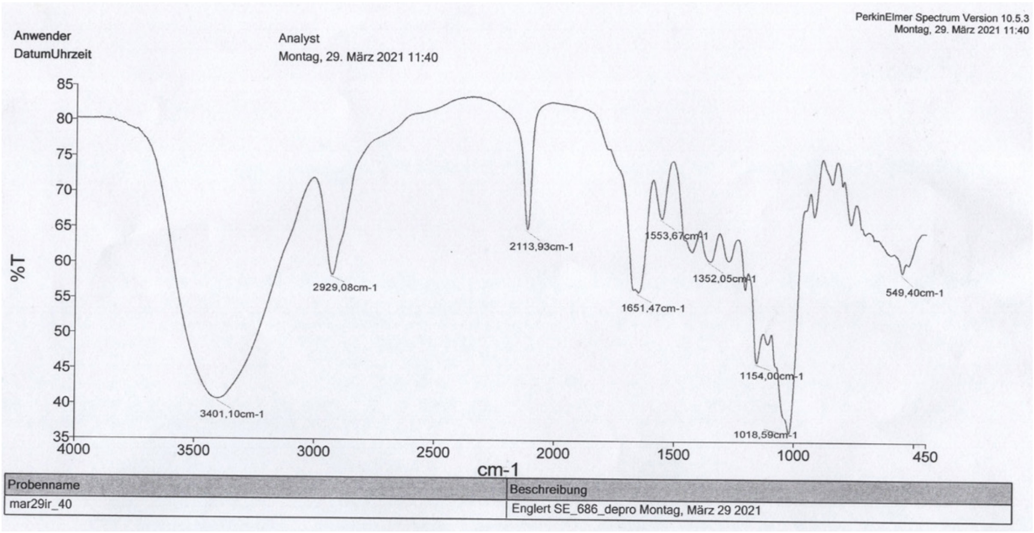

Figure S 99| IR spectrum (KBr pellet) of cadaverine-dextran-$(N_3)_{6.3}$ **65** with azide band at wavenumber 2113.93 cm^{-1}.

8.2.54 Analytical Data of Biotin-Cadaverine-Dextran-$(N_3)_{6.3}$ 66

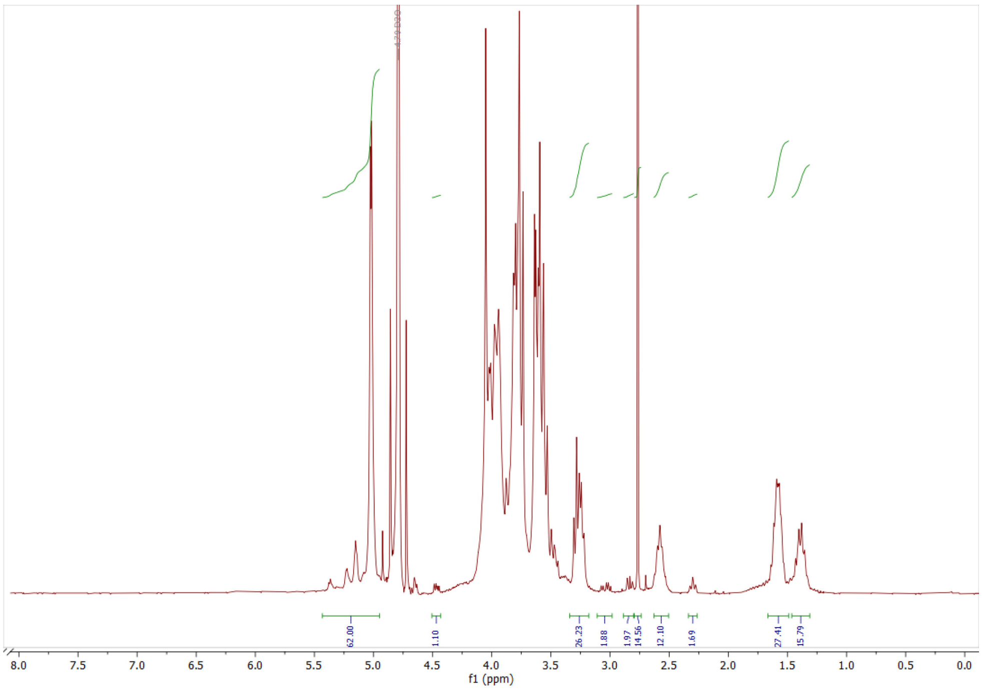

Figure S 100| ^1H NMR (300 MHz, D_2O) of biotin-cadaverine-dextran-$(N_3)_{6.3}$ **66**.

8.2.55 Analytical Data of *H*-D(OtBu)-f-K(Boc)-R(Pbf)-G-*OH* 67

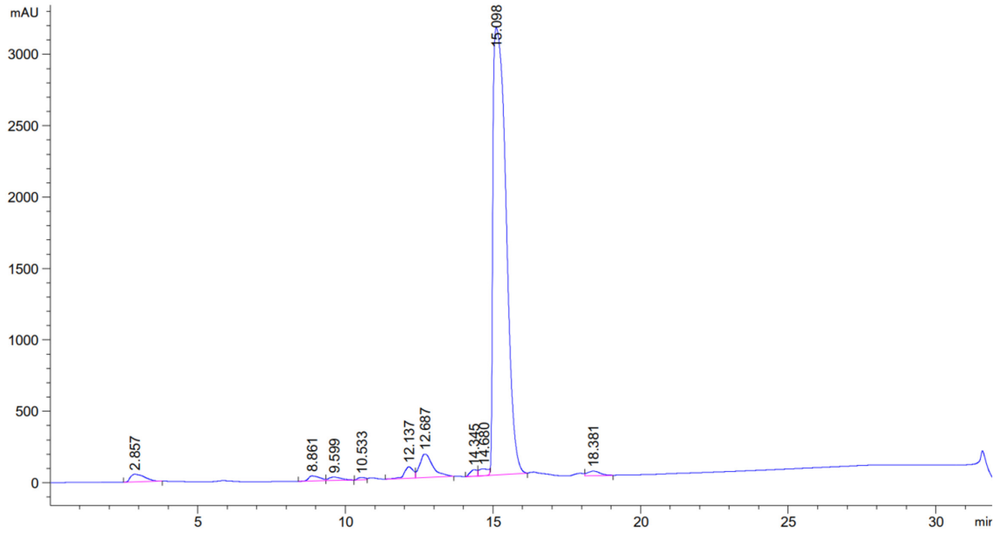

Figure S 101| Analytical RP-HPLC chromatogram of *H*-D(OtBu)-f-K(Boc)-R(Pbf)-G-*OH* **67**, 30 to 100 % eluent B (20 min gradient), 220 nm, t_R = 15.098 min.

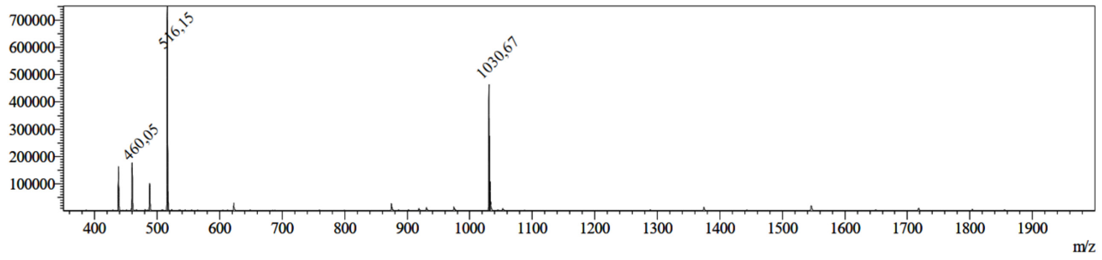

Figure S 102| ESI-MS of of *H*-D(OtBu)-f-K(Boc)-R(Pbf)-G-*OH* **67**. Calc. for $C_{49}H_{75}N_9O_{13}S$: m/z: $[M+H]^+$ = 1030.53 (obs. 1030.67), $[M+2H]^{2+}$ = 516.27 (obs. 516.15).

8.2.56 Analytical Data of *H*-D(OtBu)-f-K(Boc)-R(Pbf)-A-*OH* 68

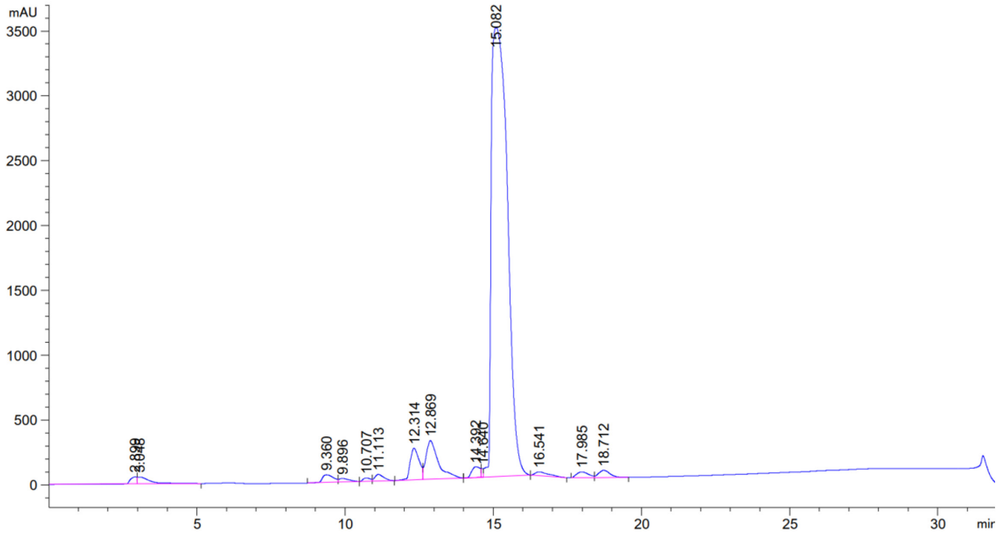

Figure S 103| Analytical RP-HPLC chromatogram of *H*-D(OtBu)-f-K(Boc)-R(Pbf)-A-*OH* **68**, 30 to 100 % eluent B (20 min gradient), 220 nm, t_R = 15.082 min.

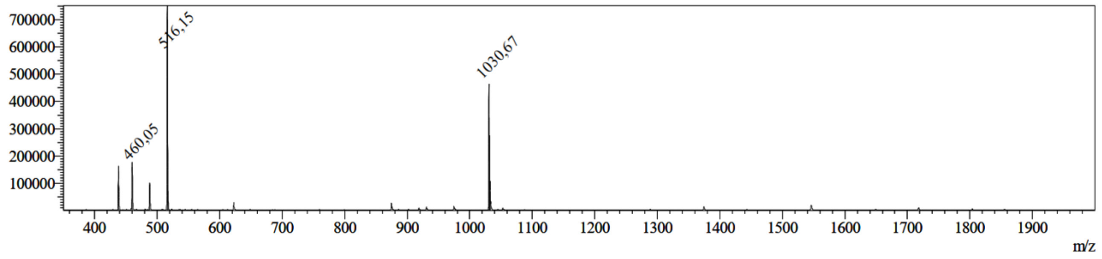

Figure S 104| ESI-MS of *H*-D(OtBu)-f-K(Boc)-R(Pbf)-A-*OH* **68**. Calc. for $C_{50}H_{77}N_9O_{13}S$: m/z: $[M+H]^+$ = 1044.54 (obs. 1044.77), $[M+2H]^{2+}$ = 522.77 (obs. 523.15).

8.2.57 Analytical Data of *Cyclo*[D(OtBu)-f-K(Boc)-R(Pbf)-G] 69

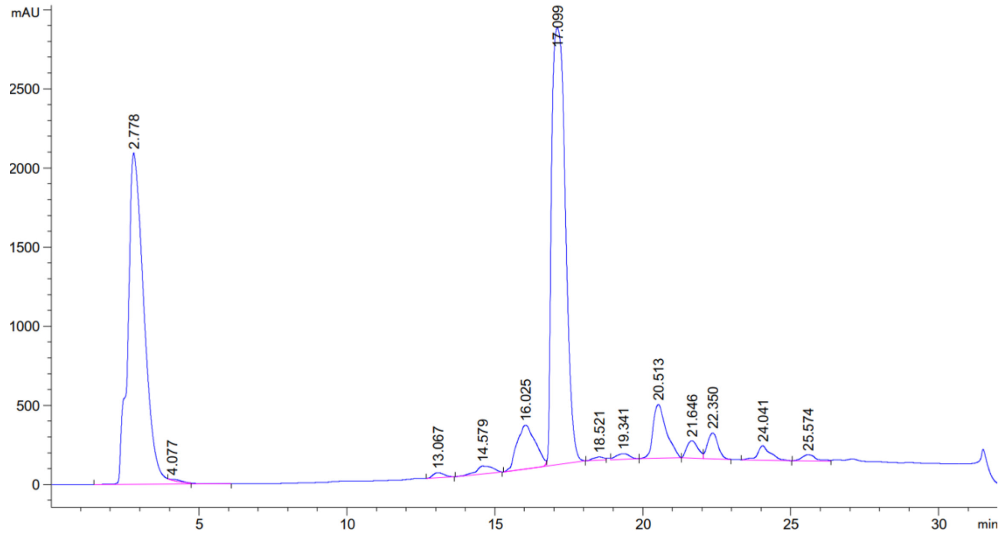

Figure S 105| Analytical RP-HPLC chromatogram of *cyclo*[D(OtBu)-f-K(Boc)-R(Pbf)-G] **69**, 30 to 100 % eluent B (20 min gradient), 220 nm, t_R = 17.099 min.

8.2.58 Analytical Data of *Cyclo*[D(OtBu)-f-K(Boc)-R(Pbf)-A] 70

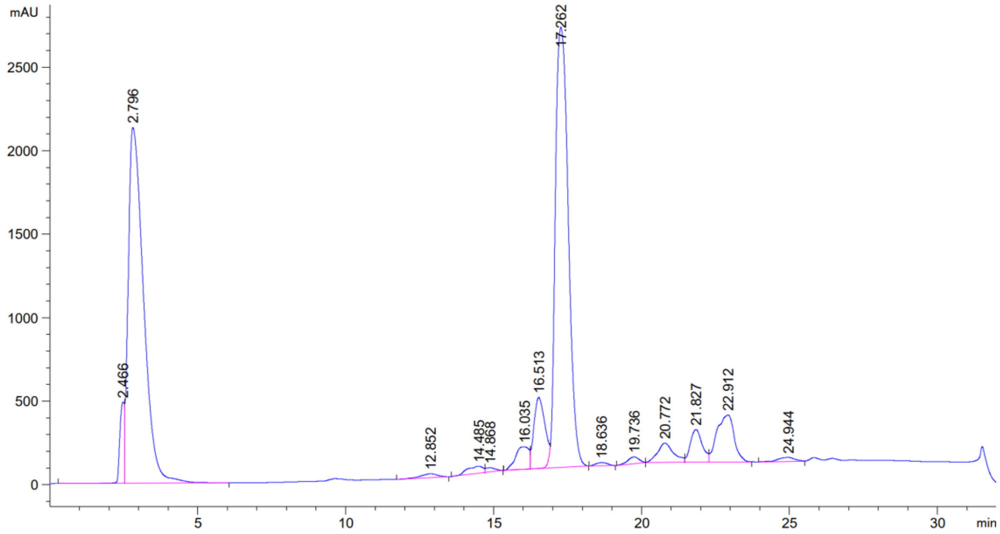

Figure S 106| Analytical RP-HPLC chromatogram of *cyclo*[D(OtBu)-f-K(Boc)-R(Pbf)-A] **70**, 30 to 100 % eluent B (20 min gradient), 220 nm, t_R = 17.262 min.

8.2.59 Analytical Data of *Cyclo*[RGDfK] 71

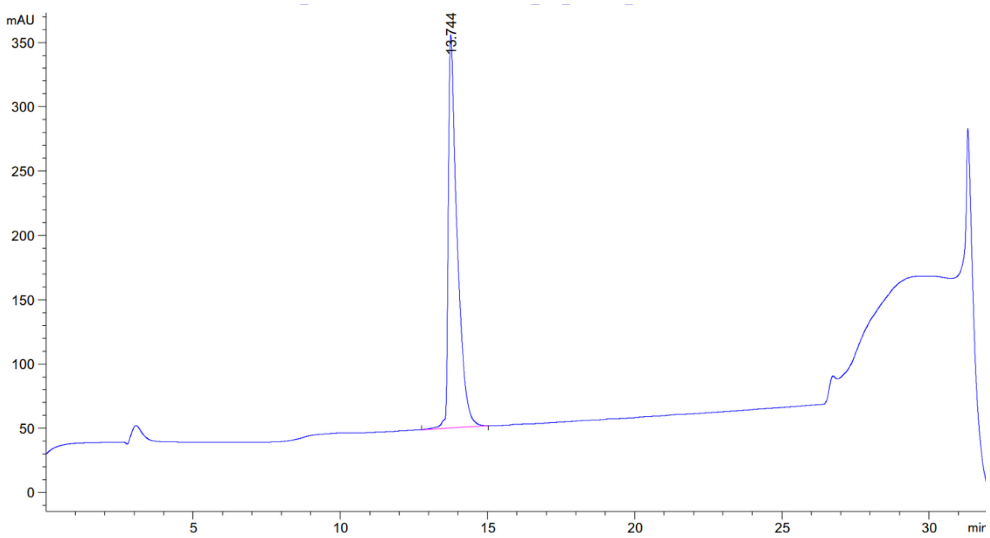

Figure S 107| Analytical RP-HPLC chromatogram of *cyclo*[RGDfK] **71**, 0 to 40 % eluent B (20 min gradient), 220 nm, t_R = 13.744 min.

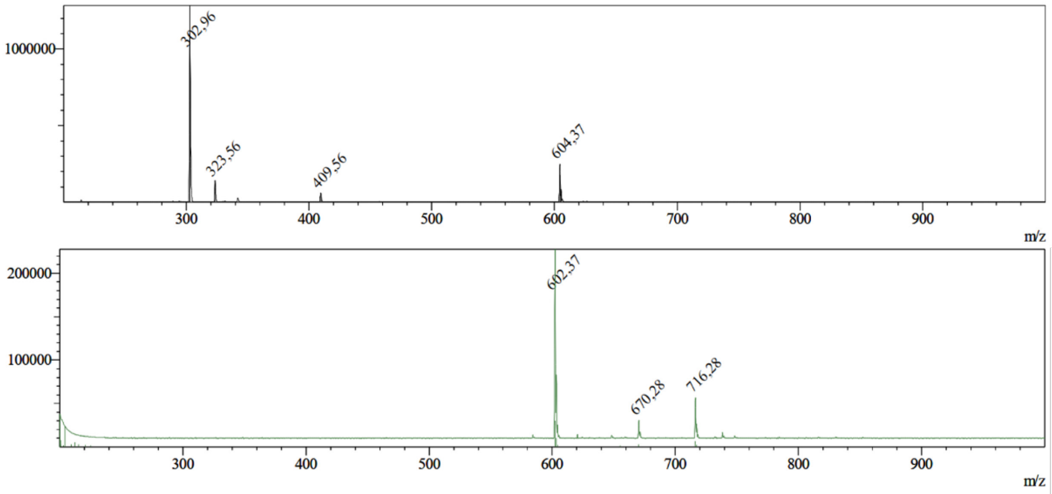

Figure S 108| ESI-MS of *cyclo*[RGDfK] **71** with positive mode (top) and negative mode (bottom). Calc. for $C_{27}H_{41}N_9O_7$: m/z: $[M+H]^+$ = 604.32 (obs. 604.37), $[M+2H]^{2+}$ = 302.66 (obs. 302.96), $[M-H]^-$ = 602.31 (obs. 602.37).

8.2.60 Analytical Data of *Cyclo*[RADfK] 72, Product Fraction 1

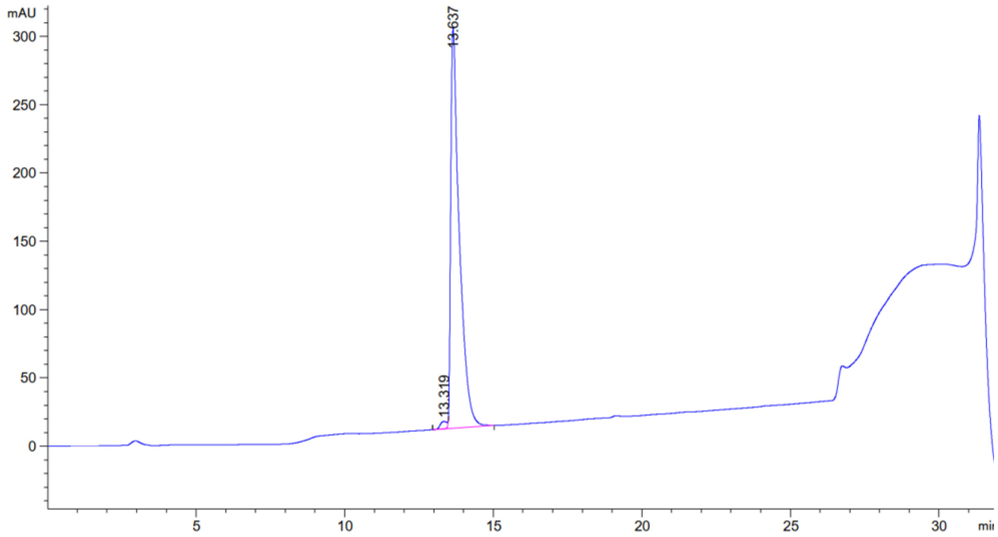

Figure S 109| Analytical RP-HPLC chromatogram of *cyclo*[RADfK] **72**, product fraction 1, 0 to 40 % eluent B (20 min gradient), 220 nm, t_R = 13.637 min.

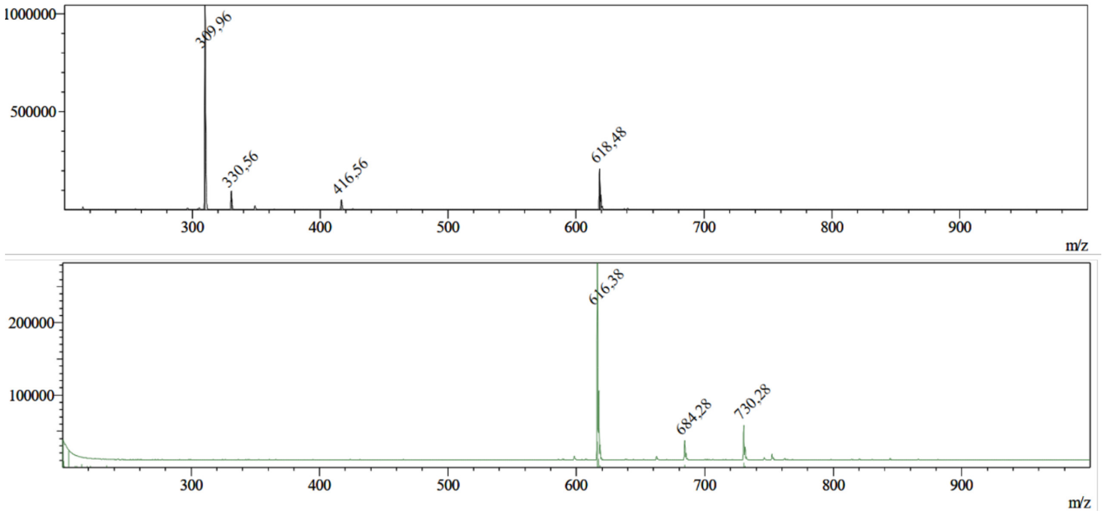

Figure S 110| ESI-MS of *cyclo*[RADfK] **72**, product fraction 1, with positive mode (top) and negative mode (bottom). Calc. for $C_{28}H_{43}N_9O_7$: m/z: $[M+H]^+$ = 618.34 (obs. 618.48), $[M+2H]^{2+}$ = 309.67 (obs. 309.96), $[M-H]^-$ = 616.32 (obs. 616.38).

8.2.61 Analytical Data of *Cyclo*[RADfK] 72, Product Fraction 2

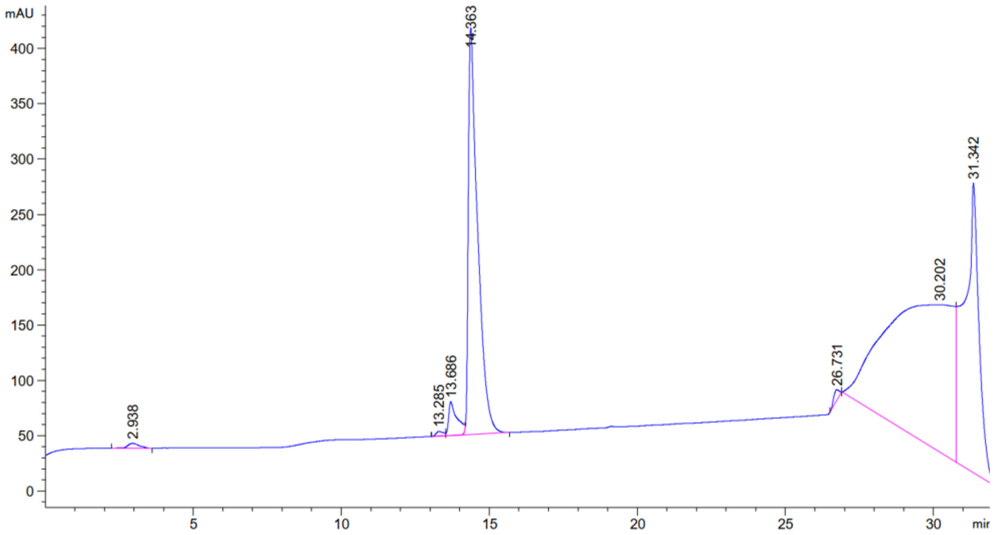

Figure S 111| Analytical RP-HPLC chromatogram of *cyclo*[RADfK] **72**, product fraction 2, 0 to 40 % eluent B (20 min gradient), 220 nm, t_R = 14.363 min.

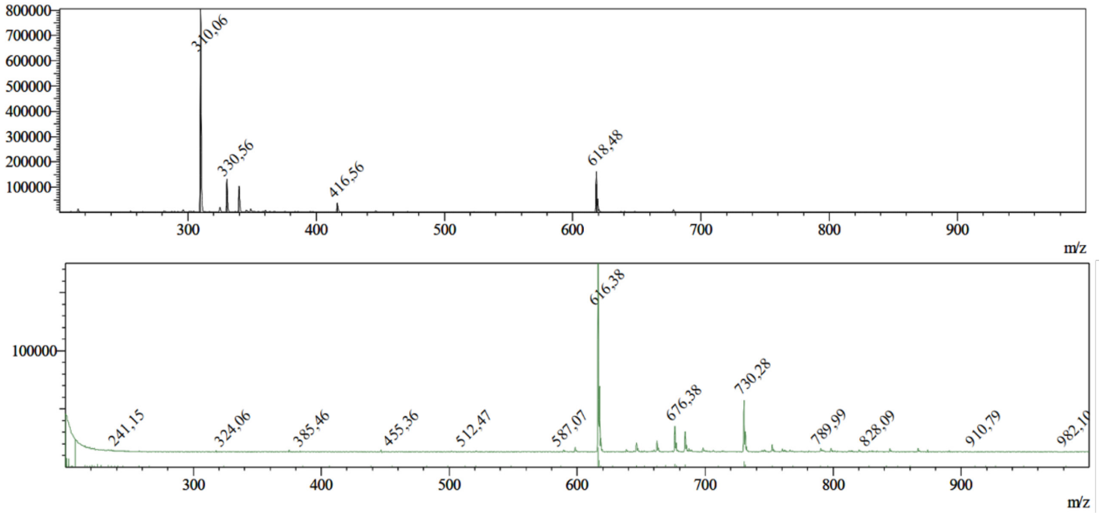

Figure S 112| ESI-MS of *cyclo*[RADfK] **72**, product fraction 2, with positive mode (top) and negative mode (bottom). Calc. for $C_{28}H_{43}N_9O_7$: m/z: $[M+H]^+$ = 618.34 (obs. 618.48), $[M+2H]^{2+}$ = 309.67 (obs. 310.06), $[M-H]^-$ = 616.32 (obs. 616.38).

8.2.62 Analytical Data of *Cyclo*[RGDfK(4-Pentynoic Acid)] 74

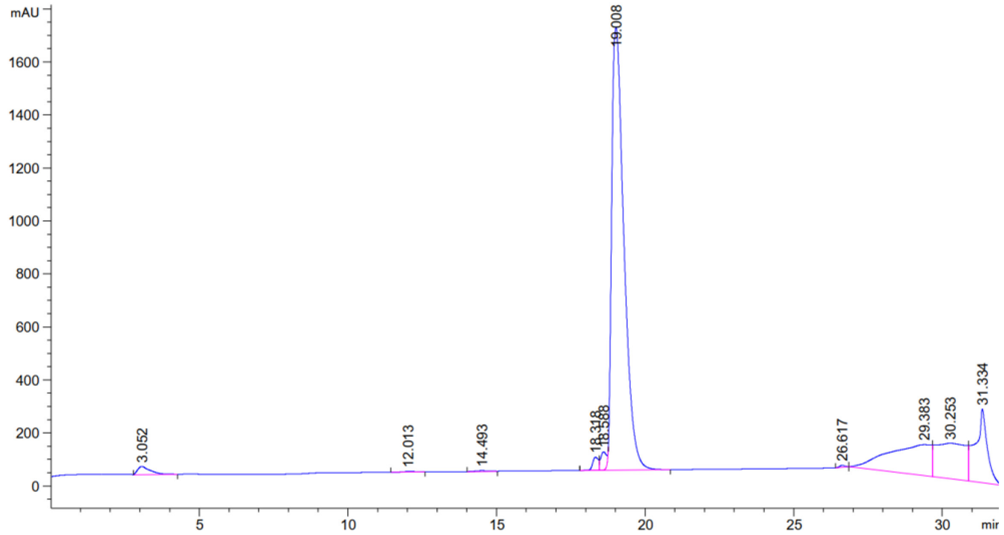

Figure S 113| Analytical RP-HPLC chromatogram of *cyclo*[RGDfK(4-pentynoic acid)] **74**, 0 to 40 % eluent B (20 min gradient), 220 nm, t_R = 19.088 min.

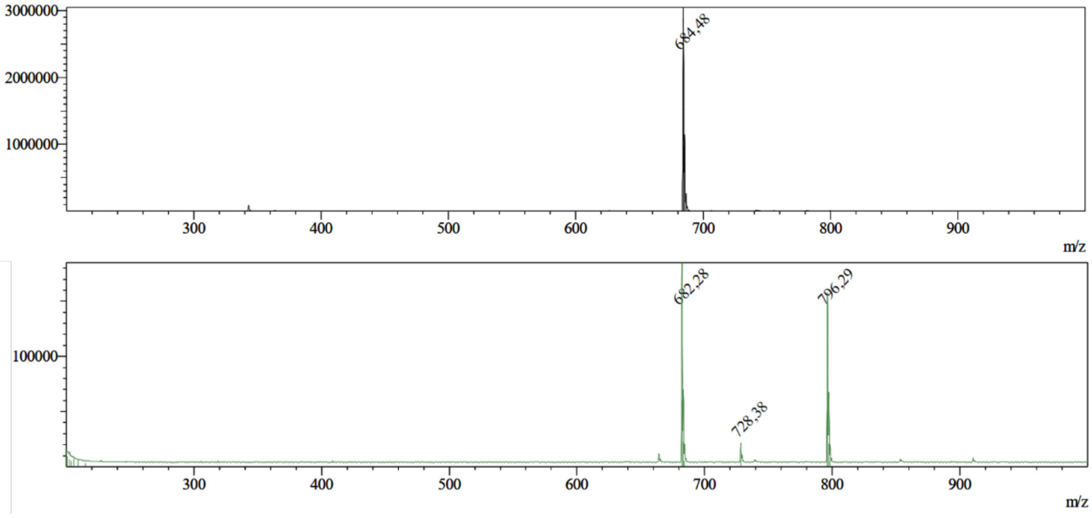

Figure S 114| ESI-MS of *cyclo*[RGDfK(4-pentynoic acid)] **74**, with positive mode (top) and negative mode (bottom). Calc. for $C_{32}H_{45}N_9O_8$: m/z: $[M+H]^+$ = 684.38 (obs. 684.48), $[M-H]^-$ = 682.38 (obs. 682.38).

8.2.63 Analytical Data of *Cyclo*[RADfK(4-Pentynoic Acid)] 75

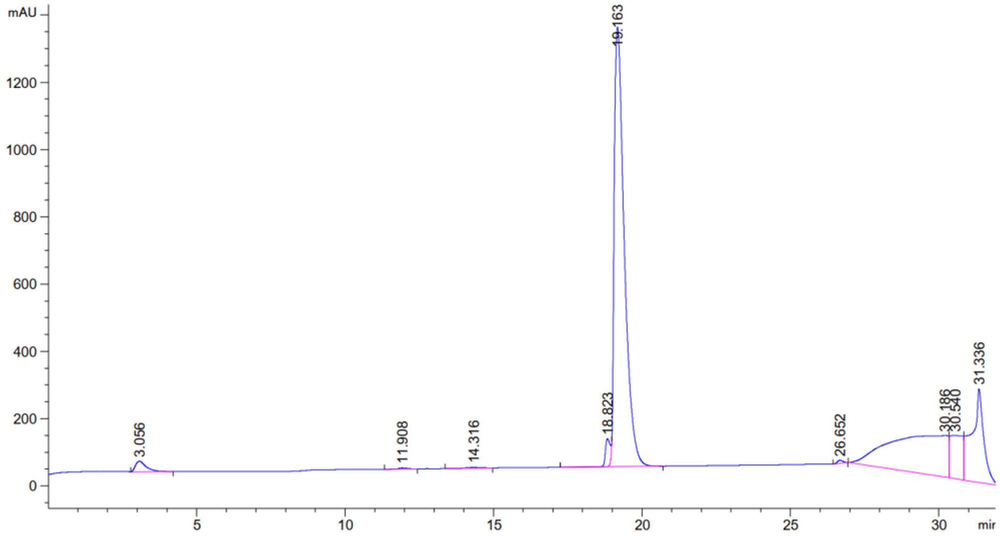

Figure S 115| Analytical RP-HPLC chromatogram of *cyclo*[RADfK(4-pentynoic acid)] **75**, 0 to 40 % eluent B (20 min gradient), 220 nm, t_R = 19.163 min.

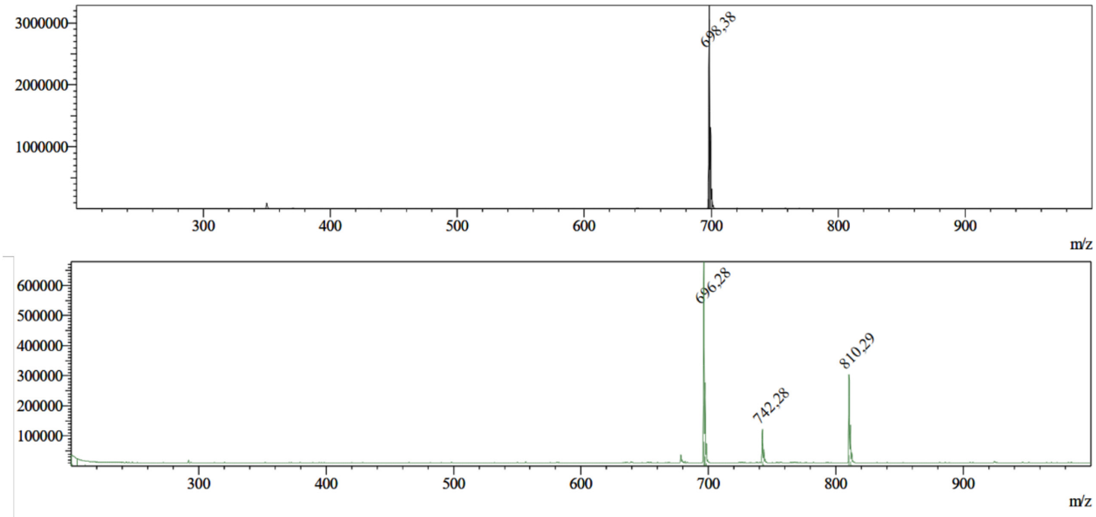

Figure S 116| ESI-MS of *cyclo*[RADfK(4-pentynoic acid)] **75**, with positive mode (top) and negative mode (bottom). Calc. for $C_{33}H_{47}N_9O_8$: m/z: $[M+H]^+$ = 698.36 (obs. 698.38), $[M-H]^-$ = 696.28 (obs. 682.35).

8.2.64 Analytical Data of Biotin-Cadaverine-Dextran-(RGD)$_{6.3}$ 76

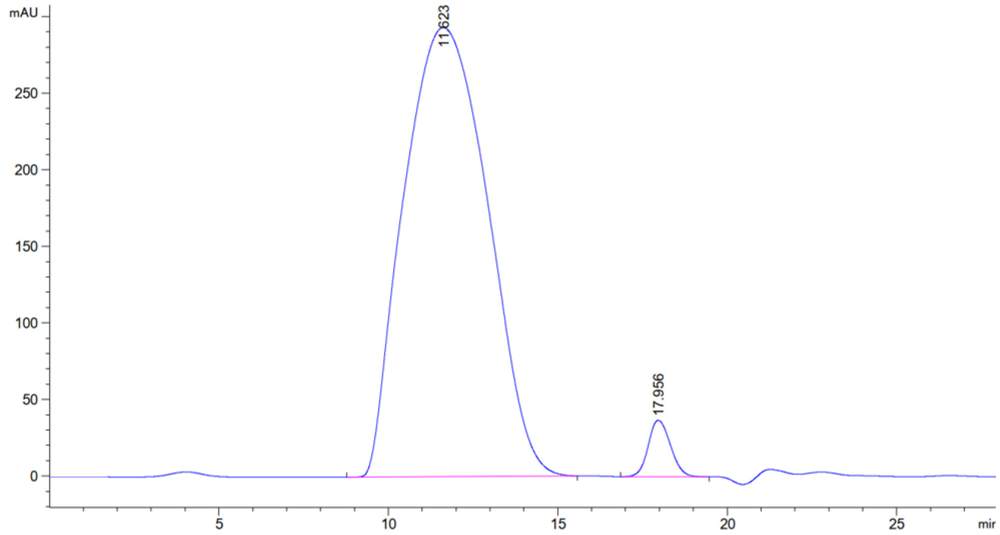

Figure S 117| Analytical SEC-HPLC chromatogram of biotin-cadaverine-dextran-(RGD)$_{6.3}$ **76**, isocratic 30% B (28 min), 220 nm, t_R = 11.623 min.

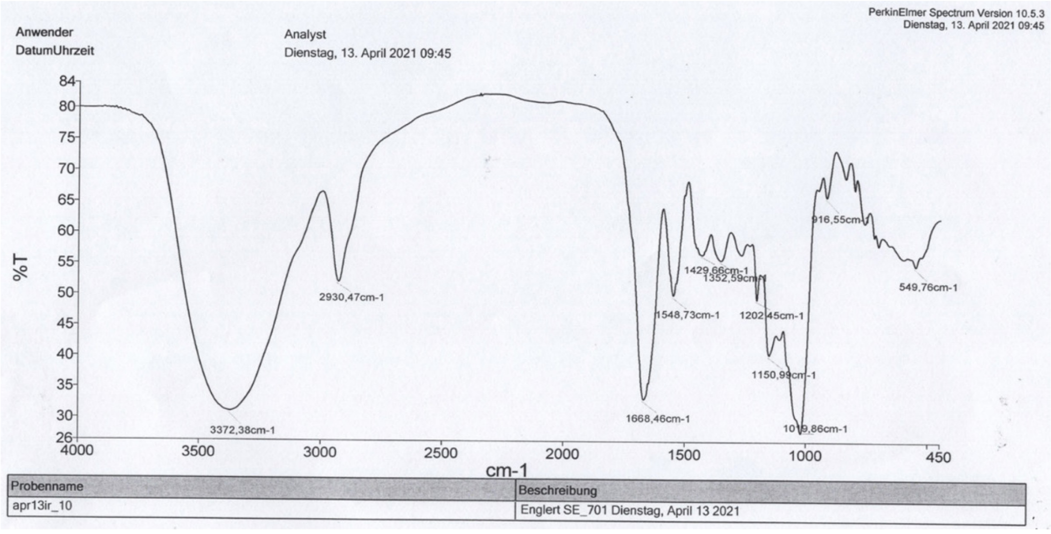
Anwender
DatumUhrzeit

Analyst
Dienstag, 13. April 2021 09:45

PerkinElmer Spectrum Version 10.5.3
Dienstag, 13. April 2021 09:45

Probenname	Beschreibung
apr13ir_10	Englert SE_701 Dienstag, April 13 2021

Figure S 118| IR spectrum (KBr pellet) of biotin-cadaverine-dextran-(RGD)$_{6.3}$ **76**. Compared to the parent dextran **65** (as progenitor of biotin-cadaverine-dextran-(N$_3$)$_{6.3}$ **66**), the azide band at 2113.93 cm^{-1} disappeared.

8.2.65 Analytical Data of Biotin-Cadaverine-Dextran-(RAD)$_{6.3}$ 77

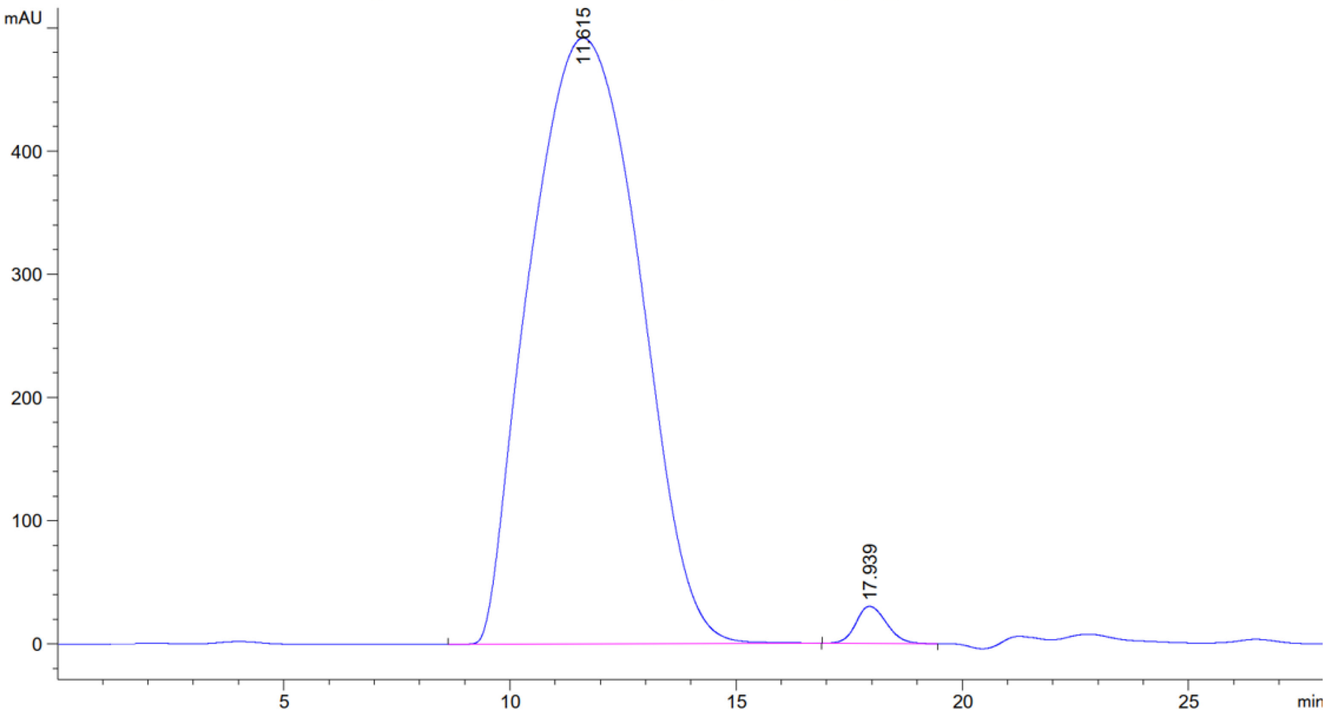

Figure S 119| Analytical SEC-HPLC chromatogram of biotin-cadaverine-dextran-(RAD)$_{6.3}$ **77**, isocratic 30% B (28 min), 220 nm, t_R = 11.615 min.

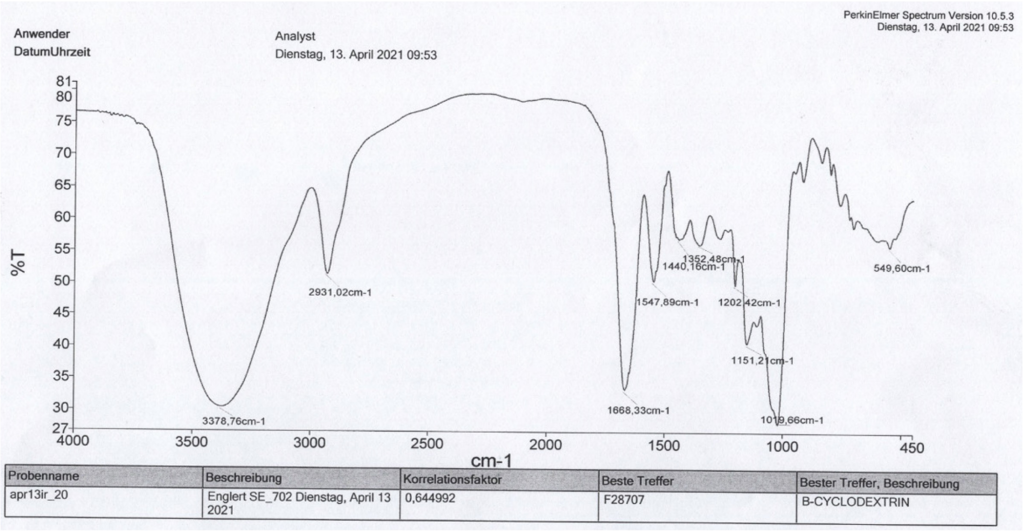

Probenname	Beschreibung	Korrelationsfaktor	Beste Treffer	Bester Treffer, Beschreibung
apr13ir_20	Englert SE_702 Dienstag, April 13 2021	0,644992	F28707	B-CYCLODEXTRIN

Figure S 120| IR spectrum (KBr pellet) of biotin-cadaverine-dextran-(RAD)$_{6.3}$ **77**. Compared to the parent dextran **65** (as progenitor of biotin-cadaverine-dextran-(N$_3$)$_{6.3}$ **66**), the azide band at 2113.93 cm^{-1} disappeared.

8.2.66 Analytical Data of Biotin-Ahx 78

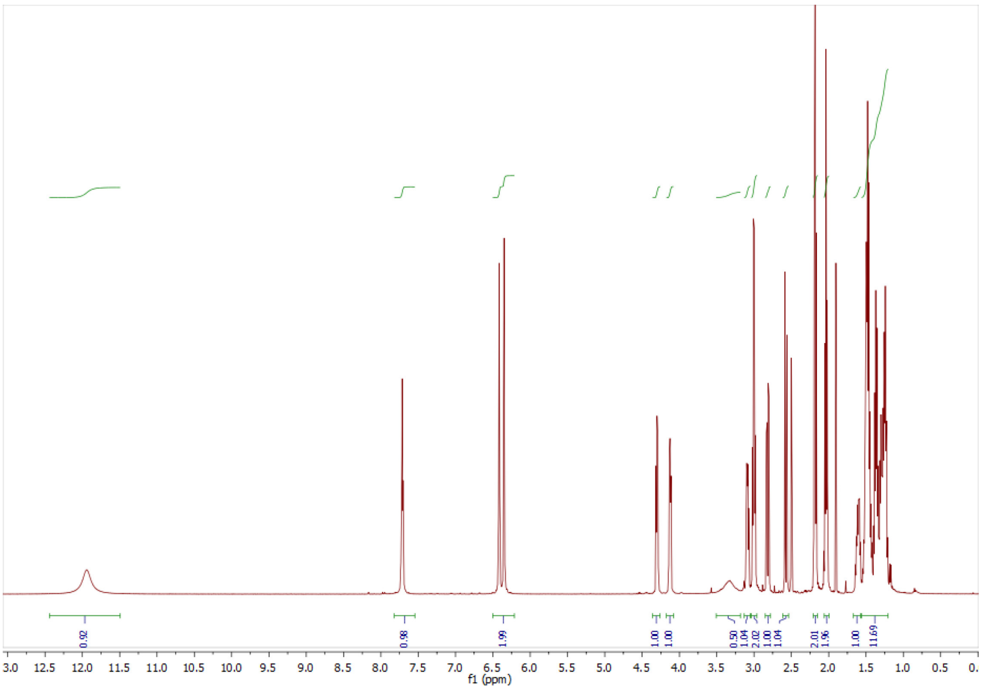

Figure S 121| ^{1}H NMR of biotin-Ahx **78** (500 MHz, DMSO-d$_6$).

8.2.67 Analytical Data of Biotin-Ahx-NHS 79

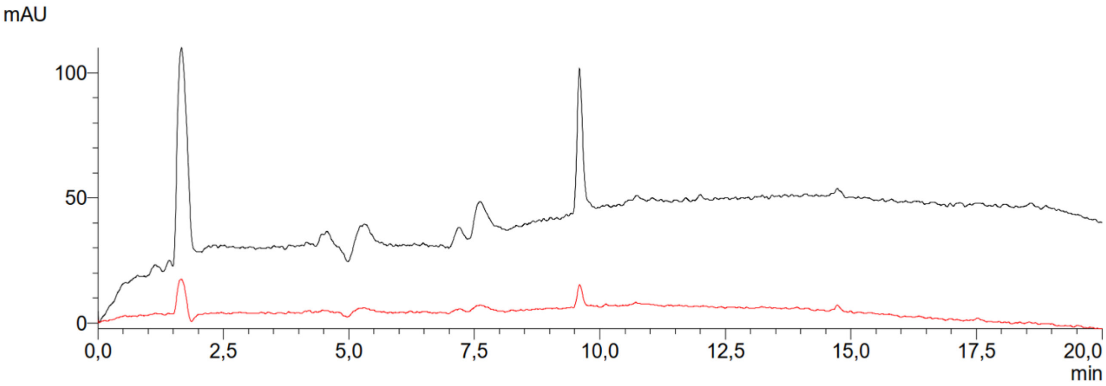

Figure S 122| Analytical RP-HPLC (ESI-MS device) chromatogram of biotin-Ahx-NHS **79**, 30 to 100 % eluent B (13.5 min gradient), 220 nm (black), 280 nm (red), t_R = 9.625 min.

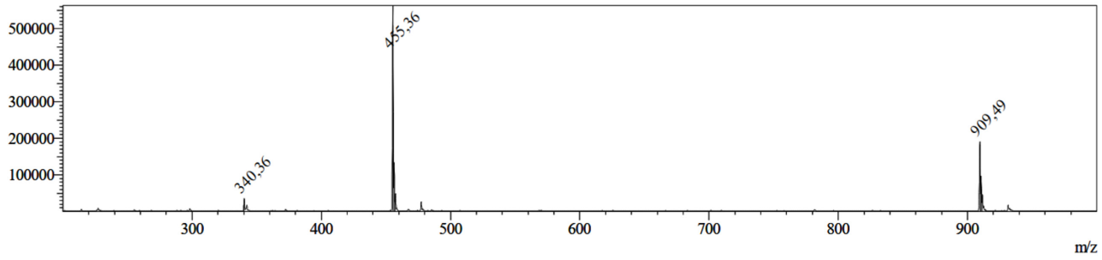

Figure S 123| ESI-MS of biotin-Ahx-NHS **79**. Calc. for $C_{20}H_{30}N_4O_6S$: m/z: $[M+H]^+$ = 455.19 (obs. 455.36), $[2M+H]^+$ = 909.36 (obs. 909.49).

8.2.68 Analytical Data of *Cyclo*[RGDfK(Ahx-Biotin)] 80

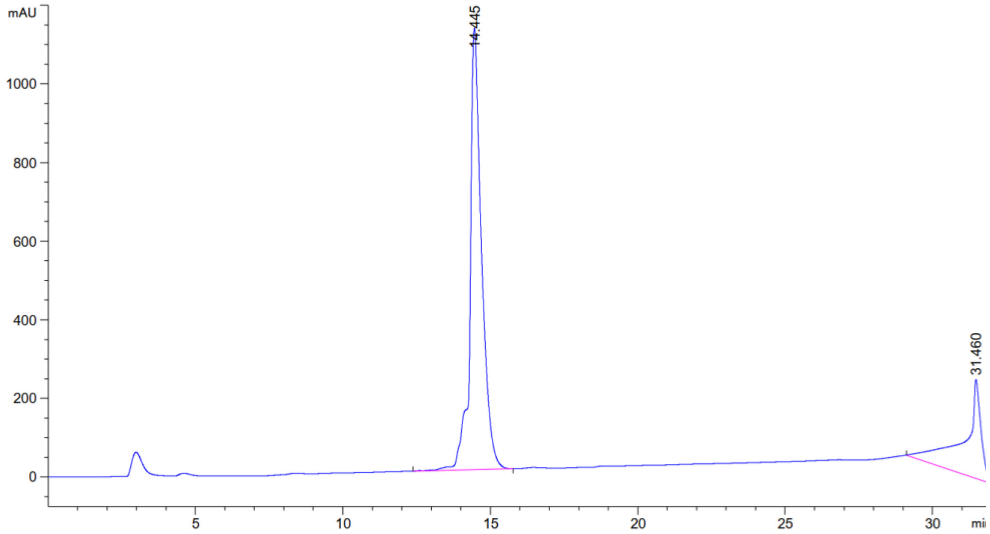

Figure S 124| Analytical RP-HPLC chromatogram of *cyclo*[RGDfK(Ahx-biotin)] **80**, 10 to 60 % eluent B (20 min gradient), 220 nm, t_R = 14.445 min.

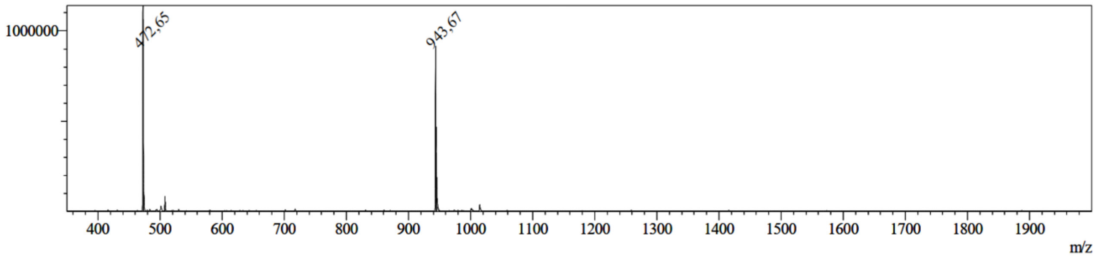

Figure S 125| ESI-MS of *cyclo*[RGDfK(Ahx-biotin)] **80**. Calc. for $C_{43}H_{66}N_{12}O_{10}S$: m/z: $[M+H]^+$ = 943.48 (obs. 943.67), $[M+2H]^{2+}$ = 472.24 (obs. 472.65).

8.2.69 Analytical Data of *Cyclo*[RADfK(Ahx-Biotin)] 81

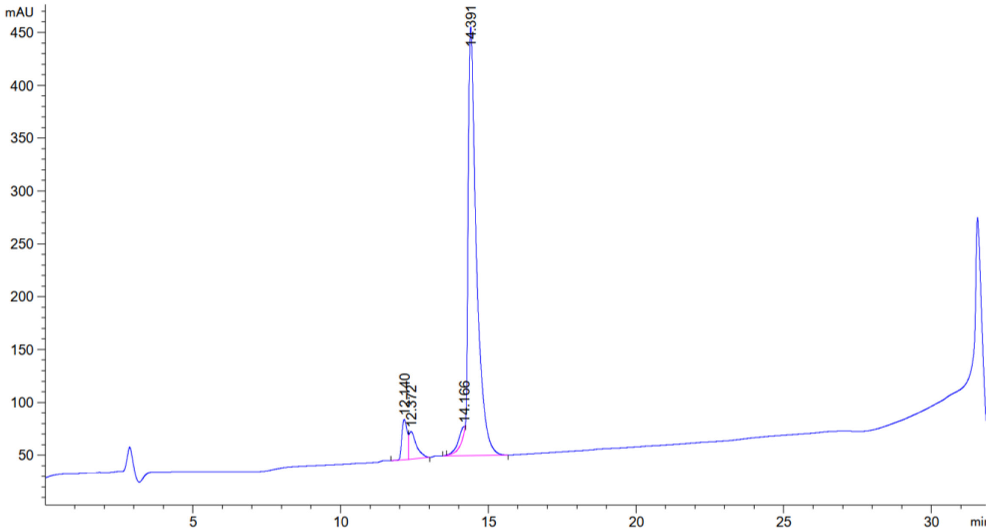

Figure S 126| Analytical RP-HPLC chromatogram of *cyclo*[RADfK(Ahx-biotin)] **81**, 10 to 60 % eluent B (20 min gradient), 220 nm, t_R = 14.391 min.

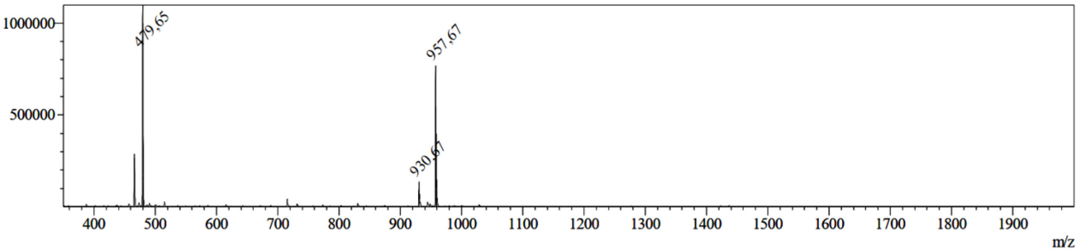

Figure S 127| ESI-MS of *cyclo*[RADfK(Ahx-biotin)] **81**. Calc. for $C_{43}H_{66}N_{12}O_{10}S$: m/z: $[M+H]^+$ = 957.50 (obs. 957.67), $[M+2H]^{2+}$ = 479.25 (obs. 479.65).

8.3 Abbreviations

2-CTC	2-chlorotrityl chloride
7-AAD	7-aminoactinomycin D
ACN	acetonitrile
ADC	antibody-drug conjugate
Ahx	6-aminohexanoic acid
ATP	adenosin triphosphate
ATR	attenuated total reflection
Bak	Bcl-2 homologous antagonist/killer
Bax	Bcl-2 associated X-protein
BCN	bicyclo[6.1.0]nonyne
Bhoc	benzhydryloxycarbonyl
Bid	BH3-interacting domain death agonist
Boc	*tert*-butyloxycarbonyl
BODIPY	boron-dipyrromethene
BTTAA	2-(4-((bis((1-(tert-butyl)-1H-1,2,3-triazol-4-yl)methyl)amino)methyl)-1H-1,2,3-triazol-1-yl)acetic acid
CDI	1,1´-carbonyldiimidazole
CE	carboxyethyl
c-FLIP	cellular FLICE-like inhibitory protein
CLSM	confocal laser scanning microscopy
CML	chronic myeloid leukemia
COC	cyclic oligochalcogenide
COSS	cube-octameric silsesquioxane
COVID-19	corona virus disease-19
CPP	cell-penetrating peptide
CPS	cell-penetrating polydisulfide
CuAAC	copper(I)-catalyzed azide-alkyne cycloaddition
DCC	*N,N´*-dicyclohexylcarbodiimide
DCM	dichloromethane
DcR1 / DcR2	decoy receptor 1 / decoy receptor 2
DD	death domain
Dde	*N*-[1-(4,4-dimethyl-2,6-dioxocyclohex-1-ylidene)ethyl]
DED	death effector domain
DEE	diethyl ether
DIC	*N,N*-diisopropylcarbodiimide
DIPEA	*N,N*-diisopropylethylamine
DISC	death-inducing signaling complex
DiSeL	diselenolipoic acid
DMEM	Dulbecco´s modified Eagle´s medium
DMF	*N,N*-dimethylformamide
DMSO	dimethylsulfoxide
DNA	deoxyribonucleic acid

DOTA	2,2′,2′′,2′′′-(1,4,7,10-Tetraazacyclododecane-1,4,7,10-tetrayl)tetraacetic acid
DPR	dye-to-protein ratio
DR4 / DR5	death receptor 4 / death receptor 5
DR5TP	DR5 targeting peptide
E. coli	*Escherichia coli*
EA	ethyl acetate
EC	extracellular
EC_{50}	effective concentration 50
ECM	extracellular matrix
EDC	1-ethyl-3-(3-dimethylaminopropyl)carbodiimide
EEDQ	*N*-ethoxycarbonyl-2-ethoxy-1,2-dihydroquinoline
EGF	epidermal growth factor
eGFP	enhanced green fluorescent protein
ELISA	enzyme-linked immunosorbent assay
ELSD	evaporative light scattering detector
ESI	electrospray ionization
ETP	epidithiodiketopiperazine
FACS	fluorescence-activated cell sorting
FADD	Fas-associated with death domain
FBS	fetal bovine serum
Fc	fragment crystallizable
FcB	Fc region binding peptide
FDA	Food and Drug Administration
FISH	fluorescence *in situ* hybridization
Fmoc	fluorenylmethoxycarbonyl
GFP	green fluorescent protein
GPCR	G protein-coupled receptor
GTP	guanosine triphosphate
GuCOSS	guanidinylated COSS
HA	hemagglutinin
HATU	1-[bis(dimethylamino)methylene]-1H-1,2,3-triazolo[4,5-b]pyridinium 3-oxide hexafluorophosphate
HBTU	3-[bis(dimethylamino)methyliumyl]-3*H*-benzotriazol-1-oxide hexafluorophosphate
HCl	hydrochloric acid
HEK	human embryonic kidney
HeLa	Henrietta Lacks
Hex	n-hexane
HIC	hydrophobic interaction chromatography
HIV	human immunodeficiency virus
HPLC	high performance liquid chromatography
HPMA	poly(*N*-(2-hydroxypropyl)methacrylamide)
HR	high resolution
HRP	horse radish peroxidase
IC	intracellular

Ig	immunoglobulin
IgG	immunoglobulin G
IgM	immunoglobulin M
IR	infrared
L.m.	*Leuconostoc mesenteroides*
LAP	lipoic acid acceptor peptide
LC_{50}	lethal concentration 50
LNA	locked nucleic acid
LplA	lipoic acid protein ligase
MD	molecular dynamics
MEM	minimum essential medium
MIDAS	metal-ion dependent adhesion site
MMAE	monomethylauristatin E
MS	mass spectrometry
mTG	microbial transglutaminase
MTS	3-(4,5-dimethylthiazol-2-yl)-5-(3-carboxymethoxyphenyl)-2-(4-sulfophenyl)-2H-tetrazolium
NHL	non-Hodgkin´s lymphoma
NHS	*N*-hydroxysuccinimide
NMR	nuclear magnetic resonance
NSAID	non-steroidal anti-inflammatory drug
NSCLC	non-small cell lung cancer
O_2Oc	8-amino-3,6-dioxaoctanoic acid
oN	over night
PAB	*p*-aminobenzyl alcohol
PAGE	polyacrylamide gel electrophoresis
PAMAM	polyamidoamine
PBS	phosphate-buffered saline
PDB	Protein Data Bank
PDC	peptide-drug conjugate
pen/strep	penicillin/streptomycin
PET	positron emission tomography
PFA	paraformaldehyde
pI	isoelectric point
PLGA	poly-(DL-lactide-co-glycolide)
PMO	phosphordiamidate morpholino oligonucleotide
PNA	peptide nucleic acid
POPC	palmitoyloleoylphosphatidylcholine
POSS	polyhedral oligomeric silsesquioxane
Pra	propargylglycine
PRIT	pretargeted radioimmunotherapy
PROTAC	proteolysis targeting chimera
PSI	plexins, semaphorins and integrins
PSMA	prostate-specific membrane antigen
PyBOP	(benzotriazol-1-yloxy)tripyrrolidinophosphonium hexafluorophosphate

QTOF	quadrupole time-of-flight
RAFT	regioselectively addressable functionalized template
RAM	Rink amide
RISC	RNA-induced silencing complex
RNA	ribonucleic acid
RP	reverse phase
RPMI	Roswell Park Memorial Institute
RT	room temperature
RTK	receptor tyrosine kinase
Sav	streptavidin
SDS	sodium dodecyl sulfate
SEC	size-exclusion chromatography
siRNA	small interfering ribonucleic acid
SOD	superoxide dismutase
SPAAC	strain-promoted azide-alkyne cycloaddition
SPPS	solid-phase peptide synthesis
TAMRA	5(6)-carboxy-tetramethylrhodamine
TAT	transactivator of transcription
tBid	truncated Bid
TES	triethyl silane
TFA	trifluoroacetic acid
THF	tetrahydrofuran
TLC	thin layer chromatography
TNF	tumor necrosis factor
TRAIL	TNF-related apoptosis inducing ligand
Tris	tris(hydroxymethyl)aminomethane
Trt	trityl

8.3.1 List of Figures

8.3.2 List of Schemes

8.3.3 List of Tables

8.4 Danksagung

An dieser Stelle möchte ich mich bei allen Personen herzlich bedanken, die mich während der Zeit meiner Promotion begleitet und unterstützt haben.

Folgenden Personen möchte ich meinen aufrichtigen Dank aussprechen:

In erster Linie möchte ich **Prof. Dr. Harald Kolmar** als meinem Doktorvater für die Möglichkeit danken, diese spannenden und interessanten Themen in seiner Arbeitsgruppe zu bearbeiten und die Arbeit zu verfassen. Danke für das stets entgegengesetzte Vertrauen und die ständige Unterstützung schon seit meiner Bachelorarbeit! Auch zu oft später Stunde hattest Du immer Antworten und Tipps bei auftretenden Problemen parat. Dank deiner wissenschaftlichen Expertise und als schier unerschöpfliche Quelle kreativer Ideen konnten so einige unerwartete Hürden im Laufe der Zeit genommen werden. Dabei hast Du uns Doktoranden immer Freiraum gelassen, unsere eigenen Ideen zu entwickeln und umzusetzen. Die Zeit in deiner Arbeitsgruppe und nicht zuletzt natürlich auch die KWT-Aufenhalte habe ich sehr genossen, vielen Dank dafür!

Bei **Prof. Dr. Katja Schmitz** möchte ich mich herzlich für die Übernahme des Korreferats bedanken. Desweiteren danke ich **Prof. Dr. Nico Bruns** und **PD Dr. Tobias Meckel** für die kurzfristige Übernahme der Rolle als Fachprüfer für meine Prüfung. Ich danke Dr. Tobias Meckel zudem für die Messungen am Konfokalmikroskop. Bei **Prof. Dr. Christina Thiele** möchte ich mich für die schnelle Zusage als Vorsitzende meiner Disputation bedanken.

Hiermit möchte ich mich auch bei meinen Co-Autoren für ihre gute Zusammenarbeit bedanken: **Dr. Hendrik Schneider**, **Dr. Bastian Becker**, **Dr. Arturo Macarrón Palacios**, **Dr. Desislava Yanakieva**, **Dr. Ataurehman Ali**, **Sarah Hofmann**, **Carolin Dombrowsky**, **Jorge Lerma Romero**, **Dr. Adrian Elter**, **Sebastian Bitsch**, **PD Dr. Tobias Meckel** und **Dr. Olga Avrutina**.

Bei **Dr. Olga Avrutina** möchte ich mich weiterhin für ihre stetige Unterstützung danken, sei es für das Lektorat meiner verfassten Texte oder im Laboralltag, vor allem bei der Peptidsynthese. Dank dir konnten so einige schwierige Peptidsequenzen gemeistert werden!

Ein großer Dank auch an meine (ehemaligen) Kollegen bei Sulfotools, **Dr. Sascha Knauer**, **Dr. Christina Uth** und **Dr. Niklas Koch**. Dank euch konnte ich so einiges auf dem Gebiet der Synthesechemie und Peptidsynthese dazu lernen. Besonderer Dank gilt **Sascha** noch als Betreuer meiner Masterarbeit und für die Hilfe beim Massenspektrometer und den HPLCs.

Ganz besonders möchte ich mich bei **Dr. Hendrik „Aal" Schneider** und **Dr. Ataurehman „Ata" Ali** bedanken. Egal ob beim Wandern und Skifahren in den Alpen, im Fitnessstudio, in der Krone oder auf der Terasse; man konnte sich immer auf euch verlassen. Riesendank dafür! Nicht zuletzt auch wegen der sehr überzeugenden Samweis „Sam" Gamdschie Einlage an den Steilhängen Mordors (a.k.a. Kleinwalsertal).

Bei **Dr. Bastian Becker** möchte ich mich sehr für die entspannte Arbeitsatmosphäre und Zusammenarbeit im Labor bedanken, die ja dann auch mit einer gemeinsamen Publikation veredelt wurde. Als Chemiker-Gang mit **Dr. Hendrik Schneider** konnten die zahlreichen Laborgeräte instand und eine Vielzahl an Praktika betreut werden. Das Kaffeetrinken in der Kuhle war eine nette Abwechslung zu den unzähligen Filterkaffees im Arbeitskreis!

Vielen Dank auch an **Dr. Adrian „Adi" Elter**, **Dr. Julius „Jules" Grzeschik** und **Steffen „C." Hinz** für die gelegentlichen abendlichen Hopfenkaltschalen auf der Terrasse und die ständigen Kaffeeheißschalen während der Arbeit. Dank der interessanten Gespräche und Diskussionen konnte ich so einiges auf dem Gebiet der Biologie dazulernen.
Besonders möchte ich mich bei **Adi** noch für die Zeit während des Studiums bedanken und natürlich auch während der „Woog-Ghetto" Ära. Es betrübt mich leider immer noch zutiefst dass du die magische Zutat bei Nudeln mit Ei weglässt :(
Vielen Dank **Jules** für deine unermütliche Motivation, mir das Skifahren beizubringen. Ich werde nie das erste Jahr KWT vergessen als ich zusammen mit **Steffen** im stilsicheren Pflug die blaue Piste am Ifen zerschrubbt habe. Desweiteren hat deine abwechslungsreiche musikalische Untermalung den Laboralltag erleichtert und meinen musikalischen Horizont erweitert!
Bei **Steffen** möchte ich mich sehr herzlich für die Planung der zahlreichen Skiurlaube bedanken und dafür, dass dank seiner Versiertheit auf dem Gebiet der *Aves*, insbesondere der *Corvus corone*, unsere geliebte Terrasse nahezu *Columba livia*-frei war. Bitte korrigiere mich, falls mir ein Fehler bei der Benennung unterlaufen ist.

Natürlich darf auch die Urlaubsgruppe um **Dr. Arturo „Arturito" Macarrón Palacios**, **Dr. Ata Ali, Dr. Steffen Hinz**, **Dominic „Ps-Ps-Ps" Happel**, **Jorge Lerma Romero**, **Jordi Pfeiffer Serrahima** und **Sebastian Bitsch** nicht fehlen. Egal ob bei meterhohen Wellen auf Kreta, gefährlichen Steilhängen in den Bergen der Schweiz oder streikendem Getriebe im Feierabendverkehr in Barcelona, die Reisen waren unvergesslich!
An **Arturo** noch ein Dankeschön dass wir so häufig in Golle am Wochenende mit Dartspielen und Lagerfeuer chillen konnten.

Desweiteren möchte ich mich bei folgenden Personen für die schöne Arbeitsatmosphäre im Labor, zahlreichen Ausflügen und netten Gesprächen auf der Terrasse bedanken: **Jan Habermann**, **Dr. Desislava Yanakieva**, **Dr. Andreas Christmann**, **Peter Bitsch**, **Dr. Valentina Liebich**, **Sarah Hofmann**, **Dr. Thomas Pirzer**, **Ingo Bork**, **Dr. Aileen Ebenig**, **Dr. Anja Hofmann** und allen ehemaligen und derzeitigen Mitgliedern des Arbeitskreises. Vielen Dank auch an die Mitglieder der Ferring Gruppe: **Dr. Lukas Deweid**, **Dr. David Fiebig**, **Dr. Stefania Carrara**, **Dr. Jan Bogen** und **Dr. Benjamin Mattes**.

An dieser Stelle auch ein Dankeschön an **Barbara Diestelmann**, **Dana Schmidt** und **Cecilia Gorus**, die unermüdlich und mit steter Hilfsbereitschaft den Laden am Laufen halten und uns Doktoranden die Arbeit sehr erleichtert haben.

Zu guter Letzt gilt mein größter Dank meiner Familie, die mich auf meiner langen akademischen Reise begleitet und stets bedingungslos mit Rückhalt und Zuspruch unterstützt haben. Ohne euch wäre das nicht möglich gewesen!

8.5 Erklärungen

Erklärungen laut Promotionsordnung

§8 Abs. 1 lit. c der Promotionsordnung der TU Darmstadt

Ich versichere hiermit, dass die elektronsiche Version meiner Dissertation mit der schriftlichen Version übereinstimmt und für die Durchführung des Promotionsverfahrens vorliegt.

§8 Abs. 1 lit. d der Promotionsordnung der TU Darmstadt

Ich versichere hiermit, dass zu einem vorherigen Zeitpunkt noch keine Promotion versucht wurde und zu keinem früheren Zeitpunkt an einer in- oder ausländischen Hochschule eingereicht wurde. In diesem Fall sind nähere Angaben über Zeitpunkt, Hochschule, Dissertationsthema und Ergebnis dieses Versuchs mitzuteilen.

§9 Abs. 1 der Promotionsordnung der TU Darmstadt

Ich versichere hiermit, dass die vorliegende Dissertation selbstständig und nur unter Verwendung der angegebenen Quellen verfasst wurde.

§9 Abs. 2 der Promotionsordnung der TU Darmstadt

Die Arbeit hat bisher noch nicht zu Prüfungszwecken gedient.

Darmstadt, den ....

____

Simon Peter Englert